2017

Gravitation

Sponsored by

- CNRS (Centre National de la Recherche Scientifique)
- CEA (Commissariat à l'Énergie Atomique et aux Énergies Alternatives)
- GRAM (Gravitation, Références, Astronomie, Métrologie: Action Spécifique du CNRS)
- ESA (European Space Agency)
- FNRS (Fond National de la Recherche Scientifique)
- BSP (Belgian Science Policy)

52nd Rencontres de Moriond
La Thuile, Aosta Valley, Italy - March 25 - April 1, 2017

2017 Gravitation

©Published by ARISF, 2017



All rights reserved. This book, or parts thereof, may not be reproduced in any form or by any means, electronic or mechanical, including photocopying, recording or any information storage and retrieval system now known or to be invented, without written permission from the publisher.

Proceedings of the 52nd RENCONTRES DE MORIOND

Gravitation

La Thuile, Aosta Valley, Italy *March 25-April 01, 2017*

2017

Gravitation

edited by

Étienne Augé

Jacques Dumarchez

and

Jean Trân Thanh Vân

The 52^{nd} Rencontres de Moriond

2017 Gravitation

was organized by

Étienne Augé (LAL, Orsay)
Jacques Dumarchez (LPNHE, Paris)

with the active collaboration of:

- Barry Barish (Caltech, Pasadena)
- Pierre Binétruy (APC, Paris)
- Marie Anne Bizouard (LAL, Orsay)
- Luc Blanchet (IAP, Paris)
- Fabien Cavalier (LAL, Orsay)
- Pacôme Delva (Observatoire de Paris)
- Jean-Marc Le Goff (Irfu-SPP, Saclay)
- Ernst Rasel (IfQO, Hannover)
- Serge Reynaud (LKB, Paris)
- Fulvio Ricci (Università La Sapienza, Rome)
- Tim Sumner (Imperial College London)
- Jean-Yves Vinet (Observatoire de Nice)
- Peter Wolf (Observatoire de Paris)

2017 RENCONTRES DE MORIOND

The 52^{nd} Rencontres de Moriond were held in La Thuile, Valle d'Aosta, Italy.

The first meeting took place at Moriond in the French Alps in 1966. There, experimental as well as theoretical physicists not only shared their scientific preoccupations, but also the household chores. The participants in the first meeting were mainly french physicists interested in electromagnetic interactions. In subsequent years, a session on high energy strong interactions was added.

The main purpose of these meetings is to discuss recent developments in contemporary physics and also to promote effective collaboration between experimentalists and theorists in the field of elementary particle physics. By bringing together a relatively small number of participants, the meeting helps develop better human relations as well as more thorough and detailed discussion of the contributions.

Our wish to develop and to experiment with new channels of communication and dialogue, which was the driving force behind the original Moriond meetings, led us to organize a parallel meeting of biologists on Cell Differentiation (1980) and to create the Moriond Astrophysics Meeting (1981). In the same spirit, we started a new series on Condensed Matter physics in January 1994. Meetings between biologists, astrophysicists, condensed matter physicists and high energy physicists are organized to study how the progress in one field can lead to new developments in the others. We trust that these conferences and lively discussions will lead to new analytical methods and new mathematical languages.

The 52^{nd} Rencontres de Moriond in 2017 comprised four physics sessions:

- March 18 - 25: "Electroweak Interactions and Unified Theories"
- March 18 - 25: "Very High Energy Phenomena in the Universe"
- March 25 - April 01: "QCD and High Energy Hadronic Interactions"
- March 25 - April 01: "Gravitation"

We thank the organizers of the 52^{nd} Rencontres de Moriond:

- A. Abada, E. Armengaud, J. Conrad, P. Fayet, J.-M. Frère, P. Hernandez, L. Iconomidou-Fayard, P. Janot, M. Knecht, J. P. Lees, S. Loucatos, F. Montanet, J. Orloff, A. Pich, S. Pokorski, V. Tisserand, D. Wood for the "Electroweak Interactions and Unified Theories" session,
- F. Cavalier, A. de Angelis, M. de Naurois, J. Dumarchez, Y. Giraud-Héraud, J.-M. Le Goff, G. Sigl for the "Very High Energy Phenomena in the Universe" session,
- E. Augé, E. Berger, S. Bethke, A. Capella, A. Czarnecki, D. Denegri, N. Glover, B. Klima, M. Krawczyk, N. Mahmoudi, L. McLerran, B. Pietrzyk, L. Schoeffel, Chung-I Tan, J. Trân Thanh Vân, U. Wiedemann for the "QCD and High Energy Hadronic Interactions" session,
- B. Barish, P. Binétruy, M. A. Bizouard, L. Blanchet, F. Cavalier, P. Delva, J.-M. Le Goff, E. Rasel, S. Reynaud, F. Ricci, T. Sumner, J.-Y. Vinet, P. Wolf for the "Gravitation" session

and the conference secretariat and technical staff:

V. de Sá-Varanda and C. Bareille, I. Cossin, G. Dreneau, F. Legrand, G. Perrin, S. Vydelingum.

We are also grateful to Giorgio Palmucci, Mimmo De Pisa, Ida Liseno, Francesco Quinto, Luca Mondelli and the Planibel Hotel staff who contributed through their hospitality and cooperation to the well-being of the participants, enabling them to work in a relaxed atmosphere.

The Rencontres were sponsored by the Centre National de la Recherche Scientifique, the Commissariat à l'Energie Atomique (CEA-Irfu), the European Space Agency, the Fonds de la Recherche Scientifique (FRS-FNRS) and the Belgium Science Policy. We would like to express our thanks for their encouraging support.

It is our sincere hope that a fruitful exchange and an efficient collaboration between the physicists and the astrophysicists will arise from these Rencontres as from previous ones.

E. Augé, J. Dumarchez and J. Trân Thanh Vân

Table of Contents

1. Gravitational Waves

Compact binary coalescence searches performed during advanced LIGO's first observational run	Damir Buskulic	3
Searching for the Stochastic Gravitational-Wave Background with Advanced LIGO and Advanced Virgo	Nelson Christensen	11
Black holes binaries from globular clusters as sources of gravitational waves	Dorota Gondek-Rosinska	21
Advanced Virgo commissioning challenges	Julia Casanueva Diaz	27
All sky search for long duration gravitational-wave transients	Valentin Frey	31
Gravitational wave signals from multi-dimensional Core-collapse Supernova explosion simulations	Eirik Endeve	37
Electromagnetic follow-up of gravitational wave transients: first results and perspectives	Barbara Patricelli	43
Status of the continuos gravitational wave searches in the advanced detector ERA	Michal Bejger	51
Multi-band gravitational wave astronomy: science with joint space- and ground-based observations of black hole binaries	Alberto Sesana	59
Detecting additional polarization modes with LISA	Lionel Philippoz	69

2. Tests of the Equivalence Principle

Progress on testing Lorentz symmetry with MICROSCOPE	Hélène Pihan-Le Bars	75
Antimatter and Gravitation	Pascal Debu	79
AEgIS experiment: status & outlook	Pierre Lansonneur	87
Constraints on Lorentz symmetry violations with Lunar Laser Ranging	Adrien Bourgoin	93
PETER: a double torsion pendulum to test quasi free-fall on two degrees of freedom	Luciano Di Fiore	97
Universality of free fall versus ephemeris	Olivier Minazzoli	101
Studies of general relativity with quantum sensors	Philippe Bouyer	105
The Quantum Sensor Challenge - Designing a System for a Space Mission	Astrid Heske	117

3. Tests of Fundamental Physics

Preparing ESPRESSO's fundamental physics tests	Ana Catarina Leite	123
Gravitational Properties of Light	Dennis Rätzel	127
Prospects for probing fundamental physics with the radio sky	Amanda Weltman	133
Atomic Clock ensemble in space	Luigi Cacciapuoti	139
ACES MWL data analysis center at SYRTE	Frédéric Meynadier	149
Optical clocks and fiber links	Jérôme Lodewyck	153
Test of special relativity using a fibre network of optical clocks	Pacôme Delva	159
Searching for scalar dark matter using six years of LNEe-SYRTE fountain clock comparison data	Aurélien Hees	165
Low-energy tests of Lorentz symmetry: new constraints with nucleons in a cold atom clock	Christine Guerlin	169
The Astrometric Gravitation Probe Concept	Mario Gai	173

4. Tests of Gravity at all ranges

Casimir-Polder shifts on quantum levitation states	Pierre-Philippe Crépin	179
Trapped atom interferometry for the study of Casimir forces and Gravitation at short range	Franck Pereira	185
The Inverse Square Law And Newtonian Dynamics space explorer (ISLAND)	Joël Bergé	191
Perspective to measure forces between macroscopic flat parallel plates	Aniello Grado	199
LARASE: Testing General Relativity with Satellite Laser Ranging	Massimo Bassan	203

5. Theory

Theories of Modified Gravity	Andrew Tolley	209
Cosmic Tsunamis : Wrecking Screening Mechanisms in Modified Gravity	David F. Mota	217
Degenerate Higher-Order Scalar-Tensor (DHOST) theories	David Langlois	221
Stability of Fundamental Couplings and Dark Energy: a pre-ESPRESSO analysis and forecast	Carlos Martins	229
Generalised Proca Theories	Lavinia Heisenberg	233
Testing general relativity from curvature & energy contents at cosmological scale	Ziad Sakr	243
Different ways for graviton mass evaluations	Alexander Zakharov	247
Conservative Dynamics of Binary Systems of Compact Objects at the Fourth Post-Newtonian Order	Guillaume Faye	251
4.5 Post-Newtonian order gravitational radiation	Tanguy Marchand	259
Effective Field theory of post-newtonian gravity including spins	Michele Levi	263
On solving post-Newtonian accurate Kepler Equation	Yannick Boetzel	269
Millisecond Pulsars at the Center of the Galaxy	Walid Majid	275
Neutron stars with realistic equations of state in scalar-tensor theories of gravity	Zahra Motahar	279
Testing the gravitational theory with short-period stars around our galactic center	Aurélien Hees	283
P Probing the hidden gauge symmetry breaking of the early universe and new physics by the phase transition gravitational waves	FaPeng Huang	287

6. Posters

de Sitter-invariant special relativity and the dark energy problem	Adriana Araujo	293
Recent advances in the determination of a high spatial resolution geopotential model using chronometric geodesy	Pacôme Delva	295
Primordial power spectrum and local features	Alexander Gallego Cadavid	297
Integrals of quasi-linear equations of gravitating dark matter at the space thermostat presence: gravitation frequency and scale	Mikhail Ivanov	299
Does a graviton gas act like a cosmological vacuum state and 'cosmological' constant parameter	Andrew Beckwith	301

Authors Index 303

List of participants 311

1.
Gravitational Waves

COMPACT BINARY COALESCENCE SEARCHES PERFORMED DURING ADVANCED LIGO's FIRST OBSERVATIONAL RUN

D. BUSKULIC on behalf of the LIGO and Virgo collaborations
Laboratoire d'Annecy-le-Vieux de Physique des Particules / Université Savoie Mont Blanc, B.P. 110, Annecy-le-Vieux, F-74941 Annecy Cedex, France



We provide in this article an overview of the compact binary coalescence search results in the first observational run -O1- of the LIGO detectors. This includes the direct detection of gravitational wave signals from two binary black hole mergers -GW150914 and GW151226-. We present the properties of the sources and the implications in terms of astrophysics and fundamental physics.

1 Introduction

A century after gravitational waves (GW) were predicted by A. Einstein as part of his theory of general relativity (GR), the Laser Interferometer Gravitational-wave Observatory (LIGO) performed its first observational run (O1) from September 12, 2015 to January 19, 2016. During this run, two signals from a binary black hole merger were detected, the first of which [1], GW150914 was recorded by the two LIGO detectors at Hanford (H1), WA, and Livingston (L1), LA, on September 14, 2015, at 09:50:45 UTC, with a signal-to-noise ratio (SNR) of 23.7 and a significance greater than 5.1σ.

2 Searches for compact binary coalescences

Dedicated searches for compact binary coalescence (CBC) signals rely on accurate models of the expected waveforms to analyze the data with matched filtering. Those searches target signals from binary neutron star, binary black hole or neutron star black-hole systems. The coalescence of compact objects is composed of three phases. In the inspiral phase, the masses orbit around each other, the system emits gravitational waves which in turn cause an increase of the orbital frequency as well as the amplitude of the emitted waves. The inspiral waveform is characterized by the so called "chirp mass" :

$$\mathcal{M} = \frac{(m_1 m_2)^{3/5}}{(m_1 + m_2)^{1/5}} \tag{1}$$

where m_1 and m_2 are the binary component masses, and to the lowest order in post-newtonian expansion can be expressed as

$$\mathcal{M} = \frac{c^3}{G}\left[\frac{5}{96}\pi^{-8/3} f^{-11/3}\dot{f}\right]^{3/5} \tag{2}$$

where f and $\dot{f}$ are the orbital frequency of the system and its first derivative. The second phase of the coalescence is the merger of the two bodies, and one has to rely on numerical relativity computation to calculate the corresponding waveform. Once the two bodies have merged, the horizon of the resulting black hole undergoes a damped perturbation that appears as a ringdown signal in the waveform which can be decomposed in quasi-normal modes.

The calculated waveforms are used as templates in a matched filtering process, which consists in the cross correlation between the output signal of the detectors and the templates, weighted by the inverse of the power spectral density of the detectors. A threshold is put on the resulting time series, giving a set of candidate events or triggers. The parameters that drive the evolution of the waveform can be split in two categories. The intrinsic parameters, which are the masses and spins of the components, drive the system dynamics and the waveform evolution. Since the matched filtering process is very sensitive to the phase evolution of the waveform, one needs to scan the 4D intrinsic parameter space with a very large number of templates, around 250 000 in our case [3] (figure 1). The extrinsic parameters, the initial phase of the signal or

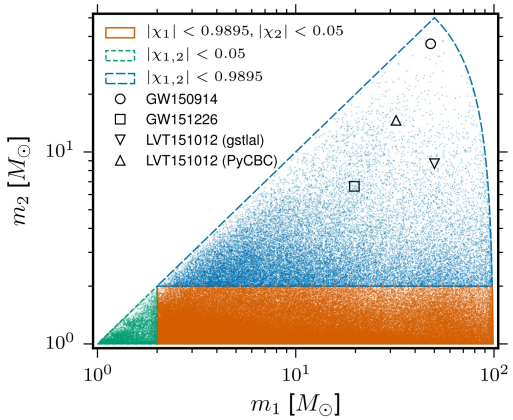


Figure 1 – The four-dimensional search parameter space covered by the template bank shown projected into the component-mass plane, using the convention $m_1 > m_2$. Symbols indicate the best matching templates for GW150914, GW151226, and LVT151012. For GW150914 and GW151226, the templates were the same in the two independent searches named PyCBC and GstLAL, while for LVT151012 they differed. The parameters of the best matching templates are consistent, up to the discreteness of the template bank, with the detector frame mass ranges provided by detailed parameter estimation.

parameters that determine the orientation of the binary, impact the arrival time of the signal and its global amplitude and phase. These parameters can be maximized over without the need for a computationally expensive matched filtering.

The triggers produced by the matched filtering process are subjected to a χ^2 test checking consistency of the signal with the expected waveform and to data quality vetoes excluding times with known perturbations in the instruments or their environments [4]. Coincidences are then identified as surviving triggers in the two detectors matching in time and parameters. Triggers are ranked according to the value of the combined reweighted SNR: $\hat{\rho}_c = \sqrt{\hat{\rho}_{H1}^2 + \hat{\rho}_{L1}^2}$, with $\hat{\rho} = \rho / \left[(1 + (\chi_r^2)^3)/2\right]^{1/6}$ and χ_r the outcome of the consistency test.

3 Observational run 1 and the observed events therein

During the first LIGO-Virgo observational run, two events - GW150914 [1] and GW151226 [5] - were considered of high enough significance to be called detections. The third most significant trigger - LVT151012 - was not significant enough to be a detection but interesting enough to be studied in depth. The reconstructed waveforms from a coherent Bayesian analysis [6] of the three aforementioned triggers is shown on fig. 2

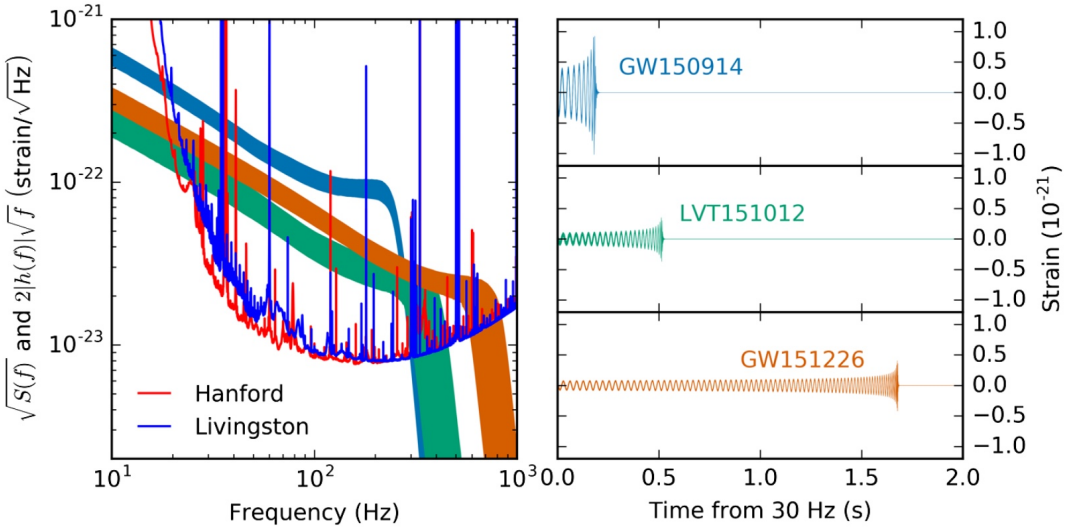


Figure 2 – Left panel: Amplitude spectral density of the total strain noise of the H1 and L1 detectors, $\sqrt{S(f)}$ in units of strain per $\sqrt{\text{Hz}}$, and the recovered signals of GW150914, GW151226, and LVT151012 plotted so that the relative amplitudes can be related to the SNR of the signal. Right panel: Time evolution of the recovered signals from when they enter the detectors sensitive band at 30 Hz. Both figures show the 90% credible regions of the LIGO Hanford signal reconstructions from a coherent Bayesian analysis using a nonprecessing spin waveform model [6].

The detectors physical environment is monitored by an array of sensors : seismometers, accelerometers, microphones, magnetometers, radio receivers, weather sensors, power line monitors and cosmic ray detectors. This array forms about 10^5 data channels for each detector, used to veto transient disturbances. Special attention is paid to the correlated sources of noise like global electromagnetic noise. In the case of the events GW150914 and GW151226, an environmental origin was ruled out because the excess power in the auxiliary channels was too small by a factor $>\sim 17$ to explain the signal. Furthermore, the observed environmental disturbances do not match the morphology of the signal events.

The signal significance is quantitatively assessed based on its false alarm rate (FAR), measured from the background estimated on the data themselves; in the case of GW150914, the analysis is repeated $\sim 10^7$ times on detector streams time-shifted by multiples of 0.1s, whereby accumulating a background time of 608000 years. As shown in fig. 3, GW140914 is louder than all background triggers, therefore bounding its false alarm rate after accounting for trial factors to be $< 6 \times 10^{-7}$ yr^{-1}, corresponding to a significance $> 5.3\sigma$. The figure 3 also shows the

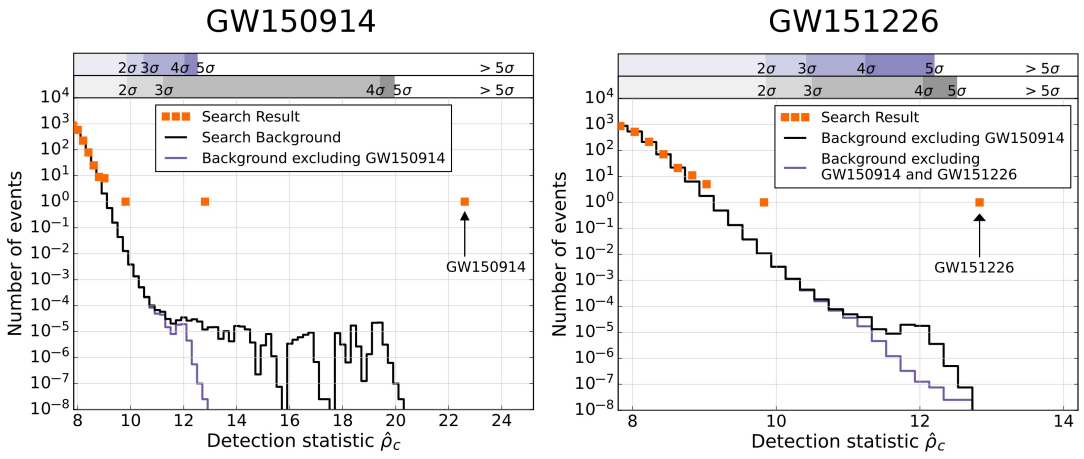


Figure 3 – Search results from one of the data analyses performed on the data. See the text for explanation.

search results from one of the two analyses performed on the data. The left-hand plot shows the result for signals with chirp mass $\mathcal{M} > 1.74\ M_\odot$ (the chirp mass of an $m_1 = m_2 = 2\ M_\odot$ binary). GW150914 is the most significant event in the data, with a combined SNR of $\hat{\rho}_c = 23.7$, and it is more significant than any background event in the data. Individual triggers in the L1 and H1 detectors, forming the event GW150914, have the highest SNR in each detector. As GW150914 is so significant, the high significance background is dominated by its presence in the data. Once it has been identified as a signal, we remove it from the background estimation to evaluate the significance of the remaining events. The right plot shows results with GW150914 removed from both the foreground and background. GW151226 is then identified as the most significant event remaining in the data, with an SNR $\hat{\rho}_c = 13.0$. GW151226 is more significant than the remaining background in this analysis, with a significance of greater than 5.3σ. The third most significant event in the search, LVT151012, is identified with a significance of 1.7σ in one of the performed analyses. The significance obtained for LVT151012 is not greatly affected by including or removing background contributions from GW150914 and GW151226. There is no instrumental or environmental artefact around LVT151210 and the parameter estimation results are consistent with an astrophysical Binary Black Hole source.

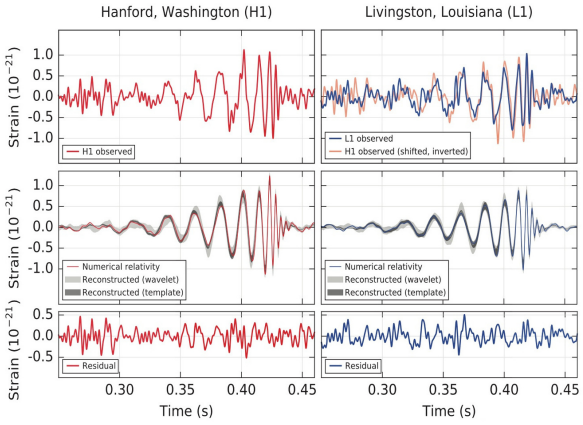


Figure 4 – GW150914 signal observed by the LIGO H1 (left) and L1 (right detectors, filtered with a 35-350 Hz bandpass filter. Top: Strain data. Middle: GW strain projected onto each detector, showing a numerical relativity waveform for a system with parameters consistent with those recovered from GW150914 (solid lines) and 90% credible regions for two independent waveform reconstructions (shaded areas). Bottom: Residuals after subtracting the filtered numerical relativity waveform from the filtered detector time series.

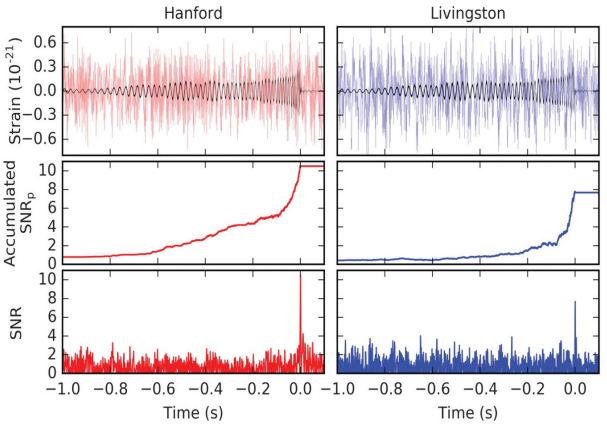


Figure 5 – GW151226 signal observed by the LIGO H1 (left) and L1 (right) detectors, filtered with a 30-600 Hz bandpass filter and band-reject filters to remove strong instrumental spectral lines . Top row: Strain data and best-match template from a nonprecessing spin waveform model reconstructed using a Bayesian analysis [6]. Middle row: Accumulated peak signal-to-noise ratio (SNR_p) when integrating from the start of the best-match template, corresponding to a gravitational-wave frequency of 30 Hz, up to its merger time. Bottom: Signal-to-noise ratio (SNR) time series produced by time shifting the best-match template waveform and computing the integrated SNR at each point in time.

Figures 4 and 5 show the strain time series measured in the H1 and L1 detectors, and compares them to various waveform reconstructions. The waveform reconstructed from the coherent signal in both detectors agrees with the best-fit CBC waveform, with a numerical relativity waveform computed for a system with parameters consistent with those recovered from GW150914, and with the data.

4 Source properties

Eight instrinsic parameters are needed to describe the source (masses and spin vectors) and nine extrinsic parameters: three for the location (luminosity distance, right ascension, declination), two for the orientation (inclination and polarization), two for the time and phase of coalescence

and two for the eccentricity of the orbit. Assuming circular orbits, parameters are estimated from a coherent analysis across the detector network, in a Bayesian framework. Stochastic sampling methods are used to explore the full multidimensional parameter space, computing the likelihood of the data according to the match between the data and the predicted waveform given a set of parameters. Parameter estimation therefore relies on accurate waveform models being available, which has made crucial progress over the past decade. There are now models that combine perturbative theory and numerical relativity and accurately describe all the phases of a BBH coalescence: inspiral, merger, and ringdown, considering aligned spins and an effective spin precession parameter. Still missing are the eccentricity, higher order gravitational modes and full spin generality.

The intrinsic parameters of the binary drive the system dynamics and are therefore encoded in the GW signal. The inspiral phase is driven at leading order by the chirp mass. The mass ratio and spin components parallel to the orbital angular momentum enter at next to leading order, and other spin degrees of freedom at higher orders. In addition, if spins have components in the orbital plane, this leads the latter to precess, causing amplitude and phase modulation of the observed GW signal. The merger and ringdown phases are primarily governed by the mass and spin of the final black hole, which are fully determined by the masses and spins of the binary in GR.

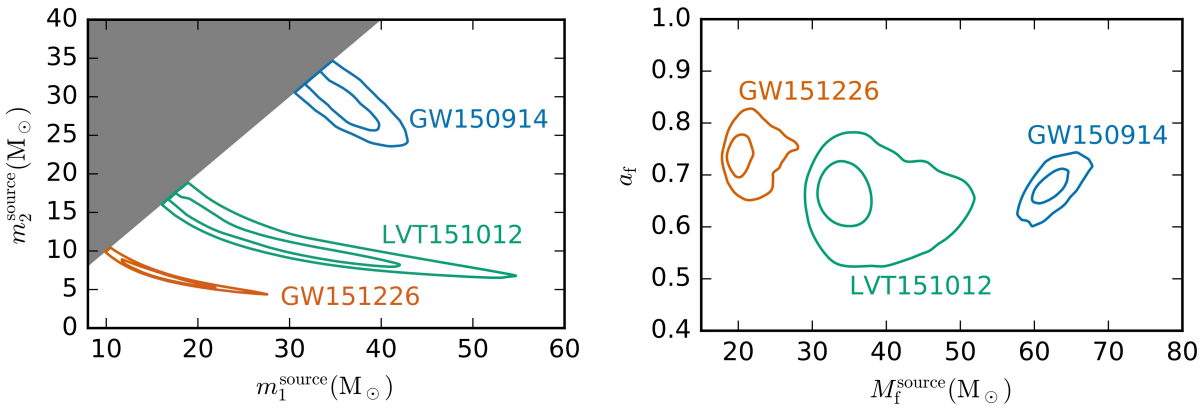


Figure 6 – Posterior probability densities (50% and 90% credible regions contours) of the initial masses, final masses and final spins to the three events GW150914, LVT151012, and GW151226. Left panel: Component masses m_1^{source} and m_2^{source} for the three events. We use the convention that $m_1^{source} \geq m_2^{source}$. Right panel: The mass and dimensionless spin magnitude of the final black holes.

Figure 6 shows the posterior probability density functions (PDF) for the source-frame component masses, mass and spin of the remnant BH of GW150914, GW151226 and LVT151012. The measured values are shown in table 1.

Table 1: Source frame component masses, final BH mass and spin for the three events of interest in the O1 run. The reported values are median values with 90% credible intervals that include statistical errors and systematic errors from averaging the results of different waveform models.

	m_1^{source}	m_2^{source}	M_f^{source}	a_f
GW150914	$36.2^{+5.2}_{-3.8}$ $\mathrm{M}_\odot$	$29.1^{+3.7}_{-4.4}$ $\mathrm{M}_\odot$	$62.3^{+3.7}_{-3.1}$ $\mathrm{M}_\odot$	$0.68^{+0.05}_{-0.06}$
GW151226	$14.2^{+8.3}_{-3.7}$ $\mathrm{M}_\odot$	$7.5^{+2.3}_{-2.3}$ $\mathrm{M}_\odot$	$20.8^{+6.1}_{-1.7}$ $\mathrm{M}_\odot$	$0.74^{+0.06}_{-0.06}$
LVT151012	23^{+18}_{-6} $\mathrm{M}_\odot$	13^{+4}_{-5} $\mathrm{M}_\odot$	35^{+14}_{-4} $\mathrm{M}_\odot$	$0.66^{+0.09}_{-0.10}$

In the case of GW150914, we estimate the system radiated in GW a total energy of $3.0^{+0.5}_{-0.4}\mathrm{M}_\odot c^2$ and reached a peak luminosity of $3.6^{+0.5}_{-0.4} \times 10^{56}$ erg/s, equivalent to $200^{+30}_{-20}\mathrm{M}_\odot c^2/\mathrm{s}$.

The estimation of extrinsic parameters is based both on measurements and statistical guesses.

The amplitude of the observed signal depends on the system intrinsic properties and its distance, as well as some geometrical factors. There is for instance a degeneracy between the distance and the inclination of the system with respect to the line of sight, with distant sources with favorable orientations being more likely. The source luminosity distance is estimated to be, for GW150914, 420^{+150}_{-180} Mpc (redshift $z = 0.09^{+0.03}_{-0.04}$), for GW151226, 440^{+180}_{-190} Mpc (redshift $z = 0.09^{+0.03}_{-0.04}$) and for LVT151210, 1000^{+500}_{-500} Mpc (redshift $z = 0.20^{+0.09}_{-0.09}$). The sky location of the source is inferred primarily from the time delay (of $6.9^{+0.5}_{-0.4}$ ms for GW150914) between the L1 and H1 detectors, as well as amplitude and phase consistency constraints, with sky locations corresponding to good detector response being preferred. The localization currently has limited accuracy, with a two detector network, and forms part of an annulus whose area is about 230 deg^2 for GW150914.

5 Infered rate of binary black hole mergers

Previous estimates of the BBH merger rate based on population modeling are reviewed in [9]. The range of rates given there spans more than three orders of magnitude, from 0.1-300 Gpc^{-3}.yr^{-1}. The inference of astrophysical rates is made by counting the signals in an experiment and estimating the sensitivity to a population of sources, depending on the mass distribution which is hardly known. Fig. 7 (left) shows the posterior probability density of mergers of the type of each observed event, as well as the sum of these. The obtained 90% range of allowed rates is $R \sim 9 - 240$ Gpc^{-3}.yr^{-1}.

Other transient searches and activities inside the Compact Binary Coalescences group lead to upper limits on the binary neutron star (BNS) and neutron star - black hole events from the O1 run [10]. Binary neutron star coalescences with neutron star masses in the range $m_{NS} \in [1, 3]$ M$_\odot$ were searched for and an upper limit on BNS merger rate was found, at 90% confidence, to $r(\text{BNS merger}) < 12600$ Gpc^{-3}.yr^{-1}. NS-BH mergers were also searched for with the same NS mass range and $m_{BH} \in [2, 99]$ M$_\odot$ and the no-detection resulting upper limit was $r(\text{NSBH merger}) < 3600$ Gpc^{-3}.yr^{-1}. An all-sky search for gravitational waves from merging intermediate mass black hole binaries (IMBHBs) was performed [12], leading to a most stringent limit obtained for black holes of individual mass 100 M$_\odot$, with spins aligned with the binary orbital angular momentum. For such systems, the merger rate is constrained to be less than 0.93 Gpc^{-3}.yr^{-1} in comoving units at the 90% confidence level.

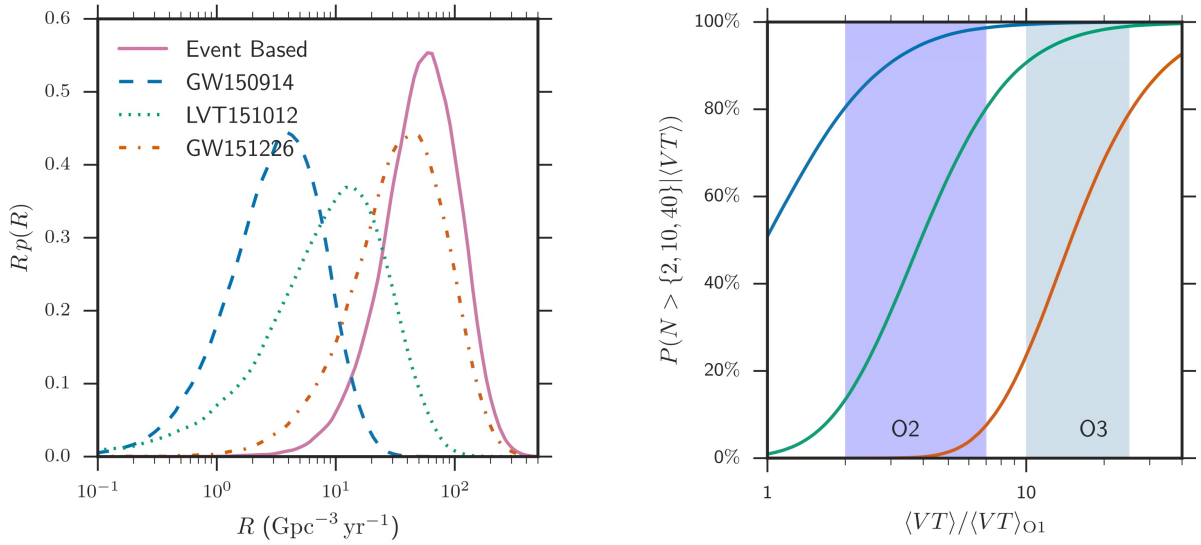


Figure 7 – Left plot: posterior densities on the rate of GW150914-like BBH, LVT151012-like BBH, and GW151226-like BBH mergers. The event-based rate is the sum of these. Right plot: probability of observing $N > 2$, $N > 10$, and $N > 40$ highly significant events, as a function of surveyed space-time volume. The vertical line and bands show, from left to right, the expected sensitive space-time volume for the second (O2) and third (O3) anticipated advanced detector observing runs.

6 Electromagnetic follow-up searches

Preliminary estimates of the time, significance, and sky location of GW150914 were shared with 63 teams of astronomy partners covering radio, optical, near-infrared, X-ray, and gamma-ray wavelengths with ground and space-based facilities. Follow-up observations were reported by 25 teams in the days and weeks that followed [8], covering a fair fraction of the preliminary sky map, as can be seen in fig. 8. As GW150914 turned out to be a binary black hole merger, there is little expectation of a detectable electromagnetic signature. Nevertheless, this first broadband campaign to search for a counterpart of a GW source represents a milestone and highlights the broad capabilities of the transient astronomy community.

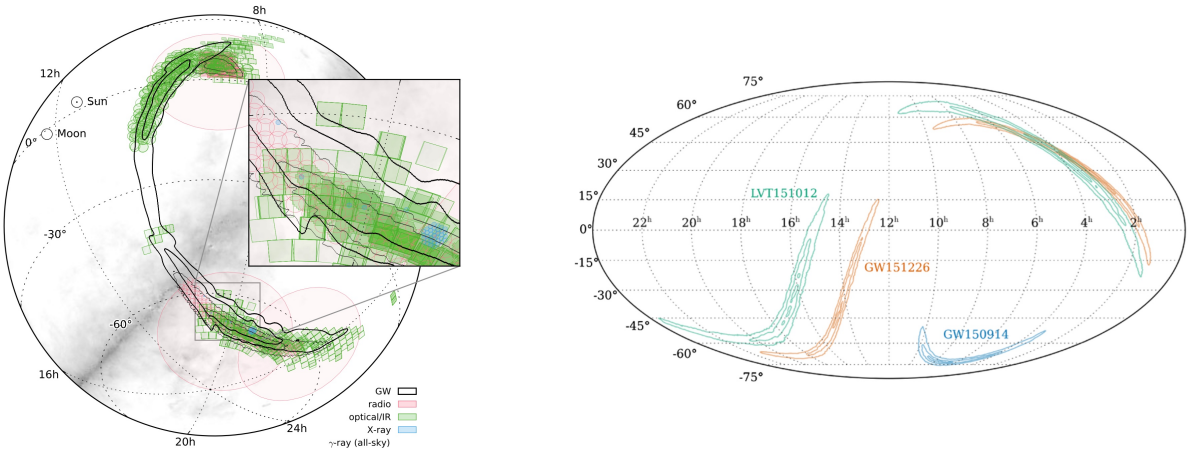


Figure 8 – Footprints of electromagnetic observations in comparison with the 50% and 90% credible levels of the initially distributed GW localization maps for GW150914.

We can use the inferred rates to estimate the number of BBH mergers expected in future observing runs [11]. The expected number of observed events scales linearly with the sensitive space-time volume $\langle VT \rangle$ of a future search. We use a fiducial BBH system with total mass $60M_{\odot}$ and mass ratio $q = 1$, to estimate a range of sensitive space-time volumes for future observing runs. The second observing run (O2) has begun in december 2016 and will last six months, and the third run (O3) is set to start in 2018 and last nine months. The right plot of fig. 7 shows the predictions for the probability of obtaining N or more high-significance events as a function of $\langle VT \rangle$ (in units of the space-time volume surveyed during O1).

7 Testing consistency with general relativity

The recorded events allow for tests of GR in the strong field, non linear, high velocity regime ($v/c \sim 0.5$). Their relatively large SNR allows to perform some coarse consistency tests with the predictions of GR [2]. It was checked that the residuals after subtraction of the best-fit waveform are consistent with instrumental noise, and that early and late parts of the observed waveforms are consistent with each other in the context of GR. By using waveform models that allow for parameterized GR violations during the inspiral and merger phases, quantitative tests were performed on the GW phase in the dynamical regime and the first empirical bounds were placed on several high-order post-Newtonian coefficients (see fig. 9). Furthermore, assuming a modified dispersion relation for gravitational waves, constraints were put on the Compton wavelength of the graviton to be $\lambda_g > 10^{13}$ km, which could be interpreted as a bound on the graviton mass $m_g < 1.2 \times 10^{22} \mathrm{eV/c^2}$.

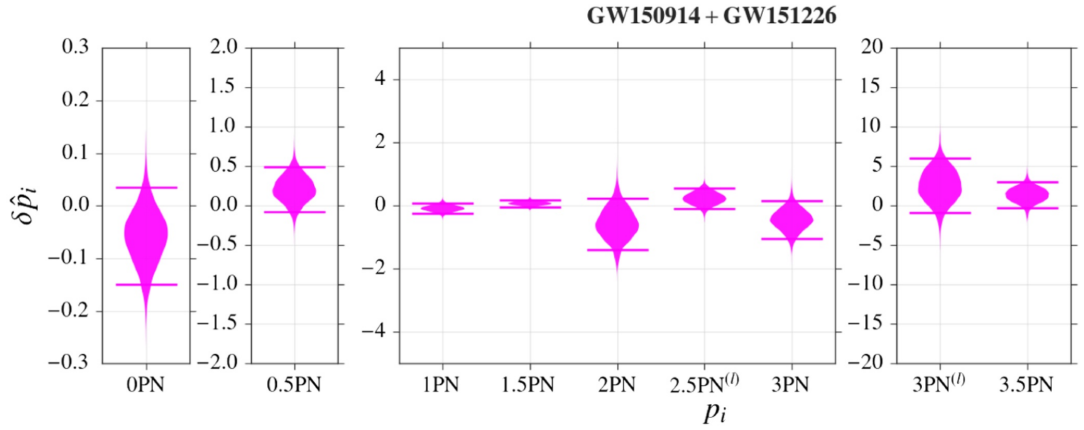


Figure 9 – Posterior PDFs of parameters caracterizing deviations from GR in the observed signals recorded during the O1 run. Each $\delta\hat{p}$ parameter represents the deviation from the $\hat{p}$ parameter at each order in the post-Newtonian expansion of the considered waveforms.

8 Some astrophysics implications

The detection and properties of the GW150914 and GW151226 demonstrate that relatively heavy stellar mass black holes (> 25 $M_\odot$) exist in nature, which implies the progenitor was formed in a low metallicity environment, to allow for weak massive-star winds [2]. Also demonstrated is the fact that binary black holes can form, although the events do not currently allow to identify the formation path, from an isolated binary or through dynamical capture in a dense stellar cluster.

9 Outlook

The first observational run of LIGO led to the detection of two strong events, GW150914 and GW151226, which were both interpreted as the coalescence of two black holes. Efforts are underway to enhance significantly the global gravitational wave detector network, both in terms of sensitivity and number of detectors, with Advanced Virgo expected to join Advanced LIGO soon. The future observing runs will lead to detecting further signals, with improved position reconstruction and parameter estimation of the sources, thus yielding a wealth of astrophysics and fundamental physics insights.

References

1. LIGO Scientific Collaboration, Virgo Collaboration (Abbott B. P. *et al.*), *Phys. Rev. Lett.* **116**, 061102 (2016)
2. LIGO Scientific Collaboration, Virgo Collaboration (Abbott B. P. *et al.*), *Phys. Rev.* X **6**, 041015 (2016)
3. LIGO Scientific Collaboration, Virgo Collaboration (Abbott B. P. *et al.*), PRD **93**, 122003 (2016)
4. S. A. Usman *et al.*, CQG **33**, 21 (2016)
5. LIGO Scientific Collaboration, Virgo Collaboration (Abbott B. P. *et al.*), PRL **116**, 241103 (2016)
6. J. Veitch, V. Raymond, B. Farr, W. Farr, P. Graff, S. Vitale, B. Aylott, K. Blackburn, N. Christensen, M. Coughlin *et al.*, *Phys. Rev.* D **91**, 042003 (2015)
7. D. V. Martynov *et al.*, *Phys. Rev.* D **93**, 112004 (2016)
8. B. P. Abbott *et al.*, *Astrophys. J.* **826**, L13 (2016)
9. J. Abadie, B.P. Abbott *et al. Class. Quantum Grav.* **173001**, 27 (2010)
10. LIGO Scientific Collaboration, Virgo Collaboration (Abbott B. P. *et al.*), *Astrophys. J. Lett.* **832**, L21 (2016)
11. LIGO Scientific Collaboration, Virgo Collaboration (Abbott B. P. *et al.*), *Living Rev. Relativ.* **1**, 19 (2016)
12. LIGO Scientific Collaboration, Virgo Collaboration (Abbott B. P. *et al.*), arXiv:1704.04628 [gr-qc]

Searching for the Stochastic Gravitational-Wave Background with Advanced LIGO and Advanced Virgo

N.L. Christensen
(For the LIGO Scientific Collaboration and the Virgo Collaboration)
Department of Physics, Carleton College, Northfield, Minnesota 55057, USA
ARTEMIS, Université Côte d'Azur, Observatoire Côte d'Azur, CNRS, 06304 Nice, France



The Advanced LIGO detectors have commenced observations with Advanced Virgo joining in the near future. Gravitational waves from the merger of binary black hole systems have been observed. A major goal for LIGO and Virgo will be to detect or set limits on a stochastic background of gravitational waves. A stochastic background of gravitational waves is expected to arise from a superposition of a large number of unresolved cosmological and/or astrophysical sources. A cosmologically produced background would carry unique signatures from the earliest epochs in the evolution of the Universe. Similarly, an astrophysical background would provide information about the astrophysical sources that generated it. The observation of gravitational waves from binary black holes implies that there will be a stochastic background from these sources that could be observed by Advanced LIGO and Advanced Virgo in the near future. The LIGO and Virgo search for a stochastic background should probe interesting regions of the parameter space for numerous astrophysical and cosmological models. Presented here is an outline of LIGO and Virgo's search strategies for a stochastic background of gravitational waves, including the search for gravitational wave polarizations outside of what is predicted from general relativity. Also discussed is how global electromagnetic noise (from the Schumann resonances) could affect this search; possible strategies to monitor and subtract this potential source of correlated noise in a the global detector network are explained. The results from Advanced LIGO's observing run O1 are presented, along with the implications of the gravitational wave detections. The future goals for Advanced LIGO and Advanced Virgo are explained.

1 Introduction

A consequence of Einstein's general theory of relativity are gravitational waves, perturbations to spacetime that travel away from their source at the speed of light. A stochastic gravitational-wave background (SGWB) signal is formed from the superposition of many events or processes that are too weak and too numerous to be resolved individually, and which combine to produce a SGWB. Cosmological sources, such as inflation, pre-Big Bang models, or cosmic strings, could create a SGWB. Astrophysical sources can also create a SGWB; this background could be produced over the history of the Universe from compact binary coalescences, supernovae, and

neutron stars. In fact, the recent observations by Advanced LIGO of gravitational waves from binary black hole mergers [1,2,3] implies that a SGWB will be created from these events happening throughout the history of the universe and it may be detectable by Advanced LIGO [4] and Advanced Virgo [5] in the coming years [6]. As Advanced LIGO and Advanced Virgo conduct their observations a major goal will be to measure the SGWB.

The spectrum of a SGWB is usually described by the dimensionless quantity $\Omega_{gw}(f)$ which is the gravitational-wave energy density per unit logarithmic frequency, divided by the critical energy density ρ_c ($\rho_c = 3c^2H_0^2/8\pi G$, where H_0 is the present value of the Hubble constant) to close the universe,

$$\Omega_{gw}(f) = \frac{f}{\rho_c}\frac{d\rho_{gw}}{df} \ . \tag{1}$$

Theoretical models of the SGWB in the observation band of LIGO and Virgo are characterized by a power-law spectrum which assumes that the fractional energy density in gravitational waves has the form

$$\Omega_{gw}(f) = \Omega_\alpha \left(\frac{f}{f_{ref}}\right)^\alpha \ , \tag{2}$$

where α is the spectral index and f_{ref} is a reference frequency. Cosmologically produced SGWBs are typically approximated by a power law in the LIGO frequency band, $\alpha = 0$, while $\alpha = 3$ is characteristic of many astrophysical models. A SGWB from binary black holes in Advanced LIGO and Advanced Virgo's most sensitive frequency band (10 Hz - 100 Hz) would have $\alpha = 2/3$.

The method by which LIGO and Virgo have attempted to measure the SGWB is, in principle, not difficult; optimally filtered correlations from the output strain data from two detectors are calculated [7,8] Initial LIGO [9] and initial Virgo [10] have used this method on their data to set upper limits on the energy density of the SGWB [11,12,13]. No signal was detected, but the results constrain the energy density of the SGWB to be $\Omega_0 < 5.6 \times 10^{-6}$ at 95% confidence [13] in the 41.5–169.25 Hz band. The advanced detectors will ultimately have about 10-times better strain sensitivity than the initial detectors; the low frequency limit of the sensitive band is also extended from 40 Hz down to 10 Hz. Furthermore, the number of detectors operating in a worldwide network will increase, eventually including sites at LIGO-Hanford, LIGO-Livingston, Virgo, GEO-HF (at high frequencies) [14], KAGRA (Japan) [15], and potentially LIGO-India [16]. The significant strain sensitivity improvements and wider bandwidth will enable real breakthroughs in the searches for the SGWB, with a potential sensitivity of $\Omega_0 < 6 \times 10^{-10}$. The detection of a cosmologically produced SGWB would be a landmark discovery of enormous importance to the larger physics and astronomy community. The detection of an astrophysically produced SGWB would also be of great interest; the loudest contribution to such an SGWB would likely be stellar mass binary black hole systems, due to their large apparent abundance [6].

Gravitational-wave signals that are too weak to be detected individually combine to form a SGWB. The SGWB that LIGO and Virgo hope to observe could be created from two classes of sources. A cosmologically produced SGWB would be created in the earliest moments of the Universe. There are a host of cosmological processes that could contribute to the SGWB, such as the amplification of vacuum fluctuations following inflation [17], phase transitions in the early universe [18,19], cosmic strings [20,21,22,23], and pre-Big Bang models [24,25]. An astrophysically produced SGWB would arise from the ensemble of what would be considered to be standard astrophysical events [26]. In total the astrophysical background would be the result of a broad spectrum of events, including core collapses to neutron stars or black holes [27,28,29,30,6], rotating neutron stars [31,32] including magnetars [33,34,35,36], phase transition [37,38] or initial instabilities in young neutron stars [39,40,41,40], compact binary mergers [42,43,44,45,46,47] and compact objects around super-massive black holes [48,49]. As LIGO and Virgo observe in the advanced detector era, the cosmologically produced SGWB and the astrophysically produced SGWB are both exciting targets for observation.

2 Results from Advanced LIGO Observing Run O1

Advanced LIGO's first observing run went from September 2015 to January 2016. The data from the two Advanced LIGO detectors, LIGO Hanford and LIGO Livingston, were used for the search for a SGWB. Data quality cuts removed problematic times and frequencies from the analysis. In total, 29.85 days of coincident data were analyzed. No SGWB was detected.

2.1 O1 Isotropic Results

Assuming that the frequency dependence of the energy density of the SGWB is flat, namely $\alpha = 0$, the constraint on the energy density is $\Omega(f) < 1.7 \times 10^{-7}$ with 95% confidence within the 20 Hz - 86 Hz frequency band [50]. This is a factor of 33 better than the upper limit set by initial LIGO and initial Virgo [13]. Assuming a spectral index of $\alpha = 2/3$ the constraint on the energy density is $\Omega(f) < 1.3 \times 10^{-7}$ with 95% confidence within the 20 Hz - 98 Hz frequency band, while for $\alpha = 3$ it is $\Omega(f) < 1.7 \times 10^{-8}$ in the 20 Hz - 300 Hz band [50] (the reference frequency is $f_{ref} = 25$ Hz when $\alpha \neq 0$). Figure 1 provides the O1 SGWB results, as well as constraints from from previous analyses, theoretical predictions, the expected sensitivity at design sensitivity for Advanced LIGO and Advanced Virgo, and the projected sensitivity of the proposed Laser Interferometer Space Antenna (LISA) [51]. The O1 results will be used to limit cosmic string parameters, similar to what was done with initial LIGO and initial Virgo [11,52].

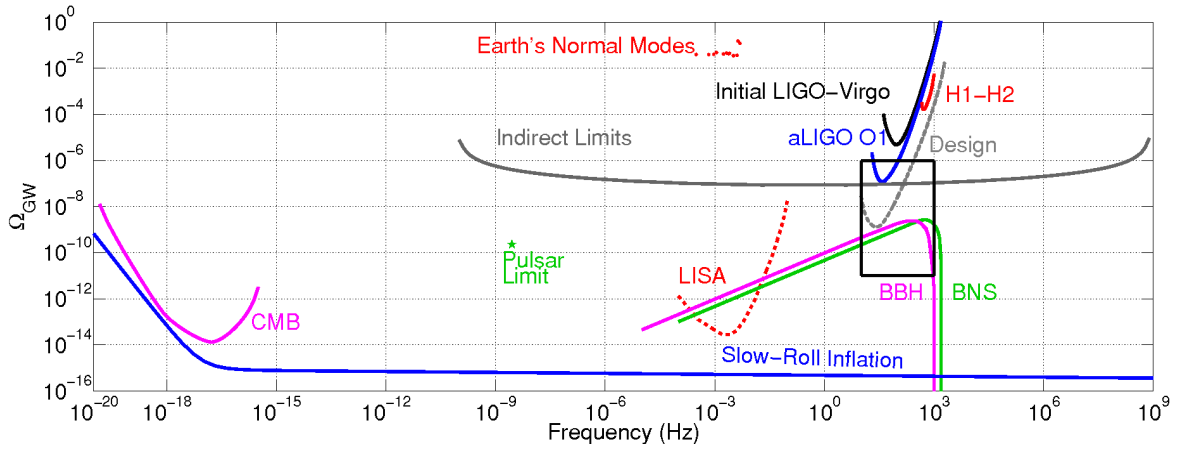


Figure 1 – Constraints on the SGWB, as well as some representative models, across many decades in frequency. Presented are the limits from ground-based interferometers from the final science run of Initial LIGO-Virgo, the co-located detectors at Hanford (H1-H2), Advanced LIGO (aLIGO) O1, and the projected design sensitivity of the advanced detector network assuming two years of coincident data, with constraints from other measurements: CMB measurements at low multipole moments [53], indirect limits from the Cosmic Microwave Background (CMB) and Big-Bang Nucleosynthesis [54,55], pulsar timing [55], and from the ringing of Earth's normal modes [56]. The predicted SGWB from binary black holes (BBH) [6] and binary neutron stars (BNS) [57] are displayed. Also given are the projected limits for the proposed space-based detector LISA [51]. Displayed in Figure 2 is the region in the black box in more detail. Figure from [50].

The dramatic improvement in the upper limit on the SGWB energy density was important, but not the most important SGWB outcome of observing run O1. The observation of the gravitational waves from stellar mass binary black hole mergers [1,2,3] implies that these events are far more numerous in the universe than previously expected. In fact, it is likely that the SGWB produced from these type of events will be at the level of $\Omega_{GW} \sim 10^{-9}$ in the observing band of Advanced LIGO and Advanced Virgo [6]. See Figure 2.

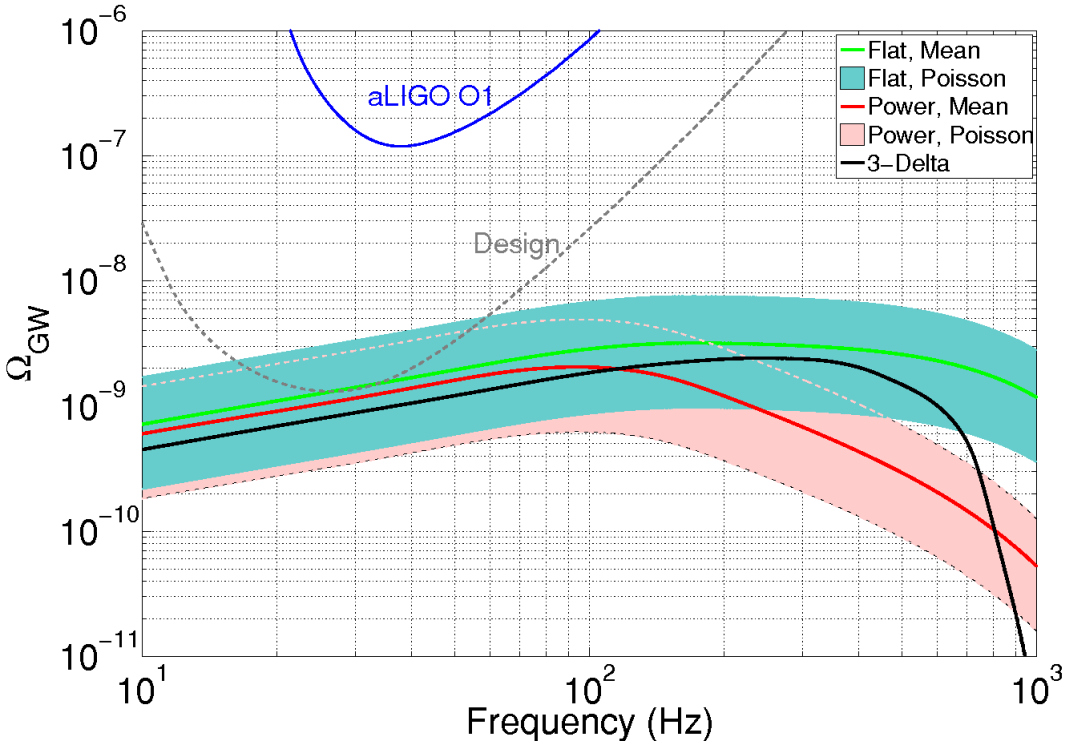


Figure 2 – The range of potential spectra for a BBH background assuming the flat-log, power-law, and three-delta mass distribution models described in [58,3], and the local rate derived from the O1 detections [3]. Also displayed is the O1 sensitivity and the projected ultimate design sensitivity for Advanced LIGO and Advanced Virgo. Figure from [50].

2.2 Anisotropic O1 Results

Within the LIGO-Virgo observational band it is expected that the SGWB will be essentially isotropic. However, LIGO and Virgo have decided to look for a SGWB that would be anisotropic. Such an anisotropic background could provide even more information about the early universe, or the astrophysical environment in our region of the universe. Using the recent O1 data there have been three different types of searches for an anisotropic background [59]. To look for extended sources, LIGO and Virgo use what is known as the spherical harmonic decomposition [60]. In order to search for point sources, a broadband radiometer analysis is used [61,62]. Finally, LIGO and Virgo employed a narrowband radiometer search to look for gravitational waves in the direction of interesting objects in the sky, such as the galactic center, Scorpius X-1 and SN 1987A.

An anisotropic SGWB was not observed with the Advanced LIGO O1 data, but important upper limits were set [59]. For broadband point sources, the gravitational wave energy flux per unit frequency was constrained to be $F_{\alpha,\Theta} < (0.1 - 56) \times 10^{-8}$ erg cm^{-2} s^{-1} Hz$^{-1}(f/25\text{ Hz})^{\alpha-1}$ depending on the sky location Θ and the spectral power index α. For extended sources, the upper limits on the fractional gravitational wave energy density required to close the Universe are $\Omega(f,\Theta) < (0.39 - 7.6) \times 10^{-8}$ sr$^{-1}(f/25\text{ Hz})^{\alpha}$, again depending on Θ and α. The directed searches for narrowband gravitational waves from Scorpius X-1, Supernova 1987 A, and the Galactic Center had median frequency-dependent limits on strain amplitude of $h_0 <$ (6.7, 5.5, and 7.0) $\times 10^{-25}$ respectively, for the most sensitive detector frequencies 130 - 175 Hz. See [59] for further details.

LIGO and Virgo have used the recent observation of gravitational waves from binary black hole coalescences to test general relativity [63,3]. The LIGO-Virgo SGWB search will also be extended in order to test general relativity. There is not necessarily a reason to expect extra polarizations of gravitational waves, nor extra polarizations in the SGWB; however, LIGO and Virgo have the ability to search for these modes, and will do so. With general relativity there are only two possible polarizations for gravitational waves, namely the two tensor modes. Alternative theories of gravity can also generate gravitational waves with scalar or vector polarizations [64].

Since there are six possible polarization modes, Advanced LIGO (with only two detectors, that are essentially co-aligned with respect to each other) cannot identify the polarization of short duration gravitational wave signals [3,65,64], such as those that have been recently observed [1,2,3]. A minimum of six detectors would be necessary to resolve the polarization content (scalar, vector and tensor) of a short duration gravitational wave [64]. A search for long duration gravitational waves, such as those from rotating neutron stars or the SGWB by the two Advanced LIGO detectors, can directly measure the polarizations of the gravitational waves [65,66,67,68]. A detection of a SGWB by Advanced LIGO and Advanced Virgo would allow for a verification of general relativity that is not possible with short duration gravitational wave searches.

The LIGO-Virgo search for a SGWB will now be expanded to a search for 6 polarizations: two tensor modes, two vector modes, and two scalar modes [68]. This will soon be applied to Advanced LIGO Observing Run O1 data. The addition of Advanced Virgo to the network does not improve detection prospects (because of its longer distance displacement from the LIGO detectors), however it will improve the ability to estimate the parameters of a SGWB of mixed polarizations. The eventual inclusion of KAGRA [15] and LIGO-India [16] will further expand the ability to resolve different polarizations of the SGWB, and further test general relativity. Bayesian parameter estimation techniques have been developed in order to search for tensor, vector and scalar polarizations in the LIGO-Virgo data [68].

3 Correlated magnetic noise in global networks of gravitational-wave detectors

A search for the SGWB uses a cross-correlation between the data from two detectors. Inherent in such an analysis is the assumption that the noise in one detector is statistically independent from the noise in the other detector. Correlated noise would introduce an inherent bias in the analysis. It is for this reason that the data from two separated detectors is used. At one time initial LIGO had two co-located detectors at the LIGO Hanford site. An attempt was made to measure the SGWB with these two detectors, but correlated noise at low frequencies contaminated the measurement, and a clean analysis could only be made for frequencies above 460 Hz [12].

The LIGO and Virgo detectors' sites are thousands of kilometers from one another, and the simple assumption is that the noise in the detectors at these sites is independent from one another. However, this assumption has been demonstrated to be false for magnetic noise. The Earth's surface and the ionosphere act like mirrors and form a spherical cavity for extremely low frequency electromagnetic waves. The Schumann resonances are a result of this spherical cavity, and resonances are observed at 8, 14, 20, 26, ... Hz [69]. Most of these frequencies fall in the important SGWB detection band (10 Hz to 100 Hz) for Advanced LIGO and Advanced Virgo. The resonances are driven by the 100 or so lightning strikes per second around the world. The resonances result in magnetic fields of order 0.5 - 1.0 pT $\mathrm{Hz}^{1/2}$ on the Earth's surface [69]. In the time domain, 10 pT bursts appear above a 1 pT background at a rate of ≈ 0.5 Hz [70].

This magnetic field noise correlation has been observed between magnetometers at the LIGO and Virgo sites [71]. Magnetic fields can couple into the gravitational wave detectors and create noise in the detectors' output strain channel. It has been determined that the correlated magnetic field noise did not affect the SGWB upper limits measured by initial LIGO and Virgo, but

it is possible that they could contaminate the future results of Advanced LIGO and Advanced Virgo [72]. If that is the case, then methods must be taken to try and monitor the magnetic fields and subtract their effects. This could be done, for example, via Wiener filtering [72,73]. Low noise magnetometers are now installed at the LIGO and Virgo sites in order to monitor this correlated magnetic noise, and to be used if Wiener filtering is necessary for the SGWB searches. In addition to long term magnetic noise correlations, short duration magnetic transients, produced from lightning strikes around the world, are seen to be coincidently visible at the detector sites and could affect the search for short duration gravitational wave events [74].

4 Future Observing Runs for LIGO and Virgo

Advanced LIGO has completed its first observing run, and the results of the search for a SGWB have been published [50,59]. At the time of this writing Advanced LIGO is in the middle of its second observing run, with Advanced Virgo to join soon. Over the next few years further observing runs will happen as Advanced LIGO and Advanced Virgo approach their target sensitivities [75]. At their target sensitivities LIGO and Virgo should be able to constrain the energy density of the SGWB to approximately $\Omega_{gw} \sim 1 \times 10^{-9}$ (in the 10 Hz to 100 Hz band) with a year of coincident data, while 3 years of data will give a limit of $\Omega_{gw} \sim 6 \times 10^{-10}$. At this point it is likely that LIGO and Virgo could observe a binary black hole produced SGWB [50,6]. Various cosmological models [18,19,24,25], or cosmic strings [20,21,22,23] might produce a detectable SGWB at this level as well. Similar sensitivity advances will also be made with the directional searches as Advanced LIGO and Advanced Virgo reach their target sensitivities. In fact, the addition of Advanced Virgo to the network, with its long distance displacement from the LIGO sites, will make a further important contribution to the directional searches and their ability to map the sky [59]. One can expect to see many important results pertaining to the search for a SGWB from LIGO and Virgo in the coming years.

Acknowledgments

This project is funded by NSF grant PHY-1505373. The LIGO Scientific Collaboration (LSC) and the Virgo Collaboration gratefully acknowledge the support of the United States National Science Foundation (NSF) for the construction and operation of the LIGO Laboratory and Advanced LIGO as well as the Science and Technology Facilities Council (STFC) of the United Kingdom, the Max-Planck-Society (MPS), and the State of Niedersachsen/Germany for support of the construction of Advanced LIGO and construction and operation of the GEO600 detector. Additional support for Advanced LIGO was provided by the Australian Research Council. The LSC and Virgo gratefully acknowledge the Italian Istituto Nazionale di Fisica Nucleare (INFN), the French Centre National de la Recherche Scientifique (CNRS) and the Foundation for Fundamental Research on Matter supported by the Netherlands Organisation for Scientific Research, for the construction and operation of the Virgo detector and the creation and support of the EGO consortium. The LSC and Virgo also gratefully acknowledge research support from these agencies as well as by the Council of Scientific and Industrial Research of India, Department of Science and Technology, India, Science & Engineering Research Board (SERB), India, Ministry of Human Resource Development, India, the Spanish Ministerio de Economía y Competitividad, the Conselleria d'Economia i Competitivitat and Conselleria d'Educació, Cultura i Universitats of the Govern de les Illes Balears, the National Science Centre of Poland, the European Commission, the Royal Society, the Scottish Funding Council, the Scottish Universities Physics Alliance, the Hungarian Scientific Research Fund (OTKA), the Lyon Institute of Origins (LIO), the National Research Foundation of Korea, Industry Canada and the Province of Ontario through the Ministry of Economic Development and Innovation, the Natural Science and Engineering Research Council Canada, Canadian Institute for Advanced Research, the Brazilian Ministry of

Science, Technology, and Innovation, Fundação de Amparo à Pesquisa do Estado de São Paulo (FAPESP), Russian Foundation for Basic Research, the Leverhulme Trust, the Research Corporation, Ministry of Science and Technology (MOST), Taiwan and the Kavli Foundation. The LSC and Virgo gratefully acknowledge the support of the NSF, STFC, MPS, INFN, CNRS and the State of Niedersachsen/Germany for provision of computational resources. This article has been assigned the document number LIGO-P1700108.

References

1. B. P. Abbott et al. Observation of Gravitational Waves from a Binary Black Hole Merger. *Phys. Rev. Lett.*, 116:061102, Feb 2016.
2. B. P. Abbott et al. GW151226: Observation of Gravitational Waves from a 22-Solar-Mass Binary Black Hole Coalescence. *Phys. Rev. Lett.*, 116:241103, Jun 2016.
3. B. P. Abbott et al. Binary Black Hole Mergers in the First Advanced LIGO Observing Run. *Phys. Rev. X*, 6:041015, Oct 2016.
4. J Aasi et al. Advanced LIGO. *Classical and Quantum Gravity*, 32(7):074001, 2015.
5. F Acernese et al. Advanced Virgo: a second-generation interferometric gravitational wave detector. *Classical and Quantum Gravity*, 32(2):024001, 2015.
6. B. P. Abbott et al. GW150914: Implications for the Stochastic Gravitational-Wave Background from Binary Black Holes. *Phys. Rev. Lett.*, 116:131102, Mar 2016.
7. N Christensen. Measuring the Stochastic Gravitational Radiation Background with Laser Interferometric Antennas. *Physical Review D*, 46:5250, 1992.
8. Bruce Allen and Joseph D. Romano. Detecting a stochastic background of gravitational radiation: Signal processing strategies and sensitivities. *Phys.Rev.*, D59:102001, 1999.
9. B Abbott et al. LIGO: the Laser Interferometer Gravitational-Wave Observatory. *Reports on Progress in Physics*, 72(7):076901, 2009.
10. T Accadia et al. Virgo: a laser interferometer to detect gravitational waves. *Journal of Instrumentation*, 7(03):P03012, 2012.
11. B. Abbott et al. Searching for Stochastic Gravitational Waves with LIGO. *Nature*, 460:990, 2009.
12. J. Aasi et al. Searching for stochastic gravitational waves using data from the two colocated LIGO Hanford detectors. *Physical Review D*, 91:022003, 2015.
13. J. Aasi et al. Improved Upper Limits on the Stochastic Gravitational–Wave Background from 2009–2010 LIGO and Virgo Data. *Physical Review Letters*, 113:231101, 2014.
14. C Affeldt, K Danzmann, K L Dooley, H Grote, M Hewitson, S Hild, J Hough, J Leong, H Lck, M Prijatelj, S Rowan, A Rdiger, R Schilling, R Schnabel, E Schreiber, B Sorazu, K A Strain, H Vahlbruch, B Willke, W Winkler, and H Wittel. Advanced techniques in geo 600. *Classical and Quantum Gravity*, 31(22):224002, 2014.
15. Yoichi Aso, Yuta Michimura, Kentaro Somiya, Masaki Ando, Osamu Miyakawa, Takanori Sekiguchi, Daisuke Tatsumi, and Hiroaki Yamamoto. Interferometer design of the KAGRA gravitational wave detector. *Phys. Rev. D*, 88:043007, Aug 2013.
16. C. S. Unnikrishnan. IndIGO AND LIGO-INDIA: SCOPE AND PLANS FOR GRAVITATIONAL WAVE RESEARCH AND PRECISION METROLOGY IN INDIA. *International Journal of Modern Physics D*, 22(01):1341010, 2013.
17. E. W. Kolb & M. S. Turner. *The Early Universe.* Westview Press, 1994.
18. A. A. Starobinskii. Spectrum of relic gravitational radiation and the early state of the universe. *JETP Lett.*, 30, 1979.
19. R. Bar-Kana. Limits on Direct Detection of Gravitational Waves. *Phys. Rev. D*, 50, 1994.
20. T. W. B. Kibble. Topology of cosmic domains and strings. *J. Phys.*, A9, 1976.
21. T. Damour & A. Vilenkin. Gravitational radiation from cosmic (super)strings: bursts,

stochastic background, and observational windows. *Phys. Rev. D*, 71, 2005.
22. S. Olmez, V. Mandic, and X. Siemens. Gravitational-Wave Stochastic Background from Kinks and Cusps on Cosmic Strings. *Phys. Rev. D*, 81:104028, 2010.
23. S. Olmez, V. Mandic, and X. Siemens. Anisotropies in the Gravitational-Wave Stochastic Background. *J. Cosmol. Astropart. Phys.*, 2012:009, 2011.
24. A. Buonanno. Spectrum of relic gravitational waves in string cosmology. *Phys. Rev. D*, 55, 1997.
25. V. Mandic and A. Buonanno. Accessibility of the Pre-Big-Bang Models to LIGO. *Phys. Rev. D*, 73, 2006.
26. T. Regimbau. The astrophysical gravitational wave stochastic background. *Research in Astronomy and Astrophysics*, 11:369–390, April 2011.
27. A. Buonanno, G. Sigl, G. G. Raffelt, H.-T. Janka, and E. Müller. Stochastic gravitational-wave background from cosmological supernovae. *Physical Review D*, 72(8):084001, October 2005.
28. P. Sandick, K. A. Olive, F. Daigne, and E. Vangioni. Gravitational waves from the first stars. *Physical Review D*, 73(10):104024, May 2006.
29. S. Marassi, R. Schneider, and V. Ferrari. Gravitational wave backgrounds and the cosmic transition from Population III to Population II stars. *Monthly Notices of the Royal astronomical Society*, 398:293–302, September 2009.
30. X.-J. Zhu, E. Howell, and D. Blair. Observational upper limits on the gravitational wave production of core collapse supernovae. *Monthly Notices of the Royal astronomical Society*, 409:L132–L136, November 2010.
31. T. Regimbau and J. A. de Freitas Pacheco. Cosmic background of gravitational waves from rotating neutron stars. *Astronomy and Astrophysics*, 376:381–385, September 2001.
32. P. A. Rosado. Gravitational wave background from rotating neutron stars. *Physical Review D*, 86(10):104007, November 2012.
33. T. Regimbau and J. A. de Freitas Pacheco. Gravitational wave background from magnetars. *Astronomy and Astrophysics*, 447:1–7, February 2006.
34. E. Howell, T. Regimbau, A. Corsi, D. Coward, and R. Burman. Gravitational wave background from sub-luminous GRBs: prospects for second- and third-generation detectors. *Monthly Notices of the Royal Astronomical Society*, 410:2123–2136, February 2011.
35. S. Marassi, R. Ciolfi, R. Schneider, L. Stella, and V. Ferrari. Stochastic background of gravitational waves emitted by magnetars. *Monthly Notices of the Royal Astronomical Society*, 411:2549–2557, March 2011.
36. C.-J. Wu, V. Mandic, and T. Regimbau. Accessibility of the stochastic gravitational wave background from magnetars to the interferometric gravitational wave detectors. *Physical Review D*, 87(4):042002, February 2013.
37. G Sigl. Cosmological gravitational wave background from phase transitions in neutron stars. *J. Cosmol. Astropart. Phys.*, JCAP04:002, 2006.
38. J. C. N. de Araujo and G. F. Marranghello. Gravitational wave background from neutron star phase transition. *General Relativity and Gravitation*, 41:1389–1406, June 2009.
39. V. Ferrari, S. Matarrese, and R. Schneider. Stochastic background of gravitational waves generated by a cosmological population of young, rapidly rotating neutron stars. *Monthly Notices of the Royal astronomical Society*, 303:258–264, February 1999.
40. X.-J. Zhu, X.-L. Fan, and Z.-H. Zhu. Stochastic Gravitational Wave Background from Neutron Star r-mode Instability Revisited. *The Astrophysical Journal*, 729:59, March 2011.
41. E. Howell, D. Coward, R. Burman, D. Blair, and J. Gilmore. The gravitational wave background from neutron star birth throughout the cosmos. *Monthly Notices of the Royal astronomical Society*, 351:1237–1246, July 2004.
42. A. J. Farmer & E. S. Phinney. The gravitational wave background from cosmological

compact binaries. *Mon. Not. R. Ast. Soc.*, 346:1197, 2003.
43. X.-J. Zhu, E. Howell, T. Regimbau, D. Blair, and Z.-H. Zhu. Stochastic Gravitational Wave Background from Coalescing Binary Black Holes. *The Astrophysical Journal*, 739:86, October 2011.
44. P. A. Rosado. Gravitational wave background from binary systems. *Physical Review D*, 84(8):084004, October 2011.
45. S. Marassi, R. Schneider, G. Corvino, V. Ferrari, and S. Portegies Zwart. Imprint of the merger and ring-down on the gravitational wave background from black hole binaries coalescence. *Physical Review D*, 84(12):124037, December 2011.
46. C. Wu, V. Mandic, and T. Regimbau. Accessibility of the gravitational-wave background due to binary coalescences to second and third generation gravitational-wave detectors. *Physical Review D*, 85(10):104024, May 2012.
47. X.-J. Zhu, E. J. Howell, D. G. Blair, and Z.-H. Zhu. On the gravitational wave background from compact binary coalescences in the band of ground-based interferometers. *Monthly Notices of the Royal astronomical Society*, 431:882–899, May 2013.
48. L Barack & C Cutler. Confusion noise from LISA capture sources. *Phys. Rev. D*, 70:122002, 2004.
49. G Sigl & J Schnittman & A Buonanno. Gravitational-wave background from compact objects embedded in AGN accretion disks. *Phys. Rev. D*, 75:024034, 2007.
50. B. P. Abbott et al. Upper Limits on the Stochastic Gravitational-Wave Background from Advanced LIGO's First Observing Run. *Phys. Rev. Lett.*, 118:121101, Mar 2017.
51. P. Amaro-Seoane et al. Laser Interferometer Space Antenna. *ArXiv e-prints*, February 2017.
52. J. Aasi et al. Constraints on cosmic strings from the LIGO-Virgo gravitational-wave detectors. *Phys.Rev.Lett.*, 112:131101, 2014.
53. Planck Collaboration, Ade, P. A. R., et al. Planck early results. I. The Planck mission. *Astronomy & Astrophysics*, 536:A1, 2011.
54. Luca Pagano, Laura Salvati, and Alessandro Melchiorri. New constraints on primordial gravitational waves from planck 2015. *Physics Letters B*, 760:823 – 825, 2016.
55. Paul D. Lasky et al. Gravitational-wave cosmology across 29 decades in frequency. *Phys. Rev. X*, 6:011035, Mar 2016.
56. Michael Coughlin and Jan Harms. Constraining the gravitational wave energy density of the Universe using Earth's ring. *Phys. Rev. D*, 90:042005, Aug 2014.
57. Duncan Meacher, Michael Coughlin, Sean Morris, Tania Regimbau, Nelson Christensen, Shivaraj Kandhasamy, Vuk Mandic, Joseph D. Romano, and Eric Thrane. Mock data and science challenge for detecting an astrophysical stochastic gravitational-wave background with Advanced LIGO and Advanced Virgo. *Phys. Rev. D*, 92:063002, Sep 2015.
58. B. P. Abbott et al. Astrophysical Implications of the Binary Black-hole Merger GW150914. *The Astrophysical Journal Letters*, 818(2):L22, 2016.
59. B. P. Abbott et al. Directional Limits on Persistent Gravitational Waves from Advanced LIGO's First Observing Run. *Phys. Rev. Lett.*, 118:121102, Mar 2017.
60. B Abbott et al. Directional limits on persistent gravitational waves using LIGO S5 science data. *Phys. Rev. Lett.*, 107:271102, 2011.
61. Stefan W Ballmer. A radiometer for stochastic gravitational waves. *Classical and Quantum Gravity*, 23(8):S179, 2006.
62. B Abbott et al. Upper limit map of a background of gravitational waves. *Phys. Rev. D*, 76:082003, 2007.
63. B. P. Abbott et al. Tests of General Relativity with GW150914. *Phys. Rev. Lett.*, 116:221101, May 2016.
64. Clifford M. Will. The confrontation between general relativity and experiment. *Living Reviews in Relativity*, 17(1):4, 2014.

65. Joseph D. Romano and Neil. J. Cornish. Detection methods for stochastic gravitational-wave backgrounds: a unified treatment. *Living Reviews in Relativity*, 20(1):2, 2017.
66. Emanuele Berti et al. Testing general relativity with present and future astrophysical observations. *Classical and Quantum Gravity*, 32(24):243001, 2015.
67. Maximiliano Isi, Matthew Pitkin, and Alan J. Weinstein. Probing Dynamical Gravity with the Polarization of Continuous Gravitational Waves. *arXiv:1703.07530*, 2017.
68. Thomas Callister, A. Sylvia Biscoveanu, Nelson Christensen, Maximiliano Isi, Andrew Matas, Olivier Minazzoli, Tania Regimbau, Mairi Sakellariadou, Jay Tasson, and Eric Thrane. Tests of General Relativity with the Stochastic Gravitational-Wave Background. *arXiv:1704.08373*, 2017.
69. D.D. Sentman. Handbook of atmospheric electrodynamics. 1:267, 1995.
70. Martin Füllekrug. Schumann resonances in magnetic field components. *Journal of Atmospheric and Terrestrial Physics*, 57(5):479 – 484, 1995.
71. E Thrane, N Christensen, and R Schofield. Correlated magnetic noise in global networks of gravitational-wave interferometers: observations and implications. *Phys. Rev. D*, 87:123009, 2013.
72. E Thrane, N Christensen, R M S Schofield, and A Effler. Correlated noise in networks of gravitational-wave detectors: subtraction and mitigation. *Phys. Rev. D*, 90:023013, 2014.
73. Michael W Coughlin, Nelson L Christensen, Rosario De Rosa, Irene Fiori, Mark Gokowski, Melissa Guidry, Jan Harms, Jerzy Kubisz, Andrzej Kulak, Janusz Mlynarczyk, Federico Paoletti, and Eric Thrane. Subtraction of correlated noise in global networks of gravitational-wave interferometers. *Classical and Quantum Gravity*, 33(22):224003, 2016.
74. Izabela Kowalska-Leszczynska, Marie-Anne Bizouard, Tomasz Bulik, Nelson Christensen, Michael Coughlin, Mark Gokowski, Jerzy Kubisz, Andrzej Kulak, Janusz Mlynarczyk, Florent Robinet, and Maximilian Rohde. Globally coherent short duration magnetic field transients and their effect on ground based gravitational-wave detectors. *Classical and Quantum Gravity*, 34(7):074002, 2017.
75. B. P. Abbott et al. Prospects for Observing and Localizing Gravitational-Wave Transients with Advanced LIGO and Advanced Virgo. *Living Reviews in Relativity*, 19(1):1, 2016.

BLACK HOLES BINARIES FROM GLOBULAR CLUSTERS AS SOURCES OF GRAVITATIONAL WAVES

M. SZKUDLAREK[1], D. GONDEK-ROSIŃSKA[1], A. ASKAR[2], T. BULIK[3], M. GIERSZ[2]

[1] *Janusz Gil Institute of Astronomy, University of Zielona Góra, Licealna 9, 65-417, Zielona Góra, Poland*

[2] *Nicolaus Copernicus Astronomical Centre, Polish Academy of Sciences, ul. Bartycka 18, 00-716 Warsaw, Poland*

[3] *Astronomical Observatory Warsaw University, 00-478 Warsaw, Poland*

Stellar mass binary black holes are the most important sources of gravitational waves for ground based interferometric detectors. We analyze about a thousand globular cluster (GC) models simulated using the MOCCA Monte Carlo code for star cluster evolution to study black hole - black hole interactions in these dense stellar systems that can lead to gravitational wave emission. We extracted information for all coalescing binary black holes (BBHs) that merge via gravitational radiation from these GC models and for those BHs that collide due to 2-body, 3-body and 4-body dynamical interactions. By obtaining results from a substantial number of realistic star clusters evolution model, that cover different initial parameters (masses, metallicities, densities etc) we have an extremely large statistical sample of two black holes which merge or collide within a Hubble time. We discuss the importance of BBH originating from GC for gravitational waves observations.

1 Introduction

The direct detections of gravitational waves (GWs) from the merger of binary black holes (BBHs) by the Advanced LIGO (aLIGO) detectors has ushered astrophysics into a new era of observing highly energetic events that were previously invisible. Following the detection of GW150914 [2], two more confirmed BBH mergers, GW151226 [3] and GW170104 [4] were observed by aLIGO. The detections confirm the existence of massive stellar black holes (BHs) in binary systems and proves that such systems can merge via GW emission within a Hubble time. Masses inferred from the GW signal of coalescing BBHs detected by aLIGO show that these BHs are typically more massive than accreting stellar mass BHs in X-ray binaries. Existence of BHs with masses higher than $20M_{\odot}$ may indicate that they were formed in low metallicity environments like GCs [9] but the formation scenario for massive BBHs and the origin of the detected coalescing binaries remains debatable. Such systems may form in the field via isolated binary evolution [26,10,29] or through dynamical interactions in dense stellar systems like GCs [28,7] or galactic nuclei [6,5]. It is also possible that the detected events maybe coalescing primordial BHs [25]. In this contribution we study the astrophysical properties of BHs which merge via GW emission in a binary system or collide in GCs due to dynamical interactions. Binary black hole coalescence will lead to the characteristic chirp signal (a signal with increasing frequency with time caused by shrinking a BBH orbit due to gravitational radiation) while collisions in dynamical interactions may produce a short, burst signal.

2 Method

We analyze about 1000 GC models generated by the MOCCA (MOnte Carlo Cluster simulAtor) code [17,14] as part of the MOCCA-Survey Database I [7]. The initial conditions for these models models cover a wide range of the parameter space (different initial masses, densities, primordial binary fraction, metallicity, central density and concentrations). The code follows most of the important physical processes that occur during the dynamical evolution of star clusters. Additionally to proper treatment of the relaxation process MOCCA includes:

1. Synthetic binary and stellar evolution using the prescriptions provided by Hurley, Pols & Tout (2000) and Hurley, Tout & Pols (2000) (BSE code) [18,19],
2. Direct integration procedures for small N sub-systems using the *fewbody* [13] code provided by Fregau *et al.* (2004),
3. Realistic treatment of escape processes in tidally limited clusters based on Fukushige & Heggie (2000) [12].

MOCCA has been extensively tested by Giersz *et al.* (2013) [14], Heggie (2014) [16], Wang *et al.* (2016) [30], Mapelli (2016) [23] and Madrid (2017) [22] against the results of N-body simulations of star cluster models comprising of thirty thousand to one million stars. The agreement between these two types of simulations was excellent. In the MOCCA-SURVEY Database I cluster models are more or less representative of the GC population in our Galaxy [7]. The code has been recently used to determine properties of coalescing binary black holes originating from GC [7]. The mass of each BH in a binary system was limited to $M < 100 M_{\odot}$ and BH natal kicks were modified according to mass fallback prescriptions given by Belczynski *et al.* (2002) [8]. In this contribution we consider all BH masses and take into account all BH-BH interactions which lead to GW emission. For BBHs that were ejected from GC, we calculated the merger times using the formulae derived by Peters (1964)[24] and the time when the BBH escaped the GC model. For coalescing BBHs retained in GC models, results from BSE code incorporated within MOCCA were used to obtain correct merger times. For BH collisions and mergers during binary-single and binary-binary interactions, the results from the FEWBODY code used in MOCCA for strong interactions were analyzed. Direct collisions between all single objects from MOCCA results were also analyzed to look for direct collisions betwen BHs. For BH collisions we consider 2-body, 3-body and 4-body interactions. This also included interactions with an Intermediate Mass Black Hole (IMBH, which is defined as a BH with mass above 100 $M_{\odot}$) that are dynamically formed in 30 % GC models. [15].

3 Merging BBHs and Colliding BHs From Globular Clusters

Globular cluster are spherical and dense group of 10^5 to 10^6 stars orbiting a host galaxy. Numerous dynamical interactions take place in these extremely dense stellar environments. Such interactions can lead to the formation of binaries, affect the parameters of existing binary systems and radically change their evolution. This is particularly important for compact objects binaries: change of orbital parameters due to gravitational interactions with nearby objects; exchange of an object in a binary system as a result of close interaction; formation of new binary systems as a result of several-body interactions; the merger or the collision of two objects as a result of dynamical interactions. The whole analysis involves BHs that merged in a binary system or collided with each other within Hubble time $T = T_{\rm H} = 13 \times 10^9$ yrs.

3.1 Characteristics of the BH-BH interactions

Analyzing the output of the MOCCA code we can distinguish five different interactions, which can lead to the emission of *chirp* GW signal due to the coalescence of two BHs in a binary

system or a *burst* GW signal due to the collision of two BHs. The number of mergers inside or outside cluster models or collisions due to 2-body, 3-body and 4-body dynamical interactions as a function of time are provided in Fig. 1.

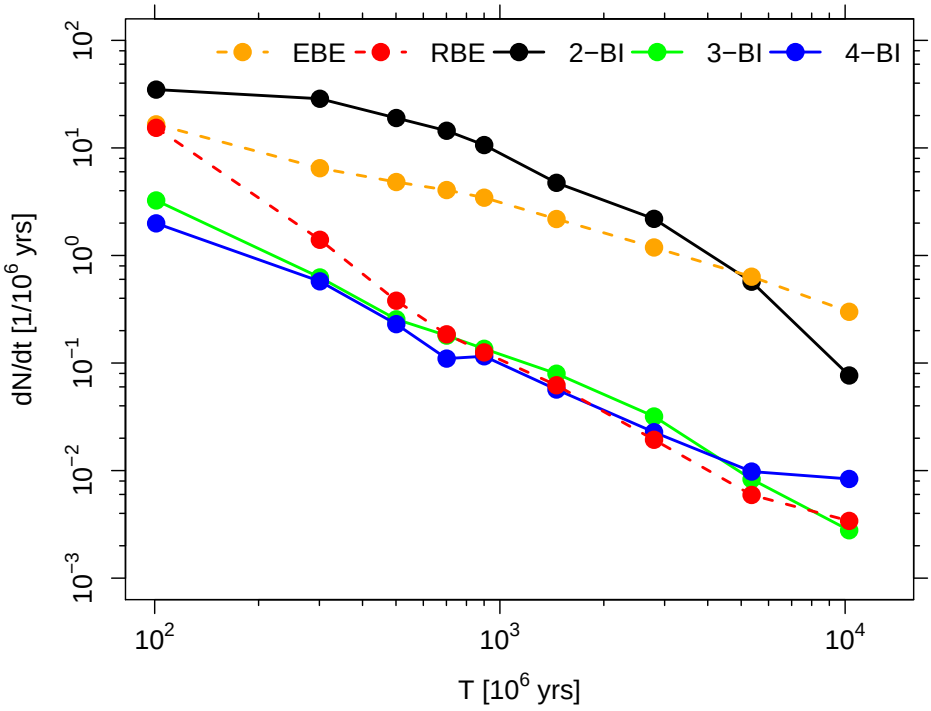


Figure 1 – Number of merging BBHs per unit time (1 Myr) as a function of merger time limited to Hubble time $T_{\rm H}$. Orange and red dashed point-lines correspond to binary mergers with *chirp* GW signal (outer and inner binary evolution respectively). Black, green and blue solid point-lines correspond to *burst* GW signal interactions, which are 2-, 3- and 4-body interactions respectively.

1. Interactions leading to the *chirp* GW signal:

   - EBE - Ejected Binary Evolution - a binary systems which, due to interactions in a cluster, gained sufficient velocity to escape the gravitational potential of GC. Such ejected BBH systems evolve in isolation outside GC. The coalescence time is determined by the orbital parameters set at the time of the escape which are taking into account while integrating Peters (1964) equations. Over 50 % of the EBE merge during the first two billion years of the cluster model evolution. This is the interaction that produces the largest number of GW *chirp* signal. By the $T_{\rm H}$, 15 236 BBH merged, and only 102 of them had the mass of one of the two BHs greater than 100 $M_\odot$.
   - RBE - Retained Binary Evolution - the BBH merger due to binary evolution or due to gravitational interaction inside the cluster. Most of these binaries, about 90% merge at early time of the cluster evolution (up to 5×10^8 years), when the most massive stars evolve rapidly, there is ongoing mass segregation process and the dynamical interactions are very common. There were 3 628 binary mergers found in this interaction, more than 80% of them are binaries in which none of the BHs exceed 100 $M_\odot$. As in the case of EBE interactions, the presence of IMBH results in a greater number of coalescencing (over 2/3 of found binaries).

2. Dynamical interactions leading to the *burst* GW signal:

   - 2-BI - 2-Body Interactions - a collision of two BHs, which is based on a physical collision (the minimum distance is less than the sum of the Schwarzschild radius of both BHs). Collisions occur only in the clusters where the IMBH was formed, and the collision percentage in which it took part is 99.9%. Such objects have a significant influence on the evolution of the entire cluster. In our analysis we found 32 122 these interactions, and only 35 of them were with BHs with masses lower than 100 $M_{\odot}$. More than 50% of 2-body collisions occur during the first billion years of globular cluster model evolution.
   - 3-BI - 3-Body Interactions - interactions involving three objects - a binary system and a star. In this interaction, as in the case of 2-BI, a dynamical physical collision occurs. To designate the relevant objects involved in a collision all possible permutations must be taken into account. These collisions are very rare (1,064 found events) and, as in the case of 2-BI interactions, the majority of the collisions occur during the first billion years of the GC model evolution. Over 97% of them are collisions in clusters with IMBH.
   - 4-BI - 4-Body Interactions - interactions involving two binary systems, in which two BHs are colliding. These interactions have properties very similar to 3-BI, but with even less statistics (783 found events), although more collisions were reported, both quantitatively and in percent, in clusters without IMBH. Just like other interactions, 4-BIs accumulate at the beginning of the cluster model evolution.

4 Local and Cosmological Merger and Collision Rate Density

In order to determine the merger and the collision rate density we used the same formalism as Bulik *et al.* (2004). We used GC star formation rate model (GCSFR) from Katz & Ricotti (2013). We found a local merger rate density for EBE and RBE in GCs of at least 5.6 $\mathrm{Gpc}^{-3}\mathrm{yr}^{-1}$ up to 30 $\mathrm{Gpc}^{-3}\mathrm{yr}^{-1}$. It is comparable to the rate calculated by Rordriguez *et al.* (2016) and consistent with the lower bound on the observed LIGO BBHs merger rate density of $12 - 213$ $\mathrm{Gpc}^{-3}\mathrm{yr}^{-1}$ [4]. In Figure 2 one can see that rate of merging BBHs depends on cluster metallicity. The obtained masses of BH are consistent with aLIGO observations. The uncertainty in the metallicity composition of GCs in early galaxies and the uncertainties connected with stellar initial mass function and the maximum stellar mass may introduce an additional increase in the merger rate. This shows that BBHs from GC could contribute to the observed events by aLIGO and other ground based detectors. The efficiency of BBH mergers is higher in GC than in the field but the total amount of star formation in dense GCs could be about 1% of the mass in the field. The local rate density for collisions due to 2-BI is at least of 1.1 $\mathrm{Gpc}^{-3}\mathrm{yr}^{-1}$.

We also determined the merger and collision rate density of two BHs as a function of redshift z. In Figure 3 different types of interactions are marked with different colours. Dashed lines correspond to the interactions leading to the *chirp* GW signal, while solid lines correspond to interactions which lead to *burst* GW signal. In the local universe, the dominant interactions are those of EBE, the binaries that escaped the cluster and evolve due to GW emission outside GC. For higher value of $z > 0.6$ 2-BI collisions dominate the rate. Aside from 2-BI, a large coalescence ratio on high values of z has also EBE and RBE interactions. Collisions due to 3-body and 4-body interactions are less significant than others in full range of z.

5 Conclusion

In conclusion, the results presented in this contribution show that dynamical interactions within dense stellar environments like GCs can lead to GW emission from merging and colliding BHs

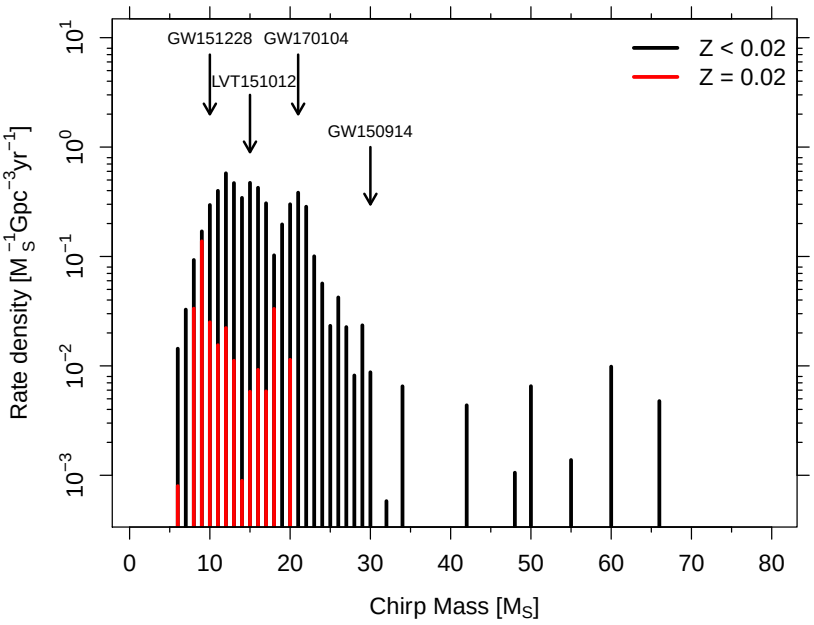


Figure 2 – Local merger rate density of two black holes with masses m_1 and m_2 in function of *chirp* mass $\mathcal{M} = (m_1 m_2)^{3/5}/(m_1 + m_2)^{1/5}$. Data includes only OBE interactions, which are divided by the initial metallicity of the cluster model: solar $Z = 0.02$ (red) and sub-solar $Z < 0.02$ (black). Arrows indicate all GW signals from merging BBHs detected by the aLIGO detector.

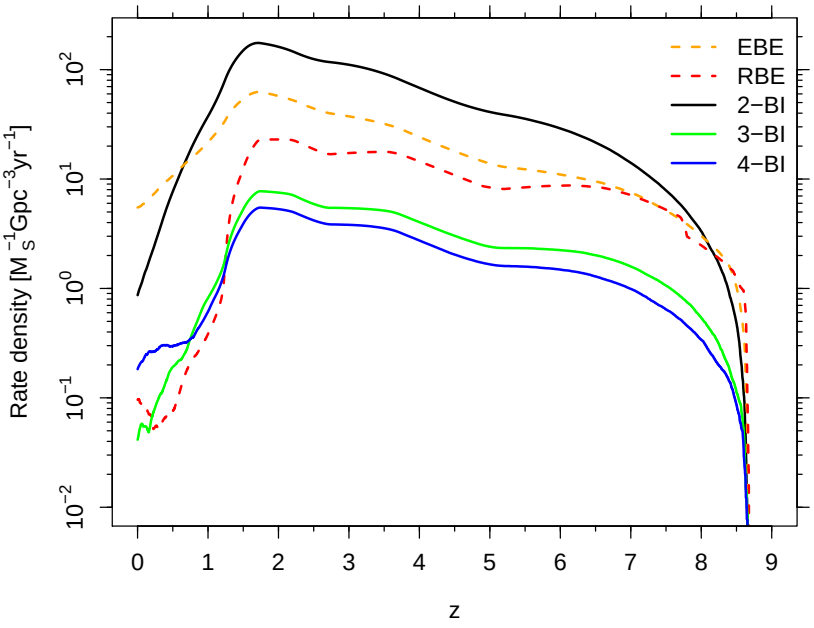


Figure 3 – Merger and collision rate density in function of redshift for fixed GCSFR [20] for all types of interactions. Orange and red dashed lines correspond to binary mergers (outer and inner binary evolution respectively) which produce *chirp* GW signal. Black, green and blue solid lines correspond to interactions, which are sources of *burst* GW signal (2-, 3- and 4-body interactions).

that maybe detected by GW observatories. GCs are efficient factories for producing BBHs that can coalesce within Hubble time producing a chirp GW signal. BH collisions during multiple body interactions can also significantly contribute to the burst like GW events under assumption that the IMBH is formed in some GC.

Acknowledgments

This work was supported by Polish National Science Centre (PNSC) grant UMO 2015/17/N/ST9 /01605 and UMO 2013/08/A/ST9/00795. Partially supported by POMOST/2012-6/11 Program of Foundation for Polish Science co-financed by the European Union within the European Regional Development Fund and by the PNSC grants UMO 2014/14/M/ST9/00707, UMO 2015/17/N/ST9/02573, UMO 2013/01/ASPERA/ST/0001, UMO 2014/15/Z/ST9/00038.

References

1. Abbott B. P., *et al.*, *Phys. Rev. Lett.* **116**, 061102 (2016)
2. Abbott B. P., *et al.*, *ApJ* **818**, L2 (2016)
3. Abbott B. P., *et al.*, *Phys. Rev. Lett.* **116**, 241103 (2016)
4. Abbot B. P., *et al.*, *Phys. Rev. Lett.* **118**, 22 (2017)
5. Antonini F. and Perets H. B., *Apj* **757**, 27 (2012)
6. Antonini F. and Rasio F. A., 2016, arXiv:1606.04889
7. Askar, A., M. Szkudlarek, D. Gondek - Rosińska, M. Giersz and T. Bulik, *MNRAS* **464**, L36-L40 (2017)
8. Belczynski K., Kalogera V., Bulik T., *ApJ* **572**, 407 (2002)
9. Belczynski K., *et al.*, *ApJ* **714**, 1217 (2010)
10. Belczynski K., *et al.*, Nature **534**, 512 (2016)
11. Bulik, T., K. Belczyski and B. Rudak, *A&A* **415**, 407 (2004)
12. Fukushige T. and Heggie D. C., *MNRAS* **318**, 753 (2000)
13. Fregeau J. M., *et al.*, *MNRAS* **352**, 1 (2004)
14. Giersz M., *el al.*, *MNRAS* **411**, 2184 (2013)
15. Giersz M., *et al.*, *MNRAS* **454**, 3150 (2015)
16. Heggie, D. C., *MNRAS* **445**, 3435 (2014)
17. Hénon, M. H., *AP&SS* **14**, 151 (1971)
18. Hurley J. R., Pols O. R. and Tout C. A., *MNRAS* **315**, 543 (2000)
19. Hurley J. R., Tout C. A. and Pols O. R., *MNRAS* **329**, 897 (2002)
20. Katz, H. and Ricotti,M. *MNRAS* **432**, 3250 (2013)
21. The LIGO Scientific Collaboration, *et al.*, 2016, arXiv:1606.04856
22. Madrid J., *el al.*, *MNRAS* **470**, 1729 (2017)
23. Mapelli M., *MNRAS* **459**, 3432 (2016)
24. Peters P. C., *PhRv* **136**, 1224 (1964)
25. Sasaki M., *et al.*, *Phys. Rev. Lett.* **117**, 061101 (2016)
26. Stevenson S., *et al.*, NatCo **8**, 14906 (2017)
27. Strader J., *et al.*, *Nature* **490**, 7418 (2012)
28. Rodriguez C. L., Chatterjee S. and Rasio F. A., *Phys. Rev.* D **93**, 084029 (2016)
29. van den Heuvel E., Portegies Zwart,S. and de Mink, S. *MNRAS Advance Access* **stx1430**, (2017)
30. Wang L., *et al.*, *MNRAS* **458**, 1450 (2016)

ADVANCED VIRGO COMMISSIONING CHALLENGES

J. CASANUEVA FOR THE VIRGO COLLABORATION
LAL, Centre Scientifique d'Orsay,
91898 Orsay, France



The second generation of gravitational wave detectors has made the first detection of a gravitational wave on September 14^{th} of 2015, opening the possibility to study new astrophysical phenomena. The Advanced Virgo detector is currently under commissioning to join the data taking. The main challenges encountered during this process will be presented in this document, together with the solutions implemented to bring the detector to its working point.

1 Introduction

The existence of Gravitational Waves (GW) was predicted by Albert Einstein's General Relativity in 1915. They are perturbations of the metric (geometry of the space-time) that are caused by a movement of mass and which propagate at the speed of light. The sources that emit powerful GWs are compact objects like Black Holes and Neutron Stars and cataclysmic events such as supernova explosions.

Gravitational Waves interact very weakly and so they carry direct information about their sources that can not be accessed by the Electromagnetic spectrum. Moreover, their study will provide a deeper understanding on General Relativity and gravitational interaction.

The first detection of a GW was done on September 14^{th} of 2015 by the LIGO-Virgo collaboration. It was emitted by the merger of a Binary Black Hole, providing the first direct proof of the existence of Black Holes. This event marks the beginning of a new way of observing the Universe.

2 Gravitational wave detectors

The effect of the passage of a GW on Earth is a change on the distance between test masses, i.e. masses experiencing only the gravitational interaction. Moreover this effect is differential so when the distance is reduced in one direction it is expanded in the perpendicular one. This distance variation is proportional to the amplitude of the GW, called h:

$$\delta L \simeq h \cdot L \tag{1}$$

where L is the distance between the test masses, δL is the distance variation induced by the passage of a GW.

Taking this into account, a Michelson interferometer is the ideal instrument to detect GWs since it measures differential distances. The particularity of GW detectors is that their mirrors are suspended to behave as test masses. Their working principle is to keep the Michelson interferometer on a Dark Fringe, where there is no light arriving to the Detection photodiode but all the light is reflected back towards the laser.

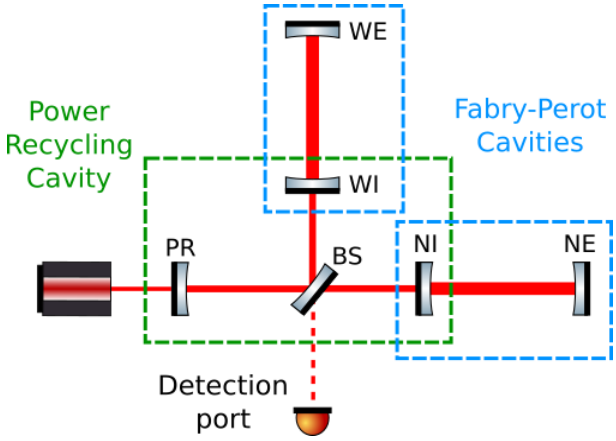


Figure 1 – Scheme of a GW detector.

In this configuration, the passage of a GW will cause a δL that will spoil the interference condition, allowing some light to leak to the Detection photodiode. However, a simple Michelson interferometer does not provide enough sensitivity for detecting GW. In order to improve the detector performance two upgrades were added to the 1^{st} generation of GW detectors:

- **Fabry-Perot cavities in the arms:** two Fabry-Perot cavities of 3 km each were added in order to increase the optical path, increasing as well the Signal-to-Noise ratio (SNR). They are marked in blue in Figure 1.

- **Power Recycling cavity:** an additional mirror was added between the Beam Splitter (BS) and the laser, as it can be seen in Figure 1. Its target is to recirculate the power that comes back towards the laser when the Michelson is in Dark Fringe. This allows to increase the effective input power and so the SNR.

With these upgrades, a sensitivity of 10^{-19} m/$\sqrt{Hz}$ was reached but the 1^{st} generation instruments did not make any detection during their Scientific Runs. For this reason it was decided to increase the sensitivity in one order of magnitude by upgrading the detector's design.

The Advanced Virgo detector is the result of this effort. There were many changes in order to reach this goal, but the main emphasis was put in reducing the fundamental noises and in reducing the stray light. The most challenging upgrades from the point of view of the commissioning will be presented here.

The first challenging upgrade was the increase of the finesse of the arm cavities from 150 to 450. The aim was to increase further the optical path and so the SNR. However this adds complexity to the length control that keeps the cavities on resonance, as it will be explained in detail in Section 3.

Regarding the thermal noise reduction it was decided to change the geometry of the Fabry-Perot cavities of the arms in order to increase the beam size on the mirrors. As a consequence the geometry of the Power Recycling Cavity (PRC) needed to be adapted. These changes had an impact on its stability, increasing the difficulty of the global control of the interferometer. The solution implemented in order to deal with this feature will be described in Section 4.

3 Arm cavities: longitudinal control acquisition

Due to the seismic noise the cavities' length is continuously changing and so a longitudinal control is needed to keep the mirrors at their working point: on resonance. The technique used for this purpose is called PDH, and provides an error signal that contains information about the cavity length and the working point. It is produced by modulating in phase the laser beam using a Radio Frequency (Ω), which in practice will add two sidebands around the laser frequency, or carrier, at $\pm\Omega$. The frequency is chosen to be anti-resonant on the Fabry-Perot cavities, acting as a phase reference for the carrier which is resonant instead. The beat note between the carrier and the sidebands is used as an error signal of a feedback loop that acts on the mirror positions to keep the cavity on resonance.

However, as the mirrors are moving, when the laser beam impinges on them there is an exchange of energy and a Doppler effect is produced. This effect is negligible if it is punctual but it accumulates each round-trip and for high finesse cavities it can become of the same order of magnitude as the linewidth of the cavity. In this case dynamical effects appear distorting the electric fields of the cavity including the error signal so that it can not be used anymore.

For the arm cavities of Advanced Virgo the critical cavity velocity above which dynamical effects start to spoil the error signals is $v_{cr} = 0.14\mu$m/s. Knowing that the cavity velocity in free-swinging is 1 μm/s rms, the control strategy needs to be adapted to overcome this problem. For this purpose a technique called *Guided Lock* was developed in Caltech [1]. Its target is to estimate the cavity velocity online and apply in consequence a single extended impulse with the maximum force available in order to bring the cavity back to the resonance but with a lower velocity. This way the second time that the resonance is crossed there are no more dynamical effects and the control can be engaged normally.

The challenging part is the velocity estimation, which is calculated using the slope of the error signal weighted by a calibration factor and a power law correction. However this is very demanding in the early stages of commissioning. For this reason an alternative method was developed to obtain the velocity already in physical units. The idea is to use the deformation of the transmitted power due to dynamical effects. In particular, the velocity is calculated with the time that the cavity takes from transmitting 10% of the power when in resonance to transmit 40% of it. Simulations proved that it exists a linear relationship between both parameters that provides the velocity online with 1% of accuracy, and the method has been implemented in Advanced Virgo arm cavities successfully. An example is shown in Figure 2.

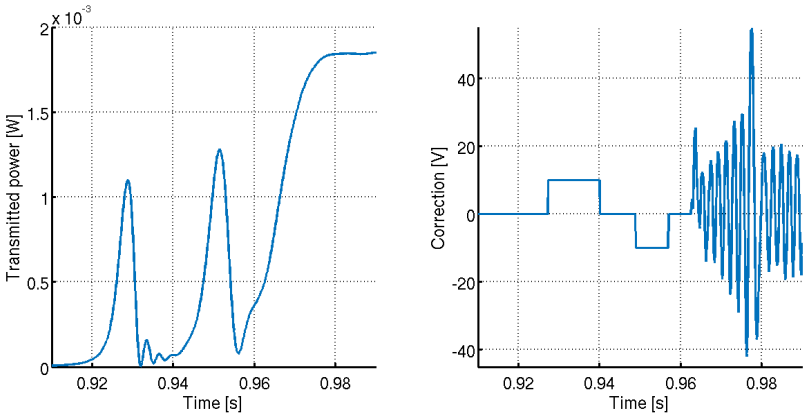


Figure 2 – Transmitted power and corrections sent to the mirror.

The advantages of this method is that it provides the velocity in physical units and that it is calculated before the resonance is crossed, increasing the success rate. The main disadvantage is that it is valid only while the velocity is slow enough that the cavity build-up reaches 40%. In the case of Advanced Virgo it is valid up to 1.4μm/s, which was enough for our needs.

4 Power Recycling Cavity stability: impact on the lock acquisition

An optical cavity is stable when it exists a Gaussian beam that can resonate inside it. The stability condition is the following:

$$0 < g_1 \cdot g_2 < 1 \tag{2}$$

where g_1, g_2 are defined as $g_i = 1 - \frac{L}{R_i}$ where L is the cavity length and R_i is the radius of curvature of the mirrors. Notice that it depends on geometrical considerations only.

The PRC of Advanced Virgo is very close to instability ($1\text{-}g_1 g_2 \sim 0.19 \cdot 10^{-5}$). This translates into Higher Order Modes (HOM) resonating very close to the fundamental mode, which means that they will couple strongly to the PRC modifying its optical configuration. These HOMs are produced by misalignments of the optical elements or by a bad matching of the beam to the cavity geometry. In particular, simulations showed that for a misalignment of 0.15μrad the optical gain of the sidebands inside the PRC cavity decreases an 80%, which can not be handled by a control loop.

The solution proposed to deal with this problem was to add a higher modulation frequency, which would experiment a lower finesse inside the PRC due to the presence of higher losses. In this case, the extra losses on the fundamental mode due to the coupling of HOMs would have a lower impact. This means that an error signal produced with a higher modulation frequency will be less sensitive to misalignment or mismatch and so the control will be more stable.

Using this new modulation frequency we have been able to reach the working point of the Advanced Virgo detector, and, in spite of the fluctuations of the optical gain, keep a stable control during long periods of time. An example of this is shown on Figure 3.

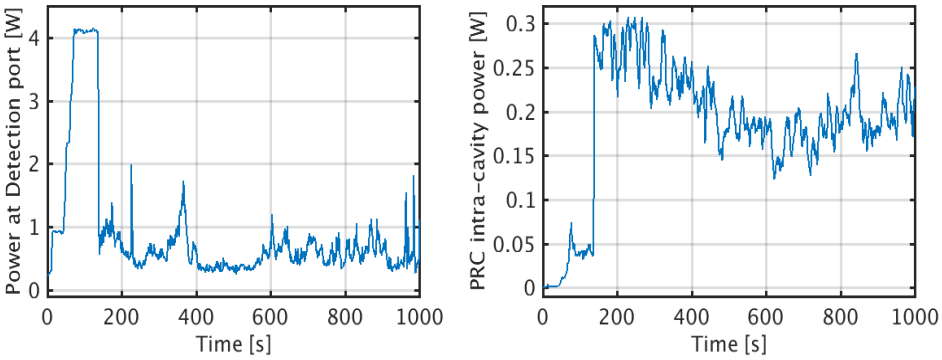


Figure 3 – Power at the Detection port and power of the sidebands inside the PRC at the working point.

5 Conclusion

The upgrades implemented to improve the sensitivity of the Advanced Virgo detector have arisen new challenges to the commissioning. Simulation work has been useful to anticipate and solve these problems. A new method for calculating the cavity velocity online has been presented as well as an alternative to deal with cavities very close to instability. The addition of an extra modulation frequency which experiences a lower finesse allows to keep a stable lock in the presence of HOMs. This work has allowed to bring the Advanced Virgo to its working point in a reliable way, and keep a stable control. In this conditions it is possible to work on reducing the presence of HOMs and then come back to the designed control strategy.

References

1. J. Camps *et al*, *Opt. Lett.* **20**, 2463 (1995).

All-sky search for long duration gravitational wave transients.

V.FREY
Laboratoire de L'Accélerateur Linéaire, ORSAY, FRANCE

The birth of gravitational wave astronomy carried out by the recent detection of Gravitational Waves (GWs) will allow a better understanding and characterization of astrophysical phenomena. For now, only signals from coalescence of two stellar-mass black holes were detected. Nevertheless it demonstrates that Advanced LIGO detectors reach a sensitivity good enough to catch interesting new sources. Among these new sources, some of them are expecting to produce long duration GWs. Between 10s up to several minutes duration, these signals are predicted to be generated by astrophysical compact sources experiencing complex dynamics, accretion and hydrodynamic instabilities. We explain the main steps of an all-sky un-modelled search dedicated to long duration GWs sources and give the most recent results obtained with LIGO data.

1 Introduction

Historically, in the LIGO/Virgo collaboration, searches for GWs fall into 4 categories depending on the knowledge we have on the signals and their duration. When the expected signal waveforms is precisely known like for compact binary coalescence, searches are based on matched filtering techniques. For poorly modelled signals we use time frequency decomposition methods. In the last few years, new searches targeting GW signals falling in between the categories have been developed. This is the case for the long duration search which bridge the burst/stochastic background/continuous waves parameters space.

Long duration transient gravitational waves signals are expected to be generated by promising sources. For example, fallback accretion onto a newborn neutron star can lead to a non-axisymmetric deformation which emits GWs until the neutron star collapses to a black hole [6,7,1]. Non-axisymmetric accretion disk instabilities can lead to material spiralling into the central stellar-mass black hole, emitting GWs [2,3]. Long-duration GWs may also be emitted by non-axisymmetric deformations in magnetars, which are possible progenitors of long and short GRBs [5]. The parameters space spanned by these sources was unexplored so far (see Section 2).

To deal with the large parameter space and to ensure an all-sky un-modelled search, we build an analysis the cross correlation between data from a pair of detector. Including a set of possible sky position we build coherent time-frequency maps where we extract significant triggers. The analysis details will be addresses in Section 3.

We have analysed all the LIGO observation runs since 2005. More precisely this concerns S5 and S6 runs where LIGO detectors reached their nominal sensitivity and advanced LIGO detectors data (O1) that recorded the first stellar mass black hole mergers. Virgo data was not included in the analyses. Even if no significant results were found, we set the first upper limit on the rate of events emitting long duration GW. We present the results of the full analysis in Section 4.

2 Sources

When evolving in extreme environment, compact objects, neutron stars and black holes, are expected to emit weak and long duration GWs. Waveforms prediction is rather inaccurate as it requires to take into account complex dynamic and hydrodynamic instabilities.

Accretion disk instability (ADIs): Massive accretion disk enclosed a stellar-mass black hole are susceptible to various non-axisymmetric instabilities that lead to fragmentation falling into the central black hole. This accretion disk instabilities (ADIs) dissipate energy via long duration GW. The resulting anti-chirp like signals last from 10s up to few hundred of seconds. The corresponding model depends on the mass of the central black hole M, the Kerr spin parameter a_*, and the fraction ϵ of the disk mass that forms clumps [2,3].

Fallback accretion disk (FA): Newly born spinning neutron stars can emit long duration GW in some unstable configurations where non-axisymmetric deformation appears. The signal lasts from $\sim$ 10 s up to $\sim$ a few 100 s and its frequency evolution is almost linear. We used a model of fallback accretion disk models described in [1].

Magnetar: Magnetic deformation of a rapidly rotating neutron star can generate long-lasting GWs that can live up to one hour with a slowly frequency and amplitude decreasing behaviour (anti-chirp). We used the model described in [4], which includes two parameters: the magnetic ellipticity ϵ_b and the spin frequency f_0 of the neutron star, that entirely describe the frequency and amplitude variations.

For all these models, waveforms are known to a mild degree of precision which renders match filtering techniques untrustable. Furthermore the multi dimensional physical parameters space of all models is huge. To cope with this, we consider the generic features, frequency and time evolution, of the waveforms. In order to completely span the parameters space, we also consider adhoc waveforms. Monochromatic waveforms (MONO) and waveforms with a linear (LINE) and quadratic (QUAD) frequency evolution, as well as white noise band-limited (WNB) and sine-Gaussian bursts (SG) [8]. All these waveforms have duration from $\sim$ 10 s up to a few $\sim$ 100 s and frequencies spanning the whole analysis range.

3 Pipeline

As already mentioned we are searching a weak signal in the data of LIGO-Virgo detectors without any assumption of its exact waveform, time of arrival or sky position of the source.

For each second of coincident data, the pipeline cross-correlates the data in the Fourrier domain and, considering a set of sky positions, compute coherent 1s $\times$ 1Hz pixels of SNR. The SNR is computed for each second of data by estimating the mean noise over the neighbouring seconds on each side. Pixels in frequency bins corresponding to known instrumental lines are suppressed. Because of computing resources limitation we don't test all sky positions. As a consequence, coherent GW signals can have negative SNR (anti-coherent). To recover these signals we apply a threshold on the absolute value of the pixels SNR. These selected pixels are then grouped to form triggers. The triggers SNR is the quadratic sum of the pixels SNR and is used as ranking statistic. Some veto are developed to get rid of triggers coming from instrumental and environmental noise. To estimate how significant is a trigger, we need to know the background trigger rate or false alarm rate (FAR) as a function of the ranking statistic.

Because the detector noise is non Gaussian we use the data themselves to estimate the background trigger rate. More precisely the background is estimated by time-shifting the data of one detector in steps of 250s.

Waveforms generated in the frame of the source, have been added coherently to the detectors' data at randomly chosen times over the full run period to estimate the search sensitivity. Sources are uniformly distributed over the sky. The signal amplitude is also varied in order to estimate the dependency of the efficiency on the strength of the signal at a given FAR. Efficiency is simply

the fraction of signals that are detected with a ranking statistic equal or larger than a value corresponding to the given FAR.

4 Results

Long duration GW signals have been searched in LIGO data recorded since 2005. In total $\sim$ 1 year of coincident data at nominal initial detector sensitivity (S5/S6), 48 days of the first advanced observation run (O1) and we are currently analysing the O2 dataset since November 2016.

4.1 S5/S6 results

Two vetoes against noise transients have been considered for the S5/S6 analysis. One, named DQFlags, is a selection of vetoes based on auxiliary channels that monitor the environment of the instrument. The other one, SNRfrac, is based on the shape of the triggers and designed to remove short (<1s) noise transients. Once the vetoes are applied, the distribution of background triggers is close to a Gaussian distribution, which is not usual in a GW transient search. Figure 1 shows the distributions of the cumulative rate of coincident data triggers and background triggers for the S5/S6 run.

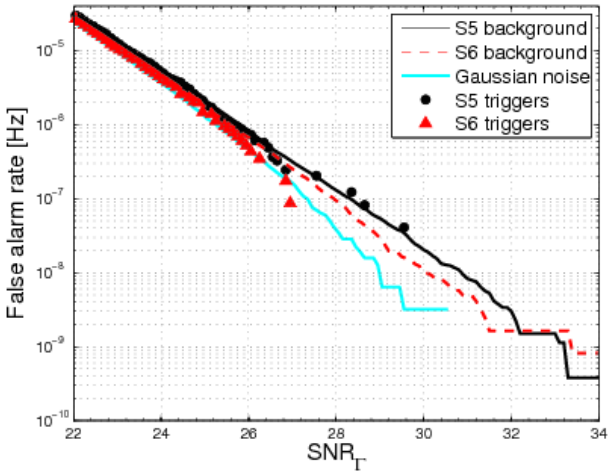


Figure 1 – Cumulative trigger rate as function of the ranking statistic for S5 and the S6 run. The search results are consistent with the expectation of accidental Gaussian noise coincidences.

The sensitivity was estimated using only adhoc and ADI waveforms. In table 1, we give the distance at which we detect 50% of the sources and the energy emitted by a source located at 10kpc and detected at 50% of efficiency using the quadripolar approximation. We are sensitive to the local Universe for ADI sources.

Table 1: S5/S6 search sensitivity for ADI waveforms for the initial generation run (S5/S6). The upper limit at 90% confidence level combines S5 and S6 dataset.

run	S5		S6		S5 + S6
Waveforms	distance$^{50\%}$[Mpc]	$E_{GW}^{50\%}$ [$M_\odot c^2$]	distance$^{50\%}$[Mpc]	$E_{GW}^{50\%}$ [$M_\odot c^2$]	$R_{90\%}$ [Mpc^{-3}yr^{-1}]
ADI A	5.4	1.5×10^{-7}	6.8	9.4×10^{-8}	9.4×10^{-4}
ADI B	16.3	1.9×10^{-7}	18.6	1.5×10^{-7}	3.4×10^{-5}
ADI C	8.9	9.9×10^{-7}	11.3	6.3×10^{-7}	2.2×10^{-4}
ADI E	11.5	3.3×10^{-7}	13.4	2.4×10^{-7}	1.1×10^{-4}

No significant triggers were detected during S5/S6 run. So we set upper limits on the rate at 90% confidence level by combining the two runs (see Figure 2). The short distance upper limit is dominated by the observation time and the far distance by the detectors' sensitivity.

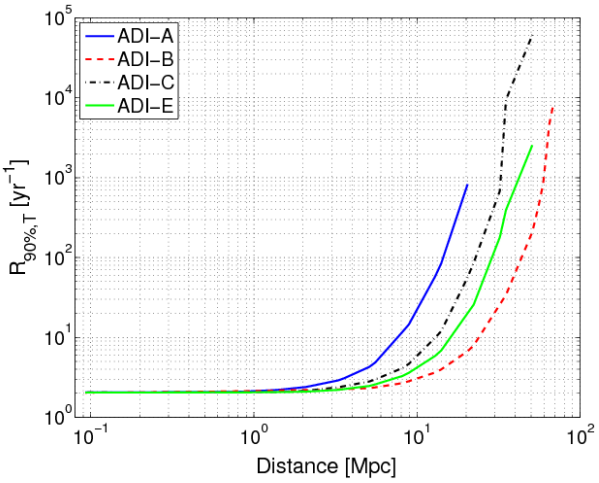


Figure 2 – Upper limits at 90% confidence level on the rate of GW events from accretion disk instability GW sources as a function of the distance of the source obtained with the S5/S6 dataset.

4.2 O1 results

The search frequency range was extended up to 2000Hz. Magnetar and FA waveforms (see section 2) were added to comple our cataclogie of GW signals.

With respect to S5/S6, the data was noisier urging us to develop two new vetoes. One to remove non stable specific lines during specific periods. These lines have instrumental origin and were exited at the beginning of some interferometer relocks. The other veto is based on the SNR ratio in each detector in order to remove the dramatic coincidence between loud instrumental triggers in one detector and a small noise fluctuation in the other. Once all vetoes are applied we expect a quasi normal distribution for the background triggers.

Concerning the sensitivity, we expect a factor 3 with respect to the first generation of detectors. Figure 3 shows the GW energy emitted by a source at 10kpc detected with an efficiency of 50%.

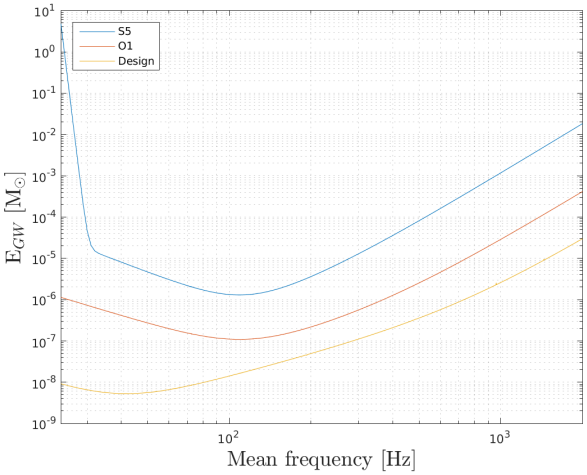


Figure 3 – GW energy emitted by a source located at 10kpc and detected with an efficiency of 50%. The S5 curve is obtained using the S5/S6 results. The O1 and design are extrapolated from the S5 curve considering the O1 and design LIGO sensitivity curves.

5 conclusion

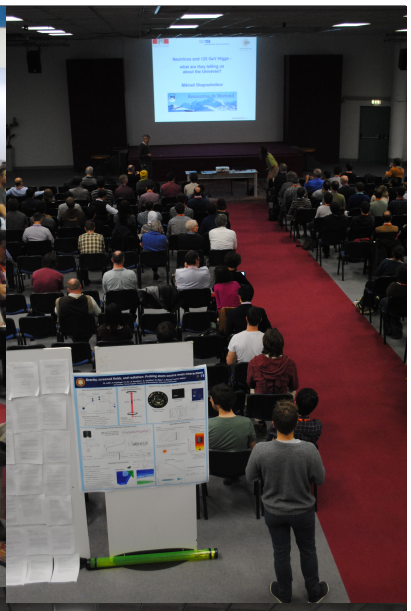
The long duration gravitational waves transient search, if is a recent one, has gain a certain maturity mitigating the lack of models with a robust analysis. Gateway between burst, stochastic background, and continuous waves searches, the long duration search has gained its letter of nobless for the LIGO/Virgo collaboration. The search becomes more an more interesting along the sensitivity increase.

The current Observing run O2 which started on November 2016 is promising : the LIGO sensitivity has now increased a bit and Virgo should join before the end of the run.

References

1. A. L. Piro and E. Thrane, Astrophys. J **761**, 63 (2012).
2. M. H. P. M. van Putten, *Phys. Rev. Lett.* **87**, 9110 (2001).
3. M. H. P. M. van Putten, Astrophys. J. Lett. **684**, (2008).
4. Simone Dall'Osso and Bruno Giacomazzo and Rosalba Perna and Luigi Stella, Astrophys. J. **798**, 2015 (.)
5. Corsi, A. and Mészáros, P., Astrophys. J. **702**, (2009)
6. Lai, Dong and Shapiro, Stuart L., Astrophys. J. **442**, (1995)/
7. Cutler, Curt", *Phys. Rev. Lett.* **66**, 084025 (2002).
8. Abbott, Benjamin P. and others, *Phys. Rev.* D **93**, 042005 (2016)






quite unexpected ... the Higgs boson is nothing else, confirming the Standard Model.


The missing piece of the SM





GRAVITATIONAL WAVE SIGNALS FROM MULTI-DIMENSIONAL CORE-COLLAPSE SUPERNOVA EXPLOSION SIMULATIONS

K.N. Yakunin[a], E. Endeve[a,b,d], A. Mezzacappa[a,b],
M. Szczpanczyk[e], M. Zanolin[e] P. Marronetti[f],
E.J. Lentz[a,b,c,g], S.W. Bruenn[h], W.R. Hix[a,c],
O.E.B. Messer[a,c,i], J.M. Blondin[j], and J.A. Harris[i,k]

[a] *Department of Physics and Astronomy, University of Tennessee, Knoxville, TN 37996-1200, USA*
[b] *Joint Institute for Computational Sciences, Oak Ridge National Laboratory, P.O. Box 2008, Oak Ridge, TN 37831-6354, USA*
[c] *Physics Division, Oak Ridge National Laboratory, P.O. Box 2008, Oak Ridge, TN 37831-6354, USA*
[d] *Computer Science and Mathematics Division, Oak Ridge National Laboratory, P.O.Box 2008, Oak Ridge, TN 37831-6164, USA*
[e] *Department of Physics, Embry Riddle Aeronautical University, Prescott, AZ 86301-3720,USA*
[f] *Physics Division, National Science Foundation, Arlington, VA 22207 USA*
[g] *Joint Institute for Nuclear Physics and its Applications, Oak Ridge National Laboratory, P.O. Box 2008, Oak Ridge, TN 37831-6374, USA*
[h] *Department of Physics, Florida Atlantic University, 777 Glades Road, Boca Raton, FL 33431-0991, USA*
[i] *National Center for Computational Sciences, Oak Ridge National Laboratory, P.O. Box 2008, Oak Ridge, TN 37831-6164, USA*
[j] *Department of Physics, North Carolina State University, Raleigh, NC 27695-8202, USA*
[k] *Lawrence Berkeley National Lab, Berkeley, CA 94720, USA*

In this work we report briefly on the gravitational wave (GW) signal computed in the context of a self-consistent, three-dimensional (3D) simulation of a core-collapse supernova (CCSN) explosion of a 15 $M_\odot$ progenitor star. We present a short overview of the GW signal, including signal amplitude, frequency distribution, and the energy emitted in the form of GWs for each phase of explosion, along with neutrino luminosities, and discuss correlations between them.

1 Introduction

The era of gravitational wave (GW) astronomy began with the first direct detections of GW signals from binary-black-hole mergers [1,2]. Among the sources of Earth-detectable GWs we can include core-collapse supernovae (CCSNe), which are physics rich. They result from the rapid collapse and violent explosion of a massive star ($M{>}8M_\odot$), and are one of the most energetic burst phenomena in the Universe. An enormous amount of energy ($\sim 10^{53}$ erg) is released in the form of neutrinos, synthesized matter, and electromagnetic and gravitational radiation. Simultaneous detection of these signals will help us reveal details of the physical processes taking place under the extreme conditions as a massive star explodes [for a comprehensive review, see, e.g., Ott (2009) [4]]. Thus, any advanced study of CCSN requires detailed simulation of the processes in the supernova core, and physical fidelity of CCSN simulations is crucial. However, self-consistent CCSN simulations that include the physics necessary for production of realistic GW templates (e.g., neutrino transport with a complete set of weak interactions and effects

of general relativity) are extremely compute intensive, and demand computing at the extreme scale. For instance, the number of processors required to perform the 3D simulation presented here was on the order of 10^5, and the full simulation, until the onset of explosion (350–400 ms) required $\sim 10^8$ CPU hours. In spite of recent advances in simulation codes and computational resources, few groups [5,9,10] have performed 3D simulations that include the necessary physics for realistic GW templates. Since CCSNe are one of the most promising sources for multimessenger astronomy due to their strong combined neutrino and GW signals, these 3D models are able to produce the most reliable GW and neutrino signals, and deduce potential correlations between them, and could help not only detect GW signals from CCSN, but also help resolve a number of open questions concerning the physics of the CCSN explosion mechanism. To contribute to these efforts, we present here a short overview of GW and neutrino signals from a 3D simulation carried out with the CHIMERA code.

2 Model Description

Our analysis is based on the 3D CCSN simulation of the $15M_\odot$ progenitor of Woosley & Heger [11], performed by Lentz *et al.* [5] (Fig. 1). The simulation is performed with the neutrino radiation hydrodynamics code CHIMERA that includes neutrino transport with a modern set of weak interactions through the "ray-by-ray-plus" approach, a nuclear equation of state, and an effective relativistic gravitational potential. The effective gravitational potential for self-gravitating fluids is build from a Newtonian potential by replacing the leading term in its spherical harmonic expansion with the TOV potential. The effective potential mimics the deeper potential well obtained in full GR [6]. Gravitational redshift of the neutrino spectrum is also included in the transport scheme. The 3D computational grid consist of $540(r)\times180(\theta)\times180(\phi)$. The θ-resolution varies from $2/3^\circ$ near the equator to 8.5° near the poles. The ϕ-resolution is uniform and equal to 2°. The radial resolution varied according to the structure of the collapsed core in our adaptive mesh, and reached $\sim$0.1 km inside the proto-neutron star (PNS).

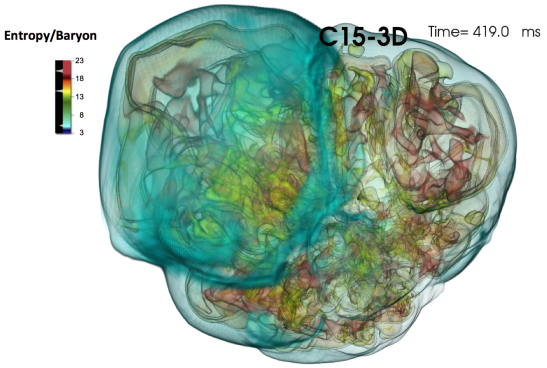


Figure 1 – Volume rendering of the specific entropy from a CCSN explosion simulation with the CHIMERA code. The large rising plumes drive the expansion of the shock, while active accretion onto the PNS surface sustains neutrino emission, and contributes to the GW signal.

3 Results

A CCSN passes through several phases before the onset of explosion. The massive star's iron core collapses, with inner core densities ultimately exceeding nuclear densities. At these extremes, the inner core rebounds due to the stiffening of the EoS and launches an outgoing shock wave. Within a $\sim$ 100 ms after bounce, the shock stalls due to energy loss by neutrino emission and dissociation of iron falling through the shock. It is revived by neutrino energy deposition behind the shock, but aided by hydrodynamical instabilities [3]. Instabilities operating inside the PNS, large scale convection in the neutrino heated, post-shock region, and the standing accretion shock instability (SASI), contribute to produce a strong GW burst signal that can be detected by GW observatories (cf. Fig. 1).

3.1 GW signal

The typical GW signal from axisymmetric (2D) explosion models, carried out to about two seconds after bounce, consists of four main phases [7]. The structure of our 3D waveform is similar to what was obtained in the 2D case. The early GW signal is produced by prompt convection inside the PNS that develops behind the quickly expanding, newly formed shock. It lasts for 70–80 ms after bounce. The GW energy emitted during the early phase is $\sim 4 \times 10^{-11} M_\odot\, c^2$ (Fig. 2 bottom right). Note that the GW energy of the early signal is much higher in 3D than in 2D. This can be explained by the inverse turbulent cascade in 2D: turbulent energy accumulates artificially in large scale eddies, decreasing the emitted GW energy. The quiescent phase (80–120 ms) is the result of shock stagnation and ceasing of the initial prompt convection. Other fluid instabilities have not yet developed. The strongest phase of the GW signal starts at around 120 ms. It is the result of a non-linear interaction between different types of instabilities. Active accretion on the PNS surface induces the density disturbances inside the PNS (g-modes) that produce the most energetic GW signal. In turn, active accretion is formed due to the superposition of neutrino-driven convection and the SASI. The GW energy emitted during the strong signal phase is $\sim 2 \times 10^{-9} M_\odot\, c^2$, which is almost two orders of magnitude higher than the GW energy emitted in the early phase. In contrast with the early phase, more GW energy is emitted in the 2D model than in the 3D model during the strong phase. Here, the additional dimension allows development of global, low frequency modes (e.g., spiral SASI modes and large scale convection) that are suppressed in the 2D models. The spectrogram of the GW signal confirms the presence of stronger low-frequency (50–200 Hz) activity in the signal (Fig. 2; top right). The fourth phase – DC offset ("tail") in the signal observed in the 2D models due to shock expansion [7] is not yet present in the 3D model. The onset of explosion in the 3D model is delayed by about 100 ms relative to the 2D model [5]. Consequently, during the 450 ms considered here, we do not observe the low-frequency tail in the GW signal. It may appear later, but will probably be less pronounced due to the different explosion morphologies in 2D and 3D. In the 2D models, the heating region is divided into 2–3 large volumes due to the presence of 1–2 accretion downflows. When these volumes acquire enough energy from neutrinos they begin to expand at the same time. The picture is different in the 3D model. There are multiple down flows splitting the heating region into multiple volumes of relatively small sizes. When one of these volumes becomes sufficiently large it starts to expand while others do not [5] (Fig. 1).

3.2 Neutrino signal

Neutrinos play a fundamental role in CCSNe. They carry most (99%) of the gravitational binding energy liberated during iron core collapse. As such, neutrinos are the major source of energy for the supernova explosion in the delayed neutrino-driven mechanism. [3]. Moreover, the observation of supernova neutrinos from a CCSN will provide not only important insights into the dynamics inside the exploding star, but will also significantly increase the chances for detection of the GW signal from the supernova event.

Neutrino luminosities from the 3D model are plotted in the bottom left panel in Fig. 2. The first prominent feature is the well-known electron neutrino, or neutronization, burst that occurs when the post-shock matter becomes transparent to neutrinos shortly after bounce. During the later phase, the electron neutrino and antineutrino luminosities are largely regulated by the mass accretion onto the PNS. (The neutrino luminosities are also sensitive to PNS parameters; e.g., compactness, surface temperature.) As the accretion rate drops, the relative contribution of the electron neutrino and antineutrino flux decreases. The significant variations in the neutrino luminosity for $t > 150$ is due to variations in mass accretion (in response to fluid instabilities operating). The variations in the ν-luminosity in 2D are larger than in 3D because multiple accretion down flows in the 3D model are less massive than the 1–2 down flows present in the 2D model. The heavy flavor neutrinos (ν_μ, ν_τ; emanating deeper in the PNS) show a steady

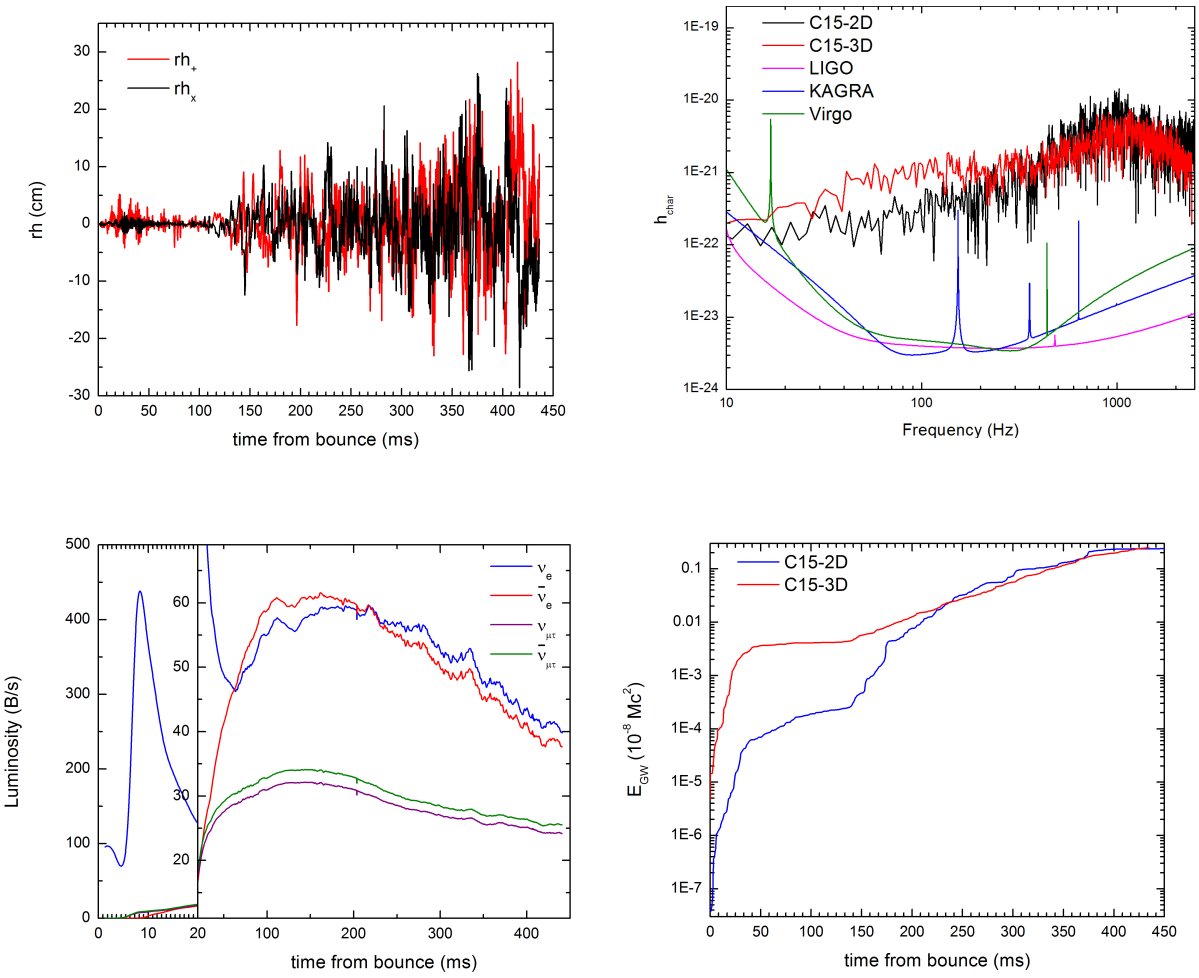


Figure 2 – Two polarizations of the GW signal as they are seen by observer at the equator (top left), characteristic spectral strain $h_{\rm char}$ of 2D and 3D models at a distance of 10 kpc compared with the design noise levels of the current and future GW detectors (top right), neutrino luminosities for each type of neutrino included in the simulation (bottom left), and energy emitted in the form of GWs for C15-2D and C15-3D models (bottom right).

decline after about 150 ms, and are not as sensitive to sudden variations in accretion. It is worth noting that the fluctuations of the ν-luminosities are a consequence of oscillations in mean shock radius. Thus, the SASI activity is imprinted on neutrino signal. When comparing the top and bottom left panels of Fig. 2, a correlation between the neutrino and GW signals can be inferred. Immediately after the neutronization burst, there are no significant variations in the neutrino luminosities. This phase coincides with the quiescent phase of the GW signal. The strongest variations in the neutrino signal coincide with the large amplitude spikes in the GW signal. This is to be expected since both features are due to variations in accretion onto the PNS, and a response to explosion dynamics.

4 Outlook

Despite the complexity of supernova physics, several groups are now able to simulate CCSN explosions with high physical fidelity, and compute GW and neutrino signals from 3D models [8,9,10]. However, only a handful of models exist today. The 3D simulations of Lentz *et al.* [5] and Andresen *et al.* [9] have similar physics input: spectral neutrino transport with full set of weak interactions and effective GR potential. The fully relativistic simulation of Kuroda *et*

al. [10] includes energy-integrated (grey) neutrino transport and a reduced set of weak interactions. Each of these groups still employs approximations to be able to complete simulations, but work on improvements are underway; e.g., better resolution, better algorithms well suited to modern computer architectures, and improved physical fidelity in both the gravity and the neutrino transport sectors. There are robust features of the GW signals that are common across simulations, but there are differences in the waveforms too [8,9]. These differences motivate us to establish closer collaborations between supernova modeling efforts and to look deeper at the problem. By continuing the work to model CCSN, with independent codes, we will obtain a larger catalog and more robust waveforms to aid in GW searches.

Acknowledgments

This research was supported by the U.S. Department of Energy Offices of Nuclear Physics and Advanced Scientific Computing Research, the NASA Astrophysics Theory and Fundamental Physics Program (grants NNH08AH71I and NNH11AQ72I), and the National Science Foundation PetaApps Program (grants OCI-0749242, OCI-0749204, and OCI-0749248) and Gravitational Physics Program (grant GP-1505933).

References

1. B.P. Abbott *et al.*, *Phys. Rev. Lett.* **116**, 061102 (2016).
2. B.P. Abbott *et al.*, *Phys. Rev. Lett.* **116**, 241103 (2016).
3. H.-T. Janka, *Ann. Rev. Nucl. Part. Sci.* **62**, 407 (2012).
4. C.D. Ott, *Class. Quant. Grav.* **26**, 063001 (2009).
5. E.J. Lentz *et al.*, *Astrophys. J. Lett.* **807**, L31 (2015).
6. A. Marek *et al.*, *Astrophys. J.* **445**, 273 (2006)
7. K.N. Yakunin *et al.*, *Phys. Rev.* D **92**, 084040 (2015).
8. K.N. Yakunin *et al.*, *arXiv:1701.07325v1*, (2017).
9. H. Andresen *et al.*, *arXiv:1607.05199*, (2016)
10. T. Kuroda *et al.*, *Astrophys. J. Lett.* **829**, 14 (2016).
11. S.E. Woosley and A. Heger, *Phys. Rep.* **442**, 269 (2007).
12. J. Cooperstein, *Nucl. Phys.* A **438**, 722 (1985).
13. J.M. Lattimer and D.F. Swesty, *Nucl. Phys.* A **535**, 331 (1991).
14. S. Bruenn *et al.*, *Astrophys. J.* **818**, 123 (2016)


Some
Slalom
Winners

ELECTROMAGNETIC FOLLOW-UP OF GRAVITATIONAL WAVE TRANSIENTS: FIRST RESULTS AND PERSPECTIVES

B. PATRICELLI
on behalf of the LIGO Scientific Collaboration and the Virgo Collaboration
Scuola Normale Superiore, Piazza della Carovana 7,
56126 Pisa, Italy
&
INFN - Sezione di Pisa, Largo B. Pontecorvo 3,
56127 Pisa, Italy



The recent detection of gravitational waves from the merger of binary black holes marked the birth of gravitational wave astronomy and opened a new chapter in the multi-messenger study of the Universe. Among gravitational wave sources, mergers of binary neutron stars and black holes are thought to be associated with electromagnetic transient phenomena, such as short Gamma Ray Bursts. Simultaneous observations with gravitational interferometers and ground-based or space telescopes will thus provide an unique opportunity to find the electromagnetic counterparts of these gravitational wave sources. In this paper I review the astrophysical sources expected to emit transient multi-messenger signals, discuss the results on the electromagnetic follow-up campaign performed during the first observing run of Advanced LIGO, and highlight the perspectives and challenges for future science runs.

1 Introduction

The detection of gravitational waves (GWs) by the two interferometers of the Advanced Laser Interferometer Gravitational-Wave Observatory (LIGO [1]) opened the era of GW astronomy. The two detected events, labeled GW150914 and GW151226, are both consistent with the coalescence of two black holes (BBH) at a distance of $\sim$400 Mpc (see Abbott et al. 2016a,b [2,3]).

Detailed analysis of the GW signals allowed to measure several of the source physical parameters. For example, the masses of the two BHs have been estimated to be (in the source frame) $36.2^{+5.2}_{-3.8}$ $M_\odot$ and $29.1^{+3.7}_{-4.4}$ $M_\odot$ for GW150914, $14.2^{+8.3}_{-3.7}$ $M_\odot$ and $7.5^{+2.3}_{-2.3}$ $M_\odot$ for GW151226 (Abbott et al. 2016c [4]). The measured BH masses in GW150914 are higher than any of the BH masses dynamically measured reliably from X-ray binaries (see, e.g., Özel et al. 2010 [9]) and represent a clear evidence that relatively "heavy" BHs ($M > 25$ $M_\odot$) can form in nature. Such heavy BHs require massive progenitors and weak star winds. Given our current understanding of massive-star winds and their dependence on metallicity, the binary systems of heavy BHs

form in an environment with a metallicity lower than about half of the solar value. The BBH formation in a dense star cluster or from an isolated binary are both consistent with GW150914 (see Abbott et al. 2016d [10]) and GW151226 (see Abbott et al. 2016c [4]).

To obtain a more complete knowledge of the environment of GW sources, as well as of the source nature, multi-messenger astronomy is needed. In fact, the detection of an EM counterpart would give a precise localization and potentially lead to the identification of the host galaxy of the source, thus also determining its redshift; furthermore, it would considerably increase the confidence in the astrophysical origin of the GW signal.

Joint EM and GW observations can be performed through the EM follow-up or the externally triggered GW searches. In the EM follow-up a GW event is detected by online data analysis pipelines and a GW alert is promptly issued to a network of EM observatories, that start observing the sky region consistent with the GW signal (see, e.g., Abadiet et al. 2012 [5], Evans et al. 2012 [6], Aasi et al. 2014a [7]). In the externally triggered GW searches a EM transient is detected, and then GW data are analyzed in detail to find a possible GW signal in temporal and spatial coincidence with the observed EM signal (see, e.g., Aasi et al. 2014b [8]).

The EM follow-up of GW transient events is challenging for several reasons. First of all, the sky localization of GW events can be very poor. In fact, GW sources are mainly localized via triangulation methods, based on the observed time delays, phase differences, and relative amplitude of the GW signal at different detectors. For this reason, the larger is the number of GW detectors in the network, the smaller is the GW error box in the sky localization; with only two detectors (i.e., the two Advanced LIGO interferometers), the GW sky localization areas are of the oder of 100-1000 square degrees. Another challenge is represented by the need of a low-latency program to detect GW candidates and send alerts to the astronomical community in nearly real-time, to allow astronomers to start EM observations as promptly as possible.

This review describes the transient sources expected to have a multi-messenger emission and summarize the results of the EM follow-up campaign associated to the first GW detections. The work is organized as follows. In section 2 we describe the GW transient sources and their expected EM and neutrino counterparts; in section 3 we explain how low-latency GW searches are performed; in section 4 we present the results obtained from multi-messenger searches during the first observing run of Advanced LIGO, while in section 5 we discuss the future observational scenario. Finally, in section 6 we present our conclusions.

2 Multi-messenger emission from transient sources

In the universe there are many transient sources expected to emit both GWs and radiation in different electromagnetic bands. In the following we will describe these sources and their expected multi-messenger emission.

2.1 GW transient sources

Besides BBHs, the most promising transient sources that emit GWs at the frequencies at which ground-based interferometers (such as Advanced LIGO) are sensitive (10 Hz - 10 kHz) are the coalescences of binary systems of compact objects (CBC) composed by two neutron stars (NS-NS) or a neutron star and a stellar mass black hole (NS-BH). These events are among the most energetic: for instance, the energy emitted in GWs from the inspiral of a NS-NS system is of the order of 10^{-2} $M_\odot$ c^2 (see Peters 1964 [11]). For CBC systems the GW waveform is accurately modeled by post-Newtonian approximation and numerical simulations, therefore the GW signals can be searched with the matched filter modeled search (see, e.g., Wainstein & Zubakov 1962 [12], Cannon et al. 2012 [13], Messick et al. 2017 [14], Adams et al. 2016 [15], Veitch et al. 2015 [16], Dal Canton et al. 2014 [17], Usman et al. 2016 [18], Nitz et al. 2017 [19]).

Another class of transient GW sources that may be observed by ground-based interferometers are the core-collapsing massive stars (see Ott 2009 [20] and Kotake et al. 2006 [21] for an overview).

These sources are expected to emit GWs if there is some asymmetry in the stellar envelope ejection phase. However, the large uncertainties affecting our knowledge on the collapsing phase of these objects makes highly uncertain the GW released energy (it is expected to be in the range 10^{-8} $M_\odot$ c^2 to 10^{-5} $M_\odot$ c^2) and, as a consequence, there is large uncertainty also in maximum distance at which these sources can be detected. Furthermore, the modeling of the GW signal is quite complicated, so the GW signals are searched with the so called "unmodeled searches", with minimal assumptions about the GW waveform.

The last class of transient GW sources is represented by rotating NSs with very intense magnetic fields, of the order of 10^{15} G (magnetars). Theoretical studies predict that when such stars undergo starquakes, asymmetric strains can temporally alterate the geometry of the star and GWs are expected to be emitted (see, e.g., Corsi & Owen 2011 [22]). Also in this case, the expected amount of GW energy emitted is highly uncertain (it might be in the range 10^{-16} - 10^{-6} $M_\odot$ c^2), and the GW waveform is uncertain as well, so the GW signals are searched with the unmodeled searches.

2.2 The EM and neutrino counterparts

The GW transient sources described in section 2.1 are expected to have also an associated EM emission. For instance, NS-NS and NS-BH mergers are thought to be the progenitors of short Gamma Ray Bursts (GRB): intense and highly variable flashes of γ-rays whose duration is $<$ 2 s (the prompt emission), sometimes followed by a long lasting afterglow emission at lower energies (X-rays, optical, radio). Coalescing NS-NS systems are also theoretically predicted to isotropically eject a quantity of neutron rich matter; the radioactive decay of heavy nuclei synthesized in this ejecta through r-processes produces a thermal optical/NIR emission: the "kilonova". Finally, a radio blast wave emission can also be observed, due to the interaction of the merger ejecta with the interstellar medium. For a review see Metzger & Berger 2012 [23].

The core-collapse of massive stars are accompanied by supernova (SN) emission at optical and radio frequencies, generally observed starting from days to weeks after the collapse and lasting from weeks to years. The SN emission can be preceded by a bright flash of radiation created as the shock wave generated by the collapsing core reaches the surface of the star: this is the so called "shock break-out" (SBO) emission, that has been observed in X-rays and optical (see, e.g., Soderberg et al. 2008 [24] and Garnavich et al. 2016 [25]). Another EM emission expected from the core-collapse of massive stars is represented by long GRBs[a], that sometimes have been observed in association with SN emission (see, e.g., Modjaz et al. 2006 [26]).

Soft Gamma Repeaters (SGRs) and Anomalous X-ray Pulsars (AXP) are sources which sporadically emit short bursts of gamma-rays and X-rays at irregular intervals (see Mereghetti 2008 [27] for a review). Both objects are largely believed to be associated to magnetars experiencing starquakes and consequent crust disruption. GW emission associated to starquakes can also be accompanied by a radio/X-ray pulsar glitch: a sudden increase in the rotational frequency of a highly magnetized, rotating NS (pulsar) followed by exponential decays, which bring back the pulsar to the initial value (see e.g. Espinoza et al. 2011 [28]).

The above described EM sources, in particular GRBs and SNe, are expected to produce relativistic outflows in which particles (protons and nuclei) can be accelerated and produce high-energy neutrinos by interacting with the surrounding medium and radiation. For instance, MeV neutrinos have bee detected from SN 1987A in the Large Magellanic Cloud (at a distance of D$\sim$50 kpc) by the Kamiokande-II (Hirata et al. 1987 [29]) and the Irvine-Michigan- Brookhaven (Bionta et al. 1987 [30]) neutrino detectors, a few hours before its optical counterpart was discovered.

[a] Long GRBs are characterized by a longer duration ($>$ 2 s) of the prompt emission and a softer spectrum with respect to short GRBs.

3 Low-latency GW data analysis

As mentioned in the Introduction, one of the challenges of successfully obtaining prompt EM observations is to identify the GW candidates quickly: the data from the interferometers must be transferred and analyzed in near-real time. The LIGO Scientific Collaboration and the Virgo Collaboration (the LVC collaboration) developed a low-latency follow-up program, that is schematized in figure 1.

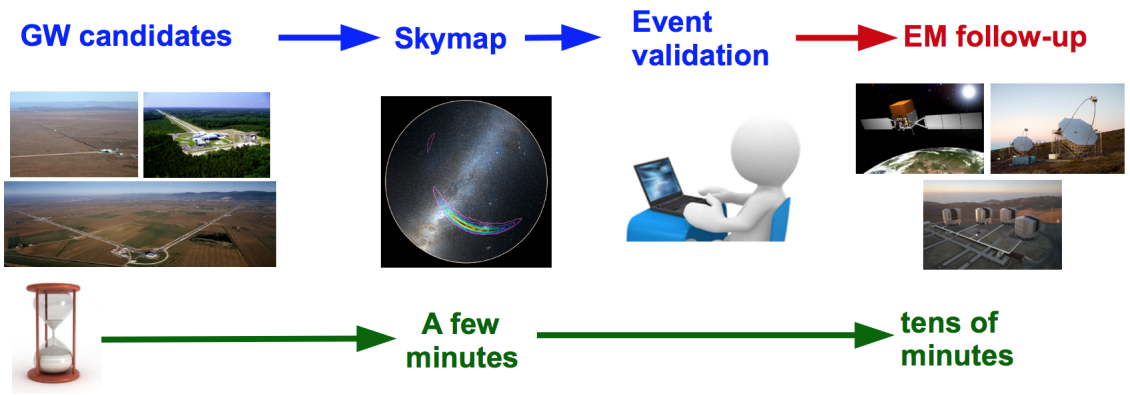


Figure 1 – Schematization of the low-latency follow-up program.

Several automatic low-latency GW data analysis pipelines have been built to continuously monitor the GW data, to search for transient GW signals that are coincident in the two detectors within the 10 ms light travel time separating them (see, e.g., Klimenko et al. 2016 [31], Lynch et al. 2015 [32], Cannon et al. 2012 [13], Messick et al. 2016 [14], Adams et al. 2015 [15], Usman et al. 2016 [18]). These pipelines report GW candidates within a few minutes of data acquisition, and estimate the potential sky position of the source. Once the candidates are identified, there is a manual "event validation": a team of experts evaluate the detector performances at the time of the trigger and the quality of the data. If the event candidate passes all the checks, a GW alert is sent to the astronomers, and the EM follow-up of the GW event can start.

Event candidate triggers as well as their skymaps are shared with astronomers through the Gamma ray Coordinates Network (GCN) protocol, consisting of machine-readable Notices plus short bulletins (Circulars) with human descriptions of the events[b]. These GCNs are currently restricted, until the GW event has been published, to astronomers who signed a Memorandum of Understanding (MoU)[c] with the LVC collaboration.

4 The EM follow-up campaign during O1 and O2

The first Advanced LIGO observational run (O1) took place from September 2015 up to January 2016. During O1, three GW alerts have been shared with the astronomers who signed a MoU. Although binary BH mergers are not expected to emit detectable EM emission nor neutrinos, the GW detections were followed by an impressive multi-messenger campaign, involving tens of instruments (satellites and ground-based telescopes) covering the whole electromagnetic spectrum, from radio to very high energy γ-rays (see Abbott et al. 2016e [33]).

On September 14, 2015, there was the first GW detection (Abbott et al. 2016 [2]): GW150914, with a statistical significance of more than 5.3 σ and a False Alarm Rate (FAR) $< 6\times10^{-7}$ yr^{-1}. An initial announcement (via email) on September 16, and a GCN Circular (GCN 18330) on September 20, were sent to the 63 teams of astronomers who signed the MoU, together with two skymaps obtained by two different data analysis pipelines: Coherent Wave Burst (cWB,

[b] https://gcn.gsfc.nasa.gov/lvc.html
[c] https://gw-astronomy.org/wiki/LVEM/PublicParticipatingGroups

Klimenko et al. 2016 [31]) and Omicron+LALInference Burst (oLIB, Lynch et al. 2015 [32]). The most accurate skymap by LALInference (Veitch et al. 2015 [16]) showed a 90% probability area of 630 deg^2 (Abbott et al. 2016f [34]). Despite this very huge GW error box, there was a good sky coverage at all wavelengths, with a contained probability of 100% in gamma-rays, 85 % in X-rays, 86 % in radio and $\sim$ 50 % in optical (see Abbott et al. 2016e [33]). Several optical candidate counterparts have been found, but all of them have been identified to be normal population type Ia and type II SN, with a few dwarf novae and active galactic nuclei (AGNs) that are all very likely unrelated to GW150914 (see, e.g., Smartt et al. 2016a [35], Kasliwal et al. 2016 [36], Copperwheat et al. 2016 [37]). A weak transient signal was found in *Fermi* GBM data 0.4 s after the time of GW150914 (Connaughton et al. 2016 [38]), but no corresponding signal was found in the INTEGRAL SPI-ACS instrument (Savchenko et al. 2016 [39]) or AGILE (Tavani et al. 2016 [40]). The IceCube and ANTARES collaborations performed a high-energy-neutrino follow-up of the GW event, but they found no neutrino candidates in both temporal and spatial coincidence with GW150914 (Adrián Martínez et al. 2016 [41]).

On October 22, 2015 a second GW candidate was observed and a GW alert was released to the astronomical community (GCN 18442). However, off-line GW data analysis found it not to be an event of interest and a retraction was submitted with a new GCN about one month later (GCN 18626).

On December 26, 2015, a third GW candidate was detected. Off-line refined analysis of the GW data confirmed this event, labeled GW151226, to be a real event, with a significance of more than 5.3 σ and a FAR $< 6\times10^{-7}$ yr^{-1} (Abbott et al. 2016 [3]). The GW alert was sent to partner astronomers nearly two days after the GW event occurred with a GCN (GCN 18728), together with a skymap. As for GW150914, many optical candidate counterparts have been found, but all of them have been identified to be normal population type Ia and type II SN, dwarf novae and AGNs, all unrelated to GW151226 (see, e.g., Copperwheat et al. 2016 [37], Smartt et al. 2016b [42], Cowperthwaite et al. 2016 [43]). The IceCube and ANTARES collaborations performed a high-energy-neutrino follow-up of the GW event, but they found no neutrino candidates in both temporal and spatial coincidence with GW151226 (Adrián Martínez et al. 2017 [44]).

The second scientific run of Advanced LIGO (O2) started on November 30, 2016 and is currently in progress. Up to now, 92 teams of astronomers have signed a MoU with LVC (this number includes ANTARES and IceCube for the neutrino follow-up). Among these groups, 84 have observational capabilities for O2 and receive alerts. As of April 23, 2017 6 triggers have been identified by the online analysis, using a loose FAR threshold of one per month, and shared with astronomers who have signed MoUs with LIGO and Virgo for electromagnetic follow-up. A thorough investigation of the data and offline analysis are in progress; results will be shared when available[d].

5 Future perspectives: observing and localizing GWs in the next LIGO and Virgo scientific runs

Advanced Virgo [45] is expected to joint Advanced LIGO in the data taking before the end of O2. In the next years, both Advanced LIGO and Advanced Virgo will be upgraded, and will progressively increase their sensitivity up to a factor of ten with respect to the initial LIGO and Virgo: this will also increase the volume of the explorable universe, enhancing the probability to detect GW sources.

From the observations of BBH mergers during O1, it has been possible to infer the stellar-mass BBH merger rate in the local Universe, that is in the range 9-240 Gpc^{-3} yr^{-1}. Given this merger rate, it has been possible to estimate the expected number of detections during O2 and the third scientific run (O3), considering the space-time volume that will be surveyed. In particular, during O2 the probability to observe more than two (ten) BBHs is higher than $\sim$

[d] http://ligo.org/news/index.php#O2Apr2017update

80% (∼15%); during O3, the probability to observe more than ten (forty) BBHs is higher than ∼ 90% (∼ 20%; see Abbott et al. 2016c [4]).

The non detection of NS-NS and NS-BH systems during O1 allowed to put upper limits on their merger rate: $R_{\rm NS-NS} < 12600$ Gpc^{-3} yr^{-1} and $R_{\rm NS-BH} < 4600$ Gpc^{-3} yr^{-1}; these rates are consistent with the expectations from many theoretical models. The no detection of these systems during O2 and O3, with higher sensitivities and longer operation time, would imply stronger upper limits on these merger rates (see Abbott et al. 2016g [46]), possibly ruling out several theoretical models (e.g., Vangioni et al. 2016 [47]).

The sky localization of GW events is expected to significantly improve when three (or more) interferometers will be operative as a network. For instance, the presence of a third GW detector such as Virgo would have improved the sky localization of GW150914 to a few tens of square degrees both for the unmodeled and CBC searches (see Abbott et al. 2016e [33]). During O3, the percentage of NS-NS mergers expected to be localized within 5 deg^2 for the network composed by the two LIGO interferometers and Advanced Virgo is > 1-2 % (Abbott et al. 2016h [49]). Within the next six years, other GW detectors are expected to join Advanced LIGO and Advanced Virgo: KAGRA in Japan [48] and another LIGO detector in India[e]: this will further improve the sky localization of the GW events. For instance, with a network composed by the three LIGO interferometers and Advanced Virgo, the percentage of NS-NS mergers expected to be localized within 5 deg^2 is > 20% (Abbott et al. 2016h [49]). This will enhance the probability to find the EM counterparts, further expanding the frontiers of GW astronomy and the multi-messenger investigation of cosmic sources.

6 Conclusions

In this paper we have discussed the GW transient sources and their expected EM counterparts; furthermore, we have summarized the main results of the EM follow-up campaign performed during the first science run of Advanced LIGO. This campaign clearly demonstrated the capability of ground-based telescopes and satellites to provide a very good sky and energy coverage, as well as an optimal coordination among many astronomical facilities (ground-based telescopes and satellites). Advanced Virgo is expected to start operations soon and, within the next few years, also KAGRA and LIGO-India will become operative. With a 4 GW detector network, the sky localization of GW events is expected to significantly improve: this will enhance the probability to find the EM counterparts. The detection of an EM signal associated to a GW event is an important milestone for the future: GWs and photons provide complementary information about the sources and their environment, and a joint GW and EM detection will allow to better understand the physics underlying the most extreme objects in the Universe.

References

1. J. Aasi *et al*, *CQG* **32**, 074001 (2015).
2. B.P. Abbott *et al*, *Phys. Rev. Lett.* **116**, 061102 (2016a).
3. B.P. Abbott *et al*, *Phys. Rev. Lett.* **116**, 241103 (2016b).
4. B.P. Abbott *et al*, *Phys. Rev.* X **6**, 041015 (2016c).
5. J. Abadie *et al*, *A&A* **541**, 155 (2012).
6. P.A. Evans *et al*, *ApJ Suppl. Series* **203**, 28 (2012).
7. J. Aasi *et al*, *ApJ Suppl. Series* **211**, 7 (2014).
8. J. Aasi *et al*, *Phys. Rev. Lett.* **113**, 011102 (2014b).
9. F. Özel *et al*, *ApJ* **725**, 1918 (2010).
10. B.P. Abbott *et al*, *ApJ Letters* **818**, 22 (2016d).
11. P. Peters, *Phys Rev* **136**, 1224 (1964).

[e] https://www.ligo.caltech.edu/page/ligo-india

12. L.A. Wainstein and V.D. Zubakov, *Extraction of Signals from Noise*, Prentice-Hall, Englewood Cliffs (1962).
13. K. Cannon *et al*, *ApJ* **748**, 136 (2012).
14. C. Messick *et al*, *Phys. Rev.* D **95**, 042001 (2017).
15. T. Adams *et al*, *CQG* **33**, 175012 (2016).
16. J.Veitch *et al*, *Phys. Rev.* D **91**, 042003 (2015).
17. T. Dal Canton *et al*, *Phys. Rev.* D **90**, 082004 (2014).
18. S.A. Usman *et al*, *CQG* **33**, 215004 (2016).
19. A.H. Nitz *et al*, *arXiv:*1705.01513.
20. C.D. Ott, *CQG* **26**, 204015 (2009).
21. K. Kotaake *et al*, *Reports on Progress in Physics* **69**, 971 (2006).
22. A. Corsi and B.J. Owen, *Phys. Rev.* D **83**, 104014 (2011).
23. B.D. Metzger and E. Berger, *ApJ* **746**, 48 (2012).
24. A. Soderberg *et al*, *Nature* **453**, 469 (2008).
25. P. M. Garnavich *et al*, *ApJ* **820**, 23 (2016).
26. M. Modjaz *et al*, *ApJ Letters* **645**, 21 (2006).
27. S. Mereghetti, *A&A Review* **15**, 225 (2008).
28. C.M. Espinoza, *MNRAS* **414**, 1679 (2011).
29. K. Hirata*et al*, *Phys. Rev. Lett.* **58**, 1490 (1987).
30. R.M. Bionta et al, *Phys. Rev. Lett.* **58**, 1494 (1987).
31. S. Klimenko *et al*, *Phys. Rev.* D **93**, 042004 (2016).
32. R. Lynch *et al*, *arXiv:*1511.05955 (2015).
33. B.P. Abbott *et al*, *ApJ Letters* **826**, 13 (2016e).
34. B.P. Abbott *et al*, *ApJ Suppl. Series* **225**, 8 (2006f).
35. S.J. Smartt *et al*, *MNRAS* **462**, 4094 (2016a).
36. M.M. Kasliwal *et al*, *ApJ* **824**, 24 (2016).
37. C.M. Copperwheat *et al*, *MNRAS* **462**, 3528 (2016).
38. V. Connaughton *et al*, *ApJ* **826**, 6 (2016).
39. V. Savchenko *et al*, *ApJ* **820**, 36 (2016).
40. M. Tavani *et al*, *ApJ* **825**, 4 (2016).
41. S. Adrián Martínez *et al*, *Phys. Rev.* D **93**, 122010 (2016).
42. S.J. Smartt *et al*, *ApJ* **827**, 40 (2016b).
43. P.S. Cowperthwaite *et al*, *ApJ* **826**, 29 (2016).
44. S. Adrián Martínez *et al*, *arXiv:1703.06298*, (2017).
45. F. Acernese *et al*, *CQG* **32**, 024001 (2015).
46. B.P. Abbott *et al*, *ApJ Letters* **832**, 21 (2016g).
47. E. Vangioni *et al*, *MNRAS* **455**, 17 (2016).
48. Y. Aso *et al*, *Phys. Rev.* D **88**, 043007 (2013).
49. B.P. Abbott *et al*, *Living Reviews in Relativity* 19, (2006h).












Rencontres de Manon
52

STATUS OF THE CONTINUOUS GRAVITATIONAL WAVE SEARCHES IN THE ADVANCED DETECTOR ERA

M. Bejger (for the LIGO-Virgo Collaboration)
Nicolaus Copernicus Astronomical Center, Polish Academy of Sciences, ul. Bartycka 18, 00-716, Warsaw, Poland

Periodic (almost monochromatic) gravitational waves emitted by rotating, asymmetric neutron stars are intriguing potential signals in the sensitivity band of Advanced LIGO and Advanced Virgo detectors. These signals are related to elastic and magnetic stresses in the neutron-star interior, as well as to various possible instabilities, and thus are interesting from the point of view of the largely-unknown neutron star structure. I will describe the main challenges related to these searches, the current state of the data-analysis methods and plans for the future.

1 Introduction

Recent first direct detections of gravitational waves with the two LIGO detectors [1,2] create an unprecedented opportunity for studying the Universe through a novel, never before explored channel of spacetime fluctuations. Advanced LIGO [3] and Advanced Virgo [4], few-kilometer long arm laser interferometric detectors are sensitive in the range of frequencies between 10 Hz and a few kHz. They registers a coherent signal emitted by a bulk movement of large, rapidly-moving masses. Once emitted, gravitational waves are weakly coupled to the surrounding matter and propagate freely without scattering. This has to be contrasted with the electromagnetic emission which originates at the microscopic level, is strongly coupled to the surroundings and often reprocessed; it carries a reliable information from the last scattering surface only. Gravitational wave observations are therefore the perfect counterpart to the electromagnetic observations as they may provide us with information impossible to obtain by other means.

In addition to inspiralling and merging binary systems, among promising sources of gravitational radiation are all asymmetric collapses and explosions e.g., supernovæ. wide binary systems, rotating deformed stars (gravitational-wave 'pulsars' of continuous and transient nature), as well as stochastic background waves produced by whole populations of sources.

In the following we will briefly describe astrophysical motivation behind continuous gravitational waves produced by rotating deformed neutron stars (Sect. 2), data-analysis methods and computational challenges related to them (Sect. 3), Advanced LIGO O1 run results (Sect. 4), and plans for the future (Sect. 5).

2 Astrophysical motivation

Neutron stars are the most relativistic, dense and compact *material* objects in the Universe. Their compactness i.e., mass-to-radius ratio $2GM/Rc^2$ reaches 0.5 (G being the Newton's constant, c the speed of light); for comparison, the compactness of the most compact objects, black holes, equals 1. Their average density surpasses the nuclear saturation density i.e., the density

of atomic nuclei. At these densities matter exists most probably in an 'exotic' phase, e.g., as de-confined quarks. Neutron stars are self-gravitating objects stabilized by strong force interactions, gigantic nuclei of masses up to $2\,M_\odot$, radii about $10-15$ km with surface magnetic fields of 10^8-10^{15} Gauss, that can spin several hundred times per second. Comparison of realistic models of neutron stars with a variety of astrophysical observations - including the gravitational waves they emit - is the only way to peek into a realm of dense matter strong interactions much above the nuclear saturation density.

Neutron stars provide truly unique conditions to study matter at the most extreme densities, pressures, and in the presence of powerful magnetic fields. These conditions cannot be reproduced (or even approximated) in terrestrial laboratories. At present, about 2500 neutron stars are known, and an estimated number of 10^8-10^9 exists in every galaxy similar to ours. Neutron stars play an important role in many astrophysical phenomena: they are observed in all the EM spectrum as radio-, X- and γ-pulsars, magnetars, are present in supernovæ remnants, in many accreting systems and in relativistic double neutron star binaries, yet very little is known about their internal composition. What is conventionally accepted is that at least some part of neutron-star interior - the outer part about 1 km thick called the crust, corresponding to densities *below* the nuclear saturation density - is in the crystalline state.

In the following we will focus on rotating, non-axisymmetric neutron stars as sources of continuous periodic gravitational wave emission. Continuous gravitational wave is by definition a long-lived phenomenon, $T > T_{obs}$, and its frequency f_{GW} is somehow proportional to the spin frequency of the star f, $f_{GW} \propto f$. There are several proposed astrophysical mechanisms providing the necessary asymmetry, which in the case of a rotating star is the source of time-varying quadrupole required for the gravitational-wave emission. Mechanisms include neutron-star "mountains", supported by elastic and/or magnetic stresses ($f_{GW} = 2f$), oscillations (e.g., r-modes [5], $f_{GW} = 4/3f$), free precession ($f_{GW} \propto f + f_{prec}$) and accretion that drives the deformation from r-modes, thermal gradients and magnetic fields ($f_{GW} \simeq f$). For a recent review see [6].

The most-commonly used and the simplest model of the non-axisymmetric rotating neutron star radiating purely quadrupolar waves consists of a triaxial ellipsoid (with moments of inertia along the axes I_1, I_2, I_3), rotating about one of the principal directions of its moment of inertia tensor (I_3, say). Such a body radiates GWs at the frequency twice the rotational frequency of the star, $2\pi f_{GW} = \Omega_{GW} = 2\Omega$. The strain signal at the detector changes in time as

$$h(t) = h_0 \left(\frac{1}{2} F_+(t,\alpha,\delta,\psi) \left(1+\cos^2\iota\right) \cos(\phi(t)+\phi_0) + F_\times(t,\alpha,\delta,\psi) \cos\iota \cos(\phi(t)+\phi_0) \right), \quad (1)$$

where h_0 is the gravitational-wave strain amplitude, α and δ are right ascension and declination of the source in the sky, ψ is the polarization angle, and ι the inclination of the rotation axis to the line of sight. Phase of the signal $\phi(t)+\phi_0$ incorporates the possible evolution of the spin frequency. F_+ and $F_\times$ are the antenna responses of the detector, corresponding to two gravitational-wave polarizations + and $\times$.

From the quadrupole formula [7], amplitude h_0 is estimated as follows:

$$h_0 = \frac{16\pi^2 G}{c^4} \frac{I\epsilon f^2}{d} = 4\times 10^{-25} \left(\frac{\epsilon}{10^{-6}}\right) \left(\frac{I}{10^{45}\ \mathrm{g\ cm^2}}\right) \left(\frac{f}{100\ \mathrm{Hz}}\right)^2 \left(\frac{100\ \mathrm{pc}}{d}\right), \quad (2)$$

where $I \equiv I_3$, $f = \Omega/2\pi$, $\epsilon = (I_1 - I_2)/I$ is is the fiducial equatorial ellipticity of the star (a "deformation"), and d is typical distance in the Galaxy. According to theoretical studies of the dense matter equation of state [8,9,10], nucleonic matter may sustain deformations up to $\epsilon \simeq 10^{-6}-10^{-7}$, whereas for quark matter ϵ can reach $10^{-4}-10^{-5}$.

Observations of the majority of known pulsars show that their spin frequency slowly decreases, $\dot{f} < 0$ (exceptions are pulsars in binary systems which can be spun-up by the angular momentum transfer from the accretion disk). A useful quantity related to the amount of kinetic

(rotational) energy of the star is the so-called spin-down limit. It is derived by assuming that the gravitational-wave emission alone is responsible for the change in the rotational energy, $\dot{E}_{\rm rot}$. For $E_{\rm rot} = 2\pi^2 I f^2$, $\dot{E}_{\rm rot} \propto I f \dot{f}$ is equated with the GW emission, $\dot{E}_{\rm GW} \propto \epsilon^2 I^2 f^6$ to obtain the spin-down limit amplitude

$$h_{\rm sd} = \frac{1}{d}\sqrt{\frac{5GI}{2c^3}\frac{|\dot{f}\,|}{f}} = 8\times10^{-24}\sqrt{\left(\frac{I}{10^{45}\ {\rm g\ cm^2}}\right)\left(\frac{|\dot{f}\,|}{10^{-10}\ {\rm Hz/s}}\right)\left(\frac{100\ {\rm Hz}}{f}\right)\left(\frac{100\ {\rm pc}}{d}\right)}. \quad (3)$$

Comparison with Eq. 2 results in the limiting deformation $\epsilon_{\rm sd}$:

$$\epsilon_{\rm sd} = 2\times10^{-5}\sqrt{\left(\frac{10^{45}\ {\rm g\ cm^2}}{I}\right)\left(\frac{100\ {\rm Hz}}{f}\right)^5\left(\frac{|\dot{f}\,|}{10^{-10}\ {\rm Hz/s}}\right)} = 0.2\left(\frac{h_{\rm sd}}{10^{-24}}\right) f^{-2} I_{45}^{-1} d_{kpc}. \quad (4)$$

A star with $\epsilon_{\rm sd}$ would spin-down solely by gravitational-wave radiation. In reality, the ellipticity is smaller, so the results 'beating the spin-down limit' probe the physically interesting range of ellipticities and set the upper limit for the ellipticity given object has. We will come back to the spin-down limit in Sect. 4.

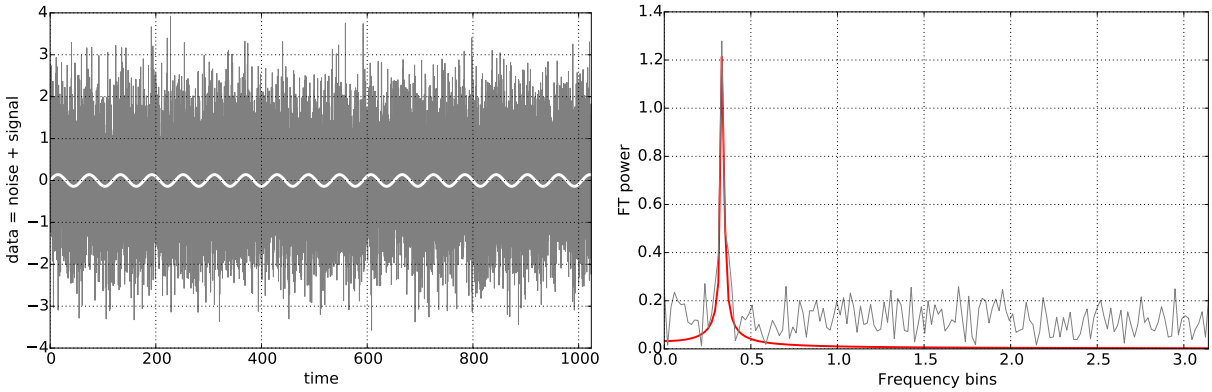


Figure 1 – Periodic signal hidden in white Gaussian noise (left), and the Fourier transform of this time series (right).

3 Data-analysis methods and computational challenges

Searching for long-lived, weak gravitational wave signals is a particularly cumbersome task, especially when nothing is known about its parameters. Eq. 2 shows that their strain amplitude is much smaller than than e.g., the characteristic strain amplitude of O1 detections, $h \simeq 10^{-21}$. Fortunately, one may search for weak signals hidden deeply in the noise provided a waveform of the signal is known. The idea of such a search would be to compute the cross correlation between the data and a parametrised template waveform in order to find parameters of the best match. Techniques of this sort are called the matched filtering methods [11,12,13]. Matched filtering provide an optimal detection statistic (it maximizes the signal-to-noise ratio) if noise is Gaussian.

3.1 Example: signal-to-noise ratio for a periodic signal

An instance of a strictly periodic signal "buried" in the stationary white Gaussian noise is presented in Fig. 1. We will estimate the signal-to-noise ratio ρ by approximating the output of the matched filter, which in the case of a periodic signal is simply the Fourier transform. The scalar product $(x|y)$ is defined using the Fourier transform as

$$(x|y) = 4\Re\int_0^\infty \frac{\tilde{x}(f)\tilde{y}^*(f)}{S_n(f)} {\rm e}^{2\pi i f t} df, \quad (5)$$

where $*$ denotes complex conjugation, $\Re$ is the real part of the integral, and $\tilde{x}(f)$ and $\tilde{y}(f)$ are the Fourier transform of the time-domain data series:

$$\tilde{x}(f) = \int_{-\infty}^{\infty} x(t) \mathrm{e}^{-2\pi i f t} dt, \quad \text{with the inverse transform} \quad x(t) = \int_{-\infty}^{\infty} \tilde{x}(f) \mathrm{e}^{2\pi i f t} df. \tag{6}$$

$S_n(f)$ is the one-sided power spectral density of the detector's noise. For a stable detector we may assume the that $S_n(f) \approx S_0 = const.$ over the data span. From the Parseval theorem,

$$(x|y) \approx \frac{2}{S_0} \int_0^T x(t) y(t) dt. \tag{7}$$

For the additive noise process, the data $s(t)$ is defined as the sum of the signal and the noise: $s(t) = h(t) + n(t)$. The matched filter output of the data stream $s(t)$ with a filter template $h_{templ.}(t)$ (correlation of the data containing a possible signal with its model) is

$$4\Re \int_0^{\infty} \frac{\tilde{s}(f) \tilde{h}^*_{templ.}(f)}{S_n(f)} \mathrm{e}^{2\pi i f t} df. \tag{8}$$

The optimal signal-to-noise ratio is defined as $\rho := \sqrt{(h|h)}$. For a periodic signal $h(t) = h_0 \cos(\phi(t) + \phi_0)$, we will assume that the data span T_0 is much longer than the period of the wave, $P_0 = 1/f_0$, and that the phase can be expanded in the series $\phi(t) = \Sigma_k a_k t^{k+1}$. Also

$$\frac{1}{T_0} \int_0^{T_0} \cos(n\phi(t)) dt \approx \frac{1}{T_0} \int_0^{T_0} \sin(n\phi(t)) dt \approx 0 \tag{9}$$

for integers $n > 0$. Integrating the ρ^2 for $h(t) = h_0 \cos(\phi(t) + \phi_0)$ gives the estimate for the optimal signal-to-noise ratio for a periodic signal of the amplitude h_0

$$\rho = \left(\frac{2}{S_0} \int_0^{T_0} \left(h(t)\right)^2 dt \right)^{1/2} \left(\frac{2}{S_0} \int_0^{T_0} h_0^2 \cos^2(\phi(t) + \phi_0) dt \right)^{1/2} \approx \; h_0 \left(\frac{T_0}{S_0} \right)^{1/2}. \tag{10}$$

It is clear that even for a small h_0 one can reach a satisfactory signal-to-noise ratio with a sufficiently long stretch of data.

In practice, on top of the secular spin-down modulation mentioned before (to describe this feature, one says that the signal is *almost monochromatic*), the signal is modulated by the movement of the detector with respect to the source. Since the Advanced LIGO and Advanced Virgo detectors are placed on Earth, the presence of other planets and Earth's rotation influences signal's amplitude and phase. Demodulation to a frame connected with the Solar System Barycenter (the place in the Solar System that moves the least with respect to the source), precise ephemerides of the movement of planets are used. The fact that the detectors are moving with respect to the source isn't necessary a bad thing, though: detector movement distinguishes a real signal from local spectral artifacts, called the "stationary lines".

3.2 Example: the $\mathcal{F}$-statistic

A conceptually relatively simple method to develop a detection statistic using the time-domain data $s(t)$ is the $\mathcal{F}$-statistic [14]. For a triaxial rotating neutron star model (Eq. 1, the statistic is obtained by maximizing the likelihood ratio function with respect to the four unknown parameters: h_0, ϕ_0, ι, and ψ. This leaves, in case when only first derivative of f is taken into account, a function of four parameters: f, $\dot{f}$, α and δ. These four parameters form a parameter space in which the signal's best match will be searched for. Assuming that the observation time T_0 is the integer multiple of sidereal days, and that the bandwidth is narrow (so that the spectral density of the noise S_0 is constant), the $\mathcal{F}$-statistic is evaluated [15] as

$$\mathcal{F} = \frac{2}{S_0 T_0} \left(\frac{|F_a|^2}{\langle a^2 \rangle} + \frac{|F_b|^2}{\langle b^2 \rangle} \right), \tag{11}$$

with

$$F_a = \int_0^{T_0} s(t)a(t)\exp(-i\phi(t))dt, \quad F_b = \ldots, \quad \langle a^2\rangle = \int_0^{T_0} a(t)^2 dt, \quad \langle b^2\rangle = \ldots, \tag{12}$$

F_a and F_b being the generalizations of the Fourier transforms from the previous section. Amplitude modulation functions $a(t)$ and $b(t)$ are related to detector's antenna response ($F_+ = a(t)\cos 2\psi + b(t)\sin 2\psi$, $F_\times = -a(t)\sin 2\psi + b(t)\cos 2\psi$) and depend on the sources' sky position α and δ, and the phase modulation function $\phi(t)$ depends also on the frequency f and spin-down of the source, $\dot{f}$. The signal-to-noise ratio ρ is related to $\mathcal{F}$ as follows: $\rho = \sqrt{2(\mathcal{F}-2)}$.

3.3 Taxonomy of search methods

Continuous gravitational-wave searches can by divided according to the amount of information one has about the sources.

The *targeted searches* are most often based on matched filtering (data of length T_0 correlated with signal templates). Position, f and $\dot{f}$, sometimes also the source's orientation are known. In this case the expected strain amplitude scales like $h_0 \propto \sqrt{S/T_0}$, where S is the amplitude spectral density at the expected gravitational-wave frequency.

Directed searches cover the intermediate cases when only some parameters are known, e.g., the position of the source. Astrophysically, they may be relevant to supernovæ remnants, the Galactic center, globular clusters, accreting neutron stars in binary systems (e.g., the brightest X-ray source in the sky, Sco X-1).

All-sky searches are the most demanding types of searches. Source parameters and positions are not known, which makes the parameter space large and the problem becomes very quickly computationally bound. In order to mediate this, hierarchical approaches are being used. Instead of analyzing the whole T_0 data span at once, the data is divided into N data segments of length T_s, which are analyzed coherently, and the resulting information is combined incoherently. The expected strain amplitude scales like $h_0 \propto \sqrt{S/T_s}/N^{1/4}$. The most sophisticated example of the hierarchical approach is the volunteer-driven Einstein@Home project [a].

3.4 Example: computational cost for an all-sky search

In order to optimally cover the $(f, \dot{f}, \alpha, \delta)$ parameter space of an all-sky search at all possible frequencies, a grid of parameters is obtained as a solution to the covering problem with constraints (a constraint being e.g., a condition that the optimal $(\dot{f}, \alpha, \delta)$ lattice coincides with points in f corresponding to the Fourier frequencies bins of the Fast Fourier Transform algorithm). Typically, the number of points in $\dot{f}, \alpha, \delta$ scales with some positive power of T_0, so, depending on the details of the implementation [16], the computational demand scales like

$$\underbrace{T_0^2}_{\dot{f}} \times \underbrace{T_0^{[0-3]}}_{\alpha,\delta} \times \underbrace{T_0 \log(T_0)}_{f \text{ by FFT}} = T_0^{[3-6]} \log(T_0), \tag{13}$$

which is very prohibitive for large T_0. A coherent search of $T_0 \simeq 1\,yr$ of data (comparable with ongoing and planned Advanced LIGO/Virgo runs) in the broad sensitivity band of the detectors (10 - 2000 Hz) requires *zettaFLOPS* (10^{21} FLOPS) scale supercomputers. The solution is a hierarchical scheme: divide the data T_0 into a number N shorter length T_s, $T_s \simeq$ days, data segments and perform a coherent search in each of them (search in narrow frequency bands of bandwidth B, Nyquist sampling time $\delta t = 1/2B$, number of data points $N_p = T_s/\delta t = 2T_sB$). This is feasible on a typical petaFLOP scale supercomputer (cluster), yet still requires millions of CPU-hours. Second incoherent stage consists of searching for coincidences between different T_s segments. Surviving outliers present in sufficiently many segments (candidate signals with

[a] `https://einsteinathome.org`

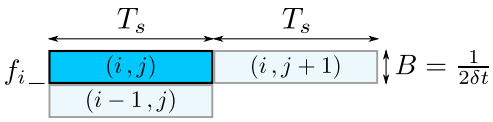


Figure 2 – Division of the time-frequency data into narrow frequency bands of bandwidth B, reference frequency f_i, and N time segments of length T_s ($NT_s = T_0$). Each time-frequency segment is then analyzed separately, allowing for effective parallelization.

relatively well-determined parameters) are subjected to a final scrutinizing follow-up (a "targeted search").

4 Continuous gravitational waves in the Advanced LIGO O1 era

The first Advanced LIGO observing run (O1) started on September 11, 2015 and finished January 19, 2016. During that time the Hanford and Livingston detectors collected 78 days and 66 days of science data, respectively.

First published result pertains to a targeted search for gravitational waves from 200 known pulsars [17]. In this list, 11 high-value target pulsars, for which the spin-down limit based on Eq. 3 could either be improved or closely approached, were identified. These selected pulsars were analyzed by three, largely independent methods: two time-domain-based methods, Bayesian [18] and $\mathcal{F}/\mathcal{G}$-statistic [19], and the frequency-domain-based 5n-vector method [20,21]. The remaining 189 targets were analyzed using the Bayesian method only. The analysis didn't find significant evidence for a gravitational-wave signal from any of these pulsars, but the most constraining upper limits to date on their gravitational-wave amplitudes and ellipticities were obtained. For eight of the high-value target pulsars, new upper limits give improved bounds over the indirect spin-down limit values. For the Crab pulsar, the 95% confidence upper limit for the gravitational-wave radiation energy is $2\times10^{-3}\ \dot{E}_{rot}$, and in case of the Vela pulsar, the upper limit is $10^{-2}\ \dot{E}_{rot}$. The limits on ellipticity correspond to the relative deformation (the "mountain") no greater than $\simeq$ 10cm and $\simeq$ 50 cm for the Crab and Vela pulsars, respectively. For another 32, values within a factor of 10 of the spin-down limit were found: it is likely that some of these will be reachable in future runs of Advanced LIGO and Advanced Virgo. The smallest upper limit was obtained for PSR J1918-0642: $h_0 = 1.6 \times 10^{-26}$. These new results improve on previous limits of Initial LIGO/Virgo by more than a factor of two (see the summary Fig. 1 of [17], where the comparison with the sensitivity curve, initial detector results and the spin-down limits is presented).

Second publication (in the time of writing available as a preprint) is related to a directed search for gravitational waves from a bright X-ray source Sco X-1 [22]. Sco X-1 is the brightest Low Mass X-ray Binary (LMXB, a binary system consisting of a neutron star or a black hole, and a normal star with lower mass) in the Galaxy. The X-ray radiation is produced during accretion; neutron stars in these systems are potential sources of continuous gravitational waves because accretion provides a natural method of building a deformation on the star and powering the gravitational-wave emission. There are however challenges in searching for gravitational waves from this particular source. First, the spin frequency of the neutron star is unknown - the search has to cover a broad range of frequencies, which means it requires much more computing power than a directed search in case of a known pulsar. Most likely the spin frequency is not constant, and not even behaving strictly monotonously, but "wandering" i.e., it changes because of the fluctuations in the amount of accreted matter; frequency is also modulated by the orbital motion of the binary system (the signal power is distributed into sidebands i.e., frequencies higher or lower than the gravitational-wave signal frequency). In order to perform an efficient search in these circumstances, a hidden Markov model (a statistical model in which it is assumed that the system is a Markov process with unobserved states, see [23] and references therein and tutorial [24]) was implemented. The search covered a band of frequencies from 60 Hz to 650 Hz. No detection was claimed from this search, but very sensitive upper limits on the gravitational-wave strain were placed (to quote one example: 95% upper limits $h_0 = 3 \times 10^{-25}$ at 100 Hz, assuming

circular polarization).

We also report on an ongoing all-sky search for periodic gravitational waves using the Advanced LIGO's O1 run, in the frequency band 20-475 Hz and a frequency time derivative range of $[-1.0, +0.1] \times 10^{-8}$ Hz/s. Several different data-analysis pipelines took part in this study: the *PowerFlux* (see [25] and references therein), the *FrequencyHough* [26], the *Skyhough* [27] and the *Time-Domain $\mathcal{F}$-stat* [28]. The pipelines employ a variety of algorithmic and parameter choices e.g., they primarily use either the frequency or time domain data, adopt different coherence times used in first-stage data processing (from 1800 s to 6 days), and treat differently the narrow spectral artifacts ("lines"). Outliers that survive all stages of any of the four pipelines are examined man-

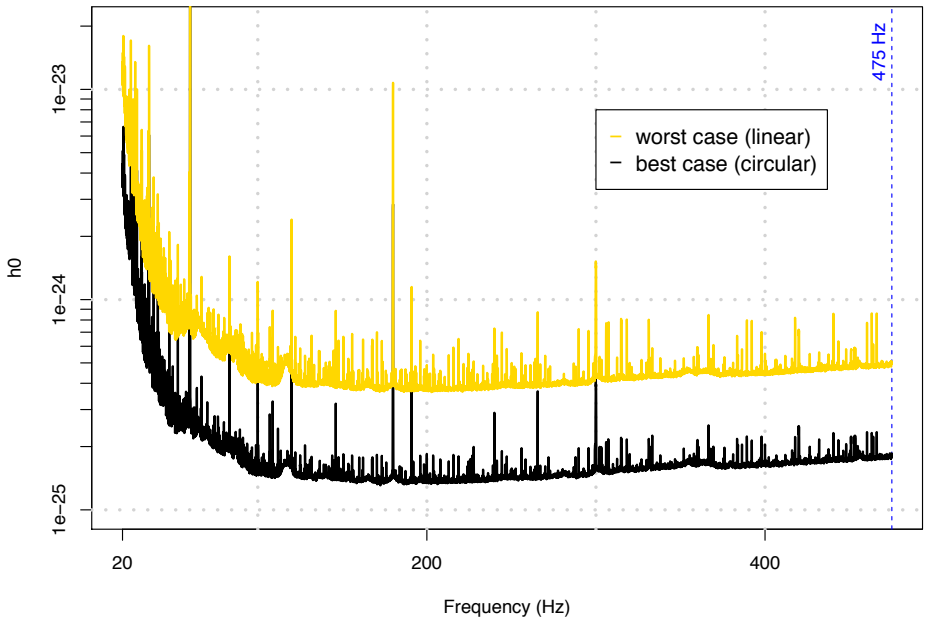


Figure 3 – Preliminary O1 all-sky upper limits for continuous gravitational waves from the *PowerFlux* pipeline. The upper (yellow) curve shows worst-case (linearly polarized) 95% CL upper limits. The lower (grey) curve shows upper limits assuming a circularly polarized source.

ually for contamination from known, or possibly new, instrumental artifacts. Survivors of this procedure are subjected to additional systematic follow-up used for Einstein@Home searches [29]. Preliminary upper limit results are presented in Fig. 3. The lowest upper limits on worst-case (linearly polarized) strain amplitude h_0 are $\simeq 4 \times 10^{-25}$ near 170 Hz. For a circular polarization (most favorable orientation of the source), the smallest upper limits obtained are $\simeq 1.5 \times 10^{-25}$.

In addition, several studies from the Initial Detector Era (LIGO S6 and Virgo VSR2, VSR4 runs) were recently published. They include an all-sky Mock Data Challenge based on the LIGO S6 data [30], a directed search towards nine supernova remnants [31], the Orion spur [32], the globular cluster NGC 6544 [33], as well as the deepest all-sky survey for continuous waves from the Initial Detector Era, the S6 Einstein@Home search in the $[50, 505]$ Hz range [34]. The reason we see merit in publishing the 'old' results is to gather experience, test algorithmic improvements and develop new methods using the well-understood data. These new tools are now being used in the O1 (and soon, the O2) searches.

5 Plans for the future

The algorithmic and implementation-related improvements acquired during the Dark Ages (2011–2015) will be used to expand the 'standard' targeted searches for high-value targets (Sco X-1, Cas A, Vela Jr and G347 supernovæ remnants, Crab and Vela pulsars) and to speed up the massive all-sky searches with relatively simple source models (aligned triaxial ellipsoid, Eq. 1). Additionally, we plan to search for signals with more complicated, realistic morphology. The models

include inclined rotating neutron stars, which emit gravitational waves at multiple frequencies at once (e.g., at f and $2f$), transient continuous gravitational waves emitters (phenomena that may last for weeks to months, and are caused by neutron-star instabilities e.g., the r-modes), and search for non-tensorial gravitational waves. In order to capture the richness of physical processes will are also improving the loosely-coherent methods taking into account the neutron-star frequency wandering, glitches, and a possible mismatch between the gravitational-wave spin frequency parameters and the parameters inferred from the electromagnetic observations.

Acknowledgments

This work was partially supported by the Polish NCN grant no. UMO-2014/14/M/ST9/00707 and ASPERA/NCN grant 2013/01/ASPERA/ST9/00001.

References

1. Abbott, B. P., Abbott, R., Abbott, T. D., et al. 2016, *Phys. Rev. Lett.*, 116, 061102
2. Abbott, B. P., Abbott, R., Abbott, T. D., et al. 2016, *Phys. Rev. Lett.*, 116, 241103
3. Aasi, J., Abbott, B. P., et al. 2015, *Class. Quant. Grav.*, 32, 074001
4. Acernese, F., Agathos, M., Agatsuma, K., et al. 2015, *Class. Quant. Grav.*, 32, 024001
5. Andersson, N., & Kokkotas, K. D. 2001, IJMP D, 10, 381
6. Lasky, P. D. 2015, PASA, 32, e034
7. Einstein, A. 1918 "Sitzungsberichte der Königlich Preussischen Akademie der Wissenschaften zu Berlin", 154
8. Johnson-McDaniel, N. K., & Owen, B. J. 2012, *Phys. Rev. D*, 86, 063006
9. Owen, B. J. 2005, *Phys. Rev. Lett.*, 95, 211101
10. Ushomirsky, G., Cutler, C., & Bildsten, L. 2000, *MNRAS*, 319, 902
11. Wiener, N. 1949, "Extrapolation, Interpolation, and Smoothing of Stationary Time Series", New York: Wiley
12. Helstrom, C. W. 1968, "Statistical Theory of Signal Detection", Pergamon Press, London
13. Schutz, B. F. 1999, *Class. Quant. Grav.*, 16, A131
14. Jaranowski, P., Królak, A., & Schutz, B. F. 1998, *Phys. Rev. D*, 58, 063001
15. Astone, P., et al. 2010, *Phys. Rev. D*, 82, 022005
16. Wette, K. 2014, *Phys. Rev. D*, 90, 122010
17. Abbott, B. P., Abbott, R., Abbott, T. D., et al. 2017, *ApJ*, 839, 12
18. Dupuis, R. J., Woan, G. 2005, *Phys. Rev. D*, 72, 102002
19. Jaranowski, P., Królak, A. 2010, *Class. Quant. Grav.*, 27, 194015
20. Astone, P., DAntonio, S., Frasca, S., Palomba, C. 2010, *Class. Quant. Grav.*, 27, 194016
21. Astone, P., et al., 2012, JPCS, 363, 012038
22. Abbott, B. P., et al., 2017, `arXiv:1704.03719`
23. Baum, L.E., 1972, Inequalities, 3, 1
24. Rabiner, L., 1989, Proceedings of the IEEE, 77, 257
25. Aasi, J. et al., 2016, *Phys. Rev. D*, 94, 042002
26. Aasi, J. et al., 2016, *Phys. Rev. D*, 93, 042007
27. Aasi, J. et al., 2014, *Class. Quant. Grav.*, 31, 085014
28. Aasi, J. et al., 2014, *Class. Quant. Grav.*, 31, 165014
29. Papa, M. A., et al., 2016, *Phys. Rev. D*,94, 122006
30. Walsh, S. et al., 2016, *Phys. Rev. D*, 94, 124010
31. Aasi, J. et al., 2015, *ApJ*, 813, 1
32. Aasi, J. et al., 2016, *Phys. Rev. D*, 93, 042006
33. Abbott, B. P., et al., 2016, `arXiv:1607.02216`
34. Abbott, B. P., et al. 2016, *Phys. Rev. D*, 94, 102002

Multi-band gravitational wave astronomy: science with joint space- and ground-based observations of black hole binaries

Alberto Sesana
School of Physics and Astronomy, University of Birmingham,
Edgbaston, Birmingham B15 2TT, United Kingdom
asesana@star.sr.bham.ac.uk

Soon after the observation of the first black hole binary (BHB) by advanced LIGO (aLIGO), GW150914, it was realised that such a massive system would have been observable in the milli-Hz (mHz) band few years prior to coalescence. Operating in the frequency range 0.1-100 mHz, the Laser Interferometer Space Antenna (LISA) can potentially detect up to thousands inspiralling BHBs, based on the coalescence rates inferred from the aLIGO first observing run (O1). The vast majority of them (those emitting at $f < 10$ mHz) will experience only a minor frequency drift during LISA lifetime, resulting in signals similar to those emitted by galactic white dwarf binaries. At $f > 10$ mHz however, several of them will sweep through the LISA band, eventually producing loud coalescences in the audio-band probed by aLIGO. This contribution reviews the scientific potential of these new class of LISA sources which, in the past few months, has been investigated in several contexts, including multi-messenger and multi-band gravitational wave astronomy, BHB astrophysics, tests of alternative theories of gravity and cosmography.

1 Introduction

The detection by advanced LIGO (aLIGO) of a $36^{+5}_{-4}M_\odot$ and $29\ ^{+4}_{-4}M_\odot$ coalescing black hole binary (BHB) at $z = 0.09^{+0.03}_{-0.04}$ on September 14, 2015 (GW150914) marked the beginning of the era of gravitational wave (GW) astronomy [1]. In the following few months, a second, lighter system (GW151226, [2]), plus a third candidate (LVT151012, [3]) were also observed.

Among the plethora of scientific consequences, those detections made possible for the first time to constrain observationally the coalescence rate of stellar BHBs in the Universe [4]. BHBs can in fact originate from a variety of astrophysical channels, including: standard evolution of field massive stellar binaries [5], dynamical formation in dense stellar clusters [6] or in dense compact remnant cusps surrounding nuclear massive black holes [7], evolution of chemically mixed massive binaries [8], population III remnants [9], primordial black holes [10]. Every channel, however, is subject to considerable uncertainties. Just to cite the mainstream ones as examples, the number of BHBs resulting from standard stellar evolution critically depends on the poorly understood physics driving common envelope evolution, supernova explosions and their subsequent kicks; similarly, the cluster dynamical formation channel is also affected by the unknown supernova kick velocities and by the retention fraction of BHs in the cluster. The net results is that BHB merger rate predictions vary wildly in the literature (see [11] for a review), including some models suggesting rates up to several hundreds events $\mathrm{yr}^{-1}\mathrm{Gpc}^{-3}$ [12,13]. An extensive analysis of the aLIGO events places the 90% confidence range between 6 and 200 $\mathrm{yr}^{-1}\mathrm{Gpc}^{-3}$ (depending on the assumed BHB mass distribution [3]), close to the upper end of theoretical predictions. Moreover, aLIGO demonstrated that coalescing BHBs can be in excess of $30M_\odot$, whereas, based on mass

estimates of BHs in X-ray binaries [14], it has been often customarily assumed those binaries would have masses around $10M_{\odot}$.

GW150914, in particular, prompted a burst of interest also within the low frequency GW community. Because of its high mass, it was immediately realised that GW150914 would have been visible by a spaceborne interferometer operating in the mHz band few years prior to coalescence [15]. Would the Laser Interferometer Space Antenna (LISA) be operating, we would have known few years in advance GW150914 would have coalesced in the LIGO band on September 14, 2015. Because of the poor constrains on the rates and the standard assumption of $10M_{\odot}$ objects, BHBs have never been considered a particularly interesting LISA sources, and multi-band GW observations have been only proposed in the context of seed [16] or intermediate mass [17] BHBs . On the contrary, analysis of the BHB population as constrained by aLIGO demonstrated that LISA might see up to thousands of these systems, with a variety of profound scientific consequences that are summarized in this contribution. The paper is organized as follows. Section 2 provides the recipe to construct the BHB population in the LISA band starting from the aLIGO rates and presents detection rates and parameter estimation precision of the observed LISA systems. Section 3 covers several scientific questions that can be tackled using those binaries, and the most relevant points are briefly summarized in Section 4.

2 Merger rates, observable sources and their properties

2.1 Merger rates

aLIGO O1 results place the 90% confidence BHB merger rate within the range $6 - 200\ \mathrm{yr}^{-1}\mathrm{Gpc}^{-3}$, with most of the uncertainty coming from the unknown shape of the underlying BHB mass function. If the BH mass function is biased-high, then aLIGO observations are consistent with lower intrinsic rates. In [4] therefore, rates' probability distributions were computed for two different mass functions: one in which both BH masses, $M_1 > M_2$, are drawn from a log-flat mass distribution (model *flat*), and one in which the primary BH of a binary is drawn from a Salpeter distribution and the secondary from a flat distribution (model *salp*). The *flat* model rate distribution peas at $\approx 35\mathrm{yr}^{-1}\mathrm{Gpc}^{-3}$, whereas the *salp* model favours relatively light BHBs, with a rate distribution peaking at ($\approx 100\mathrm{yr}^{-1}\mathrm{Gpc}^{-3}$).

as detailed in [15], having assumed a mass distribution, the differential merger rate density $d^2n/d\mathcal{M}_r dt_r$ can be converted into the number of emitting sources per unit chirp mass, redshift and frequency populating the sky *at any time* via

$$\frac{d^3N}{d\mathcal{M}_r dz df_r} = \frac{d^2n}{d\mathcal{M}_r dt_r}\frac{dV}{dz}\frac{dt_r}{df_r}, \tag{1}$$

where $\mathcal{M} = (M_1M_2)^{3/5}/(M_1+M_2)^{1/5}$ is the chirp mass, dV/dz is the standard volume shell per unit redshift in the fiducial ΛCDM cosmology ($h = 0.679$, $\Omega_M = 0.306$, $\Omega_\Lambda = 0.694$, [18]), and $dt_r/df_r \propto f_r^{11/3}$ is given by the standard quadrupole GW emission formula. Subscripts $_r$ refer to quantities evaluated in the source rest frame (as opposed to the detector frame): $t_r = t/(1+z)$, $f_r = (1+z)f$, $M_r = M/(1+z)$. Equation (1) can be used to generate Monte Carlo realizations of the BHB cosmic population emitting in the LISA band.

2.2 LISA sensitivity

The LISA concept has significantly evolved in the past few years [20,21]. In 2014, the European Space Agency (ESA) appointed a gravitational observatory advisory committee (GOAT) to issue a recommendation for a space based GW observatory. During the study, different baselines for a spaceborne interferometer were considered. Full details can be found in [19]. In the following, six baselines featuring one, two or five million km arm-length (A1, A2, A5) and two possible low frequency noises – namely the LISA Pathfinder goal (N1) and the original LISA requirement

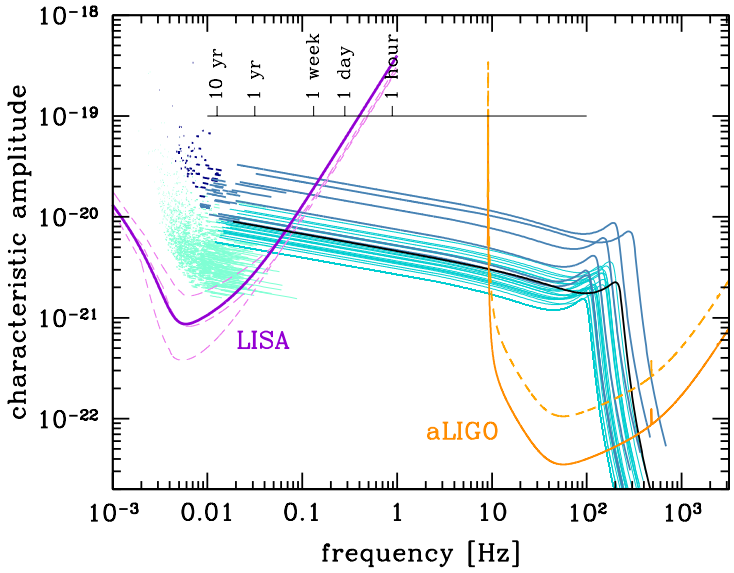


Figure 1 – Visual representation of the multi-band GW astronomy concept. Violet dashed lines are, from top to bottom, the total sensitivity curves of LISA configurations N2A1, N2A2, N2A5 (from [19]). The thick solid purple line is the LISA baseline proposed by the LISA Consortium to address ESA's L3 call. Orange lines refer to current (dashed) and design (solid) aLIGO sensitivity curves. Lines in different shades of blue represent amplitude tracks of BHBs found in a selected Monte Carlo realization of the *flat* population model (see main text) seen with S/N>1 in the new LISA configuration, integrated assuming a four year mission lifetime (baseline LISA4yr). Light and dark blue curves starting around 0.01Hz and extending to $\sim$ 100Hz are BHBs coalescing within the LIGO band during the LISA lifetime, and observable by LISA with S/N>5 and S/N>8 respectively; the dark blue ticks in the upper left corner are further sources with S/N>8 by LISA but not crossing to the aLIGO band within the mission lifetime. Light turquoise lines clustering at the bottom are sources seen in LISA with S/N<5 (for clarity those were down-sampled by a factor of 20 and sources extending to the aLIGO band were removed). The characteristic amplitude track completed by GW150914 is shown as a black solid line for comparison. The chart at the top of the figure indicates the frequency progression of this particular source in the last 10 years before coalescence. Adapted from [15].

(N2) – are considered. Those configurations, labelled N1A1, N1A2, N1A5, N2A1, N2A2, N2A5, all assume five years of observations with two equivalent Michelson interferometers (i.e. six active laser links). Building on the GOAT recommendation, the LISA Consortium proposed a somewhat different baseline [22], with slightly different technical specifications, including an armlength of 2.5M kilometres and a mission lifetime requirement of 4 years, and an extension goal to 10 years. The low frequency noise has been set to the level successfully demonstrated by the LISA Pathfinder [23]. We refer to these two latter designs as LISA4yr and LISA10yr. Numbers of detected BHBs are presented below for each of the eight configurations just described.

2.3 Observed systems and their properties

Depending on the baseline, the number of sources that can be detected above the nominal signal-to-noise ratio (S/N) threshold of eight varies by more than two orders of magnitudes, from just a few in the N1A1 configuration to about a thousand in the N2A5 configuration. Perhaps counter-intuitively, the armlength appear to have a strong impact on the number of detections. This is because, besides shifting the low frequency sensitivity, armlength also severely affects the depth of the bucket, where most of the resolvable BHBs live (see sensitivity curves in figure 1). Therefore, even with equal high frequency noise (as it is the case for all NxAy configurations), the number of detectable sources increases by about two orders of magnitude going from one (A1) to five (A5) million km. LISA4yr performs rather similarly to N2A2, as expected from the similar mission specifications. The sensitivity in the bucket of the two configurations is essentially identical, resulting in a comparable number of total detections with S/N>8 (upper

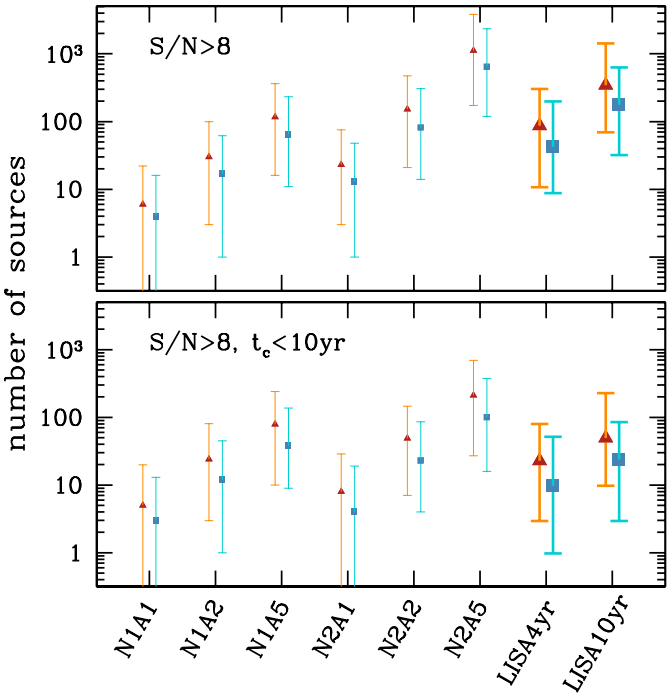


Figure 2 – Number of resolved BHBs for different LISA baselines (as labelled on the x-axis). Orange triangles and blue squares are for models *flat* and *salp* respectively. Symbols and error-bars are the median and 95% confidence interval from 200 realizations of the BHB population. The top panel show the total number of sources with S/N> 8 across the whole LISA band, whereas the lower panel is restricted to sources that will eventually coalesce in the aLIGO band within 10 years from the start of the LISA mission. Results for the LISA configuration proposed to ESA, assuming a mission lifetime of either 4 or 10 years (LISA4yr, LISA10yr) are shown with thicker symbols.

panel). Numbers are actually slightly lower for the LISA4yr configuration, because the mission lifetime was assumed to be 5 years in the N2A2 case, and S/N$\propto T^{1/2}$. There is, however, a noticeable difference in the number of sources crossing to the aLIGO band in less then 10 years (lower panel). This is because those accumulate all their S/N at $f > 10$ mHz, where the LISA4yr sensitivity becomes about 30-40% worse than the N2A2 one. Since the cumulative number of sources is proportional to $(\mathrm{S/N})^3$, this results in a difference of a factor of more than two in detected systems. LISA would definitely benefit from reaching the 10 year lifetime goal. The number of observable sources is in fact boosted by almost a factor of four in the LISA10yr case, with typical detection numbers of several hundreds. This is again because S/N$\propto T^{1/2}$ and the the cumulative number of sources is proportional to $(\mathrm{S/N})^3$. In general the flat model, in virtue of its biased-heavy mass function, results in a factor of ≈ 2 more detections in all cases. Note that for each fixed baseline and BHB population, the 95% confidence region still spans more than one order of magnitude, because of the intrinsic uncertainties on the aLIGO inferred merger rates. In summary, the current proposed LISA baseline (in its LISA4yr and LISA10yr incarnations) has the potential to observe between few tens to a thousand stellar BHBs with S/N> 8, and about 10-to-20% of them will cross to the aLIGO band within 10 years of LISA operation kick-off, realizing the promise of multi-band GW astronomy.

Early calculations by [15] also showed that LISA can achieve exquisite accuracy in the measurement of selected BHB parameters. This is shown in figure 3 for systems that *cross to the aLIGO band* within the LISA lifetime. Time to coalescence can be typically established within less than 10 seconds and sky location accuracy is generally better than a square degree. The redshifted chirp mass and symmetric mass ratio can be determined to a 10^{-6} and 0.01 relative accuracy respectively (which means that individual redshifted masses can be measured to better than 1%). Note that for these sources, LISA and aLIGO measurement can be combined to reduce parameter estimation errors [26]. Considering mildly eccentric (up to 0.1) systems, [25] showed in a follow-up paper that eccentricities in excess of 10^{-3} can be confidently measured, as shown in the right panel of figure 3, which can provide useful information on the BHB formation channel (see below). Other parameters might not be determined with comparable precision. For example, the distance to the source can only be determined to $\Delta D_l/D_l \approx A/(\mathrm{S/N})$, where in general $A > 1$; which gives rather poor results, since most BHBs have S/N< 20. Also spin determination might be problematic in general, as the two BHs are separated by thousands

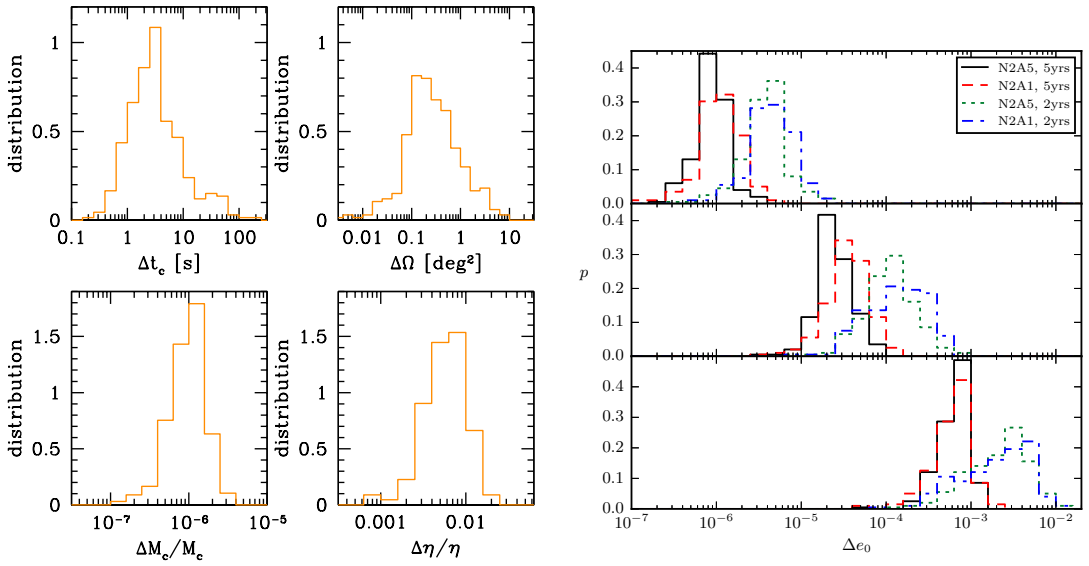


Figure 3 – Left figure (from [15]): parameter estimation precision from LISA observations of circular BHBs. Top left: coalescence time; top right: sky localization; bottom left: relative error in the chirp mass $\mathcal{M}$; bottom right: relative error in the symmetric mass ratio $\eta = M_1 M_2/(M_1 + M_2)^2$. Histograms show normalized distributions obtained from a Monte Carlo realization of 1000 sources observed with S/N$>$ 8 in the N2A5 configuration, assuming five years of mission operation (results for other configurations look similar). Estimates were obtained via Fisher Matrix analysis using 3.5 Post Newtonian non spinning waveforms [24] and the full time-dependent LISA response function. Right figure (from [25]): errors on the eccentricity measurement at frequency $f_0 = 10^{-2}$ Hz using eccentric non-spinning waveforms. From top to bottom, the three panels refer to systems with $e_0 = 0.1$, 0.01 and 0.001. Linestyles refer to different LISA baselines: N2A5 and $T_{\rm obs} = 5\,$yrs (solid black), N2A1 and $T_{\rm obs} = 5\,$yrs (dashed red), N2A5 and $T_{\rm obs} = 2\,$yrs (dotted green), N2A1 and $T_{\rm obs} = 2\,$yrs (dash-dotted blue).

of Schwarzschild radii in the LISA band and the spin-orbit and spin-spin coupling corrections on the waveform are accordingly small. An extensive study on parameter estimation precision, including precessing spinning waveforms is currently ongoing (Klein et al. in preparation).

3 Scientific potential

Because of the relatively large number of observable systems in the LISA band, the exquisite precision to which some of the parameters will be measured, and the possibility of seeing few of them sweeping through the aLIGO band within few years of the initial LISA detection, massive stellar BHBs captured the interest of the wider GW community. This fairly 'unexpected' (in terms of typical mass and rates) class of sources can be exploited in several contexts, including BHB astrophysics, fundamental physics and cosmology. This section focuses on some of the main payouts, keeping in mind that this is relatively new investigation ground, and the list is inevitably incomplete.

3.1 Multi-band and multimessenger astronomy

One of the obvious benefits of sources like GW150914 is the realization of multi-band GW astronomy. Observations of the same signal in two different detectors provides an efficient independent way to cross check and validate the instruments (which is particularly valuable for a space-based detector). Moreover, the two instruments will observe at separate frequency bands, therefore covering different evolutionary stages of BHBs; while LISA will be sensitive to their adiabatic inspiral, most of the aLIGO S/N comes from the very late inspiral, merger and ringdown. Each stage of the evolution carries information about different physical aspects of the sources, that can be combined together to push the boundary of GW astronomy in several directions, as highlighted below.

Another obvious advantage of observing BHBs several months before coalescence, is the possibility of issuing early warnings for an upcoming coalescence. LISA will allow exquisite estimation of some key parameters of the BHBs crossing to the aLIGO band. In particular, the time to coalescence can be predicted within less then ten seconds (but see [27] for potential complications) and the sky localization known within less than a square degree few weeks *before* merger. Although it is not standard to associate electromagnetic (EM) counterparts to BHB mergers, several (sometimes exotic) EM production scenarios have been proposed (see e.g.[28,29,30]), triggered by a tentative association of a gamma-ray signal detected by Fermi to GW150914 [31]. The claim is controversial, and the signal has not been confirmed, among others, by simultaneous INTEGRAL observations [32]. In any case, since the Universe is certainly not short of surprises, it is wise keep an open mind and continue to point our telescopes, and this can be done better if we know in advance when and where to observe. Knowing the sky location will facilitate the early pointing of large field of view instruments at all wavelengths. In particular, deep searches can be performed *in coincidence* to the coalescence, testing any possible exotic scenario of emission on the BHB merger dynamical timescale.

3.2 BHB astrophysics

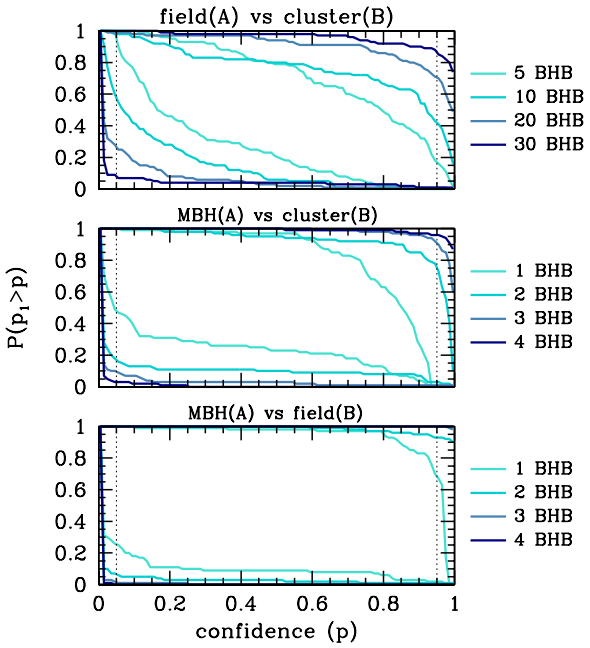


Figure 4 – Cumulative distribution function (CDF) of the confidence in a given model over 100 Monte Carlo realizations of a specific number, $N_{\rm obs}$, of observed BHBs (several $N_{\rm obs}$ are shown in each panel as labelled on the right). The N2A2 configuration is assumed, but results are weakly dependent on the adopt LISA baseline. For each pair of curves, the top one marks the CDF of confidence in model A when model A is true, whereas the bottom one marks the CDF of confidence in model A when model B is true. For example, the upper panel compares the *field* (massive binary evolution) and *cluster* (dynamical capture) scenarios; observation of 30 binaries are sufficient to distinguish among them at a 95% confidence level in more than 90% of the realizations. From [33].

Combining high and low frequency GW detection, will also help in the identification of the astrophysical channel responsible of BHB formation. Different scenarios in fact result in different mass, mass ratio, spin and eccentricity distribution of the detected sources. Ground and space based detectors are conveniently sensitive to different parameters, providing complementary information. By measuring the last few inspiral cycles with high S/N, a network of second generation ground based detectors will allow to measure individual masses within 10% precision. Information about spin magnitude and direction can be extracted by observing the effect of spin-orbit coupling induced precession, which is maximum in the late inspiral. However, because of GW circularization, BHBs will generally have a non-measurable eccentricity < 0.01 in the aLIGO band, regardless of their formation channel. LISA, on the other hand, by observing up to millions GW cycles, will allow the measurement of individual (redshifted) masses to better than 1% (and often better than 0.1%). Individual spins can be measured in a fraction of cases (Klein et al in preparation), but generally not to high precision. But perhaps most importantly, being sensitive to lower frequencies, LISA will catch GW signals from BHBs that did not have enough time to fully circularize, measuring any eccentricity in excess of $e \approx 10^{-3}$. As independently

pointed out by [33] and [34], this will allow to differentiate between competing formation scenario, chiefly between dynamically formed systems and binary stellar evolution remnants. Figure 4, shows an example of how competitive formation scenarios can be distinguished after a given number of LISA detections, on the basis of eccentricity measurements only. The two lower panels show that a handful of measurements are enough to recognize merger induced by Kozai cycles triggered by the presence of a massive black hole in the proximity of the BHB (model *MBH* from [35]). Conversely, more than 30 detections are required to efficiently differentiate between dynamical formation (model *cluster* from [36]) and stellar evolution remnants (model *field* from [37]). The currently proposed LISA design will likely detect few hundred such systems. Eccentricity information can also be combined with mass and spin measurements (from both LISA and aLIGO) to optimize astrophysical inference.

3.3 Tests of alternative theories of gravity

Multi-band detections will also enhance the potential of gravity tests in the strong, dynamical field regime of merging BHBs. Massive systems will be observed by ground based detectors with high merger (and possibly ringdown) S/N, after being tracked for years by LISA in their adiabatic inspiral. The two portions of signal can be combined to push the search for deviations from General Relativity, due for example to dipolar radiation, as first discussed in [38]. Although timing of binary pulsars excludes the emission of dipole gravitational radiation by binaries [39], entire classes of theories predict this effect predominantly (or only) in binaries involving BHs (see [40] for a review). Joint observations of GW150914-like systems by aLIGO and LISA can potentially improve current bounds on dipole emission from BHBs by more than six orders of magnitude, as shown in figure 5. The figure highlights that even if observed by LISA alone, BHBs constrain these theories better than massive BHBs (MBHBs) and extreme mass ratio inspirals (EMRIs). This is because the signal has to be phased for millions of cycles to be recovered, being therefore sensitive to minuscule phasing deviations caused by dipole emission. When combined to LIGO observations of the same system, typical bounds improve by an additional factor of about five.

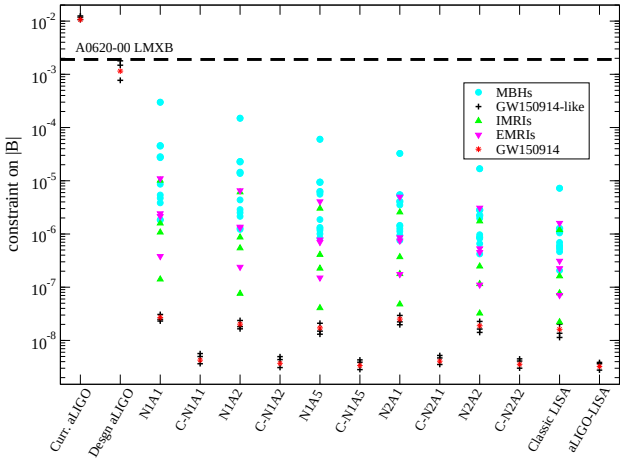


Figure 5 – 1σ constraints on the BH dipole flux parameter B as a function of the assumed GW detector from different GW sources: GW150914-like systems (stars and pluses), massive BH binaries (filled circles) and EMRIs/IMRIs (filled triangles). Shown are the NxAy designs proposed in the GOAT study as well as Classic LISA; the prefix C- indicates observations in combination with aLIGO ad design sensitivity. The current best limit on vacuum dipole radiation from LMXB A0620-00 [41] is shown as a dashed horizontal line for comparison. From [38].

3.4 Cosmography and cosmology

Stellar BHBs observed in the LISA band potentially provide a new class of standard candles. In absence of a distinctive EM counterpart, [42] estimated the number of BHBs that can be localized with enough precision that only one galaxy falls in the GW measurement error cube. They concluded that LISA might measure H_0 to a few% precision, based on the analytical scaling of the average $\Delta\Omega$ and $\Delta D_l/D_l$ and the average number density of possible host galaxies.

Although this is an useful result, it relies on average estimates of quantities ($\Delta\Omega$ and $\Delta D_l/D_l$) that vary by orders of magnitude from one source to another. Moreover, the outcome depends severely on the uncertain BHB merger rate and on the LISA design. A systematic investigation is currently ongoing (del Pozzo et al., in preparation). Preliminary results show in fact that $\Delta D_l/D_l$ errors in [42] are generally underestimated and association with an individual galaxy is not possible. One has therefore to rely on building a likelihood function based on the redshift distributions of plausible galaxy hosts in the GW measurement error cube. The technique has been first applied by [43] to EMRIs and subsequently by [44] to MBHBs. Note that LISA will provide excellent sky localization up to $\Delta\Omega < 0.1\text{deg}^2$ precision, it will not, however, provide a very good measurement of the luminosity distance, D_l, to the source. This latter might in fact be better measured by ground based detectors, that might see those sources with S/N$>$ 100 at design sensitivity. Multi-band BHBs crossing between the two detectors' windows, might therefore be particularly valuable standard candles, combining LISA sky localization with aLIGO distance determination.

3.5 Milky way BHBs

As first pointed out in [45] and then further elaborated in [46], LISA might also detect few such BHBs within the Milky Way. This specific prospect is particularly appealing for a number of reasons. Considering the typical LISA error-cube, the location of those system within the Milky Way will be rather accurate, shedding light on their formation mechanism. In case of few detections, a consistent presence of star clusters or globular clusters within the sky localization error would be a decisive element in support of the dynamical formation scenario (viceversa, the lack thereof would not discard this model, since BHBs can be efficiently ejected from their parent clusters, and the clusters themselves can evaporate by the time the BHBs merge). A frequent localization towards the Galactic centre might provide evidence of the role of dense BH cusps surrounding massive black holes in the formation of these systems, as predicted by some formation channels (see e.g. [47]). Their proximity will also allow to perform deep searches for associated EM signals. If BHBs are surrounded by debris disks left behind by partially failed supernovae, even a small amount of accretion leads to an observable photon flux within galactic distances. In the unlikely event that many such BHBs are detected, then their mass function can be linked to the metallicity content of the MW, to gather further clues about the physics driving their formation.

4 Conclusions

The first aLIGO detections showed that stellar BHBs with chirp masses in excess of $\approx 20M_\odot$ are more abundant than previously thought, and the proposed LISA has the potential to see up to about a thousand of them, depending on the adopted mission design. About 10% of these systems, those caught emitting at $f > 10$ mHz, will sweep through the LISA window, eventually coalescing in the audio band probed by aLIGO. Multi-band and multi instrument observations of these sources will open a number of new possibilities for GW astronomy. Eccentricity measurement of BHB in the LISA band will allow to disentangle between different formation channels, and their exquisite sky localization will provide an independent local measurement of the Hubble constant. The phasing of millions of waveform cycles will constrain theories of gravity allowing dynamical scalarization with unprecedented precision, especially if combined with aLIGO observations of the merger phase. In general, joint and complementary LISA-aLIGO observations of the same source will enhance the scientific potential by combining measurements of the early inspiral (LISA) to observations of merger and ringdown (aLIGO). Moreover, S/N accumulated over years of observations in the LISA band will allow to issue early warnings (with few weeks notice) about when and where the BHB will coalesce in the LIGO band. Ground and space based probes across the EM spectrum can therefore be pre-pointed in

the direction of the system, performing a deep search for possible EM precursors or for bursts coincident with the final coalescence. Multi-band GW observations of BHBs add a new exciting goal to the already rich LISA science case, opening new avenues in multi-messenger astronomy.

References

1. B. P. Abbott, R. Abbott, T. D. Abbott, M. R. Abernathy, F. Acernese, K. Ackley, C. Adams, T. Adams, P. Addesso, R. X. Adhikari, and et al. Observation of Gravitational Waves from a Binary Black Hole Merger. *Physical Review Letters*, 116(6):061102, February 2016.
2. B. P. Abbott, R. Abbott, T. D. Abbott, M. R. Abernathy, F. Acernese, K. Ackley, C. Adams, T. Adams, P. Addesso, R. X. Adhikari, and et al. GW151226: Observation of Gravitational Waves from a 22-Solar-Mass Binary Black Hole Coalescence. *Physical Review Letters*, 116(24):241103, June 2016.
3. B. P. Abbott, R. Abbott, T. D. Abbott, M. R. Abernathy, F. Acernese, K. Ackley, C. Adams, T. Adams, P. Addesso, R. X. Adhikari, and et al. Binary Black Hole Mergers in the First Advanced LIGO Observing Run. *Physical Review X*, 6(4):041015, October 2016.
4. B. P. Abbott, R. Abbott, T. D. Abbott, M. R. Abernathy, F. Acernese, K. Ackley, C. Adams, T. Adams, P. Addesso, R. X. Adhikari, and et al. The Rate of Binary Black Hole Mergers Inferred from Advanced LIGO Observations Surrounding GW150914. *ApJL*, 833:L1, December 2016.
5. K. A. Postnov and L. R. Yungelson. The Evolution of Compact Binary Star Systems. *Living Reviews in Relativity*, 17, May 2014.
6. M. J. Benacquista and J. M. B. Downing. Relativistic Binaries in Globular Clusters. *Living Reviews in Relativity*, 16, March 2013.
7. F. Antonini and F. A. Rasio. Merging Black Hole Binaries in Galactic Nuclei: Implications for Advanced-LIGO Detections. *ApJ*, 831:187, November 2016.
8. I. Mandel and S. E. de Mink. Merging binary black holes formed through chemically homogeneous evolution in short-period stellar binaries. *MNRAS*, 458:2634–2647, May 2016.
9. T. Hartwig, M. Volonteri, V. Bromm, R. S. Klessen, E. Barausse, M. Magg, and A. Stacy. Gravitational waves from the remnants of the first stars. *MNRAS*, 460:L74–L78, July 2016.
10. S. Bird, I. Cholis, J. B. Muñoz, Y. Ali-Haïmoud, M. Kamionkowski, E. D. Kovetz, A. Raccanelli, and A. G. Riess. Did LIGO Detect Dark Matter? *Physical Review Letters*, 116(20):201301, May 2016.
11. J. Abadie, B. P. Abbott, R. Abbott, M. Abernathy, T. Accadia, F. Acernese, C. Adams, R. Adhikari, P. Ajith, B. Allen, and et al. TOPICAL REVIEW: Predictions for the rates of compact binary coalescences observable by ground-based gravitational-wave detectors. *Classical and Quantum Gravity*, 27(17):173001, September 2010.
12. K. Belczynski, M. Dominik, T. Bulik, R. O'Shaughnessy, C. Fryer, and D. E. Holz. The Effect of Metallicity on the Detection Prospects for Gravitational Waves. *ApJL*, 715:L138–L141, June 2010.
13. M. Dominik, E. Berti, R. O'Shaughnessy, I. Mandel, K. Belczynski, C. Fryer, D. E. Holz, T. Bulik, and F. Pannarale. Double Compact Objects III: Gravitational-wave Detection Rates. *ApJ*, 806:263, June 2015.
14. W. M. Farr, N. Sravan, A. Cantrell, L. Kreidberg, C. D. Bailyn, I. Mandel, and V. Kalogera. The Mass Distribution of Stellar-mass Black Holes. *ApJ*, 741:103, November 2011.
15. A. Sesana. Prospects for Multiband Gravitational-Wave Astronomy after GW150914. *Physical Review Letters*, 116(23):231102, June 2016.
16. A. Sesana, J. Gair, I. Mandel, and A. Vecchio. Observing Gravitational Waves from the First Generation of Black Holes. *ApJL*, 698:L129–L132, June 2009.
17. P. Amaro-Seoane and L. Santamaría. Detection of IMBHs with Ground-based Gravitational Wave Observatories: A Biography of a Binary of Black Holes, from Birth to Death. *ApJ*, 722:1197–1206, October 2010.
18. Planck Collaboration, P. A. R. Ade, N. Aghanim, M. Arnaud, M. Ashdown, J. Aumont, C. Baccigalupi, A. J. Banday, R. B. Barreiro, J. G. Bartlett, and et al. Planck 2015 results. XIII. Cosmological parameters. *A&A*, 594:A13, September 2016.
19. A. Klein, E. Barausse, A. Sesana, A. Petiteau, E. Berti, S. Babak, J. Gair, S. Aoudia, I. Hinder, F. Ohme, and B. Wardell. Science with the space-based interferometer eLISA: Supermassive black hole binaries. *Phys. Rev. D*, 93(2):024003, January 2016.
20. Pau Amaro-Seoane et al. eLISA/NGO: Astrophysics and cosmology in the gravitational-wave

millihertz regime. *GW Notes*, 6:4–110, 2013.
21. The LISA Consortium. The Gravitational Universe. *ArXiv e-prints*, May 2013.
22. H. Audley et al. Laser Interferometer Space Antenna. *ArXiv e-prints*, February 2017.
23. M. Armano et al. Sub-Femto-g Free Fall for Space-Based Gravitational Wave Observatories: LISA Pathfinder Results. *Physical Review Letters*, 116(23):231101, June 2016.
24. E. Berti, A. Buonanno, and C. M. Will. Estimating spinning binary parameters and testing alternative theories of gravity with LISA. *Phys. Rev. D*, 71(8):084025, April 2005.
25. A. Nishizawa, E. Berti, A. Klein, and A. Sesana. eLISA eccentricity measurements as tracers of binary black hole formation. *Phys. Rev. D*, 94(6):064020, September 2016.
26. S. Vitale. Multiband Gravitational-Wave Astronomy: Parameter Estimation and Tests of General Relativity with Space- and Ground-Based Detectors. *Physical Review Letters*, 117(5):051102, July 2016.
27. C. Bonvin, C. Caprini, R. Sturani, and N. Tamanini. The effect of matter structure on the gravitational waveform. *ArXiv e-prints*, September 2016.
28. R. Perna, D. Lazzati, and B. Giacomazzo. Short Gamma-Ray Bursts from the Merger of Two Black Holes. *ApJL*, 821:L18, April 2016.
29. K. Murase, K. Kashiyama, P. Mészáros, I. Shoemaker, and N. Senno. Ultrafast Outflows from Black Hole Mergers with a Minidisk. *ApJL*, 822:L9, May 2016.
30. K. Kotera and J. Silk. Ultrahigh-energy Cosmic Rays and Black Hole Mergers. *ApJL*, 823:L29, June 2016.
31. V. Connaughton et al. Fermi GBM Observations of LIGO Gravitational-wave Event GW150914. *ApJL*, 826:L6, July 2016.
32. V. Savchenko et al. INTEGRAL Upper Limits on Gamma-Ray Emission Associated with the Gravitational Wave Event GW150914. *ApJL*, 820:L36, April 2016.
33. A. Nishizawa, A. Sesana, E. Berti, and A. Klein. Constraining stellar binary black hole formation scenarios with eLISA eccentricity measurements. *MNRAS*, 465:4375–4380, March 2017.
34. K. Breivik, C. L. Rodriguez, S. L. Larson, V. Kalogera, and F. A. Rasio. Distinguishing between Formation Channels for Binary Black Holes with LISA. *ApJL*, 830:L18, October 2016.
35. Fabio Antonini and Hagai B. Perets. Secular evolution of compact binaries near massive black holes: Gravitational wave sources and other exotica. *Astrophys. J.*, 757:27, 2012.
36. Carl L. Rodriguez, Sourav Chatterjee, and Frederic A. Rasio. Binary Black Hole Mergers from Globular Clusters: Masses, Merger Rates, and the Impact of Stellar Evolution. *Phys. Rev.*, D93(8):084029, 2016.
37. I. Kowalska, T. Bulik, K. Belczynski, M. Dominik, and D. Gondek-Rosinska. The eccentricity distribution of compact binaries. *Astron. Astrophys.*, 527:A70, 2011.
38. E. Barausse, N. Yunes, and K. Chamberlain. Theory-Agnostic Constraints on Black-Hole Dipole Radiation with Multiband Gravitational-Wave Astrophysics. *Physical Review Letters*, 116(24):241104, June 2016.
39. N. Yunes and S. A. Hughes. Binary pulsar constraints on the parametrized post-Einsteinian framework. *Phys. Rev. D*, 82(8):082002, October 2010.
40. E. Berti et al. Testing general relativity with present and future astrophysical observations. *Classical and Quantum Gravity*, 32(24):243001, December 2015.
41. Kent Yagi. New constraint on scalar gauss-bonnet gravity and a possible explanation for the excess of the orbital decay rate in a low-mass x-ray binary. *Phys. Rev. D*, 86:081504, Oct 2012.
42. K. Kyutoku and N. Seto. Gravitational-wave cosmography with eLISA and the Hubble tension. *ArXiv e-prints*, September 2016.
43. C. L. MacLeod and C. J. Hogan. Precision of Hubble constant derived using black hole binary absolute distances and statistical redshift information. *Phys. Rev. D*, 77(4):043512, February 2008.
44. A. Petiteau, S. Babak, and A. Sesana. Constraining the Dark Energy Equation of State Using LISA Observations of Spinning Massive Black Hole Binaries. *ApJ*, 732:82, May 2011.
45. N. Seto. Prospects of eLISA for detecting Galactic binary black holes similar to GW150914. *MNRAS*, 460:L1–L4, July 2016.
46. P. Christian and A. Loeb. eLISA Detection of Black Hole Binaries in the Milky Way Galaxy. *ArXiv e-prints*, January 2017.
47. I. Bartos, B. Kocsis, Z. Haiman, and S. Márka. Rapid and Bright Stellar-mass Binary Black Hole Mergers in Active Galactic Nuclei. *ApJ*, 835:165, February 2017.

DETECTING ADDITIONAL POLARIZATION MODES WITH LISA

L. PHILIPPOZ, P. JETZER
Physik-Institut, Universität Zürich,
Winterthurerstrasse 190, 8057 Zürich, Switzerland

Within the frame of General Relativity, gravitational waves possess two tensorial polarizations (h_+ and $h_\times$), whereas more general metric theories of gravity predict the existence of additional modes: up to 2 vector and 2 scalar modes. An arbitrary signal such a stochastic GW background is thus expected to contain a mixture of up to 6 polarizations with no dominant mode, and the analysis of its content could give us constraints on GR or its extensions. We addresse the question of whether a given LISA configuration can provide a sufficient sensitivity to detect additional polarization modes and then allow the extraction of the latter in order to determine the GW spectrum for each mode.

1 Introduction

The recent detections of gravitational waves (GW) announced by the LIGO Collaboration [1,2] mark the beginning of a new chapter in GW research. Furthermore, the future ESA L3 mission, the space-borne detector "Laser Interferometer Space Antenna" (LISA) [3], is expected to open new perspectives in the low-frequency domain from 0.1 mHz to 1Hz, giving access to the observation of e.g. supermassive black holes at cosmological distances or binary systems of close white dwarves, or even a stochastic GW background (SGWB).

The dynamics of those mergers can be affected by alterations of GR. The proposed design of the LISA mission [4] makes it possible to reach an unprecedented signal sensitivity and therefore measure the inprints of alternative theories, such as $f(R)$ or scalar-tensor theories. We consider the detection of a SGWB which would in general contain a mixture of all polarization modes. Depending if additional modes are effectively detected or not, this will allow in any case to put constraints and discriminate between alternative gravitation theories.

2 Mode sensitivity and mode extraction

Within the frame of GR, GW possess two tensorial polarizations, the so-called h_+ and $h_\times$ modes, but one can expect additional modes when considering more general metric theories of gravity: up to 2 vector and 2 scalar modes. The perturbed metric of a propagating GW can be expressed as:

$$h_{ij}(\omega t - \mathbf{k}\cdot\mathbf{x}) = \sum_A h_A(\omega t - \mathbf{k}\cdot\mathbf{x}) e^A_{ij} \tag{1}$$

with $A = +, \times, x, y, b, l$ the six possible polarization modes, h_A the GW amplitude of the mode A, and e^A_{ij} the following polarization tensors (tensor ($+$, $\times$), vector (x, y) and scalar (b, l) modes):

$$e^{+}_{ij} = \begin{pmatrix} 1 & 0 & 0 \\ 0 & -1 & 0 \\ 0 & 0 & 0 \end{pmatrix} \quad e^{x}_{ij} = \begin{pmatrix} 0 & 0 & 1 \\ 0 & 0 & 0 \\ 1 & 0 & 0 \end{pmatrix} \quad e^{b}_{ij} = \begin{pmatrix} 1 & 0 & 0 \\ 0 & 1 & 0 \\ 0 & 0 & 0 \end{pmatrix}$$

$$e^{\times}_{ij} = \begin{pmatrix} 0 & 1 & 0 \\ 1 & 0 & 0 \\ 0 & 0 & 0 \end{pmatrix} \quad e^{y}_{ij} = \begin{pmatrix} 0 & 0 & 0 \\ 0 & 0 & 1 \\ 0 & 1 & 0 \end{pmatrix} \quad e^{l}_{ij} = \begin{pmatrix} 0 & 0 & 0 \\ 0 & 0 & 0 \\ 0 & 0 & 1 \end{pmatrix}$$

From now on, we will not assume a particular gravitation theory, which means that a GW is in general expected to contain a mixture of up to 6 polarizations. We will focus on the determination of the detection threshold for each polarization modes present in a SGWB signal and look for a way of extracting this polarization content.

2.1 Network of detectors

The determination of the sensitivity to additional polarization modes was discussed for an earlier version of the LISA mission[5,6,7,8,9,10]. It is therefore necessary to investigate this question for the new design beforehand and establish the sensitivity curves for several time-delay interferometric (TDI) combinations (i.e. different combinations of the signals depending on the number of laser links between the satellites). We already found that the noise spectrum of the future detector presents large similarities with the older project, especially in the frequency range $f \in [10^{-2}, 1]$ Hz, and thus expect the sensitivity spectrum to be quite similar in that frequency domain where, in particular, the sensitivity to the vector and longitudinal-scalar modes is higher.

In its current proposed design (3 satellites with 3 arms, i.e. 3 times 2 laser links between the satellites), LISA is actually equivalent to two single detectors; we will describe this arrangement of three satellites as a cluster. The SGWB signal measured by a single detector can be written as

$$h(t, \mathbf{x}) = \sum_A \int_{S^2} d\hat{\mathbf{\Omega}} \int_{-\infty}^{\infty} df \; \tilde{h}_A(f, \hat{\mathbf{\Omega}}) e^{2\pi i f(t - \hat{\mathbf{\Omega}}\mathbf{x}/c)} F_A(\hat{\mathbf{\Omega}}), \tag{2}$$

with F_A the antenna pattern function of that single detector (which describes its geometry), and h_A the GW amplitude of the mode A. In a single detector, the vectors $\hat{u}$ and $\hat{v}$ give the direction of each arm and one can define the detector tensor D as

$$D_{ij} = \frac{1}{2}(\hat{u}_i \hat{u}_j - \hat{v}_i \hat{v}_j), \tag{3}$$

which describe the response of that detector to a signal.

If one now considers a network of several identical clusters [11,12,13], the first step consists in determining the so-called overlap reduction functions (ORFs), defined for a pair of detectors I and J separated by $\mathbf{\Delta x}$ as

$$\begin{aligned} \gamma^M_{IJ}(f) \;\; = \;\; & \frac{1}{\sin^2(\chi)} \left(\rho^M_1(\alpha) D^{ij}_I D^J_{ij} + \rho^M_2(\alpha) D^i_{I,k} D^{kj}_J \hat{d}_i \hat{d}_j \right. \\ & \left. + \rho^M_3(\alpha) D^{ij}_I D^{kl}_J \hat{d}_i \hat{d}_j \hat{d}_k \hat{d}_l \right), \end{aligned} \tag{4}$$

with M denoting the tensor (T), vector (V) or scalar (S) polarization modes, $\sin^2(\chi) = 1 - (\hat{u} \cdot \hat{v})^2$ a geometry factor (which is $\frac{3}{4}$ for triangular cluster like LISA), $\rho^M_i = f(j_0(\alpha), j_2(\alpha), j_4(\alpha))$ a linear combination of spherical Bessel functions, D^{ij}_I the detector tensor of the interferometer I, $\hat{d}_i = \dfrac{\mathbf{\Delta x}}{|\mathbf{\Delta x}|}$, $\alpha = \dfrac{2\pi f \, |\mathbf{\Delta x}|}{c}$. An ORF tells how much degree of correlation is preserved when one correlates the output of two detectors, according to their relative orientation.

Note that, schematically, the signal $h(t) + n(t)$ measured by a detector is composed of the GW signal $h(t)$ as well as the noise $n(t)$. Next, we can consider the one-sided power spectral density S_h^A:

$$\langle \tilde{h}_A^*(f, \hat{\mathbf{\Omega}}) \tilde{h}_{A'}(f', \hat{\mathbf{\Omega}}') \rangle = \delta(f - f') \frac{1}{4\pi} \delta^2(\hat{\mathbf{\Omega}}, \hat{\mathbf{\Omega}}') \delta_{AA'} \cdot \frac{1}{2} S_h^A(|f|), \tag{5}$$

as well as the noise spectrum $P_I(f)$:

$$\langle \tilde{n}_I(f) \tilde{n}_J(f') \rangle = \frac{1}{2} \delta(f - f') \delta_{IJ} \cdot P_I(|f|), \tag{6}$$

and the GW background energy density

$$\Omega_{\rm gw}^M(f) \propto f^3 S_h^A(f), \tag{7}$$

with e.g. $\Omega_{\rm gw}^T = \Omega_{\rm gw}^+ + \Omega_{\rm gw}^\times$ (and similarly for $M = V, S$). It is then possible to find the optimal signal-to-noise ratio (SNR) necessary to separately detect the modes:

$$SNR^M \propto \int_0^\infty df \left[\frac{(\Omega_{\rm gw}^M(f))^2 \det \mathbf{F}(f)}{f^6 \mathcal{F}_M(f)} \right]^{(1/2)}, \tag{8}$$

where $\mathbf{F}$ is a (3×3)-matrix whose elements are given by

$$F_{MM'} = \sum_{\text{det. pairs}(I,J)} \int_0^{T_{\rm obs}} {\rm d}t \frac{\gamma_{IJ}^M(t, f) \gamma_{IJ}^{M'}(t, f)}{P_I(f) P_J(f)}, \tag{9}$$

($T_{\rm obs}$ is the mission duration) and $\mathcal{F}_M(f)$ is the determinant of the matrix obtained by removing all the M-elements from the matrix $\mathbf{F}$.

The separation of the modes can then be achieved as follows [11]: we first define the statistics

$$\begin{aligned} Z_{IJ} &\propto \left| f^3 \right| \tilde{s}_I^*(f) \tilde{s}_J(f) \\ &= \sum_M \Omega_{\rm GW}^M \gamma_{IJ}^M(f) + \text{ noise }. \end{aligned} \tag{10}$$

By averaging it, one gets the matrix equation

$$\langle Z_{IJ} \rangle = \sum_M \Omega_{\rm GW}^M \gamma_{IJ}^M(f) \tag{11}$$

or shortly $\mathbf{Z} = \mathbf{\Pi}\ \mathbf{\Omega}$. By inverting so-called correlation matrix $\mathbf{\Pi}$ containing the ORF (as long as $\det(\mathbf{\Pi}) \neq 0$), one can finally find the mode densities $\mathbf{\Omega}$.

This method thus gives the detection threshold for each mode and is valid for a network of independant detectors in space, i.e. several clusters (for instance 2 independant LISA-like clusters, or 4 clusters such as in the DECIGO project [15]), in the low frequency limit and for a full polarized GW background. Moreover, it allows to extract from a signal the energy density of each mode.

2.2 Single detector

A study of the sensitivity of LISA (i.e. a cluster with 3 arms) to additional polarization modes has been performed [9] for an earlier version of the project, and the sensitivity curves for each mode as well as various TDI simply need to be updated according to the new proposed design. However, it is worth investigating a minimal version consisting of a cluster with only 2 arms (this situation could arise in case of a technical problem). Such an alternative solution requires the use of the so-called autocorrelation method [14]. As previously, we can write the output data

of the detector as $h(t) + n(t)$, with $n(t)$ the noise and $h(t)$ the GW signal. In that case, the autocorrelation of the signal reads

$$\langle \tilde{h}(f)\tilde{h}^*(f')\rangle = \frac{1}{2}\delta(f - f')S_h(|f|), \tag{12}$$

and similarly for the noise density P_n:

$$\langle \tilde{n}(f)\tilde{n}^*(f')\rangle = \frac{1}{2}\delta(f - f')P_n(|f|), \tag{13}$$

and in that case, it is possible to find the optimal SNR to detect a signal as

$$SNR = \left(\frac{T_{\rm obs}}{2}\int_{-\infty}^{\infty} df\ \frac{S_h(|f|)^2}{\left[S_h(|f|) + P_n(|f|)\right]^2}\right)^{1/2}. \tag{14}$$

This method applies to a single-detector and is valid in the high-frequency limit. Since this analysis did not assume a particular polarization content, it only gives a detection threshold for a GW signal, but it will be necessary to generalize it in order to take into account all the possible modes, similarly to the network analysis.

3 Conclusion

So far, the current analysis method for a network of space-borne detectors requires the use of multiple LISA-like clusters and presents the advantage of considering a general polarization of the signal. A study was already performed for the use of a 3-arm detector and simply needs to be adapated to the most recent LISA design. One can also focus on a single 2-arm detector, but this method does not yet address the polarization of the signal and needs to be generalized in order to fully treat the polarization content; one especially needs to take the correlation of the noise into account.

With the proposed LISA design as well as future possible projects of space-borne inteferometers, it is therefore necessary to investigate both methods in order to set limits on the detectability of each polarization mode potentially present in a SGWB.

References

1. B.P. Abbott *et al.*, *Phys. Rev. Lett.* **116**, 061102 (2016)
2. B.P. Abbott *et al.*, *Phys. Rev. Lett.* **116**, 241103 (2016)
3. P. Amaro-Seoane *et al.*, GW Notes **6**, 4-110 (2013)
4. P. Amaro-Seoane *et al.*, *Preprint* astro-ph/1702:00786 (2017)
5. J.W. Armstrong, F.B. Estabrook and M. Tinto, ApJ **527**, 814 (1999)
6. F.B. Estabrook, M. Tinto and J.W. Armstrong, *Phys. Rev.* D **62**, 042002 (2000)
7. M. Tinto, J.W. Armstrong and F.B. Estabrook, *Phys. Rev.* D **63**, 021101 (2000)
8. M. Tinto, F.B. Estabrook and J.W. Armstrong, *Phys. Rev.* D **65**, 082003 (2002)
9. M. Tinto and M.E. Alves, *Phys. Rev.* D **82**, 122003 (2010)
10. M. Tinto and S.V. Dhurandhar, Living Rev Relativity **17**, 6 (2014)
11. A. Nishizawa, A. Taruya, K. Hayama, S. Kawamura and S. Masa-aki, *Phys. Rev.* D **79**, 082002 (2009)
12. A. Nishizawa and K. Hayama, *Phys. Rev.* D **88**, 064005 (2013)
13. A. Nishizawa, A. Taruya and S. Kawamura, *Phys. Rev.* D **81**, 104043 (2010)
14. M. Tinto and J.W. Armstrong, *Preprint* gr-qc/1205.4620v1 (2012)
15. S. Kawamura *et al.*, Classical Quantum Gravity **23**, S125-S131 (2006)

2.
Tests of the Equivalence Principle

Progress on testing Lorentz symmetry with MICROSCOPE

H. Pihan-Le Bars[1], C. Guerlin[2,1], P. Wolf[1]

[1] *SYRTE, Observatoire de Paris, PSL Research University, CNRS, Sorbonne Universités, UPMC Univ. Paris 06, LNE, 61 avenue de l'Observatoire, 75014 Paris, France*

[2] *Laboratoire Kastler Brossel, ENS-PSL Research University, CNRS, UPMC-Sorbonne Universités, Collège de France*

The Weak Equivalence Principle (WEP) and the local Lorentz invariance (LLI) are two major assumptions of General Relativity (GR). The MICROSCOPE mission, currently operating, will perform a test of the WEP with a precision of 10^{-15}. The data will also be analysed at SYRTE for the purposes of a LLI test realised in collaboration with J. Tasson (Carleton College, Minnesota) and Q. Bailey (Embry-Riddle Aeronautical University, Arizona). This study will be performed in a general framework, called the Standard Model Extension (SME), describing Lorentz violations that could appear at Planck scale (10^{19} GeV). The SME allows us to derive a Lorentz violating observable designed for the MICROSCOPE experiment and to search for possible deviations from LLI in the differential acceleration of the test masses [1].

1 Lorentz violation in SME framework

1.1 Generalities

The LLI can describe the invariance under coordinate changes, called observer invariance, as well as the invariance under orientation and boost changes in a given observer frame - the particle invariance. In case of a space-time anisotropy and in the context of the SME framework, the observer invariance is preserved, but the particle invariance can possibly be violated.

The SME is a general framework built to address the issue of low-energy effects of new physics that could appear at Planck scale in both GR and Standard Model (SM), and particularly spontaneous Lorentz symmetry breaking [2]. It is an effective theory built from the combination of Standard Model (SM) fields and considering a curved spacetime. The resulting additional Lorentz violating terms appearing in the Lagrangian are parametrized by SME background coefficients (scalars, vectors or tensors) quantifying the amplitude of the deviation to the symmetry in a large variety of sectors (e.g. photon, matter, gravity). Most of these coefficients are composition-dependent, meaning that they lead to different deviations to known physics depending on the considered body or particle.

$$\mathcal{L}_{photon} = \frac{1}{4}F_{\mu\nu}F^{\mu\nu} - \frac{1}{4}(k_F)_{\kappa\lambda\mu\nu}F^{\kappa\lambda}F^{\mu\nu} \tag{1}$$

The Eq. 1 illustrates an SME modification to the pure-photon sector Lagrangian [2]. The first term is the usual Lagrangian for Maxwell's equation in absence of sources, and the second term is an SME violating term constructed from the standard Maxwell tensor and parametrized by the SME coefficient (k_F) which is a rank-4 tensor. All these coefficients are free parameters of this effective theory and need to be constrained experimentally.

1.2 SME observables

The SME intends to be independent of any given theory leading to such Lorentz violation, which enables the derivation of general observables for a large range of experiments that cannot be easily done in such theories. However the lack of assumptions on the underlying mechanism for the symmetry breaking makes the SME unable to predict the amplitude of the Lorentz violation signals arising from the coupling between dynamics and SME background coefficients.

Moreover, SME coefficients are coordinate-dependent, but are supposed to be constant in a cosmological frame as well as in any frame having a rectilinear motion with respect to it, *e.g.* the Sun Centered Frame (SCF) which is the conventional frame used to report the results of SME analyses. For a ground or a space based experiment, the transformation between the moving lab frame and the SCF leads to a time-dependent observable whose amplitude is a function of constant SCF SME coefficients, in contrast to the lab frame observable which is function of time-varying lab frame coefficients. This SCF observable can be composed of several harmonics, each having its proper amplitude and dependence on SME coefficients, and whose frequencies are related to the orbital motion of the lab frame with respect to the SCF (see Fig. 1).

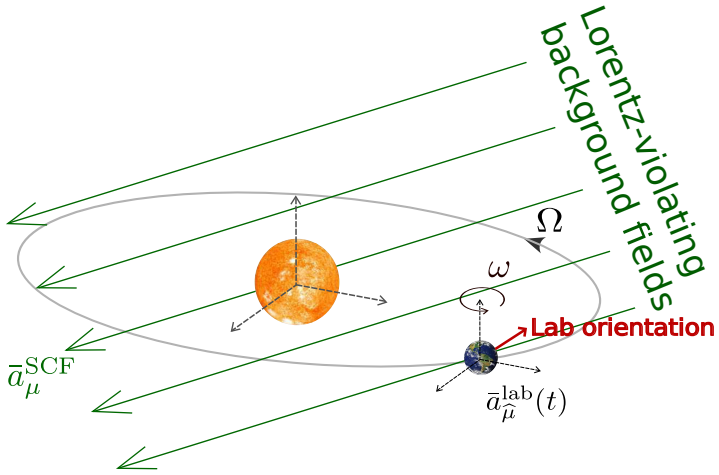
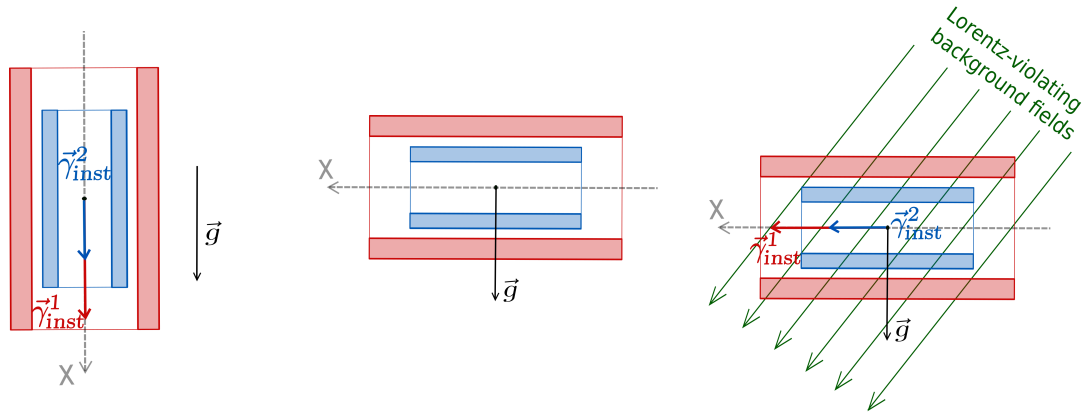


Figure 1 – Schematic view of the trajectory of a Earth based lab frame with respect to the SCF. The vector field $\bar{a}_\mu$ is an arbitrary SME background coefficient. The Earth's orbital and sidereal frequencies are respectively denoted Ω and ω.

2 Application to MICROSCOPE experiment

Several configurations that can be encountered in the WEP and SME LLI tests are described on Fig. 2. Cases (a) and (b) illustrate two typical scenarii of the WEP test: one where a violation signal could be measured (a) and one where no signal is expected (b). Configuration (a) could as well involve a violation signal in the LLI test, despite another signature, but a SME violation could also be expected when the gravitational acceleration $\vec{g}$ is perpendicular to the sensitive axis, as shown with case (c). This is due to the coupling between SME background coefficients and dynamics, such signal is specific to the SME LLI test. The performance of the SME test can easily be compared with the WEP test thanks to an analytical matching between the Eötvös parameter η and a component of a Geocentric Celestial Reference Frame (GCRF) SME coefficient, $(\bar{a}_{\mathrm{eff}})_t$.

The nature of the Lorentz violation occurring in the SME leads to harmonics that are not expected in the WEP test, which can only involve a violation signal at frequencies $\omega_o \pm \omega_s$ with ω_o the satellite orbital frequency and ω_s the satellite spinning frequency. In the SME case, a violation could be expected at frequencies $\{\omega_s, \omega_o, \omega_s \pm \omega_o, \omega_s \pm 2\omega_o, 2\omega_s \pm 2\omega_o, \omega_s \pm \omega_o \pm \Omega\}$ [1], with Ω the Earth's orbital frequency.



(a) Signal $\neq 0$ (b) No signal (c) Signal $\neq 0$

Figure 2 – Schematic view of the test masses: the blue one is in platinum and red one is the titanium mass. The acceleration of the titanium and platinum test masses in the instrument frame are respectively denoted $\vec{\gamma}^1_{\text{inst}}$ and $\vec{\gamma}^2_{\text{inst}}$. Cases (a) and (b) illustrate two scenarii of the WEP test: in (a) the sensitive axis X is parallel to the gravitational acceleration $\vec{g}$ and in (b) it is perpendicular to $\vec{g}$. Case (c) shows the SME equivalent to (b), where a violation signal can be expected.

The main systematics that could overlap with SME violation signals will be due to offcenterings, which are mainly expected to contribute at frequency $2\omega_o$. However, even if some SME harmonics are strongly correlated with offcenterings, SME coefficients could still be decorrelated from each other and from offcenterings as the SME test involves many frequency components with amplitudes ruled by a particular combination of SME coefficients for each of them. During our analysis, we will investigate this correlation between SME coefficients and offcenterings.

As we are measuring a differential acceleration, only composition-dependent coefficients can be constrained with the MICROSCOPE observable: the rank-2 tensor $\bar{c}_{\mu\nu}$ and the vector $(\bar{a}_{\text{eff}})_\mu$, with coordinates denoted by $x_\mu = (t, x, y, z)$. They both lead to different trajectories for the platinum and the titanium mass. Based on the attempted performance of the mission, it has been estimated that we could improve by up to 3 orders of magnitude the limits on some of these coefficients [1], but it will depend on the noise and systematics encountered during the flight.

3 Status

3.1 SME observable for MICROSCOPE

We chose a semi-analytical approach to obtain the MICROSCOPE instrument observable, *i.e.* the instrument frame acceleration depending on SCF SME coefficients: first through an analytical derivation of the differential acceleration in the instrument frame in terms of GCRF coefficients, and then a numerical instantaneous transformation from GCRF to SCF coefficients.

The first step is based on the Lagrangian introduced in [1] and expressed in the GCRF. In order to determine the instrument differential acceleration, one needs to change the GCRF acceleration - obtained from Euler-Lagrange equations - into the instrument acceleration through a coordinate transformation. After this process, the instrument acceleration is still a function of GCRF coefficients, which enables comparisons with WEP test, keeping only the $(\bar{a}_{\text{eff}})_t$ coefficient in the SME observable.

The instantaneous transformation from GCRF to SCF coefficients will be performed numerically using INPOP ephemerides provided by IMCCE. This last operation is needed to express the observable in terms of SCF coefficients, which is conventional in SME tests and introduces new violation frequencies in the model, as explained in Sec. 1.2.

The first expression for the LLI violating observables in Microscope was given in terms

of Keplerian elements [1]. Here we designed our model according to simulated data provided by ONERA/OCA in order to include as far as possible the in-flight parameters. This in combination with the semi-analytical approach makes our model flexible and convenient for the comparison with the WEP test.

3.2 Data analysis

For now, we worked on a first set of simulated data provided by ONERA/OCA. This enabled us to familiarise ourselves with the data and to perform some least-squares fitting on toy-models. Among other things, we identified that the contribution of the Earth's Newtonian gravitational potential, initially taken in the approximation of a uniform spherical source [1], needs to take into account higher order harmonics in order to allow direct comparison with results obtained in the standard WEP analysis. We also gradually including the contributions from angular velocity matrix, gravity gradient matrix, and so on.

The first toy-models adjustments were consistent with the parameters used in the simulations, however it has been done using unrealistic data, without noise. We are currently working on the same kind of test with new sets of simulated data including a realistic noise. Obviously, this requires the implementation of statistical methods to deal with this realistic coloured noise, which prevents the use of a simple least-squares fitting. As a first step, we are planning to use Monte-Carlo simulations based on a noise model provided by ONERA/OCA to perform the statistical analysis.

4 Conclusion

The preparation of the SME analysis of MICROCOPE data is currently ongoing at SYRTE. We are working on the derivation of an observable designed according to the in-flight parameters. The implementation of statistical methods for the data analysis is also in progress, thanks to simulated data provided by ONERA/OCA.

In the next few months, we will increase the complexity of the model and of the simulated data in order to check the consistency of both the observable and the statistical analysis methods.

Acknowledgments

We would like to acknowledge G. Métris and L. Serron for their availability and for providing us simulated data and the related documentation.

References

1. V. A. Kostelecký and J. D. Tasson, *Phys. Rev.* D **83**, 016013 (2011).
2. D. Colladay and V. A. Kostelecký, *Phys. Rev.* D **58**, 116002 (1998).

ANTIMATTER AND GRAVITATION

P. DEBU
Direction de la recherche fondamentale, CEA Saclay,
91191 Gif-sur-Yvette cedex, France



Three experiments et CERN are about to "weight" antihydrogen. We describe the objectives of the experiments trying to measure the gravitation effect on antimatter, we review some of the theoretical constraints on a possible different gravitational behavior between matter and antimatter, and give an overview of the existing experimental limits and proposals.

1 Scientific aim

1.1 The Equivalence Principle

The main objective of the measurement of the action of gravity on antimatter is to perform a direct test with antimatter of the Einstein Equivalence Principle which states that the trajectory of a test particle is independant of its composition and internal structure when its is solely subject to gravitational forces. This principle has been verified with many materials. A very high precision of around 10^{-13} has been reached. A torsion pendulum experiment [1] with Beryllium and Titanium test bodies led to the following difference between their gravitational acceleration:

$$(\Delta a/a)_{\mathrm{Be/Ti}} = (0.3 \pm 1.8) \times 10^{-13}. \quad (1)$$

A precise follow up of the relative motion of the Earth and the Moon ("Lunar Laser Ranging" [2]) gave:

$$(\Delta a/a)_{\mathrm{Earth/Moon}} = (-1.0 \pm 1.4) \times 10^{-13}. \quad (2)$$

1.2 Antimatter

In the Standard Model of particle physics, every particle comes with its own antiparticle which carries an opposite charge but, as stated by the CPT theorem, has exactly the same inertial mass and the same lifetime. The most stringent limit on the inertial mass equality is [3]:

$$(M_{K^0} - M_{\bar{K^0}})/M_{\mathrm{average}} < 6 \times 10^{-19} \ (90\ \%\ \mathrm{CL}). \quad (3)$$

As we will see, there is nos such comparison for the particle and its antiparticle *gravitational* mass, a quantity which we define in the next section.

1.3 The measured $\bar{g}$ parameter

We define the gravitational mass of an antimatter test body $\bar{m}_g$ by the following equation:

$$F = G\frac{M_E \bar{m}_g}{R_E^2}, \tag{4}$$

where F is the force acting on the body, G is the Newton gravitational constant and M_E and R_E are the mass and radius of the Earth. We define its inertial mass by:

$$F = \bar{m}_i a, \tag{5}$$

where a is its acceleration. The $\bar{g}$ parameter is then defined by:

$$\bar{g} = a = G\frac{M_E}{R_E^2}\frac{\bar{m}_g}{\bar{m}_i} = g\frac{\bar{m}_g}{\bar{m}_i}, \tag{6}$$

where g is the usual terrestrial acceleration.

Any difference between the measured $\bar{g}$ parameter and g arises from a difference between the gravitational and inertial mass of the test body and signs a violation of the Equivalence Principle or the presence of additional unknown forces.

2 Theoretical constraints

2.1 The Morrison argument

It is well known that in the framework of General Relativity, the violation of the Equivalence Principle by antimatter would lead to the violation of energy conservation [4]. Assuming that antimatter undergoes antigravity, on can raise a particle-antiparticle pair at rest at the height H without any energy cost (see fig. 1). Their annihilation gives two photons of energy $E = mc^2$, where m is the particle inertial mass. If one recombines them at the original height to form the pair again, because of the variation of the gravitational potential, the two photons have gained an energy EgH/c^2: the net balance is an energy increase of $2mgH$!

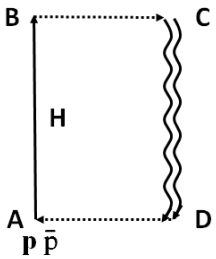


Figure 1 – Illstration of the Morrison argument (see text).

It is straightforward to extend this argument to any difference between matter and antimatter gravitational behaviour.

However, it has been shown in a seminal paper by J. Scherk [5] that antigravity may arise naturally in extensions of General Relativity, where additional fields can couple to baryon number. The potential between two test masses can be written as [6]:

$$V = -G\frac{mm'}{r}(1 \mp a\exp(-r/v) + b\exp(-r/s)). \tag{7}$$

The non-newtonian terms arise from the exchange of so-called gravi-vector and gravi-scalar fields. G is the Newton constant, m and m' are the masses of the interacting bodies and r their

distance, v and s are the range of the vector and scalar interactions, and a and b measure their intensity. In the case of matter, the first term is repulsive and may be cancelled by the second one, while both terms are attractive for one antimatter test body. As a consequence, tests of the Equivalence Principle with matter only are mostly sensitive to $|b - a|$ and do not exclude measurable effects with antimatter.

2.2 Indirect theoretical constraints

The cancellation mentioned in the previous section between scalar and vector interactions cannot be perfect since the latter has a 4-velocity dependence which is not present in the former. This fact can been exploited [7] to put very stringent limits on $|\bar{g} - g|/g$. They are based on three observations:

1. the radiative damping of binary pulsar systems depends on the nature of the gravitational interaction;
2. the vector field couples to the baryon number which is not exactly proportional to the nucleus mass;
3. the mean velocity of the nucleons within the nucleus depends on the element.

These effects are constrained by the tests of the Equivalence Principle with matter which thus lead to limits ranging from 10^{-4} to 10^{-7}.

In the same paper [7], a second class of limits is derived from an argument originally formulated by L.I. Schiff [8]: in quantum field theory, vacuum polarization effects arise from virtual particles and antiparticles (figure 2). One can say that any matter object carries an antimatter content,

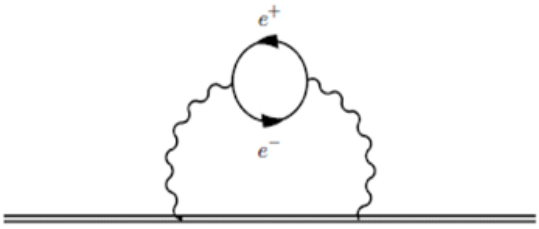


Figure 2 – Loop contribution to the self-energy of the nucleus.

the amount of which being of order of the correction on the binding energy of nuclei within the nucleus or of electrons within atoms due to these virtual pairs. Assuming this reasoning is correct, which is not obvious because of the needed renormalization of the indefinite loops in quantum field theory, the tests of the Equivalence Principle with matter translate directly to limits ranging from 10^{-2} to 10^{-9} by simply scaling them by the inverse relative energy correction.

2.3 Standard Model Extension

Models to analyze the experimental tests of CPT and Lorentz invariance have been developped. In the Standard Model Extension [9,10,11], CPT and Lorentz violating operators are introduced. This gives a framework to quantify and compare the many existing experimental constraints. Within this framework, all the previous limits can be evaded.

However, within the specific Isotropic Parachute Model [12], other limits can be put, using atomic interferometry experiments or using again the kinetic energy of the nuclei within the nucleus, down to 10^{-6} to 10^{-8}.

All these limits are strongly model dependant [13].

References to other models can be found in the presentations made at the 2015 Workshop on Antimatter and Gravity [14].

3 Cosmology

One of the fundamental questions in physics today is the origin of the matter-antimatter asymmetry of the Universe. Three minimal conditions were formulated by A. Sakharov in 1967 [15] to understand it: C and CP symmetry violation, baryon number violation, evolution out of thermal equilibrium. All of them are met within the theoretical framework of the Standard Models of particle physics and cosmology. However, the asymmetry which can be quantitatively derived is too low by many orders of magnitude [16].

The main ingredients of the today's Standard Model of cosmology needed to explain the observations are: General Relativity with a non zero cosmological constant, or equivalently dark energy; a large cold dark matter content; inflation. This model fits experimental data extremely well at large scales, but its ingredients have no observed counterpart in particle physics, and in addition, tensions with observations exist at small scales [17,18].

Motivated by these facts, some authors [19] have tried to build a cosmology without dark matter and dark energy, with as much matter as antimatter, but with a repulsive interaction between them, the origin of which is not addressed. Although this model cannot reproduce all astrophysical observations, it is rather successful in reproducing some of them: the Hubble diagram of SNIa; the abundance of ^{4}He; the order of magnitude of the baryonic acoustic scale.

In summary, whether or not one can build such a model, the question of the interplay between matter, antimatter and gravitation appears as a very relevant question for cosmology.

4 Constraints from experiments

4.1 The $K^0 - \bar{K^0}$ system

The CPLEAR experiment at CERN was dedicated to the study of discrete symmetries with the neutral kaon system [20]. $K^0 - \bar{K^0}$ pairs were produced by the annihilation of antiprotons at rest in a hydrogen target.

A very high number of K decays were recorded, and this allowed a systematic study of the $K^0 - \bar{K^0}$ oscillation parameters as a function of time and also as a function of the direction of the flying neutral kaons [21].

The CP violation parameters $\eta^{\pm}$ and $\Phi^{\pm}$ depend on the neutral kaon mass, and are sensitive to an effective mass difference δm_{eff} which would originate from a different apparent gravitational potential energy, which can be written as:

$$\delta m_{\text{eff}} = M_{K^0}(\frac{g-\bar{g}}{g})\frac{GM}{rc^2}\exp(-r/r_I)f(I), \tag{8}$$

where M is the mass of the gravitationally attracting body, r its distance to the neutral kaon system, I the spin of the particle exchanged in the interaction, r_I the range of the force, $f(I)$ a spin dependant factor.

The study of the time variation of $\eta^{\pm}$ and $\Phi^{\pm}$ or its dependence upon the flight direction of the kaons allow to test the effect of the Earth (flight direction), the Moon (monthly modulation) and the Sun (annual modulation) gravitational fields as a function of I and r_I. Depending on the assumptions made on I and r_I, limits can be put on $|g-\bar{g}|/g$ ranging from a few 10^{-5} to few 10^{-9}.

In addition, the (absolute) potential from the Galaxy or the Supercluster changes the energy (the inertial mass) of the K^0 and $\bar{K^0}$. As a consequence, the measurement by CPLEAR of the $K^0 - \bar{K^0}$ mass difference:

$$\delta m = (-2.6 \pm 2.8) \times 10^{-19}\ \text{GeV} \tag{9}$$

can be used to place limits on $|g-\bar{g}|/g$ of a few 10^{-12} to a few 10^{-14}.

4.2 The antiproton cyclotron frequency

Gabrielse and collaborators have measured the cyclotron frequencies of simultaneously trapped $\bar{p}$ and H^- ions [22] and get from this measurement the following relative difference between the antiproton and the proton cyclotron frequencies:

$$|\omega(p) - \omega(\bar{p})|/\omega(p) = (9 \pm 9) \times 10^{-11}. \tag{10}$$

In the framework of General Relativity, the cyclotron frequencies can be seen as local clocks, the rates of which undergo a shift depending on the gravitational potential U [23]:

$$\omega = \frac{qB}{m}(1 + (3\alpha - 2)U/c^2), \tag{11}$$

where B is the magnetic field, q and m the charge and mass of the (anti)particle, and $\alpha = 1$ for a particle and $\alpha = \bar{g}/g$ for an antiparticle.

The frequency measurement leads to a limit on $|g - \bar{g})|/g$ which depends on the range of an anomalous gravitational interaction which would distinguish matter and antimatter and of the potential source at stake. It is around 10^{-6} if one chooses the potential of the local Supercluster.

4.3 Neutrinos

The time arrival of photons and neutrinos produced by the explosion of the SN1987A supernova has been recorded by several detectors [24]. The gravitationally induced time delay in arrival of these particles is approximately given by [25]:

$$\delta t = MG[-R/\sqrt{R^2 + b^2} + (1 + \gamma)\ln[[R + \sqrt{R^2 + b^2}]/b]], \tag{12}$$

where M is the mass of the galaxy, R is the distance from Earth to SN1987A, b the impact parameter, and γ the post-Newtonian factor which is equal to 1 for all particles in General Relativity. Paksava et al [26] argue that the "neutrino" events are an admixture of at least one neutrino-electron scattering and 18 antineutrino-proton capture events with 90 % confidence level; under this hypothesis, the observed times of the events yield:

$$\gamma(\nu_e) - \gamma(\bar{\nu}_e) < 10^{-6}. \tag{13}$$

While the other experimental constraints give limits on $|g - \bar{g})|/g$ which can be considered as indirect because they are subject to theoretical assumptions to be translated into a test of the Equivalence Principle with antimatter, (13), if its assumption is acknowledged, can be seen as a direct test.

5 Past attempts and proposals

Positrons

The measurement of the gravitational acceleration of positrons has been proposed, but only preliminary measurements with electrons have been performed [27], the interpretation of which was questioned. This experiment is indeed extremely difficult, since the Earth gravitational acceleration on an electron is overwhelmed by a single charge closer than 5 m.

Antiprotons

A gravitation experiment with antiprotons has been proposed [28] to be performed at the Low Energy Antiproton Ring at CERN, but the latter was shutdown before the start of the experiment.

Antineutrons

The antineutron being neutral, it may be thought to be a better candidate. However, an experiment with antineutrons would be very difficult because they are produced at high energy [29] and cannot be easily slowed down.

Positronium

Positronium (Ps) is the bound $e^+ - e^-$ system. It is neutral, and its composition is a real admixture of a particle and an antiparticle, but it has a very short lifetime in its ground state (τ = 125 ps for the para-positronium, 142 ns for the ortho-positronium). This can be easily overcome if on excites it at a higher level n since the lifetime varies as:

$$\tau \simeq (n/25)^{5.236} \times 2.25 \text{ ms}. \tag{14}$$

However, Ps in a Rydberg state is highly polarisable and sensitive to stray electric fields. It is also difficult to cool and can be easily ionised by thermal radiation. The feasibility of a gravitation experiment with positronium is thoroughly discussed by Mills and Leventhal [30] and a project is being contemplated by Cassidy [31].

Muonium

An experiment with muonium (M), the $\mu^+ - e^-$ bound system, is in an R&D stage [32]. A slow M beam (6 km/s) of muonium is under development at the Paul Scherrer Institute in Switzerland. The M beam is formed by stopping muons in a thin film of superfluid helium. M formed within the film are ejected perpendicular to the film with a small energy spread at around 6 km/s velocity. They will intercept a three grating atom interferometer. The aim is to measure the gravitational deflection to better than a nanometer. It requires a very precise alignement and caliration of the gratings, at the picometer level. As acknowledged by the authors, "*the technical challenges are significant*".

6 Experiments with antihydrogen

Antihydrogen is the next simplest system to perform a gravitation experiment. Antihydrogen atoms are produced at CERN since 1995 [33]. Antiprotons of 1.94 GeV/c momentum impinged on a Xe cluster target. The production mechanism is dominated by the reaction (Z represents the target nucleus):

$$\bar{p}Z \rightarrow \bar{p}\gamma\gamma Z \rightarrow \bar{p}e^+e^-Z \rightarrow \bar{H}e^-Z, \tag{15}$$

which has a very low cross section and gives hot antihydrogen atoms, not suitable for precision experiments. Nowadays, experiments use the 3 body reaction:

$$\bar{p}Ps \rightarrow \bar{H}e^-, \tag{16}$$

which allows the production of slower antihydrogen atoms.

It took many years to improve the production mechanism, and to cool, trap and control the antiatoms to prepare for precise measurements. The confinement of antihydrogen for 1000 seconds by the **ALPHA** collaboration provided a major step forward [34], as stressed in the abstract of the article: "*These advances open up a range of experimental possibilities, including precision studies of charge-parity-time reversal symmetry and cooling to temperatures where gravitational effects could become apparent*". And indeed, they were able two years later to put a direct limit on $\bar{g}$ [35]:

$$-65 < \bar{g}/g < 110 \text{ (95 \% CL)}. \tag{17}$$

This result is derived from the distribution of the annihilation position in the ALPHA apparatus of 434 antihydrogen atoms after they were released from the magnetic trap. The ALPHA Collaboration has a project to do a 10 % measurement of $\bar{g}$ using the same technique but with a vertical detector, and a longer term project for a precise measurement using the method of atom interferometry [36].

Two other experiments are under preparation at the CERN/AD (Antiproton Decelerator): AE$\bar{g}$IS [37] and GBAR [38]. Their status is described in these proceedings respectively by Pierre Lansonneur and P. Indelicato. Both experiments will eventually take advantage of the Extremely Low Energy Antipronton ring under construction in the AD hall [39].

The **AE$\bar{g}$IS** experiment will measure the deflection of a slow (500 m/s) $\bar{H}$ beam using a Moiré deflectometer with a few μm precision. It has crossed important steps towards a few % precision measurement.

GBAR will use a novel technique to produce antihydrogen atoms: they will first produce $\bar{H}^+$ ions (an antiproton with two bound positrons, the antimatter counterpart of the H^- ion) with the successive reactions:

$$\bar{p}Ps \rightarrow \bar{H}e^- \text{ followed by } \bar{H}Ps \rightarrow \bar{H}^+e^-. \tag{18}$$

$\bar{H}^+$ ions can be sympathetically cooled to around 10 μK. The excess positron is laser photodetached to perform the free fall of $\bar{H}$ "at rest" (0.5 m/s).

Both experiments aim at an initial few % precision on $\bar{g}$. GBAR will improve this precision to better than 10^{-3} by using quantum reflection of antihydrogen atoms [40,41,42]. The experiment has just started installation at CERN.

7 Conclusion

We are convinced that the conclusions of the review by Nieto and Goldman [43] on gravity measurements on antimatter remain quite relevant and instructive in spite of its old publication date. One can still state with them that "*whether or not one now accepts the existence of non-Newtonian gravitational forces, the possibility of new non-inverse-square and/or composition-dependent components of gravity must be thoroughly studied*".

However, we have shown that any anomalous effect is expected to be quite small. All the experiments are extremely challenging. A 1 % measurement will be a major breakthrough, but should be the first step towards a much higher precision.

References

1. S. Schlamminger *et al*, *Phys. Rev. Lett.* **100**, 041101 (2008).
2. J.G. Williams *et al*, *Phys. Rev. Lett.* **93**, 261101 (2004).
3. C. Patrigani *et al* (Particle Data Group), *Chin. Phys.* C **40**, 100001 (2016).
4. P. Morrison, *American J. Phys.* **26**, 358 (1958).
5. J. Scherk, *Phys. Lett.* B **88**, 265 (1979).
6. S. Bellucci and V. Faraoni, *Phys. Lett.* B **377**, 55 (1996).
7. D.S.M. Alves *et al*, SU-ITP-09/36 (2009).
8. L.I. Schiff, *Phys. Rev. Lett.* **1**, 254 (1958).
9. D. Colladay and V.A. Kostelecký, *Phys. Rev.* D **55**, 6760 (1997), *Phys. Rev.* D **58**, 116002 (1998).
10. V.A. Kostelecký, *Phys. Rev.* D **69**, 105009 (2004).
11. V.A. Kostelecký and M. Mewes, *Phys. Rev.* D **80**, 015020 (2009), *Phys. Rev.* D **85**, 096005 (2012), *Phys. Rev.* D **88**, 096006 (2013).
12. J.D. Tasson, *Int. J. Mod. Phys. Conf. Ser.* **30**, 1460273 (2014).
13. J.D. Tasson, *Phys. Rev. Lett.* **111**, 151102 (2013).

14. 3rd International Workshop on Antimatter and Gravitation, https://indico.cern.ch/event/361413/.
15. A.D. Sakharov, *JETP Lett.* **5**, 24 (1967).
16. M. Dine and A. Kusenko, *Rev. Mod. Phys.* **76**, 1 (2004).
17. R.H. Sanders and S.S. McGaugh, *Ann. Rev. A&A* **40**, 263 (2002).
18. B. Famaey and S.S. McGaugh, *Living Rev. Relativity* **15**, 110 (2012).
19. A. Benoît-Lévy and G. Chardin, *A&A* **537**, A78 (2012).
20. A. Angelopoulos *et al* (CPLEAR Collaboration), *Phys. Report* **374**, 165 (2003).
21. A. Apostolakis *et al*, *Phys. Lett.* B **452**, 425 (1999).
22. G. Gabrielse *et al*, *Phys. Rev. Lett.* **82**, 3198 (1999).
23. R. Hughes and M. Holzsheiter, *Phys. Rev. Lett.* **66**, 854 (1999).
24. Kamiokande Collaboration, K. Hirata *et al*, *Phys. Rev. Lett.* **58**, 1490 (1987), IMP Collaboration, R.M. Bionta *et al*, *Phys. Rev. Lett.* **58**, 1494 (1987), C. Bratton *et al*, *Phys. Rev.* D **37**, 3361 (1988).
25. S. Weinberg in *Gravitation and Cosmology*, ed. Wiley (New York, 1972).
26. S. Paksava *et al*, *Phys. Rev.* D **39**, 1761 (1989).
27. F.Witteborn and W. Fairbank, *Phys. Rev. Lett.* **19**, 1049 (1967).
28. PS200 Proposal, *Los Alamos Report LA-UR* **86-260** (1986).
29. T. Brando *et al*, *Nucl. Instrum. Methods* **180**, 461 (1981).
30. A.P. Mills and M. Leventhal, *Nucl. Instrum. Methods* B **192**, 102 (2002).
31. G. Dufour *et al*, *Adv. in High Energy Physics* **2015**, 379642 (2015).
32. D.M. Kaplan *et al*, *IIT-CAP* **16-1** (2016).
33. G. Baur *et al*, *Phys. Lett.* B **368**, 251 (1996).
34. G..B Andresen *et al*, *Nature Physics* **7**, 558 (2011).
35. C. Amole *et al*, *Nature Communications* **4**, 1785 (2013).
36. P. Hamilton *et al*, *Phys. Rev. Lett.* **112**, 121102 (2014).
37. A. Kellerbauer *et al* (AEgIS Collaboration), *Nucl. Instrum. Methods* B **266**, 351 (2008).
38. G. Chardin *et al* (GBAR Collaboration), *CERN-SPSC* **P342** (2011).
39. W. Bartmann *et al*, *EPJ Web of Conferences* **95**, 04012 (2015).
40. G. Dufour *et al*, *European Phys. J.* C **64**, 2731 (2014).
41. A.Y. Voronin, P. Froelich, V.V. Nesvishevsky, *Phys. Rev.* A **83**, 032903 (2011).
42. A.Y. Voronin, V.V. Nesvishevsky, S. Reynaud, *J. Phys.* B **45**, 165007 (2012).
43. M.M. Nieto and T. Goldman, *Phys. Report* **205**, 221 (1991).

AEgIS Experiment: Status & Outlook

P. Lansonneur[1], S. Aghion[2,3], C. Amsler[5], G. Bonomi[6,7], R. S. Brusa[8,9], M. Caccia[3,10], R. Caravita[11,12], F. Castelli[3,14], G. Cerchiari[15], D. Comparat[16], G. Consolati[2,3], A. Demetrio[17], L. Di Noto[11,12], M. Doser[13], C. Evans[2,3], R. Ferragut[2,3], J. Fesel[13], A. Fontana[7], S. Gerber[13], M. Giammarchi[3], A. Gligorova[19], F. Guatieri[8,9], S. Haider[13], A. Hinterberger[13], H. Holmestad[21], A. Kellerbauer[15], O. Khalidova[13], D. Krasnicky[11,12], V. Lagomarsino[11,12], P. Lebrun[1], C. Malbrunot[13,5], S. Mariazzi[5], J. Marton[5], V. Matveev[22,23], Z. Mazzotta[3,14], S. R. Müller[17], G. Nebbia[24], P. Nedelec[1], M. Oberthaler[17], N. Pacico[19], D. Pagano[6,7], L. Penasa[8,9], V. Petracek[20], F. Prelz[3], M. Prevedelli[25], L. Ravelli[8,9], B. Rienaecker[13], J. Robert[16], O. M. Rhøne[21], A. Rotondi[7,26], M. Sacerdoti[3,14], H. Sandaker[21], R. Santoro[3,10], M. Simon[5], L. Smestad[13],[28], F. Sorrentino[11,12], G. Testera[12], I. C. Tietje[13], E. Widmann[5], P. Yzombard[16], C. Zimmer[13,15,3], J. Zmeska[5], N. Zurlo[7,29].

[1]Institute of Nuclear Physics, CNRS/IN2p3, University of Lyon 1, 69622 Villeurbanne, France
[2]Politecnico of Milano, Piazza Leonardo da Vinci 32, 20133 Milano, Italy
[3]INFN Milano, via Celoria 16, 20133, Milano, Italy
[5]Stefan Meyer Institute for Subatomic Physics, Austrian Academy of Sciences, Boltzmanngasse 3, 1090 Vienna, Austria
[6]Department of Mechanical and Industrial Engineering, University of Brescia, via Branze 38, 25123 Brescia, Italy
[7]INFN Pavia, via Bassi 6, 27100 Pavia, Italy
[8]Department of Physics, University of Trento, via Sommarive 14, 38123 Povo, Trento, Italy
[9]TIFPA/INFN Trento, via Sommarive 14, 38123 Povo, Trento, Italy
[10]Department of Science, University of Insubria, Via Valleggio 11, 22100 Como, Italy
[11]Department of Physics, University of Genova, via Dodecaneso 33, 16146 Genova, Italy
[12]INFN Genova, via Dodecaneso 33, 16146 Genova, Italy
[13]Physics Department, CERN, 1211 Geneva 23, Switzerland
[14]Department of Physics, University of Milano, via Celoria 16, 20133 Milano, Italy
[15]Max Planck Institute for Nuclear Physics, Saupfercheckweg 1, 69117 Heidelberg, Germany
[16]Laboratoire Aimé Cotton, Université Paris-Sud, ENS Cachan, CNRS, Université Paris-Saclay, 91405 Orsay Cedex, France
[17]Kirchhoff-Institute for Physics, Heidelberg University, Im Neuenheimer Feld 227, 69120 Heidelberg, Germany
[18]Department of Physics, Heidelberg University, Im Neuenheimer Feld 226, 69120 Heidelberg, Germany
[19]Institute of Physics and Technology, University of Bergen, Allégaten 55, 5007 Bergen, Norway
[20]Czech Technical University, Prague, Brehova 7, 11519 Prague 1, Czech Republic
[21]Department of Physics, University of Oslo, Sem Saelandsvei 24, 0371 Oslo, Norway
[22]Institute for Nuclear Research of the Russian Academy of Science, Moscow 117312, Russia
[23]Joint Institute for Nuclear Research, 141980 Dubna, Russia
[24]INFN Padova, via Marzolo 8, 35131 Padova, Italy
[25]University of Bologna, Viale Berti Pichat 6/2, 40126 Bologna, Italy
[26]Department of Physics, University of Pavia, via Bassi 6, 27100 Pavia, Italy
[27]Department of Physics "Ettore Pancini", University of Napoli Federico II, Complesso Universitario di Monte S. Angelo, 80126, Napoli, Italy
[28]The Research Council of Norway, P.O. Box 564, NO-1327 Lysaker, Norway
[29]Department of Civil Engineering, University of Brescia, via Branze 43, 25123 Brescia, Italy

The AEGIS experiment [1] (Antimatter Experiment: Gravity, Interferometry, Spectroscopy) is planned to perform the first measurement of the gravitational acceleration on antimatter by observing the free fall of antihydrogen atoms. By combining techniques based on recent developments in the production of positronium and its laser excitation to Rydberg states, such a study seems indeed to be feasible for neutral antimatter. We present here some of the experimental techniques involved in the experiment as well as the status of the detector test envisioned for the gravity measurement.

1 Scientific goal and challenges

The weak equivalence principle states that the motion of a particle is independent of its composition and internal structure when submitted to gravity. Although several attempts were made in the past to test this principle with antiprotons [2] or positrons [3], they lead to large uncertainties mainly due to difficulties to control coulombian effects. For this reason, neutral antihydrogen atoms, benefiting from the extensive experimental developments achieved in the 1990's at CERN appear thus to be good candidates. The goal of the AEGIS experiment is to test the weak equivalence principle for neutral antihydrogen ($\overline{\mathrm{H}}$ in the following). The challenging idea is to produce a beam of cold anti-atoms by charge-exchange reaction, involving antiprotons ($\bar{\mathrm{p}}$), provided by the antiproton decelerator (AD) at CERN and positronium (Ps), a bound-state of electron and positron:

$$\bar{\mathrm{p}} + \mathrm{Ps}^* \longrightarrow \overline{\mathrm{H}}^* + \mathrm{e}^- \tag{1}$$

This reaction reveals several advantages. Indeed, the corresponding cross-section evolves as n^4 with n the principal quantum number of positronium, which represents [1] $\sigma \sim 10^{-9}$ cm^2 for $n = 25$. Moreover, as the principal quantum number of the antihydrogen is linked with n, the final state distribution can be controlled by correctly tuning the laser excitation [1]. But since the measurement of the gravitational acceleration will rely on the vertical deflection of the beam induced by gravity, the uncertainty on the velocity of the antihydrogen atoms represents one of the largest systematic error of the measurement. The whole experiment is hence performed in a cryogenic environment (liquid helium).

2 Positronium formation and excitation

In order to form a dense positronium cloud, positrons emitted by a radioactive ^{22}Na source, are ejected onto a nanoporous silica target. Among the two possible spin configurations (aligned or anti-aligned), the orhto-positronium, triplet state decaying into three gammas, has a particularly long lifetime of 142 ns.

One important achievement of AEGIS in 2016 is the creation of positronium inside the main apparatus. To detect its formation, the annihilation of the electron and the positron nearby the target was observed by the mean of plastic scintillators surrounding the AEGIS apparatus. The technique of Single Shot Positron Annihilation Lifetime Spectroscopy (SSPALS) enabled then to extract from the spectrum of the annihilation counts as a function of the time, the lifetime of positronium, in our case equal to 142.8 $\pm$ 1 ns.

To increase the cross-section of the charge-exchange reaction, the positronium is excited by two lasers. A first ultra-violet laser ($\lambda =$ 205 nm) allows the transition from ground state to $n = 3$ while an infrared laser ($\lambda =$ 1064 nm) excite the antihydrogen to $n \sim 35$. The SSPALS spectrums of positronium with and without laser excitation, recorded outside from the main apparatus, are displayed in figure 1 (left). The plot on the right is obtained by subtracting the area below the two dark gray curves on th left as a function of the ultra-violet laser wavelength, tuned by adjusting the temperature of an optical parametric generator crystal. The spread of the curve, centered on the $n = 1$ to $n = 3$ transition wavelength, is directly linked to the

velocity distribution of the positronium cloud (Doppler broadening). A proper modeling allows one to extract from this curve the spread in velocity of the positronium atoms [4], of the order of $\sigma_v = 10^5$ m/s.

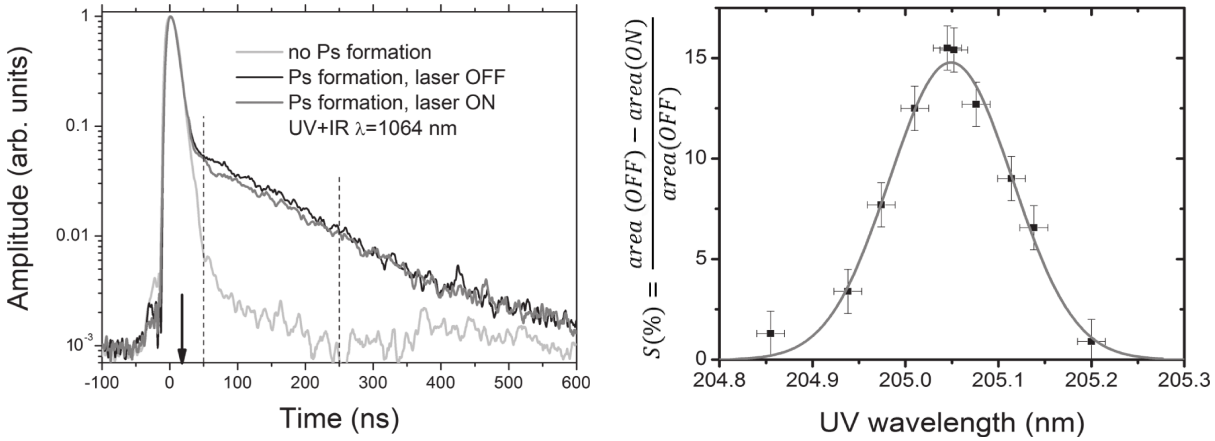


Figure 1 – (left) The SSPALS spectrum of positronium with and without laser excitation. As the positronium is excited to a state with longer lifetime, it contributes less to the beginning of the spectrum (the curve with laser ON is below the one with laser OFF). (right) The difference of the two curves in dark gray on the left as a function of the UV laser wavelength, corresponding to the $n = 1$ to $n = 3$ transition. The spread gives the velocity spread of the positronium cloud (Doppler broadening).

3 Antiprotons manipulations

The confinement of the antiprotons in the AEGIS setup is ensured by a set of Penning-Malmberg traps. In such traps, an axial magnetic field ensures the confinement of the particles radially while the longitudinal motion is restricted by applying a potential well on a set of ring-shaped electrodes. A view of the AEGIS trap system along with some of the main diagnostics is shown in figure 2.

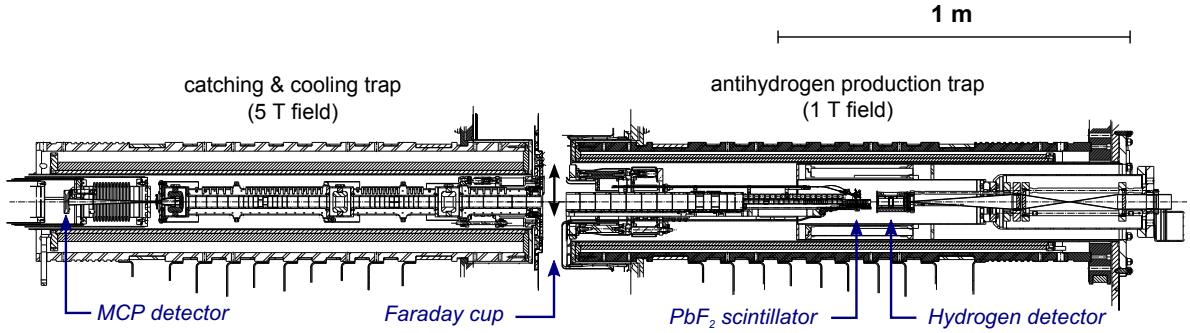


Figure 2 – Schematic view of the AEGIS traps as well as some of the detectors (blue). The cryogenic tanks surrounding the superconducting magnets are not displayed. The antiprotons exiting the AD and passing through a thin degrader from the left side are caught and cooled by electron sympathetic cooling within the trap placed in a 5 T axial field (left). A microchannel plate (MCP) as well as a segmented Faraday cup are the main diagnostics for this region of the apparatus. Once cold, the antiprotons are sent toward the 1 T trap, divided into two parts: the off-axis trap, where the positrons are transmitted toward the positronium converter, and the on-axis trap where the antihydrogen production occurs. A scintillator placed nearby the positronium converter allows one to monitor the formation of positronium. The antiproton manipulations in the 1 T region are controlled by the mean of the hydrogen detector, consisting of three ionizing electrodes stacked to a MCP.

Several steps are needed to prepare and transfer the antiprotons to the production region. The procedure adopted in AEGIS is the following:

1. Approximately 10^8 electrons are loaded in the 5 T trap. Within a few milliseconds, they cool down to the cryogenic temperature by radiative cooling;

2. A bunch of 3.10^7 antiprotons at 5.3 MeV are delivered every 110 seconds by the antiproton decelerator. After passing through a thin degrader to reduce their energy, the fraction with an energy below a few keV is caught in the 5 T trap;

3. By coulombian collisions, the antiprotons transfer their energy to electrons which in turns radiate within a few ms (sympathetic cooling). The time needed for the antiproton temperature to stabilize is typically of the order of one minute;

4. The antiprotons are compressed by applying an oscillating potential on a an electrode segmented azimuthally ("Rotating Wall" technique) and are finally sent toward the trap where the production is planned to occur, located in the 1 T region. This step reaches now 90 % of efficiency such that around 3.10^5 antiprotons are stored into the production trap for each shot of the AD.

4 Gravity measurement

Once the antihydrogen produced, the value of the gravitational acceleration for antimatter is proposed to be measured using a moiré deflectometer. It consist of three transmission gratings having a pitch d and separated by a distance L. As shown in figure 3, under the effect of gravitation, massive particles experience an acceleration a in the vertical direction leading to a parabolic trajectory while undeflected particles such as photons conserve straight trajectories throughout the whole apparatus [7]. The shift Δy between the two impacts at the level of the third grating is then given by:

$$\Delta y = a\tau^2 \tag{2}$$

where $\tau = L/v_z$ is the time of flight between two gratings. For an apparatus length of 1 meter and assuming a Maxwellian distribution of the particles velocity around a few Kelvins, it leads to a typical spatial shift of 50 μm for $a = 9.81\ m.s^{-2}$. Such a small shift can however be problematic to measure with standard particle detectors. Adding a third grating with the same pitch d but tilted by a small angle allows one to take advantage of the moiré effect to reveal macroscopic fringes orthogonal to the slits orientation. More details can be found in reference [6].

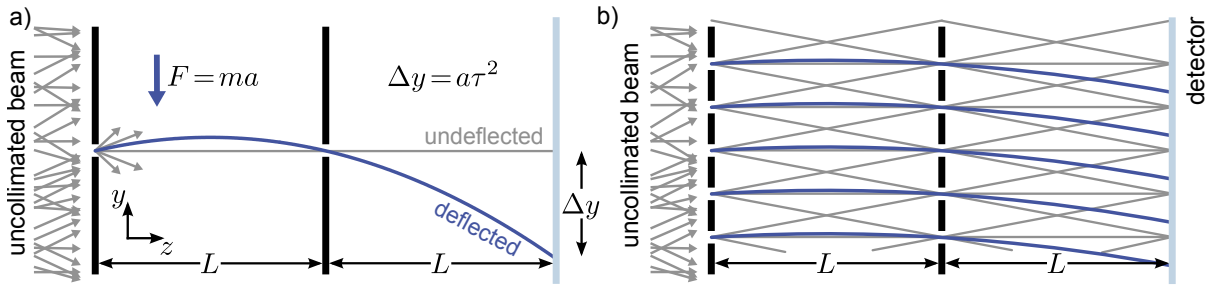


Figure 3 – a) Two slits separated by a distance L restrict the path of a beam to a specific trajectory. b) Replacing the slits by two gratings increases the flux of particles reaching the detector. A third grating (not shown here) located at the level of the detector allows one to take advantage of the moiré effect to reveal macroscopic fringes.

Several imaging detectors are envisioned for the gravity measurement. Two candidates are currently being tested on a secondary beamline: the nuclear emulsions and a silicon detector. The nuclear emulsions consist of plates of plastic covered with AgBr(I) crystals distributed homogeneously in a gelatin substrate. When excited by a charged particle, the annihilation products, such as pions, imprint on the emulsion plate a latent image. But in spite of their impressive imaging capabilities (able to reconstruct the antiproton annihilation vertices with a precision of 2 microns), the emulsions films require to open regularly the vacuum chamber and need a large amount of time to be processed. For these reasons, the choice has been oriented toward silicon detectors whose time capabilities of nanoseconds represent no issue. Among the detectors being tested, the Timepix [8], initially developed for medical imaging applications, is able to determine with 25 microns resolution the position of an antiproton annihilation with 56 % tagging efficiency [9].

5 Conclusion

The results of last antiproton runs have been numerous with the achievement of positronium formation in the production region, its excitation to n = 3 outside from the main apparatus, the transfer of around 10^5 antiprotons per shot in the production trap and the tests of possible detectors envisioned for gravity measurement. Before the long shutdown of the LHC planned from 2019 to 2021, the plan is now to produce antihydrogen in the AEGIS setup and to perform a first gravity measurement.

References

1. G. Y. Drobychev et al., Proposal for the AEGIS experiment at the CERN antiproton decelerator (Antimatter Experiment: Gravity, Interferometry, Spectroscopy), 2007.
2. N. Beverini et al., PS200 proposal Preprint, Los Alamos National Laboratory report LAUR-86-260, 1986.
3. F. Witteborn and W. Fairbank, Phys Rev Lett 19, 1049, 1967.
4. S. Aghion et al., Laser excitation of the n = 3 level of positronium for Antihydrogen production, Physical Review A 94 (2016).
5. S. Maury, The antiproton decelerator: AD, Hyperfine Interactions, 109(1), 43-52, 1997.
6. M. K. Oberthaler, S. Bernet, E. M. Rasel, J. Schmiedmayer, & A. Zeilinger, Inertial sensing with classical atomic beams, Physical Review A, vol. 54, num 4, 1996.
7. P. Bräunig, Atom Optical Tools for Antimatter Experiments, Heidelberg University PhD thesis (2015).
8. T. Poikela et al., Timepix3: a 65K channel hybrid pixel readout chip with simultaneous ToA/ToT and sparse readout, Journal of instrumentation, 9(05), C05013, 2014.
9. H. Holmestadt. Analysis of the 2015 data. GRACE/ATLIX internal note, Oct. 2016.




Dinner
Menu



Constraints on Lorentz symmetry violations with Lunar Laser Ranging.

A. Bourgoin
Dipartimento di Ingegneria Industriale, University of Bologna, via fontanella 40, Forlì, Italy

A. Hees
Department of Physics and Astronomy, University of California, Los Angeles, California 90095, USA

C. Le Poncin-Lafitte, S. Bouquillon, G. Francou, and M.-C. Angonin
SYRTE, Observatoire de Paris, PSL Research University, CNRS, Sorbonne Universités, UPMC Univ. Paris 06, LNE, 61 avenue de l'Observatoire, 75014 Paris, France

We present new constraints on Lorentz symmetry (LS) violations with lunar laser ranging (LLR). Those constraints are derived in the standard-model extension (SME) framework aiming at parameterizing any LS deviations in all sectors of physics. We restrict ourself to two sectors namely the pure gravitational sector of the minimal SME and the gravity-matter coupling. We describe the adopted method and compare our results to previous analysis based on theoretical grounds. This work constitutes the first direct experimental determination of the SME coefficients using LLR measurements.

1 Introduction

General relativity (GR) and the standard-model of particle physics provide a comprehensive description of nature. On one hand, GR describes gravitational effects as the classical consequence of space-time curvature by its energy content. On the other hand, the standard-model of particles describes all other non-gravitational forces by the quantum exchange of subatomic particles. They both assume a unique symmetry of space-time known as the Lorentz-symmetry (LS). A formulation of a quantum theory of gravity would be useful at the Planck era or for the study of black hole's singularities where quantum effects are supposed to become relevant. In many scenarios such a new physics would be expected to break some fundamental symmetry of space-time like the LS. An effective field theory built to consider all hypothetical LS violations in all sectors of physics is an efficient tool [2] to classify and enumerate LS breaking. This effective field theory is currently known as the standard-model extension (SME) framework and proposes many parametrization of LS violations in many sectors [3]. In that work, we focused on two sectors namely the pure gravitational sector [4] and the classical point-mass limit in the matter sector [5] of the SME. The main idea is to constrain the SME coefficients by analyzing lunar laser ranging (LLR) observations. In the literature, there already exist some evaluation of the SME coefficients in the pure gravitational sector using LLR observations [6], however, it is based on theoretical grounds. Unfortunately, analysis based on theoretical grounds has been shown to be not fully satisfactory [7,8] and to provide overoptimistic uncertainties. In order to provide real constraints, we have determined SME coefficient estimates directly from experimental measurements by performing a global LLR data processing directly in the SME framework [8]. To account for the effect of LS breaking upon the orbital motion of the Moon we have built a new lunar ephemeris named *éphéméride lunaire parisienne numérique* (ELPN) computed directly in the

SME framework. It integrates numerically the differential equations describing the orbital and the rotational motion of the Moon by taking into account all the theoretical effects producing a signal larger than the millimeter over the Earth-Moon distance [a].

In section 2 and 3, we describe respectively the solution obtained with ELPN in pure GR and in the SME framework. Finally, in section 4 we discuss the method used to provide real constraints on the SME coefficients and we present new results obtained in both the pure gravitational sector of the minimal SME and the classical point-mass limit in the matter sector.

2 Data analysis in pure general relativity

Analysis in the pure GR is a mandatory step which must be seen as a validation step to ensure that our ELPN solution produces residuals with a dispersion similar to the one currently obtained with other planetary and lunar ephemerides as DE430 [9] or INPOP13 [10]. To ensure that the precision of ELPN is at the same level of accuracy than other ephemerides, we have implemented the exact same equations of motion as in DE430 [b]. After integration, a direct comparison of ELPN predicted Earth-Moon distance with the one predicted by DE430 shows a maximum difference remaining below 4 cm during the time span of LLR observations. However, the true precision of our solution can only be determined after a fitting process to true LLR data by looking at the dispersion of the residuals. The residuals are obtained (i) by changing ELPN orbital predictions into observables i.e. into a prediction of the round trip light time at the date of each LLR normal points and (ii) by computing the difference between the observed light time and the computed one. The step (i) is achieved thanks to the 2010 international Earth rotation system conventions [11]. The basic procedure for building the ELPN solution in pure GR can be described as follow. First, the physical parameters and the initial conditions are taken from DE430 to perform the first numerical integration. Then, the independent solution ELPN is built at the end of an iterative process consisting of adjusting 59 parameters [c] to the LLR normal points and reintegrating the solution with the new set of constants. During this process 24022 normal points are considered spanning 48 years of LLR observations from August 1969 to December 2016. Among these normal points, we have considered 1337 observations in infrared wavelength obtained at Grasse LLR station in France. The final residuals obtained per LLR stations are shown in Fig. 1. For the most recent observations (after 2006) the dispersion of the residuals is found to be 2.8 cm for Apache-point observatory in New Mexico (United states) with no offset on the mean, and respectively 2.4 cm and 2.2 cm for the Grasse station respectively in green and infrared wavelength. For these two last ones the mean of the dispersion is found to be respectively null and equals to -1.5 cm. This offset for the infrared wavelength has not yet been fully investigated and may correspond to (i) a bad position of the Grasse station in the international terrestrial reference frame for the LLR time span (non-constant tectonic drift), or (ii) a bad modeling for the tropospheric time delay correction in infrared wavelength, or (iii) a bad experimental calibration for that wavelength. The proposition (i) seems to be the most likely, but a more rigorous investigation is mandatory. Nevertheless, a comparison of those dispersions with the one obtained e.g. with INPOP13b [12] (see Tabs. 15 and 16) shows that our residuals are typically of the same order of magnitude and even better for the most recent observations. This lunar ephemeris obtained in pure GR will be used as a starting point for considering violations of LS in order to provide real constraints on GR violations.

[a] the current observational accuracy being subcentimetric.

[b] the main difference between INPOP13 and DE430 being the inclusion of a fluid lunar core in DE430.

[c] like the position of the LLR stations and retroreflectors at J2000, the orbital and rotational lunar initials conditions at J2000, the masses of the Moon and the Earth-Moon barycenter, the Love's numbers and the time delays of degree 2 for solid body tides of both the Earth and the Moon, the total moment of inertia of the Moon, and the damping term between the mantle and the fluid core of the Moon.

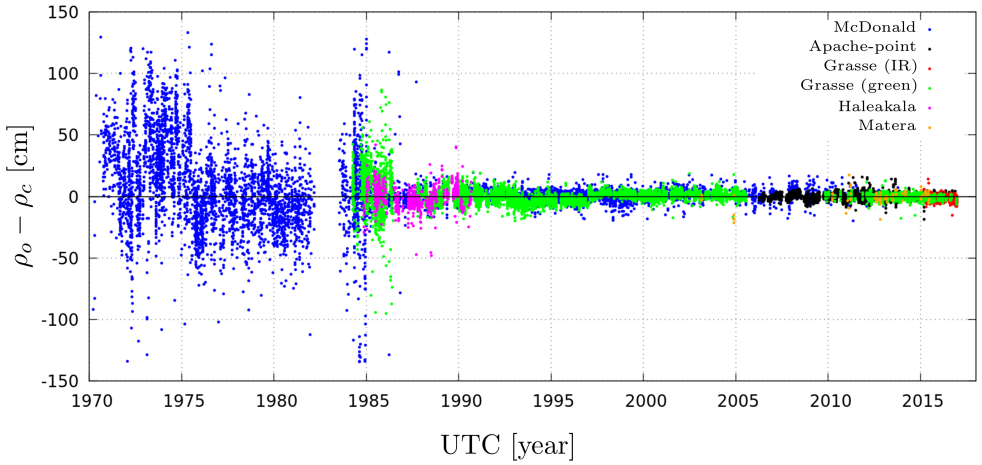


Figure 1 – Plot of the dispersion of the ELPN's residuals as a function of time per LLR stations. ρ_c is the computed time delay determined with ELPN's predictions and ρ_o is the observed time delay (normal points).

3 Data analysis in the standard-model extension framework

The most important difference between ELPN and DE430 or INPOP13 are the Lorentz violating contributions which are implemented in ELPN. The Lorentz violating terms are considered in two different parts of the modeling: (i) the orbital part, (ii) the gravitational delay for the light propagation. Each of these contributions can be split into two parts. The first one, which has already been discussed in a previous paper [8] comes from the pure gravitational sector of the minimal SME and is produced by LS violations at the level of the field equations. The second one comes from the classical point-mass limit in the matter sector of the SME framework and leads to violations at the level of the Einstein equivalence principle (EEP). The LS violations on the orbital motion of the Moon is characterized by supplementary accelerations computed in Eqs. (104) and (177) of respectively [4] and [5]. On the other hand, we have also considered the impact of LS violations on the gravitational time delay for light propagation computed by Eqs. (24) and (203) from respectively [13] and [5]. Starting from the ELPN solution computed in pure GR (cf. Sec. 2), we have have produced a new ephemeris by fitting the SME coefficients in addition to the same parameters as considered previously. Some correlations between SME coefficients are very high meaning that the LLR data does not allow to estimate all the SME coefficients independently but only some combinations of them. An iterative investigation of partial derivatives let to assess the 6 most sensitive following independent linear combinations

$$\bar{s}^1 = \bar{s}^{XY} \tag{1a}$$

$$\bar{s}^2 = \bar{s}^{YZ} \tag{1b}$$

$$\bar{s}^3 = \bar{s}^{XX} - \bar{s}^{YY}, \tag{1c}$$

$$\bar{s}^4 = 0.35\bar{s}^{XX} + 0.35\bar{s}^{YY} - 0.70\bar{s}^{ZZ} - 0.94\bar{s}^{YZ}, \tag{1d}$$

$$\bar{s}^5 = -0.62\bar{s}^{TX} + 0.78\alpha(\bar{a}^{e+p}_{\rm eff})^X + 0.79\alpha(\bar{a}^{n}_{\rm eff})^X, \tag{1e}$$

$$\bar{s}^6 = 0.93\bar{s}^{TY} + 0.33\bar{s}^{TZ} - 0.10\alpha(\bar{a}^{e+p}_{\rm eff})^Y - 0.10\alpha(\bar{a}^{n}_{\rm eff})^Y - 0.044\alpha(\bar{a}^{e+p}_{\rm eff})^Z - 0.044\alpha(\bar{a}^{n}_{\rm eff})^Z. \tag{1f}$$

Interestingly, previous work based on theoretical grounds [14] has also shown that LLR is sensitive to 6 linear combinations of the fundamental SME coefficients. Nevertheless, a look at Eqs. (1) shows that the extension to the matter sector only change 2 linear combinations compared to previous global LLR data analysis [8] in the pure gravitational sector of the minimal SME. On the opposite, theoretical work [14] expects the modification of 4 linear combinations. This determination of the linear combinations that can be constrained by direct experimental measurements highlights the limit of analyzes that rely on theoretical grounds and the need to consider a full reduction of the raw data within the SME formalism.

4 Constraints on the SME coefficients

The SME coefficients which can be constrained with LLR data are given by Eqs. (1). An adjustment of these coefficients together with the other global parameters provide an estimate of the SME coefficients as well as their statistical marginalized uncertainties. Unlike constraints derived from a postfit analysis, these uncertainties take into account the correlations with the other global parameters. However, considering subsets of our dataset reveals that the estimates of the SME coefficients depend highly on the LLR stations or retroreflectors. This is interpreted as systematics effects in our analysis which have been quantified by using a jackknife resampling method as discussed in [8]. The final estimates of SME coefficients including both statistical and systematics uncertainties are shown in Tab. 1.

Table 1: Real constraints on SME coefficients derived from a global LLR data analysis. The quoted uncertainties correspond to 1σ realistic uncertainties. The linear combinations are defined in Eqs. (1).

SME	constraints
$\bar{s}^1$	$(-0.5 \pm 3.6) \times 10^{-12}$
$\bar{s}^2$	$(+2.1 \pm 3.0) \times 10^{-12}$
$\bar{s}^3$	$(+0.2 \pm 1.1) \times 10^{-11}$
$\bar{s}^4$	$(+3.0 \pm 3.1) \times 10^{-12}$
$\bar{s}^5$	$(-1.4 \pm 1.7) \times 10^{-8}$
$\bar{s}^6$	$(-6.6 \pm 9.4) \times 10^{-9}$

5 Conclusion

Our results do not show any deviations from GR at the 68% confidence level. In addition, they constitute the first real constraints from a direct experimental measurement with LLR data in both the pure gravitational sector of the minimal SME and the classical point-mass limit in the matter sector. LLR data should be analyzed with other measurements in order to provide estimates for each individual SME coefficients [14].

Acknowledgments

A.B. thanks SYRTE from Paris Observatory for financial support. A.B. and A.H. thank the organizers for financial support to attend the conference.

References

1. C. M. Will, *Living Reviews in Relativity*, **10**, 12942 (2014).
2. V. A. Kostelecký, *Phys. Rev.* D **69**, 105009 (2004).
3. V. A. Kostelecký and N. Russell, *Reviews of Modern Physics*, **83**, 11 (2011).
4. Q. G. Bailey and V. A. Kostelecký, *Phys. Rev.* D **74**, 045001 (2006).
5. V. A. Kostelecký and J. D. Tasson, *Phys. Rev.* D **83**, 016013 (2011).
6. J. B. R. Battat *et al.*, *Phys. Rev. Lett.* **99**, 241103 (2007).
7. C. Le Poncin-Lafitte, *et al.*, *Phys. Rev.* D **94**, 125030 (2016).
8. A. Bourgoin, *et al.*, *Phys. Rev. Lett.* **117**, 241301 (2016).
9. W. M. Folkner, *et al.*, *Interplanetary Network Progress Report*, **42-196**, 1-81 (2014).
10. A. Fienga, *et al.*, *Astronomy and Astrophysics*, **507**, 1675-1686, (2009).
11. G. Petit *et al.*, *IERS Technical Note*, **36**, (2010).
12. A. Fienga, *et al.*, arXiv:astro-ph.EP/1405.0484.
13. Q. G. Bailey, *Phys. Rev.* D **80**, 044004 (2009).
14. A. Hees, *et al.*, *Phys. Rev.* D **92**, 064049 (2015).

PETER: A DOUBLE TORSION PENDULUM TO TEST QUASI FREE-FALL ON TWO DEGREES OF FREEDOM

L. DI FIORE[a], M. BASSAN[b,c], M. DE LAURENTIS[a,d], F. DE MARCHI[e], R. DE ROSA[a,d], N. FINETTI[f,g] , F. GARUFI[a,d], A. GRADO[a,h], L. MARCONI[g], L. MILANO[a,d], Y. MINENKOV[c], G. PUCACCO[b,c], R. STANGA[g,i], M. VISCO[c,j]

a INFN - Sezione di Napoli, I-80126, Napoli, Italy
b Dipartimento di Fisica, Universitá di Roma "Tor Vergat", I-00133 Roma, Italy
c INFN - Sezione Roma2, I-00133 Roma, Italy
d Dipartimento di Fisica, Universitá di Napoli "Federico II", I-80126, Napoli, Italy
e Dipartimento di Ingegneria Meccanica e Aerospaziale, DIMA, Sapienza, Universitá di Roma - 00184 Roma, Italy
f Dipartimento di Scienze Fisiche e Chimiche, Universitá degli Studi dell'Aquila, I-67100 l'Aquila, Italy
g INFN - Sezione di Firenze, I-50019 Firenze, Italy
h INAF - Osservatorio Astronomico di Capodimonte, I-80126 Napoli, Italy
i Dipartimento di Fisica ed Astronomia, Universitá degli Studi di Firenze, I-50019 Firenze, Italy
j INAF - Istituto di Astrofisica e Planetologia Spaziali, I-00133 Roma, Italy

Torsion pendulums are the best approximation, in the laboratory, to a body in free fall: the extremely low restoring force exerted by the torsion fiber approaches the absence of interaction with the surrounding, but only on a single degree of freedom (DOF), namely the rotation around the fiber. We present a peculiar pendulum where we achieved, by cascading two torsion fibers, almost-free motion on two DOFs: rotation around a vertical axis and translation along one axis. The apparatus was developed to serve as a test facility for LISA Pathfinder(LPF) pre-flight investigations of cross talk between different degrees of freedom, and is presently being upgraded to improve performances and reduce coupling of displacement noise to torsional degrees of freedom. We shall describe the instrument, review the cross-talk measurements performed on it for the electrostatic actuators of LPF and discuss how new experiments can benefit of the peculiarity of two (and potentially more) soft DOFs

1 Introduction

Thanks to the ability to approach free fall condition in laboratory down to a few mHz, ground testing with torsion pendulums played a crucial role in the development of the Gravitational Reference Sensor (GRS) of the LPF mission [1]. Single stage pendulum facilities developed at University of Trento, permitted to characterize the GRS for stray torque or force acting on the suspended TM [2,3]. This was achieved by using single mass and 4 mass torsion pendulums respectively, as illustrated schematically in figure 1. In this paper, we report on a two stage torsion pendulum, named PETER [a] that allows approaching free-fall in two DOFs, permitting simultaneous measurement of force and torque acting on the TM. A sketch of the two-fold pendulum is also reported in figure 1. This pendulum was designed [4] as a facility for, pre-flight ground testing of the LISA-Pathfinder GRS. A detailed description of the facility and measurement technique can be found in references [5,6,7,8].

[a] from Italian PEndolo Traslazionale E Rotazionale, namely Rotational and Translational Pendulum

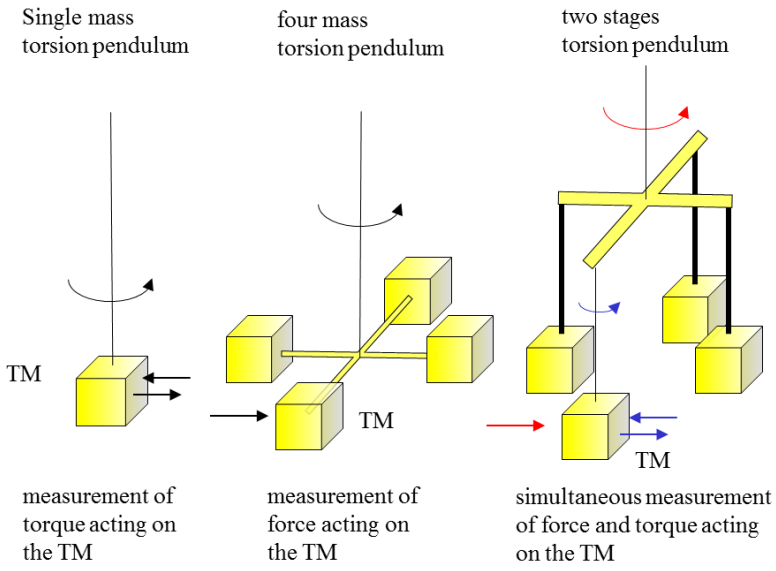


Figure 1 – single mass (left), four mass (center) and two-fold (right) pendulums

2 GRS cross-talk measurement

In 2015, we performed a campaign of six runs devoted to the measurement of actuation Cross-Talks (CT) of the Engineering Model of the LPF GRS. In table 1, we summarize the relevant information for the various measurement runs; a detailed description of the measurement technique can be found in [5,6,7,8].

Table 1: Relevant information for the six measurement runs. Run 3b was performed in constant stiffness conditions.

Run number	Run start time	Averaging time per step (hours)	Number of steps	Step size (μm)	Actuation ampl. (V^2)
Force to Torque Cross Talk (actuation force at 14 mHz)					
1a	Jun 9, 2015	3	5x5	100	50
2a	Jun 19, 2015	1.25	24 (spiral)	100	20
3a	Jun 26, 2015	2	25 (spiral)	100	20
Torque to Force Cross Talk (actuation torque at 18 mHz)					
1b	May 25, 2015	3	8	150	20
2b	May 29, 2015	3	5x5	100	20
3b	Nov 24, 2015	2	8 (spiral)	100	20

In figure 2 we report a force to torque CT measurement (run 3a) compared with an analytical model (see [8,9] and references therein for details). We also show the residuals (measured values minus model predictions) vs. x displacement. The general agreement is good with a residual small discrepancy, well represented by a linear trend along x. The results of the other force to torque CT measurements (run a1 and a2), are quite similar; the maximum difference of the three runs is below 0.05 % in CT In figure 3 we report a torque to force CT measurement (run 2b) compared wit an analytical model. We also show the residuals (measured values minus model predictions) vs. x displacement. In this case, the agreement to the model is not as good and we measure a CT much larger than expected (up to 4 %), still well represented by a linear dependence on the x coordinate. Nevertheless, in the central part of the measurement range, that is of interest for the scientific operation of LISA-Pathfinder, the measured CT is still very

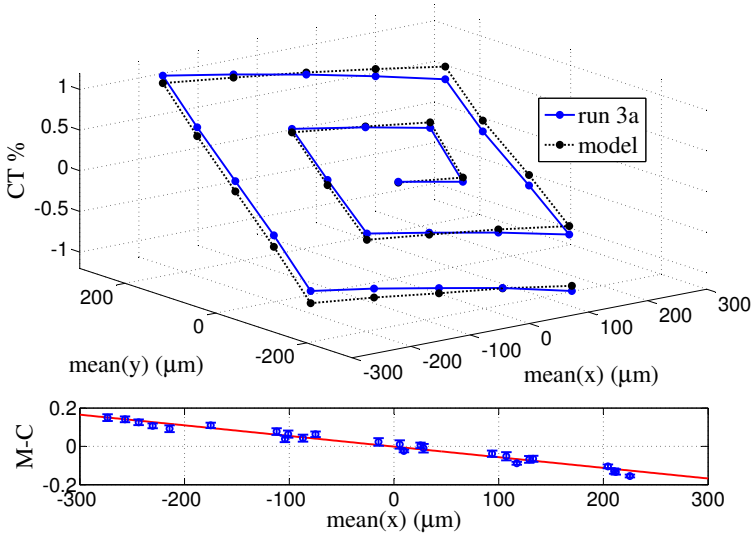


Figure 2 – Force to torque CT measurement for the run 3a, compared to the analytical model. In the lower part of the figure the M-C residuals (Measured-Computed) are shown versus the x coordinate.

small (below 0.8% in the central 50 μm and less than 0.2 % at the GRS center). Also in this case the measurement are quite repeatable and the maximum difference from run to run (run b1 and b3), stays within the experimental error.

Summarizing, we performed several CT measurement runs. In all the cases, the CT measured at the GRS electric center was always small enough to be compliant with the LPF requirements and didn't appear problematic for the on-flight GRS operation, as was then verified by the excellent performance of the LPF mission [1]

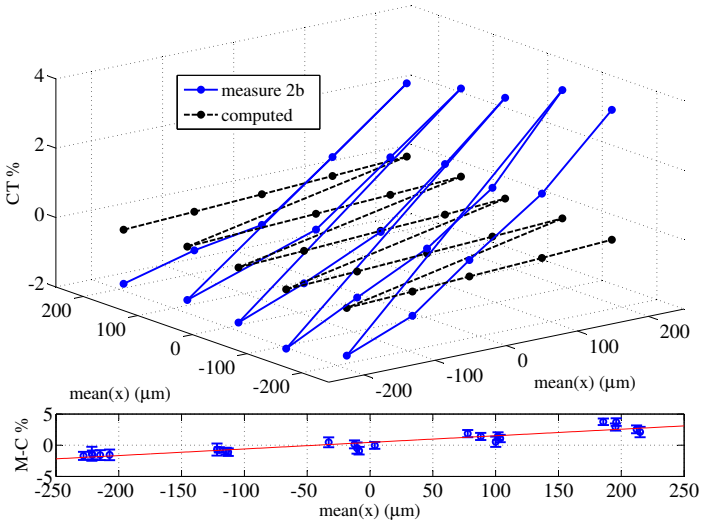


Figure 3 – Torque to force CT measurement for the run 2b, compared to the analytical model. In the lower part of the figure the M-C residuals (Measured-Computed) are shown versus the x coordinate.

3 Possible upgrades and applications

Aside to the ground-testing of the flight hardware of LISA or other drag-free space mission, a double torsion pendulum could find potential application in other field of fundamental or applied physics. As an example, we consider the measurement of the "lateral" Casimir Effect[10,11]. In this case, the usage of corrugated surfaces, generates a transverse Casimir force in addition to the "usual" Casimir pressure. From an experimental point of view, one of the main difficulties is to avoid that the transverse force is contaminated by a Cross-Talk of the, much larger, normal force. The simultaneous measurement of both normal and transverse Casimir force should simplify the analysis of the results, and permit to distinguish the different components.

Another point to mention is the possibility to extend the free fall condition to more than two DOFs (in principle, up to 6). The "easy" part is to extend to a second displacement in the horizontal plane; this can be achieved by cascading a third off-axis torsion pendulum hanging a second cross-bar to the first one. Things become more difficult if we consider the DOFs where the restoring force is dominated by the local gravitational acceleration. For what concerns the rotations around the two horizontal axis, if we move the TM attaching point close to the Center of Mass (CM), the restoring torque, for rotation around CM approaches zero and the resonance goes to low frequency. In real life, there are severe limitations due to mechanical tolerances, TM inhomogeneity, and lateral accuracy in attaching the suspending wire. As the last, perhaps more difficult, DOF, we consider the vertical direction, where we directly compete with g. In this case, we should suspend the attaching point of the first fiber to one end of a beam balance with a flexure joint. Such a setup has been realized as a tilt-meter for the LIGO interferometers[12], permitting to reach a resonance frequency as low as 10.8 mHz.

In conclusion, we think that a laboratory free-fall condition with more than two DOFs is on the reach. Several applications could benefit from the availability of such facility.

Acknowledgments

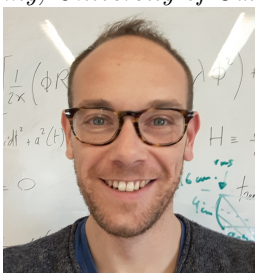
We are grateful to our technicians C. Cassese, F. Cassese, G. Pontoriere, L. Roscilli and R. Simonetti for the design and realization of several mechanical components of the PETER facility. This work is fully supported by INFN - CSN2.

References

1. M. Armano *et al*, *Phys. Rev. Lett.* **116**, 231101 (2016).
2. L. Carbone *et al*, *Phys. Rev. Lett.* **91**, 151101 (2003)
3. F. Antonucci *et al*, *Class. Quant. Grav.* **29**, 124014 (2012).
4. R. Stanga *et al*, *J. Phys. Conf. Ser.* **154**, 012032 (2009).
5. F. De Marchi *et al*, *Phys. Rev.* D **87**, 122006 (2013).
6. M. Bassan *et al*, *Phys. Rev. Lett.* **116**, 051104 (2016).
7. M. Bassan *et al*, *Measurement, with the PETER facility, of force to torque cross-talk in actuation of the LISA-Pathfinder GRS*, LFGN-NOTE-1-2015, internal note of the Laboratory of Gravitational Physics, Napoli (2015).
8. M. Bassan *et al*, *Measurement, with the PETER facility, of torque to force cross-talk in actuation of the LISA-Pathfinder GRS*, LFGN-NOTE 1-2016. internal note of the Laboratory of Gravitational Physics, Napoli (2016).
9. M. Bassan *et al*, *Actuation cross-talks in free-falling systems: torsion pendulum results for the LISA-Pathfinder gravitational reference sensor*, *Astrop. Phys.* (2017) submitted.
10. F. Chen *et al*, *Phys. Rev. Lett.* **88**, 101801 (2002).
11. T. Emig *et al*, *Phys. Rev.A* **67**, 02211 (2013).
12. Venkateswara *et al*, *Rev.Sci.Instrum.* **85**, 01500 (2014)

UNIVERSALITY OF FREE FALL VERSUS EPHEMERIS

O. Minazzoli †‡
L. Bernus[α,β], A. Fienga[β], A. Hees[γ], J. Laskar[α], V. Viswanathan [β]
†*Centre Scientifique de Monaco, 8 quai Antoine I, Monaco*
‡*Artemis, Université Côte d'Azur, Observatoire Côte d'Azur, CNRS, CS 34229, F-06304 Nice, France*
[α] *ASD/IMCCE, CNRS-UMR 8028, Observatoire de Paris, PSL, UPMC, 77 avenue Denfert-Rochereau, 75014 Paris, France*
[β] *GéoAzur, CNRS-UMR 7329, Observatoire de la Cte dAzur, Universit Nice Sophia Antipolis, 250 Av. A. Einstein, 06560 Valbonne, France*
[γ] *Department of Physics and Astronomy, University of California, Los Angeles, CA 90095, USA*



When a light scalar field with gravitational strength interacts with matter, the weak equivalence principle is in general violated, leading for instance to a violation of the universality of free fall. This has been known and tested for a while. However, recent developments [Minazzoli & Hees, PRD 2016] showed that a novel manifestation of the universality of free fall can appear in some models. Here we discuss this new scenario and expose how we intend to constrain it with INPOP ephemeris.

1 Introduction

Massless or light scalar-fields with gravitational strength that directly couple to matter are expected in the context of string theory [1,2]. A consequence of this type of fields would be that the Equivalence Principle (EP) is violated [1,2]. More precisely, the Einstein Equivalence Principle (EEP) would be violated, with several manifestations, such as violations of the Local Position Invariance (LPI) as well as violations of the Universality of Free Fall (UFF) — also known as Weak Equivalence Principle (WEP).

The most precise tests of the UFF have been made by comparing the free fall accelerations of different test bodies [3]. It is usually thought that the relative acceleration (at the Newtonian level) between two bodies that are equidistant from the source of gravity reads as follows [4]

$$\frac{\Delta a}{a} \equiv 2\frac{a_1 - a_2}{a_1 + a_2} = \left[\frac{m^G}{m^I}\right]_1 - \left[\frac{m^G}{m^I}\right]_2 = \Delta\left[\frac{m^G}{m^I}\right], \tag{1}$$

where m^G and m^I are the gravitational and inertial masses of each body respectively. However, recent phenomenological developments suggest that it may actually be more complicated than

that in some situations [5,6], as we shall see bellow. In any case, the planetary and lunar ephemeris INPOP [7,8] is an ideal tool in order to implement EP tests.

2 Brief description of INPOP

INPOP (Intégrateur Numérique Planétaire de l'Observatoire de Paris) is a planetary ephemeris that is built by integrating numerically the equations of motion of the solar system, and by adjusting to lunar laser ranging and space missions' observations [7,8,9]. In addition to the classic planetary and lunar fitted parameters, one can add parameters encoding deviations from general relativity. These parameters can be adjusted simultaneously with all the others in a global fit. With this method, good constraints were put on the PPN parameters [9] — using Mercury orbiter data (MESSENGER) [10], but also by considering a Monte Carlo exploration of the solutions' space [9]. The same methods can be used for adjusting the new parameters described in this work.

3 Acceleration at the Newtonian level

Considering a general scalar-tensor theory with non-minimal scalar-matter coupling (that cannot be gauged away by a metric redefinition such as a conformal or a disformal transformation), it has recently been shown that the acceleration of a body, say T, reads [5,6]

$$\boldsymbol{a}_T = -\sum_{A\neq T} \frac{G m_A^G}{r_{AT}^3} \boldsymbol{r}_{AT} \left(1 + \delta_T + \delta_{AT}\right), \tag{2}$$

where $\boldsymbol{r}_{AT} = \boldsymbol{x}_T - \boldsymbol{x}_A$. The coefficients δ_T and δ_{AT} parametrize the violation of the UFF. G is the "measured" constant of Newton and m_A^G is the "gravitational" mass of the body A. It is important to have in mind that G and m_A^G are not the constant of Newton and the mass that appear in the fundamental action [5,6]. One notably has $m_A^G = (1+\delta_A) m_A^I$, where m_A^I is the inertial mass of the body A [5,6]. As a consequence, from equation (2), one can check that the gravitational force in this context still satisfies Newton's third law of motion:

$$m_A^I \boldsymbol{a}_A = \frac{G m_A^I m_B^I}{r_{AB}^3} \boldsymbol{r}_{AB} \left(1 + \delta_A + \delta_B + \delta_{AB}\right) = -m_B^I \boldsymbol{a}_B. \tag{3}$$

In general, δ_T can be decomposed into two contributions: one from a violation of the WEP and one from a violation of the Strong Equivalence Principle (SEP):

$$\delta_T = \delta_T^{WEP} + \delta_T^{SEP}, \qquad \text{where} \qquad \delta_T^{SEP} = \eta \frac{|\Omega_T|}{m_T\, c^2}, \tag{4}$$

where Ω and mc^2 are the gravitational binding and rest mass energies respectively, while η is the so-called Nordtvedt parameter. On the other side, δ_T^{WEP} depends on both the scalar-matter coupling parameters and on the dilatonic charges [2,5,6]. In most cases, if $\delta_T^{WEP} \neq 0$, then $\delta_T^{WEP} \gg \delta_T^{SEP}$, such that one can usually test either the WEP (discarding SEP violations), or the SEP (discarding WEP violations).

As the parameter δ_T^{WEP}, δ_{AT} depends on both the scalar-matter coupling parameters and on the dilatonic charges [5,6]. In most situations, $\delta_T^{WEP} \gg \delta_{AT}$. However, it is not necessarily true when the scalar-matter coupling is the same in each sector of particle physics. In that situation, one can have $\delta_T^{WEP} \lesssim \delta_{AT}$ [5,6]. It is noteworthy that such kind of universality has already been suggested in the context of string theory [1].

The important thing to notice with δ_{AT}, is that it depends not only on the composition of the falling body, but also on the composition of the body that is source of the gravitational field in which the body T is falling. As a consequence, the relative acceleration of two test particles cannot only be related to the ratios between their gravitational to inertial masses.

4 The Earth-Moon system

At the Newtonian level, the relative acceleration between the Earth and the Moon reads

$$\boldsymbol{a}_M - \boldsymbol{a}_E = -\frac{G\mu}{r_{EM}^3}\boldsymbol{r}_{EM} + Gm_S^G\left[\frac{\boldsymbol{r}_{SE}}{r_{SE}^3} - \frac{\boldsymbol{r}_{SM}}{r_{SM}^3}\right] + Gm_S^G\left[\frac{\boldsymbol{r}_{SE}}{r_{SE}^3}(\delta_E+\delta_{SE}) - \frac{\boldsymbol{r}_{SM}}{r_{SM}^3}(\delta_M+\delta_{SM})\right], \tag{5}$$

With $\mu \equiv m_M^G + m_E^G + (\delta_E+\delta_{EM})m_M^G + (\delta_M+\delta_{EM})m_E^G$. With ephemeris, the first term of equation (5) does not lead to a sensitive test of the UFF, because it can be absorbed in the fit of the parameter $m_M^G + m_E^G$.[4] The last term, on the other side, does. At leading order, one can approximate both distances appearing in this last term as being approximately equal. One therefore has

$$\begin{aligned}\Delta\boldsymbol{a}^{\bar{U}FF} \equiv (\boldsymbol{a}_M - \boldsymbol{a}_E)^{\bar{U}FF} &\approx Gm_S^G\left[\frac{\boldsymbol{r}_{SE}}{r_{SE}^3}(\delta_E+\delta_{SE}) - \frac{\boldsymbol{r}_{SM}}{r_{SM}^3}(\delta_M+\delta_{SM})\right],\\ &\approx \boldsymbol{a}_E\left[(\delta_E+\delta_{SE}) - (\delta_M+\delta_{SM})\right],\end{aligned} \tag{6}$$

where $\Delta\boldsymbol{a}^{\bar{U}FF}$ is the part of the relative acceleration between the Earth and the Moon that violates the UFF. When $\delta_{SM} = \delta_{SE}$, one recovers the usual expectation, that is [4]

$$\Delta\boldsymbol{a}^{\bar{U}FF} \approx \boldsymbol{a}_E\left[\left(\frac{m^G}{m^I}\right)_E - \left(\frac{m^G}{m^I}\right)_M\right]. \tag{7}$$

The results from the comparison of the numerical integration of Eq. (2) to the measurement of the Earth-Moon distance via Lunar Laser Ranging will be published in a dedicated communication.

As one can see, there are more parameters than equations of motion. Therefore, the Earth-Moon system alone constrain a specific combination of these parameters only. In consequence, it may be useful to take advantage of the many bodies that are in the solar system.

5 Planetary orbits

One can show that the parameters δ_A and δ_{AT} mostly depend on six fundamental (or semi-fundamental) parameters — related to the couplings between the scalar field and each sector of particle physics [2,5,6]. As a consequence, in order to constrain those parameters — naively — one needs to observe at least 6 falling bodies, with sensible different compositions. Therefore, one may use solar system observations in order to constrain those parameters individually — although with a weaker accuracy than what can be achieved with the Earth-Moon system alone.

6 Acceleration at the post-Newtonian level

At current level accuracy for Solar system observations (e.g. $\sim 1cm/20yrs$ for the Moon and $\sim 1m/20yrs$ for Mars), one has to deal with the full post-Newtonian (pN) equation of motion. In the present context, it reads [5]

$$\begin{aligned}\boldsymbol{a}_T = &-\sum_{A\neq T}\frac{Gm_A^G}{r_{AT}^3}\boldsymbol{r}_{AT}\left(1+\delta_T+\delta_{AT}\right)\\ &-\sum_{A\neq T}\frac{Gm_A^G}{r_{AT}^3c^2}\boldsymbol{r}_{AT}\Bigg\{\gamma v_T^2 + (\gamma+1)v_A^2 - 2(1+\gamma)\boldsymbol{v}_A.\boldsymbol{v}_T - \frac{3}{2}\left(\frac{\boldsymbol{r}_{AT}.\boldsymbol{v}_A}{r_{AT}}\right) - \frac{1}{2}\boldsymbol{r}_{AT}.\boldsymbol{a}_A\\ &\qquad - 2(\gamma+\beta+\mathrm{d}\beta^T)\sum_{B\neq T}\frac{Gm_B^G}{r_{TB}} - (2\beta+2\mathrm{d}\beta^A-1)\sum_{B\neq A}\frac{Gm_B^G}{r_{AB}}\Bigg\}\\ &+\sum_{A\neq T}\frac{Gm_A^G}{c^2r_{AT}^3}\left[2(1+\gamma)\boldsymbol{r}_{AT}.\boldsymbol{v}_T - (1+2\gamma)\boldsymbol{r}_{AT}.\boldsymbol{v}_A\right](\boldsymbol{v}_T-\boldsymbol{v}_A) + \frac{3+4\gamma}{2}\sum_{A\neq T}\frac{Gm_A^G}{c^2r_{AT}}\boldsymbol{a}_A\,,\end{aligned} \tag{8}$$

where γ and β are the usual pN parameters. $\mathrm{d}\beta^X$ is a new parameter that depends on the composition of the body X. It indicates how non-linear is the scalar-matter coupling [5]. We do not expect that it plays a significant role in the pN dynamics though [5]. All those parameters can be expressed in terms of some of the fundamental parameters discussed in the previous section [5,6].

7 Conclusion

The solar system is ideal in order to constrain possible non-minimal couplings between gravity and matter. Here we discussed one such potential couplings, where one gravitational (massless or light) scalar field couples multiplicatively with different sectors of particle physics. Thanks to current and future advances in the solar system exploration, one can expect to greatly increase the accuracy of solar system EP tests in a foreseeable future. Based on the equations of motion presented here, the INPOP software developed at both the Paris and Nice observatories will allow such tests.

References

1. T. Damour and A. M. Polyakov. The string dilation and a least coupling principle. *Nuclear Physics B*, 423:532–558, July 1994.
2. T. Damour and J. F. Donoghue. Equivalence principle violations and couplings of a light dilaton. *Physical Review D*, 82(8):084033, October 2010.
3. S. Schlamminger, K.-Y. Choi, T. A. Wagner, J. H. Gundlach, and E. G. Adelberger. Test of the Equivalence Principle Using a Rotating Torsion Balance. *Physical Review Letters*, 100(4):041101, February 2008.
4. J. G. Williams, S. G. Turyshev, and D. H. Boggs. Lunar laser ranging tests of the equivalence principle. *Classical and Quantum Gravity*, 29(18):184004, September 2012.
5. A. Hees and O. Minazzoli. Post-Newtonian phenomenology of a massless dilaton. *ArXiv e-prints*, December 2015.
6. O. Minazzoli and A. Hees. Dilatons with intrinsic decouplings. *Physical Review D*, 94(6):064038, September 2016.
7. A. Fienga, H. Manche, J. Laskar, and M. Gastineau. INPOP06: a new numerical planetary ephemeris. *Astronomy & Astrophysics*, 477:315–327, January 2008.
8. A. Fienga, J. Laskar, P. Kuchynka, H. Manche, G. Desvignes, M. Gastineau, I. Cognard, and G. Theureau. The INPOP10a planetary ephemeris and its applications in fundamental physics. *Celestial Mechanics and Dynamical Astronomy*, 111:363–385, November 2011.
9. A. Fienga, J. Laskar, P. Exertier, H. Manche, and M. Gastineau. Numerical estimation of the sensitivity of INPOP planetary ephemerides to general relativity parameters. *Celestial Mechanics and Dynamical Astronomy*, 123:325–349, November 2015.
10. A. K. Verma, A. Fienga, J. Laskar, H. Manche, and M. Gastineau. Use of MESSENGER radioscience data to improve planetary ephemeris and to test general relativity. *Astronomy & Astrophysics*, 561:A115, January 2014.

Studies of general relativity with quantum sensors

G. Lefèvre[1,6], G. Condon[1], I. Riou[1,6], L. Chichet[1], M. Essayeh[1,6], M. Rabault[1], L. Antoni-Micollier[1], N. Mielec[2,6], D. Holleville[2,6], L. Amand[2,6], R. Geiger[2,6], A. Landragin[2,6], M. Prevedelli[3], B. Barrett[1,4], B. Battelier[1], A. Bertoldi[1,6], B. Canuel[1,5,6], and P. Bouyer[1,6]

[1] *LP2N, Laboratoire Photonique, Numérique et Nanosciences, Université Bordeaux–IOGS–CNRS:UMR 5298, rue F. Mitterrand, F–33400 Talence, France*

[2] *LNE–SYRTE, Observatoire de Paris, PSL Research University, CNRS, Sorbonne Universités, UPMC Univ. Paris 06, 61 avenue de l'Observatoire, F–75014 Paris, France*

[3] *Dipartimento di Fisica e Astronomia, Università di Bologna, Via Berti-Pichat 6/2, I–40126 Bologna, Italy*

[4] *iXblue, 34 rue de la Croix de Fer, 78100 Saint-Germain-en-Laye, France*

[5] *LSBB, Laboratoire Souterrain à Bas Bruit UNS, UAPV, CNRS:UMS 3538, AMU, La Grande Combe, F–84400 Rustrel, France*

[6] *MIGA Consortium*

We present two projects aiming to probe key aspects of the theory of General Relativity with high-precision quantum sensors. These projects use cold-atom interferometry with the aim of measuring gravitational waves and testing the equivalence principle. To detect gravitational waves, a large multi-sensor demonstrator is currently under construction that will exploit correlations between three atom interferometers spread along a 200 m optical cavity. Similarly, a test of the weak equivalence principle is currently underway using a compact and mobile dual-species interferometer, which will serve as a prototype for future high-precision tests onboard an orbiting satellite. We present recent results and improvements related to both projects.

1 Introduction

Over the past few decades, the development of laser-cooling techniques [1] has made it possible to exploit the quantum properties of matter at very low temperatures. These techniques have enabled experimentalists to coherently manipulate quantum objects with a very high degree of precision. In this context, atom interferometry has emerged as a powerful tool for metrology. Nowadays, atom interferometers (AIs) are used for a wide range of applications, such as sensitive probes of inertial forces [2,3,4,5], or studies of fundamental physics [6,7,8,9] and tests of gravitational theories [10,11].

In this frame, we are developing two AI experiments that exploit differential measurement techniques to study two aspects of the theory of General Relativity (GR). The MIGA (Matter-wave laser Interferometer Gravitation Antenna) project [12] aims to build a demonstrator for future large-scale gravitational wave (GW) detectors based on atom interferometry. The instrument will consist of a set of three AIs (each using a cold source of ^{87}Rb) that are simultaneously interrogated by the resonant field of a 200 m cavity. The ICE (Interférométrie atomique à sources

Cohérentes pour l'Espace) project [10] uses a dual-species gravimeter to test the weak equivalence principle (WEP). Here, two overlapped samples of ^{39}K and ^{87}Rb are simultaneously interrogated during free-fall—yielding a precise measurement of their differential acceleration under gravity. These experiments have been carried out on ground, and most recently in the weightless environment of parabolic flight [13] with the aim of increasing the measurement sensitivity, as well as serving as a test bed for future experiments in Space.

2 Principles of the Mach-Zehnder atom interferometer

In both the MIGA and ICE projects, the AIs utilize a sequence of three light pulses to coherently split, reflect and recombine the atoms. Using two different atomic states, $|\alpha\rangle$ representing the ground state and $|\beta\rangle$ representing the excited state with an extra momentum transferred by the light, this sequence of light-matter interactions force the atoms to follow two separate trajectories that form a closed path as in an optical Mach-Zehnder interferometer. The sensitivity of the AI to inertial effects scales as the space-time area enclosed by the atoms. The Mach-Zehnder AI pulse sequence operates as follows. Atoms initially in the state $|\alpha\rangle$ are placed in a coherent superposition of states $|\alpha\rangle$ and $|\beta\rangle$ by a "beam splitter" pulse corresponding to an area of $\pi/2$. After a time T of free evolution, the atomic population in these states are reversed are by a "mirror" pulse corresponding to an area of π. After the mirror pulse, the atoms experience a second free evolution time T followed by a recombination stage via a final $\pi/2$-pulse. By measuring the populations of the states N_α and N_β at the output of the interferometer, one can deduce the total transition probability $|\alpha\rangle \rightarrow |\beta\rangle$ given by $P = N_\beta/(N_\alpha + N_\beta)$. This probability is related to the total atomic phase $\Delta\Phi_{\mathrm{AT}}$ accumulated by the matter waves over the two interferometer pathways

$$P = \frac{1}{2}\big(1 - \mathcal{C}\cos(\Delta\Phi_{\mathrm{AT}})\big), \tag{1}$$

where $\mathcal{C}$ is the contrast of the interference fringes. This atomic phase depends on the phase $\phi(\boldsymbol{r}_i, t_i)$ of the interrogation laser pulse i that is imprinted on the matter waves at position $\boldsymbol{r}_i$ and time $t_i = \{0, T, 2T\}$

$$\Delta\Phi_{\mathrm{AT}} = \phi(\boldsymbol{r}_1, 0) - 2\phi(\boldsymbol{r}_2, T) + \phi(\boldsymbol{r}_3, 2T). \tag{2}$$

For example, in the case of an atom accelerating under gravity, the atomic phase shift can be shown to be $\Delta\Phi_{\mathrm{AT}} = \boldsymbol{k}\cdot\boldsymbol{g}T^2$, where $\boldsymbol{k}$ is the effective wavevector of the interrogation light and $\boldsymbol{g}$ is the gravitational acceleration vector. The high-sensitivity of atom interferometers to inertial effects becomes clear from this expression, since the phase scales quadratically with T and k is large for optical transitions ($\sim 10^7$ rad/m). The AI enables one to sense any effect that modifies this phase, such as the acceleration arising from an inertial force or a phase modulation of the interrogation laser induced by a GW.

On the ICE experiment, the interrogation lasers are orientated along the vertical direction to maximize the sensitivity to gravity and allowing a comparison of the gravitational acceleration for two different atomic species. In comparison, the MIGA apparatus will use interrogation beams oriented along the horizontal in a "gradiometer" configuration—enabling the detection of GWs via the phase variation between two distant ^{87}Rb AIs.

3 The MIGA project: toward a new generation of gravitational wave detectors

Gravitational waves were observed for the first time in September 2015 by the LIGO detector [14], which measured the transient event of a merging black hole binary system. This discovery has opened a new window to observe the universe, permitting for the first time the study of objects and events in the GW domain. This gravitational astronomy will benefit from the development

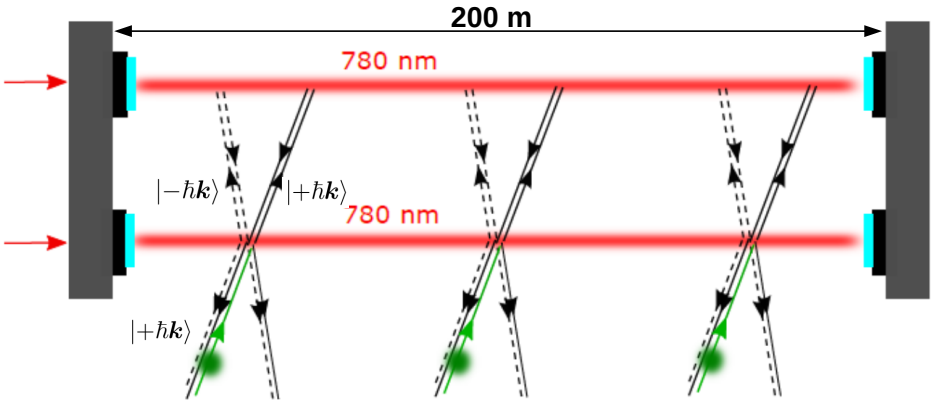


Figure 1 – Scheme of the MIGA demonstrator. Atoms are vertically launched and interrogated by three Bragg pulses resonating inside two cavities. Atoms in the external state $|+\hbar\boldsymbol{k}\rangle$ first pass through the lower cavity where they are diffracted into a coherent superposition of states $|+\hbar\boldsymbol{k}\rangle$ and $|-\hbar\boldsymbol{k}\rangle$ by a $\pi/2$-pulse. At the top of the atomic trajectory, the states are reflected by a π-pulse in the upper cavity. When the atoms pass again through the lower cavity, the states are recombined by a final $\pi/2$-pulse.

of new generations of detectors that will extend the frequency band of GW detection. State-of-the-art detectors based on optical interferometry like LIGO [15] or VIRGO [16] have a detection band starting at tens of Hz because of different sources of cavity-length noise at low frequencies. To overcome this limitation, a promising solution could rely on using correlated measurements between distant free-falling AIs. In such a configuration, the differential AI measurement enables one to read the GW phase variation induced on a common interrogation laser. The MIGA project consists of building a proof-of-principle detector by interrogating three distant AIs within the resonant field of an optical cavity. The geometry of the antenna is represented in Fig. 1: three AIs in a fountain configuration are simultaneously created by three cavity-enhanced light pulses ($\pi/2 - \pi - \pi/2$ Mach-Zehnder sequence) using Bragg diffraction [17,18] in the stationary cavity field. The transitions involve the external states $|+\hbar\boldsymbol{k}\rangle$ and $|-\hbar\boldsymbol{k}\rangle$ of the ^{87}Rb atoms in the internal ground state $|F = 2, m_F = 0\rangle$.

By measuring the atomic phase shift $\Delta\Phi_{\mathrm{AT}}(X_i)$ from the AIs placed at different locations X_i, we can extract the strain variation h induced by a GW with a strong immunity against the position noise of the cavity mirrors [19] using the differential measurement:

$$\Delta\Phi_{\mathrm{AT}}(X_i) - \Delta\Phi_{\mathrm{AT}}(X_j) \propto \frac{4\pi}{c}\frac{\nu_0}{2} s_h(X_i - X_j), \tag{3}$$

where ν_0 is the laser frequency and c is the speed of light. The term s_h is related to weighting of time-fluctuations of h by the AI sensitivity function. Assuming that (i) the measurement of each AI is limited by quantum projection noise at a level of 1 mrad, (ii) the maximum distance between AIs is given by the cavity length $L = 200$ m, and (iii) the total interferometer time is $2T = 500$ ms, we obtain from Eq. (3) a peak strain sensitivity of $2 \times 10^{-13}/\sqrt{\mathrm{Hz}}$ at a frequency of 2 Hz. To improve the measurement sensitivity, high-order Bragg diffraction [20] could be used. Instead of using transitions between the states $|+\hbar\boldsymbol{k}\rangle$ and $|-\hbar\boldsymbol{k}\rangle$ it is possible to induce transitions between the states $|+n\hbar\boldsymbol{k}\rangle$ and $|-n\hbar\boldsymbol{k}\rangle$ using matter-wave diffraction of order n. Such a process requires large optical powers that can be reached using cavity build-up.

4 Cavity-enhanced atom interferometry

We are currently working on a prototype to study cavity-enhanced atom interferometry in the MIGA configuration. This experiment consists of a single AI where atoms are manipulated by three Bragg pulses resonating inside two 80-cm-long cavities.

4.1 The atomic source and interferometer

Atoms are first cooled down in a three dimensional magneto-optical trap (3D MOT) to a temperature of ~ 140 μK. To have a fast loading rate in the 3D MOT, atoms are first trapped in a 2D MOT and pushed by a laser beam to generate an atomic flux of several 10^9 atoms/s toward the center of the 3D MOT. Atoms are launched from the 3D MOT on a vertical trajectory [see Fig. 2(a)] with a velocity of 3.0 m/s by a moving molasses technique using a frequency shift between the upper and lower cooling beams. A stage of sub-Doppler cooling reduces the sample temperature to a few μK by increasing the detuning of the cooling beams from the $F = 2$ to $F' = 3$ cycling transition to about $-20\,\Gamma$, where $\Gamma \simeq 6$ MHz is the transition linewidth. Figure 2(b) shows a typical signal of cold atoms measured by resonant fluorescence after a time of flight of 505 ms. A temperature of 4.7 μK is reached without shielding the source from external magnetic fields.

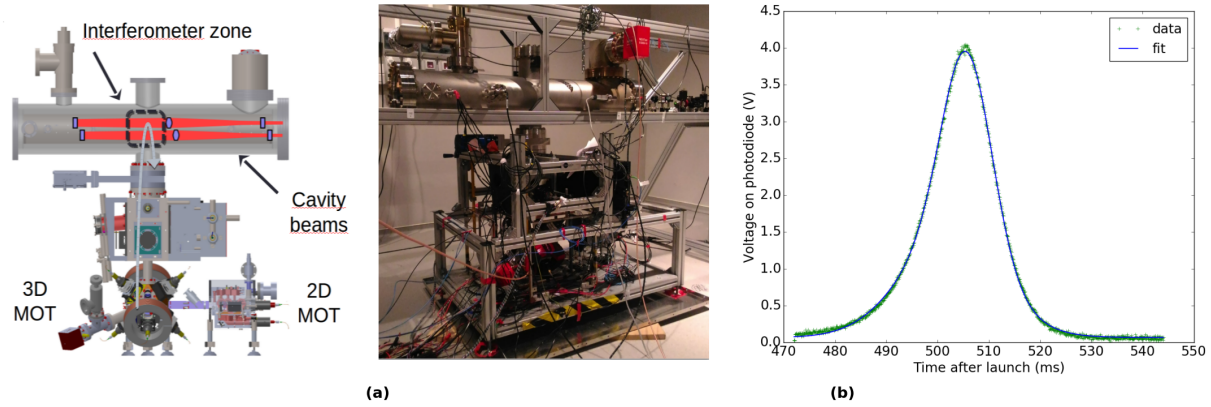


Figure 2 – (a) Left: Scheme of the atom interferometer. Atoms are loaded in a 3D MOT from a 2D MOT and are launched on vertical trajectory into the interferometer zone where they are interrogated by Bragg pulses in two optical cavities. The atoms are finally detected in the region between the 3D MOT and the cavities. Right: photo of the experiment. (b) Typical time-of-flight signal measured after 505 ms by fluorescence of the atoms. By integrating the signal we deduce an atom number of 3.6×10^8, and the full width at half maximum of the signal gives a temperature of 4.7 μK.

For the interferometer sequence, atoms need to be prepared in a well-defined velocity class and internal state. Velocity selection is performed with a horizontally-oriented Raman pulse before the atoms reach the interferometer zone. To minimize sensitivity to ambient magnetic fields, a second Raman pulse selects the atoms in the magnetically-insensitive $m_F = 0$ state by splitting the Zeeman sub-levels with a homogeneous magnetic bias field. After this preparation phase, the atoms enter the cavities where they are interrogated using a $\pi/2 - \pi - \pi/2$ pulse sequence. The π-pulse is realized at the apex of the parabolic trajectory. On their way down, the atoms pass through the detection system, where the interferometer phase shift is measured. The populations of the two states $|+\hbar k\rangle$ and $|-\hbar k\rangle$ are detected by fluorescence after a stage of state labeling is implemented using the Raman beams.

4.2 Geometry of the interrogation cavity

The waist of the Bragg beam needs to be of the order of several mm to interrogate efficiently the cold-atom clouds and obtain a high interference contrast. To achieve such a large waist in a stable 80-cm-long cavity, we opted for a marginally stable resonator geometry [21] with two plan mirrors M_1 and M_2 located at the focal point of a biconvex lens [see Fig. 3(a)], which magnifies the beam size at the cavity input. If the cavity is injected with a Gaussian beam of waist ω_{01} located on M_1, the field resonating inside the cavity after the lens will be Gaussian, with an amplified waist ω_{02} located on M_2. The atom interrogation will be performed between

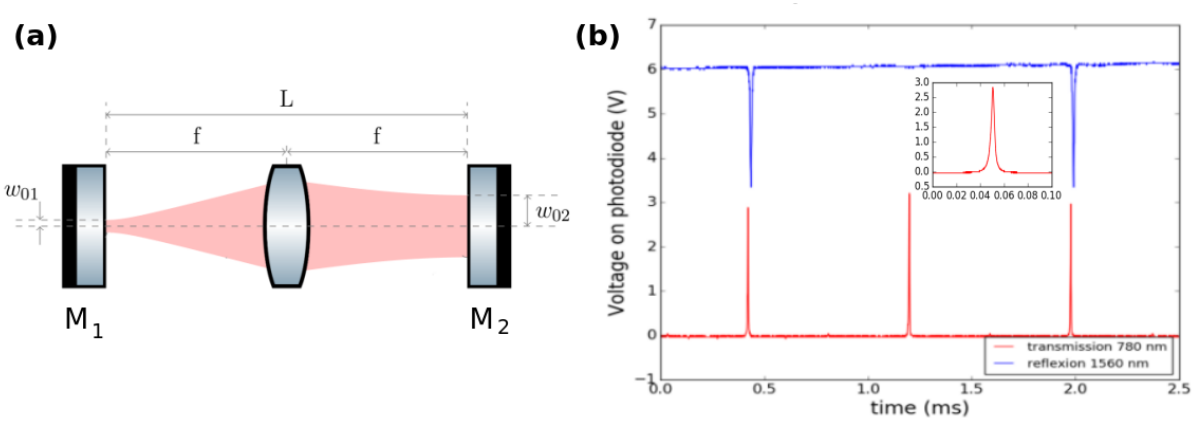


Figure 3 – (a) Scheme of the marginally-stable cavity used to interrogate the atoms. Two plane mirrors with high-reflectivity coatings at 780 nm and 1560 nm are placed at the focal distance $f = 40$ cm of a biconvex lens. An input beam with waist ω_{01} will generate a beam with a magnified waist ω_{02} on the other side of the cavity where the atoms will be interrogated. (b) Cavity transmission signal at 780 nm (red line), and reflection signal at 1560 nm (blue line) obtained by scanning the current of the master laser diode operating at 1560 nm.

the lens and M_2. The relation between the two waists is given by $\omega_{02} = \lambda f/\pi\omega_{01}$ where λ is the wavelength of the light resonating inside the cavity.

The beam at 780 nm is used to realize the interrogation pulses of the interferometer and therefore needs to be switched off most of the time, which can lead to technical issues as it also has to be kept resonant with the cavity. The 780 nm light is therefore obtained by coherently doubling the frequency of a 1560 nm laser that is constantly locked to the cavity using the Pound-Drever-Hall (PDH) technique. However, these two beams do not resonate at exactly the same frequency inside the cavity because the mirror coating has a different effective thickness at 1560 nm and 780 nm (*i.e.* the resonator lengths are not the same). To circumvent this problem, the 1560 nm beam is frequency modulated with an electro-optic modulator (EOM), and the PDH lock is realized on one of the modulation sidebands of this light. A resonant mode for both the sideband at 1560 nm and the carrier-doubled 780 nm light is obtained when the modulation frequency is 88.8 MHz.

Figure 3(b) shows the cavity transmission at 780 nm and the reflection signal at 1560 nm used for the PHD lock, when the frequency of the 1560 nm laser is scanned by modulating its driving current. The ratio between the full width at half maximum of the resonance and the free spectral range (distance between two resonances) gives the finesse of the resonator, F. We obtain for the two wavelengths $F_{780} = 236$ and $F_{1560} = 180$. The height of the resonances at 780 nm gives a measure of the power transmitted by the cavity, which is the power resonating inside the cavity attenuated by the transmission of the output mirror $T_m = 0.005$. The ratio between the power inside the cavity and the input power gives the optical gain: $G_{780} = 70$. The limitation of the optical gain, which is the key parameter for future implementation of high-order Bragg diffraction, is mainly due to light diffusion on the mirrors and optical losses from the lens. A well-aligned cavity shows a Gaussian resonating mode at 780 nm, as shown in Fig. 4(a) from an image taken of the cavity transmission. By fitting the radial profile of the Gaussian mode, we measure a waist of $\omega_{02} = 4$ mm. As previously studied theoretically [21], misalignments of the cavity optics can create an intensity variation in the beam's radial profile. For instance, for a displacement of the input mirror from the focal point of 50 μm, we observed a ring-shaped intensity distribution of the cavity field [see Fig. 4(b)].

With this experiment, we will soon be able to study the MIGA geometry on a reduced scale, which we anticipate will have an important impact on metrology and high-precision sensing with cavity-enhanced atom interferometry. This demonstrator will also help to implement future upgrades to the MIGA antenna, such as large-momentum-transfer atom optics.

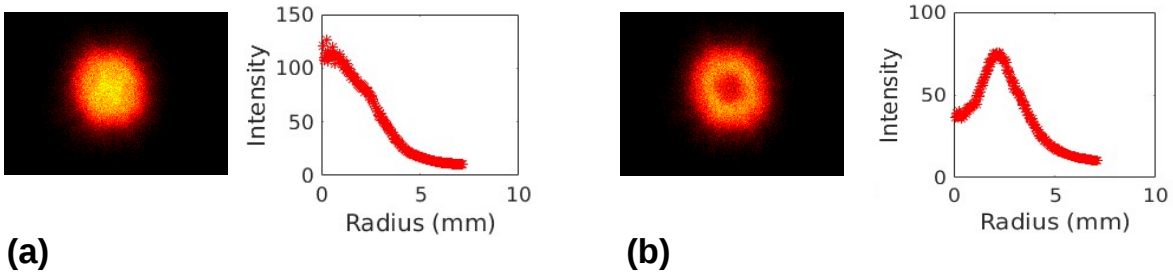


Figure 4 – (a) Left: resonating mode at 780 nm (observed via cavity transmission with a CCD camera) when the cavity is perfectly aligned. Right: azimuthal average of the image, which is well described by a Gaussian intensity profile. (b) Left: resonating mode at 780 nm when the input mirror is longitudinally displaced by 50 μm. Right: azimuthal average which shows a ring-shaped intensity profile.

5 The ICE project: testing the weak equivalence principle in weightlessness

Einstein's equivalence principle (EEP), which is a cornerstone of GR, postulates that the inertial and gravitational mass of any object are equal. This implies that, in the same gravitational field, two bodies of different masses or compositions will undergo the same acceleration. This sub-principle of the EEP is known as the weak equivalence principle (WEP), or as the universality of free fall. Various theories of quantum gravity predict a violation of the EEP [22,23], hence detecting the presence or absence of a violation at a very high precision would help to put bounds on these theories. The central parameter that characterizes the WEP is called the Eötvös parameter η, which is defined as the ratio of the differential acceleration between two bodies to their mean acceleration

$$\eta = 2\frac{|a_1 - a_2|}{|a_1 + a_2|}, \tag{4}$$

where a_1 and a_2 are the gravitational accelerations of test bodies 1 and 2, respectively. This parameter evaluates to zero if the WEP is respected.

Today, the most precise tests of the WEP have been carried out with "classical" test masses (*i.e.* masses made of bulk material) at the level of 10^{-13} via torsion pendulum [24] or lunar laser ranging [25] experiments. Recently, the MICROSCOPE space mission [26] has been launched and is anticipated to measure η at 10^{-15} by benefiting from the low background noise and permanent free fall of an orbiting satellite. In contrast, the majority of WEP tests using cold atoms have been carried out on ground, in well-controlled laboratory environments, and have not yet reached a level of precision competitive with those done with classical bodies. Nevertheless, tests using "quantum" bodies like atoms are sensitive to WEP violations resulting from quantum physics that cannot be otherwise accessed. Presently, the state-of-the-art for this type of measurement has reached a precision of 3×10^{-8} using cold samples of ^{85}Rb and ^{87}Rb [11], or more recently to low 10^{-9} with ^{87}Rb in mixtures of different internal states [27]. So far, two main approaches have been taken to reach higher sensitivities: (*i*) atoms are launched in a fountain to extend their free-fall time inside large-scale vacuum systems [28,29], or (*ii*) atoms are contained within a small-scale apparatus that is then placed in free fall, such as in a drop tower [30], a sounding rocket [31,32] or an aircraft undergoing parabolic flight [33].

The primary goal of the ICE project is to develop a mobile dual-species inertial sensor able to measure η at high precision in a weightless environment, such as that generated onboard the Novespace Zero-g aircraft. Performing WEP tests in this type of environment serves as a proof-of-concept toward using cold-atom technology onboard a satellite, as proposed by the STE-QUEST mission project [34], where future tests at the 10^{-15} level could become a reality. In the remainder of this section we will give an overview of the experiment, discuss progress toward a precision measurement on ground, and review out results from the first WEP test in weightlessness using cold-atom sensors in a free falling vehicle [13].

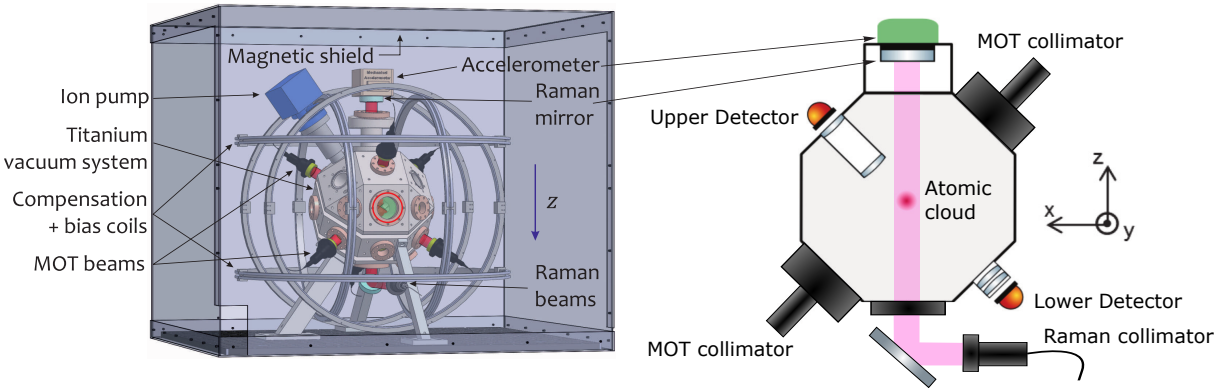


Figure 5 – Scheme of the apparatus. Left: 3D view of the titanium vacuum chamber. Right: lateral section of the chamber.

5.1 A transportable, simultaneous dual-species interferometer

The ICE project relies upon a robust and transportable apparatus comprised of a bank of fiber-based lasers, an ultra-stable frequency source and a titanium science chamber, as depicted in Fig. 5. The potassium-39 and rubidium-87 atomic sources are derived from 3DMOTs loaded from a background vapor. After laser-cooling each sample to a temperature of a few μK and preparing the atoms in the magnetically insensitive state $|F = 1, m_F = 0\rangle$, a $\pi/2 - \pi - \pi/2$ sequence of Raman pulses is applied along the vertical direction to create two Mach-Zehnder interferometers simultaneously for each species. The transition probability of each interferometer is measured via resonant fluorescence detection on the $|F = 2\rangle \rightarrow |F' = 3\rangle$ transition. This can be performed at two spatial locations by avalanche photodiodes positioned above and below the center of the chamber, as shown in Fig. 5. The upper detector collects photons with a large solid angle using a re-entrant viewport, which is useful during $0g$ operation when the atoms do not fall, or for short interrogation times during $1g$ when the samples remain close to the chamber center. The lower detector receives a strong signal after a fixed free-fall time (up to ~ 60 ms), allowing for operation with larger interrogation times, and hence increased sensitivity, on ground. Finally, the interference pattern for each species is obtained by measuring the proportion of atoms in $|F = 2\rangle$ as a function of an applied laser phase that scans the sinusoidal fringe.

In a constant gravitational field, the atomic phase shift for species j can be shown to be

$$\Delta\Phi_j = \boldsymbol{\mathcal{S}}_j \cdot \boldsymbol{a}_j + \phi_{\mathrm{vib},j} + \phi_{\mathrm{las}}, \tag{5}$$

where $\boldsymbol{\mathcal{S}}_j = \boldsymbol{k}_j T_j^2$ is the interferometer scale factor, $\phi_{\mathrm{vib},j}$ is random phase shift caused by vibrations of the retro-reflection mirror, and ϕ_{las} is a controlled phase offset from the Raman lasers. In the absence of vibration noise, since the phase shift for each species is sensitive to the gravitational acceleration $\boldsymbol{a}_j$, one can obtain the Eötvös parameter from

$$\eta = \frac{\Delta\Phi_d}{\boldsymbol{\mathcal{S}}_{\mathrm{Rb}} \cdot \boldsymbol{g}}, \tag{6}$$

where $\Delta\Phi_d = |\Delta\Phi_{\mathrm{Rb}} - (\mathcal{S}_{\mathrm{Rb}}/\mathcal{S}_{\mathrm{K}})\Delta\Phi_{\mathrm{K}}|$ is the differential phase between AIs. Equation (6) clearly states the advantage of an interferometric WEP test—the sensitivity scales quadratically with T and linearly with k, which can be further increased by using large momentum transfer processes [29].

However, as one goes to larger sensitivities, or when the vibration noise is large (such as onboard a moving vehicle), the motion of the reference mirror becomes a significant source of phase noise. In most cases, one must employ methods to either suppress or reject the phase noise resulting from mirror vibrations. A common method to suppress ambient vibrations is to place

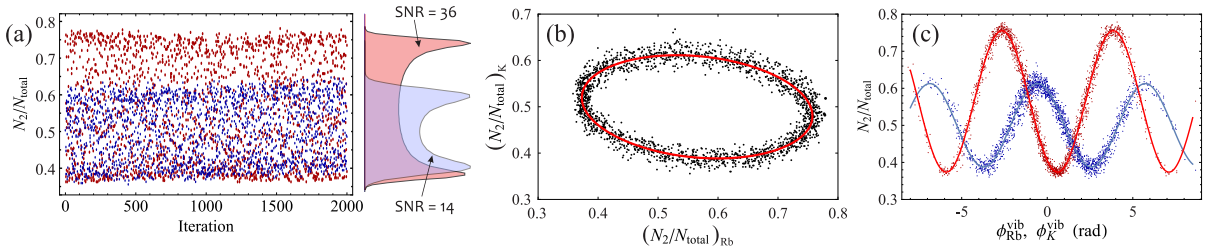


Figure 6 – (a) Raw transition probability for simultaneous ^{87}Rb (red points) and ^{39}K (blue points) interferometers with a total interrogation time of $2T = 40$ ms. The probability density measured from these 2000 measurements is shown on the right, which enables one to extract of the fringe contrast and SNR for each species. (b) Parametric plot of the raw measurements from (a). The high degree of correlation between these data results in an ellipse. A fit to these data (solid line) yields this differential phase shift between interference fringes, which is primarily caused by systematic effects. (c) Reconstruction of the fringes using the FRAC method. Here, in additional to giving the differential phase, sinusoidal fits (solid lines) can be used to directly extract the acceleration sensitivity of each species.

the apparatus on an anti-vibration platform [35,36], but this solution is not generally compatible with onboard applications. Instead, we take two approaches to reject vibration noise. The first is to perform the interferometers simultaneously and with the same scale factor (*i.e.* $\mathcal{S}_{\mathrm{Rb}} = \mathcal{S}_{\mathrm{K}}$), this ensures a maximum amount of common mode rejection. It is then possible to measure the differential phase from the ellipsoidal pattern obtained by parametrically plotting the interferometer output for each species [10] [see Fig. 6(b)]. The second method involves monitoring the mirror vibrations with a mechanical accelerometer and correcting for the noise by computing the corresponding vibration phase via [33,10]

$$\phi_{\mathrm{vib},j} = k_j \int_0^{2T_j} f_j(t) a_{\mathrm{vib}}(t) \mathrm{d}t, \tag{7}$$

where $f_j(t)$ is the interferometer response function and $a_{\mathrm{vib}}(t)$ is the common acceleration of the reference mirror due to vibrations during the interferometer sequence. We call this technique the fringe reconstruction by accelerometer correlation (FRAC) method [see Fig. 7(a)]. This latter approach is much more versatile when the mechanical accelerometer has sufficiently high signal-to-noise ratio in the desired frequency band, since it does not require the two scale factors to be equal, and it does not rely on complex ellipse fitting algorithms that can yield biased estimates of $\Delta\Phi_d$.

5.2 Testing the WEP on ground

Since the ICE apparatus is designed primarily to operate in microgravity, where the atoms remain close to the center of the science chamber, the maximum interrogation time we can achieve on ground is limited to $2T \simeq 45$ ms by our detection optics. Hence, to increase the sensitivity of our measurements, we have focused on improving the signal-to-noise ratio (SNR) of, and the degree of correlation between, both ^{87}Rb and ^{39}K interference fringes. A variety of recent improvements to our potassium source, including gray-molasses cooling and a new state preparation scheme, have enabled us to increase the fringe contrast and SNR by a factor of 4. Similarly, by using an architecture where the interrogation beams for each species travel along the same optical pathway, and have the same interaction strength with their respective atoms, we maximize the level of common-mode rejection and enhance sensitivity to differential effects.

Figure 6 shows simultaneous measurements from the laboratory using $T = 20$ ms. Here, ambient mirror vibrations are large enough to scan the interferometer fringes over a phase range of $\sim 4\pi$. Figure 6(a) displays the raw transition probability of both species for 2000 accelerations measurements (requiring ~ 30 minutes of data acquisition). These points are integrated over the horizontal axis to obtain the probability density function. By fitting a function that is

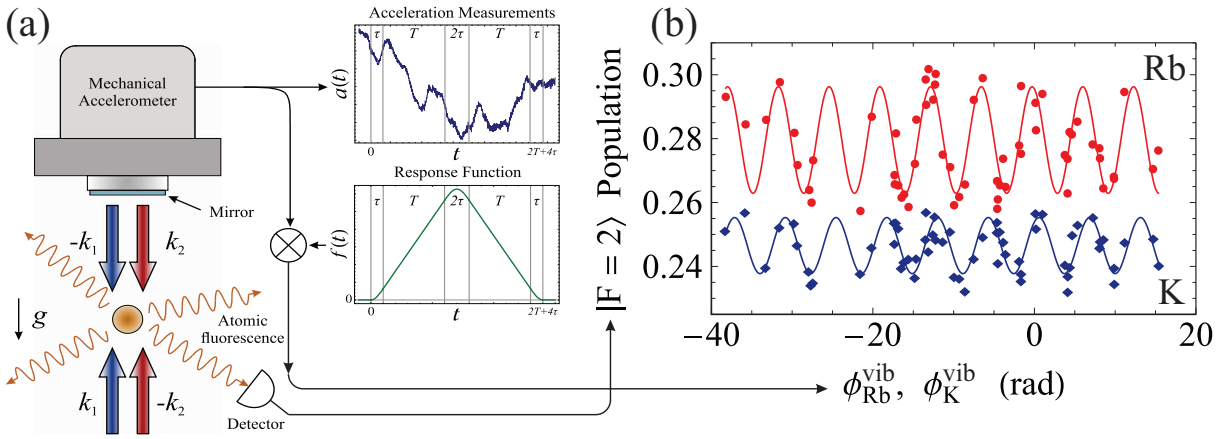


Figure 7 – (a) Schematic of the FRAC method. The acceleration is recorded during the interferometer sequence and is convolved with the interferometer response function to obtain the vibration phase $\phi_{\mathrm{vib},j}$. (b) Simultaneous ^{87}Rb (red) and ^{39}K (blue) fringes obtained using the FRAC method in $0g$ with an interrogation time of $T = 2$ ms.

the convolution of an inverse sine and a Gaussian to the probability density, we extract the contrast and SNR of each interferometer [33]. Figure 6(b) displays a parametric plot of the potassium transition probability as a function of the rubidium one for the same data presented in Fig. 6(a). Since the vibration noise is common mode for both species, there is a high degree of correlation between these data—resulting in an ellipse with an eccentricity determined by the differential phase between the two interference fringes. Fitting an ellipse to these data yields an estimate of $\Delta\Phi_d$ with a statistical precision of ~ 10 mrad—corresponding to a WEP violation sensitivity of $\delta\eta \sim 1.5 \times 10^{-7}$. Figure 6(c) shows the reconstructed interference fringes using the FRAC method, from which we can directly measure the acceleration sensitivity of each species: $\delta a_{\mathrm{Rb}} \simeq 5.2 \times 10^{-8}\, g$ and $\delta a_{\mathrm{K}} \simeq 8.3 \times 10^{-8}\, g$, corresponding to a WEP sensitivity of $\delta\eta \simeq 7.2 \times 10^{-8}$ after 30 minutes of integration. Although, further study of systematic effects is required, these results are approaching precisions competitive with the state-of-the-art [11,27].

5.3 Testing the WEP in weightlessness

In May 2015, the ICE experiment embarked on a series of parabolic flight campaigns and successfully tested the WEP for the first time in weightlessness [13]. Here, we give a review of our results and the issues that remain to be solved for future experiments.

When performing experiments in a moving vehicle, the primary challenge for an AI is to deal with the large level of vibration noise (in the case of an aircraft, this can be 5 orders of magnitude above that of a quiet laboratory), and changes in acceleration and orientation due to the vehicle's motion. Our approach to these problems has been to utilize a sensitive classical accelerometer to monitor and correct for high-frequency vibrations on the reference mirror via the aforementioned FRAC method [see Fig. 7(a)]. This sensor also gives us information about low-frequency changes in acceleration (particularly during the $0g$, $1g$ and $2g$ phases of parabolic flight) which enable us to appropriately adapt the phase modulation of our interrogation laser during the interferometer to optimize the fringe contrast [13]. During these campaigns, we obtained correlated acceleration measurements from each species during microgravity [see Fig. 7(b)] that yielded a measurement of $\eta = (0.9 \pm 3.0) \times 10^{-4}$ at $T = 2$ ms. When compared to measurements made during $1g$ on the same flights, we find a 5-fold improvement as a result of the rejection of certain systematic effects in $0g$. Although with a modest precision, this WEP test is the first of its kind—namely with cold atoms free-falling in an Einstein elevator—and serves as a test bed for future experiments in Space [34]. During these flights we also demonstrated a record-low acceleration sensitivity of $3.4 \times 10^{-5}\, g$ per shot with our ^{87}Rb interferometer operating at $T = 5$

ms—corresponding to a resolution 1600 times below the level of ambient acceleration noise. This opens the way toward inertial navigation based on cold-atom technology [37].

Presently, the sensitivity of atom-interferometric measurements on the aircraft is limited by it's rotational motion. When the rotation occurs along an axis perpendicular to that of the interrogation beams, the upper and lower pathways of the Mach-Zehnder interferometer begin to diverge and fail to overlap during the final recombination pulse. This effect results in a loss of contrast which scales as [38,13]

$$\mathcal{C} \sim e^{-(k\sigma_v T)^2(|\mathbf{\Omega}_{\rm tr}|T)^2}, \tag{8}$$

where σ_v is the width of the velocity distribution (σ_v^2 is proportional to the sample temperature) and $\mathbf{\Omega}_{\rm tr}$ is the rotation vector transverse to $\boldsymbol{k}$. In future experiments, we plan to counter-rotate the reference mirror in real-time to compensate for this effect.

6 Conclusion

Cold-atom interferometry is a very promising tool to reach the challenging sensitivities required for fundamental precision measurements such as the detection of gravitational waves or violations of the equivalence principle. Such techniques can be exploited to provide new measurement apparatuses from lab-sized to large-scale infrastructures. Beyond the impact of atom interferometry in fundamental physics, the development of such experiments brings new technologies opening applications in other fields such as geology, seismology and hydrology, for underground surveys and the detection of mass transfer, but also for the realization of quantum-sensor-based inertial navigation systems. In terms of the projects discussed here, The MIGA antenna will be a first prototype for a new type of GW detector in the 0.1–1 Hz frequency band, and the first large-scale infrastructure based on quantum technologies. We are now realizing a first-generation experiment based on an original cavity geometry that will allow the team to study future upgrades to the MIGA antenna. Similarly, the ICE project has achieved the first WEP tests in microgravity, and is presently pursuing a precision measurement of the Eötvös parameter with a very-long-baseline interferometer. Toward this goal we are preparing an evaporative cooling stage to reach ultra-cold temperatures lower than 10 nK. In addition, we have recently installed an Einstein elevator in the lab which gives access to ~ 500 ms of weightlessness every 10 s. With these new tools, we anticipate a measurement of η below 10^{-10} to be within reach.

Acknowledgments

This work was realized with the financial support of the French State through the "Agence Nationale de la Recherche" (ANR) in the frame of the "Investissement d'avenir" programs: Equipex MIGA (ANR-11-EQPX-0028), IdEx Bordeaux - LAPHIA (ANR-10-IDEX-03-02) and FIRST-TF (ANR-10-LABX-48-01). This work is also supported by the French national agencies CNES, DGA, IFRAF, action spécifique GRAM, RTRA Triangle de la Physique and the European Space Agency. This work was also supported by the Région d'Aquitaine (project IASIG-3D) and by the city of Paris (Emergence project HSENS-MWGRAV). We also thank the "Pôle de compétitivité Route des lasers - Bordeaux" cluster for his support. G. L. thanks DGA for financial support. M. P. also thanks LAPHIA–IdEx Bordeaux for partial financial support.

References

1. Chu S., Cohen-Tannoudji C., and Phillips W., *Nobel Lectures in Physics: 1996–2000*, (2003).
2. Peters A., Chung. K. Y., and Chu. S., *Metrologia* **38**, 25 (2001).
3. Gustavson T., Bouyer P., and Kasevich M. A., *Phys. Rev. Lett.* **78**, 2046 (1997).
4. Canuel B., *et al*, *Phys. Rev. Lett.* **97**, 010402 (2006).

5. Snadden M. J., McGuirk J. M., Bouyer P., Haritos K. G., and Kasevich M. A., *Phys. Rev. Lett.* **81**, 971 (1998).
6. Fixler J. B., Foster G. T., McGuirk J. M., and Kasevich M. A., *Science* **315**, 74 (2007).
7. Rosi G., Sorrentino F., Cacciapuoti L., Prevedelli M., and Tino G. M., *Nature* **510**, 518 (2014).
8. Bouchendira R., Cladé P., Guellati-Khélifa S., Nez F., and Biraben F., *Phys. Rev. Lett.* **106**, 080801 (2011).
9. Burrage C., Copeland E. J., and Hinds E. A., *J. Cosmol. Astropart. Phys.* **03**, 042 (2015).
10. Barrett B., Antoni-Micollier L., Chichet L., Battelier B., Gominet P.-A., Bertoldi A., Bouyer P., and Landragin A., *New J. Phys* **17**, 085010 (2015).
11. Zhou L., Long S., Tang B., Chen X., Gao F., Peng W., Duan W., Zhong J., Xiong Z., Wang J., Zhang Y., and Zhan M., *Phys. Rev. Lett.* **115**, 013004 (2015).
12. Canuel B., *et al*, *Proc. SPIE 9900, Quantum Optics* , 990008 (2016).
13. Barrett B., Antoni-Micollier L., Chichet L., Battelier B., Lévèque T., Landragin A., and Bouyer P., *Nat. Commun.* **7**, 13786 (2016).
14. Abbott B. P., *et al*, *Phys. Rev. Lett.* **116**, 061102 (2016).
15. Abbott B. P., *et al*, *Reports on Progress in Physics* **72**, 076901 (2009).
16. Acernese F., *et al*, *J. Opt.* A **10**, 064009 (2008).
17. Martin P., Oldaker B., Miklich A., and Pritchard D., *Phys. Rev. Lett.* **60**, 515 (1988).
18. Müller H., Chiow S., and Chu S, *Phys. Rev.* A **77**, 023609 (2008)
19. Canuel B., *et al*, *arXiv*:1703.02490 [physics.atom-ph] (2017).
20. Müller H., Chiow S., Long Q., Herrmann S., and Chu S., *Phys. Rev. Lett.* **100**, 180405 (2008).
21. Riou I., Mielec N., Lefèvre G., Prevedelli M., Landragin A., Bouyer P., Bertoldi A., Geiger R., and Canuel B., *arXiv*:1701.01473 [physics.atom-ph] (2017).
22. Will C. M., *Living Rev. Relativity* **9**, 3 (2006).
23. Damour T., Piazza F., and Veneziano G., *Phys. Rev.* D **66**, 046007 (2002).
24. Schlamminger S., Choi K.-Y., Wagner T. A., Gundlach J. H., and Adelberger E. G., *Phys. Rev. Lett.* **100**, 041101 (2008).
25. Williams J. G., Turyshev S. G., and Boggs D. H., *Phys. Rev. Lett.* **93**, 261101 (2004).
26. Touboul P., Métris G., Lebat V., and Robert A., *Class. Quantum Grav.* **29**, 184010 (2012).
27. Rosi G., D'Amico G., Cacciapuoti L., Sorrentino F., Prevedelli M., Zych M., Brukner C., and Tino G. M., *arXiv*:1704.02296 [physics.atom-ph] (2017).
28. Dickerson S. M., Hogan J. M., Sugarbaker A., Johnson D. M. S., and Kasevich M. A., *Phys. Rev. Lett.* **111**, 083001 (2013).
29. Kovachy T., Asenbaum P., Overstreet C., Donnelly C. A., Dickerson S. M., Sugarbaker A., Hogan J. M., and Kasevich M. A. *Nature* **528**, 530 (2015).
30. Müntinga H., *et al*, *Phys. Rev. Lett.* **110**, 093602 (2013).
31. Seidel S. T., Gaaloul N., and Rasel E. M. *Proceedings of 63rd International Astronautical Congress* **3**, 801 (2012).
32. Dinkelaker A. N., *et al*, *Appl. Opt.* **56**, 1388-1396 (2017).
33. Geiger R., *el al*, *Nat. Commun.* **2**, 474 (2011).
34. Aguilera D., *et al*, *Classical Quant. Grav.* **31**, 115010 (2014).
35. Le Gouët J., Mehlstäubler T. E., Kim J., Merlet S., Clairon A., Landragin A., and Pereira Dos Santos F., *Appl. Phys.* B **92**, 133 (2008).
36. Zhou M.-K., Hu Z.-K., Duan X.-C., Sun B.-L., Chen L.-L., Zhang Q.-Z., and Luo J., *Phys. Rev.* A **86**, 043630 (2012).
37. Battelier B., *et al*, *Proc. SPIE Quantum Opt.* **9900**, 990004 (2016).
38. Roura A., Zeller W., and Schleich W. P., *New J. Phys* **16**, 123012 (2014).







The Quantum Sensor Challenge - Designing a System for a Space Mission

A. HESKE
European Space Agency, Keplerlaan 1,
2201 AZ Noordwijk, The Netherlands

For fundamental physics experiments, such as probing various aspects of Einstein's Equivalence Principle or detection of gravitational waves, space missions offer a number of advantages compared to ground-based laboratory settings. Designing an instrument suite to fly on a satellite requires particular attention to a number of aspects for the instrument hardware, which are inherent to space missions. To arrive at a viable mission and spacecraft design, the science performance requirements and instrument needs have to be analyzed, drivers for the mission design need to be identified and numerical simulations of measurement performance have to be run. This iterative process of maximizing the science return while optimizing the instrument and spacecraft designs will be illustrated with examples from two mission studies carried out at the European Space Agency.

1 Introduction

Quantum sensors, devices which exploit quantum effects, such as entanglement or superposition, achieve highly sensitive measurements of physical parameters. They are employed in accelerometers, gravimeters, atomic clocks and cold atom and laser interferometers. Science applications range from geodesy, time and frequency metrology to fundamental physics experiments.This paper describes the steps required to bring such a fundamental physics experiment from a laboratory setting into space.

2 Call for Space

2.1 What Space Offers

In laboratory settings on ground, experiments are usually easily accessible and fine tuning and modifications can be made to the hardware at virtually any time. Drawbacks include the Earth gravity field, the noisy seismic environment and the short interaction times. Space platforms on the other hand offer a number of assets, and to exploit the ultimate sensitivity of quantum sensors and to push the measurement accuracy beyond what can be reached on ground, space becomes even a necessity. For fundamental physics experiments space offers:

- Infinitely long 'free-fall' times and long interaction times
- Large variations of gravitational potential and large velocities and velocity variations
- Huge free-propagation distances and variations in altitude
- Quiet environmental conditions and absence of seismic noise
- Unique requency ranges of gravitational waves inaccessible from ground

Designing and building an istrument to fly on a spacecraft requires particular attention to a number of aspects for the instrument hard- and software, which are inherent to space missions.

Autonomy and Operability: In orbit, the instrument has to carry out routine measurements and calibrations autonomously, through pre-defined measurement sequences and without frequent intervention from ground.

Reliability and Redundancy: Once in orbit, the hardware can obviously no longer be accessed or replaced, and the instrument needs to work reliably for the whole mission duration. This requires an appropriate redundancy concept, to render the instrument minimally susceptible to failures.

Radiation Environment: The instrument has to withstand a harsh radiation environment, which severely degrades the performance of the instruments' components with time, if no special measures are implemented like appropriate shielding.

Launcher and Accommodation on Spacecraft: Since the spacecraft has to fit on a launcher with given lift capabilities there are limitations for the instruments on mass, volume and power consumption and, in addition, also regarding the range of potential orbits.

Model Philosophy, Qualification and Verification: Considering the aspects described above, all instrument functions and its science performance need to be verified and qualified on ground. Building dedicated models of the instrument, these specific aspects are verified by tests thus ensuring that the instrument will work correctly in orbit, and above all, will survive the launch.

Data packages, Standards and Reviews: Data packages have become an essential part of space instrument development. They describe all aspects of the instrument such as justification of the design and plans for development and testing. The contents of these data packages as well as the design and testing of an instrument are governed by a wealth of space standards. Regular reviews are held to track progress and identify potential issues early.

3 Mission Assessment - The Theory

The aim of a space mission assessment is to analyze the science requirements and instrument performance to arrive at a viable spacecraft and overall mission design. Specific science objectives and requirements are derived from the science goals, followed by definition of mission requirements, which address the mission as a whole, including spacecraft and instrument design, orbit and operations. For design of the actual hardware, engineering requirements are derived, further breaking down the definition of the mission components. During the assessment of the engineering requirements it can - almost certainly - occur that for technical or technological reasons some of these requirements can not or only partially be fulfilled. The impact on the science objectives is evaluated, model calculations are run and a trade-off is to be found in terms of science output versus mission complexity and feasibility.

During the mission assessment and determining its feasibility the aspects addressed in Section 2.2 are to be considered together with these two related to programmatics and risks:

Technology Maturity: At the end of a mission definition phase, it is required that the critical functions of an instrument have been verified in a relevant environment. This is to reduce the risk that a low technology maturity leads to substantial delays, due to problems during the instrument development.

Management, Schedule and Funding: Spacecraft development is carried out by an industrial partner under an ESA contract, with a fixed budget and - usually - a tight schedule, to ensure the target launch date. Instrument development is carried out typically by an international consortium funded through national agencies. An appropriate consortium structure needs to be in place and funding to be secured as to align the instrument development schedule with the industry schedule.

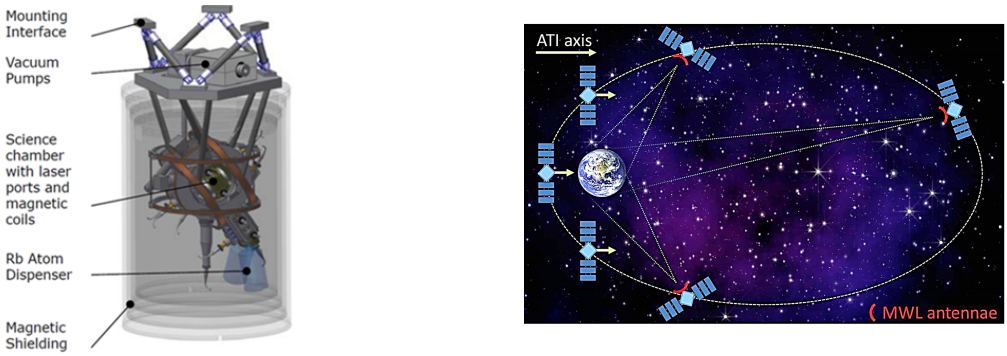


Figure 1 – STE-QUEST: Physics package of the atom interferometer (left), spacecraft attitude for ground clock comparisons and interferometry (right).

4 Mission Assessment - Case Studies

4.1 STE-QUEST - The Space Time Explorer - Quantum Equivalence Space Test

In the framework of the call for future medium-size missions issued in 2010 within the Cosmic Vision program of the European Space Agency (ESA) a three-year study was carried out assessing a fundamental physics mission candidate called STE-QUEST [1].

The primary science objectives are to test two aspects of Einstein's Equivalence Principle with quantum sensors to unprecedented accuracy: Gravitational red-shift tests in the Sun and Moon field and Weak Equivalence Principle (WEP) test, with the following measurement uncertainty requirements.

WEP Test: Uncertainty in the Eötvös ratio lower than 2×10^{-15}

Gravitational Red-shift Tests: Measurement uncertainty *Sun* - 2×10^{-6}; *Moon* - 4×10^{-4}

The payload comprised a dual species Rubidium atom interferometer to test the universality of free-fall of matter waves (see Fig. 1 left), a microwave link for simultaneous time and frequency comparisons of two atomic clocks on ground and a GNSS receiver for precise orbit determination, needed for the clock comparisons. The requirements on measurement accuracies, performances and pointing (Fig. 1 (right)) derived from the science requirements above are:

Atom Interferometry Performance: Instability $(13 \times 10^{-12} m/s^2)/\sqrt{\tau}$; Inaccuracy $< 2 \times 10^{-15}$; Gravitational acceleration $> 3 m/s^2$; Gravity gradient $< 2.5 \times 10^{-6} s^{-2}$; Rotations $< 10^{-6} rad/s$ - Inertial Pointing.

Clock Comparisons Performance: *Microwave Link:* Inaccuracy $< 5 \times 10^{-19}$; Frequency instability $< 5.2 \times 10^{-13}(1s)$; *GNSS Receiver:* Position error $2m$ Velocity error $2mm/s$ (both in post-processing); *Ground Clocks:* Inaccuracy 10^{-18}; Instability $2.5 \times 10^{-16}/\sqrt{\tau}$ - Nadir pointing.

Drivers for the orbit are a low gravity gradient and largel accelerations around perigee for atom interferometry and long common-views of ground clocks and large gravitational potential variations for the clock comparisons. The resulting reference orbit is a highly elliptical with an apogee of about 50000km, a perigee of 700 to 2000km, and a period of 16 hours (cf. Fig. 1 right). Numerical simulations confirmend that the science requirements and performance can indeed be achieved in a four-year mission.

Assessment of the technology maturity of the instrument elements concluded that the lowest risk is associated with the commercial GNSS receiver, a medium risk was identified for the upgrade of the microwave link to higher frequency and the largest development and programmatic risk was considered to be the atom interferometer, since for the dual Rubidium source as well as for the laser system critical functions had not yet been verified on full breadboards.

Under two parallel ESA contracts, industrial studies have demonstrated a viable mission and spacecraft design fulfilling all science and instrument requirements. No show-stoppers were identified, and both designs met the budget requirements for a launch on a Soyuz rocket.

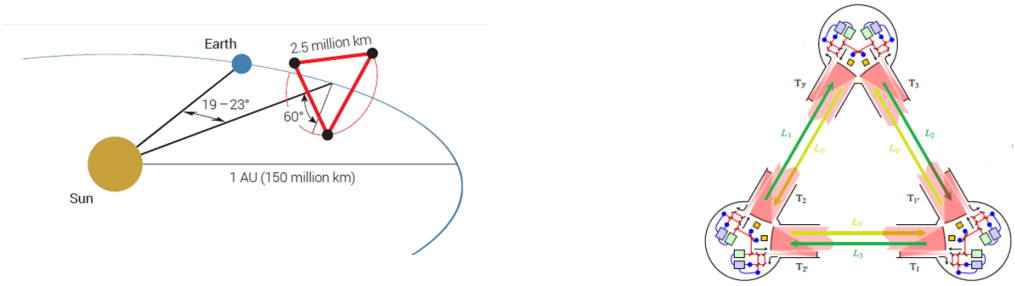


Figure 2 – LISA: Constellation and orbit (left); Three-spacecraft instrument suite configuration and laser links (right).

4.2 LISA - The Laser Interferometry Space Antenna

In response to an ESA call for mission concepts for the third large-sized mission opportunity, the Gravitational Wave Observatory, in autumn 2016, the LISA mission proposal [2] was submitted.

The science objective, in a nutshell, can be described as to detect, explore and characterize gravitational waves and their origins in a unique frequency range - from 0.1mHz to 100mHz, a frequency range inaccessible with ground-based laser interferometers. The characteristic strain sensitivity requirement ranges from $10^{-18}/\sqrt{Hz}$ at 0.1mHz, down to $10^{-21}/\sqrt{Hz}$ between 1mHz and 10mHz to $10^{-20}/\sqrt{Hz}$ at 100mHz.

The mission concept comprises three identical spacecraft flown in a triangular constellation (Fig. 2 left). with an armlength of 2.5 million km, in an Earth-trailing orbit at a distance of 50 to 65 million km. The baseline mission duration is 5 years, potentially extending up to 10 years.

The main constituents of the instrument suite (Fig. 2 right). are the telescope-optical bench-gravitational reference sensor (GRS) assembly, which contains the test masses, (two assemblies per spacecraft), a laser system and a phase meter system. Each of these hardware elements includes its own front-end control electronics. An on-board computer for instrument control and interface to the spacecraft, including power, data handling and drag-free control, completes the instrument suite per spacecraft.

5 Outcome and Outlook

5.1 STE-QUEST

The study showed that a fundamental physics mission employing quantum sensors is indeed technically feasible, provided that the technology of the dual species atom interferometer and the upgrades needed for the microwave link can be further pushed to the required maturity needed at the end of a mission definition phase, provided there will be proper funding.

5.2 LISA

LISA Pathfinder results have demonstrated that the design concept of the optical bench-GRS assembly is viable and operable, and that its performance even exeeds specifications and expectations.This concept is thus confirmed as the baseline for LISA and in an assessment study dedicated to the instrument suite it will be refined, together with a detailed analysis of the entire assembly including the telescope and the constellation acquisition system.

References

1. STE-QUEST Team, STE-QUEST Assessment Study Report, ESA/SRE(2013)6, (2013) (http://sci.esa.int/ste-quest/53445-ste-quest-yellow-book).
2. Lead proposer Prof. Dr. K. Danzmann, https://www.lisamission.org/proposal/LISA.pdf

3.
Tests of Fundamental Physics

PREPARING ESPRESSO'S FUNDAMENTAL PHYSICS TESTS

A. C. O. LEITE[a,b], C. J. A. P. MARTINS[a], P. MOLARO[c], C. S. ALVES[a,b], T. A. SILVA[a,b]
[a] *Instituto de Astrofísica e Ciências do Espaço, CAUP, Rua das Estrelas, 4150-762 Porto, Portugal*
[b] *Faculdade de Ciências da Universidade do Porto, Rua do Campo Alegre, 4150-007 Porto, Portugal*
[c] *INAF-Osservatorio Astronomico di Trieste, Via G.B. Tiepolo 11, I-34143 Trieste, Italy*

ESPRESSO is a high-resolution ultra-stable spectrograph for the VLT, whose commissioning will start this year. One of its key science goals is to test the stability of nature's fundamental couplings with unprecedented accuracy and control of possible systematics. As the first light approaches quickly, detailed studies are being done to evaluate the optimal strategy to detect a possible variation of fine-structure constant looking into metal absorption lines produced by the intervening clouds along the line of sight of QSOs. In this paper, I present the ongoing studies and emphasise the different strategy needed for fainter targets in order to improve tests of the stability of the variation of the fine-structure constant using ESPRESSO. I will also discuss the impact that these improved measurements can have on cosmology, more specifically on a Bekenstein-type model and on three different Dynamic Dark Energy models.

1 Observing with ESPRESSO

ESPRESSO is a high-resolution ultra-stable spectrograph that will be installed at the VLT - Very Large Telescope in 2017. It will allow to observe with one Unit of Telescope (UT) of the VLT individually or to combine the light of the four telescopes. This instrument has as one of his science goals to test the stability of fundamental couplings[1]. The Fundamental Physics Guaranteed Time of Observation (GTO) for this purpose will have 27 nights and a list of 14 QSO "ideal" targets was put together.[2] In order to achieve stronger constrains on the variation of the fine-structure constant, α, an ideal quasar target should present simple and strong absorption features of transitions with high sensitivities to variations of α.

The 14 targets selected for the GTO are presented in Table 1. The selection process of the target list is presented in detail in Leite et al. 2016 [2]. The first measurement on the table is not an ideal target to test α, but is a system where the proton to electron mass ratio and the T_{CMB} relation to redshift can also be measured. This makes it an interesting target to investigate the nature of the fundamental constants variation testing different theories where a relation between these three constants is predicted.[7] The GTO sample spans redshifts 1.35 to 3 and the background quasars of the targets have very different magnitudes (M=15.9-18.8).

Since most of the targets are very faint, one needs to verify if the efficiency of the collection of photons by the CCD ensures that the number of photons from our science target is higher that the number of photons coming from the instrumentation and reading of the CCD.

The limit for which the number of photons from the target and from the instrumental noise are the same was computed for the characteristics of VLT and ESPRESSO. These limits for two different cases are plotted in Figure 1: the 1 UT with no binning - 1X1 (blue line) assuming the light collected by the area of 1 VLT UT and the currently expected specifications for the ESPRESSO efficiency and CCD noise; and the 4UT with the CCD binned by 2 in the spectral direction and by 2 in the spatial direction - 2X2 (red dashed line) assuming the light collected

Table 1: List of the best measurements of the stability of the fine structure constant considering the wavelength coverage of ESPRESSO. Column 1 gives the quasar name; the redshifts of the absorption system are given in Column 2; Column 3 gives the magnitude of the emitting quasar. Column 4 and 5 gives the value of the measurement and the corresponding uncertainty. The last Column gives the references for each measurement.

Name	z_{abs}	M	$\Delta\alpha/\alpha$ (10^{-6})	$\sigma_{\Delta\alpha/\alpha}(10^{-6})$	Ref.
J034943-381031	3.02	17.3	-27.9	34.2	[3]
J040718-441013	2.59	17.3	5.7	3.4	[4]
J043037-485523	1.35	16.5	-4.0	2.3	[4]
J053007-250329	2.14	18.8	6.7	3.5	[4]
J110325-264515	1.84	15.9	5.6	2.6	[5]
J115944+011206	1.94	17.5	5.1	4.4	[4]
J133335+164903	1.77	16.7	8.4	4.4	[4]
HE1347-2457	1.43	16.3	-21.3	3.6	[5]
J220852-194359	1.92	17.0	8.5	3.8	[4]
HE2217-2818	1.69	16.0	1.3	2.4	[6]
Q2230+0232	1.86	18.0	-9.9	4.9	[3]
J233446-090812	2.15	18.0	5.2	4.3	[4]
J233446-090812	2.28	18.0	7.5	3.7	[4]
Q2343+1232	2.43	17.5	-12.2	3.8	[3]

by the area of 4 VLT UTs and the current expected specifications for the ESPRESSO efficiency and CCD noise. The area above the each line determines the photon-dominated regime, and the area below the regime where the noise dominates.

A quick analysis of the Fig. 1 shows that for a 1 hour exposure - typical times for this scientific goal - the limiting magnitude for the 1 UT mode is of 17.4. As seen in Table 1, 5 out of the 14 targets from the GTO target list are above this limit meaning that for the observation of these targets a 4UT mode should be the best strategy. The final efficiency of the instrument will only be known in detail when ESPRESSO starts commissioning, but this exercise gives us an idea of how to plan the observation of each target.

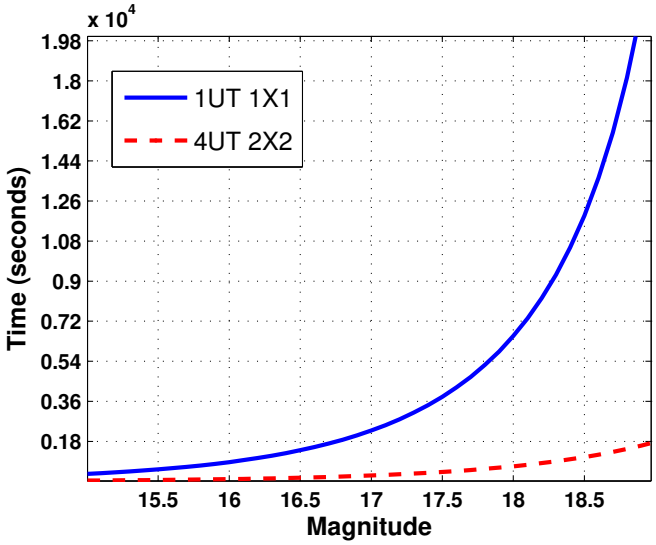


Figure 1 – The figure plots the limit for which an observation on the VLT is photon noise dominated as a function of the magnitude of a target and a given time of observation. The area above the line determines the photon-dominated regime, and the area below the regime where the noise dominates. In blue is represented this limit for the 1UT mode with no binning in the CCD, 1X1. The red dashed line represents the limit for the 4UT mode with a binning of 2X2, binned by 2 in the spectral direction and by 2 in the spatial direction of the CCD.

The instrumentation improvements that ESPRESSO will bring will allow a Baseline uncertainty per target to be of $\sigma_{\Delta\alpha/\alpha} = 0.6ppm$

2 Forecasts on Cosmology

This type of measurements are important by themselves for testing the stability of α but even a non-detection of variation can be used to constrain dark energy, as we now illustrate.

2.1 Bekenstein Type Models

The Bekenstein-Sandvik-Barrow-Magueijo [8] model assumes a variation of α that comes from the variation of the electric charge. This model can be seen as a ΛCDM-like model with an additional dynamical degree of freedom, whose dynamics is such that it leads to the aforementioned variations without having a significant impact on the Universe's dynamics. In particular, this degree of freedom can't be responsible for the dark energy (for which a cosmological constant is still invoked). In this sense, these are the simplest phenomenological models allowing for α , even if they are (arguably) less well motivated from a fundamental physics point of view.

The constraints on these kinds of models from current astrophysical and cosmological data as well as detailed forecasts for ESPRESSO are presented in Leite & Martins (2016)[9]. One important variable is the coupling ζ_α, a free parameter of the model that gives magnitude to the allowed variation on α.

Assuming the baseline uncertainties on α expected for ESPRESSO, and applying these uncertainties for the 14 targets on the GTO target list, one can expect an improvement relative to the current constraints of a factor of 5 on the coupling ζ_α. Moreover, in this type of models there are composition dependent forces which lead to a WEP violation at a level quantified by the Eotvos parameter: $\eta_\alpha \sim 3 \times 10^{-9}\zeta_\alpha$. The ESPRESSO GTO will be able to put bounds of the level of $\eta \sim 5.4 \times 10^{-15}$ to this parameter.

2.2 Dynamical Dark Energy Models

In this class of models, we consider three fiducial dynamical dark energy models where the scalar field that is responsible for dark energy also leads to α variations. In this kind of model another coupling ζ arises directly related to the variation of α.

$$\frac{\Delta\alpha}{\alpha}(z) = \zeta \int_0^z \sqrt{3\Omega_\phi(z')[1 + w_\phi(z')]}\frac{dz'}{1+z} \tag{1}$$

In Alves et al. (2017)[10], we did detailed forecasts and their analysis using Fisher matrix techniques for different scenarios. In here I will only show one specific case as an example. We considered three fiducial dynamical dark energy models:

A constant dark energy equation of state, $w_0 = const$;

A dilaton-type model where the dark energy equation of state is

$$w(z) = \frac{[1 - \Omega_\phi(1 + w_0)]w_0}{\Omega_m(1 + w_0)(1 + z)^{3[1-\Omega_\phi](1+w_0)]} - w_0}; \tag{2}$$

The Chevallier-Polarski-Linder (CPL) parametrization, where the redshift dependence of the dark energy equation of state is described by two separate parameters, w_0 and w_a, as follows:

$$w(z) = w_0 + w_a\frac{z}{1+z}; \tag{3}$$

In all cases we assumed the following fiducial values for the models: $\Omega_{m,fid}$=0.3; $w_{0,fid} = -0.9$; $w_{a,fid} = 0.3$; $\zeta_{fid} = 0$. $\zeta_{fid} = 0$ implies null results for the measurements of α. We did the analyses for the same baseline uncertainty on α expected for ESPRESSO, and applying these uncertainties on the 14 targets of GTO target list. The uncertainties retrieved for the coupling parameter ζ are presented in Table 2. This type of models also lead to a WEP violation that relates the coupling ζ with the Eotvos parameter in the following way: $\eta_\alpha \sim 10^{-3}\zeta^2$. The ESPRESSO GTO will be able to put bounds at the level of $\eta \sim 2.1 \times 10^{-16}$ to this parameter at one sigma.

Table 2: The Table shows the one sigma forecasted uncertainties on the dimensionless coupling parameter ζ, marginalizing over the remaining model parameters, for the three choices of fiducial cosmological model presented in the text.

Model	$w_0 = const$	Dilaton	CPL
$\sigma(\zeta)$	4.6×10^{-7}	3.2×10^{-7}	3.1×10^{-7}

3 Conclusion

As the first light on telescope approaches for ESPRESSO, the necessity of putting together the best observational strategy to optimize the science for the Consortium's GTO becomes more urgent. There's now a better understanding of the limitations that the instrument will face, and that not all the targets will be observed in the simple 1 UT mode. Fainter targets will gain by combining the light of several UTs even if they lose in resolution of the spectra. The definitive strategy will only be possible as the instrument becomes online and tests of efficiency are performed.

Taking conservative expectations for the ESPRESSO targets, we show that even these 14 targets for ESPRESSO GTO by themselves will be able to constraint cosmological models and put competitive bounds on the Eotvos parameter.

I emphasize that extending these forecasts with ideal uncertainties on α or with more targets would improve the output results. These are not unrealistic expectations since simply an extended Large Program on ESPRESSO, or even the future spectrograph (HIRES) planned for ELT will allow for huge improvements. More details and forecasts can be found in [2,9,10,11,12]

Acknowledgments

This work was done in the context of grant PTDC/FIS/111725/2009 from FCT (Portugal). ACL is supported by an FCT fellowship (SFRH/BD/113746/2015), under the FCT PD Program PhD::SPACE (PD/00040/2012), and by the Gulbenkian Foundation through Programa de Estímulo à Investigação 2014, grant number 2148613525. CJM. is also supported by an FCT Research Professorship, contract reference IF/00064/2012, funded by FCT/MCTES (Portugal) and POPH/FSE (EC). CSA is partially supported by grant CIAAUP-06/2017-BIC.

References

1. F. Pepe et al., The Messenger 153, 6 (2013).
2. A.C.O. Leite et al., *Phys. Rev.* D 94, 123512 (2016).
3. M.T. Murphy, Ph.D. Thesis, University of New South Wales (2002).
4. J.A. King, PhD Thesis (UNSW, 2011), arXiv:1202.6366.
5. P. Molaro et al., European Physical Journal Special Topics, 163, 173 (2008).
6. P. Bonifacio, et al., Astronomische Nachrichten, 335, 83 (2014).
7. M.C. Ferreira et al., *Phys. Rev.* D 89, 083011 (2014).
8. H. B. Sandvik, J. D. Barrow, and J. Magueijo, Phys. Rev. Lett. 88, 031302 (2002)
9. A.C.O. Leite & C.J.A.P. Martins, *Phys. Rev.* D 94, 023503 (2016).
10. C.S. Alves et al., *Phys. Lett.* B, Volume 770, 93-100 (2017).
11. A.C.O. Leite et al., *Phys. Rev.* D 90, 063519 (2014).
12. A.C.O. Leite & C.J.A.P. Martins, *Phys. Rev.* D91, 103519 (2015).

Gravitational Properties of Light

D. Rätzel
University of Vienna, Faculty of Physics, Boltzmanngasse 5, 1090 Vienna, Austria

M. Wilkens, R. Menzel
University of Potsdam, Institute for Physics and Astronomy
Karl-Liebknecht-Str. 24/25, 14476 Potsdam, Germany

As Einstein's equations tell us that all energy is a source of gravity, light must gravitate. However, because changes of the gravitational field propagate with the speed of light, the gravitational effect of light differs significantly from that of massive objects. In particular, the gravitational force induced by a laser pulse is due only to its creation and annihilation and decays with the inverse of the distance to the pulse. We can expect the gravitational field of light to be extremely weak. However, the properties of light are premises in the foundations of modern physics: they were used to derive special and general relativity and are the basis of the concept of time and causality in many alternative models. Studying the back-reaction of light on the gravitational field could give new fundamental insights to our understanding of space and time as well as classical and quantum gravity. In this article, recent work by the authors on the gravitational properties of light is reviewed. The gravitational field of a laser pulse of finite lifetime is investigated in the framework of linearized gravity.

The question of the gravitational properties of light in general relativity was raised already quite early, in 1931, in an article by Tolman, Ehrenfest and Podolsky [1]. In the article, the gravitational effect of an infinitesimally thin, cylindrical pulse of unpolarized light of finite lifetime was investigated. The central result of the article was that two light pulses that are propagating parallel do not affect each other gravitationally if they are co-propagating. In contrast, it was found that the two pulses attract each other if they are counter-propagating.

Subsequently, several other authors investigated similar situations using Einstein's equations. In an article by Bonnor [2], light was described as a null-fluid of massless particles and the corresponding full solution of Einstein's equations was constructed. In an article by Aichelburg and Sexl [3], the Lorentz-boosted Schwarzschild-metric of a point mass in the limit $v \to c$, $m \to 0$ was derived. Recently, Van Holten derived exact plane wave solutions of the coupled Maxwell-Einstein theory [4].

Here, we will shortly review the model of the laser pulse propagating in vacuum that we use and the properties of its gravitational field. A full derivation is given in our previous article about the gravitational properties of a laser pulse [6]. We start by assuming that the laser pulse is well described by the paraxial approximation. Furthermore, we assume that we can neglect the transversal spread of the pulse and that the length of the pulse is much larger than its width. Then, we model the pulse as an effectively 1-dimensional "needle of null stuff" propagating with the speed of light. The energy momentum of the pulse is given by "boxing" the energy momentum of a plane wave of a given polarization. With this model, we catch the essential ingredients of a laser pulse, which are (1) its localizability, (2) its masslessness, and (3) its polarization.

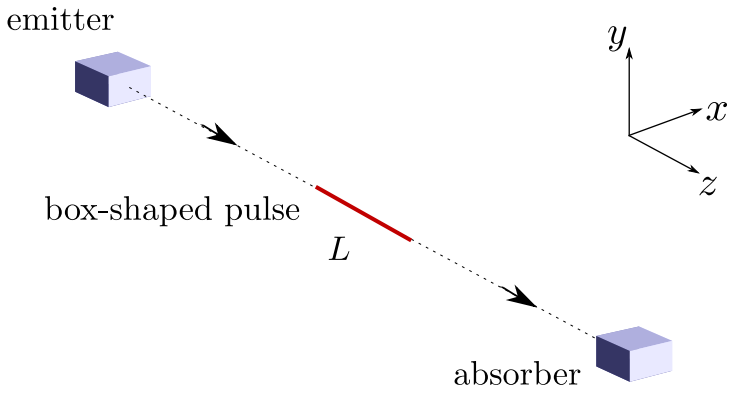


Figure 1 – The laser pulse is modeled with finite extension L in the direction of propagation, but negligible extension $\Delta(z)$ in the transverse x/y-directions, $\Delta(z) \ll L$. It travels from the emitter to the absorber over a distance D along the z-axis. The figure was originally published in Rätzel et al. NJP 18 023009 (2016) under the CC Attribution 3.0 license https://creativecommons.org/licenses/by/3.0/.

Additionally, we consider the emission and the absorption process (see Figure 1) by continuously letting the energy momentum appear and vanish. The continuity equation of general relativity would then require the inclusion of the energy momentum of the emitter and the absorber and their evolution during the pulse emission. However, we have shown in our previous article [6] that these effects are negligible for small distances to the pulse trajectory. To give a full description of the situation, we have derived the full gravitational field of the whole emission process for a specific situation - the emission of two light pulses from a single atom in another article [7].

Since the gravitational field of light can be expected to be small, we make use of the framework of linearized gravity. The metric is split as $g_{\mu\nu} = \eta_{\mu\nu} + h_{\mu\nu}$, where $\eta_{\mu\nu}$ is metric of the background, which we assume to be Minkowski space, and $h_{\mu\nu}$ is a small perturbation. We choose the set of Cartesian coordinates (ct, x, y, z) in which the experiment is at rest and the background metric takes the form $\eta = \mathrm{diag}(-1, 1, 1, 1)$. To be a small perturbation means then $|h_{\mu\nu}| \ll 1$ for all μ, ν. By imposing the gauge condition

$$\partial^\mu \left(h_{\mu\nu} - \frac{1}{2}\eta_{\mu\nu} h_\alpha{}^\alpha \right) = 0\,, \tag{1}$$

where $h_\alpha{}^\alpha = h_{\alpha\beta}\eta^{\alpha\beta}$, the Einstein field equations assume the well known form of linearized gravity

$$\left[\frac{\partial^2}{\partial x^2} + \frac{\partial^2}{\partial y^2} + \frac{\partial^2}{\partial z^2} - \frac{1}{c^2}\frac{\partial^2}{\partial t^2} \right] h_{\mu\nu} = \frac{16\pi G}{c^4} \left(T_{\mu\nu} - \frac{1}{2}\eta_{\mu\nu} T_\alpha{}^\alpha \right)\,, \tag{2}$$

where $T_{\mu\nu}$ is the energy-momentum tensor of the lase pulse, G is Newton's gravitational constant, c is the speed of light and $T_\alpha{}^\alpha = T_{\alpha\beta}\eta^{\alpha\beta}$. It is well known from classical electrodynamics that an equation like (2) can be solved by a retarded potential

$$h_{\mu\nu}(x, y, z, t) = \frac{4G}{c^4} \int \frac{\left(T_{\mu\nu} - \frac{1}{2}\eta_{\mu\nu} T_\alpha{}^\alpha \right)(x', y', z', t_{\mathrm{ret}})}{\sqrt{(x - x')^2 + (y - y')^2 + (z - z')^2}} dx' dy' dz'\,, \tag{3}$$

with t_{ret} the retarded time, $t_{\mathrm{ret}} = t - \sqrt{(x - x')^2 + (y - y')^2 + (z - z')^2}/c$.

The energy momentum tensor of the laser pulse in our model is given as $T_{00} = T_{zz} = -T_{0z} = -T_{z0} = u$, with $u = \frac{\varepsilon_0}{2}\vec{E}^2 + \frac{1}{2\mu_0}\vec{B}^2$ the energy density of the electromagnetic field, where the index 0 corresponds to ct. We obtain the non-vanishing components of the metric

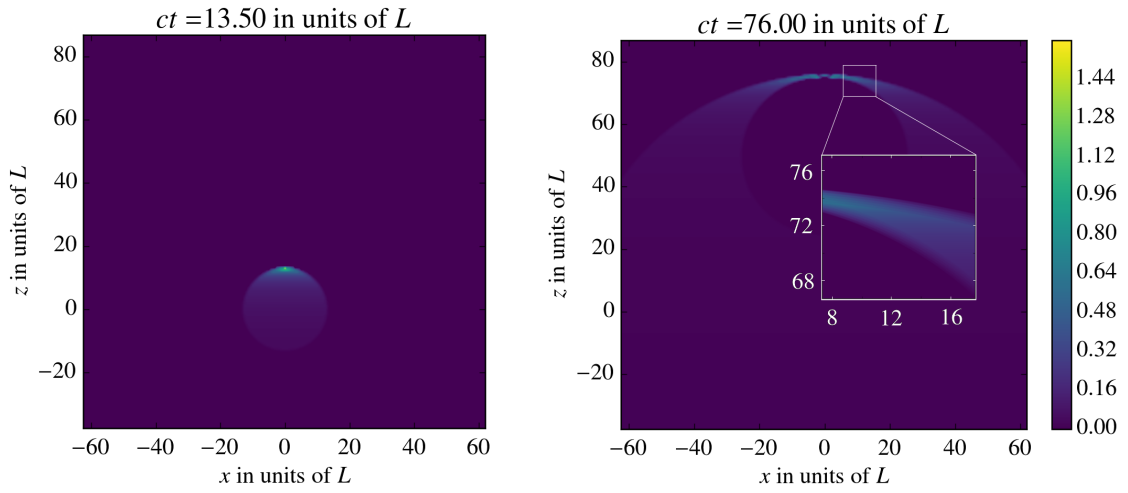


Figure 2 – The plots show the metric perturbation $h^{\mathrm{P}} = h_{00} = h_{11} = -h_{10} = -h_{01}$ for a pulse of length L in the coordinates (ct, x, y, z) in the (x, y)-plane for different times t. h^{P} is normalized to units of κ and then the logarithm of the logarithm is taken. The figures were originally published in in Rätzel et al. NJP 18 023009 (2016) under the CC Attribution 3.0 license https://creativecommons.org/licenses/by/3.0/.

as $h^{\mathrm{P}}_{00} = h^{\mathrm{P}}_{zz} = -h^{\mathrm{P}}_{0z} = -h^{\mathrm{P}}_{z0} = h^{\mathrm{P}}$, where h^{P} can be read off from (3). Plots for the function h^{P} in the x-z-plane for different times after the events of the emission of the pulse can be seen in Figure 2. It is interesting to note that the metric perturbation approaches the form of a plane fronted parallel propagating wave (pp-wave) for distances to the trajectory of the pulse much smaller than the distance from the observer to the emitter (see Figure 3). This situation coincides with the full solution of Einstein's equations constructed by Bonner [2].

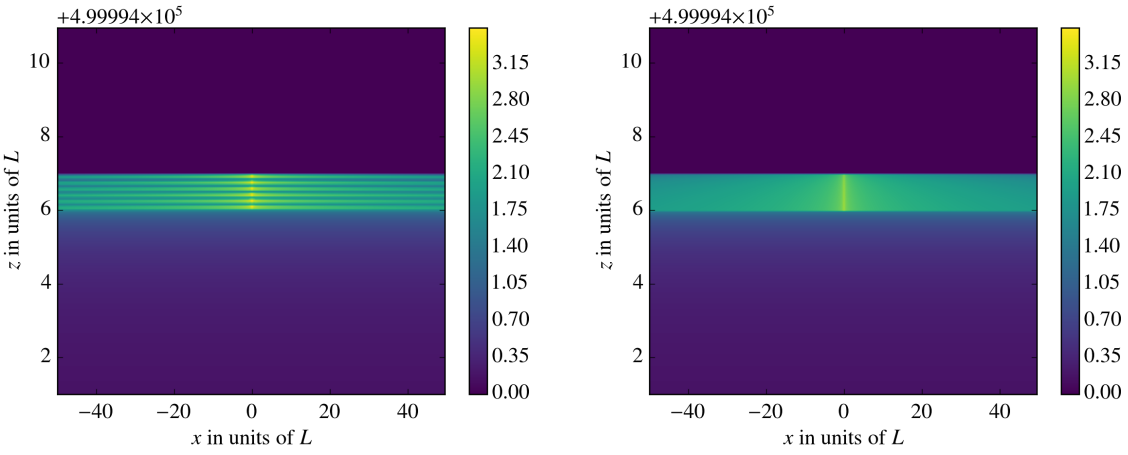


Figure 3 – These plots show the double logarithm of the metric perturbation h^{P} for a linearly polarized pulse of length L and central wavelength $\lambda = \frac{2\pi c}{\omega} = \frac{2}{3}L$ in the x-y-plane at $t = 50000L/c$, after its emission at $z = 0$. h^{P} is normalized to units of $\kappa = 4GAu_0/c^4$ and then the logarithm of the logarithm is taken. The figures were originally published in in Rätzel et al. NJP 18 023009 (2016) under the CC Attribution 3.0 license https://creativecommons.org/licenses/by/3.0/.

To understand the implications of the metric perturbation $h_{\mu\nu}$, it is best to study the Riemann curvature tensor $R^{\mu}{}_{\rho\sigma\alpha}$, which is a simple combination of second derivatives of the metric perturbation in first order in the metric perturbation. The Riemann tensor has a direct physical and geometrical interpretation as it appears naturally in the geodesic deviation equation for the relative acceleration between two infinitesimally close geodesics. This relative acceleration can

be interpreted as the effect of tidal forces on neighboring test particles. One component of the curvature tensor, R^{p}_{0x0x}, is plotted for different times in Figure (4).

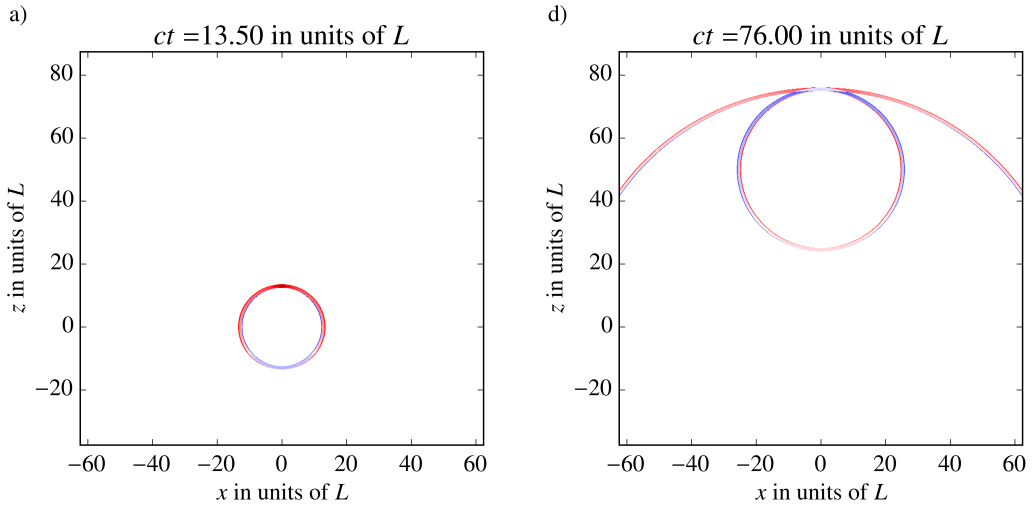


Figure 4 – The plots show the curvature component R^{p}_{0x0x} for the metric perturbation $h^{\mathrm{p}}_{\mu\nu}$ induced by a laser pulse in the coordinates (ct, x, y, z) in the (x, z)-plane for different times t. The logarithm of value of R^{p}_{0x0x} is encoded in the opacity of the color. Red is a negative value of R^{p}_{0x0x} and blue a positive value. White stands for zero. The figures were originally published in in Rätzel et al. NJP 18 023009 (2016) under the CC Attribution 3.0 license https://creativecommons.org/licenses/by/3.0/.

The most interesting feature is that the laser pulse induces curvature only on spherical shells of thickness L (pulse length) that expand from the point of creation and annihilation. If the curvature tensor vanishes in one set of coordinates, it vanishes in all sets of coordinates. Therefore, we can say that any gravitational effect due to the laser pulse must be confined to these spherical shells of non-zero curvature. It is even more interesting to note that the shells are causally disconnected from the pulse during its free propagation. Hence, we conclude that the physical effect of the laser pulse is due to its creation and annihilation alone as it was argued by Bonnor recently from a different perspective [8]. In contrast to our case, in the case of laser pulses running in wave guides [5], test particles would witness gravitational effects in the whole region causally connected with the timeline of the laser pulse propagating with $v < c$. Hence, the localization of the gravitational effect is due to the luminal motion of the laser pulse. A similar situation arises in electrodynamics with massless charges [9].

After we know about the localization of the physical effect, we can learn about the actual effect on test particles located in the spherical shells of non-zero curvature. To this end, the geodesic equation governing the trajectory of free test particles $\gamma^\mu(\lambda)$ is employed $\ddot{\gamma}^\mu = -\Gamma^\mu_{\rho\sigma}\dot{\gamma}^\rho\dot{\gamma}^\sigma$, where we have to assume $g_{\mu\nu}\dot{\gamma}^\mu\dot{\gamma}^\nu = -1$ for massive test particles and $g_{\mu\nu}\dot{\gamma}^\mu\dot{\gamma}^\nu = 0$ for massless test particles as in additional condition. We find that the emission induces an attraction towards the position of the pulse in the coordinates (ct, x, y, z). The absorption induces a repulsion away from the position the pulse would be at if it would have continued to propagate freely. In agreement with the authors of [1], we find from the geodesic deviation equation that massless test particles moving in the same direction as the pulse are not deflected while counter-propagating pulses are deflected four times more strongly than massive particles at rest containing the same energy.

Today, the strongest laser pulses available have a pulse power in the range of 10^{15}W. This means that there would be an acceleration of about $\ddot{\gamma}^x \approx -\frac{4GP}{c^3 x} \approx -10^{-18}\frac{\mathrm{m}}{\mathrm{s}^2}$ for a massive test particle at a distance of 2.5mm from the pulse trajectory. This acceleration can be compared with the acceleration experienced by a test particle in the Newtonian potential induced by a small spherical, massive object. We find that a mass of only $M = 10^{-13}$kg would be necessary

to provide the same acceleration as the laser we considered above at a distance of $r = 2.5$mm. We find a slightly different situation, if we assume a periodically pulsed laser. The induced gravitational field is periodically varying and close to the beamline, the corresponding tidal forces can be compared to those induced by a gravitational wave. If we assume a laser power of 10^{15}W again, the induced tidal forces are in the same order as those due to a gravitational wave of angular frequency $\omega = 10^3$Hz and amplitude $h_+ = 10^{-22}$. The order is similar to that of the strain induced by gravitational waves that were detected by LIGO. Of course, this comparison only holds inside a very small region close to the beamline and there is still no chance to detect the gravitational field of light with state of the art technology. It would be necessary to develop completely new technologies for narrow band detectors of oscillating tidal forces on millimeter scales. Promising approaches can be found in [10] and [11].

References

1. R C Tolman and P Ehrenfest and B Podolsky, Phys. Rev. **37 5**, 602 (1931).
2. W B Bonnor, Comm. Math. Phys. **3**, 163 (1969).
3. P C Aichelburg and R U Sexl, General Relativity and Gravitation **2 4**, 303 (1971).
4. J W van Holten, Fortschritte der Physik **59 3-4**, 284 (2011).
5. M O Scully, Phys. Rev. D **19 12**, 3582 (1979).
6. D Rätzel and M Wilkens and R Menzel, New Journal of Physics **18 2**, 023009 (2016).
7. D Rätzel and M Wilkens and R Menzel, Phys. Rev. D **95 8**, 084008 (2017).
8. W B Bonnor, General Relativity and Gravitation **41 1**, 77 (2009).
9. F Azzurli and K Lechner, Annals of Physics **349**, 1 (2014).
10. C Sabin and D E Bruschi and M Ahmadi and I Fuentes, New Journal of Physics **16 8**, 085003 (2014).
11. S Singh and L A De Lorenzo and I Pikovski and K C Schwab, arXiv:1606.04980 , (2016).

Prospects for probing fundamental physics with the radio sky

Amanda Weltman[1,2], Anthony Walters[1], Amadeus Witzemann[1,3]
[1] *Department of Mathematics and Applied Mathematics, University of Cape Town, South Africa,*
[2] *School of Natural Sciences, Institute for Advanced Study, Princeton, NJ, 08540, USA,*
[3] *Department of Physics and Astronomy, University of the Western Cape, South Africa*

The coming era of radio telescopes and arrays brings immense possibilities for probing the universe on the largest scales and quite importantly of answering some important open questions about fundamental physics. In this work, we consider one possibility, improved measurements of curvature, with a particular focus on near future radio telescope arrays in South African, in particular HIRAX.

1 Introduction

Progress in cosmology and astronomy are ultimately linked through the inexorable power of data. Although we have certainly entered the era of precision cosmology, the extent to which the precision in our observables really tells us about the physical laws underlying our universe is still not completely clear. The accuracy of our modeling really depends on our priors. Our ability to rule out theories is perhaps more powerful than repeated improvements in precision that allow for consistency checks. Inflationary theory is an exemplar. All of our data is indeed consistent with the theory of inflation, however, questions about whether inflation can be ruled out remain. In particular, the multiverse associated with inflation appears particularly slippery with claims that it can never be ruled out.

Here we will consider the possibility for radio astronomy to provide comment on this question. The prospects for radio astronomy are great, and beyond the scope of this short article. Amongst the many other exciting possibilities, radio astronomy could rule out alternative theories of the very early universe as well as alternative theories of gravity, and beyond the standard model particles. Here we consider the more narrow question - is there a single measurement that would rule out parts of the multiverse? We hope to convince you that the answer is yes, and more than that, that radio astronomy is perhaps our best chance to do this, in particular with curvature, as advances in 21 cm intensity mapping should allow us to break the dark energy curvature degeneracy, thus constraints on each should improve in the coming decades.

1.1 HIRAX

The Hydrogen Intensity and Real-time Analysis experiment (HIRAX) is a new radio astronomy interferometer currently under construction in a radio-quiet area in South Africa [1]. HIRAX will use hydrogen intensity mapping to detect the effects of dark energy on the distribution of galaxies. HIRAX has the potential to be a world-leading facility for the study of radio transients and is expected to produce a huge catalogue of several thousand Fast Radio Bursts (FRBs). In its full intended design, the HIRAX array will comprise 1024 6m dishes and will map large scale structure in a redshift range of $0.8 < z < 2.5$. HIRAX will observe in the Southern

Hemisphere, complementing CHIME in Canada which maps the Northern Hemisphere in using a similar redshift range. The location is particularly strategic, as not only will it be situated in a region of very low radio frequency interference (RFI), but the Southern location allows for cross correlations with several ongoing surveys; see [1] for further discussions on HIRAX setup and strengths. HIRAX is a 21 cm intensity mapping experiment that will measure 15 000 deg^2 of the sky mapping the neutral hydrogen in 1024 frequency bins between 400 and 800 MHz.

1.2 Intensity Mapping

Traditional late-time cosmological experiments, like galaxy surveys, rely on the ability to resolve individual sources. They either count the number of sources on a given patch of the sky, or also determine the redshifts to obtain distance data. On large scales, galaxies are assumed to be biased tracers of the underlying dark matter distribution and are used to calculate the matter power spectrum. The need for better precision in cosmology drives new surveys into covering larger survey areas and volumes. One way to achieve this is to give up on resolving individual sources, and instead measure the intensity in a given pixel, which contains the integrated radiation from many individual sources. This allows us to observe sources or frequency ranges that would otherwise be too dim to detect.

One very promising new approach, using the intensity mapping technique, is to observe the 21cm transition line of neutral hydrogen. Neutral hydrogen is greatly abundant in the universe after recombination, and similar to e.g. galaxies, neutral hydrogen is believed to be a biased tracer of the underlying dark matter distribution. It has a characteristic emission line at a rest frame wavelength of 21cm, which allows precise redshift determination. However, detecting this 21cm emission is difficult; a large collecting area is needed in order to reach the required sensitivity in intensity mapping. Furthermore, other major difficulties are the cleaning of the signal from non cosmological foregrounds, e.g. galactic emission, radio frequency interference from the earth itself, and the processing of the huge amount of data generated. In some sense, intensity mapping trades angular resolution for better radial resolution, and will achieve much larger survey areas and volumes, which is crucial for further advancement of cosmology.

2 Curvature

There is probably no single observation that could convince the community that inflation is a correct theory. However, it is possible that there will one day be observations that would be convincing that eternal inflation is not correct. In particular, as highlighted by Guth and Nomura [2], if the curvature of the universe is found to be positive at the level of $\Omega_k \leq -10^{-4}$ then eternal inflation, as it is currently understood at least, is ruled out [a]. On the other hand, should we observe negative curvature at the level $\Omega_k \geq 10^{-4}$ then our conclusions are more subtle. Amongst other things, as discussed in [2] we would then infer that diffusive eternal inflation did not occur in our immediate past, our pocket universe was born by bubble nucleation and that slow roll inflation as observed is an accidental feature of the potential rather than something fundamental ensuring a flat potential. In fact, as argued in [3] $|\Omega_k| \geq 10^{-4}$ rules out slow roll inflation.

Depending on the measure, nearly all models of inflation require eternal inflation at some point in the past, so essentially an observation of positive curvature at the level of $\Omega_k \leq -10^{-4}$ alone, is enough to rule out most models of inflation, with few caveats. It is worth understanding why this is so, as intuitively one might expect inflation to inflate away all curvature, but since inflation generates fluctuations in the curvature as well as the matter, curvature is not entirely inflated away, and indeed in eternal inflation these fluctuations are quite large. For more insights on this question, we highly recommend the reader to [2,3].

[a] Remember, by convention, a positively curved universe has negative Ω_k

So now the real question arises. Are these levels of curvature ever going to be within the reach of observation? A quick answer would appear to be no. From [4], we find a convincing argument that the so called curvature floor is at the scale 10^{-4}, beyond which we cannot claim improved constraints. We will have essentially reached the cosmic variance limit set by horizon scale perturbations. While we may not be able to constrain curvature below the level of 10^{-4} in the foreseeable future, it is still possible, indeed preferable, that we may observe a signal before that stage and essentially rule out eternal inflation. The strongest bounds currently come from Planck combined with BAO constraints from 6dFGS, SDS-MGS, and BOSS [5] and are at the level of $|\Omega_K| < 5 \times 10^{-3}$ (95% CL). So that does not look promising. However, as emphasised in [6], these bounds assume that dark energy is driven by a cosmological constant, Λ. This alone is not a proven assumption, but in the case of Planck, it is a necessary assumption as there is a degeneracy between dark energy and curvature which needs to first be broken before we can make truly strong claims on curvature. Indeed this is the purpose of [6] which shows that 21 cm intensity mapping experiments will be able to constrain curvature in a dark energy model independent way.

HIRAX is designed to precisely detect the baryon acoustic oscillations (BAO) in the fluctuations of the matter power spectrum via 21cm intensity mapping. The BAO are a standard ruler out to very high redshifts, thus these measurements are very sensitive to curvature and dark energy. Current data sets suffer from degeneracies of curvature and dark energy unless relatively strong assumptions on dark energy are made [5,6]. By using the BAO for precise distance measurements on a high redshift range, HIRAX is ideally suited to precisely constrain curvature, and to disentangle it from dark energy, even if one allows for an arbitrary dark energy equation of state. See figure 1 to see the parameter constraints compared to DETF Planck constraints [7] for a dark energy model with fixed equation of state. Here we forecast for the standard cosmological parameters, the Hubble constant $h = H_0/(100\text{km/s/Mpc})$, the curvature and dark energy density parameters, Ω_k and $\Omega_{\rm DE}$ respectively, the spectral index n_s and the late-time fluctuation amplitude σ_8. While these parameters are degenerate in DETF Planck data, combining it with HIRAX allows for good constraints. While Planck constraints were derived assuming a fixed dark energy equation of state $w = \text{const}$. A more general solution is to allow a first order Taylor expansion of the equation of state, $w(a) = w_0 + (1-a)w_a$; results for which are given in figure 1. However, even with an arbitrary equation of state curvature can still constrained, this is done for HIRAX in [6].

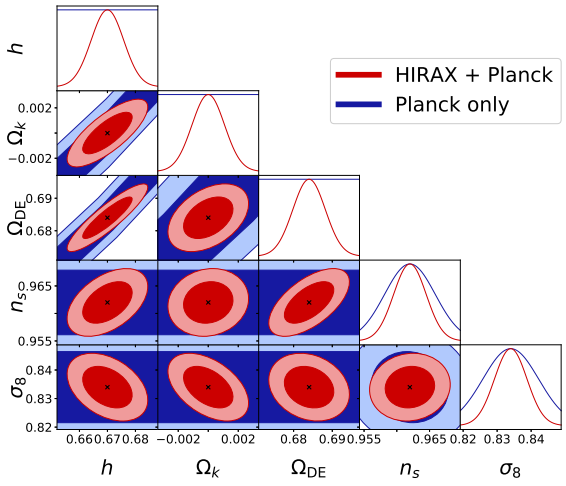


Figure 1 – Parameter constraints for HIRAX, compared to Planck alone, while fixing the dark energy equation of state. HIRAX will be able to efficiently break degeneracies. These forecasts were done assuming HIRAX with 1024 dishes, 2100 deg^2 and one year of integration time.

3 Constraints from FRB observations

Given the large numbers of FRBs that near future radio telescopes are expected to observe, it is plausible that they may soon serve as a new cosmic probe complementary to existing techniques. Should a large enough population of the observed FRBs be assigned a redshift, which may be possible by association with a host galaxy, then one could extract valuable information about the background spacetime through which they propagate. This would come in the form of constraints on the cosmological parameters - a possible further consistency check of the concordance model.

Optimistically, HIRAX is expected to detect around $50-100$ FRBs per day out to $z \sim 2.8$[11]. Should only 5% of these events be assigned a redshift the catalogue could have as many as 1000 even after 200 observing days. Initial investigations indicate that such a catalogue would constrain new regions of parameter space[8,9]. Particularly promising are the constraints forecast for the dark energy equation of state parameters [10]. Figure 2 shows the forecast 1- and 2-σ contours derived from an MCMC analysis of a mock catalogue of 1000 and 10000 FRBs, compared with forecast intensity mapping constraints [6] and the existing constraints derived by Planck + BAO + SN1a + H_0 data. The degeneracy directions are different which suggest that FRBs carry valuable complimentary information about the background metric. Additionally, curvature has been included as a free parameter in the fit of Figure 2, with $-0.1 \leq \Omega_k \leq 0.1$, which seems to suggest that FRBs may be a good probe of the dynamics of dark energy even when the exact value of Ω_k is unknown. Constraints on curvature, however, appear to be very weak, essentially unconstrained due to the degeneracy with matter and w_0.

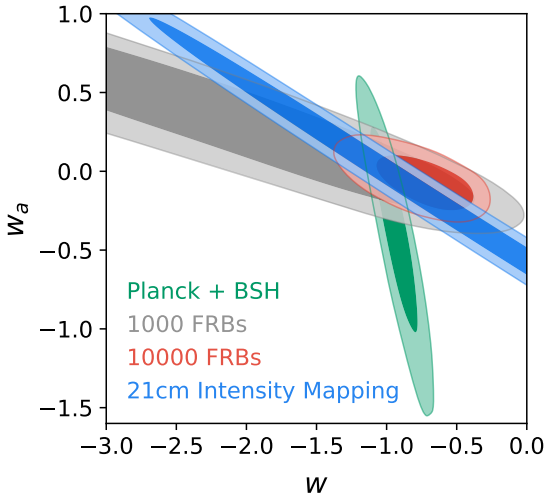


Figure 2 – Forecast 1- and 2-σ constraint contours for w_0 and w_a from FRB and intensity mapping observations, compared with the Planck 2015 + BAO + SN1a + H_0 results (green). The FRB constrains are the results from an MCMC analysis of mock catalogues containing 1000 (gray) and 10000 (red) events respectively, in both cases out to a limiting redshift $z = 3$. The blue region represents the intensity mapping results from HIRAX, with only flat priors on the parameters. These plots are preliminary results adapted from[10] and[6].

4 Conclusion

Radio astronomy will soon be burgeoning with new data. There are already many exciting flagship programmes for these experiments ranging from cosmology to searches for extraterrestrial life. In this short article, we bring attention to the fact that there is also fundamental physics to be explored and questions to be answered about the early universe. The new tools accessible to us through radio telescope arrays, bring with them the real hope of constraining cosmological observables that should be set by fundamental physics theory .There are many exciting questions about fundamental physics, that radio astronomy may help us to answer.

Acknowledgements

This work is based in part on a talk given by Weltman at the 2017 Moriond Gravity meeting, for which she would like to thank the Organisers. We gratefully acknowledge our collaborators on the projects referenced in this work, [6] and [10].Weltman is supported by the South African Research Chairs Initiative of the Department of Science and Technology and the National Research Foundation of South Africa. Any opinion, finding and conclusion or recommendation expressed in this material is that of the authors and the NRF does not accept any liability in this regard. She would also like to thank the Institute for Advanced study, the Flatiron Institute where as well as the Princeton University Astrophysics department for their generous support while this work was completed. Walters is funded by a grantholder bursary from the Competitive Programme for Rated Researchers (Grant Number 91552). Witzemann acknowledges support from the South African Square Kilometre Array Project and National Research Foundation.

References

1. L.B. Newburgh et al."HIRAX: A Probe of Dark Energy and Radio Transients". Proc.SPIE Int.Soc.Opt.Eng. 9906 (2016) 99065X
2. A. Guth and Y. Nomura " What can the observation of nonzero curvature tell us? " Phys.Rev. D86 (2012) 023534
3. M. Kleban and M. Schillo "Spatial Curvature Falsifies Eternal Inflation" JCAP 1206 (2012) 029
4. C. D. Leonard, P. Bull, R. Allison."Spatial curvature endgame: Reaching the limit of curvature determination" Phys.Rev. D94 (2016) no.2, 023502
5. Planck Collaboration: P. A. R. Ade *et. al.* "Planck 2015 results. XIII. Cosmological parameters" A&A 594, A13 (2016)
6. A. Witzemann, P. Bull, C. Clarkson, M. Santos, M. Spinelli, A. Weltman, "Model-independent curvature determination with 21cm intensity mapping experiments" To appear
7. A. Albrecht, L. Amendola, G. Bernstein, D. Clowe, D. Eisenstein, et al. 2009, [arXiv:0901.0721]
8. B. Zhou, X. Li, T. Wang, Y. Fan, D. Wei. "Fast radio bursts as a cosmic probe?" Phys.Rev. D89 (2014) no.10, 107303
9. H. Gao, Z. Li, B. Zhang."Fast Radio Burst/Gamma-Ray Burst Cosmography" Astrophys.J. 788 (2014) 189
10. A. Walters, A. Weltman, B. Gaensler, Y. Ma, "Dynamical Dark Energy with Fast Radio Bursts" To appear
11. K. Rajwade, D. Lorimer, "Detecting Fast Radio Bursts at Decametric Wavelengths" Mon.Not.Roy.Astron.Soc. 465 (2017) no.2, 2286-2293







ATOMIC CLOCK ENSEMBLE IN SPACE

L. Cacciapuoti[a], P. Laurent[b], C. Salomon[c]
[a] *European Space Agency, Keplerlaan 1, 2200 AG Noordwijk ZH - The Netherlands*
Luigi.Cacciapuoti@esa.int
[b] *SYRTE, CNRS UMR 8630, Observatoire de Paris, LNE, UPMC, 61 Av. de l'Observatoire, 75014 Paris - France*
[c] *Laboratoire Kastler Brossel, ENS-PSL Research University, CNRS, UPMC, Collège de France, 24 rue Lhomond, 75005, Paris - France*

Atomic Clock Ensemble in Space (ACES) is an ESA mission designed to test the Einstein's Equivalence Principle with high-performance atomic clocks in space and on the ground. Installed onboard the International Space Station, the ACES payload will generate a clock signal with fractional frequency instability and inaccuracy of $1 - 3 \cdot 10^{-16}$. Two links operating on microwave (MWL) and optical (ELT) frequencies will allow comparing the ACES clocks with the best atomic clocks on the ground in a global network. Space-to-ground and ground-to-ground comparisons will provide tests of Einstein's theory of general relativity, at the same time developing applications in geodesy and time & frequency metrology.
The ACES flight model is close to completion. The cold atom clock PHARAO has been tested and delivered for integration in the ACES payload. The ELT link has been completed. MWL and the active hydrogen maser SHM are presently under test. System level tests have already started and will continue all along 2017.
This paper will present the recent progress of the ACES mission and discuss future perspectives for testing fundamental physics with clocks in space.

1 ACES Mission Elements

Proposed to the European Space Agency in 1997, the *Atomic Clock Ensemble in Space* (ACES) mission relies on PHARAO, a clock based on laser-cooled caesium atoms, to generate a high stability and accuracy time reference in space [1,2,3]. The free fall conditions are crucial for PHARAO to reach or even surpass the performance of the best atomic fountain clocks on ground, while keeping a very compact volume, small mass and power consumption. Installed onboard the International Space Station (ISS), at the external payload facility of the Columbus module, the ACES payload distributes its time scale to ground clocks by using two independent time & frequency transfer links, a link operating in the microwave domain (MWL) and the ELT (European Laser Timing) optical link. On the ground, a network of MWL ground terminal and satellite laser ranging stations provides the physical interface between the ACES clock ensemble and atomic clocks on ground.

The ACES payload is shown in Fig. 1. It has a volume of about 1 m^3, for a mass of 230 kg and a power consumption of 450 W.

The main onboard instruments are the cesium clock PHARAO and the active hydrogen maser SHM. The PHARAO clock reaches a fractional frequency stability of $1.1 \cdot 10^{13}/\sqrt{\tau}$, where τ is the integration time expressed in seconds, and an accuracy of a few parts in 10^{16}. SHM is the ACES flywheel oscillator, also providing the frequency reference needed for the onboard characterization of the PHARAO clock stability and accuracy. PHARAO and SHM 100 MHz

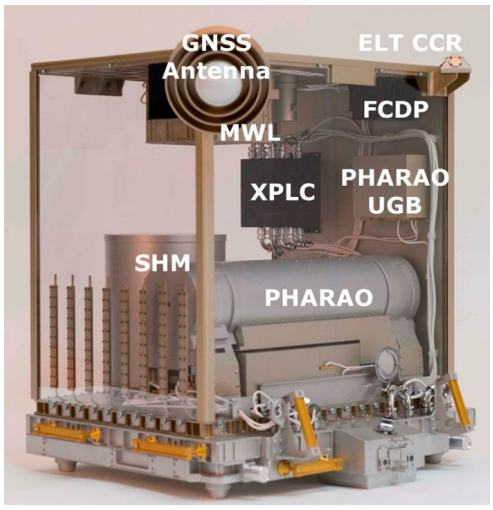


Figure 1 – The ACES payload has a volume of 1 m^3, for a mass of 230 kg and a power consumption of 450 W.

signals are compared in the phase comparator FCDP, which also distributes the ACES frequency reference to the MWL electronics. FCDP performs a phase comparison measurement between the 100 MHz clock signals generated by PHARAO and SHM and uses this information to close a phase-locked loop, which steers the PHARAO local oscillator (USO) on SHM with a typical time constant of a few seconds (short-term servo-loop). At the same time, the frequency difference (Detsynch) between the PHARAO USO and the frequency reference provided by the Cs clock transition is measured in the PHARAO resonator, sent to the ACES onboard computer (XPLC), and used to operate a frequency-locked loop steering SHM on PHARAO with a time constant of a few hundreds of seconds (long-term servo-loop). The two servo-loops lock PHARAO and SHM together generating the ACES clock signal, which now exhibits the short to medium-term stability of SHM and the long-term stability and accuracy of PHARAO.

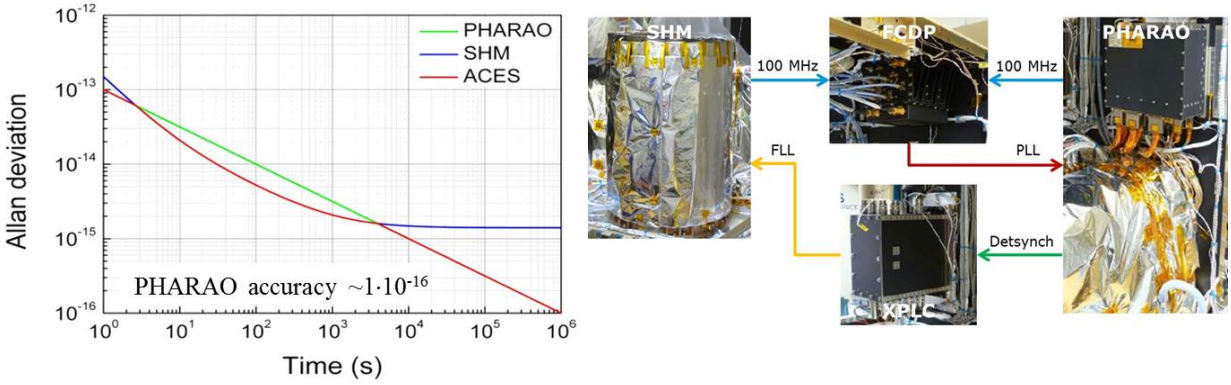


Figure 2 – The clock signal generated onboard ACES.

MWL is the ACES metrology link: coherently with the ACES clock signal, it generates the ACES time scale and compares it with the time scales locally generated by atomic clocks on the ground; furthermore, it stamps the arrival of the electrical pulses generated by the ELT detector in the onboard time. Finally, a GNSS receiver, tracking GPS, GALILEO and GLONASS signals, provides precise orbit data of the ACES clocks. The onboard receiver is driven by the ACES clock signal thus providing one additional link for comparing remote clocks in space and on the ground via the GNSS network. Figure 3 shows the ACES network of MWL ground terminals. Six fixed units will be deployed around the world, at the best institutes for time & frequency metrology: two in the US, JPL (Pasadena) and NIST (Boulder), three in Europe, at SYRTE

(Paris, FR), PTB (Braunschweig, DE), and NPL (Teddington, UK), and one in Japan, at NICT (Tokyo). One transportable MWL station will be located in Europe and shared by other institutes, including the Wettzell geodetic observatory (Wettzell, DE), METAS (Bern, CH), and INRIM (Torino, IT); a second transportable station will be dedicated to the calibration of MWL fixed terminals for time transfer experiments and for comparisons with the laser link ELT. As shown in Fig. 3, space-to-ground comparisons will occur over three continents, at the same time enabling ground-to-ground comparisons over worldwide distances by using ACES as a relay satellite.

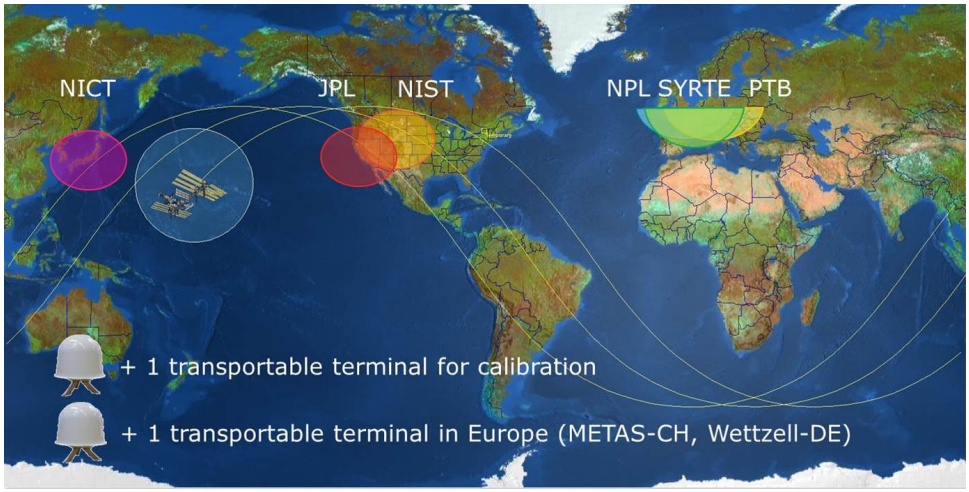


Figure 3 – The ACES network of MWL ground terminals and typical ground tracks of the ISS orbit.

Combined with the growing network of regional links using compensated optical fibers, which have already demonstrated frequency comparison capability at $1 \cdot 10^{-19}$ resolution, clock comparisons at the level of $1 \cdot 10^{-17}$ or better will soon be available with ACES on a global scale. Such performance represents one to two orders of magnitude improvement over the currently used TWSTFT and GPS time transfer systems. Several institutes, such as PTB, SYRTE, and NPL, are already interconnected by a fiber link and additional links will be operational by the time of the ACES mission. Furthermore, the fiber links between NIST and JILA (Boulder, US) as well as between NICT, NMIJ (Tsukuba, JP), and RIKEN (Tokyo, JP) will connect additional institutes sensibly enlarging the ensemble of ground clocks contributing to ACES.

The ground clocks connected to the ACES network are based on different atoms and ions, with transitions both in the microwave and in the optical domain. Microwave fountain clocks are today mature instruments, with fractional frequency stability and accuracy of a few parts in 10^{-16}, able to run on a very high duty cycle ($> 95\%$) [5,4]. They will be compared over the whole mission duration with the ACES clocks. Following the advances in optical frequency measurements using frequency combs, clocks based on the optical transitions of atoms and ions have made spectacular progress in the last years. Several optical clocks have demonstrated a stability of $3 \cdot 10^{-16}$ at 1 s, down to $2 \cdot 10^{-18}$ after 20000 s, and an accuracy in the 10^{-18} range [6,7,8,9,10,11]. These clocks are not yet as reliable as microwave fountain clocks, but with ACES they will be compared over intercontinental distances at 10^{-17} frequency resolution during dedicated measurement campaigns.

ACES, ready for launch in the fall of 2018, will be transported on orbit by Space X and automatically mated at the Clolumbus External Payload Facility (CEPF) by the ISS robotic arm. The ISS has a nearly circular orbit around the Earth with a mean elevation of 400 km, an orbital period of 5400 s, and an inclination of 51.6°. The first 6 months of operations will be devoted to the characterization and performance evaluation of the ACES clocks and links. In microgravity, it will be possible to optimize the interaction time of cesium atoms in the PHARAO clock and tune the linewidth of the atomic resonance by two orders of magnitude. After the

clocks optimization, performance in the 10^{16} range both in frequency stability and accuracy are expected. In parallel, the ACES metrology links will be calibrated and characterized. During the second part of the mission (12 months, possibly extended to 30 months), the ACES clocks will be routinely compared to ground clocks operating both in the microwave and in the optical domain.

2 Scientific Objectives

2.1 Testing General Relativity with ACES

According to Einstein's theory of general relativity, identical clocks placed in different gravitational fields experience a frequency shift that depends on the difference between the Newtonian potentials at the clock positions. The comparison between the ACES clocks and ground-based atomic clocks will measure the frequency variation due to the gravitational redshift with a 70-fold improvement on the GP-A experiment [12], testing Einstein's prediction at the 2 ppm uncertainty level.

Time variations of fundamental constants can be measured by comparing clocks based on different atomic species and transitions [13,14]. Indeed, the energy of an atomic transition can be expressed in terms of the fine structure constant α and the two dimensionless constants $m_{\mathrm{q}}/\Lambda_{\mathrm{QCD}}$ and $m_{\mathrm{e}}/\Lambda_{\mathrm{QCD}}$, depending on the quark mass m_{q}, the electron mass m_{e}, and the QCD mass scale Λ_{QCD} [15,16]. ACES will perform crossed comparisons of ground clocks both in the microwave and in the optical domain with a frequency resolution of $1 \cdot 10^{-17}$ in a few days of integration time. These comparisons will impose strong and unambiguous constraints on the time variations of the three fundamental constants reaching an uncertainty of $1 \cdot 10^{-17}$/yr after one year, down to $3 \cdot 10^{-18}$/yr after three years.

The foundations of special relativity lie on the hypothesis of Local Lorentz Invariance (LLI). According to this principle, the outcome of any local test experiment is independent of the velocity of the freely falling apparatus. In 1997, LLI tests based on the measurement of the round-trip speed of light have been performed by comparing clocks onboard GPS satellites to ground hydrogen masers [17]. In such experiments, LLI violations would appear as variations of the speed of light c with the line-of-sight direction and the relative velocity of the clocks. ACES will perform a similar experiment by measuring relative variations of the speed of light at the 10^{-10} uncertainty level.

The possibility of constraining Lorentz-violating Standard Model extension (SME) coefficients of the proton and neutron as well as dark matter models with ACES are presently under study.

2.2 Applications

ACES will also demonstrate a new technique to map the Earth gravitational potential. It relies on a precision measurement of the Einstein's gravitational redshift between two clocks to determine the corresponding difference in the local gravitational potentials. The possibility of performing comparisons of ground clocks to the 10^{-17} frequency uncertainty level will allow ACES to resolve geopotential differences down to 10 cm on the geoid height.

A dedicated GNSS receiver onboard the ACES payload will ensure orbit determination of the space clocks. The receiver will be connected to the ACES clock signal, opening the possibility of using the GNSS network for clock comparisons.

The simultaneous operation of MWL and ELT will allow to cross calibrate the two links. Optical versus dual-frequency microwave measurements will provide useful data for the study of atmospheric propagation delays and for the construction of atmosphere mapping functions in S-band, Ku-band, and at optical frequencies. The ACES links will also deliver absolute ranging measurements, both in the microwave and in the optical domain.

3 ACES Status

3.1 PHARAO

PHARAO is a primary frequency standard based on laser cooled cesium atoms developed by LNE-SYRTE, LKB, and CNES. Its concept is very similar to ground-based atomic fountains. Atoms, launched in free flight along the PHARAO tube, cross a resonant cavity composed of two spatially separated interrogation zones where they interact with a microwave field tuned on the transition between the two hyperfine levels of the cesium ground state (9.192631770 GHz, from the SI definition of the second). In microgravity, the velocity of the atoms is constant and it can be continuously changed over almost two orders of magnitude (5 to 500 cm/s), allowing the detection of atomic signals down to sub-Hz linewidth.

All PHARAO subsystems have passed their qualification tests: random vibrations, thermal cycles, etc. During ground tests, PHARAO is operated under vacuum with the cesium tube aligned vertically and the atoms launched upwards at a velocity of 3.56 m/s. The space environment is emulated by changing the temperature at the clock baseplate and the magnetic field via large external Helmholtz coils. The clock performance tests at CNES lasted 4 months and ended in Summer 2014. The capture, cooling, launch, and detection of cold atoms have been optimized. The frequency stability and the major systematic frequency shifts of the clock have been measured. $5 \cdot 10^8$ atoms can be collected in the PHARAO optical molasses for a laser power of 12 mW/beam and a loading time of 1.5 s. The PHARAO Ramsey fringes are in full agreement with numerical simulations. The central fringe has a linewidth of 5.6 Hz corresponding to an interaction time of 90 ms. In micro-gravity, the linewidth can be reduced to 0.12 Hz at a launch velocity of 50 mm/s.

The PHARAO frequency stability has been measured as a function of the integration time τ by comparing the clock to the SYRTE mobile fountain FOM [18]. PHARAO Allan deviation is $3.15 \cdot 10^{-13}/\sqrt{\tau}$, with FOM contributing $1.3 \cdot 10^{-13}/\sqrt{\tau}$. The clock model predicts a frequency stability of $1.1 \cdot 10^{-13}/\sqrt{\tau}$ in microgravity. PHARAO and FOM frequencies agree to better than $2 \cdot 10^{-15}$. All major systematic frequency shifts have been measured and the frequency accuracy of the PHARAO clock has been thoroughly characterized down to the $1 \cdot 10^{-15}$ level. When operated under microgravity conditions, the PHARAO clock is expected to have an accuracy of $1 - 3 \cdot 10^{-16}$.

PHARAO is now at ADS in Friedrichshafen, integrated on the ACES baseplate.

3.2 SHM

SHM is an active H-maser operating on the hyperfine transition of atomic hydrogen at 1.420405751 GHz. Developed by SpectraTime, SHM provides ACES with a stable fly-wheel oscillator. SHM is designed to fit into a volume of $390 \times 390 \times 590$ mm^3 and a mass of 42 kg, while delivering the typical frequency stability performance of a ground maser. To this purpose, the number of thermal shields has been reduced and a dedicated Automatic Cavity Tuning (ACT) system has been implemented to steer the resonance frequency of the maser cavity against thermal drifts. SHM ACT injects two tones, symmetrically placed around the H-maser signal. The two tones are coherently detected and the unbalance between their power levels is used to close a feedback loop acting on the cavity varactor and stabilizing the resonance frequency of the microwave cavity against temperature variations. This method allows SHM to reach fractional frequency stabilities down to $1.5 \cdot 10^{-15}$ at 10^4 s of integration time.

The SHM sensitivity to temperature and magnetic field variations has been measured. The thermal sensitivity can be counteracted by a fast servo on the ACES baseplate temperature ($<$ 600 s time constant) and by the natural filtering of temperature fluctuations due to the thermal inertia of the instrument. In addition, SHM frequency variations can be calibrated as a function of temperature. SHM sensitivity to magnetic fields has been measured to about $8 \cdot 10^{-14}$/G. At

this level, the magnetic field variations along the ISS orbit (±0.4 G) are expected to introduce a degradation to the H-maser stability of $1 - 2 \cdot 10^{-14}$. These frequency fluctuations will be corrected by the ACES servo-loops. In addition, magnetic field perturbations are suppressed to high degree when taking the frequency difference between alternating PHARAO cycles over 100 s time intervals, as needed for the PHARAO accuracy evaluation. Tests will be performed to better characterize the H-maser sensitivity to external B-fields. In addition, dedicated electronics have recently been implemented in SHM to be able to degauss the mu-metal shields of the clock while on orbit.

The SHM flight model is being completed. Its delivery for integration in the ACES baseplate is expected by the end of 2017.

3.3 ACES Integrated System Tests

The flight model of the PHARAO clock, the SHM engineering model, the flight model of FCDP and XPLC have recently been integrated in the ACES payload to verify that the clocks can be operated close to each other without interfering and to validate the main functions of ACES, including the short and long-term servo-loops. The ACES performance was measured with respect to an ensemble of ground clocks operated at ADS premises in Friedrichshafen, namely an active H-maser stabilizing a cryogenic sapphire oscillator. In addition, the H-maser was permanently compared to UTC(OP) via a GPS link to constantly monitor the PHARAO frequency and to evaluate its systematic shifts. The long-term stability of the ACES clock signal was measured against the H-maser; on the other hand, the cryogenic oscillator was used to evaluate the short-term stability and the phase noise power spectral density (PSD) of the clocks.

After the standard power-on of the payload, SHM was first initialized and tuned. The Allan deviation and the phase noise PSD were measured. SHM Allan deviation is shown in Fig. 4. The measured stability is in good agreement with the SHM performance in stand-alone configuration.

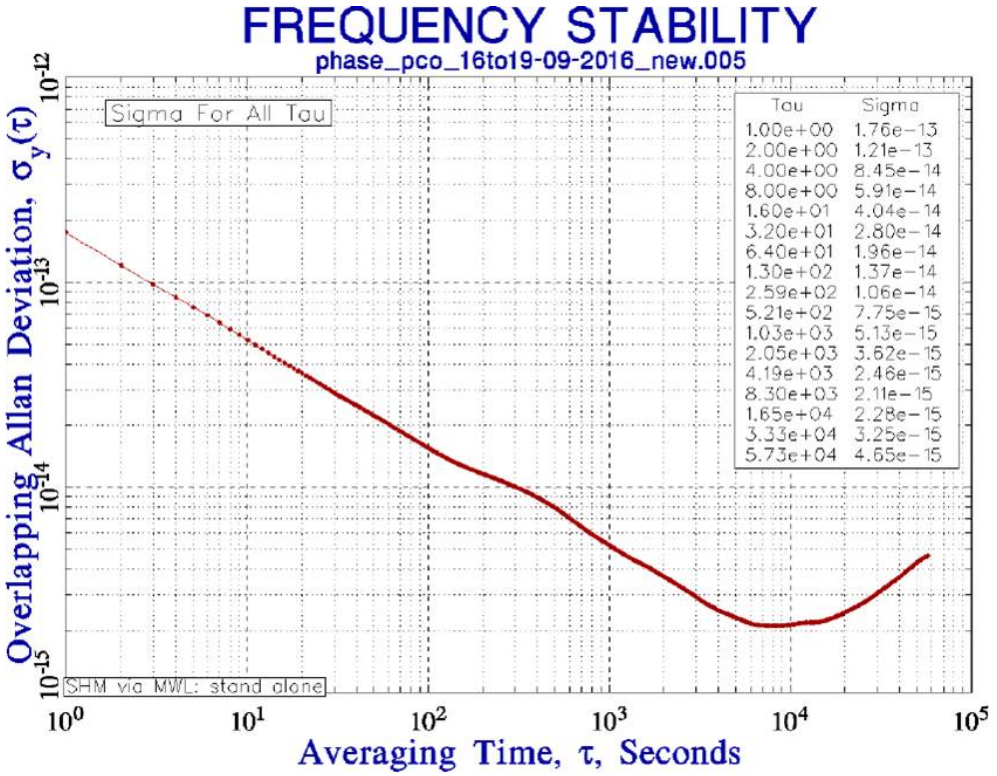


Figure 4 – Allan deviation of the SHM clock integrated in the ACES payload.

As second step, the PHARAO clock was also powered on. PHARAO was first operated in autonomous mode. In this configuration, PHARAO measures the frequency difference (Detsynch) between its local oscillator (USO) and the Cs clock transition, sends this information to the PHARAO onboard computer (UGB) that in turn closes a loop to steer the PHARAO USO on the Cs resonance. The clock stability is reported in Fig. 5, showing a good agreement with the PHARAO stability as measured during clock stand-alone tests at CNES.

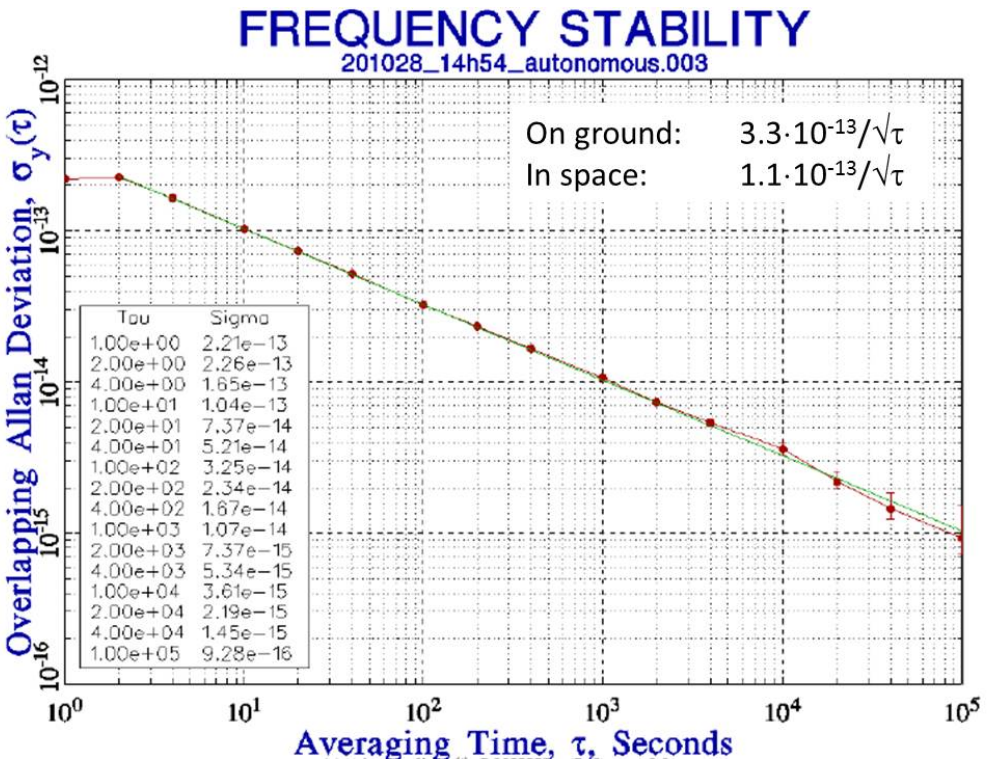


Figure 5 – Stability of the PHARAO clock when operated in autonomous mode on the ACES payload.

Finally, also FCDP was powered on and the ACES signal was distributed at the MWL output. Unfortunately, due to an error in the FCDP firmware, it was not possible to fully test the performance of the short-term servo-loop. The loop could be closed, but it was not possible to change the gain and its time constant to optimize it. On the contrary, it was possible to characterize the long-term servo-loop and evaluate the major frequency shifts affecting the PHARAO clock. This test was performed by operating ACES in its Backup mode. In this configuration, the PHARAO USO is bypassed and the clock is driven by the SHM 100 MHz signal. The long-term servo was closed with the PHARAO clock operated on two different cycles, alternating high-density and low-density clouds of laser-cooled Cs atoms. PHARAO was configured to hold the last Detsynch value when in the high-density cycle to avoid frequency jumps at the SHM output. Figure 6 shows the evolution of the long-term servo-loop error signal (Detsynch) and its Allan deviation. The loop has a time constant of about 500 s. The $1/\tau$ slope observed in the Allan deviation plot for integration times longer than 500 s shows that the loop is correctly operating. For shorter integration times, the Allan deviation shows the performance of the PHARAO clock, now $\sim 1 \cdot 10^{-12}$ at 1 s, dominated by the Dick effect due to the worse phase noise PSD of SHM compared to the PHARAO USO.

Finally, the main systematic frequency shifts at the PHARAO clock were evaluated down to the $1 \cdot 10^{-15}$ level while ACES was operated in Backup mode: the second-order Zeeman effect, the blackbody radiation shift, the cold collisions shift, and the first-order Doppler effect. As final confirmation of the accuracy of the ACES clock signal, an absolute frequency measurement with respect to the Cs fountain clocks operated at LNE-SYRTE in Paris was performed via the

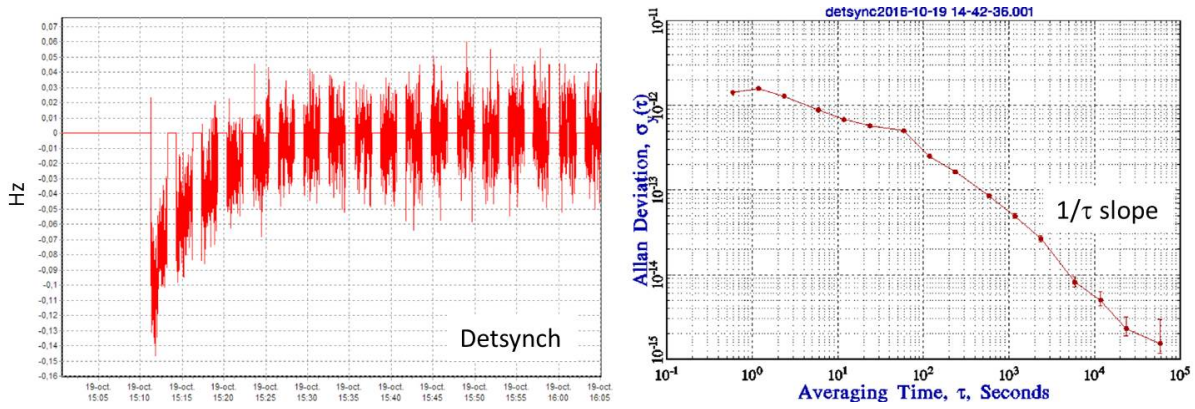


Figure 6 – ACES operated in Backup mode: (left) evolution of the error signal Detsynch when closing the long-term servo-loop; (right) Allan deviation of Detsynch.

GPS link. Figure 7 shows the Allan deviation of the remote comparison between the ground H-maser operated ADS and UTC realization in LNE-SYRTE (UTC(OP)). The comparison reaches a fractional frequency uncertainty of a few parte in 10^{15} after about 10 days of integration time. After estimating the frequency shift due to the gravitational time dilation, the absolute frequency measurement confirmed the evaluation of the PHARAO frequency shift performed in Friedrichshafen to $2 \cdot 10^{-15}$.

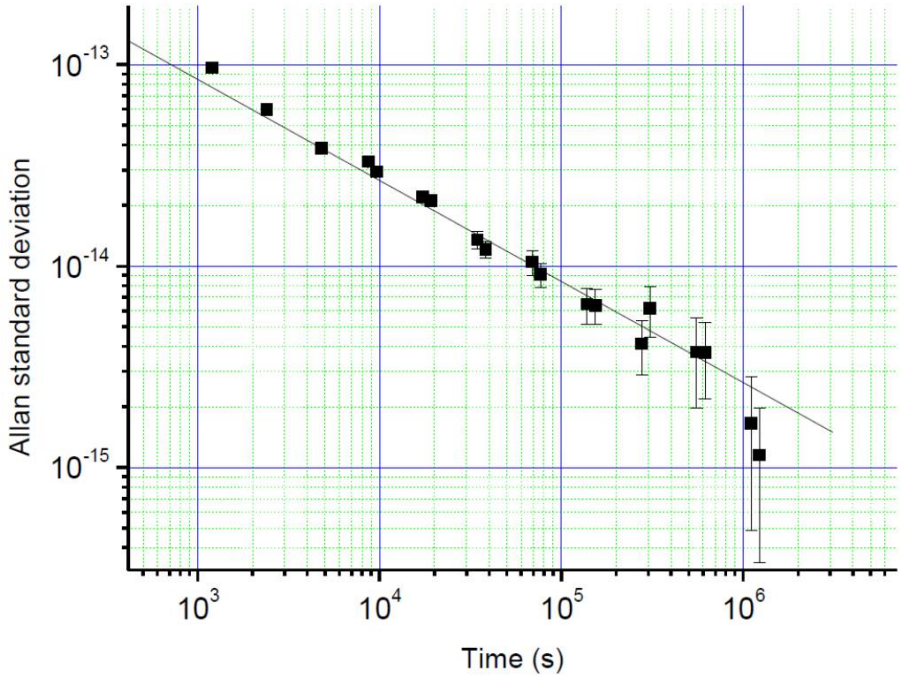


Figure 7 – Allan deviation of the remote comparison between the ground H-maser operated at ADS and UTC realization in LNE-SYRTE (UTC(OP)). The comparison reaches a fractional frequency uncertainty of a few parts in 10^15 after about 10 days of integration time.

3.4 MWL

The ACES microwave link is developed by ADS, TIMETECH, TZR, and EREMS. The proposed MWL concept is an upgraded version of the Vessot two-way technique used for the GP-A experiment in 1976 [12] and the PRARE geodesy instrument. The system operates continuously with a carrier frequency in the Ku-band. The high carrier frequencies of the up and down links

(13.5 GHz and 14.7 GHz respectively) allow for a noticeable reduction of the ionospheric delay. A third frequency in the S-band (2.2 GHz) is used to determine the Total Electron Content (TEC) and correct for the ionospheric time delay. A PN-code modulation (100 Mchip/s) on the carrier removes the phase ambiguity between successive comparison sessions separated by large dead times. The system is designed for multiple access capability, allowing up to 4 simultaneous ground users distinguished by the different PN-codes and Doppler shifts.

The engineering model of the flight segment electronic unit has been tested in end-to-end configuration with the ground terminal electronics in the presence of signal dynamics (attenuation and Doppler frequency variations as predicted along the ISS orbit). On the short-term (< 300 s), the time stability is driven by the noise performance of the Ku-band transmitter and receiver and the DLL (Delay-Locked Loop) boards. The 100 MHz chip rate allows to reach a time stability at the 5 ps level already with code measurements. However, the ultimate performance is achieved with the carrier phase measurements, whose time stability is at the level 200 fs at about 100 s of integration time in the presence of signal dynamics. The thermal sensitivity of the system has been calibrated. The sensitivity to a series of key parameters such as clock input power, received signal-to-noise density ratios, supply voltage, Doppler, and Doppler rate has also been measured.

MWL ground terminal (GT) electronics are similar to the MWL flight hardware, symmetry being important in a two-way system to reduce instrumental errors. The electronics unit of the MWL GT has been rigidly attached to the antenna unit to reduce phase instabilities due to the tracking motion. The Ku-band signal is delivered to the antenna feeder via a waveguide; a high stability RF cable is used for the S-band. The antenna is a 60 cm offset reflector with a dual-band feed system automatically pointed in azimuth and elevation by a steering mechanism. A computer controls the steering unit based on ISS orbit prediction files, collects telemetry and science data both from the local clocks and the MWL GT electronics, and it interfaces directly with the ACES Users Support and Operation Center (USOC). The system is housed below a protective radome cover, which also allows to stabilize the temperature of the enclosed volume by an air conditioning system, part of a separate service pallet. The thermal design allows to operate the MWL GT for an external temperature between -30°C and $+45$°C.

The MWL flight model is under assembly and board level tests have already started. The delivery of MWL flight segment electronics for integration in the ACES payload is expected by end 2017. The first MWL ground terminal has been deployed in PTB. The network is expected to be completed in the second half of 2018.

3.5 ELT

ELT, acronym for European Laser Timing, is an optical link based on picosecond laser pulses exchanged between Satellite Laser Ranging (SLR) stations on ground and the ACES payload. The onboard hardware consists of a corner cube reflector, a Single-Photon Avalanche Diode (SPAD), and an event timer board connected to the ACES time scale. Laser pulses fired towards the ISS are detected by the SPAD diode and stamped in the ACES scale. At the same time, the ELT reflector re-directs the laser pulses towards the ground station. The measurement of the start and return times on ground and of the detection time in space is then used to determine the desynchronization between space and ground clocks as well as the range.

Developed by the Technical University of Prague and CSRC, the SPAD diode has been tested in conjunction with a laboratory time tagging board providing sub-picosecond resolution. The time deviation of the combined system has a floor slightly below 200 fs. Peak-to-peak time fluctuations amount to a few picoseconds over several days of measurement. The detector is extremely robust against stray light and temperature variations. The temperature sensitivity has been measured between -60°C and $+70$°C showing a mean slope as low as 0.48 ps/K.

The flight model of the detector has been tested and delivered. The corner cube reflector is already integrated on the ACES payload.

Acknowledgments

The development of the ACES mission is a collective effort and the authors would like to thank all participants, in particular the ACES Investigators Working Group (IWG), the ACES project team at ESA and ADS, the PHARAO team at CNES, SYRTE, LKB, TAS, Sodern, Erems, CS, the SHM team at SpectraTime, the University of Prague team, the Technical University of Münich team, and the data analysis team at SYRTE for their contributions. This work is supported by ESA, CNES, and CNRS.

References

1. C. Salomon *et al*, C. R. Acad. Sci. Paris **t.2 Séries 4**, 1313 (2001).
2. L. Cacciapuoti and C. Salomon, Eur. Phys. J. Special topics **172**, 57 (2009).
3. P. Lauren *et al*, Comptes Rendus Physique **16**, 540 (2015).
4. R. Li *et al*, Metrologia **48**, 283 (2011).
5. J. Guéna *et al*, Phys. Rev. Lett **106**, 130801 (2011).
6. T. Rosenband *et al*, Science **319**, 1808 (2008).
7. A.D. Ludlow *et al*, Science **319**, 1805 (2008).
8. N. Hinkley *et al*, Science **341**, 1215 (2013).
9. B.J. Bloom *et al*, Nature **506**, 71 (2014).
10. I. Ushijima *et al*, Nature Photonics **9**, 185 (2015).
11. T.L. Nicholson *et al*, Nature **6**, 6896 (2015).
12. R.F.C. Vessot *et al*, Phys. Rev. Lett. **45**, 2081 (1980).
13. N. Huntermann *et al*, Phys. Rev. Lett. **113**, 210802 (2014).
14. R.M. Godun *et al*, Phys. Rev. Lett. **113**, 210801 (2014).
15. V.V. Flambaum *et al*, Phys. Rev. D **69**, 115006 (2004).
16. V.V. Flambaum *et al*, Phys. Rev. C **73**, 055501 (2006).
17. P. Wolf and G. Petit, Phys. Rev. A **56**, 4405 (199).
18. J. Guéna *et al*, IEEE Trans. Ultrason. Ferroelec. Freq. Contr. **59**, 391 (2012).
19. W. Itano *et al*, Phys Rev. A **25**, 1233 (1981).
20. K. Gibble, Phys. Rev. A **90**, 015601 (2014).

ACES MWL data analysis center at SYRTE

F. MEYNADIER[1], P. DELVA[1], C. LE PONCIN-LAFITTE[1], C. GUERLIN[2], P. LAURENT[1], P. WOLF[1]

[1] *LNE-SYRTE, Observatoire de Paris, CNRS, UPMC, LNE, 61 avenue de l'Observatoire 75014 Paris, France*

[2] *Laboratoire Kastler-Brossel, ENS, CNRS, UPMC, 24 rue Lohmond, 75005 Paris, France*

The ACES-PHARAO mission aims at operating a cold-atom caesium clock on board the International Space Station, and performs two-way time transfer with ground terminals, in order to allow highly accurate and stable comparisons of its internal timescale with those found in various metrology institutes. Scientific goals in fundamental physics include tests of the gravitational redshift with unprecedented accuracy, and search for a violation of the Lorentz local invariance. Hopefully this is our last status update in Moriond with ACES still on ground... As launch is coming closer we are getting ready to process the data expected to come from ACES Microwave Link (MWL) once on board the International Space Station. Several hurdles have been cleared in our software in the past months, as we managed to implement algorithms that reach target accuracy for ground/space desynchronisation measurement. I will present the current status of data analysis preparation, as well as the activities that will take place at SYRTE in order to set up its data processing center.

1 Introduction

This presentation follows previous status updates, notably last Rencontres de Moriond [1]. General presentation of the ACES mission may be found in Laurent *et al.*, 2012[2]. The software is now almost finished, as it is able to process what we assume to be realistic MWL simulated data over full measurement sessions ($\simeq$10 days). We were therefore able to use this software for experiments (e.g. influence of ISS orbitography uncertainty on final results).

2 A brief reminder of the MWL measurement principle

The ACES Micro Wave Link (MWL) will be the main device used for time and frequency transfer between space and ground stations. It requires a specific terminal, 5 of them will be attached permanently to several high performance clocks around the world, while additional mobile units will perform measurements for shorter period of times either in colocation for calibration purposes, or at different institutes to increase coverage.

It applies the principle of two way time transfer, in which both clocks send a timing signal to the other one. Each incoming signal is then compared to the locally produced signal, which provides a " pseudo-range" observable. The difference between the ground and space observable nullifies (at first order) the signals propagation delay and gives access to the desynchronisation between the clocks [3]. Figure 1 shows the basic configuration for signal exchange. We use one uplink (Ku-band, 13.475 GHz) and two downlinks with very different frequencies in order

to determine the Total Electron Content (TEC), Ku-band 14.703 GHz and S-band 2.24 GHz. The "lambda" configuration shown on figure minimizes the effect of our limited knowledge of ISSposition and also limits the impact of tropospheric delays estimate errors.

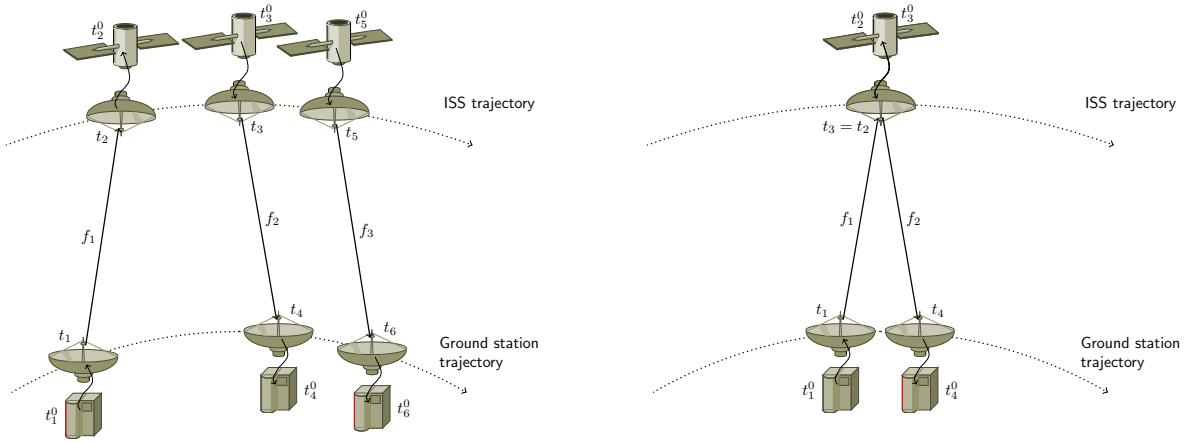


Figure 1 – Left : nominal configuration for signals exchange, the uplink signal and both downlink signals are not synchronised and both stations move during time of flight. Right : The "lambda" configuration, obtained by interpolation, where we match arrival at and departure from the space station in order to minimize the impact of its positional uncertainty.

3 Software development at Syrte

Basic ideas for the data processing where first explored in Duchayne, 2008 [4]. Actual coding of the present software started in 2011, the package now consists in roughly 6300lines of python / numpy code. For each pass of the ISSin visibility of the ground station, it takes raw (but demodulated) data + auxiliary files as input, and computes ground/space desynchronisation, Total Electron Content, and pseudo range every 80ms during the pass.

In parallel, a simulation software has been developed as independently as possible : different programming language (Matlab) and separate developers, only sharing basic understanding of the measurement principle.

3.1 Typical results

Figure 2 shows typical results coming out of the processing of one pass, from simulated data. The top row shows the actual value of the desynchronisation throughout the pass : we asked for a simulation with a $\simeq 1$ ms offset, plus a drift which is due to the difference in geopotential (i.e. Pharao is not de-tuned to compensate this). Tis means that, from the beginning to the end of the pass, the desynchronisation varie by a few tens of microseconds.

There are two measurements done simultaneously : the signal consists on an encoded modulation of the carrier, and the modem returns a "code" and a "carrier" observable. "code" is non ambiguous but as a 20 ps uncertainty on each point. "carrier" is more stable (1 ps at each point) but needs ambiguity removal and is affected by an unknown offset. The bottom graphs illustrate these characteristics.

It should be noted that the only noise source included here is the quantization noise generated by the measurement principle (which is based on counters running at $\simeq 100$ MHz, which translate into the observed spread). Therefore this represents the floor noise this technique may achieve : we expect real data to be much noisier.

One of our recent major achievements is the implementation of carrier disambiguation and offset conservation from pass to pass : as noted above, the most stable measurement (i.e.

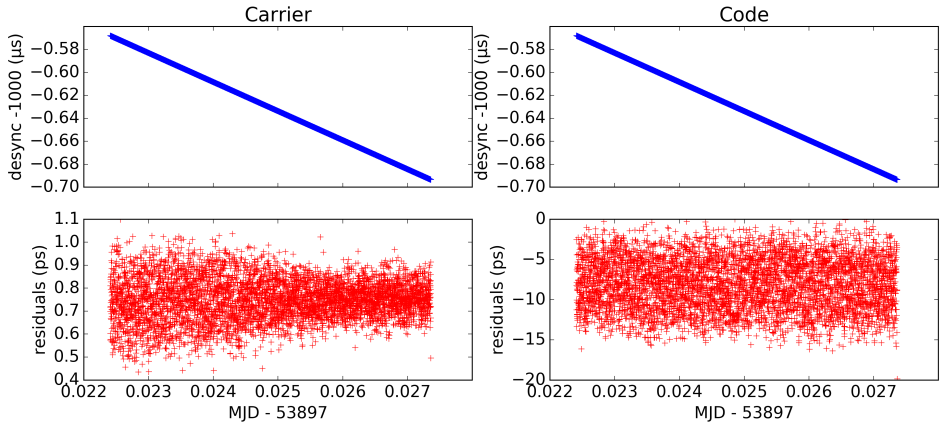


Figure 2 – A typical pass result. Top : input desynchronisation (drift = GR). Bottom : residuals (theoretical - calculated desynchronisation).

"phase") is affected by an unknown offset, but according to the specifications there is a way to link one pass to the next and therefore keep this unknown offset constant from one dataset to the next (provided no hardware reset has occurred in the mean time). This behaviour is illustrated on figure 3 : "code" measurement mean value can exhibit $\simeq$ 20 ps jitter, while "carrier" measurement stays close to the same value (here, 0.8 ps away from the theoretical value).

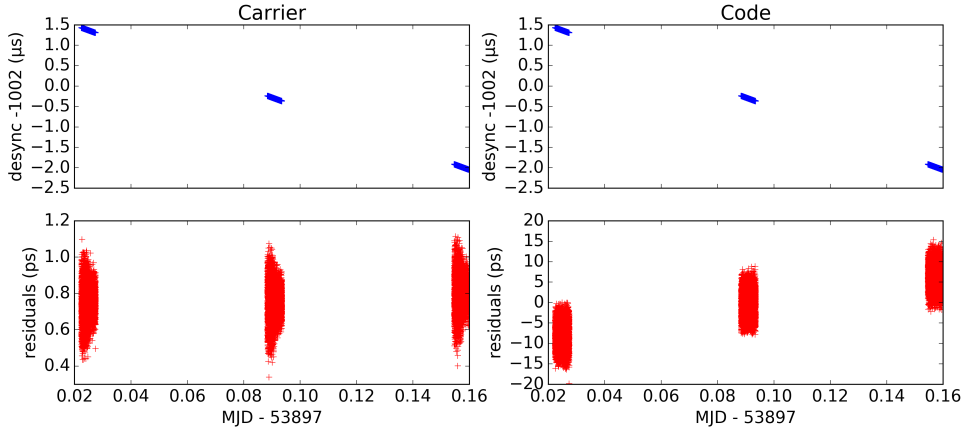


Figure 3 – Same as fig. 2, but spanning 3 consecutive passes (roughly separated by 1 ISS orbital period).

4 Experiments

Both processing and simulation software are very useful tools even before the mission start, as an efficient way to experiment on expected data : the very high flexibility of the simulation software allows to generate datasets that will test edge cases or peculiar scenarios, even non physical ones for test purposes (e.g. stop the ISS to allow "constant range" scenarios, switch atmosphere on and off, etc...). We regularly provide datasets to industrial Ground Segment developers to test their work chain. We also test our own ability to detect deviations to GR or possible technical mishaps.

For example, we have tested the impact of ISS orbitography uncertainty : we know that the ISS will always be slightly off the position we read from the orbitography files. First, with help from DLR (O. Montenbruck) we compared two orbitography datasets obtained for the ISS at the same time, one from the regular tracking device (SIGI), the other from a more precise GNSS receptor installed temporarily on the ISS in 2006. The SIGI error dominates, so the difference between the two gives an estimate of the error vector.

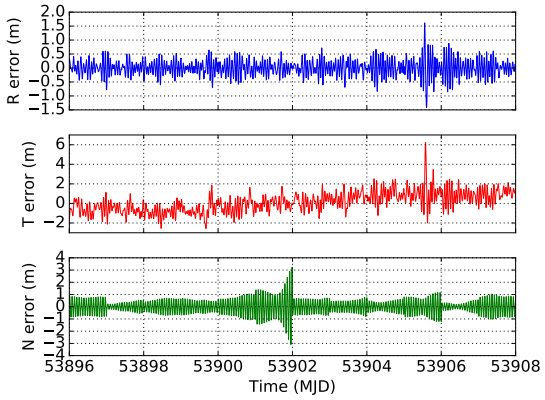


Figure 4 – Projection of ISS orbitography uncertainties.

Projection of this error vector on meaningful axes, for 12 days of data, is shown on fig 4. As expected, we observe a smaller dispersion on R (radial), i.e. a few meters, while T (transverse, along path) axis bears larger errors. N (normal) exhibits peculiar patterns due to the model used for fitting. Note that we have selected a "quiet" period, without major disturbances (such as altitude boosts, vessel docking, etc...). Once we have those projections we can re-apply them to our orbitography file, and change their amplitude (selectively on each axis) to test for degraded conditions.

This allowed us to verify theoretical calculations showing that using the "lambda" configuration effectively reduces the impact of ISS orbitography uncertainty : we show that, as far as the desynchronisation determination is concerned, our algorithm can cope with an error between 10 and 100 times worse than expected. Note however that it is another matter to check the impact of this uncertainty on our knowledge of the gravity potential during the orbit, which in turn shifts the clocks frequency during orbit. Tools are being developed to modelize and integrate this shift in various theoretical frames.

5 Conclusion

Work has progressed well and is in line for the planned launch date, one year from now. We already have demonstrated our ability to process large amounts of data within the required specifications, all remaining unknowns pending to comprehensive end-to-end hardware tests that are expected to happen this summer.

References

1. F. Meynadier, P. Delva, C. Guerlin, C. Le Poncin-Lafitte, P. Laurent, and P. Wolf. ACES MWL data analysis preparation status. In *Proceedings of the 50th Rencontres de Moriond*, 21 March 2015.
2. P. Laurent, O. Grosjean, I. Moric, M. Abgrall, F. Picard, and D. Massonnet. Cold Atoms Space Clock PHARAO: Validation and Flight Model Assembly. In *39th COSPAR Scientific Assembly*, volume 39 of *COSPAR Meeting*, page 1042, July 2012.
3. P. Delva, F. Meynadier, P. Wolf, C. Le Poncin-Lafitte, and P. Laurent. Time and frequency transfer with a microwave link in the ACES/PHARAO mission. In *Proceedings of the European Frequency and Time Forum (EFTF) 2012 held in Gothenburg, Sweden, April 2012*, June 2012.
4. L. Duchayne. *Transfert de temps de haute performance : le lien micro-onde de la mission ACES*. PhD thesis, Observatoire de Paris, France, 2008.

Optical clocks and fiber links

J. Lodewyck
LNE-SYRTE, Observatoire de Paris, PSL Research University, CNRS, Sorbonne Universités, UPMC Univ. Paris 06, LNE, 61 avenue de l'Observatoire 75014 Paris, France



Optical clocks are now the most stable and accurate frequency standards, with performances in the low 10^{-18}, outperforming by two orders of magnitude the best microwave primary standards based on cesium. This opens the question of a possible redefinition of the SI (Système International) second with an optical transition. However, several operational steps have to be demonstrated before such a redefinition can be effective: reliable and interconnected clocks are necessary to realize the definition. Here, we report on several experimental advents in this direction, including the remote comparison of optical lattice clocks via phase compensated optical fiber links between different metrology institutes across Europe.

1 Introduction

The primary microwave cesium clock, the cold atom fountain being its most accurate implementation, are currently realizing the SI and are used to build international timescales such as TAI (Temps Atomique International) and its derivative UTC (Universal Time Coordinated). The widespread usage of fountain clocks for these application relies on four pillars. First, the availability in several metrology institutes of highly reliable atomic fountains makes possible a continuous operation. Second, these remote clocks are interconnected by satellite-based microwave links, in oder to compare them. Third, repeated measurement of frequency ratios between cesium clocks and between cesium and rubidium clocks have confirmed their accuracy budget, evaluated at a few parts in 10^{16}. Finally, regular calibrations of TAI reported to the Bureau International des Poids et Mesures (BIPM) make them key players in building accurate time scales [1].

More recently, optical clocks, whose frequency is referenced to a narrow optical atomic transition in ions or neutral atoms instead of a microwave hyperfine transition, have progressed fast down to a control of systematic effect of a few parts in 10^{18} [2,3,4]. The frequency stability of optical clocks using neutral atoms confined in an optical lattice have reach a few 10^{-16} for an integration time of 1 s, effectively reaching a the statistical resolution of a few 10^{-18} in a mere hour of measurement [5,6,2]. The performances of optical clocks thus outperform the performances of microwave primary standards by two orders of magnitude, opening the way to a redefinition of the SI second using an optical transition.

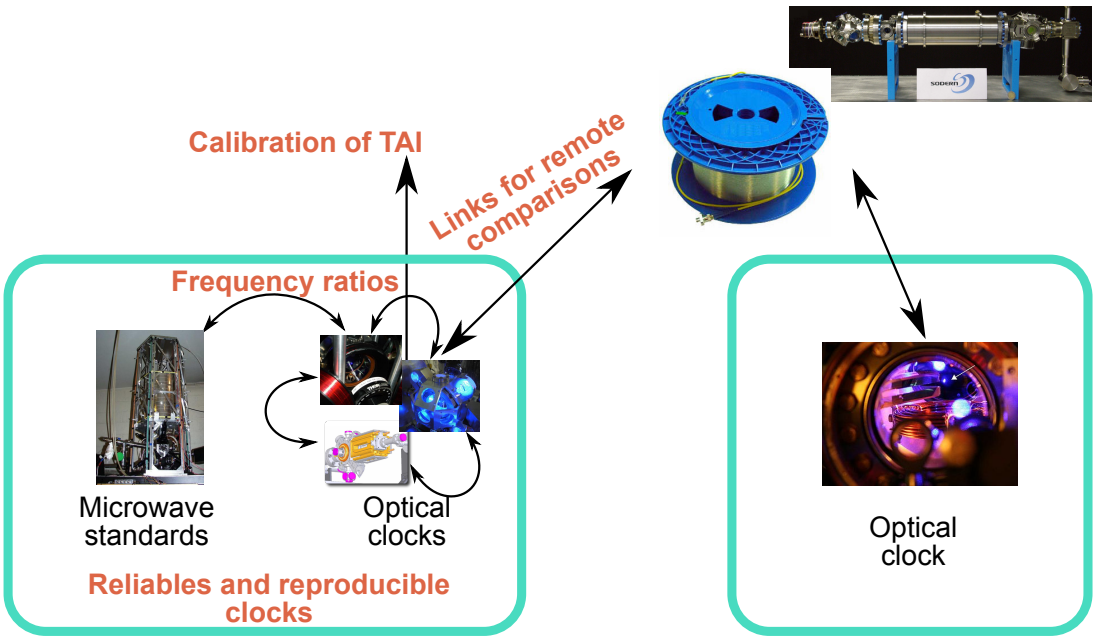


Figure 1 – Optical clock architecture proposed in this paper. It includes all four components (text in red) that integrate optical clocks into a network of clocks whose implementation is necessary to envision a SI second based on an optical transition.

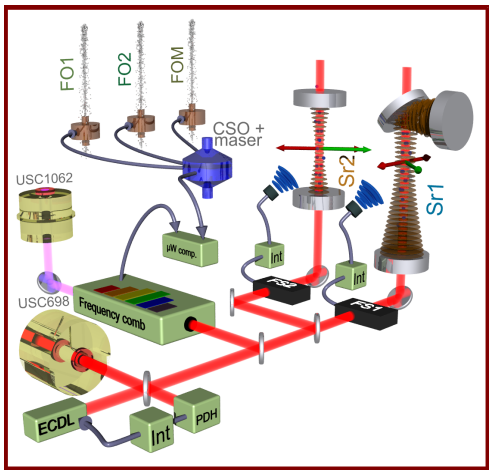
However, before optical clocks can replace the operational microwave clocks, a full network of optical clocks implementing the four pillars listed above has to be realized, as depicted in figure 1. In this paper, we report on several experimental advents that, together, are a first demonstration that optical clocks are in the process of fully reproducing the current clock architecture based on microwave clocks. First, the experimental demonstration of reliable optical lattice clocks, able to operate almost continuously over extended periods of several weeks, shows that optical clocks are now suitable for applications such as calibrating timescales. Second, reproducible measurements of frequency ratios between optical and optical clocks confirm the excellent control of systematic effects advertised for these clocks, while frequency ratio measurements between optical and microwave clocks bridge the two frequency domains. Third, linking optical clocks together enable the comparison of completely independent remote clocks located at different metrology institutes. To fully benefit from the statistical resolution of optical clocks, these comparisons are now conducted by fiber links, as the satellite comparisons methods feature a limited frequency stability. Finally, we report on the first contribution to TAI with an optical frequency standard, complementing the regular contributions of cesium and rubidium microwave standards.

2 Optical clocks

Optical clocks take advantage of the high quality factor offered by narrow electronic transitions in the optical spectrum, probed by a pre-stabilized narrow linewidth laser. Optical lattice clocks are therefore composed of two elements: a laser locked on an ultra-stable Fabry Perot resonator with relative length fluctuations on the order of 10^{-16}, and a set of ultra-cold atoms confined in an optical lattice for a Doppler-free spectroscopy. LNE-SYRTE has built a set of two optical lattice clocks with strontium atoms with frequency instability of 10^{-15} at 1 s and an accuracy of 4.1×10^{-17}. They are connected, via a frequency comb to an optical lattice clock with mercury atoms, an ultra-stable laser injected in fiber links (section 4), and a set of three microwave standards (figure 2).

The strontium optical clocks have been demonstrated to be operable over several weeks with minimal human intervention, and a time coverage ranging from 67% to 92%. This shows

that optical lattice clocks are suitable for calibrating time scale for which long term operation is necessary. It also makes possible to measurement of optical-to-microwave frequency ratio, which, because of the limited frequency stability of microwave standards, require long integration times [7].



Effect	Correction	Uncertainty
Black-body radiation shift	5208	20
Quadratic Zeeman shift	1317	12
Lattice light-shift	−30	20
Lattice spectrum	0	1
Density shift	0	8
Line Pulling	0	20
Probe light-shift	0.4	0.4
AOM phase chirp	−8	8
Servo error	0	3
Static charges	0	1.5
Black-body radiation oven	0	10
Background collisions	0	8
Total	6487.4	41

Figure 2 – Left: clock architecture at LNE-SYRTE, showing two Sr clocks, ultra-stable cavities, and the frequency comb linking these clocks to the Cs and Rb atomic fountains. Right: accuracy budget of the two strontium clocks. It is dominated by the uncertainty on the black-body radiation shift arising from temperature inhomogeneities in the vacuum environment of the atoms.

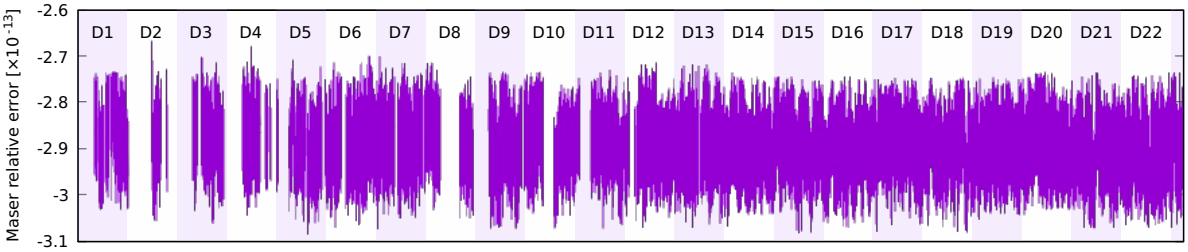


Figure 3 – 3 week operation of the two Sr optical lattice clocks at LNE-SYRTE. This graph shows the relative frequency error of SYRTE's master maser with respect to the strontium clock transition. These data are directly used to calibrate international timescales. the second half of the experiments, the Sr clock was operated unattended without failure.

3 Optical to optical and optical to microwave frequency ratios

Comparing two clocks using the same atomic species enables to confirm the accuracy budget of the clocks. We have conducted comparisons between our two strontium clocks (Sr2 and SrB) over extended periods, and found an agreement compatible with the total uncertainty:

$$\frac{\nu_{\mathrm{Sr}_2} - \nu_{\mathrm{Sr}_B}}{\nu_{\mathrm{Sr}}} = (2.3 \pm 7.1) \times 10^{-17}. \quad (1)$$

This result improves on the first comparison between two optical lattice clocks with an uncertainty beyond the best realization of the SI second [8], conducted at SYRTE.

High resolution interspecies optical-to-optical comparisons enable many applications of optical clocks, such as test of fundamental physics, by verifying that the measured frequency ratio stays constant over time. Indeed, many theories beyond the standard model predict that the constants of nature may vary with time, hence frequency ratios between clocks, whose frequency depends on these constants. At LNE-SYRTE, we measured the frequency ratio between strontium and mercury lattice clocks with a total uncertainty of 1.7×10^{16} [9]. This ratio is in agreement

with a completely independent measurement at RIKEN, Japan [10]. This quantity is thus one of the best frequency ratio measurement reproduced in different laboratories. It confirms that optical clocks can be reproduced with uncertainties better than the best realization of the SI second.

Frequency ratios between optical and microwave clocks, although they do not reach an uncertainty as low as optical to optical comparisons, bring several advantages. First, measuring the stability of these ratios tests different physical theories, owing to the different nature of the atomic transitions involved (the frequency of optical clocks is mainly determined by the electron orbit, while the frequency of microwave hyperfine transitions is mainly determined by the properties of the nucleus). Second, they are able to bridge the microwave domain and the optical domain, which is a necessary condition for a redefinition of the SI second.

At SYRTE, we conducted extensive measurements of the frequency ratio between Sr lattice clocks and Cs and Rb microwave clocks [7]. This frequency ratio has been extensively measured by different laboratories worldwide, leading to a very good agreement. Figure 4 shows the recent history of the Sr/Cs measurements.

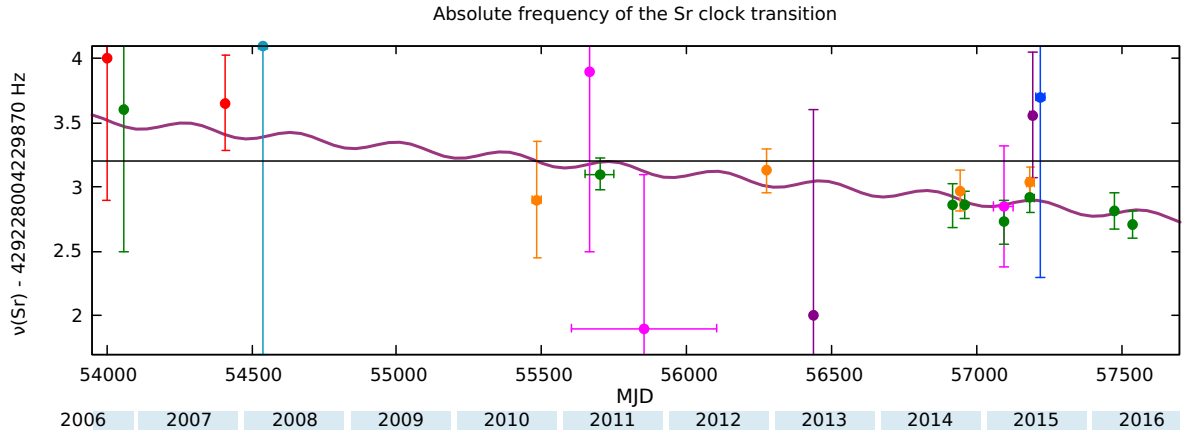


Figure 4 – International agreement of the frequency ratio between Sr optical lattice clocks and the Cs primary standard: green •: LNE-SYRTE, red •: JILA, light blue •: Tokyo University, orange •: PTB, pink •: NICT, purple •: NMIJ, blue •: NIM. The graph also shows a fit of these data points by a linear drift of the fundamental constants, as well as a fit with a possible coupling to the Sun's gravitational potential, with a yearly signature. Although no effect is resolved yet, the Sr/Cs data bring a decisive contribution to constraints on these effects.

4 Comparisons between remote optical clocks with fiber links

Remote clock comparison can provide many more application with respect to local comparisons. First, it extends the possibilities of clock comparisons by making more clock pairs available, also enabling to directly compare completely independent clocks built by different teams. But it also makes new applications possible, one of the most prominent being a mapping of the gravitational potential at long distances by comparing the rates of clocks located at different positions in the gravitational potential of the Earth, via the gravitational redshift. Geodetic models can predict this redshift with an uncertainty of several 10^{-18}, *i.e.* several centimeters on the clocks' positions with respect to a common reference geoid. When laboratories are able to compare remote clocks with uncertainties in the low 10^{-18}, these comparisons will therefore contribute previously unknown information to geophysicists [11].

Satellite comparisons methods are limited to a resolution around 10^{-16}, reached after several weeks of integration. Applications of remote optical clocks comparisons therefore require new comparison methods. For this purpose, optical fiber links are being deployed at continental scale between laboratories, especially in Europe where several of these links are being operated. These

links make use of an infrared laser as a transfer laser, sent back and forth in the link in order to measure and actively cancel the phase fluctuations in the fibers, by comparing the phase of the laser sent into the fiber with the phase of the laser coming back from the fiber. Repeater and regeneration stations are necessary to overcome the problem of the large attenuation in the fibers, and to overcome the limitation on the bandwidth of the active compensation of phase fluctuations set by the round-trip delay in the fiber.

A link between LNE-SYRTE and PTB has been used for the first time in 2015 to compare remote strontium optical lattice clocks [12]. The statistical resolution reached a few 10^{-17} after a mere hour of measurements, that is to say one order of magnitude better than satellite methods, and two orders of magnitude faster. This comparison enabled to evaluate the frequency difference to:

$$\frac{\nu_{\mathrm{Sr_{PTB}}} - \nu_{\mathrm{Sr_2}}}{\nu_{\mathrm{Sr}}} = (4.7 \pm 5.0) \times 10^{-17} \tag{2}$$

To reach this agreement, a correction of the gravitational redshift of $(-247.4 \pm 0.4) \times 10^{-17}$ was applied, independently determined by geodetic models. This comparison was the first all-optical international agreement between two optical clocks. Along with a similar comparison between SYRTE and NPL, this comparison already contributed to a first test of special relativity with optical fiber links [13]

5 Contributing to international time scales with optical clocks

The last component of the clock architecture proposed in this paper is the first contribution of an optical frequency standard to TAI. While cesium clocks routinely contribute to TAI, calibration reports from the rubidium fountain clock at SYRTE has been the only contribution so far with a secondary representation of the SI second. Before the SI second can be redefined, it is however necessary that optical standards used in practice for the calibration of TAI. However, such calibrations are challenging, as calibration intervals are composed of multiple of five continuous days. SYRTE has reported five calibration reports spanning from 2014 to 2016, with calibration intervals ranging from 10 to 20 days. This first calibration has been accepted by the BIPM, as a non steering contribution. It shows that optical clocks are closer to supersede microwave clocks.

Acknowledgments

This paper gathers several experimental achievements conducted by many contributors at SYRTE, LPL, PTB and NPL. These authors are listed in the relevant publications [7,12,9,13].

References

1. M. Abgrall, B. Chupin, L. De Sarlo, J. Guéna, P. Laurent, Y. Le Coq, R. Le Targat, J. Lodewyck, M. Lours, P. Rosenbusch, G. D. Rovera, and S. Bize. Atomic fountains and optical clocks at SYRTE: Status and perspectives. *Comptes Rendus Physique*, 16(5):461 – 470, 2015.
2. T.L. Nicholson, S.L. Campbell, R.B. Hutson, G.E. Marti, B.J. Bloom, R.L. McNally, W. Zhang, M.D. Barrett, M.S. Safronova, G.F. Strouse, et al. Systematic evaluation of an atomic clock at 2×10^{-18} total uncertainty. *Nature communications*, 6:6896, 2015.
3. Ichiro Ushijima, Masao Takamoto, Manoj Das, Takuya Ohkubo, and Hidetoshi Katori. Cryogenic optical lattice clocks. *Nature Photonics*, 9(3):185–189, 2015.
4. N. Huntemann, C. Sanner, B. Lipphardt, Chr. Tamm, and E. Peik. Single-ion atomic clock with 3×10^{-18} systematic uncertainty. *Phys. Rev. Lett.*, 116:063001, Feb 2016.

5. M Schioppo, RC Brown, WF McGrew, N Hinkley, RJ Fasano, K Beloy, TH Yoon, Gianmaria Milani, D Nicolodi, JA Sherman, et al. Ultrastable optical clock with two cold-atom ensembles. *Nature Photonics*, 11:48, 2017.
6. Sebastian Häfner, Stephan Falke, Christian Grebing, Stefan Vogt, Thomas Legero, Mikko Merimaa, Christian Lisdat, and Uwe Sterr. 8×10^{-17} fractional laser frequency instability with a long room-temperature cavity. *Opt. Lett.*, 40(9):2112–2115, 2015.
7. J. Lodewyck, S. Bilicki, E. Bookjans, J.-L. Robyr, C. Shi, Vallet G., R. Le Targat, D. Nicolodi, Y. Le Coq, J. Guéna, Abgrall M., P. Rosenbusch, and S. Bize. Optical to microwave clock frequency ratios with a nearly continuous strontium optical lattice clock. *Metrologia*, 53(4):1123, 2016.
8. R. Le Targat, L. Lorini, Y. Le Coq, M. Zawada, J. Guéna, M. Abgrall, M. Gurov, P. Rosenbusch, D. G. Rovera, B. Nagórny, R. Gartman, P. G. Westergaard, M. E. Tobar, M. Lours, G. Santarelli, A. Clairon, S. Bize, P. Laurent, P. Lemonde, and J. Lodewyck. Experimental realization of an optical second with strontium lattice clocks. *Nature Communications*, 4:2109, 2013.
9. R Tyumenev, M Favier, S Bilicki, E Bookjans, R Le Targat, J Lodewyck, D Nicolodi, Y Le Coq, M Abgrall, J Guéna, L De Sarlo, and S Bize. Comparing a mercury optical lattice clock with microwave and optical frequency standards. *New Journal of Physics*, 18(11):113002, 2016.
10. Kazuhiro Yamanaka, Noriaki Ohmae, Ichiro Ushijima, Masao Takamoto, and Hidetoshi Katori. Frequency ratio of ^{199}Hg and ^{87}Sr optical lattice clocks beyond the si limit. *Phys. Rev. Lett.*, 114:230801, Jun 2015.
11. P. Delva and J. Lodewyck. Atomic clocks: new prospects in metrology and geodesy. *Acta Futura*, 7:67, 2013.
12. C Lisdat, G Grosche, N Quintin, C Shi, SMF Raupach, C Grebing, D Nicolodi, F Stefani, A Al-Masoudi, S Dörscher, et al. A clock network for geodesy and fundamental science. *Nature Communications*, 7:12443, 2016.
13. P. Delva, J. Lodewyck, S. Bilicki, E. Bookjans, G. Vallet, R. Le Targat, P.-E. Pottie, C. Guerlin, F. Meynadier, C. Le Poncin-Lafitte, O. Lopez, A. Amy-Klein, W.-K. Lee, N. Quintin, C. Lisdat, A. Al-Masoudi, S. Dörscher, C. Grebing, G. Grosche, A. Kuhl, S. Raupach, U. Sterr, I. R. Hill, R. Hobson, W. Bowden, J. Kronjäger, G. Marra, A. Rolland, F. N. Baynes, H. S. Margolis, and P. Gill. Test of special relativity using a fiber network of optical clocks. *Phys. Rev. Lett.*, 118:221102, Jun 2017.

TEST OF SPECIAL RELATIVITY USING A FIBER NETWORK OF OPTICAL CLOCKS

P. DELVA and J. LODEWYCK
SYRTE, Observatoire de Paris, PSL Research University, CNRS, Sorbonne Universités, UPMC Univ. Paris 06, LNE, 61 avenue de l'Observatoire, 75014, Paris, France

In this paper we report on a test of special relativity theory [1] using a network of distant optical lattice clocks located in France, Germany and the UK. By exploiting the difference between the velocities of each clock in the inertial geocentric frame, due to their different positions on the surface of the Earth, we can test the time dilation effect. The connection between these clocks, achieved with phase-compensated optical fibers, allows for an unprecedented level of statistical resolution for the comparison of remote atomic clock, making such a test now competitive with the best Ives-Stillwell tests.

1 Introduction

Atomic clocks are today essential for several daily life applications, such as the building of the International Atomic Time (TAI) or Global Navigation Satellite Systems (GNSS) [2]. With the new generation of optical clocks, they reach such accuracy and stability that they are now considered in practical applications for the measurement of gravitational potential differences, thanks to the Einstein effect, or gravitational redshift. Several projects explored the possibilities of using clocks in geodesy or geophysical applications and research [3,4,5,6,7]. This context offers a fantastic opportunity to use atomic clocks to test fundamental physics [8,9,10].

Special Relativity (SR), one of the cornerstones of modern physics, assumes that Lorentz Invariance (LI) is a fundamental symmetry of nature. However, it is believed today that this symmetry could be violated at some level of energy. Moreover, a strong violation of LI at the Planck scale is likely to yield a small amount of violation at low energy, which could be measured with precise experiments [11].

Optical clocks are now the most precise measurement devices. They reach systematic uncertainties of a few 10^{-18}, which can be resolved after a mere few hours of measurement with optical lattice clocks based on trapped neutral atoms [12,13,14,15,16]. Thanks to these unparalleled performances, comparing the resonance frequencies of optical clocks has led to new tests of fundamental physics, such as bounding the time variation of fundamental constants [17,18].

2 The Robertson-Mansouri-Sexl theoretical framework

LI violations are predicted by several theoretical frameworks, categorized as kinematical and dynamical frameworks [11]. In this paper we use the Robertson–Mansouri–Sexl (RMS) kinematical framework [19,20,21,22] which contains only three parameters. It assumes the existence of a preferred frame Σ where light propagates rectilinearly and isotropically in free space with constant speed

c. The ordinary Lorentz transformations from Σ to the observer frame S with relative velocity $\vec{w}$ are generalized to allow for violations of SR:

$$T = a^{-1}(t - c^{-1}\vec{\epsilon}\cdot\vec{x}) \quad (1)$$

$$\vec{X} = d^{-1}\vec{x} - (d^{-1} - b^{-1})(\vec{w}\cdot\vec{x})\vec{w}/w^2 + \vec{w}T \ , \quad (2)$$

where a, b and d are functions of w^2, and $\vec{\epsilon}$ is a w-dependent vector specifying the clock synchronization procedure in S. In the low-velocity limit:

$$a(\vec{w}) = 1 + c^{-2}(\alpha - 1/2)w^2 + \mathcal{O}(c^{-4}w^4) \ , \quad (3)$$

where α is an arbitrary parameter quantifying the LI violation, the value of which is zero in SR.

The RMS framework has been tested with atomic clocks comparisons in the past [23,24]. However, with the advent of heavy-ion storage rings, Ives–Stillwell type experiments [25,26] gave up to now the best constraints with $|\alpha| \lesssim 2.0 \times 10^{-8}$.

3 Comparison of optical clocks

Our test is based on four optical lattice clocks using Sr atoms, two located at LNE-SYRTE, Observatoire de Paris, France [27,28], one at PTB, Braunschweig, Germany [29,30], and one at NPL, Teddington, UK [31]. These clocks are connected by two fiber links, one running from SYRTE to PTB operated in June 2015 [32], and one from SYRTE to NPL operated in June 2016.

In a simplified setup, an optical clock comparison using a phase noise compensated fiber link can be described as a two-way frequency transfer between two observers A and B [33,34,35,36,37]. Observer A emits an electromagnetic signal (e.g. an IR laser) with proper frequency ν_0, received by observer B at a proper frequency ν_1, and partly reflected back to observer A, where it is received with a proper frequency ν_2. The "redshift signal" or de-syntonization is

$$\Delta = \frac{\nu_1 - \nu_0}{\nu_0} - \frac{\nu_2 - \nu_0}{2\nu_0} \ . \quad (4)$$

The first term contains the relativistic redshift between the two observer locations as well as the first order Doppler shift, while the second term contains only the first order Doppler shift, therefore cancelling this term [23]. In addition, this compensation is active by fixing the second term at a known value, realizing a well-known "Doppler cancellation" scheme [35]. The laser frequencies ν_0 and ν_1 are then measured locally by beating with an optical clock at each end of the link.

In the low-velocity limit the de-syntonization can be written as

$$\Delta = \Delta_{cl} + \Delta_\alpha \ , \quad (5)$$

where Δ_{cl} contains the relativistic redshift due to the static part of the gravity potential as well as temporal variations [38]. The LI violating term signal is:

$$\Delta_\alpha = \alpha c^{-2}\left[2\vec{w}\cdot(\vec{v}_A - \vec{v}_B) + \left(v_A^2 - v_B^2\right)\right] + \mathcal{O}(c^{-3}) \ , \quad (6)$$

where $\vec{v}_A$ and $\vec{v}_B$ are respectively the velocities of clocks A and B in the non-rotating geocentric celestial reference system (GCRS). $\vec{w}$ is the velocity of the Earth with respect to a preferred frame, taken as the rest frame of the cosmological microwave background (CMB). The first term of the LI violation in equation (6) varies with a period of one sidereal day as the Earth rotates around its axis. It is therefore possible to bound the LI violating parameter α by looking for daily variations in the relative frequency difference y between remote clocks, located at different longitudes (*i.e.* different orientation of $\vec{v}$) and/or different latitudes (*i.e.* different norms of $\vec{v}$).

Table 1: Fits A to C use the NPL-SYRTE comparison data with A: Sr2 data only; B: SrB data only; C: Sr2 and SrB data combined. Fit D uses the PTB-SYRTE comparison data.

	$\delta t^{\mathrm{SYRTE}}$ (hours)	$\alpha_T^{\mathrm{SYRTE}}$ (10^{-16} K^{-1})	α (10^{-8})
A	–	–	$+3.81 \pm 8.41$
B	–	–	-5.87 ± 7.78
C	–	–	-2.83 ± 6.19
D	4.81 ± 0.25	1.76 ± 0.12	-0.38 ± 1.06

4 Results

We first analyzed the result of the comparison between the clocks at SYRTE and NPL. Between June 10th and 15th 2016, we accumulated about 60 hours of clock comparison data between SYRTE's Sr2 and SrB lattice clocks, and NPL's Sr clock [1]. To search for a violation of LI in the clock comparisons, we consider three different data subsets: A: Sr2 data only; B: SrB data only; C: Sr2 and SrB data combined. The relative frequency difference $y_{\text{NPL-SYRTE}}$ between the NPL Sr clock and the SYRTE Sr clock is corrected from the term Δ_{cl}. The model used to fit the data contains two (for A and B subsets) or three parameters (for C subset):

$$y_{\text{NPL-SYRTE}}(t) = \bar{y}^{\mathrm{i}}_{\text{NPL-SYRTE}} + 2\alpha c^{-2}\vec{w}\cdot[\vec{v}_{\text{SYRTE}}(t) - \vec{v}_{\text{NPL}}(t)] \ , \tag{7}$$

where $\bar{y}^{\mathrm{i}}_{\text{NPL-SYRTE}}$ allows for one or two fractional frequency offsets, depending on the chosen data subset: A: i = {Sr2}; B: i = {SrB}; C: i = {Sr2, SrB}, and α is the LI violating parameter. All parameters are determined in the fitting procedure, along with correlations and uncertainties. Fitting results are given in table 1 for the three cases A to C.

The PTB-SYRTE comparison took place between June 4th and 24th 2015. This comparison, involving SYRTE's Sr2 clock and PTB's stationary Sr clock, is reported in [32]. We use in this paper the data of the second of the two campaigns reported in [32], representing around 150 hours of clock comparison data. An analysis of the PTB-SYRTE comparison data with a model similar to equation (7) (replacing the NPL clock velocity with the PTB clock velocity, and i = {Sr2}) results in a significant bias for the parameter α, five times larger than the 1σ uncertainty on α. A detailed analysis has shown that this effect is probably due to temperature variations in the SYRTE clock laboratory [1]. Therefore, in addition to the LI violation, we included the effect of temperature in the SYRTE clock room, leading to the following model:

$$y_{\text{PTB-SYRTE}}(t) = \bar{y}^{\mathrm{Sr2}}_{\text{PTB-SYRTE}} + y_{T,\text{SYRTE}}(t) + 2\alpha c^{-2}\vec{w}\cdot[\vec{v}_{\text{SYRTE}}(t) - \vec{v}_{\text{PTB}}(t)] \ , \tag{8}$$

where $\bar{y}^{\mathrm{Sr2}}_{\text{PTB-SYRTE}}$ allows for a fractional frequency offset, $y_{T,\text{SYRTE}}$ is the temperature effect model containing two parameters, α_T a temperature coefficient and δt a lag, both to be determined in the fitting procedure, and α is the LI violating parameter. The detailed result of this analysis is given in table 1 – line D. It shows a significant effect of the temperature on the frequency comparison of the order of 10^{-16} K^{-1}, with a lag of around 4.8 hours.

5 Conclusion

By using clock comparisons between four optical clocks at NPL (UK), PTB (Germany) and SYRTE (France), linked by a leading-edge optical fiber network, we are able to put a more stringent bound on the LI violating parameter α of the RMS framework. With 1.1×10^{-8}, α is now by around a factor of two better constrained compared to the best previous determination of this parameter, which was obtained with accelerated ions, and by two orders of magnitude with respect to the best constraint previously obtained by comparing atomic clocks. Moreover, this

bound is purely limited by technical noise sources on the clock systems, which will improve in future comparisons. Projecting the comparison of distant clocks with an instability of $10^{-16}/\sqrt{\tau}$ over several weeks, a reduction in uncertainty of more than one order of magnitude for α is within reach. This shows the significant potential for tests of fundamental physics with networks of optical clocks connected by optical fiber links.

References

1. P. Delva, J. Lodewyck, S. Bilicki, E. Bookjans, G. Vallet, R. Le Targat, P.-E. Pottie, C. Guerlin, F. Meynadier, C. Le Poncin-Lafitte, O. Lopez, A. Amy-Klein, W.-K. Lee, N. Quintin, C. Lisdat, A. Al-Masoudi, S. Dörscher, C. Grebing, G. Grosche, A. Kuhl, S. Raupach, U. Sterr, R. Hill, I. R. Hobson, W. Bowden, J. Kronjäger, G. Marra, A. Rolland, N. Baynes, F. S. Margolis, H. and P. Gill. *Physical Review Letters*, 118(22):221102, 2017.
2. G. Petit, P. Wolf, and P. Delva. In S. M. Kopeikin, editor, *Frontiers in Relativistic Celestial Mechanics - Volume 2: Applications and Experiments*, De Gruyter Studies in Mathematical Physics, pages 249–279. De Gruyter, 2014.
3. P. Delva, U. Kostić, and A. Čadež. *Advances in Space Research*, 47(2):370–379, 2011.
4. P. Delva and J. Lodewyck. *Acta Futura*, 07:67–78, 2013.
5. P. Delva and J. Geršl. *Universe*, 3(1):24, 2017.
6. A. Gomboc, U. Kostić, M. Horvat, S. Carloni, and P. Delva. *Acta Futura*, 07:79–85, 2013.
7. G. Lion, I. Panet, P. Wolf, C. Guerlin, S. Bize, and P. Delva. *Journal of Geodesy*, pages 1–15, 2017.
8. C. Guerlin, P. Delva, and P. Wolf. *Comptes Rendus Physique*, 16(5):565–575, 2015.
9. P. Delva, A. Hees, S. Bertone, E. Richard, and P. Wolf. *Classical and Quantum Gravity*, 32(23):232003, 2015.
10. P. Delva, A. Hees, and P. Wolf. *Space Science Reviews*, pages 1–37, 2017.
11. D. Mattingly. *Living Rev. Relativ.*, 8, 2005.
12. A. D. Ludlow, M. M. Boyd, J. Ye, E. Peik, and P. O. Schmidt. *Rev. Mod. Phys.*, 87:637–701, 2015.
13. I. Ushijima, M. Takamoto, M. Das, T. Ohkubo, and H. Katori. *Nature Photonics*, 9(3):185–189, 2015.
14. T. L. Nicholson, S. L. Campbell, R. B. Hutson, G. E. Marti, BJ Bloom, RL McNally, W Zhang, MD Barrett, MS Safronova, GF Strouse, et al. *Nature communications*, 6:6896, 2015.
15. A. Al-Masoudi, S. Dörscher, S. Häfner, U. Sterr, and C. Lisdat.
16. M. Schioppo, R. C. Brown, W. F. McGrew, N. Hinkley, R. J. Fasano, K. Beloy, T. H. Yoon, G. Milani, D. Nicolodi, J. A. Sherman, N. B. Phillips, C. W. Oates, and A. D. Ludlow. *Nature Photonics*, 11(1):48–52, 2017.
17. N. Huntemann, B. Lipphardt, Chr. Tamm, V. Gerginov, S. Weyers, and E. Peik. *Phys. Rev. Lett.*, 113:210802, 2014.
18. R. M. Godun, P. B. R. Nisbet-Jones, J. M. Jones, S. A. King, L. A. M. Johnson, H. S. Margolis, K. Szymaniec, S. N. Lea, K. Bongs, and P. Gill. *Phys. Rev. Lett.*, 113(21):210801, 2014.
19. H. P. Robertson. *Rev. Mod. Phys.*, 21:378–382, 1949.
20. R. Mansouri and R. U. Sexl. *Gen. Relativ. Gravitation*, 8:497–513, 1977.
21. R. Mansouri and R. U. Sexl. *Gen. Relativ. Gravitation*, 8:515–524, 1977.
22. R. Mansouri and R. U. Sexl. *Gen. Relativ. Gravitation*, 8:809–814, 1977.
23. C. M. Will. *Phys. Rev. D*, 45(2):403–411, 1992.
24. P. Wolf and G. Petit. *Phys. Rev. A*, 56(6):4405–4409, 1997.
25. S. Reinhardt, G. Saathoff, H. Buhr, L. A. Carlson, Andreas Wolf, Dirk Schwalm, Sergei

Karpuk, Christian Novotny, Gerhard Huber, Marcus Zimmermann, et al. *Nat. Phys.*, 3(12):861–864, 2007.
26. B. Botermann, D. Bing, C. Geppert, G. Gwinner, Theodor W. Hänsch, Gerhard Huber, Sergei Karpuk, Andreas Krieger, Thomas Kühl, Wilfried Nörtershäuser, et al. *Phys. Rev. Lett.*, 113(12):120405, 2014.
27. J. Lodewyck, S. Bilicki, E. Bookjans, J.-L. Robyr, Chunyan Shi, Grgoire Vallet, Rodolphe Le Targat, Daniele Nicolodi, Yann Le Coq, Jocelyne Guéna, et al. *Metrologia*, 53(4):1123, 2016.
28. R. Le Targat, L. Lorini, Y. Le Coq, M. Zawada, J. Guéna, M. Abgrall, M. Gurov, P Rosenbusch, DG Rovera, B Nagórny, et al. *Nat. Commun.*, 4:2109, 2013.
29. S. Falke, N. Lemke, C. Grebing, B. Lipphardt, Stefan Weyers, Vladislav Gerginov, Nils Huntemann, Christian Hagemann, Ali Al-Masoudi, Sebastian Häfner, et al. *New J. Phys.*, 16(7):073023, 2014.
30. C. Grebing, A. Al-Masoudi, S. Dörscher, S. Häfner, V. Gerginov, S. Weyers, B. Lipphardt, F. Riehle, U. Sterr, and C. Lisdat. *Optica*, 3:563–569, 2016.
31. I. R. Hill, R. Hobson, W. Bowden, E. M. Bridge, S Donnellan, E A Curtis, and P Gill. *J. Phys. Conf. Ser.*, 723(1):012019, 2016.
32. C. Lisdat, G. Grosche, N. Quintin, C. Shi, SMF Raupach, C Grebing, D Nicolodi, F Stefani, A Al-Masoudi, S Dörscher, et al. *Nature Communications*, 7:12443, 2016.
33. P. A. Williams, W. C. Swann, and N. R. Newbury. *JOSA B*, 25(8):1284–1293, 2008.
34. G. Grosche, O. Terra, K. Predehl, R. Holzwarth, B. Lipphardt, F. Vogt, U. Sterr, and H. Schnatz. *Optics Letters*, 34(15):2270–2272, 2009.
35. G. Grosche. *Optics Letters*, 39(9):2545–2548, 2014.
36. F. Stefani, O. Lopez, A. Bercy, W.-K. Lee, Christian Chardonnet, Giorgio Santarelli, Paul-Eric Pottie, and Anne Amy-Klein. *J. Opt. Soc. Am. B*, 32(5):787, 2015.
37. J. Geršl, P. Delva, and P. Wolf. *Metrologia*, 52(4):552, 2015.
38. C. Voigt, H. Denker, and L. Timmen. *Metrologia*, 53(6):1365, 2016.









SEARCHING FOR SCALAR DARK MATTER USING SIX YEARS OF LNE-SYRTE FOUNTAIN CLOCK COMPARISON DATA

A. HEES[1,2], J. GUÉNA[2], M. ABGRALL[2], S. BIZE[2], P. WOLF[2]

[1] *Department of Physics and Astronomy, University of California, Los Angeles, CA 90095, USA*

[2] *SYRTE, Observatoire de Paris, PSL Research University, CNRS, Sorbonne Universités, UPMC Univ. Paris 06, LNE, 61 avenue de l'Observatoire, 75014 Paris, France*

We use six years of accurate hyperfine frequency comparison data of the dual rubidium and caesium cold atom fountain FO2 at LNE-SYRTE to search for a massive scalar dark matter candidate. Such a scalar field can induce harmonic variations of the fine structure constant, of the mass of fermions and of the quantum chromodynamic mass scale, which will directly impact the rubidium/caesium hyperfine transition frequency ratio. We find no signal consistent with a scalar dark matter candidate but provide improved constraints on the coupling of the putative scalar field to standard matter. Our limits are complementary to previous results that were only sensitive to the fine-structure constant, and improve them by more than an order of magnitude when only a coupling to electromagnetism is assumed.

While thoroughly tested [1], the theory of General Relativity (GR) is currently challenged by theoretical considerations and by galactic and cosmological observations. Indeed, the development of a quantum theory of gravitation or of a theory that would unify gravitation with the other fundamental interactions leads to deviations from GR. These modifications are usually characterized by the introduction of new fields in addition to the space-time metric to model the gravitational interaction. For example, string theory generically predicts the existence of new scalar fields. In addition, in the current cosmological paradigm, some galactic and cosmological observations are explained by the introduction of cold Dark Matter (DM) and of Dark Energy. Little is currently known about these two components that constitute the major part of our Universe. They can be interpreted as new types of matter (although not directly detected so far), as a modification of the gravitational theory or as a combination of the two.

The introduction of non minimally coupled scalar fields additionally to GR (tensor-scalar theories) generally leads to a space-time dependence of fundamental constants, which can then be searched for by experiments that test the Einstein equivalence principle (EEP) like weak equivalence principle (WEP) tests or tests of local position or Lorentz invariance (LPI and LLI) [1]. Such scalar fields could be a candidate for DM and/or dark energy. In several scenarios, a massive scalar field will oscillate at a frequency related to its mass, leading to a corresponding oscillation of fundamental constants [2,3]. Recently atomic spectroscopy of Dy has been used to constrain such oscillations [4] of the fine structure constant (α). In this proceeding, we present limits on possible oscillations of a linear combination of constants (α, quark mass and Λ quantum chromodynamics – QCD – mass scale) using six years of highly accurate hyperfine frequency comparison of Rb and Cs atoms [5]. This provides complementary constraints to those from Dy spectroscopy [4] which is sensitive to α alone. When assuming a variation of α only, our results improve the limits of Van Tilburg *et al* [4] by over an order of magnitude.

1 The model

The model considered is a massive scalar field of DM parametrized by the action

$$S = \frac{1}{c}\int d^4x \frac{\sqrt{-g}}{2\kappa}\left[R - 2g^{\mu\nu}\partial_\mu\varphi\partial_\nu\varphi - V(\varphi)\right] + \frac{1}{c}\int d^4x\sqrt{-g}\left[\mathcal{L}_{\rm SM}(g_{\mu\nu},\Psi) + \mathcal{L}_{\rm int}(g_{\mu\nu},\varphi,\Psi)\right] , \tag{1}$$

with $\kappa = 8\pi G/c^4$ where G is Newton's constant, R the curvature scalar of the space-time metric $g_{\mu\nu}$, φ a dimensionless scalar field, $\mathcal{L}_{\rm SM}$ is the Lagrangian density of the Standard Model of particles depending on the matter fields Ψ and $\mathcal{L}_{\rm int}$ parametrizes the interaction between the scalar field and matter. We consider a quadratic scalar self-interaction $V(\varphi) = 2\frac{c^2}{\hbar^2}m_\varphi^2\varphi^2$ where m_φ has the dimension of a mass, and linear couplings between the scalar field and the matter fields similar to the ones introduced by Damour and Donoghue [6]. The interacting part of the Lagrangian $\mathcal{L}_{\rm int}$ is given by Eq. (12) from Damour and Donoghue [6]

$$\mathcal{L}_{\rm int} = \varphi\Big[\frac{d_e}{4\mu_0}F^2 - \frac{d_g\beta_g}{2g_3}\left(F^A\right)^2 - c^2\sum_{i=e,u,d}(d_{m_i} + \gamma_{m_i}d_g)m_i\bar{\psi}_i\psi_i\Big] , \tag{2}$$

with $F_{\mu\nu}$ the standard electromagnetic Faraday tensor, μ_0 the magnetic permeability, $F^A_{\mu\nu}$ the gauge invariant gluon strength tensor, g_3 is the QCD gauge coupling, β_3 denotes the β function for the running of g_3, m_i the mass of the fermions, γ_{m_i} the anomalous dimension giving the energy running of the masses of the QCD-coupled fermions and ψ_i the fermions spinor. This Lagrangian is parametrized by five dimensionless coefficients $d_e, d_{m_e}, d_{m_u}, d_{m_d}$ and d_g that characterize the coupling between the scalar and standard model fields. It is well known that such a model will induce a violation of the Einstein Equivalence Principle for baryonic matter. In particular, Damour and Donoghue [6] have shown that the particular form of the interacting Lagrangian leads to a linear dependence of 5 constants of Nature with respect to the scalar field: the fine-structure constant α, the fermions' masses m_i (electron, up/down quark) and the QCD mass scale Λ_3.

In a Friedmann-Lemaître-Robertson-Walker space-time, when one is considering time-scales $<< 1/H$, the scalar field will have an oscillating component $\varphi = \varphi_0\cos(\omega t+\delta)$, with $\omega = m_\varphi c^2/\hbar$. This oscillating part of the scalar field behaves similarly to a pressureless fluid at the cosmological scale and can be interpreted as DM whose energy density is given by

$$\rho_{\tilde{\varphi}} = \frac{c^2}{4\pi G}\frac{\omega^2\varphi_0^2}{2} = \frac{c^6}{4\pi G\hbar^2}\frac{m_\varphi^2\varphi_0^2}{2} . \tag{3}$$

If this scalar field is non-minimally coupled to the SM Lagrangian, these oscillations will produce a similar behavior on the fine structure constant, on the masses of the fermions and on the QCD mass scale. Atomic transition frequencies are sensitive to possible variations of the constants of the Standard Model. The variation of the frequency ratio X of two atomic transitions is characterized by $d\ln X = k_\alpha d\ln\alpha + k_\mu d\ln(m_e/m_p) + k_q d\ln(m_q/\Lambda_3)$ where the k's represent sensitivity coefficients [7] that have been computed by Flambaum and coworkers [8,9] for several atomic clock transitions. Therefore, the harmonic evolution of the constants of Nature will induce a similar signature in an atomic frequency ratio, whose amplitude is given by

$$\mathcal{A} = \left[k_\alpha d_e + k_q(d_{\hat{m}} - d_g)\right]\frac{1}{\omega}\left(\frac{8\pi G}{c^2}\rho_{\rm DM}\right)^{1/2} , \tag{4}$$

where we have identified the energy density of the scalar field from Eq. (3) to the local DM energy density $\rho_{\rm DM}$.

In conclusion, a massive scalar field will experience cosmological oscillations and can be identified as DM. If this scalar field is non-minimally coupled to the SM Lagrangian, it will produce similar oscillations in the constants of Nature. This harmonic signature can be searched for by using atomic frequency ratio measurements and the amplitude of this signature is directly related to the frequency ratio sensitivity to the constants of Nature (the k's), to the coupling between the scalar field and the SM (the d_i) and to the local DM energy density.

2 The SYRTE Cs/Rb dual atomic fountain dataset

We use the dual Cs/Rb atomic fountain clock FO2 at LNE-SYRTE that operates simultaneously on both species thereby providing primary (Cs) and secondary (Rb) realizations of the SI second in parallel [10,11,12]. A detailed description of the experimental apparatus can be found in Guéna *et al* [10,11,12], here we only recall the main features. Rb and Cs atoms are simultaneously laser-cooled, launched, state-selected, and probed with the Ramsey interrogation method, and finally selectively detected using time resolved laser-induced fluorescence, in the same vacuum chamber (see e.g. Fig. 2 of Guéna *et al* [11]). The $|F = 1, m_F = 0\rangle \rightarrow |F = 2, m_F = 0\rangle$ hyperfine transition frequency of ^{87}Rb at ≈6.8 GHz and the $|F = 4, m_F = 0\rangle \rightarrow |F = 3, m_F = 0\rangle$ hyperfine transition frequency of ^{133}Cs at ≈9.2 GHz are simultaneously measured against the same ultrastable microwave reference at the 1.6 s fountain cycle, corrected for all known systematic effects (cold collisions, 2nd order Zeeman shifts, Blackbody radiation, etc... [11,12]), and then averaged over synchronous intervals of $\Delta t_0 = 864$ s duration.

Our data set consists of measurements of the Rb/Cs hyperfine frequency ratio spanning November 2009 to February 2016 with some gaps due to maintenance and investigation of systematics (overall duty cycle of ≈ 45% over more than six years, see Fig. 1 from Hees *et al* [5]). The noise is roughly stationary over the complete data set, and characterized by white frequency noise with two different amplitudes depending on the averaging time (see Fig. 7 and related discussion in Guéna *et al* [12]). This behavior is well understood and reproducible. It results from the operation of FO2 with atom numbers that are intentionally varied in order to correct for the collisional frequency shifts [12].

3 Data analysis and results

Our goal is to search for a sinusoidal signature in the Rb/Cs atomic frequency ratio measurements. Our methodology is fully described in Hees *et al* [5] and consists in using a Lomb-Scargle periodogram [13]. For each frequency considered, we can estimate the normalized power spectrum

$$P(\omega) = \frac{N_o}{4\sigma_o^2(\omega)}\mathcal{A}_\omega^2\,, \tag{5}$$

where N_o is the number of measurements and $\sigma_o^2(\omega)$ is their estimated variance and $\mathcal{A}_\omega$ is the amplitude of the harmonic signal with angular frequency ω fitted to the data. In addition, a detection threshold has been estimated. This threshold is defined as the ensemble of power levels (for each frequency) such that the statistical probability of finding at least one power larger than that level in case of only noise is smaller than $p_0 = 5\%$, i.e. if at any frequency we find a value of the power spectrum larger than this threshold value and interpret it as a detection, the probability of it being a false detection is less than 5%.

In the left of Fig. 1, we present the results of this analysis for the Rb/Cs data set. Since the measured power spectrum is always smaller than the corresponding detection threshold, we conclude that there is no evidence of a harmonic modulation in our data.

We can now transform our power spectrum into limits on $d_e + k_q/k_\alpha(d_{\hat{m}} - d_g) = d_e + 0.043(d_{\hat{m}} - d_g)$ using Eqs. (4) and (5). The right panel of Fig. 1 shows our 95% confidence upper bound on this combination as a function of the scalar field mass $m_\varphi = \hbar\omega/c^2$. We can exclude couplings larger than 5.3×10^{-4} at any m_φ within our range, with our most stringent limit being as low as 3.8×10^{-9} at $m_\varphi = 1.4 \times 10^{-23}$ eV/c^2. Our limits are complementary to those of Van Tilburg *et al* [4] and also to those coming from tests of the weak equivalence principle [6] as they probe different combinations of the coupling constants d_i. If we assume that the scalar field is coupled only to electromagnetism (only $d_e \neq 0$) then our limits improve those of Van Tilburg *et al* [4] by more than one order of magnitude.

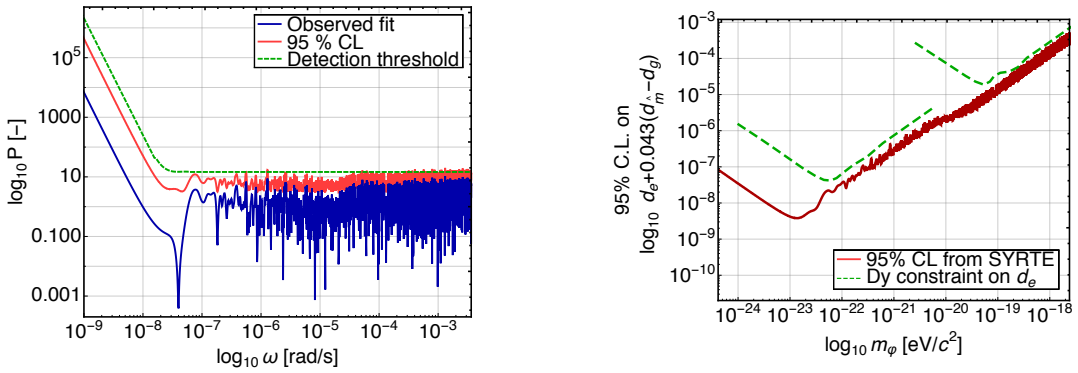


Figure 1 – Left: Normalized power spectrum (blue) obtained from the best-fit (see Eq. (5)) with the corresponding 5% detection threshold (see text). The red line corresponds to the maximum allowed signal at 95% confidence. Right: 95% confidence upper limit on the linear combination $d_e + 0.043(d_{\hat{m}} - d_g)$ of coupling constants d_i between a massive scalar field and standard matter fields as a function of scalar field mass. The red dashed line represents the 95% confidence upper bound obtained with Dy atoms in Van Tilburg *et al*[4], which is only sensitive to d_e.

4 Conclusion

In conclusion, massive scalar fields are a possible candidate for dark matter, and can be searched for by searching for a harmonic oscillation of fundamental constants, which in turn leads to an oscillation of frequency ratios of atomic transitions. We have presented such a search, using over six years of precision measurements of the Rb/Cs ground state hyperfine frequency ratio at LNE-SYRTE. We see no evidence for an oscillating massive scalar field, but set upper limits on a linear combination of coupling constants between such a field and standard matter. Our results are complementary to previous measurements which constrain other parameter combinations, and improve previous results by over an order of magnitude when allowing only coupling to electromagnetism [5]. The rapid progress of atomic clocks over the last years will allow similar searches with other types of transitions. That will further limit the parameter space for massive scalar fields as dark matter candidates and their coupling to standard matter.

Acknowledgments

AH thanks the organizers for financial support to attend the conference.

References

1. C. Will, *Living Rev. Relativ.* **17**, 4 (2014).
2. A. Arvanitaki, J. Huang, K. Van Tilburg, *Phys. Rev.* D **91**, 015015 (2015).
3. Y. V. Stadnik, V. V. Flambaum, *Phys. Rev. Lett.* **115**, 201301 (2015).
4. K. Van Tilburg *et al*, *Phys. Rev. Lett.* **115**, 011802 (2015).
5. A. Hees *et al*, *Phys. Rev. Lett.* **117**, 061301 (2016).
6. T. Damour, J. Donoghe, *Phys. Rev.* D **82**, 084033 (2010).
7. V. V. Flambaum *et al*, *Phys. Rev.* D **69**, 115006 (2004).
8. V. V. Flambaum *et al*, *Phys. Rev.* C **73**, 055501 (2006).
9. V. A. Dzuba, V. V. Flambaum, *Phys. Rev.* A **77**, 012515 (2008).
10. J. Guéna *et al*, *IEEE Transactions on Ultrasonics, Ferroelectrics and Frequency Control* **57**, 647 (2010).
11. J. Guéna *et al*, *IEEE Transactions on Ultrasonics, Ferroelectrics and Frequency Control* **59**, 391 (2012).
12. J. Guéna *et al*, *Metrologia* **51**, 108 (2014).
13. J. D. Scargle, *Astroph. Journal* **263**, 835 (1982).

LOW-ENERGY TESTS OF LORENTZ SYMMETRY: NEW CONSTRAINTS WITH NUCLEONS IN A COLD ATOM CLOCK

C. GUERLIN[1,2], H. PIHAN-LE BARS[2], R.-D. LASSERI[3], J.-P. EBRAN[4], Q. G. BAILEY[5], S. BIZE[2], E. KHAN[3], P. WOLF[2]

[1]*Laboratoire Kastler Brossel, ENS-PSL Research University, CNRS, UPMC-Sorbonne Universités, Collège de France, 75005 Paris, France*

[2]*SYRTE, Observatoire de Paris, PSL Research University, CNRS, Sorbonne Universités, UPMC Univ. Paris 06, LNE, 75014 Paris, France*

[3]*Institut de Physique Nucléaire, Université Paris-Sud, IN2P3-CNRS, F-91406 Orsay Cedex, France*

[4]*CEA, DAM, DIF, F-91297 Arpajon, France*

[5]*Embry-Riddle Aeronautical University, 3700 Willow Creek Road, Prescott, Arizona 86301, USA*



We report on a Lorentz invariance test with nucleons in a cold atom ^{133}Cs clock using spin-polarized states. We analyze this test in the Standard Model Extension framework, and improve by up to 13 orders of magnitude the constraints on some coefficients parametrizing Lorentz violations.

1 Introduction

We analyze the boost and orientation dependence of the transition frequency in a Cs fountain clock and put constraints on one possibe type of Lorentz Invariance violation (LIV) from the Standard Model Extension (SME) framework. The $\overline{c}_{\mu\nu}$ coefficient of the SME framework describes an anisotropy of the dispersion relation of electrons, protons, neutrons. Since atomic states energies depend on the bound kinetic energy, in the case of a non-isotropic density distribution of an atomic eigenstate, the energy of this state will depend on its orientation in space if $\overline{c}_{\mu\nu}$ LIV terms are non-zero. This deviation will scale with the momentum anisotropy of the wavefunction, and more precisely with its momentum quadrupole moment [1,2]. This type of test has been interpreted elsewhere as an analogue of Michelson-Morley test for a standing matter wave [3].

The Standard Model extension is an effective field theory which modifies the dynamics equations for the Standard Model and General Relativity fields at the level of the Lagrangian. For each mass dimension, only a finite number of terms exist that preserve the invariance under a change of coordinate but not the invariance under a frame change. The minimal Standard Model Extension, in which we realize our analysis, describes the set of LIV terms that are power-counting renormalizable (operators of mass dimensions 3 and 4). All LIV terms are controlled by tensor coefficients, supposed to be constant in an

inertial frame. They are allowed to be species dependent. These terms give rise to a rich phenomenology which covers effects ranging from Weak Equivalence Principle violation (see e.g. the article by H. Pihan-Le Bars in these proceedings [4]) to modified dispersion relations. This last type is explored in the present test with nucleon standing matter waves in the nucleus of ^{133}Cs. Analyzing the boost and orientation dependence of spin-polarized hyperfine transitions as the experiment daily rotates around Earth's rotation axis and annually orbits around the Sun, with the help of a more detailed trajectory description and nucleus modelization, we improve the constraints on several proton and neutron SME parameters by up to 13 orders of magnitude [5].

2 Principle of the experiment

We analyse data taken with the fountain FO2 at SYRTE operated with ^{133}Cs. Experimental details on the fountain set-up can be found in [6]. The usual transition used for the clock operation is the ground state hyperfine transition between the $m_F = 0$ states as it does not suffer from first order Zeeman shift, proportional to the magnetic field and to the value of m_F. However on this transition there is no differential shift from the SME LIV model. Thus we interrogate the clock on transitions between spin-polarized states. In order to reject the first order Zeeman systematic shift, we form a combination of transition frequencies with opposite first order Zeeman shift: $\nu_c = \nu_3 + \nu_{-3} + \nu_0$ where ν_i is the frequency of the transition $|F = 3, m_F = i\rangle \longrightarrow |F = 4, m_F = i\rangle$. In our test the clock is operated alternatively on these three transitions. Our observable is evaluated every 4 seconds.

Such data were taken during two sets of more than 10 days separated approximately by half a year interval [7]. The noise is white with a 3 mHz standard deviation. If fitting a single sinusoid on these data, for its amplitude we would reach a frequency resolution of 60 μHz. Prior to data analysis we correct for a constant -2 mHz offset from the second order Zeeman shift.

3 Model improvements

A first analysis of these data was previously done [7]. Here we bring large improvements to these results by two ways: we improve the description of the clock's frame evolution, and we use a more refined nuclear model than the Schmidt model usually used so far.

The latter describes the nucleus as shells, which is not realistic for large nuclei as the one of ^{133}Cs. Instead we use here the self-consistent relativistic mean-field (SCRMF) method, which provides a relativistic microscopic description of the nucleus with free parameters calibrated on a set of benchmarking nuclei [5]. From this we can calculate the nuclear density as shown on Fig. 1; the anisotropy of the nuclear wavefunctions can be seen on this picture. The quantity relevant for the SME model is the total momentum quadrupole moment from the N_w particles of type w with $w = p, n$ for proton, neutron:

$$\widetilde{M}_{20}^{w} = -\sum_{N=1}^{N_w} \langle I, I| \, \hat{\boldsymbol{p}}^2 - 3\hat{p}_z^2 \, |I, I\rangle$$

with I the nuclear angular momentum. The results of this method are compared to two other nuclear models recently used for SME tests and agree with the most advanced one. Unlike the Schmidt model which only accounts for the sensitivity to the proton, the SCRMF model includes the contribution from the neutron, though it appears to be 2 orders of magnitude suppressed.

The other improvement is involved when expressing the observable in terms of Sun centered celestial equatorial frame (SCCEF) SME coefficients, which involves a Lorentz transformation betweeen the SCCEF and the lab frame. This transformation was previously done at first order in v/c with v the relative velocity between the two frames, leading to a sensitivity on 8 of the 9 SME coefficients. Here we include the second order, which gives sensitivity to the ninth coefficient $\bar{c}_{TT}$, the isotropic component of the tensor, which is also the less constrained component.

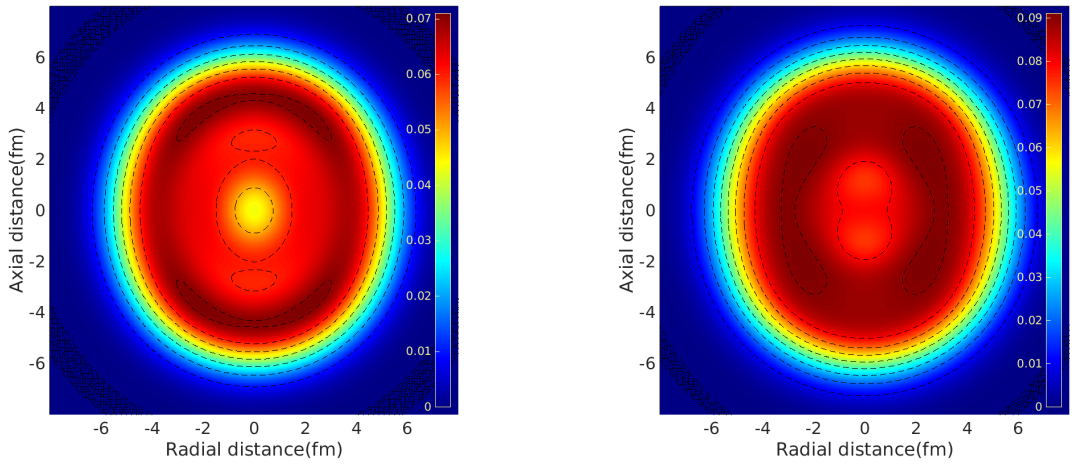


Figure 1 – Nucleonic density distriution in configuration space for ^{133}Cs calculated by SCRMF: protons (left) and neutrons (right).

4 Data analysis and results

With our model, the LIV SME shift of our observable can be expressed as:

$$\delta\nu_c = -\frac{9}{7h}\left[\frac{\widetilde{M}^p_{20}}{6m_p^2c^2}\tilde{c}^p_q + \frac{\widetilde{M}^n_{20}}{6m_n^2c^2}\tilde{c}^p_n\right]$$

where for each particle $\tilde{c}_q$ is one of the nine combinations of $\bar{c}_{\mu\nu}$ coefficients, expressed in the lab frame. When this expression is expressed in terms of SME SCCEF coefficients, it involves the 9 components of the $\bar{c}_{\mu\nu}$ tensor. The complete expression is long; its structure is described in [7].

We realize a least-squares fit to adjust directly (and simultaneously) the value of the 9 SCCEF SME coefficients. This allows to account for correlations between the 9 coefficients, unlike most previous SME analyses. We separately fit this model on data taken for the systematics calibration (residual first order Zeeman effect).

The result of the fit is shown on Table 1. All coefficients can be disentangled, although some correlations remain. For each coefficient, the relative contribution from the neutron and proton respectively can not be disentangled. We convert the results in terms of maximal sensitivity (used also in the Data Tables referencing yearly all current experimental best constraints [8]). As can be seen in the table, we improve several coefficients by up to 13 orders of magnitude over state of the art.

5 Conclusion and prospects

Clocks have the advantage of combining a high frequency resolution and systematics that are well controlled and calibrated. This allows us to use the long term stability of the clock to fit annual variations, which combined with an improved velocity description gives access in this analysis to the SME isotropic coefficient $\bar{c}_{TT}$. Thanks to a more advanced nuclear model, we also improve the constraints on neutron coefficients. In the future, this constraints will possibly be improved when analyzing future data from the ACES mission [9], thanks to a different orbital geometry.

We tentatively analyze the impact of these results for fundamental physics. Although all electron coefficients where previously constrained below the Planck suppressed scale (defined in [10] as the ratio of electroweak energy to Planck energy $E_{ew}/E_P \sim 10^{-17}$), it was not the case of all proton and neutron coefficients. With our analysis all remaining coefficients uncertainties are brought under or much closer to that scale. It can be seen as challenging the level of suppression expected for a low-energy effective

Table 1: Limits (1 sigma) on SME Lorentz violating parameters $\tilde{c}^{w}_{\mu\nu}$ for the proton and neutron, in GeV, when using SCRMF nuclear model. The last two columns show the corresponding maximal sensitivities on each nucleon as defined in [8] (2 sigma limits logarithmically rounded). In bold are the values which improve over the state-of-the-art laboratory limits published in the 2017 version of [8] and obtained with other experiments, with in bracket the improvement in orders of magnitude.

Coefficient	Value and uncertainty	Unit (GeV)	$\tilde{c}^{p}_{\max}$(GeV)	$\tilde{c}^{n}_{\max}$(GeV)
$\tilde{c}^{p}_{Q} + 0.021\ \tilde{c}^{n}_{Q}$	0.4 ± 2.8	10^{-22}	10^{-21}	$\mathbf{10^{-20(7)}}$
$\tilde{c}^{p}_{-} + 0.021\ \tilde{c}^{n}_{-}$	-0.2 ± 1.2	10^{-23}	10^{-23}	10^{-21}
$\tilde{c}^{p}_{X} + 0.021\ \tilde{c}^{n}_{X}$	2.0 ± 7.0	10^{-24}	10^{-23}	10^{-21}
$\tilde{c}^{p}_{Y} + 0.021\ \tilde{c}^{n}_{Y}$	-1.1 ± 2.2	10^{-24}	10^{-23}	10^{-22}
$\tilde{c}^{p}_{Z} + 0.021\ \tilde{c}^{n}_{Z}$	-1.3 ± 5.2	10^{-24}	10^{-23}	10^{-21}
$\tilde{c}^{p}_{TX} + 0.021\ \tilde{c}^{n}_{TX}$	2.0 ± 7.6	10^{-20}	10^{-19}	$\mathbf{10^{-17(12)}}$
$\tilde{c}^{p}_{TY} + 0.021\ \tilde{c}^{n}_{TY}$	-1.8 ± 7.8	10^{-20}	10^{-19}	$\mathbf{10^{-17(12)}}$
$\tilde{c}^{p}_{TZ} + 0.021\ \tilde{c}^{n}_{TZ}$	1.4 ± 4.6	10^{-21}	10^{-19}	$\mathbf{10^{-18(13)}}$
$\tilde{c}^{p}_{TT} + 0.021\ \tilde{c}^{n}_{TT}$	-2.2 ± 9.1	10^{-16}	$\mathbf{10^{-15(4)}}$	$\mathbf{10^{-13(2)}}$

field theory derived from Planck scale Lorentz violations. Alternatively, if one assumes the existence of an intermediate energy scale for new physics, SME limits such as ours put an upper limit for it (see the analysis in [11]), complementary to explorations made with high energy devices.

References

1. V. A.Kostelecký and C. D. Lane, *Phys. Rev.* D **60**, 116010 (1999).
2. R. Bluhm, V. A. Kostelecký, C. D. Lane and N. Russel, *Phys. Rev.* D **68**, 125008 (2003).
3. T. Pruttivarasin *et al*, Nature **517**, p. 592-595 (2015).
4. H. Pihan-Le Bars *et al*, this volume.
5. H. Pihan-Le Bars *et al*, *Phys. Rev.* D **95**, 075026 (2017).
6. J. Guéna *et al*, IEEE Trans. Ultrason. Ferroelectr. Freq. Control **59**, 391 (2012).
7. P. Wolf *et al*, *Phys. Rev. Lett.* **96**, 060801 (2006).
8. V. A. Kostelecký and N. Russell, Rev. Mod. Phys **83**, 11 (2011); arXiv:0801.0287v10.
9. P. Laurent, D. Massonnet, L. Cacciapuoti and C. Salomon, Comptes-Rendus Acad. Sciences **16**, 540 (2015).
10. V. A. Kostelecký and R. Potting, *Phys. Rev.* D , 51 (3923)1995.
11. V. V. Flambaum, *Phys. Rev. Lett.* **117**, 072501 (2016).

The Astrometric Gravitation Probe Concept

M. Gai, M.G. Lattanzi, A. Riva, A. Vecchiato, D. Busonero
Ist. Naz. di Astrofisica, Osserv. Astrof. di Torino, V. Osservatorio, 20 - 10025 Pino Torinese (Italy)

The Astrometric Gravitation Probe (AGP) is the concept of a space mission for Fundamental Physics tests in the Solar system, through coronagraphy and Fizeau interferometry for differential astrometry. We describe the science motivation, the proposed mission profile, the instrument concept and the expected performance.

1 Introduction: the AGP science goals

Gravitation is a crucial aspect of Fundamental Physics, and it is being investigated over microscopic to cosmological distances, using many different techniques. The Astrometric Gravitation Probe (AGP) concept, previously presented as GAME [1], aims at a modern rendition of two of Einstein's classical tests of General Relativity (GR), namely the gravitational deflection of light around massive bodies, in particular close to the Sun, and Mercury's excess precession observed on orbit perihelion. AGP is conceived as a modern version of the 1919 Dyson-Eddington-Davidson experiment, based on a space-borne telescope with built-in eclipse provided by a coronagraphic system.

Tests of gravity theories in the weak field conditions valid within the Solar System are usually analysed in the framework of the Parametrised Post-Newtonian (PPN) framework [2], which enables the comparison of several theories through their prediction on the value of a limited number of parameters. Among the PPN parameters, γ and β are of particular interest to Fundamental Physics, for identification of the best gravity theory; they are directly connected, respectively, with the light deflection and the excess orbit precession; in GR, $\gamma = \beta = 1$.

The AGP precision goal on the γ and β PPN parameters and competing models is respectively in the 10^{-8} and 10^{-6} range, improving by one or two orders of magnitude on the expectations on current or near future experiments. Such precision is suitable to detect possible deviations from unity value, associated to generalised Einstein models for gravitation in the weak field limit, with potentially huge impacts on our understanding of the cosmological distribution of dark matter and dark energy from a Solar system scale experiment [3,4]. Precise astrometric measurements are also important in other tests of fundamental physics citeIorio2005,Turyshev2010, since they improve on the ephemeris of the Solar System bodies.

Light deflection reaches a peak value of 1".74 at the edge of the Sun, rapidly decreasing at increasing distance; in order to estimate the γ parameter at the 10^{-6} level or better, μas level measurements of relative positions are required on many thousand stars within few degrees from the Sun. Deflection is also affected by some terms of Standard Model Extension [7] describing specific violation modes of the Lorentz invariance principle, which may therefore be tested at a precision level comparable with that of γ. Besides, high precision measurements of the dynamics within the Solar system, including bodies with different chemical composition, also support a verification of the Weak Equivalence Principle, down to the 10^{-6} level.

The AGP measurement principle is based on the differential astrometric signature on the stellar positions, i.e. based on the spatial component of the effect rather than the temporal component as in the most recent experiments using radio link delay timing variation on the space probe Cassini [8]. The instrument concept is based on multiple field, multiple aperture Fizeau interferometry, observing simultaneously regions close to the Solar limb (requiring the adoption of coronagraphic techniques), and others in opposition to the Sun. The diluted optics approach is selected for achieving an efficient rejection of the scattered solar radiation, while retaining an acceptable angular resolution on the science targets. The design is focused on systematic error control through multiple field simultaneous observation and calibration.

2 Payload and mission operation concept

Ground based eclipse observations, repeated throughout the past century, could not improve on the estimate of light deflection (and γ) beyond the 10% level, because of the short duration of the Sun obscuration, the high background flux from the solar corona, atmospheric turbulence and the limited number of bright stars in the region. The need for a space mission, overcoming such limitations, is suggested by the much quieter environment with respect to the ground.

The AGP measurement concept is shown in Fig. 1: on the left-hand side, a coronagraph, embedded in the payload design, get rid of the direct illumination from the Sun, thus allowing observation of nearby stars, which, due to the gravitational lensing effects associated to light deflection, appear to be displaced away from the Sun centre. The photons follow curved trajectories (dash-dotted lines in figure), but the observer can only deduce that the sources are in the projected directions corresponding to the tangent (dashed lines) at arrival. Without the Sun, the stars would have been observed in the unperturbed positions corresponding to the dotted lines. Ideally, a semi-reflecting mirror would allow simultaneous observation of other stars affected by negligible deflection in the direction opposite to the Sun (dashed lines on the right-hand side in Fig. 1). After six months, the satellite, following the Earth's orbit, is able to observe the same star sets, which now have complementary roles with respect to the deflection, affecting at this time the objects on the right-hand side.

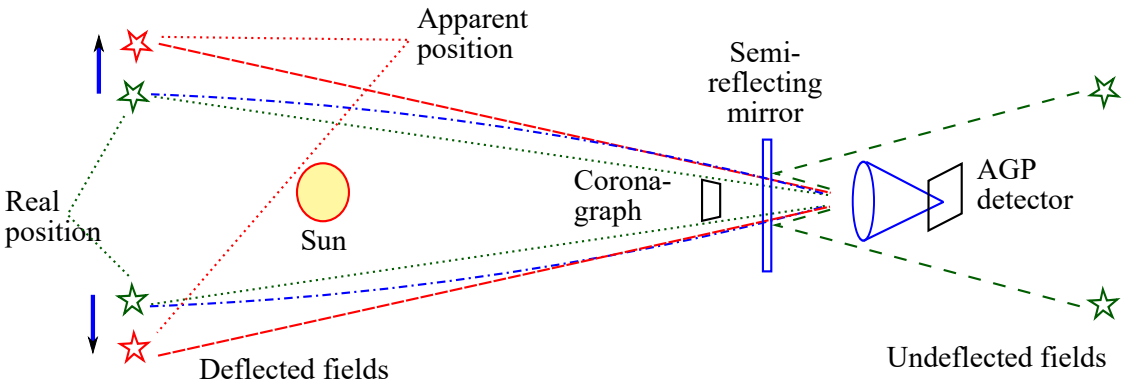


Figure 1 – Principle of AGP operation

The AGP instrument and operation design is based on systematic error minimisation, mainly thanks to differential measurement and symmetry concepts. The simultaneous observation of deflected and undeflected fields is beneficial to measurement efficiency, doubling the number of stars observed, but its main goal is to "encode" most of the instrumental characteristics at any time on both sets of sources (from left and right-hand sides in figure). This should allow clean identification of perturbations, and their efficient suppression in the differential measurement.

Calibration on the sky, which also benefits from the imposed symmetry, allows identification of several error sources in the medium to long time scale, and their suppression in the data

reduction. An on-board metrology system [9] is planned to be included, to improve on rejection of short term instrument variations.

The AGP telescope optical design [10], shown in Fig. 2 for the medium mission implementation, is derived from a classical Korsch three-mirror anastigmatic configuration with two channels (for the two lines of sight on the Sun side), endowed with a multiple aperture coronagraph [11] for Sun disc light rejection, and an actual flat mirror to feed the stellar beams from the undeflected direction. All four viewing directions are multiplexed onto a common detection system, placed "above" and close to the primary mirror, through a set of folding mirrors (FM in figure) to fit within the satellite envelope.

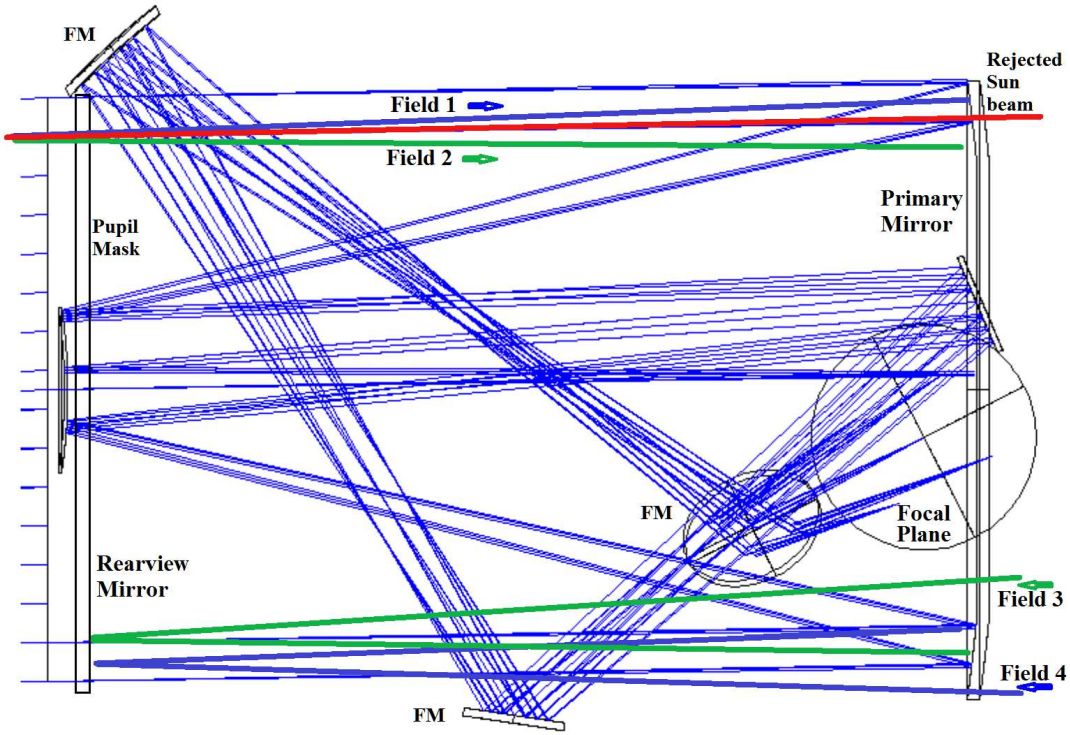


Figure 2 – Instrument optical layout, medium mission; FM: folding mirrors

The detector is a mosaic of 16 CCD imaging detectors, with technology and complexity comparable to the current Gaia [12] and Euclid [13] missions. It covers a sky region of $16' \times 16'$ in each viewing direction, thanks to the field superposition provided by the above multiple channel optical layout.

A helio-synchronous orbit at $\sim 1,500\,km$ altitude provides nearly constant observation, avoiding eclipses, and a stable thermal environment to the AGP payload.

3 Conclusions - expected performance

The AGP concept can, in principle, be implemented at the level of a small to medium class space mission, in the language of the European Space Agency, with performance scaling naturally with instrument size, complexity, and mission duration. In Fig. 3, the improvement of the cumulative precision on light deflection angle is shown as a function of time for two relevant cases, i.e. respectively a small mission (dashed line), with reduced payload size ($0.7\,m$ telescope diameter), smaller focal plane (3×3 CCD detector) and lifetime limited to three years, and a medium mission using a larger instrument ($1.2\,m$ telescope diameter) and operating for a longer period.

Within the framework of a small class mission, with a lifetime of two to three years, the expected final precision is of order of $\sigma(\gamma)/\gamma = 10^{-7}$ and $\sigma(\beta)/\beta = 10^{-5}$, whereas a medium

class mission, operating for five to seven years, would improve to the level $\sigma(\gamma)/\gamma = 10^{-8}$ and $\sigma(\beta)/\beta = 10^{-7}$, depending on a number of implementation options and details.

The AGP roadmap includes a set of technological studies for consolidation of engineering aspects, and above all the dissemination of the experiment concept among the scientific community in order to strengthen the mission goals and achieve adequate support for inclusion of AGP in the implementation plan of the interested space agencies.

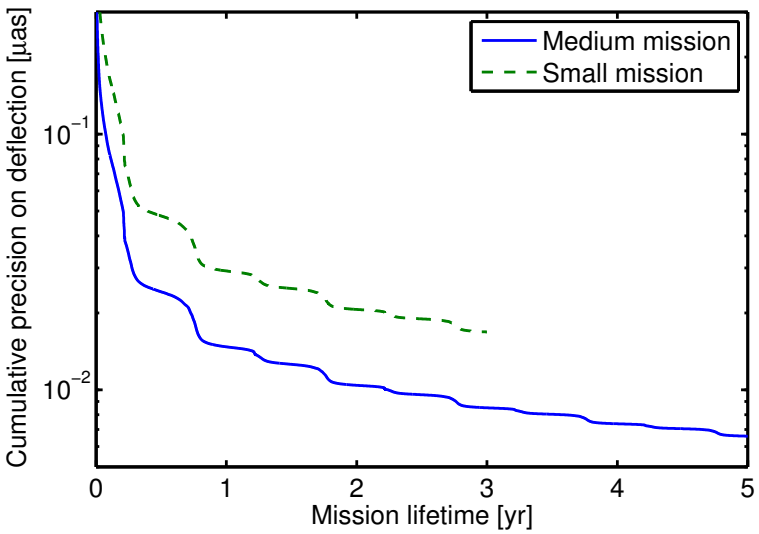


Figure 3 – AGP performance for either small or medium mission implementation cases

Acknowledgments

The AGP support team includes at the moment about 50 colleagues interested on different scientific and technological topics, from several countries in Europe and around the world.

References

1. Gai, M. et al., Exp. Astron., 34, 2, 165 (2012)
2. Will, C.M., Living Rev. Relativity **9**(3) (2006).
3. Damour, T., Piazza, F., Veneziano, G., Phys. Rev. D, 66, 4, id. 046007 (2002)
4. Capozziello, S., Stabile, A., Troisi, A., Mod. Phys. Lett. A, 21, 30, 2291 (2006)
5. Iorio, L., Astron. Astrophys., 433, 1, 385 (2005)
6. Turyshev, S.G. et al., Exp. Astron., 28, 2-3, 209 (2010)
7. Tso, R., Bailey, Q.G., Phys. Rev. D, 84, 8, id. 085025 (2011)
8. Bertotti, B., Iess, L., Tortora, P., Nature, 425, 6956, 374 (2003)
9. Gai, M. et al., Metrology for Aerospace (MetroAeroSpace), IEEE (2015)
10. Riva, A. et al., Proc. SPIE, 9907, 990742 (2016)
11. Landini, F. et al., Proc. SPIE, 9907, 990741 (2016)
12. Gaia collaboration, Astron. Astrophys., 595, id. A1(2016)
13. Racca, G.D. et al., Proc. SPIE, 9904, 99040O (2016)

4.
Tests of Gravity at All Ranges

Casimir-Polder shifts on quantum levitation states

P-P. Crépin, G. Dufour[a], R. Guérout, A. Lambrecht and S. Reynaud
Laboratoire Kastler Brossel, UPMC-Sorbonne Université, CNRS, ENS-PSL Research University, Collège de France, Campus Jussieu case 74, F-75252 Paris, France.

Ultracold atoms can be held in quantum levitation states by the joint effect of gravity and quantum reflection from the attractive Casimir-Polder interaction above a horizontal mirror. We calculate the Casimir-Polder shifts of the energies of these states with a precision sufficient to discuss spectroscopy experiments aiming at tests of the weak equivalence principle on antihydrogen.

Gravitationally bound quantum states have been observed with ultracold neutrons [1,2], but not with neutral atoms. At the low energies corresponding to such bound states, an efficient quantum reflection is produced by the Casimir-Polder (CP) tail above a surface [3,4,5,6], so that quantum levitation states of atoms can be created, where quantum reflection above a horizontal mirror balances gravity [7].

It has recently be proposed to test the weak equivalence principle with antihydrogen by timing its free fall from a trapping device [8]. The precision of this test, of the order of 1%, could be improved by spectroscopic measurements of quantum levitation states of antihydrogen above a material surface, since the properties of these states are essentially determined by gravity [9,10]. However an accurate determination of the acceleration requires a precise evaluation of Casimir-Polder shifts on quantum levitation states [11].

We consider an atom of mass m and energy E bouncing in the gravity potential mgz and reflected on a plane horizontal mirror due to quantum reflection on the CP potential $V_{\rm CP}(z)$. The wavefunction $\psi(z)$ obeys the one-dimensional Schrödinger equation

$$-\frac{\hbar^2}{2m}\frac{{\rm d}^2\psi}{{\rm d}z^2}(z)+V(z)\psi(z)=E\psi(z)\ ,\quad V(z)=mgz+V_{\rm CP}(z)\ , \tag{1}$$

with the potential V depending only on the altitude z of the particle above the mirror sitting at $z=0$. We also suppose that atoms are absorbed when touching the surface, which corresponds to the physical boundary condition for antihydrogen annihilated at contact with matter.

Length and energy scales associated with the Casimir-Polder potential are respectively much smaller and much larger than those associated with the gravitational potential

$$\ell_{\rm g}=\left(\frac{\hbar^2}{2m^2g}\right)^{1/3}\approx 5.87\ \mu{\rm m}\ ,\ \epsilon_{\rm g}=mg\ell_g\approx 0.602\ {\rm peV}\ ,\quad (\text{for } g\approx 9.81\ {\rm m.s^{-2}})\ . \tag{2}$$

An approximate solution of the problem is thus found by decoupling the effects of gravity and CP interactions. For quantum levitation states with low values of the quantum number n, the scattering amplitudes are mainly given by the scattering length a. It follows that the energies E_n^0

[a] *Physikalisches Institut, Albert-Ludwigs-Universität Freiburg, D-79104, Freiburg, Germany*

of an ideal quantum bouncer are all shifted by the same quantity mga resulting from the complex phase shift experienced by the atom upon reflection on the CP tail [9]. Within this *scattering length approximation* where energies are $\mathcal{E}_n^1 = E_n^0 + mga$, the transition frequencies between quantum states are independent of the atom-surface interaction. Spectroscopy experiments thus give a direct access to the value of ϵ_g, that is also g. In the following, we present an exact treatment of the full potential including the effects of gravity and CP interaction, which allows us to assess the accuracy of this approximation. We also give improved numerical and analytical results sufficient for discussing the proposed spectroscopic tests of free fall [9,10].

The Schrödinger equation, rewritten in the following form

$$\psi''(z) + F(z)\psi(z) = 0 \ , \quad F(z) = k_{\rm dB}(z)^2 = \frac{2m}{\hbar^2}\left(E - V(z)\right) \ , \tag{3}$$

with $F(z)$ the square of the de Broglie wavevector $k_{\rm dB}$ can be transformed by a Liouville transformation consisting in a coordinate change $z \to \boldsymbol{z}$ associated with a rescaling $\psi \to \boldsymbol{\psi}$ of the wave-function [12]. The transformed wave function obeys a Schrödinger equation (3) with the transformed $\boldsymbol{F}-$function written in terms of a transformed energy $\boldsymbol{E}$ and potential $\boldsymbol{V}$. Figure 1 shows the original potential landscape and transformed one. The potential $\boldsymbol{V}$ is the sum of a linear gravity potential and an effective potential $\boldsymbol{V}_{\rm CP}(\boldsymbol{z})$ producing quantum reflection. In sharp contrast with the CP well on Figure 1, the transformed potential $\boldsymbol{V}_{\rm CP}$ now shows a high peak close to the surface.

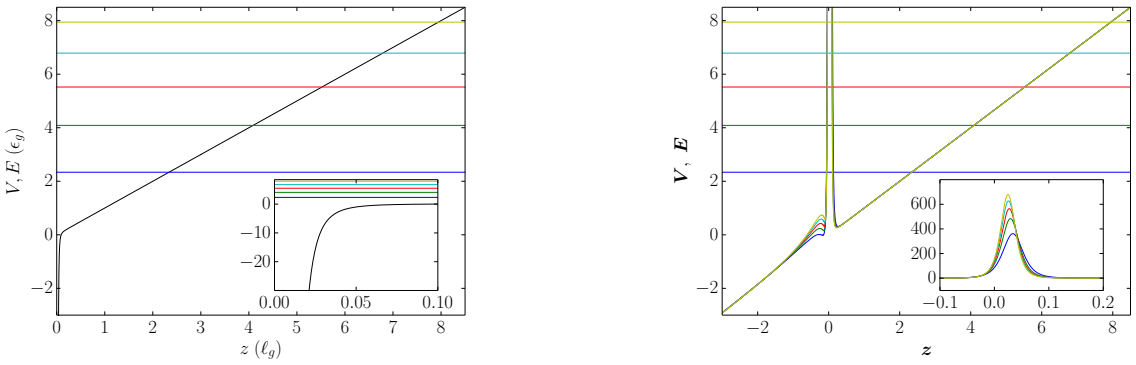


Figure 1 – Left plot: the landscape for antihydrogen atom in gravity and CP potentials above a silica bulk (black curve). Horizontal lines correspond to energies chosen as E_n^0 ($n = 1, ..., 5$ for the blue, green, red, cyan and yellow lines, respectively from bottom to top line). A zoom on the potential well near the surface is shown in the inset. Right plot: the same problem after a Liouville transformation, with energies chosen as $\boldsymbol{E}_n^0$(same color and position codes as for the left plot) and potential $\boldsymbol{V} = \boldsymbol{z} + \boldsymbol{V}_{\rm CP}$. A zoom on the wall is shown in the inset.

With quantum reflection now understood as classically expected reflection on a repulsive wall, we get a new physical picture for quantum levitation states corresponding to matter waves trapped in a Fabry-Perot cavity. Gravity plays the role of the vertical cavity's perfectly reflective top mirror, while quantum reflection corresponds to its partially reflective bottom mirror. We can then interpret the properties of quantum levitation states in terms of cavity resonances.

Above the top mirror, the solution of the Schrödinger equation is given by Airy functions, which are linear superpositions of upward and downward traveling waves Ci^+ and Ci^- ($\boldsymbol{z}_t$ is the position of the classical turning point in the transformed frame)

$$\boldsymbol{\psi}_m(\boldsymbol{z}) = \frac{a_m}{2}\left(\mathrm{Ci}^+(\boldsymbol{z} - \boldsymbol{z}_t) + \mathrm{Ci}^-(\boldsymbol{z} - \boldsymbol{z}_t)\right) \ , \quad \mathrm{Ci}^\pm(\boldsymbol{z}) = \mathrm{Ai}(\boldsymbol{z}) \pm i\,\mathrm{Bi}(\boldsymbol{z}) \ . \tag{4}$$

The amplitude a_m depends on the number m of bounces of the matter wave on the bottom mirror. With the ideal quantum bouncer model, the ideal energy levels E_n^0 would be recovered

by obtaining the stationary quantum solutions of (4). The more general problem studied in this paper is not unitary since atoms transmitted through the bottom mirror are lost.

As a consequence, the quantum levitation states can only be obtained as quasi-stationary states, with the amplitude a_m decreasing after each bounce, due to the losses. In analogy with the theory of optical Fabry-Perot cavities, we introduce a factor describing the modification of the traveling waves after one cavity round trip

$$a_{m+1} = \rho a_m \ , \tag{5}$$

with ρ obtained by solving numerically the quantum reflection problem. We may define energies E_n by requiring $\rho(E_n)$ to be a real number slightly smaller than unity. The value attained for $\rho(E_n)$ is related to the loss at each bounce, that is also the finesse of the cavity resonance. Figure 2 shows energy shifts $E_n - E_n^0$, which are close to the constant value $mg\,\mathrm{Re}(a)$ predicted by the scattering length approximation discussed above with an accuracy of the order of 10^{-4}.

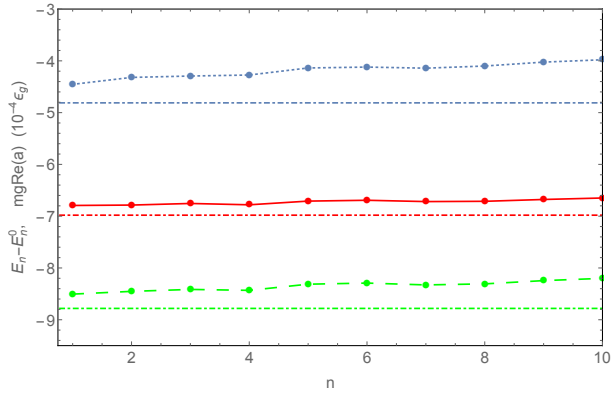


Figure 2 – Energy shift $E_n - E_n^0$ for antihydrogen interacting with a perfect mirror (blue, top lines), a silicon bulk (green, bottom lines) or a silica bulk (red, middle lines), in units of $10^{-4}\epsilon_g$. The constant shift corresponding to the real part of mga is represented by the horizontal lines.

The round trip factor ρ can be approximated as the product of two factors, the quantum reflection amplitude r on the CP tail, and a propagation phase factor deduced from the phase θ of the Airy functions

$$\rho \simeq -re^{2i\theta(-\boldsymbol{z}_t)} \ , \quad \tan\theta(x) = \frac{\mathrm{Ai}(x)}{\mathrm{Bi}(x)} \ , \quad e^{2i\theta(x)} = -\frac{\mathrm{Ci}^-(x)}{\mathrm{Ci}^+(x)} \ . \tag{6}$$

The resonance energies E_n are such that the whole phase on a round trip is an integer multiple of 2π ($2\theta(-\boldsymbol{z}_t) + \arg(-r) = 2n\pi$). We then get an *effective-range approximation* for these energies, which is much more accurate than the scattering length approximation [11].

The reflection coefficient is a function of the wavevector k and a complex length $\mathcal{A}(k)$

$$r = -\frac{1 - ik\mathcal{A}(k)}{1 + ik\mathcal{A}(k)} \ , \quad \hbar k \equiv \sqrt{2mE} \ , \tag{7}$$

with the limit $\mathcal{A}(0)$ being the scattering length a, while $\mathcal{A}(k)$ is now a function of k. For the model potential exactly described by the homogeneous form $V_4 \equiv -C_4/z^4$, the function $k\mathcal{A}$ is a known universal function of the dimensionless parameter $k\ell$. Its expansion at low values of k is

$$k\mathcal{A} = -ik\ell\ \alpha(k\ell) \ , \quad \ell = \frac{\sqrt{2mC_4}}{\hbar} \ , \quad \alpha(K) = \alpha_0 + i\frac{\pi}{3}K + \left(\alpha_2 + \frac{4}{3}\alpha_0 \ln K\right) K^2 \ , \tag{8}$$

with known coefficients $\alpha_0 = 1$ and $\alpha_2 = \frac{8}{3}(\gamma + \ln 2) - \frac{28}{9} - i\frac{2\pi}{3}$ (γ is the Euler constant).

The exact potentials describing CP interaction of an antihydrogen atom with perfectly reflecting surfaces, silicon or silica bulk contain long-range tails V_4 but are not reducible to these

tails. Using the numerical values obtained for $r(k)$ in [13], we deduce $k\mathcal{A}$ by inverting (7) and fit coefficients α_0 and α_2 in (8) to match its low energy expansion. We then solve the resonance energies as solutions of the equation given after eq.(6).

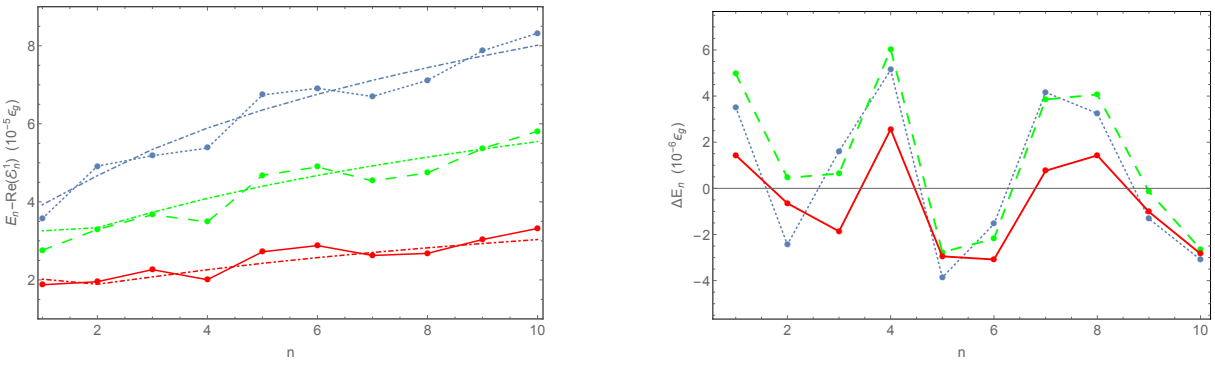


Figure 3 – Left plot : Variation of $E_n - \lambda_n\epsilon_g - mg\,\mathrm{Re}(a)$ for antihydrogen interacting with a perfect mirror (blue top lines), a silicon bulk (green middle lines) or a silica bulk (red bottom lines), in units of $10^{-5}\epsilon_g$. Points are obtained from numerical results and full lines interpolate between points. Dashed curves are analytical solutions in the effective-range approximation. Right plot : Difference ΔE_n between analytical and numerical energies (same color and line codes as on the left plot; units of $10^{-6}\epsilon_g$.

In order to assess the precision of the results, we have drawn on the left plot of Figure 3 the variation of $E_n - \mathrm{Re}\,\mathcal{E}_n^1$, for the first quantum states of antihydrogen. Points are obtained from the numerical results E_n^{num} discussed above for $n = 1, 2, \ldots, 10$ with full lines interpolating between these points. Dashed lines are obtained from the solutions E_n^{ana} of the analytical effective-range approximation (6-7).

For completeness, the differences $\Delta E_n = E_n^{\mathrm{ana}} - E_n^{\mathrm{num}}$ between the analytical and numerical values are also plotted on the right plot of Figure 3. Figure 3 shows small oscillations of the numerical values around the smoother variation obtained from the analytical approximation. These oscillations remain smaller than a few $10^{-6}\epsilon_g$ for the first ten quantum states, which means that the effective-range approximation is sufficient to compute the corrections caused by the CP interaction at this accuracy level.

Conclusion

These results show that the analytical treatment developed in [11] with the effective-range approximation is sufficient to compute the corrections caused by the CP interaction at an accuracy level better than $10^{-5}\epsilon_g$ for the positions of the resonances. This should be sufficient for analyzing spectroscopic tests of the weak equivalence principle with antihydrogen [9,10] up to an accuracy of this order.

Acknowledgements

Thanks are due to M.-T. Jaekel, V.V. Nesvizhevsky, A. Yu. Voronin for insightful discussions and to the GBAR and GRANIT collaborations.

References

1. V. V. Nesvizhevsky, H. G. Borner, A. K. Petukhov, et al. Quantum states of neutrons in the Earth's gravitational field. *Nature*, 415:297–299, 2002.
2. V. V. Nesvizhevsky and A. Yu. Voronin. *Surprising quantum bounces*. Imperial College Press, 2015.

3. F. Shimizu. Specular reflection of very slow metastable neon atoms from a solid surface. *Phys. Rev. Letters*, 86:987–990, 2001.
4. T. A. Pasquini, Y. Shin, C. Sanner, et al. Quantum reflection from a solid surface at normal incidence. *Phys. Rev. Lett.*, 93:223201, 2004.
5. T. A. Pasquini, M. Saba, G.-B. Jo, et al. Low velocity quantum reflection of Bose-Einstein condensates. *Phys. Rev. Letters*, 97:093201, 2006.
6. G. Dufour, A. Gerardin, R. Guerout, et al. Quantum reflection of antihydrogen from the Casimir potential above matter slabs. *Phys. Rev. A*, 87:012901, 2013.
7. J. Madronero and H. Friedrich. Influence of realistic atom wall potentials in quantum reflection traps. *Phys. Rev. A*, 75:022902, 2007.
8. P. Indelicato, G. Chardin, P. Grandemange, et al. The GBAR project, or how does antimatter fall? *Hyperfine Interactions*, 228:141–150, 2014.
9. A. Yu Voronin, P. Froelich, and V. V. Nesvizhevsky. Gravitational quantum states of antihydrogen. *Phys. Rev. A*, 83:032903, 2011.
10. A. Yu Voronin, V. V. Nesvizhevsky, G. Dufour, and S. Reynaud. Quantum ballistic experiment on antihydrogen fall. *J. Phys. B*, 49:054001, 2016.
11. P. P. Crepin, G. Dufour, R. Guerout, A. Lambrecht, and S. Reynaud. Casimir-Polder shifts on quantum levitation states. *Phys. Rev. A*, 95:032501, 2017.
12. G. Dufour, R. Guerout, A. Lambrecht, and S. Reynaud. Quantum reflection and Liouville transformations from wells to walls. *EPL*, 110:30007, 2015.
13. G. Dufour, R. Guerout, A. Lambrecht, and S. Reynaud. Liouville transformations and quantum reflection. *J. Phys. B*, 48:155002, 2015.




Dinner
Menu





Trapped atom interferometry for the study of Casimir forces and Gravitation at short range

F. Pereira dos Santos, X. Alauze, C. Solaro, A. Bonnin
LNE-SYRTE
Observatoire de Paris, PSL Research University, CNRS, Sorbonne Universités, UPMC Univ. Paris 06
61 Avenue de l'Observatoire, 75014 Paris, France



We report on the recent progress on an experiment which aims at measuring short range forces with a high sensitivity force sensor based on trapped atom interferometry. The spatial resolution of the sensor was improved to a few microns by cooling the atomic sample down to ultracold temperatures by evaporative cooling in a crossed dipole trap. Having now in hand a much denser atomic sample, we have to face deleterious effects arising from atomic interactions, which reduce the coherence time of the interferometer. We finally propose how to mitigate these effects in order to preserve the excellent sensitivity of the sensor.

1 Introduction

Cold atom interferometers allow for sensitive and accurate measurements of inertial forces, which make them ideal sensors for a variety of fundamental tests in physics, such as tests of the equivalence principle [1,2], measurements of fundamental constants, such as the fine structure constant [3] and the Newtonian gravitational constant G [4], tests of atom neutrality [5], tests of exotic fields [6] and detection of gravitational waves [7,8]. These measurements are performed in most cases with Raman light pulses interferometers using free falling atoms as tests masses. This configuration is by far the most mature, but is not suited to local measurements because of the motion of the atoms. Instead, we realize here a trapped atom interferometer to be used as a sensor for short range interactions between the atoms and the surface of a mirror. This sensor will allow for sensitive measurements of Casimir-Polder forces and tests of gravity at short range [9].

Our sensor is described in detail in [10,11] and we recall here its main features. We use atoms trapped in the wells of a vertical optical lattice. Raman transitions allow to induce coherent tunneling between neighboring wells. A sequence of two such pulses, acting as a beamsplitter and a recombination pulse, and separated by a free evolution time T, allows to create a Ramsey interferometer with separated arms. The interferometer phase shift is proportional to the difference in potential energy between states separated by typically a ten of wells. Far from the

surface of the mirror which retroreflects the lattice laser, this energy difference is the difference in gravitational potential energy, $\Delta m \times h\nu_B$, where Δm is the difference in well index between the separated states, h the Planck constant and ν_B the Bloch frequency. The Bloch frequency is given by $\nu_B = m_a g\lambda/2h$, where m_a is the mass of the atom (^{87}Rb in our case), g the Earth gravity acceleration and λ the wavelength of the lattice laser.

Using a separation of $\Delta m = 6$ wells and an interferometer time of 2 s, our interferometer reaches a state of the art short term relative sensitivity in the Bloch frequency of 2×10^{-6} at 1s. Operating this sensor close to the surface of the lattice mirror will allow for a very sensitive measurement of short range forces, and more specifically of the Casimir-Polder force with an uncertainty better than the %. Yet, this interferometer was performed so far with atoms distributed in thousands of wells, and does not offer the spatial resolution required for short range measurements.

We describe in this paper our efforts to increase the spatial resolution of the measurement while preserving the sensitivity of the measurement. Evaporative cooling in a crossed dipole trap is performed to decrease the vertical size of the atomic sample, and hence increase drastically the atomic density. We reach a regime of atomic densities where interactions between the atoms play an important role, and constitute a limitation in the coherence of the interferometer. We study quantitatively the contrast loss rate versus the number of atoms and the trap parameters. We show that diluting the cloud in the transverse direction allows to mitigate the effect of the interactions and to improve the sensitivity of the measurement.

2 Preparation of an ultracold atomic sample

To cool down the atoms even further and decrease the size of the sample, we have setup a dipole trap, by crossing two beams of a 100 W Yb fiber laser in the horizontal plane, with an angle of 43°. The two beams are focused onto the atoms with 50μm and 70μm radii at $1/e^2$ and maximum powers of respectively 10 and 20 W. We start by loading within 600 ms 1.5×10^9 atoms in a magneto-optical trap, while ramping up linearly the power of the dipole trap laser up to its maximum power. After the loading of the MOT, the cloud is compressed for 100 ms in a dark mot, by lowering the intensity of the repumper laser. We then turn off the magnetic field of the MOT and the cooling and repumping beams, and trap about 10^7 atoms in the crossed trap predominantly in the $F = 1$ state. We then lower the power of the two beams from 10 and 20 W to 0.23 and 0.12 W within 1.25 s and obtain a sample of 10^5 atoms at a temperature of 300 nK. We end up at a phase space density of about 0.5, not far from degeneracy. At the beginning of the evaporation, we apply a small vertical bias field and the atoms are optically pumped into the $F = 1, m_F = 0$ state with 70 % efficiency with a 1.2 ms long pulse of light tuned on the $F = 1 \rightarrow F' = 0$. We attribute this imperfect pumping to the absorption of the pumping light by the optically thick sample of atoms. In order to purify the sample, we then use at the end of the evaporation a sequence of microwave and pusher pulses. We first drive a microwave pulse which transfers the atoms from $F = 1, m_F = 0$ into $F = 2, m_F = 0$. A subsequent 12 ms long pulse of optical pumping heats up the atoms remaining in $F = 1$, which escape from the trap. A second microwave pulse transfers the atoms from $F = 2, m_F = 0$ back into $F = 1, m_F = 0$. We finally push the small fraction of atoms which remained in $F = 2$ (about 3%).

The atoms are then transferred into a mixed trap, composed of two vertically aligned lasers: a lattice laser (wavelength 532 nm, waist 700 μm) for the vertical confinement and a fiber laser (wavelength 1064 nm, waist 200 μm) for the radial confinement. Both lasers forming the mixed trap are switched on within 0.1 s at the end of the evaporation, before switching off the crossed dipole trap. Finally, we end up in the mixed trap at a lattice depth of $1.8E_r$ with a maximum number of atoms of about 5×10^4 at transverse temperatures in the range 50-500 nK, depending on the power of the IR transverse laser.

3 Effects of atomic interactions on the contrast

The density in the mixed trap is of order of 10^{11} atoms/cm^3, which is 3 orders of magnitude higher than when loading the mixed trap directly from the molasses. In this high density regime, we observe a significant loss of contrast when increasing the number of atoms. This is illustrated with the left graph on figure 1, which displays Ramsey fringes for increasing interrogation times T for two different numbers of atoms.

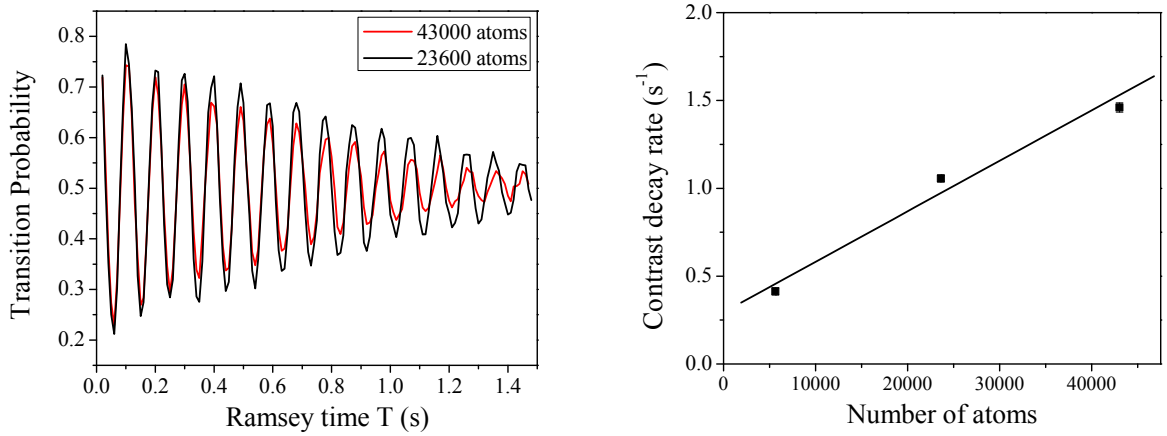


Figure 1 – Ramsey fringes and the contrast decay as a function of the interferometer duration, for two different numbers of atoms.

We have recorded such fringe patterns for various atom numbers, and fitted the contrast decays with an exponential law : $C_0 e^{-\gamma T}$. Loss rates γ are found to increase with the number of atoms, as displayed on the right of figure 1, with a slope β of $2.8(4) \times 10^{-5}\mathrm{s}^{-1}$ per atom, and an offset α of $0.29(12)s^{-1}$. For these measurements, the power in the transverse IR laser is 613 mW. The offset α is comparable to the one previously measured with atoms directly loaded from the molasses [11].

4 Optimizing the short term sensitivity

The relative short term sensitivity on the Bloch frequency at 1 s measurement time is given by

$$\frac{\sigma\nu_B}{\nu_B} = \frac{1}{\Delta m \nu_B} \frac{\sigma_P}{\pi C(T) T} \sqrt{T_c} \tag{1}$$

with σ_P the standard deviation of shot to shot fluctuations of the transition probability, Δm is the separation in units of well, $T_c = T + T_p$ the cycle time and $T_p = 2.3$s the preparation and detection dead time. The contrast $C(T)$ is given by $C_0 e^{-(\alpha+\beta N)T}$.

Assuming a detection noise limited measurement of the transition probability, σ_P is given by

$$\sigma_P^2 = \frac{a^2}{N^2} + \frac{1}{4N} + b^2 \tag{2}$$

where the first contribution is related to electronics noise (such as related to digitization noise, background light or voltage noise of the transimpedance circuit), the second to quantum projection noise and the third to technical noise (such as related to normalization noise or detection laser intensity and frequency noise). A detailed characterization of our detection scheme, based on the measurement of the populations in the two hyperfine states by fluorescence, gives $a = 100$ and $b = 10^{-3}$.

Figure 2 displays for three different numbers of atoms (N_{max}, $N_{max}/3$ and $N_{max}/10$, with $N_{max} = 43000$ the maximum number of trapped atoms) the calculated short term sensitivity

as a function of the interferometer duration T. It shows that for any given number of atoms, there is an optimal interferometer duration which optimizes the short term sensitivity. Because of the detrimental effect of interactions, this optimal performance does not correspond to the combination of the larger number of atoms and the larger interrogation time.

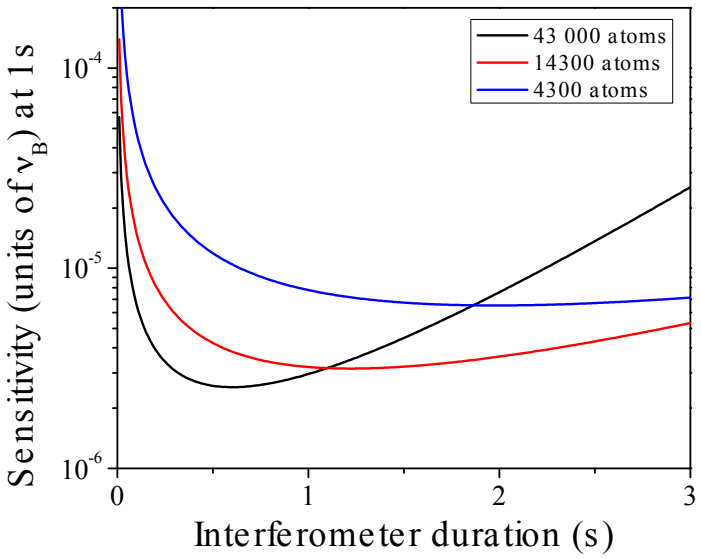


Figure 2 – Expected relative short term sensitivity on the Bloch frequency at 1 s measurement time for three different numbers of atoms

Figure 3 displays the optimal sensitivities one can expect as a function of the optimal interferometer durations, and the corresponding optimal number of atoms. This shows that optimizing the sensitivity at long interrogation times requires reducing the number of atoms.

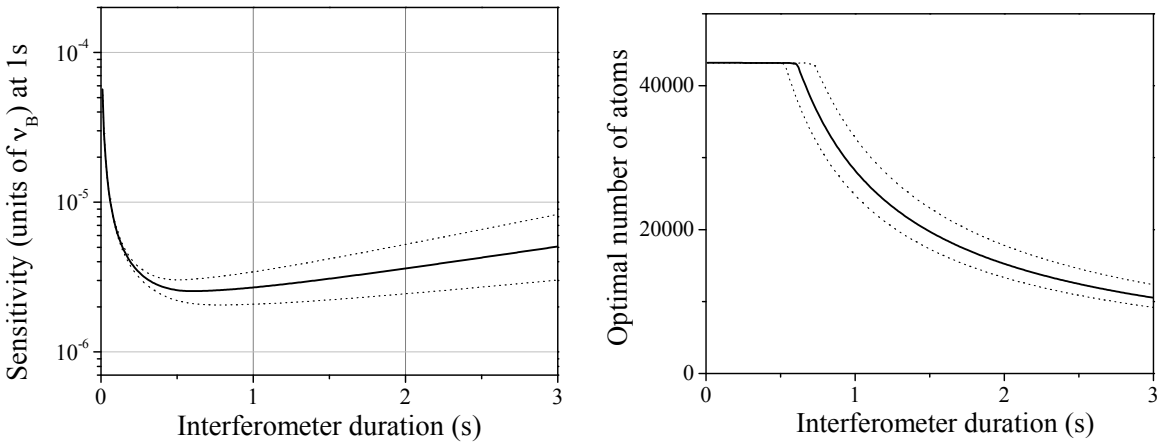


Figure 3 – Left : Optimal sensitivity as a function of the interrogation time. The dotted lines correspond to the limits obtained, given the error bars of the fit of the contast decay. Right: corresponding optimal number of atoms.

We infer a (detection noise limited) best relative short term sensitivity of $2.5(5) \times 10^{-6}$ on the Bloch frequency at an interferometer duration of 0.6 s and for a number of atoms of 43000.

In comparison, we obtain, with the same parameters, a short term sensitivity of 5×10^{-6} at best with our interferometer, which shows that the phase noise in the measurement, originating most probably by vibration noise, lies above the detection noise limit.

5 Improving spatial resolution even further

For the final measurement close to the surface of the mirror, an even better spatial resolution is desirable in the vertical direction. Assuming that we will select the atoms in a single well (out of the 10-20 wells currently populated), the number of atoms will be reduced by an order of magnitude while keeping the same atomic density. This will increase the detection noise without changing the contrast decay rate, and lead to the optimal sensitivity displayed as a blue line on figure 4.

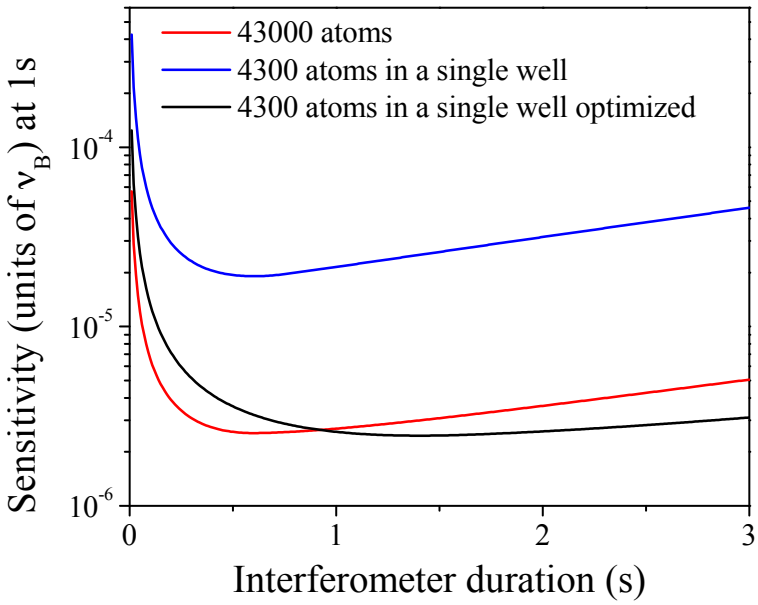


Figure 4 – Optimal sensitivities as a function of the interrogation time, for the initial situation (red curve), for atoms selected in a single well (blue curve), for atoms selected in a single well, optimized detection and reduced density (black curve)

To improve and recover a state of the art sensitivity, the detection noise can be improved down to the level of quantum projection noise, by imaging the cloud on a CCD camera. In addition, the contrast decay rate can be reduced by increasing the waist of the transverse confinement laser: with a twice larger waist of 400μm, the density and hence the decay rate constant β would then be reduced by a factor 4.

Using these asumptions, we now calculate the corresponding optimal short range sensitivities displayed in figure 4 as a black line. This shows that a best short term sensitivity of 2.5×10^{-6} could be obtained close to the surface, for an interferometer duration of 1.5 s. The corresponding optimal number of atoms is found to be about 1000. Such a sensitivity would allow to measure the CP interaction at a distance of 5 μm with a relative uncertainty of 0.1% with a measurement time of only 100 s.

Acknowledgments

We thank Peter Rosenbusch, Wilfried Maineult, and Kurt Gibble for useful discussions. We also acknowledge financial support by the IDEX PSL (ANR-10-IDEX- 0001-02 PSL) and ANR (ANR-13-BS04-0003-01). A. B. thanks the Labex First-TF for financial support.

References

1. Lin Zhou, Shitong Long, Biao Tang, Xi Chen, Fen Gao, Wencui Peng, Weitao Duan, Jiaqi Zhong, Zongyuan Xiong, Jin Wang, and et al. Test of equivalence principle at 10^8 level by a dual-species double-diffraction raman atom interferometer. *Physical Review Letters*, 115(1), Jul 2015.
2. Brett Altschul et al. Quantum tests of the Einstein Equivalence Principle with the STE-QUEST space mission. *Adv. Space Res.*, 55:501–524, 2015.
3. Rym Bouchendira, Pierre Cladé, Saïda Guellati-Khélifa, François Nez, and François Biraben. New determination of the fine structure constant and test of the quantum electrodynamics. *Phys. Rev. Lett.*, 106:080801, Feb 2011.
4. G Rosi, F Sorrentino, L Cacciapuoti, M Prevedelli, and GM Tino. Precision measurement of the newtonian gravitational constant using cold atoms. *Nature*, 510(7506):518–521, 2014.
5. Asimina Arvanitaki, Savas Dimopoulos, Andrew A. Geraci, Jason Hogan, and Mark Kasevich. How to test atom and neutron neutrality with atom interferometry. *Physical Review Letters*, 100(12), Mar 2008.
6. Benjamin Elder, Justin Khoury, Philipp Haslinger, Matt Jaffe, Holger Mller, and Paul Hamilton. Chameleon dark energy and atom interferometry. *Physical Review D*, 94(4), Aug 2016.
7. S. Dimopoulos, P. W. Graham, J. M. Hogan, and M. A. Kasevich. Atomic gravitational wave interferometric sensor. *Phys. Rev. D*, 78:122002, 2008.
8. B. Canuel, S. Pelisson, L. Amand, A. Bertoldi, E. Cormier, B. Fang, S. Gaffet, R. Geiger, J. Harms, D. Holleville, and et al. Miga: combining laser and matter wave interferometry for mass distribution monitoring and advanced geodesy. *Quantum Optics*, Apr 2016.
9. Peter Wolf, Pierre Lemonde, Astrid Lambrecht, Sébastien Bize, Arnaud Landragin, and André Clairon. From optical lattice clocks to the measurement of forces in the casimir regime. *Physical Review A*, 75(6):063608, 2007.
10. B. Pelle, A. Hilico, G. Tackmann, Q. Beaufils, and F. Pereira dos Santos. State-labeling wannier-stark atomic interferometers. *Phys. Rev. A*, 87:023601, Feb 2013.
11. A. Hilico, C. Solaro, M.-K. Zhou, M. Lopez, and F. Pereira dos Santos. Contrast decay in a trapped-atom interferometer. *Phys. Rev. A*, 91:053616, May 2015.

The Inverse Square Law And Newtonian Dynamics space explorer (ISLAND)

J. BERGÉ
ONERA – The French Aerospace Lab, 29 avenue de la Division Leclerc, 92320 Châtillon, France

The ISLAND (Inverse Square Law And Newtonian Dynamics) Space Explorer is a new concept to test the gravitational Inverse Square Law at: (1) submillimeter scale and (2) at the largest Solar System scales (dozens of Astronomical Units –AU). The main idea is to embark a torsion pendulum at the center of gravity of a dedicated, possibly drag-free and attitude-controlled, interplanetary probe whose gravitational environment is accurately probed by, and corrected for thanks to six ultrasensitive accelerometers arranged as a cross around the torsion pendulum.

1 Introduction

In its century of existence, General Relativity (GR) has been extremely successful at describing gravity. From Mercury's perihelion to gravitational lensing, to gravitational waves indirect and, recently, direct detection, it has passed all experimental tests. Yet, gravitation remains puzzling, as it poses unresolved challenges: on the one hand, observations on cosmological scales cannot be explained by the adjunction of GR to the standard model of particle physics; on the other hand, it is difficult to unify with other known interactions.

Zwicky [1] was the first to understand the problem of missing matter: galaxies rotate faster than expected based on their observed luminosity. The "dark matter" conundrum have puzzled astronomers for eighty years, and yet, despite intensive direct and indirect searches in the last decade, no new particle that could account for dark matter has been discovered. Alas, dark matter cannot be explained by a simple observational bias, since it is needed to explain how large scale structures formed in the early Universe: it is the second most significative component of the ΛCDM cosmological model, accounting for 25% of the mass-energy budget of the Universe.

Moreover, GR is usually considered to be the "correct" theory of gravitation on cosmological scales (i.e., at low energy). The ΛCDM model has been built from this assumption, and from the observation of both dark matter and of the accelerated expansion of the Universe [2]. This unexpected behavior may be explained by the presence of some dynamical, repulsive, "dark energy". This new component (which accounts for 70% of the mass-energy budget of the Universe) could be an evolving scalar field (quintessence), or more simply Einstein's cosmological constant Λ, which may be linked to the vacuum energy. However, at least two problems are encountered: (1) the *cosmological constant problem* arises from the fact that the observed value of Λ is around 120 orders of magnitude smaller than the naive expectation from Quantum Field Theory (QFT), that should be of the Planck mass, and (2) the *concordance problem* arises from the fact that the current energy density of dark energy is of the same order as that of dark matter, which is surprising since dark matter and dark energy are separate fields that should evolve independently.

GR (and by extension Newtonian gravity) describes low energy phenomena, but does not take into account the quantum nature of matter, and therefore fails at describing gravity for high-

energy phenomena, that are well described by QFT. On the opposite, QFT and its extensions assume that spacetime is flat, whereas GR's spacetime is intrinsically curved. It is not clear, neither, why gravity is so weak compared with the other interactions (it is 10^{32} times weaker than the weak force), nor how to unify it with them.

GR describes the gravitational force as mediated by a single rank-2 tensor field. There is good reason to couple matter fields to gravity in this way, but there is no good reason to think that the field equation of gravity should not contain other fields. The simplest way to go beyond GR and modify gravity is then to add an extra scalar field: such scalar-tensor theories are well established and studied theories of Modified Gravity (MG). From a phenomenological point of view, they link the cosmic acceleration to a deviation from GR on large scales. They can therefore be seen as candidates to explain the accelerated rate of expansion without the need to consider dark energy as a physical component. Furthermore, they arise naturally as the dimensionally reduced effective theories of higher dimensional theories, such as string theory; hence, testing them can allow us to shed light on the low-energy limit of quantum gravity theories.

Scalar fields that mediate a long range force able to affect the Universe's dynamics should also significantly modify gravity in the Solar System, in such a way that GR should not have passed any experimental test. Screening mechanisms have been proposed to alleviate this difficulty [3]. In these scenarios, (modified) gravity is environment-dependent, in such a way that gravity is modified at large scales (low density) but is consistent with the current constraints on GR at small scale (high density).

All theoretical attempts at explaining the three limitations mentioned above (string theory, MG, MOND) modify GR and Newton dynamics, either at small scale or very large scales, or both. In particular, if one of them is correct, we should detect a violation of the gravitational Inverse Square Law (ISL). Hence, in the weak field limit, measurements of the dynamics of gravitationally bound objects (e.g. the behavior of a torsion balance in the Earth gravity field, the trajectory of an interplanetary probe, or the receding of galaxies) should show a deviation from what is expected from Newton's equations.

We introduce the Inverse Square Law And Newtonian Dynamics space explorer (ISLAND) to look for such deviations on the submilliter and Solar System scales.

2 Tests of the inverse square law at small and large scales

Deviations from the ISL are usually parametrized with a Yukawa potential. The gravitational potential created by a point-mass of mass M at a distance r is then given by

$$V(r) = -\frac{GM}{r}\left(1 + \alpha e^{-r/\lambda}\right), \tag{1}$$

where G is the gravitational constant, α is the (dimensionless) strength of the Yukawa potential relative to Newtonian gravity, and λ is its range. Fig. 1 shows the current constraints on ISL-violations from a Yukawa potential. The left panel focuses on subcentimeter experiments. . The right panel focuses on scales larger than the centimeter; the best constraints come from the measurement of the Moon orbit with the Lunar Laser Range and from planetary motion.

Adelberger et al [4] provide a thorough review of experimental tests of small scale gravitation. Most notably, the Eöt-Wash group of the University of Washington uses low-frequency torsion pendulums to test the ISL [5]. Their pendulum consists in two parallel disks with regularly placed cylindrical missing parts, separated by a given gap: the upper disk (the detector) hangs from a thin wire and is let free to oscillate when the lower disk (the attractor) rotates. They then use an optical device to measure the deviation of the detector from its equilibrium position, and relate it to the torque created by the rotation of the attractor. They could provide strong constraints on the Yukawa (α, λ) plane [6], as shown by the "Eöt-Wash" curves in the left panel of Fig. 1. It is clear that a large part of the (α, λ) plane at submilliter scale is already excluded, with a strong degeneracy between 95% confidence level of the allowed strength α and range

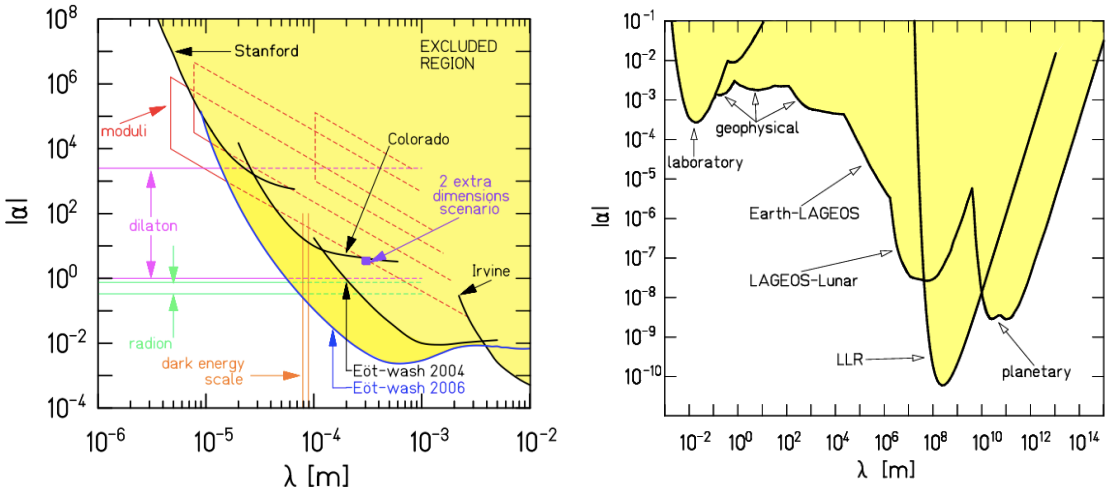


Figure 1 – 95% CL constraints on ISL violating Yukawa interactions. Left panel: $\lambda < 1$cm. Right panel: $\lambda > 1$cm

λ. The allowed region still gives possibilities for new physics, but improving the constraints on $\lambda \leqslant 10\mu$m, with a sensitivity on α similar to that of Eöt-Wash, may provide significant constraints on string-inspired theories.

Gravity at cosmogical scales can be tested through observations (eg. weak gravitational lensing or baryon acoustic oscillations). Surveys like Euclid will most probably bring tight constraints on dark matter and dark energy.

Solar-System-scale observations and/or experiments can allow us to fill the gap between submilliter- and laboratory-scale measurements, and cosmological constraints. The tightest constraints come from measurements by the Lunar Laser Range (LLR [7]). Larger scales can be probed through planetary ranging and ephemeris [8]. Such techniques provide a tight constraint on α; however, this constraint becomes quickly loose as the scale increases towards the outer solar system scale. Probing those scales can be done by measuring the orbit of an outbound spacecraft as it drifts away from the Sun and the planets. The most notable test was performed by NASA during the extended Pioneer 10 & 11 missions. The test resulted in the so-called Pioneer anomaly, finally accounted for by an anisotropic heat emission from the spacecrafts themselves [9]. However, with no direct measurement of the non-gravitational forces acting on the Pioneer 10 & 11 spacecrafts, one could still argue that the case is not completely closed.

The effect of non-gravitational forces could be definitely accounted for if we were able to measure them directly, instead of relying on spacecraft and environment models. This can be easily done with an onboard accelerometer, as proved by missions like LISA Pathfinder [10] or MICROSCOPE [11]. Combining radio tracking data with the accelerometer's direct and model-independent measurements of non-gravitational accelerations, it becomes possible to improve the comparison between the estimated spacecraft's gravitational acceleration and theory by orders of magnitude. The Outer Solar System (OSS) mission [12] investigated the opportunity to fly an accelerometer in deep space. More recently, it was shown that we could improve the constraints of Fig. 1 by at least two orders of magnitude, if we are able to measure the orbit with a 1 meter accuracy, and to measure an absolute acceleration of order 10^{-17} m/s^2, albeit with a mission plan different from that of ISLAND [13].

3 ISLAND

ISLAND aims to improve experimental constraints on those two scales that are currently loosely constrained: under the millimiter, and at the largest Solar System scales. On submilliter scales, improving the constraints on the Yukawa strength about $\lambda \approx 10\mu$m by two orders of magnitude

would allow us to constrain string-theory inspired models. Flying ISLAND up to 100 AU would then allow us to improve the constraints on the Yukawa strength for $10^{12}\text{m} \leqslant \lambda \leqslant 10^{13}\text{m}$ by at least two orders of magnitude.

3.1 Need to go to space (for submilliter-scale tests)

Current on-ground torsion pendulum experiments are mostly limited by thermal noise from the wire, by the difficulty to align the plates with the Earth gravity field, and by seismic noise. In particular, seismic noise limits the smallest separation between the attractor and detector to a few dozens microns [14], which in turn limits the region of the Yukawa parameters plane that can be probed. Those difficulties are alleviated when performing the experiment in space, in a drag-free probe, with an electrostatic torsion pendulum at the center of gravity of the spacecraft: there is no wire anymore, there is no gravity field to which the apparatus should be aligned, and no seismic noise, allowing us to probe smaller scales. Furthermore, if the torsion pendulum lies at the center of a gradiometer, all remaining gravity gradients (e.g. from the Sun gravitational field) can be measured and corrected for. Finally, a space environment is needed to optimize the electrostatic levitation and control of the torsion pendulum's detector.

Going to space will be necessary to experimentally investigate screening mechanisms. Indeed, environment-dependent screenings can prevent an experiment from detecting any deviation from the ISL on the Earth, while allowing the same experiment to detect a deviation in a space environment. Similarly, testing for screening mechanisms at different distances from the Sun might improve our understanding on their environment-dependence.

3.2 Measurement concept

Although both tests can be done independently, the small scale test takes advantage of being done at the center of mass of a gradiometer onboard a drag-free spacecraft. The gradiometer allows us to control the spacecraft's drag-free and to perform the small scale test on an optimal local gravitational environment. In turn, the gradiometer's accelerometers measure the non-gravitational accelerations required by the large scale test. Both tests thus share the same hardware.

The test of the ISL at submilliter scales will be performed with an electrostatic torsion pendulum, made of two parallel plates, based on the Eöt-Wash pendulum. The pendulum will be set at the center of gravity of a gradiometer (whose position will coincide with the center of mass of the spacecraft) in order to take advantage of an optimally clean gravitational environment.

The test of the ISL at large scale will be performed by precisely tracking the orbit of the spacecraft as it cruises the Sun's gravitational field. The gradiometer's accelerometers will allow us to measure and correct for non-gravitational forces, in a model-independent way.

3.3 Submilliter-scale test: torsion pendulum

ISLAND will perform submilliter-scale tests with an electrostatic torsion pendulum based on the Eöt-Wash concept [4]. The Eöt-Wash torsion pendulums consist in two parallel disks with regularly placed cylindrical missing parts, separated by a given gap: the upper disk (the detector) hangs from a thin wire and is let free to oscillate when the lower disk (the attractor) rotates. An optical device is used to measure the deviation of the detector from its equilibrium position, and relate it to the torque created by the rotation of the attractor. The interaction between the two disks is gravitational (electromagnetic forces are minimized), which allow them to set constraints on a possible deviation from the gravitational ISL.

As the ISLAND torsion pendulum is in microgravity onboard the spacecraft, there is no preferred direction for a disk to hang from a wire. That is why we plan to replace the wire by a capacitive system able to control the detector and measure its deviation (Fig. 2). ONERA

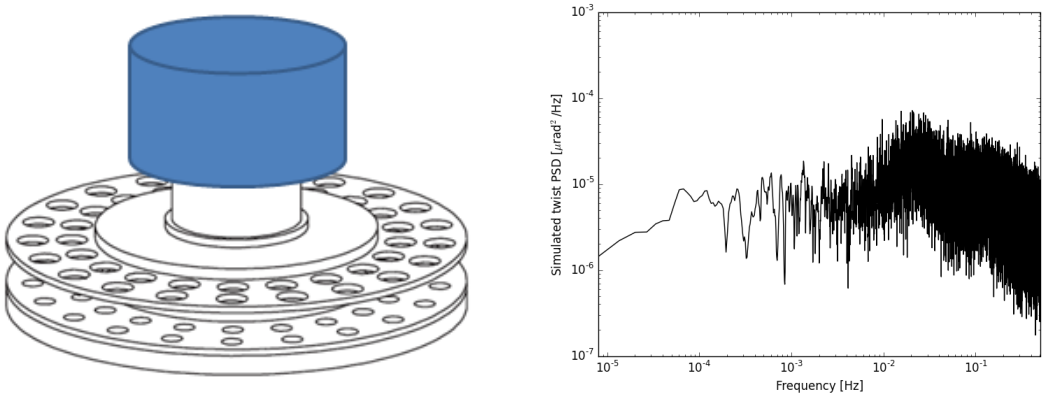


Figure 2 – Left: Torsion pendulum concept; a lower disk rotates and applies a torque to the upper disk (detector); its deviation from its equilibrium position is measured through a capacitive device (blue); the capacitive device also permits the levitation of the detector, thereby acting as a wire in a gravity field. Right: expected twist noise level.

has already built a prototype [15] of an electrostatic torsion pendulum, thereby proving that it can be possible to replace the wire by a capacitive system. As shown in Fig. 2, the envisioned capacitive system would consist of an inner cylinder controled by electrodes glued to an external cylinder (blue). The pendulum detector would be attached to the inner cylinder, and hence its motion would be directly measured by the capacitive system through the deviation of the inner cylinder from its equilibrium position.

This geometry is reminiscent of the cylindrical differential electrostatic accelerometers on-board the MICROSCOPE mission. The level of their noise up to 10^{-2} Hz is of the order of 10^{-5} μrad^2/Hz, almost one order of magnitude lower than the noise of the Eöt-Wash pendulum at the frequency of their test (right panel of Fig. 2) . Hence, with a technology adapted from that of MICROSCOPE, we should be able to reach the desired accuracy in twist measurement.

Given this expected noise level, we should perform the test of the ISL at a frequency ranging from 10^{-4} Hz to 10^{-2} Hz. As we will show below, this is in agreement with the bandwith of the GAP accelerometer, needed to clean the gravitational environment of the torsion pendulum. Assuming that the attractor and detector are made up of $N \approx 10$ holes, the attractor rotation rate ω should then be fixed between 10^{-5} Hz and 10^{-3} Hz to ensure that $N\omega$, the frequency of the expected Yukawa signal, lies in the bandwidth of the accelerometers.

The ISLAND spacecraft should be able to be in a drag-free and fine attitude-control mode when the pendulum will be in function. As a consequence, all non-gravitational backgrounds will be canceled at the position of the pendulum. Therefore, in the spacecraft reference frame, where the test will be performed, only the spacecraft self-gravity will then contribute, but it should be easy to correct for it, either by design of the spacecraft or *a posteriori* data analysis correction.

3.4 Large-scale test: orbit determination

To test gravity at large scales, ISLAND will rely on the accurate determination of its trajectory, as it cruises the Solar System and is affected by gravitational forces from the Sun, planets, moons and other bodies, as well as relativistic effects. ISLAND's orbit can be determined through ranging, Doppler tracking and Very Long Baseline Interferometry (VLBI).

The ISLAND mission will use modern radio-techniques that have been developed for deep space planetary missions. The availability of range observables will significantly reduce the uncertainty in the determination of the heliocentric distances of the probe. Meanwhile the VLBI techniques give new angular observables related to transverse motion with respect to the line of

sight. The combination of measurements based on these radio techniques and accelerometry will allow ISLAND to measure gravity in the Solar System with a greatly improved measurement accuracy and better control of the systematics. As mentioned by Buscaino et al [13], a one-meter precision in the spacecraft ranging is attainable by ranging measurement with the Deep Space Network (DSN). Such a precision would significantly improve the constraints on a Yukawa deviation at scales higher than 10 AU.

With the presence of the accelerometer, the navigation of the probe is no longer affected by uncertainties or inaccuracies in the models of the non-gravitational acceleration. This approach has been used for geodesy missions such as CHAMP, GRACE and GOCE, as well as MICROSCOPE [16]. The additional accelerometry observable removes parameters to be fitted in the orbit determination process and consequently improves its quality. It also measures the temporal fluctuations of the non-gravitational acceleration, which are not taken into account by models. Finally, it removes the correlations that appear in the orbit determination process between the non-gravitational acceleration and the gravitational acceleration, when the former are not measured.

3.5 Gradiometer and accelerometers

We want to be able to accurately measure the gravity gradients around ISLAND's torsion pendulum. One way to achieve it is to design a gradiometer with six accelerometers, that should be placed in a cross figure, like ESA's GOCE's gradiometer. Placing the torsion pendulum at the center of gravity of such a gradiometer will allow us to efficiently estimate any gravity gradient to which it is subjected. This knowledge will allow us to correct for gravity gradients at the data analysis stage.

A gradiometer can use biased accelerometers, since it is possible to correct for the bias between accelerometers, and because what is important for a gradiometer is relative accelerations. The situation would be identical, for a drag-free spacecraft, when tracking its trajectory: a drag-free system works well with relative acceleration. However, if the spacecraft is not always in a drag-free mode during its cruise phase, correcting for non-gravitational accelerations can be done only if we are able to have unbiased acceleration measurements. Therefore, an unbiased (DC) accelerometer is needed. ISLAND could use six such accelerometers, or only one, that would serve as a reference during non-drag-free periods (between torsion pendulum experiments).

Such a DC accelerometer is currently under development at ONERA: the Gravity Advanced Package (GAP) is composed of an electrostatic accelerometer (MicroSTAR), based on ONERA's expertise in the field of accelerometry and gravimetry (CHAMP, GRACE, GOCE and MICROSCOPE missions), and a bias calibration system. Ready-to-fly technology is used with original improvements aimed at reducing power consumption, size and weight. The bias calibration system consists in a flip mechanism which allows for a 180° rotation of the accelerometer to be carried out at regularly spaced times. The flip allows the calibration of the instrument bias along 2 directions, by comparing the acceleration measurement in the two positions [17].

The three axes electrostatic accelerometers developed at ONERA are based on the electrostatic levitation of the instrument inertial mass with almost no mechanical contact with the instrument frame. The test-mass is then controlled by electrostatic forces and torques generated by six servo loops applying well measured equal voltages on symmetric electrodes. Measurements of the electrostatic forces and torques provide the six outputs of the accelerometer.

MicroSTAR is optimized for measurements in a bandwith of $[10^{-5}$ - $10^{-1}]$ Hz. Assuming that the rotation rate of the torsion pendulum is between 10^{-5} Hz and 10^{-3} Hz, the signal from the torsion pendulum will be at a frequency well within MicroSTAR's bandwidth. Furthermore, in order to reach the requirement for the orbit tracking, MicroSTAR's bias must be rejected. The left panel of Fig. 3 shows the current noise of the MicroSTAR accelerometer, with different contributors: a level of 10^{-9} m/s^2/Hz$^{1/2}$ is obtained over $[10^{-5}$ - 1] Hz, with a measurement range of 1.8×10^{-4} m/s^2. The bias modulation signal, consisting in regular 180° flips of the

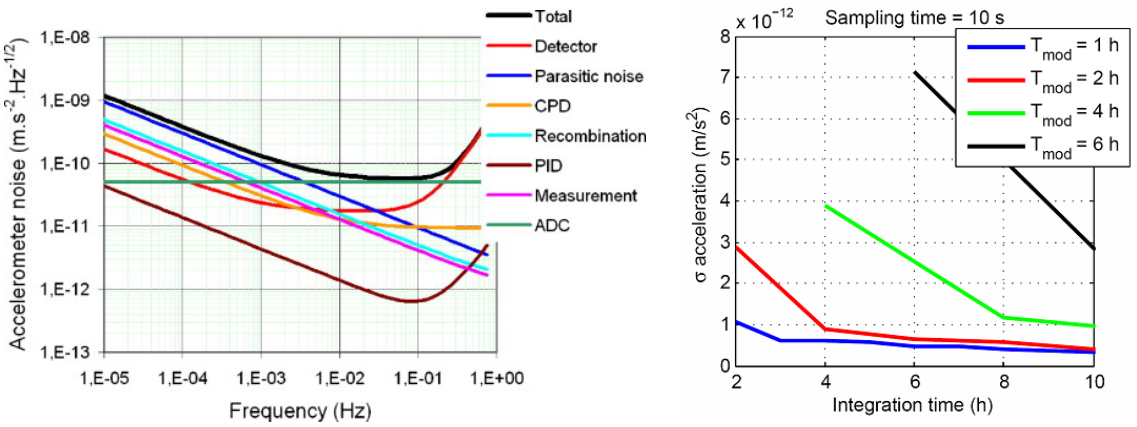


Figure 3 – Current GAP performance. *Left*: MicroSTAR's noise. *Right*: Bias rejection system's resolution.

accelerometer, allows us to band-pass filtering the accelerometer noise around the modulation frequency. The right panel of Fig. 3 shows, for different periods of modulation and calibration, that after rejecting the bias, GAP is able to measure absolute accelerations down to 10^{-12} m/s^2.

4 Conclusion

The yet unexplained acceleration of the cosmic expansion, as well as the conflict between general relativity and quantum field theory at high energy, force us to think beyond, and finely test, established frames. Any deviation from the gravitational inverse square law will be a smoking gun for new physics beyond Einstein, and will shed light towards a viable new theory of gravitation. We propose to look for such a deviation both at submilliter scales with an electrostatic torsion pendulum onboard a dedicated drag-free and attitude-controlled spacecraft; additionally, monitoring the trajectory of the spacecraft and measuring the non-gravitational accelerations that are acted upon it will allow us to test gravity at large scales.

Acknowledgments

I acknowledge financial support from the UnivEarthS Labex program at Sorbonne Paris Cité (ANR-10-LABX-0023 and ANR-11- IDEX-0005-02). I want to thank the members of the ISLAND team, from ONERA, IAP, CEA and ZARM, for useful discussions.

References

1. Zwicky, F. 1933, Helvetica Physica Acta, 6, 110
2. Riess, A. G., Filippenko, A. V., Challis, P., et al. 1998, Astronomical Journal, 116, 1009; Perlmutter, S., Aldering, G., Goldhaber, G., et al. 1999, ApJ, 517, 565
3. Joyce, A., Jain, B., Khoury, J., & Trodden, M. 2015, Physics Reports, 568, 1; Khoury, J., & Weltman, A. 2004, Phys. Rev. D, 69, 044026; Khoury, J., & Weltman, A. 2004, Physical Review Letters, 93, 171104; Hinterbichler, K., & Khoury, J. 2010, Physical Review Letters, 104, 231301; Vainshtein, A. I. 1972, Physics Letters B, 39, 393; Barreira, A., Brax, P., Clesse, S., Li, B., & Valageas, P. 2015, Phys. Rev. D, 91, 123522; Brax, P., Rizzo, L. A., & Valageas, P. 2015, Phys. Rev. D, 92, 043519; Damour, T., & Donoghue, J. F. 2010, Phys. Rev. D, 82, 084033; Damour, T., & Donoghue, J. F. 2010, Classical and Quantum Gravity, 27, 202001
4. Adelberger, E. G., Heckel, B. R., & Nelson, A. E. 2003, Annual Review of Nuclear and Particle Science, 53, 77

5. Hoyle, C. D., Schmidt, U., Heckel, B. R., et al. 2001, Physical Review Letters, 86, 1418; Hoyle, C. D., Kapner, D. J., Heckel, B. R., et al. 2004, Phys. Rev. D, 70, 042004; Kapner, D. J., Cook, T. S., Adelberger, E. G., et al. 2007, Physical Review Letters, 98, 021101
6. Kapner, D. J., Cook, T. S., Adelberger, E. G., et al. 2007, Physical Review Letters, 98, 021101; Schlamminger, S., Choi, K.-Y., Wagner, T. A., Gundlach, J. H., & Adelberger, E. G. 2008, Physical Review Letters, 100, 041101; Wagner, T. A., Schlamminger, S., Gundlach, J. H., & Adelberger, E. G. 2012, Classical and Quantum Gravity, 29, 184002
7. Murphy, T. W. 2013, Reports on Progress in Physics, 76, 076901
8. Fienga, A., Laskar, J., Kuchynka, P., et al. 2010, Relativity in Fundamental Astronomy: Dynamics, Reference Frames, and Data Analysis, 261, 159; Fienga, A., Laskar, J., Manche, H., & Gastineau, M. 2016, arXiv:1601.00947
9. Anderson, J. D., Laing, P. A., Lau, E. L., et al. 1998, Physical Review Letters, 81, 2858; Anderson, J. D., Laing, P. A., Lau, E. L., et al. 2002, Phys. Rev. D, 65, 082004; Rievers, B., & Lämmerzahl, C. 2011, Annalen der Physik, 523, 439; Turyshev, S. G., Toth, V. T., Ellis, J., & Markwardt, C. B. 2011, Physical Review Letters, 107, 081103
10. Armano, M., Audley, H., Auger, G., et al. 2016, Physical Review Letters, 116, 231101
11. Bergé, J., Touboul, P., Rodrigues, M., & MICROSCOPE Team 2015, Journal of Physics Conference Series, 610, 012009; Touboul, P. et al, submitted to PRL; Touboul, P. et al, submitted to CQG
12. Christophe, B., Spilker, L. J., Anderson, J. D., et al. 2012, Experimental Astronomy, 34, 203
13. Buscaino, B., DeBra, D., Graham, P. W., Gratta, G., & Wiser, T. D. 2015, Phys. Rev. D, 92, 104048
14. Kapner, D. J., Cook, T. S., Adelberger, E. G., et al. 2007, Physical Review Letters, 98, 021101
15. Willemenot, E., & Touboul, P. 2000, Review of Scientific Instruments, 71, 310
16. Touboul, P. 2003, Space Science Reviews, 108, 393; Touboul, P., Métris, G., Lebat, V., & Robert, A. 2012, Classical and Quantum Gravity, 29, 184010
17. Lenoir, B., Lévy, A., Foulon, B., et al. 2011, Advances in Space Research, 48, 1248; Lenoir, B., Christophe, B., & Reynaud, S. 2013, Advances in Space Research, 51, 188

PERSPECTIVE TO MEASURE FORCES BETWEEN MACROSCOPIC FLAT PARALLEL PLATES

A. GRADO[1], M. BASSAN[2], M. DE LAURENTIS[3], R. DE ROSA[3], L. DI FIORE[4]
[1] *INAF-Osservatorio Astronomico di Capodimonte, Via Moiariello 16 Napoli, Italy*
[2] *Dipartimento di Fisica, Università di Roma "Tor Vergata", I-00133 Roma, Italy*
[3] *Dipartimento di Fisica, Università di Napoli "Federico II", I-80126, Napoli, Italy*
[4] *INFN - Sezione di Napoli, I-80126, Napoli, Italy*



We propose to use a torsion pendulum to measure the force between macroscopic (of the order of few centimetres) flat metallic plates at distance of the order of 10 microns. We present the experimental setup and discuss how to cope with crucial aspects like absolute distance measurement and plates parallelism. We also discuss how the modulation at a proper frequency and amplitude of plates distance can help in disentangling the different forces contribution acting at such short distances.

1 Introduction

In the last two decades there has been an increase in the number of tests on Newtonian gravity at sub-millimeter scales due to the formulation of several specific theoretical predictions of modifications to gravity in this regime (see review [1,2]). In particular there may be possible signatures of large extra dimensions which could modify gravity directly below the millimeter range[3]. Additional effects at these scales are predicted to arise as a consequence of new particles propagating in the extra dimensions[4]. Other predictions emerge from models attempting to explain the observed smallness of the cosmological constant[5]. These developments have motivated a variety of novel experiments, and there has been substantial progress in setting constraints on non-Newtonian effects. that are usually parametrized with a Yukawa-like interaction.

The most sensitive current test[6] has shown that any inverse-square law (ISL) violating interactions with gravitational strength must have a length scale less than about 50 μm. Furthermore Upadhye, Hu and Khoury[7] noted that the 2007 ISL test[6] excludes almost all "chameleon field theories whose quantum corrections are well controlled and couple to matter with nearly gravitational strength regardless of the specific form of the chameleon potential". They argue that a two-fold improvement in the minimum distance probed would test all such theories. Finally, measurements at such scale could unravel the Drude-Plasma model debate for the real metal, finite temperature corrections to the Casimir force.

2 Forces measurement at short distances

From the previous discussion it follows that a measurement of the forces at distances of the order of $\sim 10\mu m$ is very interesting for the fundamental physics implications that may come out. At these distances the forces we consider are the gravitational force, possible new long range forces, the Casimir force with its thermal corrections and the stray force due to electrostatic noise (we are assuming magnetic clearness of the bodies). To evaluate these forces we will assume a configuration made of two parallel flat plates. There are several reasons for choosing a flat plates configuration: a) "concerning the Casimir force, it is the only one where the comparison of experiment with theory does not require either the Proximity Force Approximation or more sophisticated exact computational methods which can be effectively used so far solely in some restricted ranges of parameters" [8]; b) Flat-flat (FF) is the best geometry to put constraints on long range forces [9]; c) FF allows to increase S/N ratio giving better chance to measure Casimir thermal corrections; d) compared to sphere-plate, in the FF geometry the unwanted patch effect dominates at larger distances. The drawbacks in using such configuration are basically technical: a more stringent requirement on the accuracy of the measurement of the distance between the plates and the difficulty in keeping the two plates parallel. The second aspect is clearly missing for the flat-spherical configuration, this is the reason why up to now only few experiments choose FF configuration.

We assume that one of the plates, we call it attractor, is much wider that the other, named test mass, so that it can be considered infinite. This is the simplest and cleanest case where analytical expressions for the forces are given. Let define A_t, t_t and ρ_t the area, thickness and density of the test mass and t_a and ρ_a the thickness and density of the attractor. The gravitational force due to the infinite plate attractor is $F_N = 2\pi G\rho_a t_a A\rho_t t_t$. The force due to a Yukawa interaction between the two plates is [10]

$$F_Y = 2\pi\alpha G\rho_t\rho_a\lambda^2 A_t[1-e^{-t_a/\lambda}][1-e^{-t_t/\lambda}]e^{-d/\lambda} \tag{1}$$

where α and λ are respectively the strength and interaction length of the Yukawa force. The other force we have to consider at such short distance is the Casimir force. In a pioneering paper Casimir[11] calculated the attractive force between two neutral, perfectly conducting and indefinite parallel plates at absolute temperature equal to zero. The effect of finite metal conductivity has an appreciable effect for distances smaller than or of the order of the plasma wavelength that is around 0.2 μm [12]. As the experiments are performed at room temperature the effect of thermal fluctuations has to be taken into account beside that of vacuum fluctuations. The thermal contribution becomes predominant above few microns. The calculation of the force between dissipative mirrors at non-zero temperatures remains a matter of debate. Indeed, the calculation of the Casimir force at high temperatures or large distances gives, for dissipative mirrors described by the Drude model, a result two times smaller than the same calculation performed for non-dissipative mirrors that are described by plasma model. The correction to the Casimir force calculated with the Drude model is expressed by the formula [12] $dF_{thermal} \sim 1.22K_BTA_t/(8\pi d^3)$. The last force we consider is the electrostatic force due to patch potential [13,14,15,16]. The main limitation in performing the measurement of forces at short distances comes from this kind of stray force. Experiments show that even with precautions for extreme cleanliness, typical surface potential variations are on the order of several millivolts due to work functions variations over the surface. As an example, measurements of the patch potential for different substrate and coating materials, gave values around 6 mV peak to peak over an area of 10×10 mm^2 [17]. The electrostatic force between the plates due to a non constant potential on the surfaces with rms value V_{rms} and assuming a null average difference of potential is $F_{elect} = \epsilon_0 A_t V_{rms}^2/(2d)$

3 Experimental setup

Several experiments setup have been proposed and/or realised to measure the force between bodies at short distances. These include micro resonator, torsion pendulum, neutrons, trapped atoms, atomic force microscope [18,19,10,20,21,22,23,6,24,25]. Presently no experiments have been performed in the distance range from few microns [23] to 44 μm [6]. Measurements in the 10 μm range are very challenging and call for maximisation of the S/N ratio. The first optimization one can think on is a proper choice of the body shape. Several geometry have been adopted so far: sphere-cylinder [26], cylinder-plate [27], sphere-flat (SF) [23], FF plates [10]. The FF configuration was used by Sparnaay [18] in the first attempt to measure the Casimir effect and then by Bressi et al. [10].

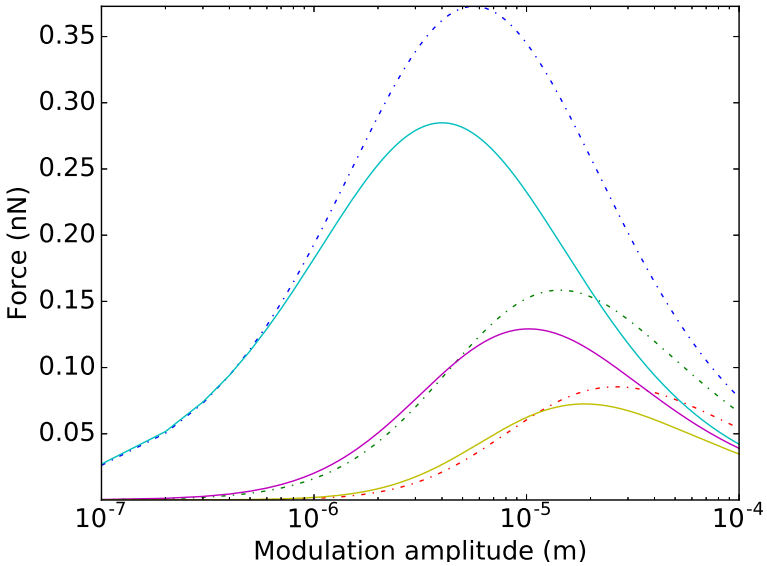


Figure 1 – First three harmonics of the Casimir forces with Drude correction at 300 K (line-dot) and patch force with 4 mV (solid line) between two flat plates. For each kind of force, in decreasing amplitude are shown the first (fundamental), second and third harmonic.

We propose to use a torsion pendulum to measure in a dynamic way the forces between two parallel flat plates. The test mass is on the pendulum, the attractor will be located on a three degrees (two tilts and one translation) nano position actuator. To face the challenge of keeping the plates parallel we propose to use three shadow sensor at 120 degrees placed on the edges of the plates. This kind of simple and effective sensors have enough sensitivity to meet the requirements on the plates parallelism. The signals from the shadow sensors will be properly filtered and sent to the piezo actuators. The control loops will allow the attractor to follow the test mass that is swinging together with the pendulum. Concerning the absolute calibration of the shadow sensors, the task can be easily accomplished using three small capacitive sensors located at 120 degrees. One face of the capacitor is made by a small area electrically isolated located on the attractor, the other face of the capacitor is the test mass. Once the calibration has been performed, the three capacitor armatures will be short circuited to the attractor in order to have one equipotential surface. The piezo actuators will also be used to modulate the plates distance to allow a synchronous detection of the forces between the plates. For a fixed minimum distance, changing the modulation amplitude allows to disentangle the various force components acting between the plates [28]. Figure 1 shows the first three harmonics of the Casimir force with the Drude correction and the patch force. As example the minimum distance is set to 8 μm and the rms patch voltage is assumed to be 4 mV. As can be seen, for each harmonic and force type, the maximum occurs at a specific modulation amplitude.

4 Conclusion

We propose to use a torsion pendulum to measure the forces between two flat parallel plates at $\sim 10\mu m$. Three shadow sensors together with a proper control loop and piezo actuators will allow to keep the plates parallel. The modulation of the distance between the plates is the key to disentangle the various force contributions.

References

1. Lamoreaux, S. K., Annual Review of Nuclear and Particle Science, 62, issue 1, 37 (2012).
2. Mostepanenko, V., The Tenth Marcel Grossmann, Rio de Janeiro, Brazil, 20-26 July 2003, Eds.: Mrio Novello; Santiago Perez Bergliaffa; Remo Ruffini. Singapore: World Scientific Publishing, XLVIII + 2492, 1183 (2006).
3. Arkani-Hamed N., Dimopoulos S., Dvali G., Phys. Lett. B 429, 263 (1998).
4. Arkani-Hamed N., Dimopoulos S., Phys. Rev. D 65 (2002) 052003.
5. Sundrum R., J. High Energy Phys. 7 (1999).
6. D.J. Kapner, T.S. Cook, E.G. Adelberger et al. Phys. Rev. Lett. 98 021101 (2007).
7. A. Upadhye, W. Hu and J. Khoury, Phys. Rev. Lett. 109, 041301 (2012).
8. Geyer, B., Klimchitskaya, G. L., Mostepanenko, V. M., Physical Review A, vol. 82, Issue 3, id. 032513 (2010)
9. Mostepanenko, V. M. and Sokolov, I. Yu., Phys. Rev. D, 47, 7, 2882 (1993)
10. G Bressi, G Carugno, A Galvani et al. , Class. Quantum Grav. 18 (2001) 3943-3961
11. H. B. G. Casimir, Proc. K. Ned. Akad. Wet. 51, 793 (1948).
12. Genet, C., Lambrecht, A., Reynaud, S., Phys. Rev. A 62, 012110 (2000)
13. Garrett, J. L., Somers, D., Munday, J. N. Journal of Physics: Condensed Matter, Volume 27, Issue 21, article id. 214012 (2015)
14. Behunin, R. O., Intravaia, F., Dalvit, D. A. R. et al. Physical Review A, vol. 85, Issue 1, id. 012504 (2012)
15. Behunin, R. O.; Dalvit, D. A. R.; Decca et al., Physical Review D, Volume 89, Issue 5, id.051301 (2014)
16. Speake, C. C. and Trenkel, C. Physical Review Letters, vol. 90, Issue 16, id. 160403 (2003)
17. N. A. Robertson et al., Class. Quantum Grav. 23, 2665 (2006)
18. Sparnaay, M.J., Physica 24, 751 (1958)
19. Lamoreaux, S. K., Phy. Rev. Letters, 78, Issue 1, 5 (1997)
20. Decca, R., Vladimir A., Lpez, D., Casimir Physics, Lecture Notes in Physics, 834. ISBN 978-3-642-20287-2. Springer-Verlag Berlin Heidelberg, p. 287 (2011)
21. Adelberger, E.G., Gundlach, J.H., Heckel, B.R. et al., Prog. Part. Nucl. Phys. 62, 102 (2009).
22. Antoniadis, I., Baessler, S., Bchner, M., C. R. - Physique, 12, Issue 8, 755 (2011)
23. Sushkov, A. O., Kim, W. J., Dalvit, D. A. R. et al., Nature Physics, 7, Issue 3, 230 (2011).
24. Chiu, Hsiang-Chih, Chang, Chia-Cheng, Castillo-Garza, R. J. of Phys. A, 41, Issue 16, 164022, 14 (2008).
25. Antonini, P., Bimonte, G., Bressi, G. et al. Journal of Physics: Conference Series, Volume 161, Issue 1, article id. 012006, 10 (2009).
26. Mukhopadhyay, S., Noruzifar, E., Wagner, J. et al. American Physical Society, APS March Meeting 2013, March 18-22, (2013)
27. Rahi, S. J.; Emig, T.; Jaffe, R. L. et al. M., Phys. Rev. A, 78, Issue 1, id. 012104 (2008)
28. Grado, A.; Calloni, E.; Di Fiore, L., Phys. Rev. D, 59, Issue 4, 042002 (1999)

LARASE: Testing General Relativity with Satellite Laser Ranging

Luciano Anselmo[1], Massimo Bassan[2,3], David Lucchesi[4,1,2],Carmelo Magnafico[4,2], Carmen Pardini[1], Roberto Peron[4,2], Giuseppe Pucacco[2,3], Ruggero Stanga[5,6], Massimo Visco[4,2].

[1] *Istituto di Scienza e Tecnologie dell'Informazione (ISTI/CNR), Via Moruzzi 1, Pisa, Italy*

[2] *Istituto Nazionale di Fisica Nucleare, Sez. Tor Vergata, Via della Ricerca Scientifica 1, Roma, Italy*

[3] *Dipartimento di Fisica, Univ. di Tor Vergata, Via della Ricerca Scientifica 1, Roma, Italy*

[4] *Istituto di Astrofisica e Planetologia Spaziali -INAF, Via Fosso del Cavaliere 100, Roma, Italy*

[5] *Dipartimento di Fisica e Astronomia, Univ. Firenze, Via Sansone 1, Sesto Fiorentino, Firenze, Italy*

[6] *Istituto Nazionale di Fisica Nucleare, Sez. Firenze, Via Sansone 1, Sesto Fiorentino, Firenze, Italy*

LARASE is an experiment devoted to test General Relativity in its weak-field linearized approximation using the geodetic satellites LAGEOS and LARES. One main target is the measurements of the Lense-Thirring effect with an accuracy higher than in the past. We present the LARASE activitities and a preliminary measurement of the effect.

1 Introduction

The Solar System is the classical laboratory for testing General Relativity (GR) in its weak field and slow motion (WFSM) limit. Measurement of the so-called gravitomagnetic effects represents one of the classical goals in this field. In GR, rotating bodies drag a freely falling reference frame, causing a precession that takes the name of Lense-Thirring [1](L-T) or gravitomagnetic effect. "Mass-currents" produce effects on the near moving masses, a phenomenon that is formally equivalent to magnetism. Einstein named this effect frame-dragging.

A first accurate measurement of the L-T effect was obtained by Ciufolini and Pavlis [2] in 2004. They reached an uncertainty of 10% in the evaluation of the main systematic error sources by analyzing about 11 years of the Satellite Laser Ranging measurements of the two LAGEOS satellites. The NASA/Stanford experiment Gravity Probe B (GP-B)[3] in 2011 succeeded in the measurement of frame dragging by measuring the precession of superconducting gyroscopes orbiting the Earth, the so-called Schiff effect. The uncertainty was about 20%.

The main scientific goal of the LAser RAnged Satellites Experiment (LARASE) is the measurement of the Lense-Thirring effect using the data of the two LAGEOS and of the newer LARES satellite, with improved precision and accuracy with respect to the best measurements to date. We refer to Lucchesi et al. [4] for a detailed description of the program.

2 The satellites of the LARASE experiment

The "tools" of LARASE measurements are geodetic satellites that orbit around the Earth. They are equipped with corner cube reflectors (CCR) and tracked with great precision using laser beams from a network of stations of the International Laser Ranging Service (ILRS) [5]. The ILRS stations provide satellites' range data, obtained with the measurement of the round-trip time, that have currently reached RMS errors around one millimeter: this allows reconstruction of the orbit, using precise orbit determination (POD) techniques, at a level of about 1 *cm*. The

ILRS data are freely available, both as high frequency measurements (called full rate) and as "normal points", i.e. values averaged over a period of two minutes for the LAGEOS satellites. We use ranging data for the two LAGEOS and the LARES satellites. The first LAGEOS was launched in 1976 by NASA, has a mass of about 400 kg, a diameter of 60 cm and hosts 426 CCR. LAGEOS II, launched in 1992 by NASA/ASI, is almost identical to LAGEOS.

LARES was launched in 2012 by ASI, it is smaller but denser than LAGEOS, with a diameter of 36 cm and a mass of about 390 kg. It is equipped with 92 CCR. The mean orbital parameters of the three satellites are reported in table 1. One relevant difference between LAGEOS and LARES is the height of their orbit: indeed, LARES is on a much lower orbit, and is therefore more sensitive to the non-uniformity of the Earth's gravitational field (higher multipoles), to tidal effects and to the drag effects from the residual atmosphere.

Table 1: Keplerian parameters of the LAGEOS and LARES satellites. The right ascension of the ascending node and argument of the pericenter are estimated at October 24th, 1992 for LAGEOS and LAGEOS II, and at February 18th, 2012 for LARES.

Orbital Element		LAGEOS	LAGEOS II	LARES
Semi-major axis (m)	a	$1.23 \cdot 10^7$	$1.22 \cdot 10^7$	$7.82 \cdot 10^6$
Eccentricity	e	$4.43 \cdot 10^{-3}$	$1.38 \cdot 10^{-2}$	$1.20 \cdot 10^{-3}$
Inclination (deg.)	i	109.84	52.66	69.49
Right ascension of the ascending node (deg.)	Ω	289.74	113.75	230.84
Argument of pericenter (deg.)	ω	53.12	212.57	296.99

3 LARASE activities

The main objective of LARASE is the measurement of the L-T effect with an improved error budget: to this purpose, we need to account for all perturbations and to keep under tight control all the systematic errors, in order to produce a robust, reliable and uncontestable result. This target requires a careful study of all the effects of both gravitational and non-gravitational origin that act on the satellite and may mask the GR effects.

The main observables used for the measurement are the rate of right ascension of the ascending node $\dot{\Omega}$ of the orbit of the satellites. Also the rate of the argument of pericenter $\dot{\omega}$ of the orbit can be used. Both these drifts are proportional to the gravitomagnetic parameter μ, which is equal to 1 in Einstein's GR and 0 in Newtonian classical physics:

$$\dot{\Omega}^{LT} = \mu \frac{2GJ_\oplus}{c^2 a^3 (1-e^2)^{\frac{3}{2}}} \qquad \dot{\omega}^{LT} = \mu \frac{-6GJ_\oplus}{c^2 a^3 (1-e^2)^{\frac{3}{2}}} \cos i \tag{1}$$

where G is the gravitational constant, a the semi-major axis, e the eccentricity, i the inclination, c the speed of light and finally $J_\oplus$ is the Earth's angular momentum.

Other phenomena, beside GR, can cause the drift of the satellite node Ω and pericenter ω. These parameters are perturbed also in the Newtonian sense: indeed, a similar effect can be produced by the non-sphericity of Earth's mass distribution, and in particular by the even terms of the geopotential multipole expansion. This disturbing effect can be reduced using the measured Keplerian parameters of several satellites and properly combining their residuals [7,8]. For example, we can use a combination of the right ascension of the nodes of the 3 satellites [8]:

$$\dot{\Omega}_{comb} = \dot{\Omega}_{L1} + k_1 \dot{\Omega}_{L2} + k_2 \dot{\Omega}_{LR}, \tag{2}$$

This weighted sum, where the coefficients k_1 and k_2 are defined by the orbital parameters, defines an equivalent shift $\dot{\Omega}_{comb}$ that is insensitive to all errors related to the first two even zonal harmonics, i.e. the quadrupole and octupole coefficients of the gravitational field. Alternative

combinations are possible using also the argument of pericenter of LAGEOS II, the most eccentric among the 3 satellites [9].

In order to reduce and properly evaluate the errors affecting the relativistic measurements, a careful study of the gravitational and non-gravitational forces acting on the satellite is required. The recent activities of LARASE have focused on:
- Study of thermal effects: these have an impact on the satellite attitude dynamics. We started with a critical analysis of the satellites physical characteristics available in literature: this enabled us to build 3D models, to evaluate e.g. the moments of inertia [6] of the satellites. These models will also be used for thermal studies based on finite-element techniques. Figure 1 shows a rendering of LARES obtained using the 3D model of the satellite.
- Study of neutral particle drag effects: due to its lower orbit, LARES is more sensitive to the perturbing effects of the neutral drag. Using a modified version of SATRAP [10] software, we evaluated the perturbations acting on LARES, in particular the decay of its semi-major axis [11]. We considered the evolution of solar and geomagnetic activities using different thermospheric density models.
- Study of Earth tides, both solid and ocean: the tides of the Earth affect the dynamics of the satellites in a threefold way: i) they modify the Earth's shape, changing the position of the ground stations, ii) they change the Earth gravitational field that influences the orbit of the satellites and iii) they change the reference frame adopted in the measurements, as they modify the Earth's rotation. Also in this case a larger effect is expected on LARES with respect to the two LAGEOS.



Figure 1 – CAD Rendering of LARES satellite

4 Preliminary results

We show a preliminary analysis on the ranging data of about 3.4 years of the LAGEOS and LARES satellites. The data were subdivided in single time spans (*arcs*) of 7 days. The *best orbit* was estimated on each arc using a least-squares approach. The measured position and velocity in each arc were used as initial conditions in a numerical evaluation of the orbit based on a model that includes all known effects, except the L-T effect to be measured. The reconstructed (propagated) orbit at the end of each arc and the measured orbit at the same initial epoch of the subsequent arc are compared, obtaining the so called (O-C) or *residuals*. These residuals should contain the "displacement" due to the L-T precession of the orbit.

The node residuals calculated for each of satellite are combined using Eq. (2). Figure 2 displays the time dependence of the integrated residuals for Ω_{comb}. Since the L-T effect produces a secular effect (see Eq. (1)), we expect a linear behaviour for the integrated residuals of the satellites nodes.

In practice, some periodic disturbances superimpose the linear behaviour predicted by GR. When these effects (typically tides and thermal effects) have periods longer than the analyzed

time span, they are hard to be discriminated: on time intervals shorter than half their period, their time evolution can be confused with a monotonic trend. We fitted many of these oscillating disturbances, taking into account a number of tides (both solid and ocean) varying between 3 and 12. In this way their oscillating behaviour can be removed, at least partially.

The computed linear fit to the data is the red line in figure 2, corresponding to a drift of 50.11 $mas/year$, to be compared with the GR prediction represented by the green line, with a slope of 50.18 $mas/year$. The statistical error is therefore around 0.1%, but the sensitivity to the number of the tides absorbed in the fit can increase this error to a few percent level. A careful analysis of the main systematic error sources is underway.

We plan, for the near future, to reduce the errors that depend on the dynamical models included in the POD, especially for the thermal and gravitational effects.

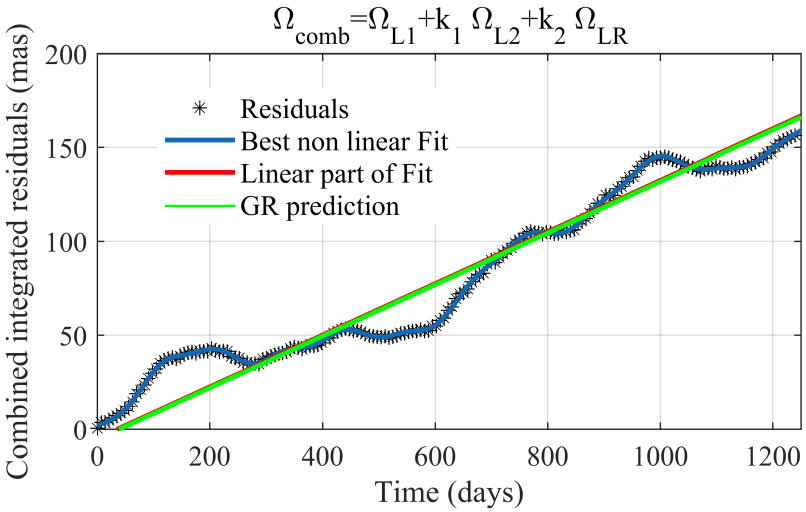


Figure 2 – Integrated residuals for the combined right ascension of the ascending node of the satellites (Ω_{comb} of eq.2). The residuals are fitted with a linear term plus a number (up to 12) of periodic terms to model slow tides.

Acknowledgments

This activity is funded by the CSN2 of INFN. We thank the ICT Service of ARTOV-CNR, and expecially G. Chionchio and E. Costantini, for providing expertise to the experiment.

References

1. W. J. Lense and H. Thirring, Phys. Zeits. **19**, 156 (1918).
2. I. Ciufolini and E. C. Pavlis, *Nature* **431**, 958 (2004).
3. C. W. F. Everitt *et al*, *Phys. Rev. Lett.* **106**, 221101 (2011).
4. D. Lucchesi *et al*, *Class. Quantum Grav.* **32**, 155012 (2015).
5. M. R. Pearlman, J. J. Degnan and J. M. Bosworth Adv. Space Res. **30**, 135143 (2002).
6. M. Visco and D. Lucchesi, *Adv. Space Res.* **57**, 1928 (2016).
7. D. M. Lucchesi and G. Balmino Planet. Space Sci. **54**, 581593 (2006).
8. I. Ciufolini, A. Paolozzi, E. C. Pavlis et al., European Phys. Journ. **C 76**, 120 (2016).
9. I. Ciufolini, D. Lucchesi, F. Vespe, A. Mandiello: *Nuovo Cimento* **A109**, 575-590 (1996).
10. C. Pardini and L. Anselmo, SATRAP: Satellite Reentry Analysis Program Internal Report C94-17 (1994). (Pisa, Italy: CNUCE Consiglio Nazionale delle Ricerche)
11. D. M. Lucchesi et al. IEEE Metrology for Aerospace 71-76 (2015)
12. D. Lucchesi and R. Peron, *Phys. Rev. Lett.* **105**, 231103 (2010).

5. Theory

Theories of Modified Gravity

Andrew J. Tolley
Theoretical Physics, Blackett Laboratory, Imperial College, London, SW7 2AZ, U.K.



I briefly review modified theories of gravity, and in particular discuss massive theories of gravity and current observational bounds placed on the graviton mass.

1 Introduction

1.1 Why modify gravity at large distances?

Why modify gravity at large distances? The principal motivation is cosmological. The main driver for exploring modifications to general relativity are the intertwined dark energy and cosmological constant problems, i.e. the theoretical attempts to reconcile the now compelling picture that the universe is undergoing late time acceleration, together with our understanding of gravity:

- **Old Cosmological Constant Problem**: Why is the Universe not accelerating at a rate determined by the vacuum energy?
- **New Cosmological Constant Problem**: Assuming the above is solved, what gives rise to the remaining vacuum energy or dark energy which leads to the acceleration we observe?
- **Testing GR**: Because it allows us to put better constraints on Einstein Gravity.

Gravity has only been tested over a special range of scales and curvatures[1]. Just as Weinberg constructed his nonlinear version of quantum mechanics, to provide a means to test experimentally the linearity of ordinary quantum mechanics [2], it is important to explore cosmological alternatives to general relativity (and a cosmological constant), to better probe the possible validity of this theory.

1.2 Guiding Principle

The central guiding principle to constructing modifications of general relativity is the theorem that:

General Relativity (with a cosmological constant) is the unique local and Lorentz invariant theory describing an interacting single massless spin two particle that couples to matter.

This theorem goes back to the work of Feynman, Weinberg, Deser, Wald and many others [3,5,4,6] and has been approached both from the perspective of the consistency of the equations of motion, the consistency of the non-linear symmetries, and the existence of an S-matrix. Any modification will thus give up one of these properties:

1. Locality,
2. Lorentz Invariance,
3. Massless,
4. Single Spin Two.

A corollary of this theorem is that any theory which preserves Lorentz invariance and locality (1 and 2) leads to new degrees of freedom since we require either new states (4) or the spin 2 field is massive (3), which by Lorentz invariance then has 3 new degrees of freedom. New gravitational degrees of freedom that couple to matter are highly constrained by a variety of tests including: fifth force constraints (e.g. solar system tests), equivalence principle tests, binary pulsar timing, nucleosynthesis, cosmological moduli problems. We thus need some kind of screening mechanism to hide extra degrees of freedom.

1.3 Screening Mechanisms

The different screening mechanisms that arise in theories of dark energy and modified gravity can be understood in relatively simple terms as follows. Let us suppose for simplicity, that the new degrees of freedom that arise are scalars. Let us denote one of these scalar fields by ϕ, and take into account the fact that in a cosmological or astrophysical background it may take on some time/space dependent background value ϕ_b. Accounting for fluctuations we denote $\phi = \phi_b + \delta\phi$. Similarly let us collectively denote the various components of the stress energy tensor by $\rho = \rho_b + \delta\rho$. The generic form of the equations of motion for perturbations is schematically

$$Z(\phi_b, \rho_b)\left[\frac{d^2\delta\phi}{dt^2} - c_s^2(\phi_b, \rho_b)\nabla^2\delta\phi\right] + m^2(\phi_b, \rho_n)\delta\phi = \beta(\phi_b, \rho_b)G_{\rm Newton}\delta\rho\,. \tag{1}$$

The static force between two point masses M_a, M_b will take the schematic form[a]

$$F \approx \frac{M_a M_b G}{r^2}\frac{\beta^2(\phi_b, \rho_b)}{Z(\phi_b, \rho_b)c_s^2(\phi_b, \rho_b)}\exp\left(-m(\phi_b, \rho_b)r\right). \tag{2}$$

Generically these fifth forces may be as strong as the ordinary Newtonian contribution unless one or more of the following conditions are met:

1. The coupling is small, at least in the presence of matter $\beta(\phi_b, \rho_b) \ll 1$. This is realised by quintessence models (where $\beta \approx 0$) or the symmetron mechanism [7] where this occurs in the regions of dense environments.
2. The mass becomes large in the region of dense environments $m(\phi_b, \rho_b) \gg 1/r_{\rm exp}$, as is realised for example by the chameleon mechanism [8].
3. The kinetic term becomes large in dense environments $Z(\phi_b, \rho_b) \gg 1$. This is known as the Vainshtein mechanism [9] and is most famously realised in the context of massive theories of gravity.

[a] Assuming an interaction $\mathcal{L}_{\rm int} \sim \beta(\phi_b, \rho_b)G_{\rm Newton}\delta\phi\delta\rho$

In what follows we shall focus on theories of massive gravity that incorporate the Vainshtein screening mechanism. For a recent review of Vainshtein screening see Ref. [10]. In brief this mechanism works as follows. Associated with the graviton mass scale m, the Planck scale $M_{\rm Pl}$ and mass of a source M, there is a characteristic length scale known as the Vainshtein radius r_V determined by

$$r_V^3 = \frac{1}{M_{\rm Pl} m^2} \frac{M}{M_{\rm Pl}} \,. \tag{3}$$

This is the scale at which the helicity-zero modes of the massive graviton, the would-be progenitors of fifth forces become strongly coupled. At distance $r \ll r_V$ the effective kinetic term for fluctuations around the background takes the form

$$Z \sim \left(\frac{r_V}{r}\right)^A \,, \tag{4}$$

with A a positive power such that $Z \gg 1$. This arises from the nonlinearities of the strong coupling mechanism. This screening of the fifth forces means that the predictions of general relativity are recovered with small corrections. Stated differently, this region is the one for which the spacetime curvature $R \gg m^2$ and so the mass term in massive gravity is negligible relative to the Einstein-Hilbert term. At distances $r \gg r_V$ the mass term comes into play and there are noticeable departures from general relativity, until eventually we reach $r \gg 1/m$ at which point the Yukawa suppression effect kicks in.

2 Massive Gravity

What does it mean to have massive gravity? To understand this we can think of the analogy of how the W and Z bosons become massive in the standard model. There the electroweak symmetry is broken by the vev of the Higgs field via

$$SU(2) \times U(1)_Y \to U(1)_{\rm EM} \,, \tag{5}$$

with the result that the W and Z bosons become massive. The would-be Goldstone mode in the Higgs field becomes the Stückelberg field which gives the boson mass. For instance in the simplified version of the Abelian Higgs model, the single complex Higgs field can be parameterized as

$$\Phi \to (v + \rho) e^{i\pi} \,, \tag{6}$$

where v is the Higgs vev, ρ is the Higgs boson and π is the Stückelberg field (which in the global limit is the Goldstone mode). Under the $U(1)$ symmetry $A_\mu \to A_\mu + \partial_\mu \chi$ and $\pi \to \pi + \chi$.

In massive gravity, the symmetries are the direct product of a local diffeomorphism group and an additional global Poincaré group. The breaking mechanism that gives rise to a mass is the one that leaves behind the diagonal subgroup

$$Diff(M) \times Poincare \to Poincare_{\rm diagonal} \,. \tag{7}$$

Similarly in bigravity models, two copies of the local diffeomorphim group are broken down to a single copy of the diffeomorphism group

$$Diff(M) \times Diff(M) \to Diff(M)_{\rm diagonal} \,. \tag{8}$$

Despite much blood, sweat and tears, an explicit Higgs mechanism for gravity is not known. However, if such a mechanism exists, we do know how to write down the low energy effective theory in the spontaneously broken phase. For an Abelian Higgs this corresponds to integrating out the Higgs boson and working at energy scales lower that the mass of the Higgs boson ρ.

This will then be an effective theory for the Stückelberg field π coupled to the gauge field A_μ.

In massive gravity we follow the same procedure [11]. Diffeomorphism invariance is spontaneously broken, but can be recovered with the introduction of 4 Stuckelberg fields ϕ^a. This is achieved by replacing the Minkowski reference metric for the global Poincare symmetry η_{ab} with the spacetime tensor $f_{\mu\nu} = \eta_{ab}\partial_\mu\phi^a\partial_\nu\phi^b$. In this way the mass term can be constructed out of scalar combinations of $f_{\mu\nu}$ and $g_{\mu\nu}$ in a way which respects diffeomorphism invariance. The reference metric η_{ab} can be viewed as the vev of a spin-2 Higgs (possibly composite) field $\eta_{ab} = \langle\hat{O}_{ab}\rangle$. The additional 3 degrees of freedom in massive graviton are made manifest by the decomposition

$$\phi^a = x^a + \frac{1}{mM_{\rm Pl}}A^a + \frac{1}{\Lambda_3^3}\partial^a\pi\,, \tag{9}$$

where $\Lambda_3^3 = m^2M_{\rm Pl}$ and scales introduced are inferred by canonical normalization. A^a caries the 2 helicity-one degrees of freedom of the massive spin 2 field (there is an additional $U(1)$ symmetry $A_\mu \to A_\mu + \partial_\mu\psi$, $\pi \to \pi - m\psi$ which keeps it at 2), and π the helicity-zero. The full form of Lorentz invariant massive gravity with the highest strong coupling scale possible Λ_3 was given in Ref [12]. The precise form is

$$\mathcal{L} = \frac{1}{2}\sqrt{-g}\left(M_{\rm Pl}^2R - m^2\sum_{n=0}^{4}\beta_n\mathcal{U}_n\right) + \mathcal{L}_M\,, \tag{10}$$

where the characteristic polynomials $\mathcal{U}_n(K)$ are defined via

$$Det[1+\lambda K] = \sum_{n=0}^{4}\lambda^n\mathcal{U}_n(K)\,, \tag{11}$$

and the matrix K is defined via $K = 1 - \sqrt{g^{-1}f}$ which may be equivalently written as $g^{\mu\alpha}f_{\alpha\nu} = g^\mu_\nu - 2K^\mu_\nu + K^\mu_\alpha K^\alpha_\nu$. The square root structure is determined entirely by the requirement that the strong coupling scale is Λ_3. A generic mass term, would give rise to an effective theory whose cutoff is $\Lambda_5 = (m^3M_{\rm Pl})^{1/5}$.

3 Constraints on the Graviton Mass

Constraints on the graviton mass are summarized in Figure (1) and are discussed at length in Ref. [13] [b]. They arise from probing three distinct physical consequences of the graviton having a mass. These are as follows:

- Yukawa Suppression: Due to the mass, static weak field forces will be exponentially suppressed at large distances $V \sim \frac{mMG}{r} \to \frac{mMG}{r}e^{-mr}$.

- Modified Dispersion Relation: Gravitational waves now propagate with a dispersion relation of the form $\omega^2 \approx c^2k^2 + m^2c^2$.

- Fifth forces/New degrees of freedom: Since generically massive gravity theories have additional degrees of freedom which couple to the stress-tensor, then they induces fifth forces which as we have discussed in the previous section must be screened in some sense in dense environments, to avoid immediate conflict with current observations.

[b] We shall review various aspects of this discussion here, and we refer to Ref. [13] for a fairly exhaustive list of references

Figure 1 – A summary of constraints on the graviton mass from de Rham, Deskins, Tolley and Zhou, 2017.

Dispersion Relation

m_g (eV)	λ_g (km)	
10^{-22}	10^{11}	aLIGO bound
10^{-20}	10^{9}	Pulsar timing
10^{-30}	10^{20}	B–mode's in CMB

Yukawa

m_g (eV)	λ_g (km)	
10^{-23}	10^{12}	Solar System tests
10^{-32}	10^{21}	Weak lensing
10^{-29}	10^{19}	Bound clusters

Fifth Force

m_g (eV)	λ_g (km)	
10^{-32}	10^{22}	Lunar Laser Ranging
10^{-27}	10^{17}	Binary pulsar
10^{-32}	10^{22}	Structure formation

3.1 Fifth Forces/New degrees of freedom

Traditionally the strongest constraint on the mass of the graviton comes from lunar laser ranging experiments which probe modifications in the earth-moon system. Despite only testing solar system scales, the accuracy and length of time they can be performed significantly compensates the otherwise negligible physical modification in the orbits due to fifth forces. For models whose effective theory is described by a cubic Galileon, such as the Dvali-Gabadadze-Porratti model then the constraint on the graviton mass implied by a modification of the Newtonian potential $\delta\Phi$ is of order

$$m_g < \delta\Phi \left(\frac{r_S}{a^3}\right)^{1/2} \quad \rightarrow m_g < 10^{-32}\text{eV}\,. \tag{12}$$

where a is the semi-major axis of the lunar orbit and r_S the Schwarzschild radius of the earth. For 'hard-mass' models of massive gravity, or those whose effective theory is described by a quartic Galileon the constraint is slightly weaker

$$m_g < \delta\Phi^{3/4} \left(\frac{r_S}{a^3}\right)^{1/2} \quad \rightarrow m_g < 10^{-30}\text{eV}\,. \tag{13}$$

It should be noted that these are already remarkably strong constraints, and are far stronger than the equivalent constraints on the mass of the photon [21].

Observations of binary pulsars provide a more direct probe of the possible existence of extra degrees of freedom [14, 15] since the extra polarizations of the graviton imply additional modes of gravitational waves. Consequently binary pulsars lose energy faster than in general relativity and so the orbit slows down more rapidly. This gives a constraint of order $m_g < 10^{-27}$eV.

3.2 Yukawa Potential Bounds

In the weak field approximation, a graviton mass leads to a Yukawa potential in place of a Newtonian potential. As such structures cannot be gravitationally stable at distances larger than the Compton wavelength of the graviton. Given that the core of clusters being a typical size of 1-10 Mpc are virialized, then we obtain a constraint $m_g < 10^{-29}$eV [16]. Within the solar system, we can check the force law by the validity of Kepler's law a^3/T^2 =constant, for Earth and Mars. This gives a constraint $m_g < 10^{-23}$eV [17]. In weak lensing, the power spectrum of effective convergence gets corrected by a factor of $k^2/(k^2+m_g^2)$, and so assuming ΛCDM we get $m_g < 10^{-32}$eV [18].

3.3 Direct Detection of Gravitational Waves

Given the recent direct detection of gravitational waves by advanced LIGO [19], associated with the merger of two binary black holes, we have a direct opportunity to put constraints on the mass of the graviton from the modified dispersion relation for gravitational waves. This is through observations of the waveform. During the merger process, the frequency of gravitational waves increases sharply at the end (the so-called 'chirp'). Taking the simplest assumption that $\omega^2 = c^2k^2 + m^2c^2$ then the gravitational waveform would be more squeezed in a theory of massive gravity than in GR. This is because the speed of near luminal gravitational waves increases with frequency as

$$\frac{v_g}{c} \approx 1 - \frac{1}{2}\left(\frac{c}{\Lambda_g f}\right)^2 \tag{14}$$

and so the later emitted parts of the waveform would travel faster, causing the overall waveform to bunch up [20]. If Δt_e is the emitted signal duration and Δt_o the observed duration, then accounting for any possible redshifting, the effective time difference due to any possible squeezing of the signal is

$$\Delta t = \Delta t_o - \Delta t_e(1+z)\,. \tag{15}$$

This effect places a constraint on the graviton mass in the form

$$m_g < 4\times 10^{-22}\text{eV}\left(f\Delta t\frac{f}{100\text{Hz}}\frac{200\text{Mpc}}{D}\right)^{1/2}\,, \tag{16}$$

where D is the luminosity distance of the source. The phase distortion $f\Delta t$ can be measured up to $1/\rho$, where ρ is the signal to noise ratio. For the gravitational wave detection $GW150914$ we have $D \sim 400$Mpc, $f \sim 100$Hz and $\rho \sim 23$ implying $m_g < 10^{-22}$eV. For LISA we could in principle have $\rho \sim 10^3$, $D \sim 3$Gpc and $f \sim 10^{-3}$Hz which could put a constraint $m_g < 10^{-26}$eV.

While the above constraint on the graviton mass was discussed already after the first direct detection of gravitational waves [19], this is far from the end of the story of what can be learned about massive gravity from strong gravity physics and gravitational waves. We known in realistic nonlinear theories of massive gravity, such as that discussed above, the graviton mass actually depends on the environment, for instance it can depend on the distance to the black holes, via the background metric. The graviton mass is also likely to vary non-adiabatically during the merger, creating additional non-adiabatic effects in the waveform. The effects of the additional scalar and vector gravitational modes has not been taken into account, and in certain stages of the merger the scalar radiation could feasibly dominate the effect of the tensors. The black hole or neutron star solutions may themselves be modified, which will lead to different quasi-normal modes modifying the final ring-down stages. The Vainshtein suppression may not be active in the merger region and this would need to be dealt with by a proper numerical simulation accounting for the additional degrees of freedom. For instance it is expected that the PN expansion almost certainly doesn't working in the Vainshtein region. Given all these extra effects that have not

yet been taken into account, it is not unreasonable to conjecture that the current advanced LIGO constraints on massive gravity theories are already much stronger than those quoted in the literature so far.

4 Summary

Realistic, nonlinear, diffeomorphism invariant effective field theories of modified gravity do exist and can be tested. Many models designed to modify late time cosmology can also be constrained by solar system, astrophysical (e.g. pulsars), strong gravity physics, gravitational waves. The various different screening mechanisms that arise in these theories play a crucial role in their theoretical and observational viability.

Nonlinear theories of massive gravity are examples which will lead to many physical effects different from general relativity, and these theories arise whenever diffeomorphism invariance is spontaneously broken. Constraints on the graviton mass arise from probing essentially three different distinct physical consequences of the existence of a graviton mass, (1) Yukawa suppression, (2) dispersion relation and (3) fifth forces. Looking to the future, strong gravity and gravitational wave physics will place strong constraints on these theories. For example, current constraints on the graviton mass from advanced Ligo need to be improved to better understand the nonlinear dynamics of the helicity-0 mode (Vainshtein effect), and the properties of the black holes and neturon stars in massive gravity (be it Lorentz invariant or Lorentz violating), how the binary merger is modified, and how the quasi-normal modes are modified.

Acknowledgments

AJT thanks the Royal Society for support at ICL through a Wolfson Research Merit Award. AJT wishes to thank the organizers of the Rencontres de Moriond for an excellent meeting.

References

1. D. Psaltis, "Probes and Tests of Strong-Field Gravity with Observations in the Electromagnetic Spectrum," Living Rev. Rel. **11**, 9 (2008) doi:10.12942/lrr-2008-9 [arXiv:0806.1531 [astro-ph]].
2. S. Weinberg, "Testing Quantum Mechanics," Annals Phys. **194**, 336 (1989). doi:10.1016/0003-4916(89)90276-5
3. R. P. Feynman, F. B. Morinigo, W. G. Wagner and B. Hatfield, "Feynman lectures on gravitation," Reading, USA: Addison-Wesley (1995) 232 p. (The advanced book program)
4. S. Weinberg, "Photons and gravitons in perturbation theory: Derivation of Maxwell's and Einstein's equations," Phys. Rev. **138**, B988 (1965). doi:10.1103/PhysRev.138.B988
5. S. Deser, "Selfinteraction and gauge invariance," Gen. Rel. Grav. **1**, 9 (1970) doi:10.1007/BF00759198 [gr-qc/0411023].
6. R. M. Wald, "Spin-2 Fields and General Covariance," Phys. Rev. D **33**, 3613 (1986). doi:10.1103/PhysRevD.33.3613
7. K. Hinterbichler and J. Khoury, "Symmetron Fields: Screening Long-Range Forces Through Local Symmetry Restoration," Phys. Rev. Lett. **104**, 231301 (2010) doi:10.1103/PhysRevLett.104.231301 [arXiv:1001.4525 [hep-th]].
8. J. Khoury, "Chameleon Field Theories," Class. Quant. Grav. **30**, 214004 (2013) doi:10.1088/0264-9381/30/21/214004 [arXiv:1306.4326 [astro-ph.CO]].
9. A. I. Vainshtein, "To the problem of nonvanishing gravitation mass," Phys. Lett. **39B**, 393 (1972). doi:10.1016/0370-2693(72)90147-5

10. E. Babichev and C. Deffayet, "An introduction to the Vainshtein mechanism," Class. Quant. Grav. **30**, 184001 (2013) doi:10.1088/0264-9381/30/18/184001 [arXiv:1304.7240 [gr-qc]].
11. N. Arkani-Hamed, H. Georgi and M. D. Schwartz, "Effective field theory for massive gravitons and gravity in theory space," Annals Phys. **305**, 96 (2003) doi:10.1016/S0003-4916(03)00068-X [hep-th/0210184].
12. C. de Rham, G. Gabadadze and A. J. Tolley, "Resummation of Massive Gravity," Phys. Rev. Lett. **106**, 231101 (2011) doi:10.1103/PhysRevLett.106.231101 [arXiv:1011.1232 [hep-th]].
13. C. de Rham, J. T. Deskins, A. J. Tolley and S. Y. Zhou, "Graviton Mass Bounds," Rev. Mod. Phys. **89**, no. 2, 025004 (2017) doi:10.1103/RevModPhys.89.025004 [arXiv:1606.08462 [astro-ph.CO]].
14. C. de Rham, A. J. Tolley and D. H. Wesley, "Vainshtein Mechanism in Binary Pulsars," Phys. Rev. D **87**, no. 4, 044025 (2013) doi:10.1103/PhysRevD.87.044025 [arXiv:1208.0580 [gr-qc]].
15. C. de Rham, A. Matas and A. J. Tolley, Phys. Rev. D **87**, no. 6, 064024 (2013) doi:10.1103/PhysRevD.87.064024 [arXiv:1212.5212 [hep-th]].
16. A. S. Goldhaber and M. M. Nieto, "Mass of the graviton," Phys. Rev. D **9**, 1119 (1974). doi:10.1103/PhysRevD.9.1119
17. C. Talmadge, J. P. Berthias, R. W. Hellings and E. M. Standish, "Model Independent Constraints on Possible Modifications of Newtonian Gravity," Phys. Rev. Lett. **61**, 1159 (1988). doi:10.1103/PhysRevLett.61.1159
18. S. R. Choudhury, G. C. Joshi, S. Mahajan and B. H. J. McKellar, "Probing large distance higher dimensional gravity from lensing data," Astropart. Phys. **21**, 559 (2004) doi:10.1016/j.astropartphys.2004.04.001 [hep-ph/0204161].
19. B. P. Abbott *et al.* [LIGO Scientific and Virgo Collaborations], "GW151226: Observation of Gravitational Waves from a 22-Solar-Mass Binary Black Hole Coalescence," Phys. Rev. Lett. **116**, no. 24, 241103 (2016) doi:10.1103/PhysRevLett.116.241103 [arXiv:1606.04855 [gr-qc]]. B. P. Abbott *et al.* [LIGO Scientific and Virgo Collaborations], "Observation of Gravitational Waves from a Binary Black Hole Merger," Phys. Rev. Lett. **116**, no. 6, 061102 (2016) doi:10.1103/PhysRevLett.116.061102 [arXiv:1602.03837 [gr-qc]]. B. P. Abbott *et al.* [LIGO Scientific and Virgo Collaborations], "Tests of general relativity with GW150914," Phys. Rev. Lett. **116**, no. 22, 221101 (2016) doi:10.1103/PhysRevLett.116.221101 [arXiv:1602.03841 [gr-qc]].
20. C. M. Will, "Bounding the mass of the graviton using gravitational wave observations of inspiralling compact binaries," Phys. Rev. D **57**, 2061 (1998) doi:10.1103/PhysRevD.57.2061 [gr-qc/9709011].
21. A. S. Goldhaber and M. M. Nieto, "Photon and Graviton Mass Limits," Rev. Mod. Phys. **82**, 939 (2010) doi:10.1103/RevModPhys.82.939 [arXiv:0809.1003 [hep-ph]].

Cosmic Tsunamis Wrecking Screening Mechanisms in Modified Gravity

David F. Mota
Institute of Theoretical Astrophysics, University of Oslo, 0315 Oslo, Norway

High energy astrophysical phenomena, such as supernovae explosions or collapse of domain walls, create waves in the new degrees of freedom of modified theories of gravity. The propagation of such waves into our galaxy and solar system significantly impacts the efficiency of screening mechanisms, thereby threatening the viability of these theories.

1 Introduction

Any modification to Einstein's gravity must include a screening mechanism to hide the new extra degree of freedom and reduce the theory to general relativity in the well tested regimes [1]. The common feature to all the screening mechanisms is that they are built, and their efficiency tested, assuming the so called quasistatic approximation for the field equations. We find that, when relaxing the quasistatic approximation, the presence of waves may result in striking consequences for the efficiency and viability of the screening mechanism. In particular, we show that energetic waves in the extra degree of freedom strongly weaken the screening process for a theory with a standard kinetic term. Therefore, modified gravity theories previously considered viable may, in fact, be ruled out by the present days gravity experiments and observational data. To understand the implications of these waves in greater detail, we simulate a scalar degree of freedom with externally generated waves. The waves propagate radially in towards a spherically symmetric matter distribution, modeled after the Milky Way halo.

1.1 The symmetron

As a working example, we implement a specific form of modified gravity called the *symmetron* [2]. In spite of this specificity, the results presented here should be considered for any modified gravity theories that have extra degrees of freedom with wave-type equations of motion. We consider the following general scalar-tensor action for canonical scalar fields:

$$S = \int \left[\sqrt{-g} \left(\frac{R}{16\pi G} - \frac{1}{2}\phi^{,\mu}\phi_{,\mu} - V(\phi) \right) + \sqrt{-\tilde{g}}\tilde{\mathcal{L}}_m \right] \mathrm{d}^4x, \tag{1}$$

$V(\phi)$ is the quartic symmetron potential with the three free parameters μ, λ, and V_0

$$V(\phi) = -\frac{1}{2}\mu^2\phi^2 + \frac{1}{4}\lambda\phi^4 + V_0. \tag{2}$$

The Jordan frame metric $\tilde{g}$ is related to the Einstein frame metric according to the conformal transformation $\tilde{g}_{\mu\nu} = C(\phi)\, g_{\mu\nu}$. The specific form of C for the symmetron is $C(\phi) = 1 + (\phi/M)^2$. The mass scale M is a free parameter that gives the strength of the interaction with the matter

fields. The equation of motion for the scalar field is

$$\ddot{\phi} + 3H\dot{\phi} - \frac{1}{a^2}\nabla^2\phi = -\rho\frac{C_{,\phi}(\phi)}{2C(\phi)} - V_{,\phi}(\phi), \tag{3}$$

The Einstein frame metric is assumed to be a flat Friedmann-Lemaître-Robertson-Walker metric with a single scalar perturbation Ψ_E, specifically

$$\mathrm{d}s^2 = -(1+2\Psi_E)\,\mathrm{d}t^2 + a^2(t)(1-2\Psi_E)\,\mathrm{d}r^2. \tag{4}$$

As a working example, we fix the symmetron parameters such that $\beta = 1$, $a_{\rm SSB} = 0.5$, and $\lambda_0 = 0.25\,\mathrm{Mpc}/h$. This is equivalent to a symmetron mass $M = 3.4 \times 10^{-4}\,M_{\rm pl}$. These parameters are being widely assumed to represent a viable model that evades all the bounds from both Solar System and astrophysical data. With this choice of parameters, we aim to prove that even such a model may, in fact, be ruled out when one fully integrates the equations of motion of the field without the quasistatic assumption and, thereby, allow for the effects of the scalar waves.

2 Solar System constraints

To test how screening mechanisms work in the Solar System, the community generally chooses a static, spherically symmetric matter distribution to mimic the Galaxy. We follow this approach and choose the Navarro-Frenk-White density profile with the characteristics to represent the Milky Way Galaxy, specifically with a virial radius of $r_{\rm vir} = 137\,\mathrm{kpc}/h$ and concentration $c = 28$, resulting in a halo mass of $1.0 \times 10^{12} M_\odot$ and a circular velocity of 220 km/s at 8 kpc. The reason for the high value of the concentration is simply that we are modeling not only dark matter, but the total matter of the Milky Way, which is more concentrated than the pure dark matter halo [5].

One of the most precisely measured gravity parameters to probe deviations from general relativity is the parametrized post-Newtonian (PPN) parameter γ. It can be expressed as the ratio of the metric perturbations in the Jordan frame, Ψ_J and Φ_J:

$$\gamma - 1 = -\frac{\phi^2}{M^2}\frac{2}{\frac{\phi^2}{M^2} - 2\Psi_E - 2\Psi_E\frac{\phi^2}{M^2}}. \tag{5}$$

In general relativity, $\gamma = 1$ exactly. The strongest constraint to date, measured by the Cassini spacecraft, is $\gamma - 1 = (2.1 \pm 2.3) \times 10^{-5}$.

The symmetron screening works by modifying the effective potential such that the field value is pushed towards zero in high density regions – like the inner regions of the Galaxy. This results in $\gamma - 1 \to 0$, such that the deviations from general relativity in the proximity of the Solar System are small. The same occurs for the fifth force F_ϕ associated to the scalar field [3,4].

3 Results

Figure 1 shows an example of how the PPN parameter γ changes when a wave enters the inner 100 kpc of the Milky Way. The vertical line shows the position of the Solar System, which we assume to be 8 kpc from the Galactic center. The modifications to gravity are initially screened very well in the regions around this position, with $|\gamma - 1| < 10^{-8}$ (blue dashed line). However, after the wave has arrived (black solid line), the scalar field is perturbed enough to breach the Solar System constraints, $|\gamma - 1| > 2 \times 10^{-5}$. In other words, the screening mechanism breaks down under these circumstances. The wave in this particular simulation has an amplitude $A = 0.01$ and a frequency $\omega = 40\ \mathrm{Myr}^{-1}$. The cusps are regions where the scalar field is zero, which exist since the wave oscillates both above and below $\chi = 0$.

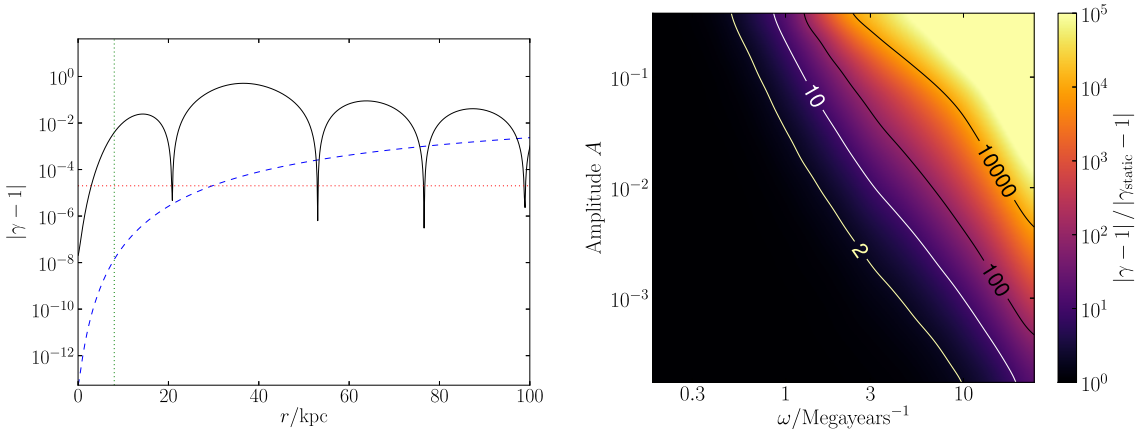


Figure 1 – LEFT: The PPN parameter $|\gamma - 1|$, plotted against distance from the center of the Galaxy. The curves show $|\gamma - 1|$ in the quasistatic case (blue dashed line), as well as after a scalar wave has entered the halo (black solid line). The vertical (green dotted) line indicates the position of the Solar System, and the horizontal (red dotted) line indicates the highest allowed value of $\gamma - 1$ in the Solar System from the Cassini experiment. When the wave enters the Milky Way, it increases the value of $|\gamma - 1|$ by several orders of magnitude. RIGHT: Maximum increase in the PPN parameter $|\gamma - 1|$ due to incoming scalar field waves at the position of the Sun in the Galaxy (8 kpc from the center) as a function of amplitude and frequency of the incoming waves. The color indicates by which factor $|\gamma - 1|$ is increased when compared to the quasistatic case with no waves.

When measuring γ arising from a single sinusoidal wave with low frequency, there is a possibility that the local wave is between two extrema at the time of measurement. This could render this kind of detection difficult for several thousand years. Nevertheless, given that various astrophysical events—such as supernovae—can generate waves, the probability that one of the wavefronts would bring us away from the minima at the present time is not negligible [6]. In order to investigate how our result depends on the frequency ω and amplitude A of the waves, we simulate incoming waves with several values of these two parameters. Figure 1 shows the maximum growth of $|\gamma - 1|$ that we found at 8 kpc from the Galactic center. Brighter colors mean a larger increase of $|\gamma - 1|$ compared to the quasistatic approximation. The values of the frequency and amplitude that lie in the black region of the plot, give waves that do not significantly impact γ compared to the quasistatic solution. Therefore, in this region of parameter space, the screening mechanism is efficient and hides the extra degree of freedom from gravity experiments.

From Figure 1, one concludes that higher frequencies and amplitudes for the incoming scalar waves give larger deviations from the general relativity result (i.e., $\gamma = 1$). The limit where amplitude and frequency go to zero is equivalent to the quasistatic limit, where no waves are produced and their energy is zero. As one goes into the high frequency and amplitude regime, the waves carry more energy, and therefore, the PPN parameter γ starts deviating significantly from the quasistatic limit. Note that, since in the symmetron model, the fifth force is $F_\phi \propto \nabla\phi^2/M^2$, these values can be immediately extrapolated to the impact of the waves on this quantity.

The dependence of the γ PPN parameter on the wave amplitude is straightforward to understand: When a wave propagates through the screened regions of the halo, a larger amplitude wave will lead to larger displacements of the field from the screening value $\phi \approx 0$. Therefore, $|\gamma - 1| \propto \phi^2$ will increase accordingly.

The frequency dependence of the γ parameter is a consequence of the following: The effective potential of the symmetron grows steeper and narrower in high density areas. In other words, the mass of the field increases towards the center of the halo. Therefore, it becomes more difficult to perturb the field away from the minimum, and a higher wave energy is needed to displace it. Specifically, if the energy of the external waves is small compared to the mass of the field, the field will not be perturbed and the γ parameter will not be affected.

The results obtained imply that if waves with sufficient amplitude or frequency can somehow

be generated in a given model for modified gravity, they will have to be taken into account when constraining the model parameters. Cosmic tsunamis, resulting from extreme events, could even completely ruin the screening mechanisms in modified gravity by increasing the deviations from general relativity by several orders of magnitude compared to the quasistatic case. A subject that that must be discussed now is the generation of such waves. Extreme events on small scales, such as collision of neutron stars, stellar, or super-massive black holes are obvious examples. Generation of waves by pulsating stars are another possibility.

In the specific case of the symmetron model, it is possible to obtain waves from events that occur on cosmological scales. First, the symmetron model undergoes a phase transition when the density falls below a specific threshold. This transition first occurs in voids when the expansion factor is close to $a_{\rm SSB}$. When this happens, the scalar field receives a kick, which produces waves traveling from the center of the voids towards the dark matter halos. We find that, in a symmetron model with slightly different parameters, the amplitude of cosmological waves is typically smaller that 0.1 and the associated frequencies are of the order of 1/Myr. Note that these values depend on the model parameters and, hence, must be taken only as indicative. Scalar waves can also be created through the collapse of topological defects, which are known to exist in any model in which such phase transition occurs.

4 Conclusions

The viability of modified theories of gravity is strongly dependent on the existence of a screening mechanism that suppresses any extra degrees of freedom at these scales. Here, we show that waves propagating in an additional gravity degree of freedom, may significantly spoil the screening mechanism and, hence, jeopardize the viability of the given modified gravity theory. Specifically, we show that waves in a given model can increase the amplitude of the fifth force and the PPN parameter $|\gamma - 1|$ by several orders of magnitude, rendering theories previously assumed to be viable unfeasible. To demonstrate that similar effects can be expected in other theories, we propose a simple calculation regarding a viable chameleon model ($n = 1$, $M = 10^{-3} M_{\rm Pl}$, $\Lambda = 2\,{\rm meV}$). When a white dwarf explodes as a type Ia supernova, waves in the chameleon field will be measurable at several Mpc distance.

The applicability of the quasistatic approximation should be carefully analyzed when obtaining constraints for modified gravity theories from Solar System experiments. Our results show that, in modified gravity, the Solar System—and indeed, the Galaxy—can not be studied in isolation; events that occur on cosmological scales might actually impact events that happen in the inner Solar System. While our conclusions make it more difficult to build viable modified gravity theories based on screening mechanisms, the existence of nonstatic effects opens a completely new window for developing new tests of gravity.

Acknowledgments

DFM thanks R. Hagala and C. Llinares whose collaboration resulted in the Letter this proceeding is based on.

References

1. P. Brax, Acta Phys. Polon. B **43**, 2307 (2012) doi:10.5506/APhysPolB.43.2307
2. K. Hinterbichler and J. Khoury, Phys. Rev. Lett. **104** (2010) 231301
3. D. F. Mota, M. Sandstad and T. Zlosnik, JHEP **1012** (2010) 051
4. D. F. Mota, D. J. Shaw and J. Silk, Astrophys. J. **675** (2008) 29
5. C. Llinares and D. Mota, Phys. Rev. Lett. **110** (2013) no.16, 161101
6. R. Hagala, C. Llinares and D. F. Mota, Phys. Rev. Lett. **118** (2017) no.10, 101301

Degenerate Higher-Order Scalar-Tensor (DHOST) theories

David Langlois
APC (Astroparticules et Cosmologie), CNRS-Université Paris Diderot,
10, rue Alice Domon et Léonie Duquet, 75013 Paris, France

This contribution reviews scalar-tensor theories whose Lagrangian contains second-order derivatives of a scalar field but nevertheless propagate only one scalar mode (in addition to the usual two tensor modes), and are thus not plagued with the Ostrodradsky instability. These theories, which encompass the so-called Horndeski and Beyond Horndeski theories, have recently been fully classified up to cubic order in second-order derivatives. After introducing these theories, I present a few phenomenological aspects. In cosmology, these theories can be included in the unified effective description of dark energy and modified gravity. Finally, neutron star solutions in some specific models are discussed.

1 Introduction

There have been numerous attempts to modify or extend general relativity, with either the motivation to account for dark energy (and sometimes dark matter) or, more modestly, to construct benchmark models that are useful to test general relativity quantitatively. Scalar-tensor theories have often played a prominent role in these attempts and, lately, special attention has been devoted to scalar-tensor theories whose Lagrangians contain second-order derivatives of a scalar field.

Lagrangians of this type, which contain "accelerations", are generically plagued by an instability due to the presence, in addition to the usual scalar mode and tensor modes, of an extra scalar degree of freedom (unless the higher order terms can be treated as perturbative terms in the sense of low energy effective theories). Until recently, it was believed that only theories that yield second-order Euler-Lagrange equations were free of this dangerous extra degree of freedom. In the last couple of years, it has been realized that there in fact exists a much larger class of theories that satisfy this property.

2 From Horndeski to DHOST theories

2.1 Higher-Order Scalar-Tensor theories

In this section, we introduce scalar-tensor theories whose action is a functional of a metric $g_{\mu\nu}$ and of a scalar field ϕ, allowing for a dependence not only on ϕ and its gradient $\phi_\mu \equiv \nabla_\mu\phi$ as usual, but also on its second derivatives $\phi_{\mu\nu} \equiv \nabla_\mu\nabla_\nu\phi$. Restricting our investigation to Lagrangians that depend on $\phi_{\mu\nu}$ up to cubic order, we are interested by actions of the form

$$S[g,\phi] = \int d^4x\,\sqrt{-g}\,\Big[f_0(X,\phi) + f_1(X,\phi)\Box\phi + f_2(X,\phi)\,R + C^{\mu\nu\rho\sigma}_{(2)}\,\phi_{\mu\nu}\,\phi_{\rho\sigma} + \\ + f_3(X,\phi)\,G_{\mu\nu}\phi^{\mu\nu} + C^{\mu\nu\rho\sigma\alpha\beta}_{(3)}\,\phi_{\mu\nu}\,\phi_{\rho\sigma}\,\phi_{\alpha\beta}\Big]\ , \qquad (1)$$

where the functions f_i depend only on ϕ and $X \equiv \phi_\mu \phi^\mu$, while R and $G_{\mu\nu}$ denote, respectively, the usual Ricci scalar and Einstein tensor associated with the four-dimensional metric $g_{\mu\nu}$. The tensors $\mathbf{C}_{(2)}$ and $\mathbf{C}_{(3)}$ are the most general tensors constructed with the metric $g_{\mu\nu}$ and the scalar field gradient ϕ_μ.

It is easy to see that the terms quadratic in $\phi_{\mu\nu}$ can be rewritten as

$$C^{\mu\nu\rho\sigma}_{(2)}\,\phi_{\mu\nu}\,\phi_{\rho\sigma} = \sum_{A=1}^{5} a_A(X,\phi)\,L^{(2)}_A\,, \tag{2}$$

with

$$\begin{aligned} &L^{(2)}_1 = \phi_{\mu\nu}\phi^{\mu\nu}\,, \qquad L^{(2)}_2 = (\Box\phi)^2\,, \qquad L^{(2)}_3 = (\Box\phi)\phi^\mu\phi_{\mu\nu}\phi^\nu\,, \\ &L^{(2)}_4 = \phi^\mu\phi_{\mu\rho}\phi^{\rho\nu}\phi_\nu\,, \qquad L^{(2)}_5 = (\phi^\mu\phi_{\mu\nu}\phi^\nu)^2\,, \end{aligned} \tag{3}$$

where the a_A are five arbitrary functions of X and ϕ. Similarly, the cubic terms can be written in terms of ten arbitrary functions b_A, as

$$C^{\mu\nu\rho\sigma\alpha\beta}_{(3)}\,\phi_{\mu\nu}\,\phi_{\rho\sigma}\,\phi_{\alpha\beta} = \sum_{A=1}^{10} b_A(X,\phi)\,L^{(3)}_A\,, \tag{4}$$

where

$$\begin{aligned} &L^{(3)}_1 = (\Box\phi)^3\,, \quad L^{(3)}_2 = (\Box\phi)\,\phi_{\mu\nu}\phi^{\mu\nu}\,, \quad L^{(3)}_3 = \phi_{\mu\nu}\phi^{\nu\rho}\phi^\mu_\rho\,, \quad L^{(3)}_4 = (\Box\phi)^2\,\phi_\mu\phi^{\mu\nu}\phi_\nu\,, \\ &L^{(3)}_5 = \Box\phi\,\phi_\mu\phi^{\mu\nu}\phi_{\nu\rho}\phi^\rho\,, \quad L^{(3)}_6 = \phi_{\mu\nu}\phi^{\mu\nu}\phi_\rho\phi^{\rho\sigma}\phi_\sigma\,, \quad L^{(3)}_7 = \phi_\mu\phi^{\mu\nu}\phi_{\nu\rho}\phi^{\rho\sigma}\phi_\sigma\,, \\ &L^{(3)}_8 = \phi_\mu\phi^{\mu\nu}\phi_{\nu\rho}\phi^\rho\,\phi_\sigma\phi^{\sigma\lambda}\phi_\lambda\,, \quad L^{(3)}_9 = \Box\phi\,(\phi_\mu\phi^{\mu\nu}\phi_\nu)^2\,, \quad L^{(3)}_{10} = (\phi_\mu\phi^{\mu\nu}\phi_\nu)^3\,. \end{aligned} \tag{5}$$

Theories described by an action of the form (1) in general contain, in addition to the usual scalar mode and two tensor modes, an extra scalar mode leading to the so-called Ostrogradsky instability [1]. However, by imposing some restrictions on the functions f_2, f_3 and a_A and b_A, it is possible to find theories that only one propagating scalar mode.

Historically, theories of this type were found in several steps. The starting point was the construction of higher-order theories leading to at most second-order Euler-Lagrange equations for the metric and for the scalar field, due to Horndeski [2]. Until recently, it was (wrongly) believed that requiring at most second-order Euler-Lagrange equations was necessary to get rid of the extra scalar degree of freedom and, as a consequence, Horndeski theories were considered to be the most general theories without Ostrogradsky instability. This belief was challenged by a new class of theories, now often called Beyond Horndeski (or GLPV), proposed in [3], extending Horndeski's theories and leading to higher-order equations of motion [a]. Beyond Horndeski theories were finally superseded by a larger class of theories, the DHOST theories, once it was understood that the crucial element that characterizes higher-order theories propagating a single scalar degree of freedom is the degeneracy of their Lagrangian [5], rather than the order of their equations of motion [b]. By using the degeneracy criterium, the quadratic DHOST theories were first identified in [5], extending both quadratic Horndeski and Beyond Horndeski Lagrangians [c]. More recently, all DHOST theories up to cubic order have been systematically classified [9].

[a] It is also worth noting that [4] had already pointed out the possibility to construct theories "beyond Horndeski" by applying disformal transformations of the metric to the Einstein-Hilbert action.

[b] In [6], after showing that the equations of motion of Beyond Horndeski theories, written in an arbitrary gauge, can be reformulated as a system of equations with at most second-order time derivatives, it was suggested that this property could provide a characterization of theories with a single scalar DOF. However, one can notice that this reformulation also applies to theories that are not degenerate (and thus propagate an extra scalar DOF), therefore invalidating this diagnostic. Note that, for scalar-tensor theories, the presence of redundant variables, due to the diffeomorphism invariance, makes it difficult to count the number of degrees of freedom just from the order of the equations of motion; instead, one needs to identify the number of independent initial conditions that are physically relevant.

[c] The name DHOST was not coined in the original paper but later in [7]. Note that the very same (quadratic) theories were also dubbed "Extended Scalar-Tensor" in [8].

2.2 Degeneracy of the Lagrangian

As mentioned above, the crucial ingredient that singles out higher-order theories with a single scalar degree of freedom is the degeneracy of their Lagrangian [5]. To better understand this notion of degeneracy, it is instructive to present a very simple toy model based on classical point dynamics. Let us consider the Lagrangian

$$L = \frac{1}{2}a\,\ddot{\phi}^2 + b\,\ddot{\phi}\,\dot{q} + \frac{1}{2}\dot{\phi}^2 + \frac{1}{2}c\,\dot{q}^2 - V(\phi, q)\,, \tag{6}$$

where a, b and c are constant coefficients and $V(\phi, q)$ is some potential. This Lagrangian involves the acceleration of ϕ but not that of q. If $a \neq 0$, one gets fourth-order equations of motion, whereas, if $a = 0$ but $b \neq 0$, one obtains third-order equations of motion.

In order to work with a more familiar Lagrangian containing only velocities, let us introduce, following [5], the auxiliary variable

$$Q \equiv \dot{\phi}\,, \tag{7}$$

leading to the new (and equivalent) Lagrangian

$$L = \frac{1}{2}a\,\dot{Q}^2 + b\,\dot{Q}\,\dot{q} + \frac{1}{2}c\,\dot{q}^2 + \frac{1}{2}Q^2 - V(\phi, q) - \lambda(Q - \dot{\phi})\,, \tag{8}$$

which does not include any acceleration.

Let us now try to identify the number of independent physical degrees of freedom in the system. Equivalently, one can count the number of initial conditions that are needed to fully determine the system at some initial time. From the equations of motion, it is easy to see that two cases arise, depending on the nature of the Hessian matrix, defined by

$$M \equiv \left(\frac{\partial^2 L}{\partial v^a \partial v^a}\right) = \begin{pmatrix} a & b \\ b & c \end{pmatrix}\,, \tag{9}$$

where the symbol v^a denotes the velocities, i.e. $v^a \equiv \{\dot{Q}, \dot{q}\}$.

In the generic case where M is invertible, one finds that six initial conditions are needed, which corresponds to the existence of three degrees of freedom. While the variable q describes as usual one degree of freedom, the variable ϕ is associated with two degrees of freedom. By contrast, in the particular cases where M is degenerate, i.e.

$$\det M = ac - b^2 = 0\,, \tag{10}$$

only four initial conditions are necessary, which means that only two degrees of freedom are present. The extra mode associated with ϕ is eliminated when M is degenerate. By extension, it can be said that the initial Lagrangian (6) is degenerate in this situation.

The number of degrees of freedom can also be determined by resorting to a Hamiltonian analysis. When the Lagrangian is degenerate, the conjugate momenta satisfy a (primary) constraint. By writing down the time evolution of this constraint, one finds that it leads to a secondary constraint in phase space. These two constraints eliminate one degree of freedom, in agreement with the analysis based on the equations of motion.

The above discussion can be generalised to the case of n variables similar to ϕ. In order to get rid of all of the n extra degrees of freedom that arise in general, one must not only impose a degeneracy of order n of the Hessian matrix, which guarantees the existence of n primary constraints, but also require additional constraints to ensure the presence of n secondary constraints [10, 11].

2.3 Horndeski and Beyond Horndeski theories

Well-known particular examples of DHOST theories are Horndeski's theories. They are characterized by four arbitrary functions of ϕ and X, corresponding to the four functions f_A that appear in the general action (1). The other functions a_A and b_A are then completely determined in terms of f_2 and f_3, respectively. The quadratic part of the Horndeski action, which it is convenient to denote $L^{\rm H}_{(2)}[f_2]$, is thus fully determined by the function f_2, with the quadratic coefficient a_A given by

$$a_1 = -a_2 = 2f_{2,X}\,, \qquad a_3 = a_4 = a_5 = 0\,. \tag{11}$$

Similarly, the cubic part of Horndeski theories, $L^{\rm H}_{(3)}[f_3]$, depends only on the functions f_3, while

$$3b_1 = -b_2 = \frac{3}{2}b_3 = f_{3,X}\,, \qquad b_A = 0 \ (A = 4, \ldots, 10)\,. \tag{12}$$

The so-called Beyond Horndeski (or GLPV) theories, introduced in [3], extend Horndeski theories by including two additional Lagrangians, each characterized by a single arbitrary function. The first of these Lagrangians, which can be written as $L^{\rm bH}_{(2)}[g_2]$, is quadratic and characterized by the coefficients

$$a_1 = -a_2 = Xg_2\,, \qquad a_3 = -a_4 = 2g_2\,, \qquad a_5 = 0\,. \tag{13}$$

The second new Lagrangian, which is cubic and will be denoted $L^{\rm bH}_{(3)}[g_3]$, depends on a single arbitrary function g_3 and its non vanishing coefficients b_A are given by

$$\frac{b_1}{X} = -\frac{b_2}{3X} = \frac{b_3}{2X} = -\frac{b_4}{3} = \frac{b_5}{6} = \frac{b_6}{3} = -\frac{b_7}{6} = g_3\,. \tag{14}$$

In the original paper [3], it was not yet fully clear whether arbitrary sums of the four Horndeski Lagrangians and of the two new Lagrangians $L^{\rm bH}_{(2)}[g_2]$ and $L^{\rm bH}_{(3)}[g_3]$ were viable. It was first pointed out in [12] that some Beyond Horndeski theories could be related to Horndeski theories via (invertible) conformal-disformal transformations, in which case they should have the same number of degrees of freedom as their Horndeski counterparts [d]. But it was only with the concept of degeneracy that this question was finally settled, with the results of [5] and [13].

Let us briefly summarize these results, by stressing that the sum of two degenerate Lagrangians is not necessarily degenerate. Moreover the terms f_0 and $f_1\Box\phi$ can always be added in the action without modifying the degeneracy of the total Lagrangian, so we do not need to worry about these terms any further. For the remaining terms, the following combinations involving Beyond Horndeski terms are degenerate: $L^{\rm H}_{(2)} + L^{\rm bH}_{(2)}$, $L^{\rm H}_{(3)} + L^{\rm bH}_{(3)}$ and $L^{\rm bH}_{(2)} + L^{\rm bH}_{(3)}$. By contrast, the following combinations are not degenerate: $L^{\rm H}_{(2)} + L^{\rm bH}_{(2)} + L^{\rm H}_{(3)}$, $L^{\rm H}_{(2)} + L^{\rm bH}_{(2)} + L^{\rm bH}_{(3)}$.

2.4 DHOST theories

As discussed above, the crucial element that characterizes higher-order theories with a single scalar degree of freedom is the degeneracy of their Lagrangian, hence their name DHOST [e].

DHOST theories were originally identified at quadratic order in $\phi_{\mu\nu}$ (i.e. with the functions f_2 and a_A only) in [5] and a complete Hamiltonian analysis in [14] soon confirmed that they indeed contained only one scalar degree of freedom. Quadratic DHOST theories were further studied in [7, 8, 15]. More recently, the identification of DHOST theories has been extended up to cubic order, i.e. by including the second line of (1), in [9] and the interested reader will find the full classification there.

[d] Note that the calculation in the final part of [12], directly inspired by a similar calculation in [4], does not lead to a manifestly second-order system, as originally claimed. But the main point of the paper, based on disformal transformations, remains valid.

[e] Amusingly, this acronym can be obtained by substituting the initial of 'ghost' with 'D' of 'degeneracy'.

In summary, DHOST theories include seven subclasses of quadratic theories (four classes with $f_2 \neq 0$ and three classes with $f_2 = 0$) and nine subclasses of cubic theories (two with $f_3 \neq 0$ and seven with $f_3 = 0$). These quadratic and cubic subclasses can be combined to yield degenerate hybrid theories, involving both quadratic and cubic terms, but all combinations are not possible: only 25 combinations (out of 63) lead to degenerate theories, often with extra conditions on the functions a_A and b_A in the Lagrangian (see [9] for details and for the explicit form of the functions in each subclass).

2.5 Disformal transformations

A legitimate question about this classification is whether seemingly different DHOST theories could correspond the same theory in different guises, in other words whether some theories could be identified via field redefinitions[f]. Since the Lagrangian depends on a metric and on a scalar field, natural field redefinitions of the metric involve disformal transformations [16]

$$\tilde{g}_{\mu\nu} = C(X,\phi) g_{\mu\nu} + D(X,\phi)\, \phi_\mu\, \phi_\nu \,. \tag{15}$$

Via this transformation, any action $\tilde{S}$ given as a functional of $\tilde{g}_{\mu\nu}$ and ϕ induces a new action S for $g_{\mu\nu}$ and ϕ, when one substitutes the above expression for $\tilde{g}_{\mu\nu}$ in $\tilde{S}$:

$$S[\phi, g_{\mu\nu}] \equiv \tilde{S}\left[\phi, \tilde{g}_{\mu\nu} = C\, g_{\mu\nu} + D\, \phi_\mu \phi_\nu\right] \,. \tag{16}$$

The actions S and $\tilde{S}$ are then said to be related by the disformal transformation (15). The disformal transformations of all quadratic DHOST theories have been investigated in [7], where it was shown that all seven subclasses are stable under the action of disformal transformations.

Interestingly, there is a nice correspondence between the type of disformal transformations and the extent of the corresponding stable class of theories:

- Horndeski theories are stable under disformal transformations characterized by $C(\phi)$ and $D(\phi)$, i.e. conformal and disformal factors that depend only on ϕ, but not on X [17].
- Beyond Horndeski theories are stable under disformal transformations characterized by $C(\phi)$ and $D(\phi, X)$ [12].
- Finally, DHOST theories are stable under the most general disformal transformations where C and D depend on both ϕ and X [7].

3 Cosmology and astrophysics

After the short introduction to DHOST theories given in the previous section, let us now discuss briefly some phenomenological consequences of these theories in the context of cosmology and of astrophysics.

3.1 Cosmology

In order to study the cosmology of DHOST theories, it is very convenient to resort to the unified formalism that has been developed for an effective description of Dark Energy and Modified Gravity (see e.g. [18] for a review).

This approach is based on a $3+1$ decomposition of spacetime, in which the spatial slices coincide with uniform scalar field hypersurfaces. In this particular gauge, sometimes called unitary gauge, the action of DHOST theories is of the form

$$S = \int d^3x\, dt\, N\sqrt{h}\, L[N, K_{ij}, {}^3R_{ij}; t] \,, \tag{17}$$

[f] The coupling to matter is ignored here. If, after a redefinition of the metric, two related theories are minimally coupled to matter, then they are physically distinct.

where N is the lapse function [which appears in the $3+1$ form of the spacetime metric $ds^2 = -N^2dt^2 + h_{ij}(dx^i + N^i dt)(dx^j + N^j dt)$, N^i being the shift vector, h_{ij} the spatial metric]; K_{ij} is the extrinsic curvature tensor and ${}^3R_{ij}$ the intrinsic curvature tensor.

The Friedmann equations associated with a spatially flat Friedmann-Lemaître-Robertson-Walker (FLRW) spacetime $ds^2 = -\bar{N}^2(t)dt^2 + a^2(t)\delta_{ij}dx^i dx^j$, are then simply derived from the homogeneous action

$$S_{\rm homog} = \int dt\, N a^3 L[N = \bar{N}(t), K^i_j = \frac{\dot{a}}{\bar{N}a}\delta^i_j, {}^3R_{ij} = 0; t]\,. \tag{18}$$

To study the dynamics of linear perturbations, one needs to write down the action at quadratic order in perturbations. These perturbations are associated with the three basic ingredients of the action:

$$\delta N \equiv N - \bar{N}\,, \qquad \delta K^i_j = K^i_j - H\delta^i\,, \qquad \delta\, {}^3R^i_j = {}^3R^i_j\,, \tag{19}$$

where $H = \dot{a}/\bar{N}a$ is the Hubble parameter, and ${}^3R^i_j$ is already a perturbation since it vanishes in the background. The Lagrangian at quadratic order is then obtained via a Taylor expansion, which is formally written as

$$L(q_A) = \bar{L} + \frac{\partial L}{\partial q_A}\delta q^A + \frac{1}{2}\frac{\partial^2 L}{\partial q_A \partial q_B}\delta q^A \delta q^B + \dots\,. \tag{20}$$

where $q^A = \{N, K^i_j, {}^3R^i_j\}$.

All (quadratic and cubic) DHOST theories lead to a Lagrangian quadratic in linear perturbations of the form [19]

$$\begin{aligned} S_{\rm quad} \;=\; & \int d^3x\, dt\, a^3 \frac{M^2}{2}\Bigg\{\delta K_{ij}\delta K^{ij} - \left(1+\frac{2}{3}\alpha_{\rm L}\right)\delta K^2 + (1+\alpha_{\rm T})\left({}^3R\frac{\delta\sqrt{h}}{a^3} + \delta_2{}^3R\right) + H^2\alpha_{\rm K}\delta N^2 \\ & + 4H\alpha_{\rm B}\delta K\delta N + (1+\alpha_{\rm H})\,{}^3R\,\delta N + 4\beta_1\delta K\delta\dot{N} + \beta_2\delta\dot{N}^2 + \frac{\beta_3}{a^2}(\partial_i\delta N)^2\Bigg\}\,, \end{aligned} \tag{21}$$

where $\delta_2{}^3R$ denotes the second order term in the perturbative expansion of ${}^3R$, where the parameters M, $\alpha_{\rm L}$, $\alpha_{\rm T}$, $\alpha_{\rm K}$, $\alpha_{\rm B}$, $\alpha_{\rm H}$, β_1, β_2 and β_3 are time-dependent functions. Moreover, one finds that these parameters, for DHOST theories, are restricted to satisfy either one of the following sets of conditions:

$$\mathcal{C}_{\rm I}: \qquad \alpha_{\rm L} = 0\,, \qquad \beta_2 = -6\beta_1^2\,, \qquad \beta_3 = -2\beta_1\left[2(1+\alpha_{\rm H}) + \beta_1(1+\alpha_{\rm T})\right]\,, \tag{22}$$

or

$$\mathcal{C}_{\rm II}: \qquad \beta_1 = -(1+\alpha_{\rm L})\frac{1+\alpha_{\rm H}}{1+\alpha_{\rm T}}\,, \quad \beta_2 = -6(1+\alpha_{\rm L})\frac{(1+\alpha_{\rm H})^2}{(1+\alpha_{\rm T})^2}\,, \quad \beta_3 = 2\frac{(1+\alpha_{\rm H})^2}{1+\alpha_{\rm T}}\,. \tag{23}$$

The category $\mathcal{C}_{\rm I}$ contains the subclass of Horndeski theories and of those related to Horndeski via disformal transformations.

In the static linear regime around Minkowski, one can define an effective Newton's constant given by [19]

$$8\pi G_{\rm N} = M^{-2}\left[\frac{(1+\alpha_{\rm H})^2}{1+\alpha_{\rm T}} - \frac{\beta_3}{2}\right]^{-1}\,, \tag{24}$$

which diverges for theories satisyfing $\mathcal{C}_{\rm II}$.

The coupling to matter can be minimal or nonminimal. One can derive the transformation of the parameters that describe the matter coupling at linear level under disformal transformations (15). Similar transformations exist for the parameters of (21). See [19] for details.

3.2 Stars in Beyond Horndeski theories

Even if the main motivation for modified gravity arises from the observed acceleration of the cosmological expansion, it is indispensable to verify that any viable theory remains compatible with astrophysical observations and solar system constraints.

As part of this programme, let us concentrate on Beyond Horndeski theories. In these models, it has been noticed that the Vainshtein mechanism is partially broken inside matter [20]. For spherical bodies, a new term appears in the gravitational law,

$$\frac{d\Phi}{dr} = \frac{G_{\rm N} M(r)}{r^2} + \frac{\Upsilon}{4} G_{\rm N} \frac{d^2 M(r)}{dr^2} \,, \tag{25}$$

where Φ is the gravitational potential and $M(r)$ is the mass inside a sphere of radius r. This leads to a modified profile of Newtonian stars [21, 22].

Following the recent works [23] and [24], let us discuss neutron stars in a specific model described by the action

$$S = \int d^4x \sqrt{-g} \left[M_{\rm P}^2 \left(\frac{R}{2} - k_0 \Lambda \right) - k_2 X - \frac{\zeta}{2} X^2 + \mathcal{L}_{(2),{\rm bH}}[g_2] \right] \,, \tag{26}$$

where k_0, k_2, ζ and g_2 are assumed to be constant. By writing the Friedmann equations for this model, one can easily find de Sitter solutions where the Hubble parameter H is constant. In order to embed a spherical object within such cosmological spacetime, it is useful to rewrite the de Sitter solution in Schwarzschild-like coordinates,

$$ds^2 = -(1 - H^2 r^2) dt^2 + \frac{dr^2}{1 - H^2 r^2} + r^2 \left(d\theta^2 + \sin^2\theta d\phi^2 \right) \,, \tag{27}$$

$$\phi(r,t) = v_0 t + \frac{v_0}{2H} \ln(1 - H^2 r^2) \,. \tag{28}$$

One can then insert a spherical symmetric object in this cosmological solution by trying to solve the Einstein equations for a metric of the form

$$ds^2 = -e^{\nu(r)} dt^2 + e^{\lambda(r)} dr^2 + r^2 \left(d\theta^2 + \sin^2\theta d\phi^2 \right) \,, \tag{29}$$

going asymptotically to (27). The energy-momentum tensor receives a contribution from the scalar field as well as a contribution from a perfect fluid which is assumed to model the neutron star's matter. Remarkably, one can find an exact solution outside the star, corresponding to a Schwarzschild-de Sitter geometry. Inside the star, the equations of motion can be solved numerically, assuming some equation of state, in order to determine the matter density profile and the internal geometry.

When $\Upsilon < 0$, one finds that stars with fixed mass have a larger radius than their GR counterparts. Moreover, for the same equation of state, the maximum mass can increase significantly with respect to GR [23]. Modified gravity could thus provide a solution to the hyperon puzzle. Moreover, one can derive a relation between the dimensionless moment of inertia Ic^2/G^2M^3 and the compactness GM/Rc^2, which is robust in the sense that it weakly depends on the equation of state and which can discriminate between modified gravity and GR [24].

Acknowledgments

I would like to thank my numerous collaborators, especially Karim Noui and Filippo Vernizzi, for their contributions to the works I have presented here.

References

1. R. P. Woodard, Scholarpedia **10**, no. 8, 32243 (2015) [arXiv:1506.02210 [hep-th]].
2. G. W. Horndeski, Int. J. Theor. Phys. **10**, 363 (1974).
3. J. Gleyzes, D. Langlois, F. Piazza and F. Vernizzi, Phys. Rev. Lett. **114**, no. 21, 211101 (2015) [arXiv:1404.6495 [hep-th]].
4. M. Zumalacarregui and J. Garcia-Bellido, Phys. Rev. D **89**, 064046 (2014) [arXiv:1308.4685 [gr-qc]].
5. D. Langlois and K. Noui, JCAP **1602**, no. 02, 034 (2016) [arXiv:1510.06930 [gr-qc]].
6. C. Deffayet, G. Esposito-Farese and D. A. Steer, Phys. Rev. D **92**, 084013 (2015) [arXiv:1506.01974 [gr-qc]].
7. J. Ben Achour, D. Langlois and K. Noui, Phys. Rev. D **93**, no. 12, 124005 (2016) [arXiv:1602.08398 [gr-qc]].
8. M. Crisostomi, K. Koyama and G. Tasinato, JCAP **1604**, no. 04, 044 (2016) [arXiv:1602.03119 [hep-th]].
9. J. Ben Achour, M. Crisostomi, K. Koyama, D. Langlois, K. Noui and G. Tasinato, JHEP **1612**, 100 (2016) [arXiv:1608.08135 [hep-th]].
10. H. Motohashi, K. Noui, T. Suyama, M. Yamaguchi and D. Langlois, JCAP **1607**, 007 (2016) [arXiv:1603.09355 [hep-th]].
11. R. Klein and D. Roest, JHEP **1607**, 130 (2016) [arXiv:1604.01719 [hep-th]].
12. J. Gleyzes, D. Langlois, F. Piazza and F. Vernizzi, JCAP **1502**, 018 (2015) [arXiv:1408.1952 [astro-ph.CO]].
13. M. Crisostomi, M. Hull, K. Koyama and G. Tasinato, JCAP **1603**, no. 03, 038 (2016) [arXiv:1601.04658 [hep-th]].
14. D. Langlois and K. Noui, JCAP **1607**, no. 07, 016 (2016) [arXiv:1512.06820 [gr-qc]].
15. C. de Rham and A. Matas, JCAP **1606**, no. 06, 041 (2016) [arXiv:1604.08638 [hep-th]].
16. J. D. Bekenstein, Phys. Rev. D **48**, 3641 (1993) [gr-qc/9211017].
17. D. Bettoni and S. Liberati, Phys. Rev. D **88**, 084020 (2013) [arXiv:1306.6724 [gr-qc]].
18. J. Gleyzes, D. Langlois and F. Vernizzi, Int. J. Mod. Phys. D **23**, no. 13, 1443010 (2015) [arXiv:1411.3712 [hep-th]].
19. D. Langlois, M. Mancarella, K. Noui and F. Vernizzi, JCAP **1705**, no. 05, 033 (2017) [arXiv:1703.03797 [hep-th]].
20. T. Kobayashi, Y. Watanabe and D. Yamauchi, Phys. Rev. D **91**, no. 6, 064013 (2015) [arXiv:1411.4130 [gr-qc]].
21. K. Koyama and J. Sakstein, Phys. Rev. D **91**, 124066 (2015) [arXiv:1502.06872 [astro-ph.CO]].
22. R. Saito, D. Yamauchi, S. Mizuno, J. Gleyzes and D. Langlois, JCAP **1506**, 008 (2015) [arXiv:1503.01448 [gr-qc]].
23. E. Babichev, K. Koyama, D. Langlois, R. Saito and J. Sakstein, Class. Quant. Grav. **33**, no. 23, 235014 (2016) [arXiv:1606.06627 [gr-qc]].
24. J. Sakstein, E. Babichev, K. Koyama, D. Langlois and R. Saito, Phys. Rev. D **95**, no. 6, 064013 (2017) [arXiv:1612.04263 [gr-qc]].

STABILITY OF FUNDAMENTAL COUPLINGS AND DARK ENERGY: A PRE-ESPRESSO ANALYSIS AND FORECAST

C. J. A. P. MARTINS, A. C. O. LEITE, A. M. M. PINHO, C. S. ALVES,
F. M. O. MOUCHEREK, T. A. SILVA
Centro de Astrofísica da Universidade do Porto and IA, Universidade do Porto, Rua das Estrelas, 4150-762 Porto, Portugal

We highlight some recent developments in tests of the stability of nature's fundamental couplings, which provide a direct handle on new physics: a detection of variations will be revolutionary, but even improved null results provide competitive constraints on a range of cosmological and particle physics paradigms. A joint analysis of all currently available data shows a preference for variations of α and μ at about the two-sigma level, but inconsistencies between different sub-sets (likely due to hidden systematics) suggest that these statistical preferences need to be taken with caution. On the other hand, these measurements strongly constrain Weak Equivalence Principle violations. Plans and forecasts for forthcoming studies with facilities such as ALMA, ESPRESSO and the E-ELT, which should clarify these issues, are also briefly discussed, showing how a new generation of precision consistency tests of the standard paradigm will soon become possible.

1 Scalars, because they are there

We now know, from experiments at the LHC, that fundamental scalar fields are among Nature's building blocks and that Nature's fundamental dimensionless couplings run with energy. Whenever one such field is included in the Lagrangian, it will naturally couple to the rest of the model's degrees of freedom, unless a new (unknown) principle is postulated to suppress them. This leads to potentially observable long-range forces and spacetime varying couplings [1,2,3], which can therefore roll in time (or equivalently redshift) and ramble in space (in practice, depending on the local environment).

Tests of the stability of nature's fundamental couplings, whether they reveal detections of variations or simply null results, constrain fundamental physics and cosmology. Varying dimensionless physical constants imply a violation of the Einstein Equivalence Principle (demonstrating that gravity is not a purely geometric phenomenon) as well as the presence of a fifth force of nature. There will also be violations of the temperature-redshift relation and the distance duality relation, which provide key consistency tests [4,5]. Conversely, null results provide upper bounds on Equivalence Principle violations as well as on dynamical dark energy and several particle physics paradigms. These constraints ensure a 'minimum guaranteed science', which is relevant when developing the science cases and technical designs of future facilities.

The importance of improved bounds can be ascertained by comparison to constraining the dark energy equation of state or, to be more specific, its present-day value w_0. The dynamically relevant parameter $(1 + w_0)$ (the ratio of the square of the field speed to its total density, in the simple case of a canonical scalar field) is naively or order unity, but observationally known to be less than 0.1. But if this is not of order unity, there is no known natural physical scale to set its value: either there is fine-tuning, or a new (currently unknown) symmetry forces it

to be zero. The same argument can be made for the relative variation of say the fine-structure constant α, henceforth defined as $\Delta\alpha/\alpha(z) = (\alpha(z) - \alpha_0)/\alpha_0$, with α_0 being its present-day laboratory value, the difference being that this parameter is observationally constrained to be (conservatively) less that 10^{-5}, as we will discuss in the rest of this article. Stringent as this bound is, it is important to go further, as illustrated by the strong CP Problem in QCD: a parameter naively expected to be of order unity is known to be smaller than 10^{-10}, leading to the postulate of Peccei-Quinn symmetry and the axion (an interesting dark matter candidate) [6]. A sufficiently tight bound would either indicate that there are no dynamical fields in cosmology or that a new symmetry suppresses the couplings—whose existence would be as significant as that of the original field.

2 Current measurements

A compilation of the current astrophysical tests of the stability of fundamental couplings has recently been published in [7]. They comprise 293 archival measurements of the fine-structure constant α of Webb *et al.* [8], 21 more recent dedicated measurements of α, 16 measurements of the proton-to-electron mass ratio μ, and 29 measurements of various combinations of α, μ and the proton gyromagnetic ratio g_p.

A global likelihood analysis of all this data, assuming a single redshift-independent astrophysical value for each of the dimensionless couplings, yields

$$\frac{\Delta\alpha}{\alpha} = -1.6 \pm 0.5\, ppm\,, \quad \frac{\Delta\mu}{\mu} = -0.2 \pm 0.1\, ppm\,, \quad \frac{\Delta g_p}{g_p} = 1.7 \pm 1.3\, ppm\,, \tag{1}$$

where the values are given in units of parts per million (10^{-6}), and unless otherwise stated all values are quoted with one-sigma (68.3%) confidence level. A more detailed tomographic analyis, dividing the data into several redshift bins has also been done [7]. This reveals inconsistencies at the one to two sigma level beween radio/mm and optical/UV measurements. Since the former and the latter typically yield measurements at redshifts $z < 1$ and $z > 1$ respectively, naive theorists may interpret this as differences between acceleration and matter era values (which are indeed expected in realistic models for varying couplings) while skeptical observers will suspect hidden systematics in one or both types of measurements. Efforts are ongoing to clarify these issues through obervations with APEX and ALMA, while the forthcomng ESPRESSO spetrograph will play a key role in this endeavour.

The archival data of Webb *et al.* [8] provides a 4.2σ statistical evidence for a dipole in the values of α. An updated analysis including all currently available data [7] lowers this statistical evidence to only 2.3σ, with the posterior likelihood for the amplitude of the dipole (marginalized over sky direction) being $A_\alpha = 5.6 \pm 1.8\, ppm$. A similar analysis can be done for the μ measurements. In this case the statistical preference for a dipole is less than 2σ, and the two sigma (95.4% confidence) upper bound on its amplitude is $A_\mu < 1.9\, ppm$; furthermore the preferred directions of both putative dipoles differ by about 3σ. A defintive test of a parts per million level dipole will be carried out by ESPRESSO. Meanwhile, a more robust method to constrain spatial variation will be discussed below.

3 Dark energy and Equivalence Principle constraints

The energy content of the Universe is dominated by a component whose gravitational behavior is known to be quite similar to that of a cosmological constant. This may well turn out to be the case, but given the well known theoretical problems associated with this explanation a dynamical scalar field is (arguably) more likely. Such a field must be slow-rolling (which is mandatory for a negative pressure) and be dominating the cosmological dynamics around the present day. These are enough to ensure that couplings of this field will lead to potentially observable long-range forces and varying 'constants' [1,2,3]. As we presently show, current measurements already

provide competitive constraints on fundamental physics and cosmology, and the improvement of these constraints is among the flagship science cases (and design drivers) for forthcoming ESO facilities, including ESPRESSO and the E-ELT.

If the same degree of freedom is responsible for dark energy and varying α, the latter's evolution is parametrically determined. In the simplest case of a canonical quintessence-type scalar field, one has

$$\frac{\Delta\alpha}{\alpha}(z) = \zeta \int_0^z \sqrt{3\Omega_\phi(z')(1+w_\phi(z'))}\frac{dz'}{1+z'}\,, \tag{2}$$

where ζ is the dimensionless coupling between the scalar field and the electromagentic part of the Lagrangian and $\Omega_\phi(z) = \rho_\phi(z)/(\rho_\phi(z)+\rho_m(z))$ is the fraction of the universe's energy in the dark energy component, where for simplicity we have neglected the contribution form the radiation density since the astrophysical measurements under consideration are all at low redshifts. Current constraints, combining the aforementioned astrophysical measurements of α with atomic clock constraints on its present-day drift rate [9] and background cosmology measurements of Type Ia supernova and Hubble parameter measurements [10,11] lead to the following 2σ upper bound [12,13,14] $|\zeta| < 4\times10^{-6}$. The ESPRESSO GTO measurements, discussed in Ana Catarina Leite's contribution to these proceedings, should improve this bound by a factor of 10, assuming null results [15].

In these models the scalar field will inevitably couple to nucleons (through the α dependence of their masses) and lead to violations of the Weak Equivalence Principle [2,3,16]. Thus measurements of α constrain the Eotvos parameter η: the current 2σ bound for these models is [13,14]

$$\eta < 1.6\times10^{-14}\,. \tag{3}$$

This is an order of magnitude stronger than the current best direct bounds from torsion balance and lunar laser ranging experiments [17,18]. We therefore predict that the MICROSCOPE satellite, whose foreseen sensitivity on η should be around 10^{-15} (cf. the contributions by M. Rodrigues and G. Métris in these proceedings) will not find violations at least up to the above level. On the other hand, with the ESPRESSO GTO measurements we expect to reach a sensitivity on η of 2×10^{-16} (about 5 times better than MICROSCOPE). In the longer term, the ELT-HIRES sensitivity is expected to be at the level of a few times 10^{-18}, similar to that of proposed STEP satellite.

4 Other models: rollng tachyons and symmetrons

Astrophysical measurements of α constrain other classes of models. A rolling tachyon is a Born-Infeld scalar motivated in string theory which naturally yields coupling to gauge fields. The tachyon Lagrangian generalizes the one for a relativistic particle, like quintessence one generalizes that of a non-relativistic one. In these models the potential slope determines both $w(z)$ and $\alpha(z)$, unavoidably leading to thawing models with $\Delta\alpha/\alpha < 0$. Nhe current α measurements lead to the extremely tight constraint on the present-day dark energy equation of state, at the 3σ (99.7%) confidence level $(1+w_0) < 2.4\times10^{-7}$. Therefore background cosmology probes can not distinguish these models from standard ΛCDM, while α data can.

Above we discussed constraints on pure spatial α dipoles. While one can also fit a dipole to any such dataset, physically such a behavior is not expected to ensue from any realistic model (except perhaps at the cost of significant fine-tuning). In these cases one rather expects that α will have environmental variations (e.g., it can depend on the local density). In [20] we have introduced a methodology to test models with spatial variations of α, based on the calculation of the angular power spectrum of these measurements. This enables comparisons of observations and theoretical models through their predictions on the statistics of the α variation. Applying it to the case of symmetron models we find no deviations from the standard behavior, with current data providing an upper limit to the strength of the symmetron coupling to gravity

$\log \beta^2 < -0.9$ when this is the only free parameter, and not able to constrain the model when also the symmetry breaking scale factor is also free to vary. The forthcoming ESPRESSO data will enable more stringent constraints on this and other models with spatial variations.

5 Conclusions

Precision spectroscopy is a direct and competitive probe of the (unknown) new physics behind the universe's acceleration. It provides the best current constraints on Weak Equivalence Principle violations, and it offers unique opportunities to map the behavior of the dark energy equation of state deep into the matter era [21].

The ESPRESSO spectrograph is coming soon, and will be a game changer. It will provide a consistency test of the MICROSCOPE results (and enable interesting joint analyses) as well as a range of competitive 'guaranteed science' implications for dark energy and fundamental physics. In the 2020's the E-ELT will be the flagship tool in a new generation of precision consistency tests, which together have a unique value of complementarity, redundancy, and synergies with other facilities, including ALMA, Euclid and the SKA.

Acknowledgments

This work was done in the context of project PTDC/FIS/111725/2009 (FCT, Portugal), with additional support from grant UID/FIS/04434/2013. CJM is supported by an FCT Research Professorship, contract reference IF/00064/2012, funded by FCT/MCTES (Portugal) and POPH/FSE (EC). CSA is partially supported by grant CIAAUP-06/2017-BIC, ACL is supported by an FCT fellowship (SFRH/BD/113746/2015), under the FCT PD Program PhD::SPACE (PD/00040/2012), and by the Gulbenkian Foundation through *Programa de Estímulo à Investigação 2014*, grant number 2148613525.

References

1. S. M. Carroll, *Phys. Rev. Lett.* **81**, 3067 (1998).
2. G. R. Dvali and M. Zaldarriaga, *Phys. Rev. Lett.* **88**, 091303 (2002).
3. T. Chiba and K. Kohri, *Prog. Theor. Phys.* **107**, 631 (2002).
4. A. Avgoustidis *et al*, *J. Cosmol. Astropart. Phys.* **1202**, 013 (2012).
5. A. Avgoustidis *et al*, *Phys. Rev.* D **93**, 043521 (2016).
6. R. D. Peccei and H. R. Quinn, *Phys. Rev. Lett.* **38**, 1440 (1977).
7. C. J. A. P. Martins and A. M. M. Pinho, *Phys. Rev.* D **95**, 023008 (2017).
8. J. K. Webb *et al.*, *Phys. Rev. Lett.* **107**, 191101 (2011).
9. T. Rosenband *et al.*, *Science* **319**, 1808 (2008).
10. N. Suzuki *et al.*, *Astrophys. J.* **746**, 85 (2012).
11. O. Farooq *et al*, *Astrophys. J.* **835**, 26 (2017).
12. C. J. A. P. Martins and A. M. M. Pinho, *Phys. Rev.* D **91**, 103501 (2015).
13. C. J. A. P. Martins *et al.*, *J. Cosmol. Astropart. Phys.* **1508**, 047 (2015).
14. C. J. A. P. Martins *et al.*, *Phys. Rev.* D **93**, 023506 (2016).
15. C. S. Alves *et al.*, *Phys. Lett.* B **770**, 93 (2017).
16. T. Damour and J. F. Donoghue, *Class. Quant. Grav.* **27**, 202001 (2010).
17. T. A. Wagner *et al.*, *Class. Quant. Grav.* **29**, 184002 (2012).
18. J. Miller *et al.*, *Class. Quant. Grav.* **29**, 184006 (2012).
19. C. J. A. P. Martins and F. M. O. Moucherek, *Phys. Rev.* D **93**, 123524 (2016).
20. A. M. M. Pinho *et al.*, *Phys. Lett.* B **769**, 491 (2017).
21. A. C. O. Leite *et al.*, *Phys. Rev.* D **94**, 123512 (2016).

GENERALISED PROCA THEORIES

LAVINIA HEISENBERG
Institute for Theoretical Studies, ETH Zurich,
Clausiusstrasse 47, 8092 Zurich, Switzerland



In this work we will summarise the recent progress made in constructing consistent theories for a massive vector field with derivative self-interactions. The construction is such that only the three desired polarisations of the Proca field propagate. We apply a systematic construction of the interactions by using the anti-symmetric Levi-Civita tensors. This finite family of allowed derivative self-interactions can be also obtained from the decoupling limit by imposing that the Stückelberg field only contains second derivatives both with itself and with the transverse modes. These interactions can be generalised to curved backgrounds, which relies on the presence of non-minimal couplings and constitutes a general family of vector-tensor interactions. We discuss also some extensions of these interactions by alleviating the restriction of second order nature of the equations or by imposing global symmetries. We will also comment on their interesting cosmological applications.

1 Introduction

The Standard Model of Big Bang cosmology constitutes the prevailing cosmological model, which is able to satisfactorily represent the physics on cosmological scales using the two fundamental pillars of General Relativity and the Cosmological Principle. The latter stands for the homogeneity and isotropy. The combined inquiry of the available cosmological observations has firmly established ΛCDM as the standard model for our universe in a simple picture. It describes the evolution of the universe from its earliest known periods through the subsequent formation of large-scale structures and it provides comprehensive explanation for most of the observed phenomena. Despite being elegant and simple, the model relies on the presence of three unknown ingredients, namely a cosmological constant acting as dark energy, a cold dark matter and an inflaton field, and it still faces some theoretical challenges. The most troublesome is the Cosmological Constant Problem and is a permanent reminder of our worrisome lack of a fully satisfactory and deep theoretical understanding for the value of the cosmological constant. Our theoretical foundation is shaky because we can not account for the enormous discrepancy between observations and the radiative corrections of massive particles to the vacuum energy using known standard techniques of quantum mechanics [1]. Along this line manifests itself another tenacious fundamental problem: we do not know how to construct a consistent theory of

quantum gravity. Naive attempts of applying the principles of quantum mechanics to gravity immediately fail. The constructed theory of graviton bosons is not renormalisable and loses its predictive power. We are also prone to encounter classical primordial and black hole singularities. These singularities might be cured by the quantum nature of the interactions or by classical modifications of gravity at high curvatures (see for instance [2]).

Concerning the dark matter component of the standard model, it is as essential and inevitable as the dark energy. It is fundamental for a successful description of the rotation curves of galaxies, Cosmic Microwave Background (CMB) anisotropies, large scale structures and weak lensing measurements. If dark matter exists, then we believe that it should be a distinctive matter from the ordinary baryonic matter beyond the standard model of particle physics. Its unique manifestation comes uniquely from its gravitational effect and it does not interact with photons. Notwithstanding the tremendous efforts, it has never been directly observed. Leaving aside the theoretical challenges, from purely observational side, the standard model with a cosmological constant and a cold dark matter fits the data almost impeccable. The word "almost" reflects the fact, that there are still some remaining anomalies. Just to mention a few, there is the tension in the Hubble constant obtained from local measurements versus from the CMB, the CMB hemispherical asymmetry together with the lack of power on large scales. There seem to be also some unusual large scale correlations and large scale bulk flows referred from distant quasar measurements. Even in the presence of dark matter, a slightly different cosmology is implied by the galaxy clusters than by the CMB measurements. It is also worth mentioning that there are unobserved predictions of the standard model, for instance the phase-space correlation of galaxy satellites and the generic formation of dark matter cusps in galaxies's central regions. On the contrary, the observations seem to indicate some tight correlations between the dynamical versus luminous mass, as the baryonic Tully-Fisher relation, which is not accounted for by the standard model. Most of the above mentioned anomalies do not have yet an overwhelming statistical significance, nonetheless, combined they might point out the failure of the assumptions of the Cosmological Principle and General Relativity.

The above mentioned theoretical challenges together with the remaining observational anomalies have motivated the exploration of modifications of gravity both in UV and IR. Thanks to the advances in observational cosmology in high precision measurements, cosmology is the ideal place to test fundamental physics and get to the heart of the true nature of gravitational interactions. Most extensively studied modifications of gravity are based on scalar fields since they can for instance naturally give rise to accelerated expansion without changing the Cosmological Principle. A homogeneous and isotropic universe can be realised with a time dependent scalar field and the non-vanishing vev of the scalar field could naturally support a (quasi) de Sitter solution. However, as a candidate for dark energy the scalar field needs to be extremely light resulting unavoidably in long-range forces. Nonetheless, these additional fifth forces have never been observed in local gravity tests and therefore without any further mechanisms would be ruled out by observations. Luckily, screening mechanisms come to rescue. The presence of a successful screening mechanism makes it possible to disguise the scalar field on small scales while being unleashed on large scales producing the wanted cosmological effects. There are many modifications of General Relativity that bear an additional scalar field with these promising properties. Just to mention a few, for instance massive gravity [3,4,5,6,7] and higher dimensional frameworks [8] naturally contain a scalar field as the helicity-0 part of the graviton with very specific non-linear interactions.

The Standard Model of elementary particles contains both abelian and non-abelian vector fields as the fundamental fields of the gauge interactions. Therefore, it is well motivated to explore the role of bosonic vector fields in the cosmological evolution. Traditionally, there is the worry that vector fields might generate large scale anisotropic expansion, which would make them not a natural candidate for dark energy. However, cosmic vector fields would naturally explain some of the aforementioned anomalies, specially those in relation with a possible preferred

direction. A possible way to make the vector field to support isotropic cosmological solutions would be to promote the vector field to be a Proca field. A promising route in this respect has been considered in the works [9,10,11] (see also [12,13,14,15,16]). These vector-tensor theories can indeed support isotropic cosmological solutions with the temporal component of the vector field [17,18,19,20,21,22,23]. They also feature screening mechanisms [24]. Interesting extensions of these generalised Proca interactions can be constructed by alleviating some of the requirements or enriching some of the symmetries [25,26,27,28,29,30,31].

1.1 Generalised Proca theories

We would like to generalize the interactions of a massive vector field without changing the propagating number of degrees of freedom, namely two transverse and one longitudinal mode of the vector field. To start with, we can promote the mass term to a general potential term $V(A^2)$. This will not alter the spectrum of propagating degrees of freedom, since there is not any derivative of the vector field involved. In a similar way, we can consider any gauge invariant interactions constructed out of the field strength tensor $F_{\mu\nu} = \partial_\mu A_\nu - \partial_\nu A_\mu$ and its dual and also any contraction of those with the vector field, since they will not contain any dynamics for the zeroth component of the vector field A_0. Collecting all these type of interactions gives

$$\mathcal{L}_2 = f_2(A_\mu, F_{\mu\nu}, \tilde{F}_{\mu\nu}). \tag{1}$$

The independent contractions will be in form of $X = -A_\mu A^\mu/2$, $F = -F_{\mu\nu}F^{\mu\nu}/4$ and $Y = A^\mu A^\nu F_\mu{}^\alpha F_{\nu\alpha}$ [9,32]and therefore this function can be also rewritten as $f_2(X, F, Y)$ (ignoring the partiy violating terms). In first order in derivatives of A_μ, we can start with the interaction

$$\mathcal{L}_3 = f_3(A^2)\ \ \partial \cdot A\,, \tag{2}$$

with the arbitrary function $f_3(A^2)$. Note, that this interaction does not give a total divergence due to f_3. The temporal component of the vector field remains non-dynamical and the corresponding Hessian matrix vanishes identically. Alternatively, we can write this interaction in terms of the Levi-Civita tensor

$$\mathcal{L}_3 = -\frac{f_3(A^2)}{6}\epsilon^{\mu\nu\rho\sigma}\epsilon^\alpha{}_{\nu\rho\sigma}\partial_\mu A_\alpha = f_3(A^2)\partial \cdot A\,. \tag{3}$$

It is clear that there is only one way of contracting the indices of the Levi-Civita tensors at this order. This term would correspond to the cubic Galileon interaction for the longitudinal mode if we take the decoupling limit. The indices of the Levi-Civita tensors were contracted among themselves. We could have also contracted them with two additional vector fields, like so $\tilde{f}_3(A^2)\epsilon^{\mu\nu\rho\sigma}\epsilon^{\alpha\beta}{}_{\rho\sigma}\partial_\mu A_\alpha A_\nu A_\beta$. This would have resulted in an interaction that is conformally related to the previous one $\tilde{f}_3(A^2)A^\mu A^\nu(\partial_\mu A_\nu)$. As next order in derivatives of the vector field we can consider the following three possible ways of contracting the Lorentz indices

$$\mathcal{L}_4 = f_4(A^2)\ \left[c_1(\partial \cdot A)^2 + c_2\partial_\rho A_\sigma \partial^\rho A^\sigma + c_3\partial_\rho A_\sigma \partial^\sigma A^\rho\right]\,, \tag{4}$$

where f_4 is again an arbitrary function and the parameters c_1, c_2 and c_3 need to be constrained in order to maintain the required property of three propagating degrees of freedom. In other words, we have to guarantee the presence of a second class constraint. We can ensure that by demanding that the corresponding determinant of the Hessian matrix $\det(H^{\mu\nu}_{\mathcal{L}_4}) = 2(c_1 + c_2 + c_3)(-2c_2)^3$ is zero. Hence, we need to ensure $c_1 + c_2 + c_3$ in order to obtain the required constraint. Choosing $c_1 = 1$ together with the condition $c_3 = -(1 + c_2)$, the Lagrangian then becomes

$$\mathcal{L}_4 = f_4\ \left[(\partial \cdot A)^2 + c_2\partial_\rho A_\sigma \partial^\rho A^\sigma - (1 + c_2)\partial_\rho A_\sigma \partial^\sigma A^\rho\right]\,. \tag{5}$$

We can obtain these interactions in terms of the Levi-Civita tensors immediately. The anti-symmetric structure of the two tensors will directly impose the conditions that we just worked

out by hand. Since the vector field has the symmetric and antisymmetric parts of $\partial_\mu A_\nu$ we can contract the indices in two ways

$$\begin{aligned}\mathcal{L}_4 &= -\frac{1}{2}\epsilon^{\mu\nu\rho\sigma}\epsilon^{\alpha\beta}{}_{\rho\sigma}(f_4(A^2)\partial_\mu A_\alpha\partial_\nu A_\beta + c_2\tilde{f}_4(A^2)\partial_\mu A_\nu\partial_\alpha A_\beta)\\ &= f_4\left[(\partial\cdot A)^2 - \partial_\rho A_\sigma\partial^\sigma A^\rho\right] + c_2\tilde{f}_4(\partial_\rho A_\sigma\partial^\rho A^\sigma - \partial_\rho A_\sigma\partial^\sigma A^\rho)\,. \end{aligned} \tag{6}$$

One recognises that the terms proportional to c_2 are just the field strength tensor F

$$\mathcal{L}_4 = f_4\left[(\partial\cdot A)^2 - \partial_\rho A_\sigma\partial^\sigma A^\rho\right] + c_2\tilde{f}_4 F^2_{\rho\sigma} \tag{7}$$

and can be thus absorbed into f_2. In a very similar way, we can construct the other interactions at next orders. We can either consider all the possible contractions of the interactions at each order and demand the vanishing of the determinant of the Hessian matrix, or we can directly apply the corresponding contractions with the Levi-Civita tensors. Both techniques result in the same terms. The self-interactions of the vector field can be summarised as the following Lagrangians at each order [9,11]

$$\begin{aligned}\mathcal{L}_2 &= f_2(X,F,Y)\\ \mathcal{L}_3 &= f_3(A^2)\ \partial\cdot A\\ \mathcal{L}_4 &= f_4(A^2)\ \left[(\partial\cdot A)^2 - \partial_\rho A_\sigma\partial^\sigma A^\rho\right]\\ \mathcal{L}_5 &= f_5(A^2)\ \left[(\partial\cdot A)^3 - 3(\partial\cdot A)\partial_\rho A_\sigma\partial^\sigma A^\rho + 2\partial_\rho A_\sigma\partial^\gamma A^\rho\partial^\sigma A_\gamma\right] + \tilde{f}_5(A^2)\tilde{F}^{\alpha\mu}\tilde{F}^\beta{}_\mu\partial_\alpha A_\beta\\ \mathcal{L}_6 &= f_6(A^2)\tilde{F}^{\alpha\beta}\tilde{F}^{\mu\nu}\partial_\alpha A_\mu\partial_\beta A_\nu\,. \end{aligned} \tag{8}$$

Note, that the series stops after $\mathcal{L}_6$ and there are not any higher order interactions. All these interactions give rise to second order equations of motion for the vector field and by construction they do not give rise to any dynamics of the temporal component of the vector field [9,10,11] .

2 Alternative construction from the decoupling limit

In a similar way we could have obtained the previously discussed systematic form of these interactions starting from the consistent interactions in the decoupling limit. In this limit the interactions of the transverse and longitudinal modes can be schematically written as an expansion

$$\mathcal{L} \sim \sum_{m,n,p} c_{m,n,p}\left(\frac{A}{\Lambda_M}\right)^m\left(\frac{F}{\Lambda_F^2}\right)^n\left(\frac{S}{\Lambda_S^2}\right)^p\,, \tag{9}$$

where we introduced the symmetric part of the interactions as $S_{\mu\nu} = \partial_\mu A_\nu + \partial_\nu A_\mu$ and the scales Λ_M, Λ_F and Λ_S of the objects with some coefficients $c_{m,n,p}$. One very useful trick is to restore the broken gauge invariance of the vector field using the Stückelberg field as $A_\mu \to A_\mu + \partial_\mu\pi/M$, where M stands for the mass of the vector field. In this language the scalar field π represents the longitudinal mode of the original massive vector field. One can now very easily take the decoupling limit by sending $M \to 0$ with the leading order contributions $A_\mu \to \partial_\mu\pi/M$ and similarly $S_{\mu\nu} \to \partial_\mu\partial_\nu\pi/M$. The aforementioned expansion of the interactions in this limit becomes

$$\mathcal{L}_{\rm dec} \sim \sum_{m,n,p} c_{m,n,p}\left(\frac{\partial\pi}{M\Lambda_M}\right)^m\left(\frac{F}{\Lambda_F^2}\right)^n\left(\frac{\partial\partial\pi}{M\Lambda_S^2}\right)^p\,. \tag{10}$$

We can now go order by order in the derivative of the scalar field and impose the conditions on $c_{m,n,p}$ after the summation. At the lowest order $p = 0$, we only have one derivative per scalar field

$$\mathcal{L}^{p=0}_{\rm dec} \sim \sum_{m,n} c_{m,n,0}\left(\frac{\partial\pi}{M\Lambda_M}\right)^m\left(\frac{F}{\Lambda_F^2}\right)^n\,. \tag{11}$$

A glance at the interactions reveals that one would obtain three types of interactions at this order after summation in m and n. The summation in n maintaining $m = 0$ would correspond just to functions of F^2. In the same way the summation in m with $n = 0$ would give rise to functions of the vector norm A^2. The third type of interactions at this order with $m \neq 0$ and $n \neq 0$ would just give rise to functions of $F_\mu{}^\alpha F_{\nu\alpha} A^\mu A^\nu$ type. Summarizing, the schematic interactions in (11) correspond exactly to the interactions $f_2(X, F, Y)$ in (17) when one takes the decoupling limit. In the same way, we can analyse the next order interactions with $p = 1$

$$\mathcal{L}^{p=1}_{\rm dec} \sim \sum_{m,n} c_{m,n,1} \left(\frac{\partial\pi}{M\Lambda_M}\right)^m \left(\frac{F}{\Lambda_F^2}\right)^n \left(\frac{\partial\partial\pi}{M\Lambda_S^2}\right) . \tag{12}$$

We will again have the interactions with $n = 0$ and they represent nothing else but the standard Galileon interactions at cubic order $f_3(\partial\pi^2)\partial_\mu\partial^\mu\pi$. In fact, they represent the leading order interactions of $f_3(A^2)\ \ \partial \cdot A$ in $\mathcal{L}_3$. The novel interesting interactions arise for the case $n \neq 0$, which gives rise to the first non-trivial mixing between the gauge field and the scalar field, where the scalar field comes in with second derivatives acting on it. After perfoming the summation in m and n, the resulting symmetric rank-2 tensor will be contracted with $\partial_\mu\partial_\nu\pi$ and one has to impose that the $00-$ component of this tensor does not contain any time derivatives other than $\dot\pi$. In other words, this symmetric rank-2 tensor can only be built out of $f_3(\partial\pi^2)\tilde F^{\mu\alpha}\tilde F^\nu{}_\alpha$ in order to satisfy this requirement, since its magnetic part $\tilde F^{0\alpha}\tilde F^0{}_\alpha \propto B^2$ is purely potential. Hence, the decoupling limit interactions at this order can only be

$$\mathcal{L}^{p=1}_{\rm dec} \sim \left(c_{2,0,1}(\partial\pi)^2\eta^{\mu\nu} + c_{0,2,1}\tilde F^{\mu\alpha}\tilde F^\nu{}_\alpha\right)\frac{\partial_\mu\partial_\nu\pi}{M\Lambda_S^2} . \tag{13}$$

The coefficients can be arbitrary functions of $(\partial\pi^2)$. The first type of interactions are the leading order terms of $f_3(A^2)\partial\cdot A$ in $\mathcal{L}_3$ and the second type interactions are the leading order contributions of $\tilde f_5(A^2)\tilde F^{\alpha\mu}\tilde F^\beta{}_\mu\partial_\alpha A_\beta$ in $\mathcal{L}_5$ in the decoupling limit. We see in the decoupling limit, that these are the only allowed interactions that give rise to second order equations of motion for both the scalar field and the gauge field. In complete analogy we can build the next order interactions with $p = 2$

$$\mathcal{L}^{p=2}_{\rm dec} \sim \sum_{m,n} c_{m,n,2} \left(\frac{\partial\pi}{M\Lambda_M}\right)^m \left(\frac{F}{\Lambda_F^2}\right)^n \left(\frac{\partial\partial\pi}{M\Lambda_S^2}\right)^2 . \tag{14}$$

We have to impose again that the purely scalar interactions have to correspond to the scalar Galileon interactions whereas the mixed interactions with $n \neq 0$ need to be constructed in a similar way as before, in other words the magnetic field of the gauge field should be allowed only to couple to the second time derivatives of π. This leads uniquely to

$$\mathcal{L}^{p=2}_{\rm dec} \sim c_{2,0,2}(\partial\pi)^2\frac{(\partial_\alpha\partial^\alpha\pi)^2 - (\partial_\mu\partial_\nu\pi)^2}{M^2\Lambda_S^4} + c_{0,2,2}\tilde F^{\mu\nu}\tilde F^{\alpha\beta}\frac{\partial_\mu\partial_\alpha\pi\partial_\nu\partial_\beta\pi}{M^2\Lambda_S^4} , \tag{15}$$

with the coefficients being arbitrary functions of $(\partial\pi^2)$. The first type interactions is the purely quartic Galileon interactions, which are the leading order terms of the interactions $f_4(A^2)\left[(\partial\cdot A)^2 - \partial_\rho A_\sigma\partial^\sigma A^\rho\right]$ in $\mathcal{L}_4$ whereas the second type of interactions are the leading order mixed terms of $f_6(A^2)\tilde F^{\alpha\beta}\tilde F^{\mu\nu}\partial_\alpha A_\mu\partial_\beta A_\nu$ in $\mathcal{L}_6$ in the decoupling limit. Finally, the cubic order interactions in $\partial\partial\pi$ with $p = 3$

$$\mathcal{L}^{p=3}_{\rm dec} \sim \sum_{m,n} c_{m,n,3} \left(\frac{\partial\pi}{M\Lambda_M}\right)^m \left(\frac{F}{\Lambda_F^2}\right)^n \left(\frac{\partial\partial\pi}{M\Lambda_S^2}\right)^3 \tag{16}$$

contain only the pure Galileon interactions and there is no consistent mixing between the scalar field and the gauge field at this order. One can not construct any new interactions with $n \neq 0$.

Note also, that the series stop here and hence the decoupling limit Lagrangian has a finite order of allowed interactions for the mixed couplings. From these decoupling limit Lagrangian one can obtain the full interactions by performing $\partial_\mu\pi \to A_\mu$ and $\partial_\mu\partial_\nu\pi \to S_{\mu\nu}$. They correspond to the same exact interactions that we constructed above using the Levi-Civita tensors. The total Lagrangian written in terms of the symmetric and antisymmetric parts is $\mathcal{L}_{\rm gen.Proca} = \sum_{n=2}^{5}\alpha_n\mathcal{L}_n^S$ with

$$\begin{aligned}
\mathcal{L}_2^S &= f_2(A_\mu, F_{\mu\nu}, \tilde{F}_{\mu\nu}) \\
\mathcal{L}_3^S &= f_3(A^2)[S] \\
\mathcal{L}_4^S &= f_4(A^2)\,\Big([S]^2 - [S^2]\Big) \\
\mathcal{L}_5^S &= f_5(A^2)\,\Big([S]^3 - 3[S][S^2] + 2[S^3]\Big) + \tilde{f}_5(A^2)\tilde{F}^{\alpha\mu}\tilde{F}^{\beta}{}_{\mu}S_{\mu\nu} \\
\mathcal{L}_6^S &= f_6(A^2)\tilde{F}^{\alpha\beta}\tilde{F}^{\mu\nu}S_{\alpha\mu}S_{\beta\nu}\,.
\end{aligned} \tag{17}$$

For the construction of these interactions the requirement of second order equations of motion and the absence of any dynamics for the temporal component of the vector field were very crucial. The latter condition reflects itself in the absence of higher order equation of motion for the scalar field once the broken gauge field is reintroduced using the Stückelberg trick. For more details see [9,11].

3 Curved background

The interactions we constructed above were so far on a flat background and it would be crucial to promote these interactions to the curved background case for different applications. In the presence of gravity the interactions have to be adjusted by counter-terms in order to maintain the property of second order equations of motion. If we simply replace the partial derivatives by covariant derivatives, then this would result in higher order equations of motion. In fact, specific non-minimal couplings have to be added for some of the interactions in order to guarantee the nature of second order equations of motion. For the construction of these non-minimal couplings the divergenceless tensors of the gravity sector play an important role. The pure Stückelberg field should this time possess the scalar Horndeski interactions [33]. This helps to construct the interactions for the vector field in curved backgrounds. The Lagrangian becomes $\mathcal{L}^{\rm curved}_{\rm gen.Proca} = \sqrt{-g}\sum_{n=2}^{6}\beta_n\mathcal{L}_n$ with [9,11]

$$\begin{aligned}
\mathcal{L}_2 &= G_2(A_\mu, F_{\mu\nu}) \\
\mathcal{L}_3 &= G_3(X)\nabla_\mu A^\mu \\
\mathcal{L}_4 &= G_4(X)R + G_{4,X}\Big[(\nabla_\mu A^\mu)^2 - \nabla_\rho A_\sigma\nabla^\sigma A^\rho\Big] \\
\mathcal{L}_5 &= G_5(X)G_{\mu\nu}\nabla^\mu A^\nu - \frac{1}{6}G_{5,X}\Big[(\nabla\cdot A)^3 \\
&+ 2\nabla_\rho A_\sigma\nabla^\gamma A^\rho\nabla^\sigma A_\gamma - 3(\nabla\cdot A)\nabla_\rho A_\sigma\nabla^\sigma A^\rho\Big] \\
&- g_5(X)\tilde{F}^{\alpha\mu}\tilde{F}^{\beta}{}_{\mu}\nabla_\alpha A_\beta \\
\mathcal{L}_6 &= G_6(X)\mathcal{L}^{\mu\nu\alpha\beta}\nabla_\mu A_\nu\nabla_\alpha A_\beta + \frac{G_{6,X}}{2}\tilde{F}^{\alpha\beta}\tilde{F}^{\mu\nu}\nabla_\alpha A_\mu\nabla_\beta A_\nu\,,
\end{aligned} \tag{18}$$

where we have now the covariant derivatives ∇ instead of partial and the vector field couples to the Ricci scalar, Einstein tensor and the double dual Riemann tensor $\mathcal{L}^{\mu\nu\alpha\beta} = \frac{1}{4}\epsilon^{\mu\nu\rho\sigma}\epsilon^{\alpha\beta\gamma\delta}R_{\rho\sigma\gamma\delta}$ in order to counter balance the corresponding derivative interactions of the vector field. Note, that the interaction $\tilde{G}_5(Y)\tilde{F}^{\alpha\mu}\tilde{F}^{\beta}{}_{\mu}\nabla_\alpha A_\beta$ does not require the introduction of a non-minimal coupling.

4 Extensions of Generalized Proca theories

The interactions we constructed so far satisfy the condition of second order equations of motion for both the vector field and the graviton. One could alleviate this restriction and construct more general interactions. In accordance with the beyond Horndeski construction for scalar fields [34,35], one can construct similar beyond generalized Proca interactions allowing higher order nature of the equations of motion but still maintaining the correct number of propagating degrees of freedom [25,26]. The interactions need to be constructed such that the presence of a constraint equation is not jeopardised. With these less restrictive conditions one can for instance construct new beyond generalized Proca interactions $\mathcal{L}^{\rm N} = \mathcal{L}_4^{\rm N} + \mathcal{L}_5^{\rm N} + \tilde{\mathcal{L}}_5^{\rm N} + \mathcal{L}_6^{\rm N}$, where in terms of the Levi-Civita tensors their novelty becomes apparent [25]

$$\mathcal{L}_4^{\rm N} = f_4(X)\hat{\delta}^{\beta_1\beta_2\beta_3\gamma_4}_{\alpha_1\alpha_2\alpha_3\gamma_4}A^{\alpha_1}A_{\beta_1}\nabla^{\alpha_2}A_{\beta_2}\nabla^{\alpha_3}A_{\beta_3}\,, \tag{19}$$

$$\mathcal{L}_5^{\rm N} = f_5(X)\hat{\delta}^{\beta_1\beta_2\beta_3\beta_4}_{\alpha_1\alpha_2\alpha_3\alpha_4}A^{\alpha_1}A_{\beta_1}\nabla^{\alpha_2}A_{\beta_2}\nabla^{\alpha_3}A_{\beta_3}\nabla^{\alpha_4}A_{\beta_4}\,, \tag{20}$$

$$\tilde{\mathcal{L}}_5^{\rm N} = \tilde{f}_5(X)\hat{\delta}^{\beta_1\beta_2\beta_3\beta_4}_{\alpha_1\alpha_2\alpha_3\alpha_4}A^{\alpha_1}A_{\beta_1}\nabla^{\alpha_2}A^{\alpha_3}\nabla_{\beta_2}A_{\beta_3}\nabla^{\alpha_4}A_{\beta_4}\,, \tag{21}$$

$$\mathcal{L}_6^{\rm N} = f_6(X)\hat{\delta}^{\beta_1\beta_2\beta_3\beta_4}_{\alpha_1\alpha_2\alpha_3\alpha_4}\nabla_{\beta_1}A_{\beta_2}\nabla^{\alpha_1}A^{\alpha_2}\nabla_{\beta_3}A^{\alpha_3}\nabla_{\beta_4}A^{\alpha_4}\,, \tag{22}$$

where we introduced $\hat{\delta}^{\beta_1\beta_2\gamma_3\gamma_4}_{\alpha_1\alpha_2\gamma_3\gamma_4} = \epsilon_{\alpha_1\alpha_2\gamma_3\gamma_4}\epsilon^{\beta_1\beta_2\gamma_3\gamma_4}$. The presence of these interactions results in a detuning between the relative coefficients of the non-minimal couplings to gravity and the derivative self interactions of the vector field and gives rise to higher order equations of motion. However, due to the constraint equation one still has five propagating degrees of freedom, namely the two transverse graviton modes and the three vector modes. Instead of using the systematical construction in terms of the Levi-Civita tensors, one can on a similar footing write down all the possible interactions between the fields and their derivatives with a priori arbitrary coefficients and put constraints on them afterwards coming from the vanishing of the determinant of the Hessian matrix as we did in 1.1 for the interactions in flat space-time. This reasoning was applied in [26] to construct the corresponding interactions up to $\mathcal{L}_4$ on curved space-time.

Another natural extension of the generalised Proca interactions can be constructed by promoting the broken gauge symmetry from $U(1)$ to the $SU(2)$ case. By breaking the non-abelian gauge symmetry, can we construct derivative self-interactions for a set of massive vector fields? One can indeed do that by following the same construction scheme using the antisymmetric Levi-Civita tensors and demanding that the equations of motion for A^a_μ remain second order while keeping the zero components non-dynamical [28,29,30,31]. Some of these interactions will correspond to the straightforward generalisation of the single Proca field to the multi-Proca interactions with global $SO(3)$ symmetry [29]

$$\begin{aligned}
\mathcal{L}_2 &= G_2(A^a_\mu, F^a_{\mu\nu}) \\
\mathcal{L}_4 &= G_4 R + G_4'\delta_{ab}\frac{S^a_{\mu\nu}S^{b\mu\nu} - S^{a\mu}_{\mu}S^{b\nu}_{\nu}}{4} \\
\mathcal{L}_6 &= G_6 L^{\mu\nu\alpha\beta}F^a_{\mu\nu}F_{a\alpha\beta} + \frac{G_6'}{2}\tilde{F}^{a\alpha\beta}\tilde{F}^{\mu\nu}_a S^b_{\alpha\mu}S_{b\beta\nu}.
\end{aligned} \tag{23}$$

It is worth to mention at this point that the restriction of the global $SO(3)$ symmetry diminishes the allowed interactions and for that reason one can not construct the analog of $\mathcal{L}_3$ and $\mathcal{L}_5$ interactions of the single Proca. Besides these direct extensions, there will be also genuine new interactions, which do not have the single Proca field analog [29]

$$\begin{aligned}
\mathcal{L}_3 &= S^{a\mu\nu}A^b_\mu A^d_\nu A^c_\alpha A^{e\alpha}\delta_{de}\epsilon_{abc} \\
\mathcal{L}_4 &= \epsilon^{\alpha\beta\gamma\delta}\tilde{F}^a_{\alpha\lambda}S^{b\lambda}{}_\beta A^a_\gamma A^b_\delta \\
\mathcal{L}_5 &= \epsilon_{abc}A^a_\mu A^{\mu d}\tilde{F}^{\alpha\nu}_d\tilde{F}^{b\beta}_\nu S^c_{\alpha\beta}\,.
\end{aligned} \tag{24}$$

In difference to the interactions $\mathcal{L}_4$ and $\mathcal{L}_6$ in (23), these genuine new interactions do not require the presence of non-minimal interactions. All these different extensions of the generalised Proca interactions offer promising routes to investigate further and may offer richer phenomenology.

5 Cosmological applications of generalized Proca theories

If one deals with massless abelian gauge fields, then the only possible cosmological application can be realised by considering N vector fields that are randomly distributed. In the case of a non-abelian vector field, one can construct interactions with global $SO(3)$ symmetry and consider field configurations where three vector fields point along the spatial directions. In the context of massive vector fields, one can achieve isotropic expansion with yet another field configuration. One can use the temporal component of the vector field as an auxiliary field in order to construct homogeneous and isotropic solutions. Compatible with the background of the metric $ds^2 = -dt^2 + a^2(t)d\vec{x}^2$, one can assume the following field configuration for the vector field:

$$A^\mu = (\phi(t), 0, 0, 0)\,. \tag{25}$$

From the action one can easily obtain the corresponding Einstein field equations for the background [18,20]

$$\begin{aligned} &G_2 - G_{2,X}\phi^2 - 3G_{3,X}H\phi^3 - 6(2G_{4,X} + G_{4,XX}\phi^2)H^2\phi^2 \\ &+6G_4H^2 + G_{5,XX}H^3\phi^5 + 5G_{5,X}H^3\phi^3 = \rho_M\,, \end{aligned} \tag{26}$$

$$\begin{aligned} &G_2 - \dot{\phi}\phi^2 G_{3,X} + 2G_4\,(3H^2 + 2\dot{H}) - 2G_{4,X}\phi\,(3H^2\phi + 2H\dot{\phi} + 2\dot{H}\phi) \\ &-4G_{4,XX}H\dot{\phi}\phi^3 + G_{5,XX}H^2\dot{\phi}\phi^4 + G_{5,X}H\phi^2(2\dot{H}\phi + 2H^2\phi + 3H\dot{\phi}) = -P_M\,, \end{aligned} \tag{27}$$

where $H = \dot{a}/a$ is the Hubble function. In a similar way, the vector field equations can be obtained in a straightforward way

$$\phi\left(G_{2,X} + 3G_{3,X}H\phi + 6G_{4,X}H^2 + 6G_{4,XX}H^2\phi^2 - 3G_{5,X}H^3\phi - G_{5,XX}H^3\phi^3\right) = 0\,, \tag{28}$$

where ρ_M and P_M represent the energy density and pressure of the matter fields. One immediate observation is that the temporal component of the vector field has only an algebraic equation and hence we can integrate it out in terms of the Hubble function. One also sees that the de Sitter solutions will correspond to $\dot{H} = 0$ and $\dot{\phi} = 0$, and will be attractor de Sitter fixed points. This type of cosmological solutions will be very relevant for the dark energy applications. However, because of their attractor nature, these solutions will not be so interesting for the early universe applications. Instead, a better application will be delivered from the multi-Proca generalisations. Apart from the standard field configurations $A^a_i = A(t)\delta^a_i$, as it was for instance considered in non-abelian gauge theories, one can assume that the vector fields rather acquire the field configurations $A^a_\mu = \phi^a(t)\delta^0_\mu + A(t)\delta^a_\mu$. These new field configurations open new promising possibilities for cosmological scenarios for the early universe, that have not been considered so far in the literature [29].

Acknowledgments

LH thanks financial support from Dr. Max Rössler, the Walter Haefner Foundation and the ETH Zurich Foundation.

References

1. S. Weinberg, Rev. Mod. Phys. **61**, 1 (1989).
2. J. Beltran Jimenez, L. Heisenberg, G. J. Olmo and D. Rubiera-Garcia, arXiv:1704.03351 [gr-qc].

3. C. de Rham and G. Gabadadze, Phys. Rev. D **82**, 044020 (2010).
4. C. de Rham, G. Gabadadze, L. Heisenberg and D. Pirtskhalava, Phys. Rev. D **83**, 103516 (2011).
5. C. de Rham and L. Heisenberg, Phys. Rev. D **84**, 043503 (2011).
6. C. Burrage, C. de Rham, L. Heisenberg and A. J. Tolley, JCAP **1207**, 004 (2012).
7. C. de Rham, G. Gabadadze, L. Heisenberg and D. Pirtskhalava, Phys. Rev. D **87**, no. 8, 085017 (2013).
8. G. R. Dvali, G. Gabadadze and M. Porrati, Phys. Lett. B **485**, 208 (2000).
9. L. Heisenberg, JCAP **1405**, 015 (2014).
10. E. Allys, P. Peter and Y. Rodriguez, JCAP **1602**, no. 02, 004 (2016).
11. J. Beltran Jimenez and L. Heisenberg, Phys. Lett. B **757**, 405 (2016).
12. M. Hull, K. Koyama and G. Tasinato, Phys. Rev. D **93**, no. 6, 064012 (2016).
13. J. Beltran Jimenez and T. S. Koivisto, Phys. Lett. B **756**, 400 (2016).
14. N. Khosravi, Phys. Rev. D **89**, no. 12, 124027 (2014).
15. J. Beltran Jimenez, L. Heisenberg and T. S. Koivisto, JCAP **1604**, no. 04, 046 (2016).
16. J. Beltran Jimenez, R. Durrer, L. Heisenberg and M. Thorsrud, JCAP **1310**, 064 (2013).
17. G. Tasinato, JHEP **1404**, 067 (2014).
18. A. De Felice, L. Heisenberg, R. Kase, S. Mukohyama, S. Tsujikawa and Y. l. Zhang, JCAP **1606**, no. 06, 048 (2016).
19. G. Tasinato, Class. Quant. Grav. **31**, 225004 (2014).
20. A. De Felice, L. Heisenberg, R. Kase, S. Mukohyama, S. Tsujikawa and Y. l. Zhang, Phys. Rev. D **94**, no. 4, 044024 (2016).
21. L. Heisenberg, R. Kase and S. Tsujikawa, JCAP **1611**, no. 11, 008 (2016).
22. M. Lagos, T. Baker, P. G. Ferreira and J. Noller, JCAP **1608**, no. 08, 007 (2016).
23. A. de Felice, L. Heisenberg and S. Tsujikawa, arXiv:1703.09573 [astro-ph.CO].
24. A. De Felice, L. Heisenberg, R. Kase, S. Tsujikawa, Y. l. Zhang and G. B. Zhao, Phys. Rev. D **93**, no. 10, 104016 (2016).
25. L. Heisenberg, R. Kase and S. Tsujikawa, Phys. Lett. B **760**, 617 (2016).
26. R. Kimura, A. Naruko and D. Yoshida, JCAP **1701**, no. 01, 002 (2017).
27. L. Heisenberg, R. Kase and S. Tsujikawa, Phys. Rev. D **94**, no. 12, 123513 (2016).
28. E. Allys, P. Peter and Y. Rodriguez, Phys. Rev. D **94**, no. 8, 084041 (2016).
29. J. Beltran Jimenez and L. Heisenberg, Phys. Lett. B **770**, 16 (2017).
30. M. Hull, K. Koyama and G. Tasinato, JHEP **1503**, 154 (2015).
31. R. Emami, S. Mukohyama, R. Namba and Y. l. Zhang, JCAP **1703**, no. 03, 058 (2017).
32. P. Fleury, J. P. Beltran Almeida, C. Pitrou and J. P. Uzan, JCAP **1411**, no. 11, 043 (2014)
33. G. W. Horndeski, Int. J. Theor. Phys. **10**, 363 (1974).
34. M. Zumalacrregui and J. Garca-Bellido, Phys. Rev. D **89**, 064046 (2014).
35. J. Gleyzes, D. Langlois, F. Piazza and F. Vernizzi, Phys. Rev. Lett. **114**, no. 21, 211101 (2015).











TESTING GENERAL RELATIVITY FROM CURVATURE & ENERGY CONTENTS AT COSMOLOGICAL SCALE

ZIAD SAKR, ALAIN BLANCHARD

Université de Toulouse, UPS-OMP, CNRS, IRAP, F-31028 Toulouse, France

In this work we examine what are the cosmological implications of allowing the geometrical curvature density to behave independently from the energy density contents. Using the full data extracted by Planck mission from CMB, combined with BAO and SNIa measurements, we derive, in the light of this approach, new constraints on the cosmological parameters. In particular we determine the behavior of the curvature dark energy degeneracy when allowing a varying equation of state for the latter. We also examine whether this approach could bridge the gap recently found between the Hubble parameter value determined from CMB and that from the local universe measurements

1 Introduction

One of the prediction of the theory of inflation is that the universe is spatially flat [1]. The spatial curvature parameter Ω_k was found smaller than $< 10^{-4}$ when constrained [2], with very high accuracy, using the observed cosmic microwave background (CMB) fluctuations [6] combined with other cosmological observations, like type Ia supernova (SNIa)[3] and baryon acoustic oscillation (BAO) [5]. Observations [7] [8] have shown that the expansion of the universe is accelerating, leading to the existence of what is called dark energy. This relies on the general relativity (GR) paradigm in which a geometrical tensor is set equal to the matter-energy tensor. Consequently, according to GR, for the curvature parameter of the universe Ω_k is uniquely related to its energy contents. Therefore, testing this relation allows to test GR at cosmological scales. This can be done by introducing on one side a geometrical curvature parameter denoted $\Omega_{k_{geo}}$ and the other side another parameter related to the energy contents: $\Omega_{k_{dyn}} = 1 - \sum \Omega_i$.
Zolnierowski & Blanchard [9], ZB hereafter, (see also Clarkson [10]), tried, using datasets from BAO, SNIa and reduced CMB parameters, to perform this test and to analyze the relation between the two curvature parameters and dark energy. One of the main result they found was that the fiducial values $\Omega_{k_{geo}} = \Omega_{k_{dyn}} = 0$ were consistent with data but a significant degeneracy exists when allowing a dark energy equation of state parameter w different from the value -1. Yu [11] performed a similar analysis with full treatment of CMB and didn't find as much degeneracy as the former study. In the present work, we follow the same approach as Yu using newly released data, trying to set the degeneracy limits. We also examine, whether in this approach, the tension found between the two determination of the Hubble expansion parameter H_0 from local and distant universe probes could be alleviated.

2 Methods

To derive a solution of GR field equations :

$$G_{\mu\nu} = \frac{8\pi G}{c^4} T_{\mu\nu} \tag{1}$$

for an homogenous and isotropic universe, one uses Robertson-Walker metric:

$$ds^2 = -c^2 dt^2 + a(t)^2 \left(\frac{dr^2}{1 - kr^2} + r^2(d\theta^2 + \sin^2\theta d\phi^2) \right) \tag{2}$$

in which $a(t)$ is the expansion factor of the universe and $k = -1, 0, +1$ according to the geometry of space.
That leads to the Friedman-Lemaître equations:

$$\begin{aligned} H(z)^2 &= H_0^2 E(z)^2 \\ &= H_0^2 \left[\Omega_m (1+z)^3 + \Omega_k (1+z)^2 + \Omega_{DE}(z) \right]. \end{aligned} \tag{3}$$

where $\Omega_k = -kc^2/(Ha)^2$, which we note $\Omega_{k_{geo}}$, is the cosmological curvature parameter arising from the LHS of Equ. 1. Equ. 3 set the equality in GR between $\Omega_{k_{dyn}}$ and $\Omega_{k_{dyn}} = 1 - \sum \Omega_i$. In the following these two quantities are treated as independent. The evolution of the background of the universe described by Equ. 3 involving $\Omega_{k_{dyn}}$, while for deriving the angular and luminosity distance we need $\Omega_{k_{geo}}$ in addition of $\Omega_{k_{dyn}}$. The luminosity distance for SNIa becomes:

$$D_L = \frac{c\ (1+z)}{H_0\ \sqrt{|\Omega_{k_{geo}}|}}\ S_k \left(\sqrt{|\Omega_{k_{geo}}|} \int_0^z \frac{du}{E(u)} \right). \tag{4}$$

with $\Omega_{k_{dyn}}$ entering $E(z)$. The same applies for BAO probe which is determined using the angular diameter distance D_A. The later being related to D_L through: $D_L(z) = D_A(z)(1+z)^2$. We show in Fig 1 the dependence of the SN luminosity variation function of redshift on the two curvature parameters change.

While for the CMB measurements, the two curvature parameters enter in the determination of the fluctuations temperature, polarization and lensing power spectrum, first with $\Omega_{k_{dyn}}$, entering the expansion and propagating in the whole derivation of the former spectrums, second with $\Omega_{k_{geo}}$ playing a significant role in different places, mainly in projections of angular correlations or distances used to derive lensing effects.

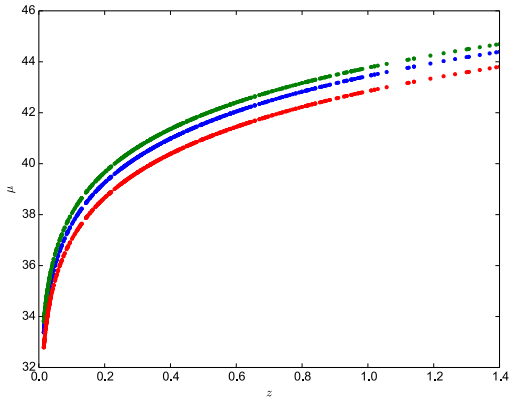


Figure 1 – The effect of changing the value of the parameters $\Omega_{k_{dyn}} = 0.25$ (lower red line) or $\Omega_{k_{geo}} = 0.25$ (upper green line) on the SN distance modulus as a function of redshift, compared to the fiducial value $\Omega_k = 0$ (middle blue line)

We show in Fig. 2 the effect of changing $\Omega_{k_{dyn}}$ or $\Omega_{k_{geo}}$ parameter on the angular power spectrum from CMB measurements.

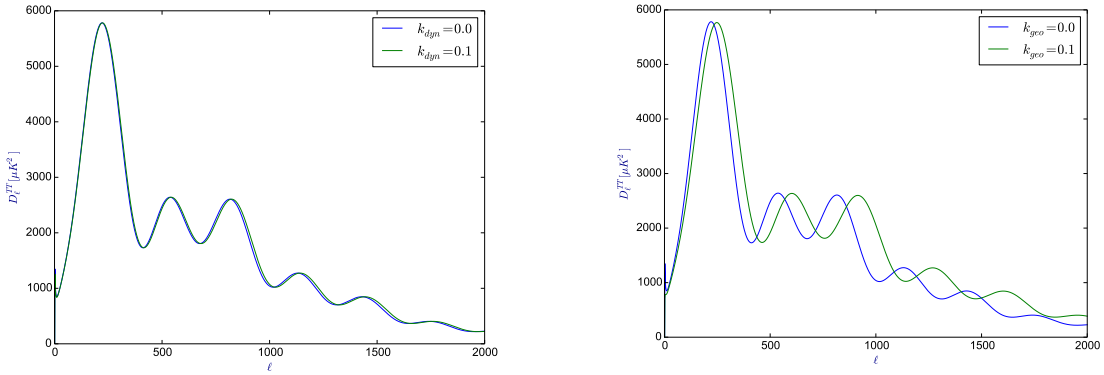


Figure 2 – The effect of $\Omega_{k_{dyn}}$ or $\Omega_{k_{geo}}$ parameters change on the angular power spectrum from CMB measurements, with the following priors $\{\omega_b, \omega_{cdm}, h, A_s, n_s, \tau_{reio}\} = \{0.022, 0.12, 0.67, 2.3e^{-9}, 0.09\}$

3 Results

To perform our analysis, we use the CMB's $C\ell s$ temperature, polarization and lensing measurements from Planck 2015 [6] releases. For the BAO probe we use datasets from Boss 2014 measurements [5] while for luminosity distance from supernovae, we use UnionII 2010 observations [4].

To constrain our parameters we use MontePython [13] to perform a Monte Carlo Markov Chain analysis in which the two curvature parameters assumption is implemented by changing the underlying Boltzman code and cosmological solver CLASS [12]. The latter can calculate the theoretical cosmological distances as well as the CMB temperature, polarization and lensing spectrums that are compared to observations in an appropriate likelihood.
All the cosmological parameters of the cosmological model as well as the nuisance parameters and the two curvature parameters $\Omega_{k_{dyn}}$ and $\Omega_{k_{geo}}$ are left free. The dark energy equation of state parameter w is set to -1 in the first case and can take any constant value in the second case.

Let us know examine how constraints on cosmological parameters may change when we relax the $\Omega_{k_{dyn}}$ and $\Omega_{k_{geo}}$ equality.

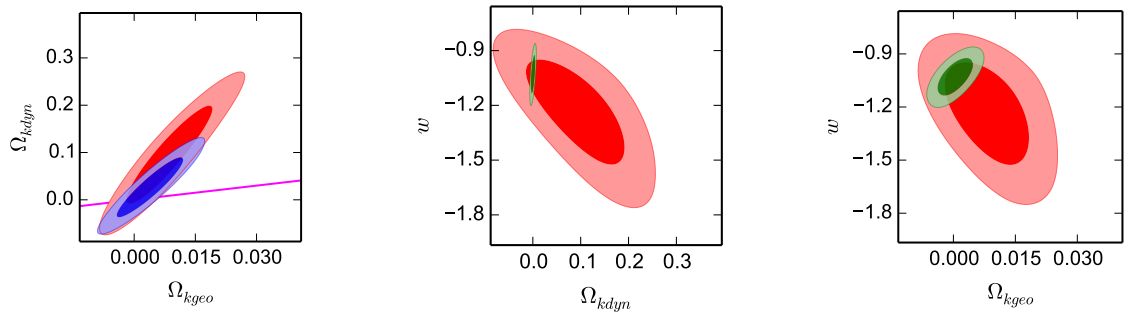


Figure 3 – 2D 68%, 95% contours for $\Omega_{k_{dyn}}$ vs $\Omega_{k_{geo}}$ (first panel), $\Omega_{k_{dyn}}$ vs w (second panel) and $\Omega_{k_{geo}}$ vs w (third panel), derived from MCMC analysis using CMB Planck2015 TT, EE, TE, BAO boss 2014 and SNIa UnionII. The (purple) line corresponds to GR prediction in the first panel while red CC corresponds to w free to vary in all panels and blue to the fiducial case $w = -1$ in the first panel. Green CC corresponds to w free vs Ω_k in GR assumption.

In Fig 3 we show in the first panel the confidence contours (CC) of $\Omega_{k_{dyn}}$ vs $\Omega_{k_{geo}}$: with $w = -1$ we observe a small degeneracy but the two values are well constrained around the

fiducial null value while when we allow w to vary, we observe a bigger degeneracy. As can be seen from the plots of Fig 1 and 2, the variation in $\Omega_{k_{dyn}}$ is one order of magnitude higher than that of $\Omega_{k_{geo}}$. This result agrees with both studies of ZB and Yu for that case ($w = -1$). In the second and the third panel, we consider the variation of the two Ω_k with w, as one can see, $\Omega_{k_{dyn}}$ is much degenerate with w, in agreement with the result obtained by ZB. One may wonder whetehr the degeneracy of the two Ω_k primarily comes from having let w free and not from having relaxed the equality of the two curvature parameters. We examine this issue where we plot CC in both cases, i.e. in GR, i.e. with $\Omega_{k_{dyn}} = \Omega_{k_{geo}}$ (green) and without (grey). As one can the above large degeneracy results from having relaxed the equality $\Omega_{k_{dyn}} = \Omega_{k_{geo}}$.

Lastly in Fig 4, we examine if the tension found between the determination of the Hubble parameter H_0 by Riess et al. [14] from probes in the local universe and the one determined from our used probes in the more deep universe, can be alleviated. For that, we show the likelihood of the Hubble parameter H_0 for three cases: one with the traditional Ω_k and $w = -1$, the other with the same hypothesis but w free and the last with our approach with w free to vary. We notice that the tension with H_0 is reduced only when we allow the two curvature parameters assumption with w free while the tension remains the same within the standard picture with or without letting w free to vary.

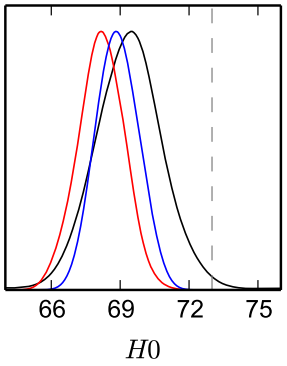


Figure 4 – 1D Likelihood of H_0 (in $km.s^{-1}.Mpc^{-1}$) using Planck, BAO and SNIa: with the standard Ω_k and $w = -1$ (blue), the same hypothesis but with w free (red) and the last with $\Omega_{k_{dyn}}$ different from $\Omega_{k_{geo}}$ with w free to vary (black). The dashed line corresponds to the central value measured in the local universe by Riess et al.

4 Conclusions

In this work we tested a scenario in which the curvature parameter and the energy density content parameter are distinct and vary with dark energy using the BAO, SN and the CMB measurements with a full treatment of the latter. We found that the standard picture in which $\Omega_{k_{dyn}} = \Omega_{k_{geo}} = 0$ with $w = -1$ is consistent with present day data with Ω_k well constrained but that a significant degeneracy is observed if the equation of state parameter w is allowed to vary. We also found that using this approach and letting dark energy parameter vary reduces the tension on the value of the Hubble parameter measured between local and deep universe. This shows the need of more model independent studies when analyzing cosmological observations.

References

1. Guth, A. H., *Phys. Rev.* D, **23**, 347 (1981)
2. A. Linde, *Lect. Notes Phys.* **738**, 1 (2008)
3. M. Betoule *et al.*, *Astron. Astrophys.* **568**, A22 (2014).
4. Amanullah, R., Lidman, C., Rubin, D., *et al.*, *Astron. J.* **716**, 712 (2010)
5. L. Anderson *et al.*, *Mon. Not. Roy. Ast. Soc.* **441**, 24 (2014)
6. Planck Collaboration, Ade, P. A. R., *Astron. Astrophys.* **594**, A13 (2016)
7. A. G., Riess *et al.*, *Astron. J.* **116**, 1009 (1998)
8. S. Perlmutter *et al.*, *Astrophys. J.* **517**, 565 (1999)
9. Zolnierowski, Y., & Blanchard, A., *Phys. Rev.* D, **91**, 083536 (2015)
10. Clarkson, C., Clifton, T., Coley, A., & Sung, R., *Phys. Rev.* D, **85**, 043506 (2012)
11. Yu, B., *Phys. Rev.* D, **92**, 083514 (2015)
12. Lesgourgues, J., arXiv:1104.2932 (2011)
13. Audren, B., Lesgourgues, J., Benabed, K., & Prunet, S. *JCAP* **2**, 001 (2013)
14. Riess, A. G., Macri, L. M., Hoffmann, S. L., et al., *Astrophys. J.* **826**, 56 (2016)

DIFFERENT WAYS FOR GRAVITON MASS EVALUATIONS

A. F. ZAKHAROV[1,2,3,4,5], P. JOVANOVIĆ[6], D. BORKA[7] and V. BORKA JOVANOVIĆ[7]
[1]*National Astronomical Observatories of CAS,Beijing, 100012 China*
[2]*Institute of Theoretical and Experimental Physics, 117218 Moscow, Russia*
[3]*Bogoliubov Laboratory for Theoretical Physics, JINR, 141980 Dubna, Russia*
[4]*National Research Nuclear University MEPhI (Moscow Engineering Physics Institute), Kashirskoe highway 31, Moscow, 115409, Russia*
[5]*North Carolina Central University, Durham, NC 27707, USA*
[6]*Astronomical Observatory, Volgina 7, 11060 Belgrade, Serbia*
[7]*Atomic Physics Laboratory (040), Vinča Institute of Nuclear Sciences & University of Belgrade, P.O. Box 522, 11001 Belgrade, Serbia*

A graviton detection is an extremely hard problem[1] but if a graviton exists then it relatively easier to evaluate a graviton mass. In February 2016 the LIGO & VIRGO collaboration reported the discovery of gravitational waves in merging black holes, therefore, the team confirmed GR predictions about an existence of black holes and gravitational waves in the strong gravitational field limit. Moreover, in their papers the joint LIGO & VIRGO team presented an upper limit on graviton mass such as $m_g < 1.2 \times 10^{-22}$ eV [2] analyzing gravitational wave signal as it was suggested earlier [3]. So, the authors concluded that their observational data do not show any violation of classical general relativity. We show that an analysis of bright star trajectories could constrain graviton mass with a comparable accuracy with accuracy reached with gravitational wave interferometers and the estimate is consistent with the one obtained by the LIGO & VIRGO collaboration. This analysis gives an opportunity to treat observations of bright stars near the Galactic Center as a useful tool to obtain constraints on the fundamental gravity law such as modifications of the Newton gravity law in a weak field approximation. In that way, based on a potential reconstruction at the Galactic Center we obtain bounds on a graviton mass.

1 Introduction

In spite of a great success of a general relativity (GR) development in a more than a century we know only a few cases where we really need a strong gravitational field approximation to describe a physical reality. If we speak about observable manifestations of black hole features we need models with a strong gravitational field to describe 1) inspiraling, merging and ring down stage of binary black hole evolution; and 2) shapes of shadows around black holes. Perhaps, very soon observers will need GR corrections and later a full GR approach to fit observational data for bright stars near the Galactic Center. Assuming that a radiation in a spectral line is emitted from a region near a black hole horizon, it was found (and after that it was observed the X-ray K_α-line) that an observed shape of the spectral line can be an important indicator of a strong gravitational field near a black hole, moreover, one can evaluate a black hole spin analyzing a spectral line structure [4,5]. Another phenomenon, where one really needs a strong gravitational field approach, is a shadow formation started since papers [6,7,8] (see also calculations of shadows for different cases [9,10,11,12,13,14,15] and recent reviews on the subject [16,17]). The problem is connected with attempts to resolve the smallest spot at the Galactic Center with VLBI interferometry in mm-

band [18]. Simulations show that in general cases shadows (dork spots in the sky) are surrounded by bright images [7,8]. As it was noted earlier, observations of bright star trajectories near the Galactic Center could provide an efficient tool to evaluate a gravitational potential in particular, analyzing these trajectories one can obtain constraints on parameters of black hole and stellar cluster [19] and on parameters of dark matter distribution [20,21].

Two groups of astronomers with VLT and Keck telescopes observe stars near the Galactic Center, see papers[22,23,24] and references therein. An analysis of S2 like star trajectories gives an opportunity to obtain stringent constraints on alternative theories of gravity, including R^n theory which is a generalization of the classical GR and $n = 1$ corresponds to GR[25,26] (there are also stringent constraints from Solar system data [27]), and Yukawa gravity[28]. In the paper we describe a procedure to obtain a graviton mass constraint from analysis of trajectories of bright stars at the Galactic Center.

2 Gravity Theories with Massive Graviton

A gravity theory with massive graviton was introduced in M. Fierz and W. Pauli[29]. However, some unexpected properties of such theories have been found such as van Dam–Veltman–Zakharov (vDVZ) discontinuity and a presence of ghosts (and related instabilities) and other pathologies from quantum field theory point of view [30]. However, there is a significant progress to overcome such problem and build a consistent theory without Boulware – Deser ghosts[31,32]. Here, we will not discuss theoretical aspects of massive gravity theory and we will consider only observational features of such an approach. There are different suggestions to evaluate a graviton mass, some of them are rather exotic and based on hardly verified assumptions[32,33]. Systematics of proposed experiments and observations is not well investigated, moreover, some weaknesses of the proposals for a graviton mass evaluation are pointed out in the review[32].

3 Graviton Mass Estimate from Gravitational Wave Signal

If a graviton has a mass m_g, then in this case a speed of gravitational wave propagation could differ from c and we have a dispersion relation[3,34]

$$\frac{v_g^2}{c^2} = 1 - \frac{m_g^2 c^4}{E^2}, \tag{1}$$

where E is a graviton energy. Gravitons with different energies propagate with different velocities. Assume that we have gravitational waves and electromagnetic waves from the same source (from supernovae exoplosion, for instance). In this case we have[3,34]

$$1 - \frac{v_g}{c} = 5 \times 10^{-17} \left(\frac{200\ \mathrm{Mpc}}{D}\right) \left(\frac{\Delta t}{1\ \mathrm{s}}\right), \tag{2}$$

where $\Delta t = \Delta t_a - (1+z)\Delta t_e$ is the time difference, where Δt_a and Δt_e are the differences in arrival time and emission time of the two signals, respectively, and z is the redshift of the source. Usually Δt_e is unknown, however, one could find an upper limit for Δt_e (for instance from a theoretical model), therefore, one could evaluate $1 - \dfrac{v_g}{c}$, therefore, m_g. Following papers[3,34] and assuming that the frequency of gravitational wave is ν and $h\nu \gg m_g c^2$ (h is Planck's constant), therefore, we have $\dfrac{v_g}{c} \approx 1 - \dfrac{1}{2}\dfrac{h}{\lambda_g \nu}$, where $\lambda_g = \dfrac{h}{m_g c}$ or $\lambda_g \approx \dfrac{1}{2}\dfrac{1}{\sqrt{1 - v_g/c}}$. If one has an upper limit for $1 - v_g/c$, it can be re-written as a lower limit for λ_g, as the following expression [3,34]

$$\lambda_g = 3 \times 10^{12}\mathrm{km} \left(\frac{200\ \mathrm{Mpc}}{D}\frac{\nu}{100\mathrm{Hz}}\right) \left(\frac{1}{\nu \Delta t}\right). \tag{3}$$

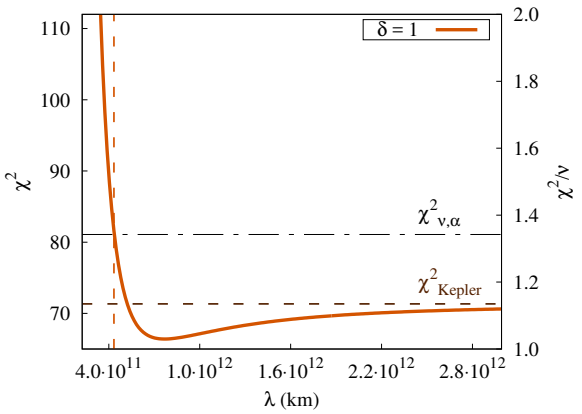


Figure 1 – χ^2 (solid lines) as a function of Yukawa range of interaction λ. The values $\lambda_g < \lambda_x$ can be excluded with 90% probability.

It is a lucky case if one observe electromagnetic and gravitational radiation from the same source. But even in the case if only gravitational radiation has been detected as it was noted[3] because gravitational wave signal with a massive graviton will be different from signal for a graviton with a vanishing mass and in this case for $D \approx 200\text{Mpc}, \nu \approx 100\text{Hz}, \nu\Delta t \sim \rho^{-1} \approx 0.1$. The result is $\lambda_g > 10^{13}$ km. Based on ideas expressed in [3,34], the LIGO/VIRGO collaboration obtained the same estimate for the Compton wavelength of a massive graviton[2,35,36].

4 Graviton Mass Estimates from Trajectories of Bright Stars near the Galactic Center

We use a modification of the Newtonian potential corresponding to a massive graviton case[3,34]:

$$V(r) = -\frac{GM}{(1+\delta)r}\left[1 + \delta e^{-\left(\frac{r}{\lambda}\right)}\right], \tag{4}$$

where δ is a universal constant (we put $\delta = 1$). In our previous studies[28] we found constraints on parameters of Yukawa gravity. As it was described in papers[37,38] we used observational data from NTT/VLT[22]. If we wish to find a limiting value for λ_x, so that $\lambda > \lambda_x$ with a probability $P = 1 - \alpha$ (where we select $\alpha = 0.1$) normalized χ^2 depending on λ_x has to be equal to the threshold depending on degree of freedom ν and parameter α or in other words, $\chi^2(\lambda_x) = \chi^2_{\nu,\alpha}$. Computing these quantities we obtain $\lambda_x = 2900$ AU $\approx 4.3 \times 10^{11}$ km. Now we obtain the upper limit on a graviton mass and we could claim that with a probability $P = 0.9$, a graviton mass should be less than $m_g = 2.9 \times 10^{-21}$ eV (since $m_g = h\,c/\lambda_x$) in the case of $\delta = 1$ [37,38,39,40], see also Fig. 1 (the plot is adopted from the paper[38]) .

5 Conclusions

As it was noted earlier, our graviton mass estimate is slightly greater than estimate with LIGO interferometer, however, a) our estimate was obtained in independent way with other observational data; b) our estimate is consistent with LIGO's one; c) our estimate will definitely improved with forthcoming facilities such as GRAVITY, E-ELT and TMT because more precise observations of bright star orbits will give an opportunity to reconstruct a gravitational potential at the Galactic Center in a more accurate way, therefore, one can expect a better estimates for λ parameter and a graviton mass. However, such a progress will be not very rapid because of an exponential dependence of a potential on λ.

Acknowledgements

A F Z thanks the organizers of the 52^{nd} Rencontres de Moriond (Gravitation Session) for their kind invitation to present a talk at the conference. A F Z appreciates NSF (HRD-1345219) and NASA (NNX09AV07A) at NASA CCFASE and CREST Centers (NCCU, Durham, NC, USA) for a partial support. P J, D B and V B J wish to acknowledge the support by the Ministry of Education, Science and Technological Development of the Republic of Serbia through the project 176003 "Gravitation and the large scale structure of the Universe". P J also thanks ICTP - SEENET-MTP project PRJ-09 Cosmology and Strings for a partial support.

References

1. F. Dyson, *Intern. J. Mod. Phys.* A **28** 1330041 (2013).
2. B. P. Abbott *et al.*, *Phys. Rev. Lett.* **116**, 061102 (2016).
3. C. Will, *Phys. Rev.* D **57**, 2061 (1998).
4. A.C. Fabian *et al.*, *Mon. Not. R. Astron. Soc.* **238** 729 (1989).
5. Y. Tanaka *et al.*, *Nature* **375**, 659 (1995).
6. S. Chandrasekhar, *Mathematical Theory of Black Holes* (Clarendon Press, Oxford, 1983).
7. H. Falcke, F. Melia and E. Agol, *Astrophys. J.* **528**, L13 (2000).
8. F. Melia and H. Falcke, *Ann. Rev. Astron. Astrophys.* **39** 309 (2001).
9. A. F. Zakharov *et al.*, *Astron. & Astrophys.* **442**, 795 (2005).
10. A. F. Zakharov *et al.*, *New Astron.* **10**, 479 (2005).
11. F. De Paolis *et al.*, *Gen. Rel. Grav.* **43**, 977 (2010).
12. A. F. Zakharov *et al.*, *New Astron. Rev.* **56**, 64 (2012).
13. A. F. Zakharov, *Phys. Rev.* D **90**, 062007 (2014).
14. A. F. Zakharov, *J. Astrophys. Astr.* **36**, 539 (2015).
15. A. F. Zakharov, in *Gravitation, Astrophysics, and Cosmology*, eds. V. N. Melnikov and J.-P. Hsu, p. 176 (World Scientific, Singapore, 2016).
16. H. Falcke and S. B. Markoff, *Class. Quan. Grav.* **30**, 244003 (2013).
17. T. Johannsen, *Class. Quan. Grav.* **33**, 113001 (2016).
18. S. S. Doeleman *et al.*, *Nature* **455**, 78 (2008).
19. A. A. Nucita *et al.*, *Publ. Astron. Soc. Pac.* **119**, 349 (2007).
20. A. F. Zakharov A F *et al. Phys. Rev.* D **76**, 062001 (2007).
21. A.F. Zakharov *et al.*, *Space Sci. Rev.* **48**, 301 (2009).
22. S. Gillessen *et al.*, *Astrophys. J.* **707**, L114 (2009).
23. S. Gillessen *et al.*, *Nature* **481**, 51 (2012).
24. L. Meyer *et al.*, *Science* **338**, 84 (2012).
25. D. Borka *et al.*, *Phys. Rev.* D **85**, 124004 (2012).
26. A. F. Zakharov *et al.*, *Adv. Space Res.* **54**, 1108 (2014).
27. A. F. Zakharov *et al.*, *Phys. Rev.* D **74**, 107101 (2006).
28. D. Borka *et al.*, *J. Cosmol. Astropart. Phys.* JCAP **11**, 050 (2013).
29. M. Fierz and W. Pauli, *Proc. R. Soc. London Ser. A* **173**, 211 (1939).
30. D. G. Boulware and S. Deser, *Phys. Rev.* D **6**, 3368 (1972).
31. C. de Rham, G. Gabadadze and A.G. Tolley, *Phys. Rev. Lett.* **106**, (2011).
32. C. de Rham *et al.*,*Preprint* arXiv:1606.08462v1 [astro-ph.CO].
33. A. S. Goldhaber and M. M. Nieto, *Rev. Mod. Phys.* **82** 939 (2010).
34. C. Will, *Liv. Rev. Relat.* **17**, 4 (2014).
35. B. P. Abbott *et al.*, LIGO Document P1500213-v27 (*Preprint* arXiv:1602.03841).
36. B. P. Abbott *et al.*, *Phys. Rev.* X **6** 041015 (2016); LIGO-P1600088 (*Preprint* arXiv:1606.04856 [gr-qc]).
37. A. F. Zakharov *et al.*, *J. Cosmol. Astropart. Phys.* JCAP **05**, 045 (2016).
38. A. F. Zakharov *et al.*, *EPJ Web of Conferences* **125**, 01011 (2016).
39. A. F. Zakharov *et al.*, *EPJ Web of Conferences* **138**, 010010 (2017).
40. A. F. Zakharov *et al.*, *Journal of Physics: Conference Series* **798**, 012081 (2017).

Conservative Dynamics of Binary Systems of Compact Objects at the Fourth Post-Newtonian Order

Laura BERNARD
CENTRA, Departamento de Física, Instituto Superior Técnico – IST, Universidade de Lisboa – UL, Avenida Rovisco Pais 1, 1049 Lisboa, Portugal

Luc BLANCHET
$\mathcal{GR}\varepsilon\mathbb{C}\mathcal{O}$, Institut d'Astrophysique de Paris, UMR 7095, CNRS, Sorbonne Universités & UPMC Univ Paris 6, 98^{bis} boulevard Arago, 75014 Paris, France

Alejandro BOHÉ
Max Planck Institute for Gravitational Physics (Albert Einstein Institute), Am Muehlenberg 1, 14476 Potsdam-Golm, Germany

Guillaume FAYE
$\mathcal{GR}\varepsilon\mathbb{C}\mathcal{O}$, Institut d'Astrophysique de Paris, UMR 7095, CNRS, Sorbonne Universités & UPMC Univ Paris 6, 98^{bis} boulevard Arago, 75014 Paris, France

Sylvain MARSAT
Max Planck Institute for Gravitational Physics (Albert Einstein Institute), Am Muehlenberg 1, 14476 Potsdam-Golm, Germany

We review our recent derivation of a Fokker action describing the conservative dynamics of a compact binary system at the fourth post-Newtonian (4PN) approximation of general relativity. The two bodies are modeled by point particles, which induces ultraviolet (UV) divergences that are cured by means of dimensional regularization combined with a renormalization of the particle's wordlines. Associated with the propagation of wave tails at infinity is the appearance of a non-local-in-time conservative tail effect at the 4PN order in the Lagrangian. In turn this implies the appearance of infrared (IR) divergent integrals which are also regularized by means of dimensional regularization. We compute the Noetherian conserved energy and periastron advance for circular orbits at 4PN order, paying special attention to the treatment of the non-local terms. One ambiguity parameter remaining in the current formalism is determined by comparing those quantities, expressed as functions of the orbital frequency, with self-force results valid in the small mass ratio limit.

1 Introduction

Inspiraling and merging black-hole binary systems are the most common sources of gravitational waves detectable by ground or space-based laser interferometric detectors. [1] Banks of extremely accurate replica of theoretical templates are a compulsory ingredient of a successful data analysis for these detectors — both on-line and off-line. In the early inspiral phase, the post-Newtonian (PN) approximation of general relativity should be pushed to extremely high order. Furthermore, high accuracy comparison and matching of PN results are performed with numerical relativity computations appropriate for the final merger and ringdown phases. In this context,

we have undertaken the derivation of the equations of motion for binary systems of compact (non-spinning) objects at the 4PN order. Solving this problem is of great importance for various applications, most notably numerical/analytical self-force comparisons [2] and effective-one-body calculations, [3] and paves the way to the determination of physical observables in the radiation field such as the orbital phase at the 4PN order beyond the Einstein quadrupole formalism.

After the introduction by Lorentz & Droste [4] of the perturbative PN scheme for solving the Einstein field equations (EFE) for weakly gravitating, slowly moving sources, it was further explored in several historical works, including the famous paper on the motion of N planets at the 1PN order by Einstein, Infeld & Hoffmann. [5] In the 1980s, the PN scheme was successfully applied to the derivation of the equations of motion of compact binaries up to the 2.5PN order, where radiation reaction effects first appear, [6] which put an end to the radiation reaction controversy raging at the time. [7] The 3PN dynamics was tackled in the 2000s with the help of various methods, and the 4PN order has been investigated since the early 2010s.

After first partial results obtained by means of the effective field theory (EFT) [8,9] and the Arnowitt-Deser-Misner (ADM) formalism, [10] the important effect of gravitational wave tails at the 4PN order was included into the ADM Hamiltonian. [11,12] This allowed a better control of the IR divergences and the completion of the full 4PN dynamics, in spite of the appearance of one unfixed numerical constant which could only be set by comparison with self-force calculations. We report here on our alternative approach, [13,14,15] based on the construction of a Fokker Lagrangian in harmonic coordinates, and whose end result is physically equivalent to the one of the ADM Hamiltonian formalism. [10,11,12]

2 Fokker action for post-Newtonian sources

The two compact objects are represented by means of non-spinning, structureless particles, with masses m_A and trajectories $y^\mu_A(t) = (c\,t, \boldsymbol{y}_A(t))$ (with $A = 1, 2$), where c represents the speed of light. The corresponding matter action reads

$$S_m = -\sum_A m_A c^2 \int \mathrm{d}t \sqrt{-(g_{\mu\nu})_A \, v^\mu_A v^\nu_A / c^2}\,, \tag{1}$$

with $v^\mu_A = \mathrm{d}y^\mu_A/\mathrm{d}t = (c, \boldsymbol{v}_A)$. The time-dependent tensor $(g_{\mu\nu})_A$ stands for the metric evaluated at the location of the particle A. We deal with the divergences arising there by means of dimensional regularization. On the other hand, the gravitational sector is described by the Einstein-Hilbert action in Landau-Lifshitz form with the usual harmonic gauge-fixing term

$$S_g = \frac{c^3}{16\pi G} \int \mathrm{d}^4x \, \sqrt{-g} \left[g^{\mu\nu} \left(\Gamma^\rho_{\mu\lambda} \Gamma^\lambda_{\nu\rho} - \Gamma^\rho_{\mu\nu} \Gamma^\lambda_{\rho\lambda} \right) - \frac{1}{2} g_{\mu\nu} g^{\alpha\beta} g^{\rho\sigma} \Gamma^\mu_{\alpha\beta} \Gamma^\nu_{\rho\sigma} \right], \tag{2}$$

where G is the Newton constant, $g = \det g_{\mu\nu}$, and $\Gamma^\rho_{\mu\nu}$ stands for the Christoffel symbols.

The gravitational action can be written in terms of the deviation of the gothic metric from the inverse flat metric $\eta^{\mu\nu} = \mathrm{diag}(-1, 1, 1, 1)$, namely $h^{\mu\nu} = \sqrt{-g} g^{\mu\nu} - \eta^{\mu\nu}$. The action appears then as an infinite non-linear power series in h, in which indices on h and on partial derivatives ∂ are lowered and raised with the Minkowski metric η. The Lagrangian density $\mathcal{L}_g$ can take various forms, obtained from each other by integrations by parts. For our purpose, we adopt the form that starts at quadratic order by terms like $\sim h \Box h$, i.e., the "propagator" form, with $\Box = \eta^{\rho\sigma} \partial^2_{\rho\sigma}$ denoting the flat d'Alembertian operator. Therefore, the general structure of our Lagrangian density is $\mathcal{L}_g \sim h \Box h + h \partial h \partial h + h\, h \partial h \partial h + \cdots$.

The harmonic gauge fixed action yields the following "relaxed" EFE:

$$\Box h^{\mu\nu} = \frac{16\pi G}{c^4} \tau^{\mu\nu}\,, \qquad\qquad \tau^{\mu\nu} \equiv |g| T^{\mu\nu} + \frac{c^4}{16\pi G} \Sigma^{\mu\nu}[h, \partial h, \partial^2 h]\,. \tag{3}$$

The quantity $\tau^{\mu\nu}$ denotes the pseudo stress-energy tensor of the matter and gravitational fields, with $T^{\mu\nu} = \frac{2}{\sqrt{-g}}\delta S_m/\delta g_{\mu\nu}$. The gravitational source term $\Sigma^{\mu\nu}$ is at least quadratic in h or its first and second derivatives. Those wave-like equations have the same Green function as in harmonic gauge, although the harmonicity conditions $\partial_\nu h^{\mu\nu} = 0$ do not hold unless the evolution equations for the matter are also satisfied.

The Fokker action is obtained by inserting back into (1)–(2) an explicit PN iterated solution of the field equations (3) given as a functional of the particle's trajectories, i.e., an explicit PN metric $g_{\mu\nu}(\boldsymbol{x}; \boldsymbol{y}_B(t), \boldsymbol{v}_B(t), ...)$ at point $\boldsymbol{x}$. The extra variables indicated by ellipsis are higher derivatives such as accelerations $\boldsymbol{a}_B(t)$ or derivatives of accelerations $\boldsymbol{b}_B(t)$. Their presence is due to the fact that we solve Eqs. (3) without replacing accelerations because we are off-shell at this stage. Thus, the Fokker generalized PN action, depending not only on positions and velocities but also on accelerations and their derivatives, reads

$$\begin{aligned} S_{\rm F}\left[\boldsymbol{y}_B(t), \boldsymbol{v}_B(t), ...\right] &= \int {\rm d}^4x\, \mathcal{L}_g\left[\boldsymbol{x}; \boldsymbol{y}_B(t), \boldsymbol{v}_B(t), ...\right] \\ &\quad - \sum_A m_A c^2 \int {\rm d}t \sqrt{-g_{\mu\nu}\left(\boldsymbol{y}_A(t); \boldsymbol{y}_B(t), \boldsymbol{v}_B(t), ...\right) v_A^\mu v_A^\nu/c^2}\,. \end{aligned} \tag{4}$$

Now, by the stationarity of the total action $S = S_g + S_m$ for the PN iterated solution, the PN equations of motion are nothing but the Euler-Lagrange equations of $S_{\rm F}$ for the particles. Once they have been obtained, they may then be order reduced as usual, by replacing all accelerations by the PN equations of motion themselves. The classical Fokker action is completely equivalent, in the "tree-level" approximation, to the effective action used in the EFT. [8,9,16,17]

In (4), the gravitational term integrates over the whole space a PN solution of the EFE that is valid only in the near zone of the source. Denoting by $\overline{h}$ the *PN expansion* of the full-fledged gravitational field $h \equiv h(\boldsymbol{x}; \boldsymbol{y}_A(t), \boldsymbol{v}_A(t), ...)$, solution of the EFE (3), we have the equality $h = \overline{h}$ in the near zone of the matter system. By contrast, outside the near zone, $\overline{h}$ is not expected to agree with h and typically diverges at infinity. On the other hand, the *multipole expansion* of the metric perturbation, denoted $\mathcal{M}(h)$, agrees with h in all the exterior region of the source, but blows up when formally extended inside the near zone as $r \to 0$. [18] To properly define the Fokker action, we initially introduced [13] a *Hadamard regularization* (HR). With that regularization, we demonstrated that the gravitational part of the Fokker Lagrangian, say $L_g^{\rm HR}$, can be written as a space integral over the looked-for PN Lagrangian density, plus an extra contribution involving the multipole expansion:

$$L_g^{\rm HR} = \underset{B=0}{\rm FP} \int {\rm d}^3\boldsymbol{x} \left(\frac{r}{r_0}\right)^B \overline{\mathcal{L}}_g + \underset{B=0}{\rm FP} \int {\rm d}^3\boldsymbol{x} \left(\frac{r}{r_0}\right)^B \mathcal{M}(\mathcal{L}_g)\,. \tag{5}$$

Here, we have introduced a regulator $(r/r_0)^B$, with B being a complex number, and a finite part (FP) at $B = 0$ in order to cure the divergences of the PN expansion when $r \equiv |\boldsymbol{x}| \to +\infty$ in the first term while dealing with the singular behaviour of the multipole expansion when $r \to 0$ in the second one. The constant r_0, representing an IR scale in the first term and a UV scale in the second, cancels out between the two contributions. We have proved, though, that the second term in (5) does not contribute to $S_{\rm F}$ below the 5.5PN order, hence we consider at 4PN order:

$$L_g^{\rm HR} = \underset{B=0}{\rm FP} \int {\rm d}^3\boldsymbol{x} \left(\frac{r}{r_0}\right)^B \overline{\mathcal{L}}_g\,. \tag{6}$$

3 The 4PN conservative dynamics

The general PN solution that matches an exterior solution with retarded boundary conditions at infinity may be decomposed in two pieces. The first one consists of the naive near zone expansion of the retarded integral of the PN source, each term being regularized by means of

the same FP procedure as in Eq. (6). The second piece is a homogeneous multipolar solution regular inside the source, expanded in the near zone, [19,20]

$$\overline{h}^{\mu\nu} = \frac{16\pi G}{c^4}\overline{\Box}^{-1}_{\rm ret}\overline{\tau}^{\mu\nu} - \frac{2G}{c^4}\sum_{\ell=0}^{+\infty}\frac{(-)^\ell}{\ell!}\,\partial_L\overline{\left\{\frac{\mathcal{R}^{\mu\nu}_L(t-r/c)-\mathcal{R}^{\mu\nu}_L(t+r/c)}{r}\right\}}\,. \tag{7}$$

The multipole moments $\mathcal{R}^{\mu\nu}_L$ in (7) are functionals of the multipole expansion of the effective gravitational source in the EFE, $\mathcal{M}(\tau^{\mu\nu})$, thus depending on the boundary conditions imposed at infinity. Most importantly, the functions $\mathcal{R}^{\mu\nu}_L$ are responsible for the tail effects in the near zone metric. At the 4PN order, where they first appear in $\overline{h}^{\mu\nu}$, it is sufficient to consider only quadrupolar tail terms corresponding to the interaction between the total ADM mass M of the source and its Symmetric Trace-Free (STF) quadrupole moment I_{ij}. Inserting them into the original Fokker action, we obtain, after redefining the matter variables $\boldsymbol{y}_A$ with the help of an appropriate non-local-in-time 4PN shift, a net contribution

$$S^{\rm tail}_{\rm F} = \frac{G^2M}{5c^8}\underset{2s_0/c}{\rm Pf}\iint\frac{{\rm d}t{\rm d}t'}{|t-t'|}\,I^{(3)}_{ij}(t)\,I^{(3)}_{ij}(t')\,, \tag{8}$$

where the upper indices (3) represent third order time differentiation. With HR, a dependence on the scale s_0 [*a priori* different from r_0 in (6)] occurs through the definition of the Hadamard *partie finie* Pf.[a] Varying the action (8) with respect to the particle's worldlines, we recover the conservative part of the known 4PN tail effect. [21]

Following previous works on the 3PN equations of motion [22,23] we shall proceed in several steps. First, we parametrize the particular solution $\overline{\Box}^{-1}_{\rm ret}$ in the metric by means of specific PN potentials. Next, those potentials are computed at any point in three-dimensional space and inserted into the action. To deal with quadratic source terms, we extensively make use of the important Fock function $g = \ln(r_1 + r_2 + r_{12})$, such that $\Delta g = r_1^{-1}r_2^{-1}$ with $r_A = |\boldsymbol{x} - \boldsymbol{y}_A|$ and $r_{12} = |\boldsymbol{y}_1 - \boldsymbol{y}_2|$. We also need to integrate a cubic source term for which we resort to more complicated elementary solutions. [24] The integration of the Lagrangian density is then implemented by means of a Hadamard regularization, later corrected to a dimensional regularization (DR) for the UV divergences. The UV poles $\propto 1/(d-3)$ are then renormalized through a redefinition of the particle's worldlines. [23]

4 IR divergences and ambiguity parameters at the 4PN order

The ensuing Fokker Lagrangian [13] depends on the IR length r_0 and on the scale s_0 in the tail term (8). However, we have shown that these two scales combine into a single undetermined constant $\alpha = \ln(r_0/s_0)$ after suitable shifts of the particle's worldlines. Then, the tail integral (8) simply involves the separation distance r_{12} as "partie finie" scale. The constant α cannot be eliminated and is considered to be an *ambiguity* parameter, equivalent to the ambiguity parameter called C in the ADM Hamiltonian formalism.[11,12]

The ambiguity parameters are associated with IR divergences, which are in turn linked to the presence of the tail effect at the 4PN order.[21] It is thus important to check the "stability" of the calculation under a change of regularization procedure for the IR divergences, and eventually to determine which regularization should be used. We argued [14] that the Fokker Lagrangian derived by resorting to dimensional regularization for both IR and UV divergences is not dynamically equivalent to the HR Lagrangian obtained via our original approach, the difference being

[a] For any regular function $f(t)$ tending to zero sufficiently rapidly when $t \to \pm\infty$, we have

$$\underset{\tau_0}{\rm Pf}\int_{-\infty}^{+\infty}{\rm d}t'\,\frac{f(t')}{|t-t'|} \equiv \int_0^{+\infty}{\rm d}\tau\,\ln\left(\frac{\tau}{\tau_0}\right)\left[f^{(1)}(t-\tau)-f^{(1)}(t+\tau)\right]\,.$$

composed of two and only two types of terms (modulo some irrelevant shifts of the trajectories):

$$L^{\rm DR} = L^{\rm HR} + \frac{G^4 m\, m_1^2 m_2^2}{c^8 r_{12}^4}\Big(\delta_1 (n_{12}v_{12})^2 + \delta_2 v_{12}^2\Big)\,, \tag{9}$$

where $(n_{12}v_{12})$ denotes the scalar product between the unit separation vector $\boldsymbol{n}_{12} = (\boldsymbol{y}_1 - \boldsymbol{y}_2)/r_{12}$ and the relative velocity $\boldsymbol{v}_{12} = \boldsymbol{v}_1 - \boldsymbol{v}_2$, while $v_{12}^2 = (v_{12}v_{12})$ and $m = m_1 + m_2$. A pragmatic way to circumvent the problem is to acknowledge our (provisional) ignorance about the real values of δ_1, δ_2 and regard them as ambiguity parameters. Moreover, the terms containing α in $L^{\rm HR}$ can be put precisely in the form of the extra terms in (9) so that α can be absorbed into a redefinition of the two ambiguity parameters δ_1 and δ_2 without loss of generality.

Now, it turns out that the two ambiguity parameters are *uniquely fixed* by making our dynamics compatible with existing gravitational self-force (GSF) calculations of the conserved energy and periastron advance for circular orbits in the small mass-ratio limit $\nu = m_1 m_2/m^2 \to 0$ (see the next section). Nonetheless, it is important to determine them from *first principles*, i.e., without resorting to external calculations. A recent progress has been made in that direction: [15] We have replaced the HR prescription for Eq. (6) above by a full DR evaluation based on

$$L_g^{\rm DR} = \int {\rm d}^d \boldsymbol{x}\, \overline{\mathcal{L}}_g\,, \tag{10}$$

for the instantaneous terms, and computed the analogue of the tail term (8) in $d = 3 + \varepsilon$ dimensions. Notably, the computation of the difference between the two prescriptions for the instantaneous terms, i.e., $L_g^{\rm DR} - L_g^{\rm HR}$, is quite lengthy as it depends on the detailed structure of the expansion of the integrand at infinity. We proved that, in DR, the instantaneous terms develop an IR pole, but that it is exactly cancelled by a corresponding UV pole coming from the tail term in d dimensions (related cancellation of poles has been discussed in the EFT formalism [16,17]). Finally, with our full DR calculation, we found that the two ambiguity parameters can be expressed with a single parameter κ as

$$\delta_1 = \frac{1733}{1575} - \frac{176}{15}\kappa\,, \qquad \delta_2 = -\frac{1712}{525} + \frac{64}{5}\kappa\,. \tag{11}$$

This parameter κ comes from our computation of the tails and is (provisionally) left undetermined. It is equivalent to our former parameter α or to the ambiguity parameter C in the Hamiltonian formalism. [11] Let us now see how to compute κ thanks to the circular orbit limit of the invariants of the motion.

5 Conserved energy and periastron advance at 4PN order

To investigate the notions of conserved energy and angular momentum in the case of a non-local-in-time dynamics, we adopt the Hamiltonian formalism where the two-body system is described by the canonical conjugate variables $\boldsymbol{y}_A$ and $\boldsymbol{p}_A$. The Hamiltonian is made of a local instantaneous piece (containing many instantaneous terms up to 4PN order) and the non-local-in-time tail part which is the analogue of Eq. (8), namely

$$H^{\rm tail}[\boldsymbol{x}_A, \boldsymbol{p}_A] = -\frac{G^2 M}{5c^8}\, \hat{I}_{ij}^{(3)}(t) \underset{2s_0/c}{\rm Pf} \int_{-\infty}^{+\infty} \frac{{\rm d}\tau}{|\tau|}\, \hat{I}_{ij}^{(3)}(t+\tau)\,. \tag{12}$$

The hat over the quadrupole moment means that all time derivatives must be explicitly evaluated by means of the Newtonian equations of motion. It is crucial to realize that, in Hamilton's equations, the tail part of the Hamiltonian is to be differentiated in the sense of functional derivatives, e.g.,

$$\frac{\delta H^{\rm tail}}{\delta y_A^i} = -\frac{2G^2 M}{5c^8} \frac{\partial \hat{I}_{jk}^{(3)}}{\partial y_A^i} \underset{2s_0/c}{\rm Pf} \int_{-\infty}^{+\infty} \frac{{\rm d}\tau}{|\tau|}\, \hat{I}_{jk}^{(3)}(t+\tau)\,. \tag{13}$$

Since the time derivative of H computed on shell is linked to the partial derivatives of H, through the chain rule, the usual cancellations implying $\mathrm{d}H(t)/\mathrm{d}t = 0$ do not occur when non-local-in-time contributions are present. We find instead a more complicated "non-conservation" law $\mathrm{d}H/\mathrm{d}t = \mathcal{P}^{\rm tail}$, where $\mathcal{P}^{\rm tail}$ involves non-local integrals constructed from the tail term (12). From that law, we can derive explicitly the conserved energy E associated with the non-local Hamiltonian. [14] We start by performing a Taylor expansion of $\hat{I}_{ij}(t+\tau)$ when $\tau \to 0$. To remedy the appearance of divergent integrals, we introduce in the integrand an exponential cut-off factor $\mathrm{e}^{-\epsilon|\tau|}$ for some $\epsilon > 0$, and let ϵ tend to zero at the end of our calculation. It is then straightforward to recast $\mathcal{P}^{\rm tail}$ as a total time derivative, say $-\mathrm{d}\Delta H^{\rm tail}/\mathrm{d}t$, so that $E = H + \Delta H^{\rm tail}$. Aiming at getting a non-perturbative (resummed) expression for $\Delta H^{\rm tail}$, we notice that the Newtonian quadrupole moment, being a periodic function of time, may be conveniently decomposed in discrete Fourier series, with coefficients ${}_p\mathcal{I}_{ij}$ ($p \in \mathbb{N}$). All integrals entering $\Delta H^{\rm tail}$ can be evaluated in closed (albeit Fourier-expanded) form, which yields

$$\Delta H^{\rm tail} = -\frac{2G^2 M\omega^6}{5c^8}\left[\sum_p |\underset{p}{\mathcal{I}_{ij}}|^2 p^6 - \frac{1}{2}\sum_{p+q\neq 0} \underset{p}{\mathcal{I}_{ij}}\,\underset{q}{\mathcal{I}_{ij}}\,\frac{p^3q^3(p-q)}{p+q}\ln\left|\frac{p}{q}\right|\,\mathrm{e}^{\mathrm{i}(p+q)\ell}\right], \tag{14}$$

where ω represents the orbital frequency. Remarkably, this expression contains a constant (DC) contribution [first term in Eq. (14)] proportional to the gravitational wave energy flux, $\mathcal{F}^{\rm GW} = \frac{G}{5c^5}\langle (I^{(3)}_{ij})^2\rangle$. The remaining (AC) terms average to zero, and are strictly zero in the case of circular orbits. A similar procedure allows us to construct the conserved angular momentum. [14]

The complete expression of the energy through 4PN order in the limiting case of circular orbits is the sum of the instantaneous part of the 4PN dynamics, composed of many different terms, and of the tail part, composed of (12) plus the crucial DC contribution in (14). After reducing to the frame of the center of mass and specializing to circular orbits, we obtain

$$\begin{aligned} E = -\frac{m\nu c^2 x}{2}\Bigg\{1 &+ \left(-\frac{3}{4} - \frac{\nu}{12}\right)x + \left(-\frac{27}{8} + \frac{19}{8}\nu - \frac{\nu^2}{24}\right)x^2 + \left(-\frac{675}{64} + \left[\frac{34445}{576} - \frac{205}{96}\pi^2\right]\nu\right. \\ &\left. - \frac{155}{96}\nu^2 - \frac{35}{5184}\nu^3\right)x^3 + \left(-\frac{3969}{128} + \left[-\frac{123671}{5760} + \frac{9037}{1536}\pi^2 + \frac{896}{15}\gamma_{\rm E} + \frac{448}{15}\ln(16x)\right]\nu\right. \\ &\left. + \left[-\frac{498449}{3456} + \frac{3157}{576}\pi^2\right]\nu^2 + \frac{301}{1728}\nu^3 + \frac{77}{31104}\nu^4\right)x^4\Bigg\}. \end{aligned} \tag{15}$$

The PN parameter reads $x = (Gm\omega/c^3)^{2/3}$ and we have used the approximation $M = m_1 + m_2$ in the tail terms. We adjust the remaining ambiguity parameter in (11) by comparing to the circular energy obtained in the GSF framework, at first order in the perturbative expansion in the small mass ratio limit. [25,26] The correct value is $\kappa = \frac{41}{60}$. Such value agrees with the one found in the computation of the tail term in d dimensions (including both conservative and dissipative effects) by means of EFT methods. [16]

Finally we report the complete expression of the periastron advance at the 4PN order, for a slightly non-circular orbit, in the limit where the eccentricity goes to zero: [27,14]

$$\begin{aligned} K = 1 + 3x + \left(\frac{27}{2} - 7\nu\right)x^2 + \left(\frac{135}{2} + \left[-\frac{649}{4} + \frac{123}{32}\pi^2\right]\nu + 7\nu^2\right)x^3 + \left(\frac{2835}{8} + \left[-\frac{275941}{360}\right.\right. \\ \left.\left. + \frac{48007}{3072}\pi^2 - \frac{1256}{15}\ln x - \frac{592}{15}\ln 2 - \frac{1458}{5}\ln 3 - \frac{2512}{15}\gamma_{\rm E}\right]\nu + \left[\frac{5861}{12} - \frac{451}{32}\pi^2\right]\nu^2 - \frac{98}{27}\nu^3\right)x^4. \end{aligned} \tag{16}$$

Note that, for the previous value of κ, the result agrees directly with GSF calculations. The GSF contribution to the periastron is generally described by means of the function $\rho(x)$ such

that $K^{-2} = 1 - 6x + \nu\rho(x) + \mathcal{O}(\nu^2)$:

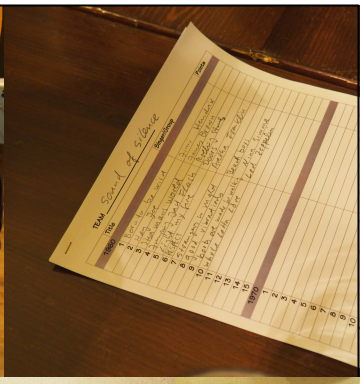
$$\rho = 14x^2 + \left(\frac{397}{2} - \frac{123}{16}\pi^2\right)x^3 + \left(-\frac{215729}{180} + \frac{58265}{1536}\pi^2 + \frac{1184}{15}\ln 2 + \frac{2916}{5}\ln 3 + \frac{5024}{15}\gamma_{\rm E} + \frac{2512}{15}\ln x\right)x^4 \,. \qquad (17)$$

The 4PN coefficient $\rho_{\rm 4PN} = a_{\rm 4PN} + b_{\rm 4PN}\ln x$, in particular the coefficient $a_{\rm 4PN}$ with numerical value $a_{\rm 4PN} \simeq 64.6406$, is in perfect agreement with GSF numerical results. [28] It is worth mentionning that the GSF periastron advance (analytical or numerical) is not computed directly but indirectly deduced from the so-called redshift variable via the first law of binary mechanics, but the latter has been checked to hold even at the 4PN order for the non-local-in-time dynamics. [29]

References

1. A. Buonanno and B.S. Sathyaprakash. Sources of gravitational waves: Theory and observations. In A. Ashtekar, B.K. Berger, J. Isenberg, and M.A.H. MacCallum, editors, *General Relativity and Gravitation: A Centennial Perspective*, page 513, 2015.
2. S. Akcay, A. Le Tiec, L. Barack, N. Sago and N. Warburton. *Phys. Rev. D*, 91:124014, 2015.
3. A. Buonanno and T. Damour. *Phys. Rev. D*, 59:084006, 1999.
4. H.A. Lorentz and J. Droste. *The motion of a system of bodies under the influence of their mutual attraction, according to Einstein's theory*, page 330. Nijhoff, The Hague, 1937. Versl. K. Akad. Wet. Amsterdam **26**, 392 and 649 (1917).
5. A. Einstein, L. Infeld, and B. Hoffmann. *Ann. Math.*, 39:65–100, 1938.
6. T. Damour. Gravitational radiation and the motion of compact bodies. In N. Deruelle and T. Piran, editors, *Gravitational Radiation*, pages 59–144, Amsterdam, 1983. North-Holland Company.
7. J. Ehlers, A. Rosenblum, J.N. Goldberg and P. Havas. *Astrophys. J.*, 208:L77, 1976.
8. S. Foffa and R. Sturani. *Phys. Rev. D*, 87:064011, 2012.
9. S. Foffa and R. Sturani. *Phys. Rev. D*, 87:044056, 2013.
10. P. Jaranowski and G. Schäfer. *Phys. Rev. D*, 87:081503(R), 2013.
11. T. Damour, P. Jaranowski and G. Schäfer. *Phys. Rev. D*, 89:064058, 2014.
12. T. Damour, P. Jaranowski, and G. Schäfer. *Phys. Rev. D*, 93:084014, 2016.
13. L. Bernard, L. Blanchet, A. Bohé, G. Faye and S. Marsat. *Phys. Rev. D*, 93:084037, 2016.
14. L. Bernard, L. Blanchet, A. Bohé, G. Faye and S. Marsat. *Phys. Rev. D*, 95:044026, 2017.
15. L. Bernard, L. Blanchet, A. Bohé, G. Faye and S. Marsat. arXiv:1706:08480, 2017.
16. C. R. Galley, A. K. Leibovich, R. A. Porto and A. Ross. *Phys. Rev. D*, 93:124010, 2016.
17. R. A. Porto and I. Z. Rothstein. arXiv:1703.06433, 2016.
18. L. Blanchet and T. Damour. *Phil. Trans. Roy. Soc. Lond. A*, 320:379–430, 1986.
19. O. Poujade and L. Blanchet. *Phys. Rev. D*, 65:124020, 2002.
20. L. Blanchet, G. Faye and S. Nissanke. *Phys. Rev. D*, 72:044024, 2005.
21. L. Blanchet and T. Damour. *Phys. Rev. D*, 37:1410, 1988.
22. L. Blanchet and G. Faye. *Phys. Rev. D*, 63:062005, 2001.
23. L. Blanchet, T. Damour, and G. Esposito-Farèse. *Phys. Rev. D*, 69:124007, 2004.
24. L. Blanchet, G. Faye, and B. Ponsot. *Phys. Rev. D*, 58:124002, 1998.
25. A. Le Tiec, L. Blanchet and B. Whiting. *Phys. Rev. D*, 85:064039, 2012.
26. D. Bini and T. Damour. *Phys. Rev. D*, 87:121501(R), 2013.
27. T. Damour, P. Jaranowski, and G. Schäfer. *Phys. Rev. D*, 91:084024, 2015.
28. M. van de Meent. *Phys. Rev. Lett.*, 118:011101, 2017.
29. A. Le Tiec and L. Blanchet. arXiv:1702.0639, 2017.












RENCONTRES DE MORIOND
50
Music Quizz

4.5 Post-Newtonian order gravitational radiation

Tanguy Marchand
Institut d'Astrophysique de Paris, 98 bis bd Arago, 75014 Paris, FRANCE



Post-Newtonian (PN) theory enables us to predict the waveform and the phase evolution of the gravitational waves emitted by a system of two compact objects coalescing in its inspiral phase. State-of-the-art works provide the phase of the expected signal up to 3.5PN [5] (i.e. up to $1/c^7$). Comparison with numerical relativity, as well as the promising evolution of gravitational wave detectors and the new discoveries incite us to pursue this computation to a higher order. In our current program, we are aiming at reaching the phase of the signal at the 4.5PN order (i.e. $1/c^9$). For this purpose, the energy flux emitted by such a system for circular orbits has to be known at 4.5PN. One difficulty of this computation is the high-order interactions - commonly called tails- between the mass of the system and its mass and current multipole moments during the propagation of the signal. In *Marchand et al. 2016* [1] , we have computed the contribution of all the tails entering the flux at the 4.5PN order, and in particular the third-order mass-quadrupole interactions known as "tails-of-tails-of-tails". Our work enables to fully determine the 4.5PN coefficient of the flux for circular orbits (while the 4PN coefficient is still unknown).

1 Introduction

With the spectacular discoveries by the LIGO/VIRGO collaboration of gravitational waves from the coalescence of black-hole binaries, we foresee the possibility of extremely accurate measurements of the so-called post-Newtonian (PN) coefficients that describe the gravitational waveform of these systems in the inspiral phase prior to the final coalescence. The PN coefficients are especially important because they probe the non-linear structure of general relativity (GR) and provide thus very constraining tests of this theory. In turn, they permit accurate measurements of the physical parameters of the binary, essentially the masses of the compact objects and their moments of rotation or spins. The PN coefficients of the phase of a gravitational signal is known up to 3.5PN (i.e. up to $(\frac{v}{c})^7$) [5] . Our current goal is to determine the phase (as well as other interesting physical quantities like the polarization modes) up to 4.5PN for a spinless compact binary system in circular orbit. For that, different tasks need to be fullfill. In particular, the contribution of the third-order tails effect (or "tails-of-tails-of-tails") in the flux is required. In this work, we have completely determined this contribution.

2 The Multipolar Post-Minkowskian (MPM) algorithm

2.1 Introduction to the MPM algorithm

The goal of our work is to understand the gravitational field in the region outside an isolated matter source. For that, we have to solve the Einstein field equations in the exterior of that source by using the Multipolar Post-Minkowskian (MPM) algorithm in harmonic coordinate developed in Blanchet and Damour 1986 [2] (cf also Blanchet 1998 [3] for more details). The gravitational field in the region outside an isolated matter source, solving the vacuum Einstein field equations in the exterior of that source, is written in "gothic" Minkowskian deviation form. We have thus $h^{\mu\nu} = \sqrt{-g}g^{\mu\nu} - \eta^{\mu\nu}$ where $\eta^{\mu\nu}$ is the (inverse) Minkowski metric, while g and $g^{\mu\nu}$ are the determinant and the inverse of the covariant metric $g_{\mu\nu}$. Our signature is almost plus, i.e., $\eta_{\mu\nu} = \mathrm{diag}(-1,1,1,1) = \eta^{\mu\nu}$. We use Cartesian coordinates and solve iteratively the Einstein field equations using the harmonic coordinates condition $\partial_\nu h^{\mu\nu} = 0$ (indices will always be raised and lowered with respect to $\eta_{\mu\nu}$). We formally develope $h^{\mu\nu}$ as a post-Minkowskian or non-linearity expansion:

$$h^{\mu\nu} = \sum_n G^n h^{\mu\nu}_{(n)}, \tag{1}$$

G being the Newton constant. If we inject (1) into the vacuum Einstein field equations, we find:

$$\Box h^{\mu\nu}_{(i)} = \Lambda^{\mu\nu}(h^{\alpha\beta}_{(1)}, \ldots, h^{\alpha\beta}_{(i-1)}) \tag{2}$$

$$\partial^\mu h_{(i)\mu\nu} = 0 \tag{3}$$

where i $geq1$ and $\Box = \eta^{\rho\sigma}\partial_{\rho\sigma}$ is the flat d'Alembertien operator and $\Lambda^{\mu\nu}$ is a complicated non linear source term depending only on the previous iteration. The MPM algorithm provides an explicit solution (computed iteratively) of the latter equations starting at linear order by Thorne's [8] linearized multipolar solution $h^{\mu\nu}_{(1)}[M_L, S_L]$ depending on two sets of multipole moments M_L (mass-type) and S_L (current-type). This linearized solution is[a]:

$$h^{00}_{(1)} = -\frac{4}{c^2}\sum_{l\geq 0}\frac{(-1)^l}{l!}\partial_L\left(\frac{1}{r}M_L(u)\right) \tag{4a}$$

$$h^{0i}_{(1)} = \frac{4}{c^3}\sum_{l\geq 1}\frac{(-1)^l}{l!}\left\{\partial_{L-1}\left(\frac{1}{r}I^{(1)}_{iL-1}(u)\right) + \frac{l}{l+1}\epsilon_{iab}\partial_{aL-1}\left(\frac{1}{r}S_{bL-1}(u)\right)\right\} \tag{4b}$$

$$h^{ij}_{(1)} = -\frac{4}{c^4}\sum_{l\geq 2}\frac{(-1)^l}{l!}\left\{\partial_{L-2}\left(\frac{1}{r}I^{(2)}_{ijL-2}(u)\right) + \frac{2l}{l+1}\partial_{aL-2}\left(\frac{1}{r}\epsilon_{ab(i}J^{(1)}_{j)bL-2}(u)\right)\right\} \tag{4c}$$

The sets of function $\{M_L\}$ and $\{S_L\}$ can be interpreted as the set of mass multipole moments and current multipole moments of the source. The function M ($l = 0$) is the ADM-mass of the source and $M_i = const$, $S_i = const$. It is always possible to achieve $M_i = 0$ by translating the origin of our coordinates to the center of mass. In this work, we will only study the interactions between the ADM-mass M and the mass quadrupole moments M_{ij} and we will focus on the following terms[b]: $h^{\mu\nu}_{(1)} = h^{\mu\nu}_{M} + h^{\mu\nu}_{M_{ij}}$, $h^{\mu\nu}_{(2)} = h^{\mu\nu}_{M^2} + h^{\mu\nu}_{M\times M_{ij}} + h^{\mu\nu}_{M_{ij}\times M_{kl}}$, $h^{\mu\nu}_{(3)} = h^{\mu\nu}_{M^3} + h^{\mu\nu}_{M^2\times M_{ij}} + h^{\mu\nu}_{M\times M_{ij}\times M_{kl}} + h^{\mu\nu}_{M_{ij}\times M_{kl}\times M_{mn}}$ etc. The final goal of this algorithm is to reach the term $h^{\mu\nu}_{M^3\times M_{ij}}$ contained in $h_{(4)}$ that corresponds to the "tails-of-tails" and that is required in order to know the 4.5PN contribution of non-local terms in the flux.

[a] Here, $L = i_1\cdots i_\ell$ denotes a multi-index composed of ℓ spatial indices (ranging from 1 to 3); we pose $L-1 = i_1\cdots i_{\ell-1}$, and so on; $\partial_L = \partial_{i_1}\cdots\partial_{i_\ell}$ is the product of ℓ partial derivatives $\partial_i \equiv \partial/\partial x^i$. Symmetrization over indices is denoted by $T_{(ij)} = \frac{1}{2}(T_{ij}+T_{ji})$. The STF projection is indicated with a hat, e.g., $\hat{n}_L \equiv \mathrm{STF}[n_L]$, or with angular brackets $\langle\rangle$ surrounding the relevant indices, e.g., $x_{\langle i}v_{j\rangle} = x_{(i}v_{j)} - \frac{1}{3}\delta_{ij}x_k v_k$. The indices of multipole moments M_L and S_L are symmetric and trace-free (STF). Time derivatives of the moments are indicated by superscripts (n) and u denotes the retarded time $u = t - r$.

[b] In our notations, $h^{\mu\nu}_{M_{ij}}$ corresponds to the terms in (4a)-(4b)-(4c) that depends on M_{ij} and $h_{M\times M_{ij}}$ to the terms in $h_{(2)}$ sourced in equation (2) by $\Lambda(h_M, h_{M_{ij}})$ etc.

2.2 First step: Finite-Part regularization

The first difficulties to address is the existence of U.V. divergences due to the multipolar expansion of the metric. In fact, the MPM solution of the metric will correspond to the true metric in the far-zone region, outside the source. Inside the matter source, the MPM metric is no long valid and divergences appear. These infinities occur when we want to solve the d'Alembertien equation. For example, the equation:

$$\Box u^{\mu\nu}_{(n)} = \Lambda^{\mu\nu}(h^{\alpha\beta}_{(1)}, \ldots, h^{\alpha\beta}_{(n-1)}), \tag{5}$$

is usually solved using the usual retarded propagator $\Box^{(-1)}_{\rm ret}$. However, applying this propagator will lead to divergences if $\Lambda^{\mu\nu}(h^{\alpha\beta}_{(1)}, \ldots, h^{\alpha\beta}_{(n-1)}) \sim_{r\to 0} \frac{1}{r^k}$ with $k \geq 3$. In order to solve this issue, we multiply the source $\Lambda^{\mu\nu}(h^{\alpha\beta}_{(1)}, \ldots, h^{\alpha\beta}_{(n-1)})$ by a regulartor $\left(\frac{r}{r_0}\right)^B$ and define

$$u^{\mu\nu}_{(n)B} = \Box^{-1}_{\rm ret}\left[\left(\frac{r}{r_0}\right)^B \Lambda^{\mu\nu}(h^{\alpha\beta}_{(1)}, \ldots, h^{\alpha\beta}_{(n-1)})\right] \tag{6}$$

The solution we are looking for is then defined by the MPM algorithm to be the finite part of the analytical continuation of $u^{\mu\nu}_{(n)B}$ when $B \to 0$, i.e. the coefficient of the zeroth power of B (i.e. B^0) in the Laurent expansion of $u^{\mu\nu}_{(n)B}$ when $B \to 0$. In order words, if we denote $\mathrm{FP}_{B=0}$ this regularization procedure, we have:

$$u^{\mu\nu}_{(n)} = \underset{B=0}{\mathrm{FP}}\, \Box^{-1}_{\rm ret}\left[\left(\frac{r}{r_0}\right)^B \Lambda^{\mu\nu}(h^{\alpha\beta}_{(1)}, \ldots, h^{\alpha\beta}_{(n-1)})\right] \tag{7}$$

Such a definition yields a solution of the wave equation $\Box u^{\mu\nu}_{(n)} = \Lambda^{\mu\nu}(h^{\alpha\beta}_{(1)}, \ldots, h^{\alpha\beta}_{(n-1)})$.

2.3 Second step: Harmonic coordinate condition

Once the solution $u^{\mu\nu}_{(n)}$ is computed, we need to add an extra homogeneous solutions to it in order to satisfy the harmonic coordinates equation (3). In order words, according to the MPM algorithm we define $h^{\mu\nu}_{(n)} = u^{\mu\nu}_{(n)} + w^{\mu\nu}_{(n)}$ with $\Box w^{\mu\nu}_{(n)} = 0$ and $\partial_\mu w^{\mu\nu}_{(n)} = -\partial_\mu u^{\mu\nu}_{(n)}$. For explicit on the definition of $w^{\mu\nu}_{(n)}$, see Blanchet 1998 [3].

2.4 The matching equation

The MPM algorithm provides an explicit solution of the vacuum Einstein equations expressed with yet unspecified functions $\{M_L, S_L\}$. By matching this MPM expansion to a post-Newtonian expansion valid inside the source and in the near-zone (i.e. in a region smaller than the gravitational wavelength of the source), explicit formulae for M_L and S_L can be found for any post-Newtonian order (cf Blanchet 1999 [4]).

3 Results

3.1 Radiative quadrupole moments

We have applied the algorithm in order to compute the effects of non-local terms in the mass-quadrupole interactions up to the 4.5PN order. The result can be expressed as a radiative multipole mass quadrupole describing the metric in the radiative zone (cf Thorne 1980 [8] for a definition of the radiative multipole moments). The mass-quadrupole interactions in the radiative moments were known up to the 3.5PN order [5] and we pushed it up to the 4.5PN order.

The result yields [c]:

$$U_{ij}(T_R) = M_{ij}^{(2)}(T_R) + \frac{GM}{c^3}\int_0^{+\infty} \mathrm{d}\tau\, M_{ij}^{(4)}(T_R-\tau)\left[2\ln\left(\frac{c\tau}{2b_0}\right)+\frac{11}{6}\right] + \frac{G^2M^2}{c^6}\int_0^{+\infty} \mathrm{d}\tau\, M_{ij}^{(5)}(T_R-\tau)\left[2\ln^2\left(\frac{c\tau}{2b_0}\right)+\frac{11}{3}\ln\left(\frac{c\tau}{2b_0}\right) -\frac{214}{105}\ln\left(\frac{c\tau}{2r_0}\right)+\frac{124627}{22050}\right] + \frac{G^3M^3}{c^9}\int_0^{+\infty} \mathrm{d}\tau\, M_{ij}^{(6)}(T_R-\tau)\left[\frac{4}{3}\ln^3\left(\frac{c\tau}{2b_0}\right)+\frac{11}{3}\ln^2\left(\frac{c\tau}{2b_0}\right) +\frac{124627}{11025}\ln\left(\frac{c\tau}{2b_0}\right)-\frac{428}{105}\ln\left(\frac{c\tau}{2b_0}\right)\ln\left(\frac{c\tau}{2r_0}\right) -\frac{1177}{315}\ln\left(\frac{c\tau}{2r_0}\right)+\frac{129268}{33075}+\frac{428}{315}\pi^2\right]+\mathcal{O}\left(\frac{1}{c^{12}}\right). \quad (8)$$

3.2 Energy flux for circular orbits

We can specify our result for compact binary systems in circular orbits and compute the energy flux emitted by such a system (by substituting the expression of M and M_{ij} for circular orbits). The result is express as a function of the symmetric mass ratio $\nu = \frac{m_1 m_2}{(m_1+m_2)^2}$ and the frequency-related quantity $x = \left(\frac{Gm\omega}{c^3}\right)^{2/3}$ which is a 1-PN parameter. We can check that all the gauge constants (i.e. r_0 and b_0) disappear. We found the energy flux to be:

$$\mathcal{F}_{\text{total}} = \frac{32c^5}{5G}\nu^2x^5\Bigg\{1+\left(-\frac{1247}{336}-\frac{35}{12}\nu\right)x+4\pi x^{3/2}+\left(-\frac{44711}{9072}+\frac{9271}{504}\nu+\frac{65}{18}\nu^2\right)x^2 +\left(-\frac{8191}{672}-\frac{583}{24}\nu\right)\pi x^{5/2}+\left[\frac{6643739519}{69854400}+\frac{16}{3}\pi^2-\frac{1712}{105}\gamma_E -\frac{856}{105}\ln(16x)+\left(-\frac{134543}{7776}+\frac{41}{48}\pi^2\right)\nu-\frac{94403}{3024}\nu^2-\frac{775}{324}\nu^3\right]x^3 +\left(-\frac{16285}{504}+\frac{214745}{1728}\nu+\frac{193385}{3024}\nu^2\right)\pi x^{7/2}+\big(\text{unknown coefficients}\big)x^4 +\left(\frac{265978667519}{745113600}-\frac{6848}{105}\gamma_{\mathrm{E}}-\frac{3424}{105}\ln(16x)+\left[\frac{2062241}{22176}+\frac{41}{12}\pi^2\right]\nu -\frac{133112905}{290304}\nu^2-\frac{3719141}{38016}\nu^3\right)\pi x^{9/2}+\mathcal{O}(x^5)\Bigg\}. \quad (9)$$

This flux was already known up to 3.5PN [5]. We can test our result by comparing the test particle limit when $\nu \to 0$ with results from black holes perturbation theory [6]. Besides, our work has been recently confirmed by Effective-One-Body computation [7].

References

1. T. Marchand, L. Blanchet, G. Faye, Class. Quant. Grav. 33, 244003 (2016), arXiv:1607.07601 [gr-qc]
2. L. Blanchet and T. Damour, Philos. Trans. R. Soc. London A 320, 379 (1986)
3. L. Blanchet, Class. Quant. Grav. 15, 89 (1998), gr-qc/9710037
4. Class.Quant.Grav. 15 (1998) 1971-1999, arXiv:gr-qc/9801101
5. L. Blanchet, Living Rev. Rel. 17, 2 (2014), arxiv:1310.1528 [gr-qc]
6. T. Tanaka, H. Tagoshi, and M. Sasaki, Prog. Theor. Phys. 96, 1087 (1996), gr-qc/9701050.
7. Francesco Messina, Alessandro Nagar 2017 arXiv:1703.08107 [gr-qc]
8. K. Thorne, Rev. Mod. Phys. 52, 299 (1980).

[c] r_0 is a constant introduced by the regularization procedure described in 2.2 while b_0 is another constant introducing when going from the harmonic coordinates to the radiative coordinates used in the far zone (cf Marchand et al. 2016 [5] for more information). $T_R = T - R$ is the retarded time in the new radiative coordinate system.

EFFECTIVE FIELD THEORY OF POST-NEWTONIAN GRAVITY INCLUDING SPINS

MICHELE LEVI
Institut de Physique Théorique, CEA Saclay, Université Paris-Saclay, 91191 Gif-sur-Yvette, France

We present in detail an Effective Field Theory (EFT) formulation for the essential case of spinning objects as the components of inspiralling compact binaries. We review its implementation, carried out in a series of works in recent years, which leveled the high post-Newtonian (PN) accuracy in the spinning sector to that, recently attained in the non-spinning sector. We note a public package, "EFTofPNG", that we recently created for high precision computation in the EFT of PN Gravity, which covers all sectors, and includes an observables pipeline.

1 Introduction

A new era of high precision Gravity has been launched with the recent direct detection of gravitational waves (GWs) from compact binary coalescence [1,2]. The influx of improved GW data is expected to increase, and more accurate GWs templates will be required to optimally analyze the signal. The continuous GW signal comprises various kinds of physics, corresponding to the different phases in the evolution of the radiating binary. The initial inspiral phase, where the components of the binary orbit with a non-relativistic velocity, can only be treated analytically with the post-Newtonian (PN) theory of General Relativity [3,4]. Indeed, in recent years there has been a remarkable progress in high order PN theory, in particular also involving the essential *spins* of the components of the binary. In what follows we detail the formal progress, which has been obtained within an extension of the Effective Field Theory (EFT) for the binary inspiral to spinning objects [5,6]. We also review its specific applications, which we carried out.

2 Effective Field Theory of Post-Newtonian Gravity including Spinning Objects

Effective Field Theories (EFTs) and their setup are universal. Once a hierarchy of scales is identified in the physical problem, be it classical or quantum, the robust EFT framework can then be applied. For the compact binary coalescence in the inspiral phase of its evolution, this observation was made by Goldberger *et al.* [7,8]. Indeed, there are three distinct characteristic length scales in the problem: r_s, r, and λ, corresponding to the scales of the internal structure of the single compact component of the binary, the orbital separation of the binary, and the wavelength of radiation emitted from the binary, respectively. They are widely separated by powers of $v \ll 1$, the typical non-relativistic orbital velocity at the inspiral phase, as we have that $r_s \sim r\, v^2 \sim \lambda\, v^3$. Goldberger *et al.* [7,8] put forward a program to tackle the binary inspiral problem with a tower of EFTs, corresponding to each of the scales. We note that the only scale in the full theory is the UV scale m, the mass of the isolated compact object, where $r_s \sim m$. For the general case that we tackle in our work, where the compact object is *spinning*, and hence also characterized by its spin length [6], S^2, we also have that $S \lesssim m^2$.

The construction of an EFT follows one of two general procedures, top-down and bottom-up. These approaches differ on how the effective action, which formally represents the EFT, is obtained. The bottom-up approach constructs the effective action from scratch as an infinite sum of operators, constrained by symmetry considerations. The top-down approach obtains the effective action by explicitly eliminating degrees of freedom (DOFs) from the action of the high energy (small scale) theory. We apply, in fact, both of these approaches in our construction of the EFTs. First, we remove the scale r_s, using a bottom-up approach, by eliminating the strong field modes $g^s_{\mu\nu}$, where the gravitational field is decomposed into $g_{\mu\nu} \equiv g^s_{\mu\nu} + \bar{g}_{\mu\nu}$, and $\bar{g}_{\mu\nu}$ represents the field modes in scales above r_s. The effective action for an isolated compact object can then be generically written as:

$$S_{\text{eff}}\left[\bar{g}_{\mu\nu}, y^\mu, e^\mu_A\right] = -\frac{1}{16\pi G}\int d^4x\sqrt{\bar{g}}R\left[\bar{g}_{\mu\nu}\right] + \underbrace{\sum_i C_i \int d\sigma O_i(\sigma)}_{S_{pp}\equiv\text{point particle action}} , \tag{1}$$

where we introduce a point particle action, S_{pp}, with an infinite tower of worldline operators, $O_i(\sigma)$. These should contain the DOFs relevant at this scale, and satisfy the symmetries of the theory. Hence, it is crucial to accurately identify the DOFs and symmetries for the general case of spinning gravitating objects as we further elaborate below [6]. Here, y^μ, and e^μ_A, are the particle worldline coordinate, and tetrad DOFs, respectively. All of the UV physics is encapsulated in the Wilson coefficients, $C_i(r_s)$, in the point particle action, S_{pp}.

For the next EFT in the tower, where the orbital scale r is removed, we use the top-down approach. First, we decompose the field into $\bar{g}_{\mu\nu} \equiv \eta_{\mu\nu} + H_{\mu\nu} + \widetilde{h}_{\mu\nu}$, where $H_{\mu\nu}$ represents the field modes at the orbital scale, and $\widetilde{h}_{\mu\nu}$, the radiation modes. These different field modes scale with a definite power of the small PN parameter v: $\partial_t H_{\mu\nu} \sim \frac{v}{r}H_{\mu\nu}$, $\partial_i H_{\mu\nu} \sim \frac{1}{r}H_{\mu\nu}$, $\partial_\rho \widetilde{h}_{\mu\nu} \sim \frac{v}{r}\widetilde{h}_{\mu\nu}$. Then, we use the effective action of two compact objects, with a copy of S_{pp} for each object, to integrate out the field modes $H_{\mu\nu}$ by computing the following functional integral:

$$e^{iS_{\text{eff(composite)}}\left[\widetilde{h}_{\mu\nu}, y^\mu, e^\mu_A\right]} \equiv \int \mathcal{D}H_{\mu\nu}\; e^{iS_{\text{eff}}\left[\bar{g}_{\mu\nu}, y^\mu_1, y^\mu_2, {e_{(1)}}^\mu_A, {e_{(2)}}^\mu_A\right]}, \tag{2}$$

taking only the tree level for the classical limit. This defines the effective action of the composite object with y^μ, and e^μ_A, now being its worldline coordinate, and tetrad, respectively. In general, we should proceed to integrate out the radiation modes, $\widetilde{h}_{\mu\nu}$, to get the final EFT. However, this is not required in the conservative sector, where no radiation modes are present. Therefore, we stress that the final effective action at this stage should consist of no remaining field modes at the orbital scale [9,10,6].

As we noted, in order to construct the point particle action in Eq. 1, it is crucial to accurately identify the DOFs and symmetries of the theory [6]. As for the DOFs for a spinning object, of which we have three kinds, it is important to note the following: 1. As for the gravitational field we should consider the tetrad field, $\eta^{ab}\tilde{e}_a{}^\mu(x)\tilde{e}_b{}^\nu(x) = g^{\mu\nu}(x)$, rather than just $g_{\mu\nu}(x)$; 2. As for the particle worldline coordinate, $y^\mu(\sigma)$, the particle worldline position does not in general coincide with the object's "center"; 3. As for the particle worldline rotating DOFs, from the worldline tetrad, $\eta^{AB}e_A{}^\mu(\sigma)e_B{}^\nu(\sigma) = g^{\mu\nu}$, we define the angular velocity, $\Omega^{\mu\nu}(\sigma) \equiv e^\mu_A \frac{De^{A\nu}}{D\sigma}$, and add its conjugate, the worldline spin, $S_{\mu\nu}(\sigma) \equiv -2\frac{\partial L}{\partial \Omega^{\mu\nu}}$, as further DOFs. Later, we switch to the worldline Lorentz matrices, $\eta^{AB}\Lambda_A{}^a(\sigma)\Lambda_B{}^b(\sigma) = \eta^{ab}$, and the conjugate local spin, $S_{ab}(\sigma)$.

Regarding the symmetries of the theory, it is crucial to note the additional symmetries that play a role for the spinning case, i.e. beyond general covariance, and worldline reparametrization invariance. These additional symmetries are: 1. Parity invariance; 2. Internal Lorentz invariance of the local frame field; 3. $SO(3)$ invariance of the worldline spatial triad; 4. Spin gauge invariance, that is invariance under the choice of completion of the worldline spatial triad through a timelike vector. This is a gauge of the rotational variables, i.e. of both the worldline tetrad,

and spin. In addition to these symmetries, we assume that the isolated object has no intrinsic permanent multipole moments beyond the mass monopole, and the spin dipole.

For a spinning object we can write the point particle action in Eq. 1 in the form [11,12,6]:

$$S_{\rm pp} = \int d\sigma \left[-m\sqrt{u^2} - \frac{1}{2} S_{\mu\nu}\Omega^{\mu\nu} + L_{\rm SI}\left[u^\mu, S_{\mu\nu}, \bar{g}_{\mu\nu}\left(y^\mu\right)\right] \right], \tag{3}$$

where $u^\mu \equiv dy^\mu/d\sigma$, and $L_{\rm SI}$ denotes the Lagrangian part, which is nonminimal coupling, and as we assume, contains only spin-induced higher multipoles. While the minimal coupling here is fixed only from covariance and reparametrization invariance, it can still be worked out to further incorporate the other symmetries related with the worldline tetrad. As for nonminimal coupling, parity invariance also plays a role in constraining it. Indeed, in [6] we work out the point particle action of a spinning object, required for the first EFT of a single spinning particle.

In the spirit of Stueckelberg, we first want to introduce the gauge freedom of the rotational variables into the effective action. We do this by applying a 4-dimensional covariant boost-like transformation on the worldline tetrad [6]. This introduces new gauge DOFs, w_μ, as the timelike vector of the tetrad, $\hat{e}_{[0]\mu} = w_\mu$, and also leads to a generic gauge condition for the spin:

$$\hat{S}^{\mu\nu}\left(p_\nu + \sqrt{p^2}\hat{e}_{[0]\nu}\right) = 0. \tag{4}$$

All in all, these constitute the $3+3$ necessary gauge conditions for the redundant unphysical DOFs, that are contained in the 4-dimensional antisymmetric angular velocity, and spin tensors. The minimal coupling term then yields:

$$\frac{1}{2} S_{\mu\nu}\Omega^{\mu\nu} = \frac{1}{2}\hat{S}_{\mu\nu}\hat{\Omega}^{\mu\nu} + \frac{\hat{S}^{\mu\nu}p_\nu}{p^2}\frac{Dp_\mu}{D\sigma}, \tag{5}$$

where an extra term appears in the action. This extra term, originating from minimal coupling, is of course not preceded by any Wilson coefficient, although it contributes to finite size effects. As for the spin that appears in spin-induced nonminimal couplings in the action, it is transformed to the generic spin variable as:

$$S_{\mu\nu} = \hat{S}_{\mu\nu} - \frac{\hat{S}_{\mu\rho}p^\rho p_\nu}{p^2} + \frac{\hat{S}_{\nu\rho}p^\rho p_\mu}{p^2}. \tag{6}$$

As we noted, the nonminimal coupling action with spin should also be constrained, using the full set of symmetries of the theory, that we detailed above. Based on these symmetries, and further considerations and properties of the problem, the leading order (LO) nonminimal couplings are indeed fixed to all orders in spin [6]:

$$\begin{aligned} L_{\rm SI} =& \sum_{n=1}^{\infty} \frac{(-1)^n}{(2n)!}\frac{C_{ES^{2n}}}{m^{2n-1}} D_{\mu_{2n}}\cdots D_{\mu_3}\frac{E_{\mu_1\mu_2}}{\sqrt{u^2}} S^{\mu_1}S^{\mu_2}\cdots S^{\mu_{2n-1}}S^{\mu_{2n}} \\ &+ \sum_{n=1}^{\infty} \frac{(-1)^n}{(2n+1)!}\frac{C_{BS^{2n+1}}}{m^{2n}} D_{\mu_{2n+1}}\cdots D_{\mu_3}\frac{B_{\mu_1\mu_2}}{\sqrt{u^2}} S^{\mu_1}S^{\mu_2}\cdots S^{\mu_{2n-1}}S^{\mu_{2n}}S^{\mu_{2n+1}}, \end{aligned} \tag{7}$$

where new spin-induced Wilson coefficients precede each of the nonminimal coupling terms. These operators are composed from either the electric, or magnetic curvature tensors, $E_{\mu\nu}$, or $B_{\mu\nu}$, respectively, together with the spin vector S^μ. Of the above operators, the quadrupole, octupole, and hexadecapole couplings should notably be taken into account up to the fourth PN (4PN) order [13,6,14]. These couplings explicitly read:

$$L_{ES^2} \equiv -\frac{C_{ES^2}}{2m}\frac{E_{\mu\nu}}{\sqrt{u^2}} S^\mu S^\nu, \tag{8}$$

$$L_{BS^3} \equiv -\frac{C_{BS^3}}{6m^2}\frac{D_\lambda B_{\mu\nu}}{\sqrt{u^2}} S^\mu S^\nu S^\lambda, \tag{9}$$

$$L_{ES^4} \equiv \frac{C_{ES^4}}{24m^3}\frac{D_\lambda D_\kappa E_{\mu\nu}}{\sqrt{u^2}} S^\mu S^\nu S^\lambda S^\kappa. \tag{10}$$

We recall that for the second EFT we need to remove the field modes at the orbital scale. To this end the field DOFs should be disentangled from the particle DOFs. This can only be attained if the gauge of the rotational variables is fixed in the action, as was put forward in [9]. We stress that as we work in an action approach the gauge of the rotational variables can be directly inserted at any stage. But first we need to switch to new rotational variables: the locally flat angular velocity with worldline Lorentz matrices, $\hat{\Omega}^{ab}_{\rm flat} = \hat{\Lambda}^{Aa}\frac{d\hat{\Lambda}_A{}^b}{d\sigma}$, and the local spin, $\hat{S}_{ab} = \tilde{e}^{\mu}_a\tilde{e}^{\nu}_b\hat{S}_{\mu\nu}$. Then, using the Ricci rotation coefficients with the tetrad field, defined by $\omega_\mu{}^{ab} \equiv \tilde{e}^b{}_\nu D_\mu \tilde{e}^{a\nu}$, we can rewrite the minimal coupling term in Eq. 5 in the form [5,6]:

$$\frac{1}{2}\hat{S}_{\mu\nu}\hat{\Omega}^{\mu\nu} = \frac{1}{2}\hat{S}_{ab}\hat{\Omega}^{ab}_{\rm flat} + \frac{1}{2}\hat{S}_{ab}\omega_\mu{}^{ab}u^\mu. \tag{11}$$

Now, before we integrate out the field modes at the orbital scale, we need to fix all gauges in the action, which also eliminates all unphysical DOFs from the action. To begin with, we apply the beneficial non-relativistic space+time Kaluza-Klein decomposition on the gravitational field, i.e. we switch to the non-relativistic gravitational (NRG) fields [15,16]. The tetrad field gauge is then accordingly fixed to Schwinger's time gauge with the NRG parametrization, and finally we fix the gauge of the rotational variables to a gauge, that is dubbed the "canonical" gauge.

3 Summary of formal results and applications

In conclusion, we have provided an EFT formulation for the essential case of spinning objects as the components of inspiralling compact binaries, which constitutes a challenging extension of the EFT of PN Gravity [6]. In particular, we have also provided spin-induced nonminimal couplings to all orders in spin for a gravitating spinning particle. Moreover, the equations of motion (EOMs), and Hamiltonians are simply derived from the resulting effective action of the composite object. The (physical) EOMs of both the position, and spin, take a simple form, and are obtained directly via a proper variation of the action. Notably, for the precession equations it should be stressed, that one makes an independent variation with respect to the spin, and to its conjugates, the Lorentz matrices [10,6]. In addition, the useful Hamiltonians are obtained in the standard manner similarly to the non-spinning case.

As for the implementation, we have completed in a series of works all of the interaction potentials, as well as their derivatives and observables, in the spinning sectors up to the 4PN order, on par with the PN accuracy recently attained in the generally simpler point mass sector. These potentials include: the linear-in-spin next-to-next-to-leading order (NNLO) spin-orbit at 3.5PN order [17], and NNLO spin1-spin2 at 4PN order [18,10], the NNLO spin-squared at 4PN order [14,19], and the LO cubic, and quartic in spin at 3.5PN, and 4PN orders, respectively [13].

Moreover, we have recently created a new public package, "EFTofPNG", for high precision computation in the EFT of PN Gravity (PNG), including spins [20]. The "EFTofPNG" package version 1.0 covers the point mass sector, and all the spin sectors, up to the 4PN order, and two-loop level. It is released as a public repository in GitHub, and can be found in the URL: "https://github.com/miche-levi/pncbc-eftofpng". The "EFTofPNG" package is self-contained, modular, and designed to be accessible to the classical Gravity community. Its final unit provides the full computation of derivatives of interest, and gauge invariant observables, and serves as a pipeline chain for the modeling of GW templates for the detectors.

Acknowledgments

ML acknowledges the prolific collaboration with Jan Steinhoff on this line of research. ML would like to thank John Joseph Carrasco for his constant support. ML is grateful for the generous grant from the Moriond conference. The work of ML is supported by the European Research Council under the European Union's Horizon 2020 Framework Programme FP8/2014-2020 grant no. 639729, preQFT project.

References

1. B. P Abbott et al. Observation of Gravitational Waves from a Binary Black Hole Merger. *Phys. Rev. Lett.*, 116:061102, 2016.
2. B. P. Abbott et al. GW151226: Observation of Gravitational Waves from a 22-Solar-Mass Binary Black Hole Coalescence. *Phys. Rev. Lett.*, 116:241103, 2016.
3. B. P. Abbott et al. Tests of general relativity with GW150914. *Phys. Rev. Lett.*, 116:221101, 2016.
4. Luc Blanchet. Gravitational Radiation from Post-Newtonian Sources and Inspiralling Compact Binaries. *Living Rev.Rel.*, 17:2, 2014.
5. Michele Levi. Next to Leading Order gravitational Spin-Orbit coupling in an Effective Field Theory approach. *Phys.Rev.*, D82:104004, 2010.
6. Michele Levi and Jan Steinhoff. Spinning gravitating objects in the effective field theory in the post-Newtonian scheme. *JHEP*, 09:219, 2015.
7. Walter D. Goldberger and Ira Z. Rothstein. An Effective field theory of gravity for extended objects. *Phys.Rev.*, D73:104029, 2006.
8. Walter D. Goldberger. Les Houches lectures on effective field theories and gravitational radiation. arXiv:hep–ph/0701129, [hep-ph].
9. Michele Levi. Next to Leading Order gravitational Spin1-Spin2 coupling with Kaluza-Klein reduction. *Phys.Rev.*, D82:064029, 2010.
10. Michele Levi and Jan Steinhoff. Equivalence of ADM Hamiltonian and Effective Field Theory approaches at next-to-next-to-leading order spin1-spin2 coupling of binary inspirals. *JCAP*, 1412:003, 2014.
11. Andrew J. Hanson and T. Regge. The Relativistic Spherical Top. *Annals Phys.*, 87:498, 1974.
12. I. Bailey and W. Israel. Lagrangian Dynamics of Spinning Particles and Polarized Media in General Relativity. *Commun.Math.Phys.*, 42:65–82, 1975.
13. Michele Levi and Jan Steinhoff. Leading order finite size effects with spins for inspiralling compact binaries. *JHEP*, 06:059, 2015.
14. Michele Levi and Jan Steinhoff. Next-to-next-to-leading order gravitational spin-squared potential via the effective field theory for spinning objects in the post-Newtonian scheme. *JCAP*, 1601:008, 2016.
15. Barak Kol and Michael Smolkin. Non-Relativistic Gravitation: From Newton to Einstein and Back. *Class.Quant.Grav.*, 25:145011, 2008.
16. Barak Kol, Michele Levi, and Michael Smolkin. Comparing space+time decompositions in the post-Newtonian limit. *Class.Quant.Grav.*, 28:145021, 2011.
17. Michele Levi and Jan Steinhoff. Next-to-next-to-leading order gravitational spin-orbit coupling via the effective field theory for spinning objects in the post-Newtonian scheme. *JCAP*, 1601:011, 2016.
18. Michele Levi. Binary dynamics from spin1-spin2 coupling at fourth post-Newtonian order. *Phys.Rev.*, D85:064043, 2012.
19. Michele Levi and Jan Steinhoff. Complete conservative dynamics for inspiralling compact binaries with spins at fourth post-Newtonian order. arXiv:1607.04252, [gr-qc].
20. Michele Levi and Jan Steinhoff. EFTofPNG: A package for high precision computation with the Effective Field Theory of Post-Newtonian Gravity. arXiv:1705.06309, [gr-qc].




LA THUILE
22


WANNA BE!


LA THUILE
33






LA THUILE
39
37
38




LA THUILE
24

LA THUILE
44
LA THUILE
33
LA THUILE
22
LA THUILE
11

On solving post-Newtonian accurate Kepler Equation

Yannick Boetzel
Physik-Institut, Universität Zürich, Winterthurerstrasse 190, 8057 Zürich

We provide an elegant way of solving analytically the third post-Newtonian (3PN) accurate Kepler equation, associated with the 3PN-accurate generalized quasi-Keplerian parametrization for compact binaries in eccentric orbits. We perform comparisons between our PN-accurate analytic solution and a very accurate numerical solution of the PN-accurate Kepler equation. Our approach can be adapted to compute crucial 3PN-accurate inputs that will be required to compute analytically both the time and frequency domain ready-to-use amplitude-corrected PN-accurate search templates for compact binaries in inspiralling eccentric orbits. This work is based on a publication submitted to Physical Review D in May 2017, in collaboration with A. Susobhanan, A. Gopakumar, A. Klein and P. Jetzer.

1 Introduction

The present paper provides an elegant analytical solution to the PN-accurate Kepler equation associated with the 3PN accurate generalized quasi-Keplerian parametrization, available in Ref. [1]. Specifically, we derive analytical 3PN-accurate infinite series expression for the eccentric anomaly u in terms of the mean anomaly l. This solution requires us to derive compact PN-accurate infinite series expressions for certain trigonometric functions of the true anomaly v in terms of u. We manipulate complex exponential representations of various trigonometric functions of v and u for these derivations. We invoke an improved version of Mikkola's method, detailed in Refs. [2,3], to compare the accuracy of our analytical solution for various values of the orbital eccentricity. Our PN-accurate analytic solution shows excellent agreement with its numerical counterpart for moderate values of eccentricity.

2 Derivation of analytic solution to PN-accurate Kepler Equation

2.1 The Bessel function approach to tackle the classic Kepler Equation

We begin by reviewing the classical Keplerian parametrization that describes semi-analytically the Newtonian-accurate orbital motion of a binary in non-circular orbits [4,5]. In polar coordinates and in the center-of-mass reference frame, this approach provides a parametric description for an eccentric orbit of Newtonian dynamics using

$$r = a(1 - e\cos u)\,, \quad \phi - \phi_0 = v \equiv 2\arctan\left[\left(\frac{1+e}{1-e}\right)^{1/2}\tan\frac{u}{2}\right], \tag{1}$$

where r and ϕ define the components of the relative separation vector $\mathbf{r} = r(\cos\phi, \sin\phi, 0)$. The auxiliary angles u and v are called eccentric and true anomaly. The classical Kepler equation defines the temporal evolution of these auxiliary angles and is given by

$$l \equiv n(t - t_0) = u - e\,\sin u\,, \tag{2}$$

where l is the mean anomaly.

In what follows, we sketch the derivation of a widely used analytic solution of the Kepler equation, involving the Bessel functions [6]. We start by expressing $u-l$ as a Fourier series in l:

$$u-l=e\,\sin u=\sum_{s=1}^{\infty}A_s\sin(sl)\,,\quad A_s=\frac{2}{\pi}\int_0^{\pi}(u-l)\sin(sl)dl\,. \tag{3}$$

Integrating by parts leads to

$$A_s=\frac{2}{\pi}\int_0^{\pi}(u(l)-l)\sin(sl)dl=\frac{2}{s\pi}\int_0^{\pi}\cos(sl)du=\frac{2}{s}\left\{\frac{1}{\pi}\int_0^{\pi}\cos(su-se\sin u)du\right\}. \tag{4}$$

The expression in the curly brackets can be identified with $J_s(se)$, namely the Bessel functions of the first kind. This allows us to write

$$u=l+\sum_{s=1}^{\infty}\frac{2}{s}J_s(se)\sin(sl)\,. \tag{5}$$

This expression provides the most popular solution of the transcendental Kepler equation. In what follows, we adapt a similar approach to tackle the PN-accurate Kepler equation.

2.2 3PN-accurate solution to PN-accurate Kepler equation

It is possible to obtain a Keplerian-type parametric solution to the PN-accurate orbital dynamics of compact binaries in non-circular orbits [5,7,8,1]. At the third post-Newtonian order, the conservative orbital dynamics of compact binaries in eccentric orbits is specified by providing the following parametrization for the dynamical variables r and ϕ:

$$r = a_r\left(1-e_r\cos u\right)\,, \tag{6}$$

$$\begin{aligned}\phi-\phi_0 &= (1+k)v+(f_{4\phi}+f_{6\phi})\sin(2v)\\ &\quad+(g_{4\phi}+g_{6\phi})\sin(3v)+i_{6\phi}\sin(4v)+h_{6\phi}\sin(5v)\,.\end{aligned} \tag{7}$$

The following 3PN accurate Kepler equation links the eccentric anomaly u to the mean anomaly $l=n\,(t-t_0)$

$$l=\;u-e_t\sin u+(g_{4t}+g_{6t})\,(v-u)+(f_{4t}+f_{6t})\sin v+i_{6t}\sin(2v)+h_{6t}\sin(3v)\,. \tag{8}$$

The expressions g, f, i and h are orbital functions entering at 2PN and 3PN order.

In what follows, we derive an elegant solution to the 3PN accurate Kepler equation. It is possible to bring in a compact infinite series expansion, similar to Eq. (3), by invoking the following exact relations:

$$v-u = 2\sum_{j=1}^{\infty}\frac{\beta_\phi^j}{j}\sin(ju)\,, \tag{9}$$

$$\sin v = \frac{2\sqrt{1-e_\phi^2}}{e_\phi}\sum_{j=1}^{\infty}\beta_\phi^j\sin(ju)\,, \tag{10}$$

$$\sin(2v) = \frac{4\sqrt{1-e_\phi^2}}{e_\phi^2}\sum_{j=1}^{\infty}\beta_\phi^j\left(j\sqrt{1-e_\phi^2}-1\right)\sin(ju)\,, \tag{11}$$

$$\sin(3v) = \frac{2\sqrt{1-e_\phi^2}}{e_\phi^3}\sum_{j=1}^{\infty}\beta_\phi^j\Big(4-e_\phi^2-6j\sqrt{1-e_\phi^2}+2j^2(1-e_\phi^2)\Big)\sin(ju)\,, \tag{12}$$

with $\beta_\phi = (1-\sqrt{1-e_\phi^2})/e_\phi$. These compact expressions allow us to express Eq. (8) as

$$l = u - e_t \sin u + \sum_{j=1}^{\infty} \alpha_j \sin(ju)\,, \tag{13}$$

where the explicit expressions for the PN-accurate orbital functions α_j can be extracted with the help of Eqs. (8) and (9-12). They are given by

$$\begin{aligned}\alpha_j &= 2\beta_\phi^j \frac{\sqrt{1-e_\phi^2}}{e_\phi^3}\Bigg((f_{4t}+f_{6t})e_\phi^2 + \frac{(g_{4t}+g_{6t})e_\phi^3}{j\sqrt{1-e_\phi^2}} \\ &\quad +2i_{6t}e_\phi\left[j\sqrt{1-e_\phi^2}-1\right] + h_{6t}\left[4-e_\phi^2-6j\sqrt{1-e_\phi^2}+2j^2(1-e_\phi^2)\right]\Bigg)\,. \end{aligned}\tag{14}$$

It is worth noting that the functional forms of α_j are identical in both the modified harmonic (MH) and Arnowitt-Deser-Misner (ADM) coordinates, since Eq. 8 takes an identical form in both gauges [1]. However, the explicit expressions for these orbital functions in terms of the conserved orbital energy and angular momentum or the parameters x and e_t differ.

The functional form of the PN-accurate Kepler equation, namely Eq. (13), allows us to write the following PN-accurate Fourier series for $u-l$

$$u - l = \sum_{s=1}^{\infty} A_s \sin(sl)\,, \quad A_s = \frac{2}{\pi}\int_0^\pi (u-l)\sin(sl)dl\,. \tag{15}$$

Integrating by parts and using Eq. (13) gives

$$\begin{aligned} A_s &= \frac{2}{\pi}\int_0^\pi (u-l)\sin(sl)dl = \frac{2}{s\pi}\int_0^\pi \cos(sl)du \\ &= \frac{2}{s\pi}\int_0^\pi \cos\Big(su - se_t\sin u + s\sum_{j=1}^{\infty}\alpha_j\sin(ju)\Big)du\,. \end{aligned}\tag{16}$$

We can expand the above result to first order in α_j and this leads to

$$\begin{aligned} A_s &= \frac{2}{s\pi}\int_0^\pi \cos\left(su - se_t\sin u\right)du - \frac{2}{\pi}\sum_{j=1}^{\infty}\alpha_j\int_0^\pi \sin\left(su-se_t\sin u\right)\sin(ju)du \\ &= \frac{2}{s\pi}\int_0^\pi \cos\left(su - se_t\sin u\right)du \\ &\quad +\frac{1}{\pi}\sum_{j=1}^{\infty}\alpha_j\int_0^\pi \left\{\cos\left((s+j)u - se_t\sin u\right) - \cos\left((s-j)u - se_t\sin u\right)\right\}du \\ &= \frac{2}{s}J_s(se_t) + \sum_{j=1}^{\infty}\alpha_j\left\{J_{s+j}(se_t) - J_{s-j}(se_t)\right\}\,, \end{aligned}\tag{17}$$

where we employed the usual integral definitions for $J_n(x)$ to reach the last step. This step allows us to write down a simple and elegant solution to 3PN-accurate generalized Kepler equation in terms of Bessel functions as

$$u = l + \sum_{s=1}^{\infty}\left(\frac{2}{s}J_s(se_t) + \sum_{j=1}^{\infty}\alpha_j\left\{J_{s+j}(se_t) - J_{s-j}(se_t)\right\}\right)\sin(sl)\,. \tag{18}$$

2.3 Comparison to numerical solution

We now compare our analytic solution against a very accurate way of solving PN-accurate Kepler Equation, detailed in Refs [9,10]. This numerical approach is based on an efficient and accurate (numerical) way of solving the classical Kepler Equation, developed by Mikkola [2] and is valid for all l and for $0 \leq e_t \leq 1$. Our analytic solution is expected to be valid only up to certain values of the PN-expansion parameter x and it will diverge for large values of x. It will be useful to concentrate on the differences between u and l values due to the nature of Eq. (18). These considerations influenced us to probe how the fractional relative error, namely $|((u_{\rm num}-l)-(u_{\rm anl}-l))/(u_{\rm num}-l)|$, varies as a function of e_t for few x values while incorporating 200 terms in the analytic solution.

We invoke the more familiar integrated error over one period using the L2-norm, namely

$$f_{L_2} = \left(\frac{1}{2\pi}\int_0^{2\pi} f^2 dl\right)^{1/2}, \quad (19)$$

where f stands for the above mentioned fractional relative error. The results in MH gauge is displayed in Fig. 1. We find that our L2-norm error estimate is small ($< 1\%$) for eccentricities up to $e_t = 0.95$ for x values relevant for the early inspiral phase like $x \approx 0.01$. However, it diverges quickly for higher x values and this is true even for moderate e_t values like 0.5.

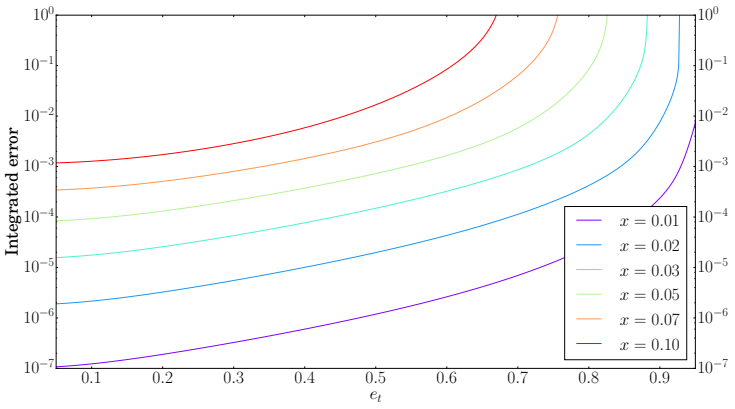


Figure 1 – Integrated relative error as a function of e_t for different x values. We let $\eta = 0.25$ and truncate the analytic series solution at $j = 200$. $x \approx 0.01$ corresponds to a binary neutron star system entering the aLIGO band at 10Hz, while a binary black hole system with masses around $10M_\odot$ enters at $x \approx 0.03$.

3 A brief summary

We derived a compact and elegant solution to the 3PN-accurate Kepler equation, present in the generalized quasi-Keplerian parameterization for compact binaries in eccentric orbits. This result crucially depends on certain 3PN-accurate infinite series expressions for trigonometric functions of v in terms of u. We probed the accuracy and correctness of our solution using analytical and numerical methods.

It will be interesting to extend the present analysis for compact binaries in hyperbolic orbits. This requires a 3PN-accurate Keplerian-type parametric solution for compact binaries in hyperbolic orbits and this is currently under investigation. It will also be interesting to include spin effects into these computations with the help of Ref. [11]. Additionally, it will be worthwhile to compute fully analytic 3PN-accurate amplitude-corrected expressions for $h_{+,\times}$ with the help of our compact expressions and Ref. [12], that provides inputs to compute amplitude-corrected $h_{+,\times}$ in terms of dynamical variables.

Acknowledgments

Y. B. is supported by the Swiss National Science Foundation.

References

1. Raoul-Martin Memmesheimer, Achamveedu Gopakumar, and Gerhard Schäfer. Third post-Newtonian accurate generalized quasi-Keplerian parametrization for compact binaries

in eccentric orbits. *Phys. Rev. D*, 70(10):104011, 2004.
2. S. Mikkola. A cubic approximation for Kepler's equation. *Celestial Mechanics*, 40:329–334, September 1987.
3. Manuel Tessmer and Achamveedu Gopakumar. Accurate and efficient gravitational waveforms for certain galactic compact binaries. *Mon. Not. Roy. Astron. Soc.*, 374:721–728, 2007.
4. P. Colwell. *Solving Kepler's equation over three centuries*. 1993.
5. T. Damour and N. Deruelle. General relativistic celestial mechanics of binary systems. I. The post-Newtonian motion. *Ann. Inst. Henri Poincaré Phys. Théor., Vol. 43, No. 1, p. 107 - 132*, 43:107–132, 1985.
6. G. N. Watson. *A Treatise on the Theory of Bessel Functions*. 1922.
7. T. Damour and G. Schafer. Higher-order relativistic periastron advances and binary pulsars. *Nuovo Cimento B Serie*, 101:127–176, 1988.
8. G. Schäfer and N. Wex. Second post-Newtonian motion of compact binaries. *Physics Letters A*, 174:196–205, March 1993.
9. M. Tessmer and A. Gopakumar. Accurate and efficient gravitational waveforms for certain galactic compact binaries. *Mon. Not. R. Astron. Soc.*, 374:721–728, January 2007.
10. S. Tanay, M. Haney, and A. Gopakumar. Frequency and time-domain inspiral templates for comparable mass compact binaries in eccentric orbits. , 93(6):064031, March 2016.
11. A. Klein and P. Jetzer. Spin effects in the phasing of gravitational waves from binaries on eccentric orbits. , 81(12):124001, June 2010.
12. C. K. Mishra, K. G. Arun, and B. R. Iyer. Third post-Newtonian gravitational waveforms for compact binary systems in general orbits: Instantaneous terms. , 91(8):084040, April 2015.


SCUOLA SCI
LA THUILE
Lo Ratrak
food & drink
ONLY SKI

Millisecond Pulsars at the Center of the Galaxy

W. A. Majid
Jet Propulsion Laboratory, California Institute of Technology,
4800 Oak Drive, Pasadena, CA, USA



The black hole in the center of the Milky Way, Sagittarius A* (Sgr A*) is an ideal candidate for testing general relativity in the strong-field regime. The tracking of young stars at very close orbits has already led to a direct measurement of its mass. The discovery and subsequent timing of a single radio pulsar in orbit around Sgr A* will also allow for a direct measurement of the black holes spin and quadrupole moment. The presence of a cluster of young, massive stars in orbit around Sgr A* makes it highly likely that a large population of such pulsars exist. Moreover, the detection of excess gamma-rays in this region of the galaxy by the Fermi LAT instrument provides further hints that a population of millisecond pulsars maybe the culprit in the production of excess gamma-rays. I will provide an overview of the recent findings and will discuss prospects for near and long term radio searches and challenges.

1 Introduction

Millisecond pulsars (MSPs) are rapidly rotating neutron stars that are spun up by transfer of material from a companion star over long timescales. MSPs, loosely defined with $P \leq 30\,\mathrm{ms}$ and $\dot{P} \sim 10^{-20}\mathrm{ss}^{-1}$ is a distinct population of pulsars, occupying the lower left part of the $P - \dot{P}$ diagram (Figure 1). MSPs exhibit a multi-wavelength emission spectrum that include both pulsed and un-pulsed emission from radio wavelengths up to GeV gamma-rays. Roughly 350 MSPs are currently known, discovered mostly through their pulsed emission in radio frequencies. The majority of these MSPs, ~ 250 of them are field MSPs in the Galactic disk, the remainder are associated with 28 different globular clusters[a]. Globular clusters have long been known to harbor MSPs due to the high stellar density and consequently high rate of stellar interactions, which result in an abundance of low-mass X-ray binaries (LMXBs), the progenitors of MSPs. The notion that such dense stellar clusters become nurseries for MSPs is borne out by the fact that over 90% of pulsars in globular clusters have spin periods that are shorter than 30 ms.

In analogy with globular clusters, the dense stellar environment at the Galactic Center (GC) is expected to harbor a large population of MSPs through frequent interactions with neighboring stars (Verbunt 1987). In fact the stellar density in the central region of the GC reaches values close to $10^6\mathrm{pc}^{-3}$ (Schödel et al. 2007), roughly two orders of magnitude larger than the stellar density in globular clusters. Estimates based on Monte Carlo methods by (Zhang & Cheng 1997)

[a] http://www.naic.edu/~pfreire/GCpsr.html.

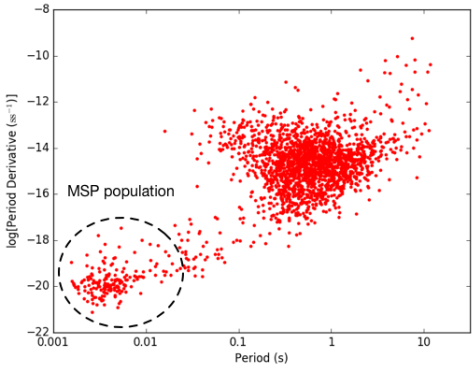


Figure 1 – The $P - \dot{P}$ diagram of known pulsars from the ATNF catalog (Manchester et al. 2005). The population of millisecond pulsars are shown in the bottom left region of the figure, noted by the dashed circle.

suggest 6000 MSPs residing within 200 pc of Sgr A*. More recent analysis put the number of pulsars in the inner regions of the GC in a few thousands (Pfah & Loeb 2004, Wharton et al. 2012), with $\sim$ 1000 pulsars beamed toward Earth, and therefore, at least in principal potentially detectable with further observations.

2 Tests of GR and the Fermi GeV Excess

Over two decades of infrared (IR) monitoring of $\sim$ 30 stellar orbits in the center of our Galaxy (e.g. Gillessen et al. 2009) has yielded the mass of the central object to be $\sim 4 \times 10^6 M_\odot$, unambiguously classifying it as a super massive black hole (SMBH). A massive black hole at a distance of $\sim$8.5 kpc is an ideal laboratory for extreme physics. The detection of even a single MSP, at distances similar to IR stars with an orbital period $P_{orb} \leq 100\,yr$ in this region would serve as an excellent probe of strong-field gravity, making it possible to carry out precision tests of Einsteins General Relativity (GR) in the strong-field regime through measurements of time dilation, gravitational redshifts, frame dragging, Shapiro delays and possibly even determine the spin of the black hole (Pfahl & Loeb 2004; Liu et al. 2012). Although GR is empirically accurate to high precision, tests that have been conducted are in the weak field regime, with the exception of compact binary pulsars. In comparison with the best forecasted precisions of IR astrometry and doppler measurements, timing of pulsars in this region has the potential of increasing the astrometric precision by at least three orders of magnitude. MSPs offer this prospect because the precise clock-like stability of the emitted pulses, now demonstrated to reach in some cases below 100 ns, translate in extraordinary astrometric precision that is orders of magnitude better than 10 μas precision expected from the next generation of proposed IR interferometric experiments.

Furthermore, recent analysis of the Fermi LAT data has shown a persistent excess of gamma-rays from the Galactic Center region of the Galaxy. This excess is measured above the predicted diffuse gamma-ray emission models and gamma-ray source catalogs (Hooper & Goodenough 2011). While several interpretation of this excess has been offered in the literature, the two primary interpretations are direct annihilation of dark matter (DM) particles in the galactic halo and an unresolved population of gamma-ray pulsars located in the inner region of the galaxy. The DM annihilation scenario, however, also implies a measurable emission from dwarf spheroidal satellites of the Milky Way. However, no such evidence of gamma-ray flux from these dwarf galaxies has been detected, which puts the DM interpretation of the GC excess in tension with observations (Albert et al. 2017). The latter interpretation, on the other hand, is supported by an excellent agreement of the energy spectrum of the GeV excess with Fermi observations of MSPs in the galactic field. Combined emission from several thousand MSPs are required to explain the detected gamma-ray signal from this region of the Galaxy (Abazajian 2011).

3 Radio Searches for MSPs

Several radio pulsar searches have been conducted within a degree of the GC and have resulted in the detection of 5 pulsars and one magnetar. All the pulsars are within $15'$ of Sgr A*, with none closer than $11'$. However, all five of these pulsars are considered canonical pulsars with spin periods $\sim$1 s. The reason for this deficit, despite the expected large number of pulsars in this region, is well understood and attributed to hyper-strong scattering of radio waves by the turbulent, ionized gas within the central 100 pc of Sgr A* (corresponding to an angular width of $40''$, using a GC distance of 8.5 kpc from the Earth), which results in temporal smearing of pulsed signals. This pulse broadening has a strong frequency dependence, $\tau_{\rm scat} \propto \nu^{-4}$, where ν is the observing frequency, making it nearly impossible to detect MSPs at low observing frequencies. Even with the more recent searches at 5 and 15 GHz, carried out with the Green Bank Telescope (GBT), no detections in the inner few parsecs around Sgr A* have been made (Deneva et al. 2009; Macquart et al. 2010). Using the 1 GHz scattering time from the NE2001 model of Cordes & Lazio (2002), scatter broadening times of (1.0, 0.01) s at observing frequencies of (5,15) GHz are expected, which explains the absence of any MSP detections.

The recent discovery of J1745-2900, a magnetar (neutron star with extremely high magnetic field) orbiting Sgr A* at a projected separation of 0.1 pc (Mori et al. 2013, Kennea et al. 2013) has unleashed a wave of excitement and re-examination about radio scattering in this region of the galaxy with significantly less pulse broadening than predicted from the NE2001 model, assuming the magnetar is at the location of Sgr A*. Unfortunately, magnetars as a class of objects have very large spin-down rates and are not sufficiently stable for astrometric measurements. Magnetars are also quite intermittent and transient in nature, typically detected in radio during large flares in gamma and X-rays. However, since radio magnetars are a rare class of pulsars (1 in 500 radio pulsars), the detection of J1745-2900 suggests that there may be a large GC pulsar population of such objects to be discovered through multi-wavelength monitoring campaigns of the GC region.

4 Future Surveys

Observations at higher radio frequencies are needed to mitigate the severe effects of pulse broadening. Pulsars, however, have steep spectra with a typical spectral index of 1.7, implying lower fluxes at higher frequencies, therefore necessitating increased sensitivity of the radio survey.



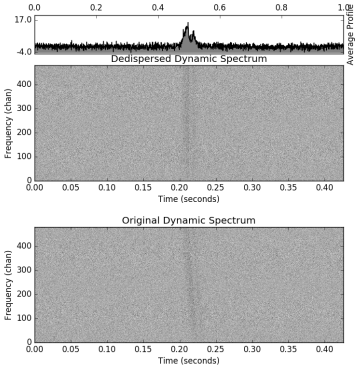


Figure 2 – DSS-43: DSN's 70-m diameter antenna in Canberra, Australia (left). A single pulse from the GC magnetar, J1745-2900 (right): The bottom subpanel shows the original dynamic spectrum; the middle subpanel shows the dedispersed dyanamic spectrum; the top subpanel shows the projected lightcurve of the single pulse.

In the short term, we are planning to use one of the Deep Space Network's (DSN) 70-m diameter antenna (Figure2 - left panel) in Canberra, Australia, to search for pulsars in this region of the galaxy. The instrument, currently the most sensitive radio telescope in the southern

hemisphere, is equipped with a number of receivers with center frequencies of 1.6, 2.2, 8.4, and 20 GHz, the latter two being more appropriate for MSP searches. We have recently carried out a few pilot observations of the GC magnetar, J1745-2900, with this instrument, resulting in clear detections of this pulsar at its nominal period of 3.76 s and a DM of 1720 pc cm-3. A typical single pulse detection from these pilot observations is shown in Figure 2 (right panel).

In the longer run, the Square Kilometer Array (SKA), currently in development phase, will make substantial progress in probing this region of galaxy for pulsars, owing to its higher sensitivity. However, even with the SKA, it will be quite challenging to detect MSPs in the inner degree of the GC region due to increased scattering at SKA operating frequencies. In addition, future gamma-ray telescopes like GAMMA-400, ASTROGRAM, and PANGU, now in various planning stages, will allow the detection of many more point sources and may therefore lead to the discovery of MSPs in this region of the galaxy.

5 Conclusions

The detection of even a single MSP in the inner regions of the GC would constitute a major discovery, that will enable precision tests of GR in the strong-field regime. In addition, the detection of MSPs would achieve a breakthrough in our understanding of the gamma-ray excess seen by Fermi, enabling the study of radio and gamma-ray properties of these sources, better understanding of the diffuse emission from the inner regions of the Galaxy, and even shedding light on the DM annihilation channels proposed to explain the excess. However, significant challenges in carrying out such surveys include overcoming the severe scatter broadening due to the turbulent interstellar medium in the vicinity of Sgr A*. Despite these challenges, surveys of the inner region of the galaxy with current and upcoming radio instruments, could yield important results over the next few years.

Acknowledgments

I would like to thank our collaborators from JPL (Tatyana Dobreva, Manuel Franco, Jonathon Kocz, Tom Kuiper, Joseph Lazio, & Leslie White), Caltech (Jonas Lippuner & Thomas Prince), and CSIRO (Shinji Horiuchi). I would also like to thank the organizers of the Moriond Gravitation 2017 meeting for the opportunity to give this presentation. This work was performed at the Jet Propulsion Laboratory, California Institute of Technology, under a Research And Technology Development Grant. Copyright 2017 California Institute of Technology. Government sponsorship acknowledged.

References

1. K. Abazajian, *Journal of Cosmology and Astroparticle Physics* **3**, 10 (2011).
2. A. Albert *et al*, *The Astrophysical Journal* **834**, 110 (2017).
3. J. Cordes & J. Lazio, arXiv:astro-ph/0301598 (2003).
4. J. Deneva *et al*, *The Astrophysical Journal* **702**, L177 (2009).
5. S. Gillessen *et al*, *The Astrophysical Journal* **692**, 1075 (2009).
6. D. Hooper & L. Goodenough, *Physics Letters* **697**, 412 (2011).
7. J. Kennea *et al*, ATel, 5124, 1 (2013).
8. K. Liu *et al*, *The Astrophysical Journal* **747**, 1 (2012).
9. J.P. Macquart *et al*, *The Astrophysical Journal* **715**, 939 (2010).
10. J.P. Macquart & N. Kanekar, *The Astrophysical Journal* **805**, 172 (2015).
11. K. Mori *et al*, *The Astrophysical Journal Letters* **770**, L23 (2013).
12. E. Pfah & A. Loeb, *The Astrophysical Journal* **615**, 253 (2004).
13. R. Schodel *et al*, *Astronomy & Astrophysics* **469**, 125 (2007).
14. F. Verbunt, *The Astrophysical Journal* **312**, L23 (1987).
15. R. Wharton *et al*, *The Astrophysical Journal* **753**, 108 (2012).

NEUTRON STARS WITH REALISTIC EQUATIONS OF STATE IN SCALAR-TENSOR THEORIES OF GRAVITY

ZAHRA A. MOTAHAR, JOSE BLÁZQUEZ-SALCEDO, BURKHARD KLEIHAUS, JUTTA KUNZ
Institute of Physics, Carl von Ossietzky University of Oldenburg, Germany



In this study, we address static spherically symmetric realistic neutron stars as well as slowly rotating ones in Scalar-Tensor Theories (STT) of gravity. We consider several realistic Equations Of State (EOS) with the values of the scalar field coupling constants constrained by current observations. We already know that in addition to the solutions of General Relativity (GR) with a trivial scalar field, STT can allow for solutions with a nontrivial scalar field, which are energetically more favorable. Our numerical results show the existence of neutron star models with a nontrivial scalar field also in the case of alternative scalar field coupling functions. We further compute the moments of inertia of neutron stars in STT which are slowly rotating. We present various results to illustrate the deviation of our models from GR.

1 Introduction

The properties of neutron stars as obtained in GR with realistic EOS have been tested successfully by observations in diverse astrophysical scenarios. However, there are various reasons to expect that GR will be superseded by a generalized theory of gravity. [1] STT are one of the most natural extensions of GR. In these theories a scalar field is included as an additional mediator of the gravitational interaction besides the metric tensor mediator of GR. Some of the alternative theories of GR like STT are indistinguishable from GR in the weak field regime but can differ significantly for strong fields. Neutron stars are good examples of the strong field regime because of their high densities and compactness. Therefore they provide an ideal laboratory for testing gravity.

The study of neutron stars in STT revealed an interesting phenomenon called spontaneous scalarization. [2,3] When a scalar field is nonminimally coupled to gravity, a nontrivial configuration of the scalar field can appear, because the scalar field nonlinearities can intensify the attractive nature of the scalar field interactions. Then it can become energetically favorable to generate more scalar-field energy without any external source. This clearly leads to neutron star models which can possess significantly different properties than their GR counterparts as shown in the static and slowly rotating case by Damour and Esposito-Farese [2,3] and for rapidly rotating neutron stars by Doneva *et al.* [4] Here we address the effect of alternative scalar field coupling

functions in STT on static spherically symmetric and slowly rotating neutron stars for several realistic EOS.

2 Basic Equations and Numerical Method

We consider the gravitational action in the Einstein frame

$$S = \frac{1}{16\pi G_*}\int d^4x\sqrt{-g}\,[R - 2g^{\mu\nu}\partial_\mu\varphi\partial_\nu\varphi - 4V(\varphi)] + S_m[\Psi_m; \mathcal{A}^2(\varphi)g_{\mu\nu}], \tag{1}$$

where G_* is the gravitational constant, and the Ricci scalar curvature R is defined with respect to the metric in Einstein frame $g_{\mu\nu}$. The matter action involves the non-minimal coupling function $\mathcal{A}(\varphi)$ to the scalar field φ. We here assume a vanishing scalar potential $V(\varphi) = 0$, and set $G_* = 1$ and $c = 1$. The Einstein-matter equations then read

$$R_{\mu\nu} - \frac{1}{2}g_{\mu\nu}R = 8\pi T_{\mu\nu} + 2\partial_\mu\varphi\partial_\nu\varphi - g_{\mu\nu}g^{\alpha\beta}\partial_\alpha\varphi\partial_\beta\varphi, \tag{2}$$

$$\nabla^\mu\nabla_\mu\varphi = -4\pi k(\varphi)T, \tag{3}$$

where $k(\varphi) = \frac{d\ln(\mathcal{A}(\varphi))}{d\varphi}$. The energy momentum tensor is given by $T_{\mu\nu} = (\varepsilon + p)u_\mu u_\nu + pg_{\mu\nu}$, where ε, p and u_μ are the energy density, the pressure and the four-velocity in the Einstein frame, which are related to the corresponding quantities in the Jordan frame by $\varepsilon = \mathcal{A}^4(\varphi)\tilde{\varepsilon}$, $p = \mathcal{A}^4(\varphi)\tilde{p}$, and $u_\mu = \mathcal{A}^{-1}(\varphi)\tilde{u}_\mu$. From the Bianchi identities the conservation law for the Einstein frame energy-momentum tensor $\nabla_\mu T^\mu{}_\nu = k(\varphi)T\partial_\nu\varphi$ is obtained.

In our study we have considered two STT with the following coupling functions

1. $\mathcal{A}(\varphi) = \exp(\frac{1}{2}\beta_1\varphi^2)$,
2. $\mathcal{A}(\varphi) = \frac{1}{\cosh(\beta_2\varphi)}$,

where the first coupling function has been investigated before,[2,3,4] whereas the second coupling function is new. There are observational constraints on the possible values of β, that should be taken into account.[5] Considering $\frac{d^2\ln(\mathcal{A}(\varphi))}{d\varphi^2}|_{\varphi=0} > -4.8$, we have employed β_1 = -4.5 and -4.8 for the exponential coupling function, while we have used $\beta_2 = \sqrt{4.8}$ and $\sqrt{4.5}$ for the new coupling function.

The metric describing a slowly rotating neutron star can be chosen as

$$ds^2 = -e^{f(r)}dt^2 + \frac{1}{n(r)}dr^2 + r^2d\theta^2 + r^2\sin^2\theta(d\phi + \omega(r)dt)^2, \tag{4}$$

where the metric function $\omega(r)$ vanishes in the static case. With the metric ansatz Eq. (4) and the scalar field $\varphi = \varphi(r)$, the pressure $p = p(r)$, and the energy density $\varepsilon = \varepsilon(r)$, the Einstein field equations for static neutron stars reduce to the following system of ordinary differential equations to be solved numerically

$$\frac{dn}{dr} = -\frac{1}{r}\left[8\pi r^2\mathcal{A}^4(\varphi)\tilde{\varepsilon} + nr^2\left(\frac{d\varphi}{dr}\right)^2 + n - 1\right], \tag{5}$$

$$\frac{df}{dr} = \frac{1}{nr}\left[8\pi r^2\mathcal{A}^4(\varphi)\tilde{p} + nr^2\left(\frac{d\varphi}{dr}\right)^2 - n + 1\right], \tag{6}$$

$$\frac{d^2\varphi}{dr^2} = \frac{4\pi r\mathcal{A}^4(\varphi)}{nr}\left[r\left(\frac{d\varphi}{dr}\right)(\tilde{\varepsilon} - \tilde{p}) + k(\varphi)(\tilde{\varepsilon} - 3\tilde{p})\right] - \left(\frac{d\varphi}{dr}\right)\frac{(n+1)}{nr}, \tag{7}$$

$$\frac{d\tilde{p}}{dr} = -(\tilde{\varepsilon} + \tilde{p})\left[\frac{4\pi r\mathcal{A}^4(\varphi)\tilde{p}}{n} + \frac{r}{2}\left(\frac{d\varphi}{dr}\right)^2 + k(\varphi)\left(\frac{d\varphi}{dr}\right) - \frac{n-1}{2nr}\right]. \tag{8}$$

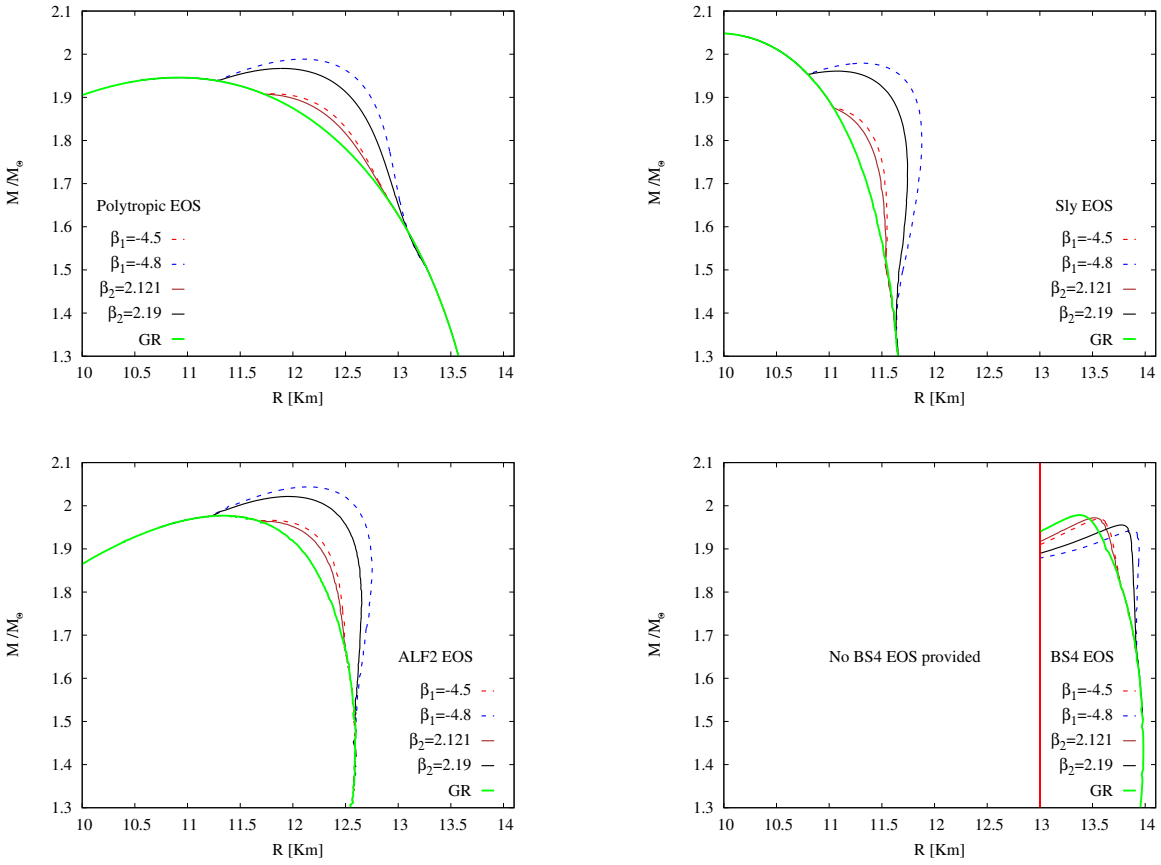


Figure 1 – Mass M vs radius R for different EOS

We have first solved these equations to obtain the spherically symmetric neutron stars (static case). Then we have considered the first order perturbation equation for the slowly rotating case

$$\frac{d^2\omega}{dr^2} = \frac{4\pi r\mathcal{A}^4(\varphi)}{n}(\tilde{\varepsilon}+\tilde{p})\left[\left(\frac{d\omega}{dr}\right)+\frac{4\omega}{r}\right]+\left(\frac{d\omega}{dr}\right)\left[r\left(\frac{d\varphi}{dr}\right)^2-\frac{4}{r}\right]. \tag{9}$$

In solving these ODEs numerically, we have used the COLSYS (COLlocation for SYStems) code. For the static solutions we have chosen the boundary conditions $n(\infty)=1$, $f(\infty)=0$, $\tilde{p}(0)=\tilde{p}_c$, $\varphi(\infty)=0$, $\left(\frac{d\varphi}{dr}\right)(0)=0$, and we have assumed slow rigid rotation with $\omega(0)=\omega_c$ and $\omega(\infty)=0$.

3 Equations of State

For the static and slowly rotating neutron stars in STT we have studied a polytropic EOS and several realistic ones. In a polytropic EOS the pressure $\tilde{p}$ and the baryonic mass density $\tilde{\rho}$ are related according to $\tilde{\varepsilon}=K\frac{\tilde{\rho}^\Gamma}{\Gamma-1}+\tilde{\rho}$, $\tilde{p}=K\tilde{\rho}^\Gamma$, where we have chosen for the polytropic constant $K=1186.0$, and for the adiabatic index $\Gamma=1+\frac{1}{N}$ the polytropic index $N=0.7463$.

We have also used various realistic EOS. But due to lack of space we here present only some examples of our results, which have been obtained using SLy [6] for nuclear matter, ALF2 [7] for quark matter, and BS4 [8] for hybrid quark-nuclear matter.

4 Results

Let us now discuss some of our results obtained in the study of static and slowly rotating neutron stars in STT with the two coupling functions $\mathcal{A}(\varphi)=\exp(\frac{1}{2}\beta_1\varphi^2)$ and $\mathcal{A}(\varphi)=1/\cosh(\beta_2\varphi)$, using realistic EOS. Fig. 1 illustrates the effects of the spontaneous scalarization on the mass–radius relationship of static neutron stars. Here the mass $M/M_\odot$ is shown versus the radius

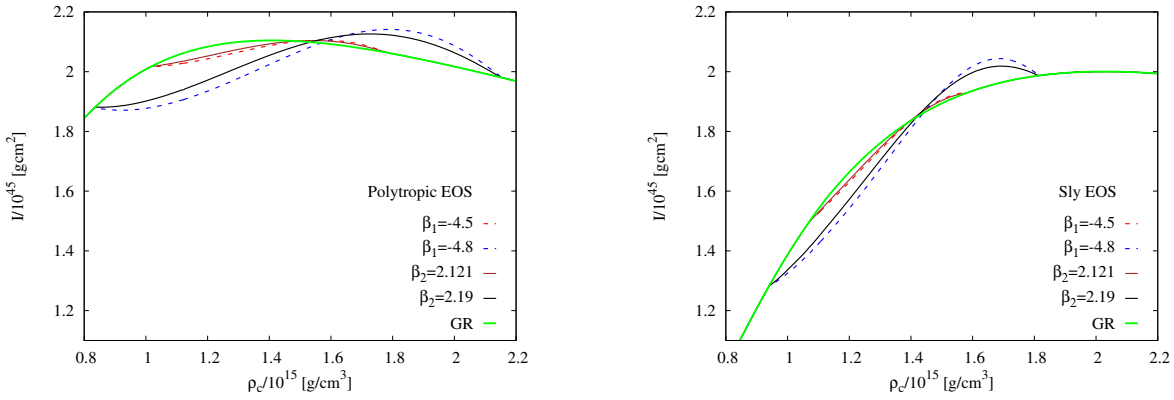


Figure 2 – Moment of inertia I vs central density ρ_c for two EOS

R for a polytropic EOS and for three realistic ones. For comparison the GR results are also exhibited. Also, both coupling functions are used, where the respective values of the coupling constants are chosen to obtain the same quadratic expansion coefficients of $\mathcal{A}(\varphi)$. Then the scalarization arises for both coupling functions at the same GR configurations, independent of the EOS. Clearly, since the exponential coupling function is smaller for larger φ than the new coupling function, the effects concerning the scalarization are larger for the exponential coupling. Thus the results for the new coupling function are closer to the GR results. We observe that for larger values of $|\beta_i|$ the maximum mass is reached at a larger radius. For smaller values of $|\beta_i|$ the maximum mass is reached only close to the upper bifurcation point for the polytropic EOS and ALF2. For Sly the maximum mass is smaller than in GR. Fig. 2 shows the moment of inertia I versus the central density ρ_c for two EOS, the polytropic EOS and the Sly EOS, to present also an example for a realistic EOS (see also Staykov *et al.*[9]).

In further studies we might consider rapidly rotating neutron stars with realistic EOS in STT with new coupling functions. It would also be interesting to study a massive scalar field for new coupling functions. Indeed, Yazadjiev *et al.*[5,10] have studied a massive scalar field for slowly and rapidly rotating neutron stars and shown that the inclusion of a mass term for the scalar field leads to very interesting new results.

Acknowledgments

We gratefully acknowledge support by the DFG Reasearch Training Group 1620 *Models of Gravity* as well as by FP7, Marie Curie Actions, People, International Research Staff Exchange Scheme (IRSES-606096).

References

1. E. Berti *et al*, *Class. Quant. Grav.* **32**, 243001 (2015).
2. T. Damour and G. Esposito-Farese, *Phys. Rev. Lett.* **70**, 2220 (1993).
3. T. Damour and G. Esposito-Farese, *Phys. Rev.* D **54**, 1474 (1996).
4. D.D. Doneva *et al*,*Phys. Rev.* D **88**, 084060 (2013).
5. S.S. Yazadjiev, D.D. Doneva and D. Popchev, *Phys. Rev.* D **93**, 084010 (2016).
6. F. Douchin and P. Haensel, *A&A* **380**, 151 (2001).
7. M. Alford, M. Braby, M. Paris, and S. Reddy, *ApJ* **629**, 969 (2005).
8. L. Bonanno and A. Sedrakian, *A&A* **539**, A16 (2012).
9. K. V. Staykov, D. D. Doneva, and S. S. Yazadjiev, *Phys. Rev.* D **93**, 084010 (2016).
10. D.D. Doneva, S.S. Yazadjiev, *JCAP* **1611**, 11, 019 (2016).

TESTING THE GRAVITATIONAL THEORY WITH SHORT-PERIOD STARS AROUND OUR GALACTIC CENTER

A. HEES[1], A. M. GHEZ[1], T. DO[1], J. R. LU[3], M. R. MORRIS[1], E. E. BECKLIN[1], G. WITZEL[1], A. BOEHLE[1], S. CHAPPELL[1], Z. CHEN[1], D. CHU[1], A. CIURLO[1], A. DEHGHANFAR[1], E. GALLEGO-CANO[2], A. GAUTAM[1], S. JIA[3], K. KOSMO[1], G. D. MARTINEZ[1], K. MATTHEWS[4], S. NAOZ[1], S. SAKAI[1], R. SCHÖDEL[2]

[1] *Department of Physics and Astronomy, University of California, Los Angeles, CA 90095, USA*
[2] *Instituto de Astrofísica de Andalucía (CSIC), Glorieta de la Astronomía S/N, 18008 Granada, Spain*
[3] *Astronomy Department, University of California, Berkeley, CA 94720, USA*
[4] *Division of Physics, Mathematics, and Astronomy, California Institute of Technology, MC 301-17, Pasadena, CA 91125, USA*

Motion of short-period stars orbiting the supermassive black hole in our Galactic Center has been monitored for more than 20 years. These observations are currently offering a new way to test the gravitational theory in an unexplored regime: in a strong gravitational field, around a supermassive black hole. In this proceeding, we present three results: (i) a constraint on a hypothetical fifth force obtained by using 19 years of observations of the two best measured short-period stars S0-2 and S0-38 ; (ii) an upper limit on the secular advance of the argument of the periastron for the star S0-2 ; (iii) a sensitivity analysis showing that the relativistic redshift of S0-2 will be measured after its closest approach to the black hole in 2018.

1 Introduction

Testing General Relativity (GR) and constraining alternative gravitational theories has been a long-standing endeavor in the scientific community. The primary motivation is the development of a quantum theory of gravitation, of a theory that would unify all fundamental interactions and by models of dark matter and dark energy. While GR is extremely well tested in the Solar System and with binary pulsars (e.g. Will [1]), observations of stars orbiting the supermassive black hole (SMBH) at the center of our Galaxy offer the opportunity to probe gravity in a strong field regime [2,3] as depicted on the left of Fig. 1.

The motion of short-period stars around our Galactic Center (GC) has been monitored for more than 20 years by two experiments: one carried out at the Keck Observatory [4,5] and the other with the Very Large Telescope [6,7]. These observations have provided proof for existence of a SMBH in our GC [4,6] and have been used to determine the distance to our GC with a 2% relative accuracy [5,7].

In this proceeding, we show that we are currently entering an era where observations of short-period stars around our GC can be used to probe fundamental physics. We report a constraint on a hypothetical fifth force obtained using observations of the two best measured stars in our GC. In addition, we present an upper limit on the secular advance of the argument of the periastron for the star S0-2 which can be used to constrain various theoretical and astrophysical scenarios in our GC. Finally, we present a sensitivity analysis that shows that S0-2's closest approach in 2018 will enable the first measurement of relativistic effects with S-stars.

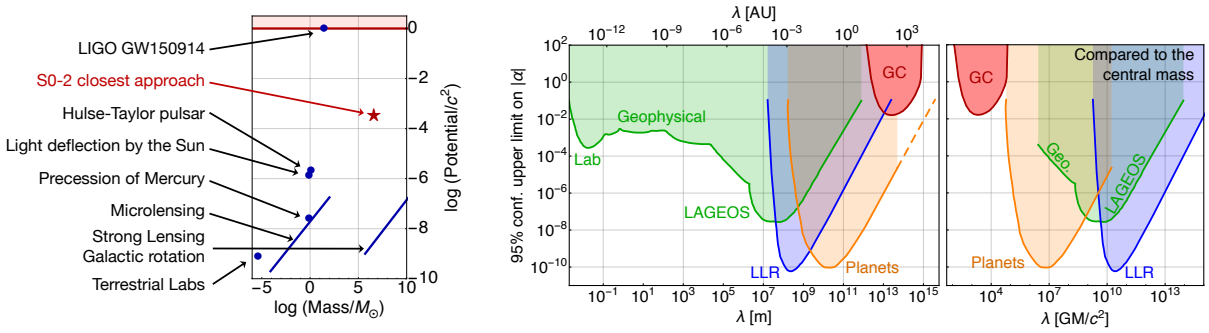


Figure 1 – Left: The gravitational potential probed by different tests of gravitation against the mass of the central body that generates gravity in these tests. Short-period stars, such as S0-2, around our Galactic Center explore a new region in this parameter space. Figure inspired by Psaltis [8].
Right: 95% confidence upper limit on the fifth force parameter $|\alpha|$ as a function of λ. The shaded regions are excluded by various experiments. Our analysis is represented by the red shaded area (GC) [9] while the other curves are from Fig. 31 of Konopliv *et al* [10]. The dashed curve is a reasonable extrapolation based on Solar System results [10]. Left panel: the horizontal axis is λ in meters or in AU. Right panel: the horizontal axis is λ expressed in term of the gravitational radius of the central mass that generates gravitation in the different experiments.

2 Constraint on a hypothetical fifth force

The fifth force formalism considers a modification from Newtonian gravity in which the gravitational potential takes the form of a Yukawa potential

$$U = \frac{GM}{r}\left[1 + \alpha e^{-r/\lambda}\right] , \tag{1}$$

where G is the Newton's constant, M is the mass of the central body, r is the distance to the central body, α is the strength of the fifth interaction and λ is its length scale. This phenomenological framework is motivated by several theoretical scenarios such as: theories with additional interactions, massive gravity, massive tensor-scalar theories, higher dimensional theories, etc [11,12]. This phenomenology has motivated many experiments at a wide variety of scales [12]: in the lab, with geophysical measurements, with satellite and lunar laser ranging and with planetary ephemerides. In addition, it has been shown that a fifth force would impact the short-period star S0-2 [13].

We used 19 years of observations of the two stars with the highest orbital phase coverage S0-2 and S0-38 to constrain a hypothetical fifth force in our GC [9]. The dataset used is fully described in Boehle *et al*[5]. The model used in our orbital fit includes 21 parameters consisting of 6 orbital parameters for each star and of 9 global parameters: the fifth force parameter α, the SMBH GM, the amount of extended mass enclosed within 0.011 parsec, the distance to our GC, the positions and velocities of the SMBH. The positions and velocities of the SMBH are important to take into account imperfections in the construction of our reference frame. In addition, in order to estimate the systematics uncertainties arising in the construction of the absolute reference frame, a Jackknife resampling method is used [5,9]. No deviation from Newtonian gravity is found and upper limit on the fifth force strength α has been derived and is presented on the right of Fig. 1. Our best constraint is at the level of $\lambda \sim 150$ astronomical units, with a 95% confidence upper limit of $|\alpha| < 0.016$. These constraints are complementary to the ones obtained in the Solar System in the sense that they are probing space-time in a new region of the parameter space (see left panel of Fig. 1): around a SMBH, which is conceptually different from Solar System tests where the space-time curvature is generated by weakly gravitating bodies and in a much higher gravitational potential. This is highlighted in the right panel from Fig. 1 where λ is expressed in term of the gravitational radius of the central body. In addition, some alternative theories of gravity exhibit screening mechanisms which may screened the deviations from GR in the Solar System. In this context, searches for deviations from GR in other environments are important.

3 Upper limit on the advance of the argument of periastron of the star S0-2

Most alternative theories of gravitation predict a different secular drift of the argument of periastron ω than GR. In addition, several astrophysical scenarios produce a similar effect. Therefore, we derived an upper limit on a linear drift of the argument of the periastron $\dot{\omega}$ for the star S0-2 [9] using the 19 years of observations described in Boehle *et al* [5]. Our orbital fit includes 7 parameters for each star: the 6 standard orbital parameters and the secular drift of the argument of periastron $\dot{\omega}$. The global parameters included in our fit consist of the SMBH GM, the distance to our GC and the positions and velocities of the SMBH (important to take into account imperfections in the construction of our global reference frame). As a result of our analysis including the Jackknnife resampling to estimate systematics uncertainties, we obtained an upper limit on a linear drift of the argument of periastron for S0-2 given by

$$|\dot{\omega}_{\text{S0-2}}| < 1.7 \times 10^{-3} \text{ rad/yr} \qquad \text{at } 95\% \text{ C.L.}\,. \tag{2}$$

This limit is one order of magnitude larger than the relativistic advance of the periastron $\dot{\omega}_{\text{GR}} = 1.6 \times 10^{-4}$ rad/yr for S0-2. Nevertheless, this limit can be used to derive preliminary constraints on various theoretical and astrophysical scenarios in our GC. A similar, although not as stringent, limit can be obtained for the star S0-38 and is given by $|\dot{\omega}_{\text{S0-38}}| \lesssim 7.6 \times 10^{-3}$ rad/yr.

4 Measurement of the relativistic redshift

In 2018, the star S0-2 will reach its closest approach to the SMBH. As anticipated by many [2,3], this event will allow us to measure the first post-Newtonian effect around a SMBH: the relativistic redshift that impacts S0-2's radial velocity. The contribution of the first order relativistic redshift on the radial velocity is given by

$$[RV]_{\text{rel}} = \frac{v^2}{2c} + \frac{GM}{rc}\,, \tag{3}$$

where r/v are the norm of the position and velocity of the star with respect to the SMBH and c the speed of light. The first term is a contribution due to special relativity while the second term corresponds to the gravitational redshift. The relativistic redshift contribution to S0-2's radial velocity reaches 200 km/s as shown on the left of Fig. 2. One way to measure the relativistic redshift is to model the total radial velocity as $RV = [RV]_{\text{Newton}} + \Upsilon\,[RV]_{\text{rel}}$, where $[RV]_{\text{Newton}}$ is the standard Newtonian radial velocity and Υ is a dimensionless parameter whose value is equal to 1 in GR. The idea is to fit Υ simultaneously with the other parameters in the orbital fit: a value significantly different from 0 but compatible with 1 would be evidence of a successful detection of the relativistic redshift while a value significantly different from 1 would indicate a deviation from GR. The current observations of S0-2 are compatible with GR and exclude the Newtonian model at 1.2σ.

In order to maximize the use of telescope time in 2018, we developed an adaptive scheduling tool that determines the optimal observation nights in order to measure the relativistic redshift, as shown in Fig. 2 (left). The optimal observation epochs for a detection of the redshift correspond to the turning points of the radial velocity curve (i.e. the extremal points, see left of Fig. 2). The right of Fig. 2 shows the evolution of the signal-to-noise ratio (defined as $1/\sigma_\Upsilon$) of the relativistic redshift measurement with the additional observations. The optimal observations ensure a successful detection of the relativistic redshift above 5σ at the end of the 2018 observation campaign.

5 Conclusion

In this proceeding, we show that we are currently entering an era where observations of short-period stars in our GC can be used to probe fundamental physics. We presented a constraint

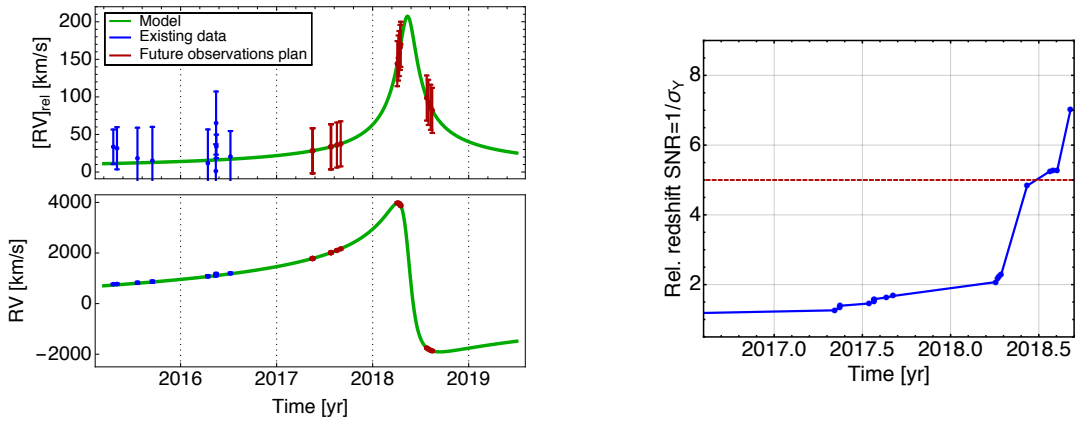


Figure 2 – Left: S0-2's radial velocity for the total RV (bottom panel) and the relativistic contribution (top panel) from Eq. 3. The blue points correspond to existing data from Keck and VLT [7]. The red points correspond to the an observation plan for 2017 and 2018 optimally designed to detect the relativistic redshift. The optimal observations are the ones corresponding to the turning points of the RV curve.
Right: evolution of the signal-to-noise ratio of the relativistic redshift measurement with future observations. The blue points correspond to the future observations.

on a hypothetical fifth force and an upper limit on the secular drift of S0-2's argument of periastron obtained using 19 years of observations [9]. Finally, we have shown that a carefully designed observations plan for 2018 will lead to a successful measurement of the relativistic redshift of the star S0-2. In the longer term, tests of GR using short-period stars are expected to be complementary to other types of observations that will probe the space-time around the SMBH at the center of our Galaxy, as for example with the Event Horizon Telescope [14].

Acknowledgments

AH thanks the organizers for financial support to attend the conference. Support for this work was provided by NSF grant AST-1412615, the Heising-Simon Foundation, the Levine-Leichtman Family Foundation, the Galactic Center Board of Advisors, and Janet Marott for her support of research on S0-38 through the Galactic Center stellar patron program.

References

1. C. Will, *Living Rev. Relativ.* **17**, 4 (2014).
2. G. F. Rubilar and A. Eckart, *A & A* **374**, 95 (2001).
3. S. Zucker *et al*, *ApJ* **639**, L21 (2006).
4. A. Ghez *el al*, *ApJ* **509**, 678 (1998).
5. A. Boehle *et al*, *ApJ* **830**, 17 (2016).
6. R. Genzel *et al*, *MNRAS* **291**, 219 (1997).
7. S. Gillessen *et al*, *ApJ* **837**, 30 (2017).
8. D. Psaltis in *X-ray Timing 2003: Rossi and Beyond*, ed. P. Kaaret, F. K. Lamb, and J. H. Swank (American Institute of Physics Conference Series, 2004).
9. A. Hees *el al*, to appear in *Phys. Rev. Lett.* , (2017).
10. A. S. Konopliv *et al*, *Icarus* **211**, 401 (2011).
11. E. Fischbach and C. Talmadge, *Nature* **356**, 207 (1992).
12. E. G. Adelberger *et al*, *Progress in Particle and Nuclear Physics* **62**, 102 (2009).
13. D. Borka *el al*, *JCAP* **11**, 50 (2013).
14. D. Psaltis *el al*, *ApJ* **818**, 121 (2016).

Probing the symmetry breaking patterns of the early universe and new physics by the phase transition gravitational waves

Fa Peng Huang

Theoretical Physics Division, Institute of High Energy Physics, Chinese Academy of Sciences, P.O.Box 918-4, Beijing 100049, P.R.China

Motivated by the observation of gravitational waves (GWs) by aLIGO, and the absence of dark matter an other new physics signals at current experiments, we study the possibility to explore the nature of Higgs boson, the baryon asymmetry of the universe, dark matter, new physics models, symmetry breaking history of the early universe by the phase transition GWs if a strong first-order phase transition can be induced therein.

1 Introduction

The observation of gravitational waves (GWs) by aLIGO has initiated a new era of exploring the nature of gravity, cosmology as well as the fundamental particle physics by the GWs. Obvious shortcomings in our understanding of particle cosmology (such as the baryon asymmetry of the universe and the dark matter) and no evidence of new physics at current experiments may just point us towards the novel universe with hidden new physics, which might only be visible for GWs detection. GWs may helps to probing the nature of Higgs boson, the baryogenesis, dark matter, new physics models, symmetry breaking patters of the universe since they may be the triggers for a strong first-order phase transition (FOPT). Then a strong FOPT can produce detectable phase transition GWs.

2 Phase transition gravitational waves in a nutshell

A strong FOPT can drive the plasma of the early universe out of thermal equilibrium, and then bubble nucleate during it, which will produce GWs through three mechanisms: the well-known bubble collision, turbulence in the plasma fluid (a fraction of the bubble wall energy converted into turbulence) and sound wave in the plasma fluid (after the collision a fraction of bubble wall energy converted into motion of the fluid, and is only later dissipated). The phase transition GWs spectrum depend on four parameters. The first parameter is $\alpha \equiv \frac{\epsilon(T_*)}{\rho_{\rm rad}(T_*)}$, which represents the strength the FOPT, namely, a larger value of α produces stronger GWs signature. The second parameter is $\frac{\beta}{H_*} = T\frac{d(S_3/T)}{dT}\Big|_{T=T_*}$, where one has $\beta \equiv -\frac{dS_E}{dt}|_{t=t_*} \simeq \frac{1}{\Gamma}\frac{d\Gamma}{dt}|_{t=t_*}$, namely, β^{-1} corresponds to the typical time scale of the phase transition. The third parameter is the efficiency factor λ_i (i=co,tu,sw), and the last parameter is the bubble wall velocity v_b. Especially, electroweak phase transition GWs becomes more interesting and realistic after the discovery of Higgs boson by LHC and GWs by aLIGO.

3 GWs related to Higgs nature and baryogenesis

A long standing problem in particle cosmology is to unravel the origin of baryon asymmetry of the universe (BAU). After the discovery of the 125 GeV Higgs boson, electroweak baryogenesis becomes a interesting and testable scenario for explaining the BAU. (To produce the observed BAU, three necessary conditions are needed: baryon number violation, C and CP violation, departure from thermal equilibrium or CPT violation.) A strong FOPT can provide the departure from thermal equilibrium, which can be realized in various of new physics models by modify the standard model(SM) Higgs potential. And probing the true Higgs potential is the urgent scientific goal after the discovery of Higgs boson. Instead of investigating the Higgs nature or electroweak phase baryogenesis in a UV-complete theory, which is difficult to make experimental predictions from unknown model parameters, we take a bottom-up approach to explain the BAU and study the possible collider and GWs signals with the effective Lagrangian of the Higgs doublet ϕ as $\delta\mathcal{L} = -\frac{\kappa}{\Lambda^2}(\phi^\dagger\phi)^3$. These effective operators could come from various renormalizable extensions of the SM. Thus, the combined results are shown in Fig.3 with the details in Ref.[1] and references therein. We conclude that the GWs interferometers can provide a complementary approach to probe the nature of the electroweak phase transition alternative to particle colliders, and vice versa.

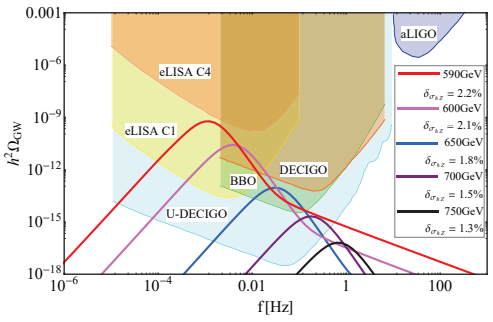


Figure 1 – The phase transition GWs spectra $h^2\Omega_{\rm GW}$ from FOPT during the evolution of our universe. The colored regions represent the expected sensitivities of GWs detectors aLIGO, eLISA, BBO and SKA, respectively. The red line depicts the possible GWs spectrum where the FOPT occurs at the energy scale of $\mathcal{O}(100)$ MeV in some dark QCD models. The black line represents the GWs spectrum for the FOPT at about 4 TeV in some hidden gauge group models, such as some 3-3-1 models. The purple line corresponds to the GWs spectrum when the FOPT takes place at the energy scale of $\mathcal{O}(10000)$ TeV in some models with high symmetry breaking scale.

4 GWs induced by dark matter

Motivated by the absence of dark matter signals in direct detection experiments (such as the recent LUX and PandaX-II experiments) and the discovery of gravitational waves (GWs) at aLIGO, we discuss the possibility to explore a generic classes of scalar dark matter models using the complementary searches via phase transition GWs and the future lepton collider signatures. We focus on the inert scalar multiplet dark matter models and the mixed inert scalar dark matter models, which could undergo a strong FOPT during the evolution of the early universe, and might produce detectable phase transition GWS signals at future GWs experiments, such as eLISA, DECIGO and BBO. We find that the future GWs signature, together with circular electron-positron collider (CEPC), could further explore the model's *blind spot* parameter region, at which the dark matter-Higgs coupling is identically zero, thus avoiding the dark matter spin-independent direct detection constraints. One example is the inert doublet model (IDM) with the relevant tree-level potential

$$\begin{aligned} V_0(\Phi, H_2) &= V(\Phi) + M_D^2 H_2^2 + \lambda_2 H_2^4 \\ &+ \lambda_3 \Phi^2 H_2^2 + \lambda_4 |\Phi^\dagger H_2|^2 + \lambda_5/2 \left[(\Phi^\dagger H_2)^2 + h.c. \right]. \end{aligned}$$

Another exmaple is the mixed singlet-doublet model(MSDM) with the tree-level potential

$$V_0 = \frac{1}{2} M_S^2 S^2 + M_D^2 H_2^\dagger H_2 + \frac{1}{2}\lambda_S S^2 |\Phi|^2 + \lambda_3 \Phi^\dagger \Phi H_2^\dagger H_2$$

$$+ \quad \lambda_4|\Phi^\dagger H_2|^2 + \frac{\lambda_5}{2}[(\Phi^\dagger H_2)^2 + h.c.] + A\left[S\Phi H_2^\dagger + h.c.\right] .$$

The final results are shown in Fig.2 with the details in the Ref.[2] and references therein.

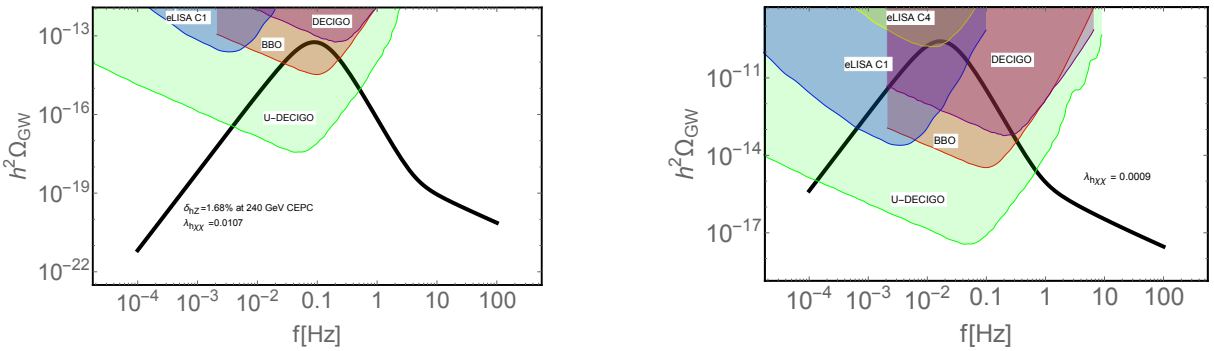


Figure 2 – The phase transition GWs spectra $h^2\Omega_{\rm GW}$ in the IDM (left) and MSDM (right). The colored regions represent the expected sensitivities of GWs interferometers U-DECIGO, DECIGO, BBO and eLISA, respectively. The black line depicts the GWs spectra in the IDM for the set of benchmark points, which also represents the corresponding hZ cross section deviation at the 240 GeV CEPC and the corresponding dark matter coupling.

5 GWs in 3-3-1 models and general new phyics models

In a generic classes of extended new physics models with hidden gauge group could undergo one or several times FOPT associated with the gauge group symmetry breaking during the evolution of the universe as shown in Fig.3, which might produce detectable phase transition GWs signals at future GWs experiments.

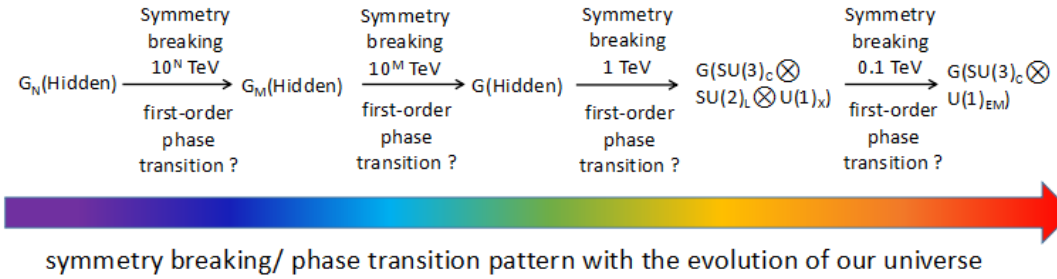


Figure 3 – Symmetry breaking (phase transition) patterns for the non-Abelian gauge group extended models with the evolution of our universe, where the first-order phase transitions may happen.

In Fig. 4, the FOPT GWs spectra $h^2\Omega_{\rm GW}$ during the evolution of our universe are shown for a generic classes of hidden gauge group extended models at the different energy scales. The colored regions represent the expected sensitivities of GWs detectors SKA, BBO, eLISA and aLIGO, respectively. The red line depicts the possible GWs spectrum where the FOPT occurs at the energy scale of $\mathcal{O}(100)$ MeV in some dark QCD models (such as the famous relaxion model), which can be detected by the pulsa timing array (PTA) experiments, such as the planned SKA or the FAST. The black line represents the GWs spectrum for the FOPT at about 4 TeV in some hidden gauge group extended models, such as some versions of 3-3-1 models. We have shown that all the three versions of the 3-3-1 models discussed above could produce FOPT GWs at TeV scale when the hidden gauge symmetry $SU(3)_L \otimes U(1)_Y$ breaks to $SU(2)_L \otimes U(1)_X$. Especially, in the economical and reduced minimal 3-3-1 models two times FOPT may take place, which will produce two GWs spectra with different characteristic peak frequencies. In general, the phase transition GWs produced at the scale from $\mathcal{O}(100)$ GeV to several TeV can be tested at future laser interferometer GWs detectors in space, such as the planned eLISA, BBO, Taiji and

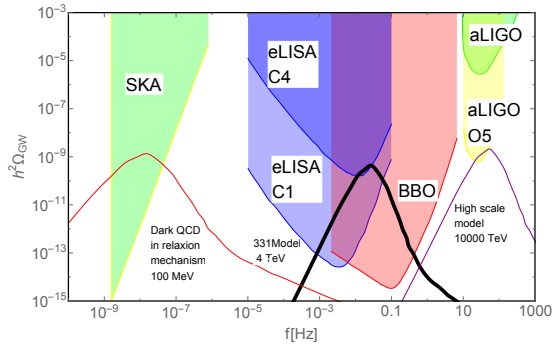


Figure 4 – The phase transition GWs spectra $h^2\Omega_{\rm GW}$ from FOPT during the evolution of our universe. The colored regions represent the expected sensitivities of GWs detectors aLIGO, eLISA, BBO and SKA, respectively. The red line depicts the possible GWs spectrum where the FOPT occurs at the energy scale of $\mathcal{O}(100)$ MeV in some dark QCD models. The black line represents the GWs spectrum for the FOPT at about 4 TeV in some hidden gauge group models, such as some 3-3-1 models. The purple line corresponds to the GWs spectrum when the FOPT takes place at the energy scale of $\mathcal{O}(10000)$ TeV in some models with high symmetry breaking scale.

Tianqin. The purple line corresponds to the GWs spectrum when the FOPT takes place at the energy scale of $\mathcal{O}(10000)$ TeV in some high scale models, which may be within the sensitivity of the future aLIGO and provide us with a unique detection of the hidden gauge symmetry breaking at high energy scales beyond the abilities of particle colliders. Besides these schematic models, many other hidden gauge group extended models may also undergo one or several FOPT at different energy scale as shown in Fig.4, where the corresponding phase transition GWs spectra can be produced and tested at the corresponding GWs detectors. The details are given in Ref.[3] and references therein.

6 summary and outlook

For cosmology, our universe may undergo one or several times phase transition during the early evolution of the universe. And we can hear the cosmological phase transition using GWs if there exists FOPT. For particle physics, this phase transition GWs approach can compensate for the collider experiments to explore the new physics models(especially the hidden sector) and provide a novel approach to probe the symmetry breaking or phase transition patterns. For particle cosmology, GWs provides a unique way to unravel the dark matter, baryogenesis and so so. New physics models in particle physics can provide abundant GWs sources. GWs becomes a new and realistic approach to explore the particle cosmology and fundamental physics, such as probing the extra dimension through gravitational wave observations of compact binaries and their electromagnetic counterparts [4]. Let us ski on the exciting journey of GWs physics.

Acknowledgments

FPH was supported in part by the NSFC (Grant Nos. 11121092, 11033005, 11375202), the CAS pilotB program. and the China Postdoctoral Science Foundation under Grant No. 2016M590133.

References

1. Fa Peng Huang, Youping Wan, Dong-Gang Wang, Yi-Fu Cai, Xinmin Zhang, *Phys. Rev.* D **94**, 041702 (2016).
2. Fa Peng, Jiang-hao Yu, arXiv:1704.04201
3. Fa Peng Huang, Xinmin Zhang, arXiv:1701.04338
4. Hao Yu, Bao-Min Gu, Fa Peng Huang, Yong-Qiang Wang, Xin-He Meng, Yu-Xiao Liu, JCAP 1702 (2017) no.02, 039.

6.
Posters

DE SITTER INVARIANT SPECIAL RELATIVITY AND THE DARK ENERGY PROBLEM

A. ARAUJO, D. F. LÓPEZ and J. G. PEREIRA
Universidade Estadual Paulista (UNESP)
Instituto de Física Teórica
São Paulo, Brazil

Due to the existence of an invariant length at the Planck scale, Einstein special relativity is believed to break down at the scale. A possible solution to this problem is to replace the Poincaré invariant special relativity by a de Sitter invariant special relativity. Such replacement produces concomitant changes in general relativity, the most relevant being the fact that both the background de Sitter curvature and the gravitational dynamical curvature are now included in the same curvature tensor

.

The de Sitter spacetime is usually interpreted as the simplest *dynamical* solution of the sourceless Einstein equation in the presence of a cosmological constant, standing on an equal footing with all other gravitational solutions, like for example Schwarzschild and Kerr. However, as a non-gravitational spacetime (in the sense that its metric does not depend on Newton's gravitational constant), the de Sitter solution should instead be interpreted as a fundamental background for the construction of physical theories, standing on an equal footing with the Minkowski solution. In fact, as quotient spaces, both Minkowski and de Sitter are known *a priori*, independently of Einstein equation. General relativity, for instance, can be constructed on any one of them. Of course, in either case gravitation will have the same dynamics, only their local kinematics will be different. When the underlying spacetime is Minkowski, the local kinematics will be ruled by the Poincaré group of ordinary special relativity. When the underlying spacetime is de Sitter, the local kinematics will be ruled by the de Sitter group, *which amounts then to replace ordinary special relativity by a de Sitter invariant special relativity*.[1]

Now, it so happens that there is a physical reason for making such replacement. It is related to the existence of an invariant length parameter at the Planck scale, represented by the Planck length l_P, which implies that ordinary special relativity breaks down at that scale. The problem is that the Lorentz group is believed no to allow the existence of an invariant length parameter. Since Lorentz is a subgroup of Poincaré—which is the group that rules the kinematics in ordinary special relativity—the kinematics at Planck scale cannot be described by ordinary special relativity. This, however, does not mean that Lorentz symmetry must be violated at the Planck scale. To see that, let us recall that Lorentz transformations can only be performed in *homogeneous spacetimes*, whose Ricci scalar has the form

$$R = 12\, l^{-2}\,, \tag{1}$$

where l is the de Sitter length-parameter, or pseudo-radius. Then comes the point: by definition, Lorentz transformations do not change the curvature of the homogeneous spacetime in which they are performed. Since the scalar curvature is given by (1), *Lorentz transformations are found to leave the length parameter l invariant*. Although somewhat hidden in Minkowski spacetime, because what is left invariant in this case is an infinite length, in de Sitter spacetime, whose

pseudo-radius is finite, this property becomes manifest. Contrary to the usual belief, therefore, *Lorentz transformations do leave invariant a very particular length parameter: that defining the scalar curvature of the homogeneous spacetime in which they are performed.* If the Planck length l_P is to be invariant under Lorentz transformations, it must then represent the pseudo-radius of spacetime at the Planck scale, which will be a de Sitter space with a Planck cosmological term

$$\Lambda_P = 3/l_P^2 \simeq 1.2 \times 10^{70}\,\mathrm{m}^{-2}. \tag{2}$$

In a de Sitter-invariant special relativity, therefore, the existence of an invariant length-parameter at the Planck scale does not clash with Lorentz invariance, which remains a symmetry at all scales. In the same way Einstein special relativity may be thought of as a generalization of Galilei relativity for velocities near the speed of light, the de Sitter-invariant special relativity may be thought of as a generalization of Einstein special relativity for energies near the Planck energy. It holds, for this reason, at all energy scales.

Implicit in de Sitter modified general relativity is the idea that any physical system with energy density ε_m induces a local cosmological term Λ in spacetime, with an energy density ε_Λ, which is necessary to comply with the local symmetry of spacetime, now ruled by the de Sitter group. Note that the ensuing cosmological term Λ is different from the usual notion in the sense that it is not constant. For example, outside the region occupied by the physical system, where ε_m vanishes, Λ vanishes as well. The question then arises: given a physical system, how to obtain the local value of the cosmological term? To answer this question, let us recall that, at the Planck scale, the cosmological term assumes the Planck value given by (2). Now, the very definition of Λ_P can be considered an extremal particular case of a general expression relating the local cosmological term to the corresponding energy density of a physical system. Accordingly, to a physical system of energy density ε_m will be associated the local cosmological term

$$\Lambda = \frac{4\pi G}{c^4}\,\varepsilon_m\,. \tag{3}$$

When the Poincaré invariant Einstein special relativity is replaced by a de Sitter invariant special relativity, general relativity changes to what we have called *de Sitter modified general relativity.* In this theory, the kinematic curvature of the underlying de Sitter spacetime and the dynamical curvature of general relativity are both included in the very same Riemann tensor. This means that the cosmological term Λ no longer appears explicitly in Einstein's equation, and consequently the second Bianchi identity does not require it to be constant. When applied to the present-day universe, the de Sitter modified Friedmann equations in the newtonian approximation gives a good account of the observed relation between the matter and the dark energy densities, providing in this way an explanation for the coincidence problem.[2]

Acknowledgements

AA and DFL would like to thank CAPES for fellowship grants. JGP thanks CNPq for partial financial support.

References

1. R. Aldrovandi and J. G. Pereira, *An Introduction to Geometrical Physics*, Second Edition (World Scientific, Singapore, 2016), Chapter 37.
2. A. Araujo, D. F. López and J. G. Pereira, *Class. Quantum Grav.*, DOI: 10.1088/1361-6382/aa6bbb e-Print: arXiv:1704.02120 [gr-qc]

Recent advances in the determination of a high spatial resolution geopotential model using chronometric geodesy

G. LION[1,2], P. DELVA[1], C. GUERLIN[1,3], S. BIZE[1], D. COULOT[2], P. WOLF[1], I. PANET[2]
[1]*SYRTE, Observatoire de Paris, PSL Research University, CNRS, Sorbonne Universits, UPMC Univ. Paris 06, LNE, 61 avenue de l'Observatoire, 75014 Paris, France*
[2]*LASTIG LAREG, IGN, ENSG, Univ Paris Diderot, Sorbonne Paris Cité, 35 rue Hélène Brion, 75013 Paris, France*
[3]*Laboratoire Kastler Brossel, ENS-PSL Research University, CNRS, UPMC-Sorbonne Universités, Collège de France, 24 rue Lhomond, 75005 Paris, France*

This work aims to evaluate the contribution of optical atomic clocks in the determination of the geopotential at high spatial resolution. The quality of the geopotential reconstruction is evaluated by comparing solutions computed from synthetic gravimetric data, combined or not with synthetic clock data. Our synthetic tests are performed in a French area with a moderate relief, which leads to variations of the gravitational field over a range of spatial scales. We show that adding few clock data into a gravimetric network permits to reduce the reconstruction bias significantly and to improve the standard deviation by a factor 3. Optimization of a clock data network with a genetic algorithm is also investigated.

1 Introduction

Comparisons between highly precise optical clocks are opening new perspectives for the direct determination of geopotential at a centimeter-level accuracy in geoid height [1,5]. Indeed, two clocks with an accuracy of 10^{-18} in terms of relative frequency shift would detect a 1-cm geoid height variation between them, corresponding to a geopotential variation ΔW of about 0.1 $\mathrm{m^2\,s^{-2}}$(see e.g. [3]). However, so far detailed quantitative estimates of the possible improvement in geoid determination when adding such clock measurements to existing data are lacking.

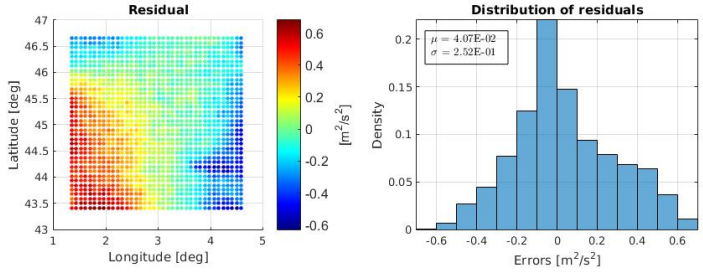
In this context, the present work aims at evaluating the contribution of this new kind of direct measurements in determining the geopotential at high spatial resolution (10 km). We investigate to what extent clocks could contribute to filling the gap between the satellite and near-surface gravity spectral, and spatial coverages, in order to improve our knowledge of the geopotential and gravity field at all wavelengths. We consider the Massif Central area, marked by smooth, moderate altitude mountains and volcanic plateaus leading to variations of the gravitational field over a range of spatial scales. This type of region is interesting because the scarcity of gravity data is a limitation in deriving accurate high resolution geopotential models.

2 Methodology and results

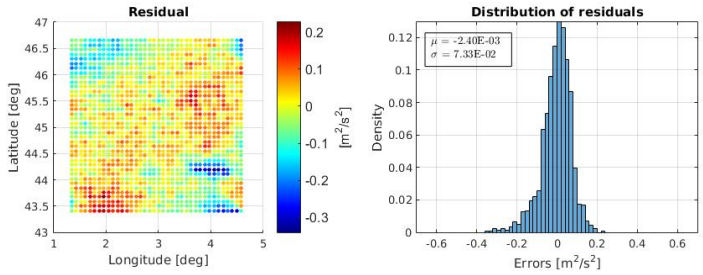
Our study is based on synthetic noised data. The gravity anomalies δg and the disturbing potential T are generated with GEOPOT [6], allowing to compute the gravity field related quantities at given locations. The synthetic data are sampled from a spherical harmonics geopotential model, and a topography model, up to 10 km resolution. The long wavelengths of the gravity field

covered by the satellites and longer than the extent of the local area are removed, providing centered data for the determination of local covariance function. A white noise is added to the simulated data, and we estimate the disturbing potential by least-squares collocation from the gravimetric data with and without the clock data. Their locations are chosen to reproduce a realistic distribution of measurements. Finally, we assess the quality of the reconstructed potential by comparing residuals of these solutions to that of the control grid.

We demonstrate in Figure 1 that adding the clock-based potential values to the existing gravimetric data set can notably improve the final gravity field solution. In Figure 1a, the estimation is realized from the 4374 gravimetric data only, and in Figure 1b by adding 33 potential data to the gravity data. The noise level is respectively 1 mGal and 0.1 $m^2\,s^{-2}$. We show that adding clock data reduces the reconstruction bias significantly and improves the standard deviation by a factor 3. Another important conclusion stemming from our simulations is that in solving the problem of gravity field recovery it is not required to have a dense clock network, only a very few percent of clock measurements compared to the number of needed gravity data is sufficient. More details about the methodology and results can be found in Lion et al. [4]. We are also investigating ways to optimize clock networks in order to find an optimal design and to improve further the determination of the gravity field. First simulations using genetic algorithms such as ϵ-MOEA [2] give promising results. Several distributions of clock data obtained with the genetic algorithm give better residual than those presented here with about 20 potential data.



(a) Without clock data.



(b) With clock data.

Figure 1: Accuracy of the disturbing potential T reconstruction on a regular 10-km step grid in Massif Central, obtained by comparing the reference model and the reconstructed one.

Acknowledgments

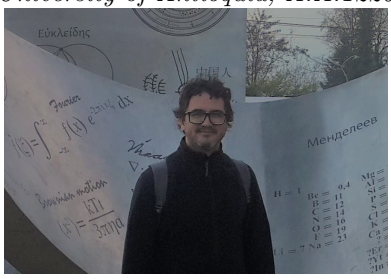
We gratefully acknowledge financial support from Labex FIRST-TF and ERC AdOC.

References

1. Bjerhammar A., 59(3), p 207–220 (1985).
2. Deb K., Manikanth M., Shikhar M., Evolutionary computation, 13.4 (2005).
3. Delva P., Lodewyck J., Acta Futura, Issue 7, p 67–78 (2013).
4. Lion G., Panet I., Wolf P., Guerlin C., Bize S., Delva P., *J. Geodesy*, p 1–15 (2017).
5. Mai E., Reihe A., Theoretische Geodäsie, Beck (2013).
6. Smith D. A., IGeS Bulletin 8, p 17–28 (1998).

PRIMORDIAL POWER SPECTRUM AND LOCAL FEATURES

ALEXANDER GALLEGO CADAVID
Institute of Physics, University of Antioquia, A.A.1226, Medellín, Colombia



We study the effects of local features (LF) of the inflaton potential on the spectrum of primordial curvature perturbations. We show that the LF affect the potential in a narrow range of the scalar field value. We compute the primordial spectrum and show that it is only affected in a limited range of scales, which leave the horizon during the time interval corresponding to the modification of the potential. Due to their local nature these features could be used to model local glitches found in the primordial spectrum without affecting other scales.

1 Introduction

The study of features of the primordial spectrum of perturbations is one of the most exciting extensions of the ΛCDM model [1,2,3,4,5]. In the past years a remarkable attention has been given to the detection of primordial features since it could pin down details of the inflationary theory, from discriminating between different models to improving the fit to CMB temperature data [1,2,5].

2 The inflationary model

We consider inflationary models with a single scalar inflaton field ϕ according to the action

$$S = \int d^4x\sqrt{-g}\left[\frac{1}{2}M_{Pl}^2 R - \frac{1}{2}g^{\mu\nu}\partial_\mu\phi\partial_\nu\phi - V(\phi)\right], \tag{1}$$

where $g_{\mu\nu}$ is the flat FLRW metric, M_{Pl} the reduced Planck mass, R the Ricci scalar, and V is the inflaton potential. To study the effects of the feature we consider the potential [4,5]

$$V(\phi) = V_0(\phi) + V_{LF}(\phi)\,, \tag{2}$$

where $V_0(\phi) = \gamma\phi^2$ is the chaotic potential used to model the featureless behavior and

$$V_{LF}(\phi) = \lambda e^{-(\frac{\phi-\phi_0}{\sigma})^2}\,, \tag{3}$$

The parameters λ, σ, and $\phi_0 \equiv \phi(t_0)$, where t_0 is the feature time, are related to the amplitude, width, and scale of the feature, respectively. This type of modification of the potential corresponds to LF [4,5], where V deviates from the featureless case only in a limited range of the field

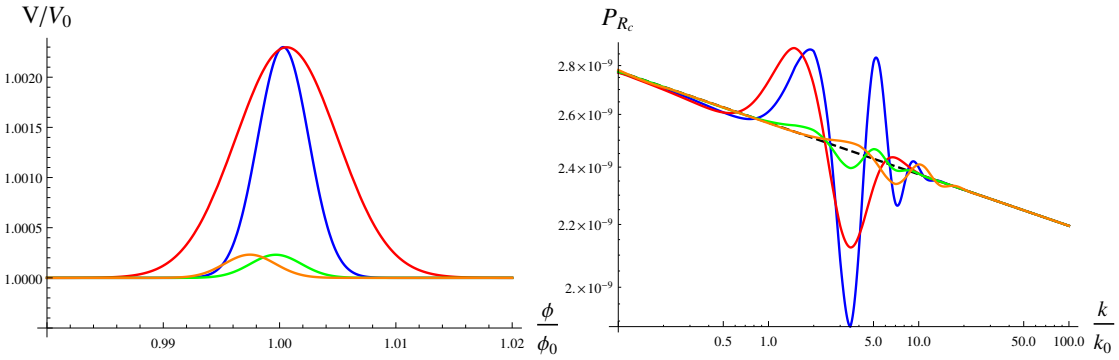


Figure 1 – We plot the effects of the features on the inflaton potential (left) and on the power spectrum of primordial curvature perturbations (right). For the features we use $\lambda = 10^{-11}, \sigma = 0.05$, and $\phi_0 = 16.16$ (blue), $\lambda = 10^{-11}, \sigma = 0.1$, and $\phi_0 = 16.16$ (red), $\lambda = 10^{-12}, \sigma = 0.05$, and $\phi_0 = 16.16$ (green), and $\lambda = 10^{-12}, \sigma = 0.05$, and $\phi_0 = 16.12$ (orange). The dashed lines correspond to the featureless case. In all cases we use $\gamma = 1.66 \times 10^{-11}$.

value around ϕ_0. The effects of the feature on the potential are shown in Fig. 1. From now on we use units in which $c = \hbar = M_{Pl} = 1$.

3 Primordial power spectrum of curvature perturbations

The power spectrum of primordial curvature perturbations is defined as [4]

$$P_{\mathcal{R}_c}(k) \equiv \frac{2k^3}{(2\pi)^2}|\mathcal{R}_c(k)|^2, \tag{4}$$

where $\mathcal{R}_c$ is the comoving curvature perturbation and k its comoving wave number. As can be seen in Fig. 1, $P_{\mathcal{R}_c}$ is affected by oscillations only around the scale k_0 exiting the horizon. This is opposed to branch features (BF) [3,4] which produce a step with respect to the featureless spectrum at large or small scales.

4 Conclusions

We have shown the effects of LF of the inflaton potential on the spectrum of primordial curvature perturbations. We have seen that the LF affect the spectrum in a narrow range of scales. The amplitude and width of the oscillations depend on the parameters defining the feature. In the future it would be interesting to study phenomenologically the combined effects of LF and BF on the primordial spectrum for different inflationary models.

References

1. Dhiraj Kumar Hazra, Arman Shafieloo, George F. Smoot, and Alexei A. Starobinsky. Primordial features and Planck polarization. *JCAP*, 1609(09):009, 2016.
2. Xingang Chen, Cora Dvorkin, Zhiqi Huang, Mohammad Hossein Namjoo, and Licia Verde. The Future of Primordial Features with Large-Scale Structure Surveys. *JCAP*, 1611(11):014, 2016.
3. Alexander Gallego Cadavid and Antonio Enea Romano. Effects of discontinuities of the derivatives of the inflaton potential. *Eur. Phys. J.*, C75(12):589, 2015.
4. Alexander Gallego Cadavid, Antonio Enea Romano, and Stefano Gariazzo. Effects of local features of the inflaton potential on the spectrum and bispectrum of primordial perturbations. *Eur. Phys. J.*, C76(7):385, 2016.
5. Alexander Gallego Cadavid, Antonio Enea Romano, and Stefano Gariazzo. CMB anomalies and the effects of local features of the inflaton potential. *Eur. Phys. J.*, C77(4):242, 2017.

Integrals of quasi linear equations of gravitating Dark Matter at space thermostat presence: gravitation frequency and scale

Mikhail Ja. Ivanov
Central Institute of Aviation Motors, Moscow, 111116, Russia



The paper presents some integrals of quasi-linear equations of gravitating dark matter motion at the Space Thermostat (ST) presence. As this ST we take Cosmic Microwave Background Radiation (CMBR) with known temperature $T = 2.73K$. The exact and numerical solutions of the equation system have been obtained and analyzed. Also we present Dark Matter (DM) visual registration by the Hubble telescope in ultraviolet light.

1 Gravitation frequency and scale

In physics problems the thermostat is called greater thermodynamic system, in which the number of particles far exceeds the number of particles of a studied system with its in thermal contact. In our case as such external ST we take CMBR with known temperature $T = 2.73K$ and with certain massive particles $m = kT/c^2 = 5.6 \cdot 10^{-40} kg = 3 \cdot 10^{-4} eV$ (particles of DM - holders and carriers of thermal radiation [1,2]). We naturally believe any natural or technical studied system in the thermal contact with the ST (CMBR). The presence of the ST introduces important adjustments in the general equations of a dynamic system motion. In the paper we are basing on the classic gravitational theory [3]. The important key is the equation of force gravitational field $\bar{F}$ may be written here accounting non-zero density ρ_0 at "infinity" in the form

$$div\vec{F} = 4\pi G(\rho_0 - \rho). \tag{1}$$

From two dimension parameters G and ρ_0, defining gravitational interaction in our case, we obtain the gravitational frequency ω_g and the gravitational period T_g of our Universe by methods of dimension. We get

$$\omega_g = sqrt(4\pi G\rho_0), Tg = 1/\omega_g. \tag{2}$$

In case if speed of light c in vacuum is assumed as a constant defining the process, we shall get the characteristic linear scale of the Universe

$$L_g = cT_g. \tag{3}$$

When $\rho_0 \approx 0.5 \cdot 10^{-29} g/cm^3$, value T_g corresponds to a periodical Universe age $T_g \approx 1.4 \cdot 10^{10}$ years. We would like to emphasis here analogy with the plasma frequency. The relation for ω_g

follows easily from the model one dimensional problem for oscillation of a mass point around the layer of gravitating DM of width x and density ρ_0.

2 Integrals and exact solutions of equations for gravitating dark matter motion

Initial equations for ideal (non-viscous and non-heat conducting) gaseous medium (Euler equations) taking into account own gravitational interaction of particles are [3]

$$\frac{\partial \rho}{\partial t} + div(\rho\bar{\nu}) = 0, \frac{\partial \bar{\nu}}{\partial t} + (\bar{\nu} \cdot \nabla)\bar{\nu} = -\frac{1}{\rho} grad\, p + \bar{F}. \quad (4)$$

Figure 1 shows the pattern of integral curves of one dimensional variant of these equations [3]. Modeling "superlumina" cosmic jet (CJ) solution corresponds moving along the bold line separatrix from the singular point 1 towards the singular point 2. Numerical CJ simulation also presents on fig. 1. We apply the special shock capture scheme [1].

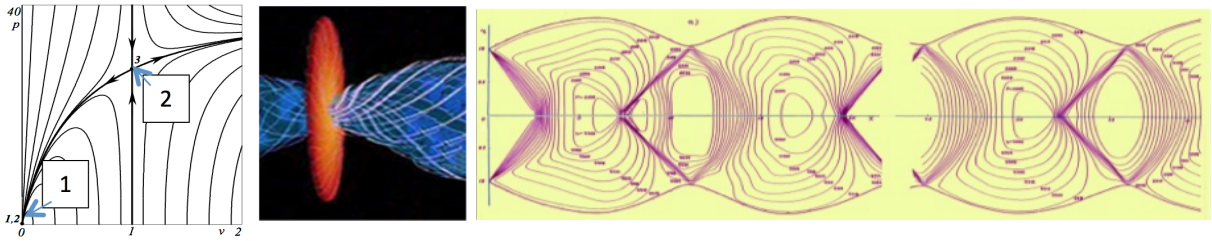


Figure 1 – Integral curves of equations in the phase plane (v,p) and numerical CJ simulation.

3 Hubble Dark Matter visual registration

Here we would like to show only one of the last DM image in visible and ultraviolet lights. Figure 2 (on the left) presents the Hubble extreme deep field image of space in the Draco constellation (group of galaxies Abell 2218) [4]. The density of DM for the Draco constellation in ultraviolet light is shown in fig. 2 on the right [5]. It's experimental confirmation of our simulations.

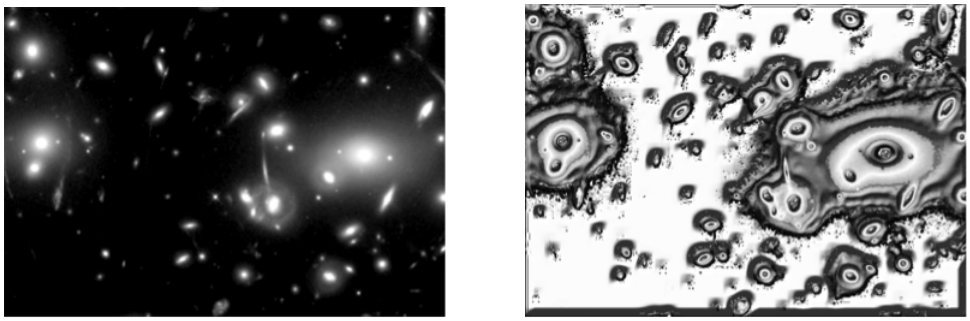


Figure 2 – The Hubble Draco constellation images in visible and ultraviolet lights.

4 Conclusion

The Universe presents itself the greatest ST of DM with the nonzero temperature $T = 2.73K$, which is holders and carriers of CMBR. The DM presents itself the gaseous medium with certain massive particles $m = kT/c^2 = 5.6 \cdot 10^{-40}kg = 3 \cdot 10^{-4}eV$.

References

1. Ivanov M.Ja. Space Energy. "Energy Conservation", In Tech, 2012, DOI:10-5772/52493.
2. Ivanov M.Ja., Mamaev V.K. Hidden mass boson. J. Modern Phys. 3(8), 2012, pp. 686 - 693.
3. Ivanov M.Ja., Terentieva L.V. Gas dynamics elements of dispersive medium. M: 2004.
4. The European Homepage for the NASA/ESA Hubble Space Telescope - Fact Sheet. EKA. 2012.
5. Saveliev G.F. Microlepton method of registration for different fields. Russian Acad. of Trinitarizm, M., $N^{\underline{o}}$ 77-6567, 23216, 01.04.2017.

DOES A GRAVITON GAS ACT LIKE A COSMOLOGICAL VACUUM STATE AND "COSMOLOGICAL" CONSTANT PARAMETER

A.W. BECKWITH
College of Physics, Chongqing University Huxi Campus
No. 55 Daxuechen Nanlu, Shapingba District, Chongqing 401331
Chongqing, P. R. China, 400014

If a nonzero graviton mass exists, one might wonder if a release of gravitons, possibly as a *graviton gas* at the onset of inflation could be considered an initial vacuum state. Pros and cons to this idea are raised, in part based on Bose gasses. The analysis starts with Volovik's condensed-matter treatment of GR and ends with the consequences the author sees if the supposition is true.

1 Introduction

The manuscript is based on Volovik's book,[1,2] which, as of 2003, has a chapter on how a Bose gas can be used to obtain a vacuum energy. We extrapolate from this idea and link it to Glinka's[1,3] WdW treatment of semi-classical style physics in his boson treatment of a graviton gas to make a analogy to Park's[4] version of a temperature-sensitive cosmological-constant parameter. Then, afterwards, we explore link to how entropy may be connected with an evolution of the resulting cosmological vacuum-energy expression for a graviton gas.

2 Review of the Volovik Model for Bose Gases

On page 24 of his manuscript, Volovik[1,2] derives a description of a total vacuum energy via an integral over three dimensional space:

$$E_{\rm vac}(N) = \int {\rm d}^3 r \cdot \varepsilon(n) \tag{1}$$

The integrand to be considered is, using a potential defined by $U = \frac{c^2 m}{n}$ as given by Volovik[1,2] for weakly interacting Bose gas particles,

$$\varepsilon(n) = \frac{1}{2} U \cdot n^2 + \frac{8}{15\pi^2 \hbar^3} m^{\frac{3}{2}} U^{\frac{5}{2}} = \frac{1}{2} \cdot c^2 \cdot \left[n \cdot m + \frac{4}{15} \cdot \left(\frac{m^5}{\hbar^2 \cdot \sqrt{c}} \right) \cdot \frac{1}{n^2} \right]. \tag{2}$$

For the sake of argument, m, as given above, will be called the mass of a graviton, and n a numerical count of gravitons in a small region of space. Afterwards, we will consider adaptations for what this expression means in terms of entropy generation. A simple graph of the second term of Eq. (2) with comparatively large m and $\hbar = c = 1$ has the following qualitative behavior.[1]

$$E_1 = \left[\frac{c^2}{2} \right] \cdot \left[\frac{4}{15} \cdot \left(\frac{m^5}{\hbar^2 \cdot \sqrt{c}} \right) \cdot \frac{1}{n^2} \right] \tag{3}$$

$E_1 \neq 0$ when n is very small, and $E_1 = 0$ as $n \to 10^{10}$ at the onset of inflation. If we view this as an indication of start of the deviation from the usual quantum linearity, the implication is that there is a cutoff right at the start of graviton production. That is, the implications for 't Hooft's[1,5] nonlinear embedding of quantum systems for gravitons would be in that the conditions for such embedding are likely in place before graviton production. We are observing right at the start of graviton production, the moment gravitons states emerge. We have extinguishment of a contribution of classical embedding, but the precursor to that would mean graviton production would be initially "framed" by a nonlinear contribution

3 Conclusion

In conclusion, the range of accessible frequencies for gravitons as linked to Eq. 3 is in sync with $h_0^2 \Omega_{\rm gw}(f) \sim 10^{-10}$ for peak frequencies with values of 10 MHz.[1] The net affect of such thinking is to rule out examining early-universe gravitons as measurable and to rule out being able to measure relic GW and gravitons via the premise that all relic GW are inaccessible. Looking at Figure 5 Beckwith,[1] $\Omega_{\rm gw} > 10^{-6}$ for frequencies as high as up to 10^6 Hz, counters what was declared by Turner and Wilzenk[6] that inflation will terminate with observable frequencies in the range of 100 Hz or so. The only way one may be able to observe a signal for relic GW or gravitons may be to consider how to obtain a numerical count of gravitons or neutrinos for (R. Weiss, personal communications):

$$h_0^2 \Omega_{\rm gw}(f) \cong \frac{3.6}{2} \bullet \left[\frac{n_f[\text{graviton}] + n_f[\text{neutrion}]}{10^{37}} \right] \times \left(\frac{\langle f \rangle}{1\,\text{kHz}} \right)^4 . \tag{4}$$

This leads to the question of how to account for a possible mass or information content of the graviton and confirming 't Hooft's speculations about quantum mechanics.[7]

Acknowledgments

This work is supported in part by National Nature Science Foundation of China grant No. 11375279.

References

1. A. W. Beckwith. *Analyzing If a Graviton Gas Acts Like a Cosmological Vacuum State and "Cosmological" Constant Parameter* (2016). http://vixra.org/abs/1004.0090
2. G. Volovik, *The Universe in a Helium Droplet, International series of Monographs on physics,* vol. 117 (Oxford Press, Oxford, 2003).
3. L. Glinka, *SIGMA* **3**, 87 (2007).
4. D. Park, H. Kim, and S. Tamarayan, *Phys. Lett.* B **535**, 5 (2002).
5. G. 't Hooft. *Beyond the Quantum,* ed. T. M. Nieuwenhuizen *et al.* (World Press Scientific, Singapore, 2006) https://arxiv.org/abs/quant-ph/0212095
6. S. Turner and F. Wilzenk, *Phys. Rev. Lett.* **65**, 3080 (1990).
7. G. 't Hooft, *Determinism beneath Quantum Mechanics* (2002). http://arxiv.org/PS_cache/quant-ph/pdf/0212/0212095v1.pdf

Authors Index

Authors Index

Abgrall, M.	Searching for scalar dark matter using six years of LNEe-SYRTE fountain clock comparison data	165
Alauze , X.	Trapped atom interferometry for the study of Casimir forces and Gravitation at short range	185
Alves, C.	Preparing ESPRESSO's fundamental physics tests	123
Alves, C.	Stability of Fundamental Couplings and Dark Energy: a pre-ESPRESSO analysis and forecast	229
Amand, L.	Studies of general relativity with quantum sensors	105
Angonin, M.-C..	Constraints on Lorentz symmetry violations with Lunar Laser Ranging	93
Anselmo, L.	LARASE: Testing General Relativity with Satellite Laser Ranging	203
Antoni-Micollier, L.	Studies of general relativity with quantum sensors	105
Araujo, A.	de Sitter-invariant special relativity and the dark energy problem	293
Askar, A.	Black holes binaries from globular clusters as sources of gravitational waves	21
Bailey, Q.	Low-energy tests of Lorentz symmetry: new constraints with nucleons in a cold atom clock	169
Barret, B.	Studies of general relativity with quantum sensors	105
Bassan, M.	PETER: a double torsion pendulum to test quasi free-fall on two degrees of freedom	97
Bassan, M.	Perspective to measure forces between macroscopic flat parallel plates	199
Bassan, M.	LARASE: Testing General Relativity with Satellite Laser Ranging	203
Battelier, B.	Studies of general relativity with quantum sensors	105
Becklin, E.	Testing the gravitational theory with short-period stars around our galactic center	283
Beckwith, A.	Does a graviton gas act like a cosmological vacuum state and 'cosmological' constant parameter	301
Bejger, M.	Status of the continuos gravitational wave searches in the advanced detector ERA	51
Bergé, J.	The Inverse Square Law And Newtonian Dynamics space explorer (ISLAND)	191
Bernard, L.	Conservative Dynamics of Binary Systems of Compact Objects at the Fourth Post-Newtonian Order	251
Bernus, L.	Universality of free fall versus ephemeris	101
Bertoldi, A.	Studies of general relativity with quantum sensors	105
Bize, S.	Searching for scalar dark matter using six years of LNEe-SYRTE fountain clock comparison data	165
Bize, S.	Low-energy tests of Lorentz symmetry: new constraints with nucleons in a cold atom clock	169
Bize, S.	Recent advances in the determination of a high spatial resolution geopotential model using chronometric geodesy	295
Blázquez-Salcedo, J.	Neutron stars with realistic equations of state in scalar-tensor theories of gravity	279
Blanchard, A.	Testing general relativity from curvature & energy contents at cosmological scale	243
Blanchet, L.	Conservative Dynamics of Binary Systems of Compact Objects at the Fourth Post-Newtonian Order	251
Blondin, J.	Gravitational wave signals from multi-dimensional Core-collapse Supernova explosion simulations	37
Boehle, A.	Testing the gravitational theory with short-period stars around our galactic center	283
Boetzel, Y.	On solving post-Newtonian accurate Kepler Equation	269
Bohé, A.	Conservative Dynamics of Binary Systems of Compact Objects at the Fourth Post-Newtonian Order	251
Bonnin, A.	Trapped atom interferometry for the study of Casimir forces and Gravitation at short range	185
Borka, D.	Different ways for graviton mass evaluations	247
Borka Jovanović, V.	Different ways for graviton mass evaluations	247
Bouquillon, S.	Constraints on Lorentz symmetry violations with Lunar Laser Ranging	93
Bourgoin, A.	Constraints on Lorentz symmetry violations with Lunar Laser Ranging	93

Bouyer, P.	Studies of general relativity with quantum sensors	105
Bruenn, S.	Gravitational wave signals from multi-dimensional Core-collapse Supernova explosion simulations	37
Bulik, T.	Black holes binaries from globular clusters as sources of gravitational waves	21
Buskulic, D.	Compact binary coalescence searches performed during advanced LIGO's first observational run	3
Busonero, D.	The Astrometric Gravitation Probe Concept	173
Cacciapuoti, L.	Atomic Clock ensemble in space	139
Canuel, B.	Studies of general relativity with quantum sensors	105
Casanueva Diaz, J.	Advanced Virgo commissioning challenges	27
Chapell, S.	Testing the gravitational theory with short-period stars around our galactic center	283
Chen, Z.	Testing the gravitational theory with short-period stars around our galactic center	283
Chichet, L.	Studies of general relativity with quantum sensors	105
Christensen, N.	Searching for the Stochastic Gravitational-Wave Background with Advanced LIGO and Advanced Virgo	11
Chu, D.	Testing the gravitational theory with short-period stars around our galactic center	283
Ciurlo, A.	Testing the gravitational theory with short-period stars around our galactic center	283
Condon, G.	Studies of general relativity with quantum sensors	105
Coulot, D .	Recent advances in the determination of a high spatial resolution geopotential model using chronometric geodesy	295
Crépin, P.-P.	Casimir-Polder shifts on quantum levitation states	179
De Laurentis, M.	PETER: a double torsion pendulum to test quasi free-fall on two degrees of freedom	97
De Laurentis, M.	Perspective to measure forces between macroscopic flat parallel plates	199
De Marqui, F.	PETER: a double torsion pendulum to test quasi free-fall on two degrees of freedom	97
De Rosa, R.	PETER: a double torsion pendulum to test quasi free-fall on two degrees of freedom	97
De Rosa, R.	Perspective to measure forces between macroscopic flat parallel plates	199
Debu, P.	Antimatter and Gravitation	79
Dehghanfar, A.	Testing the gravitational theory with short-period stars around our galactic center	283
Delva, P.	ACES MWL data analysis center at SYRTE	149
Delva, P.	Test of special relativity using a fibre network of optical clocks	159
Delva, P.	Recent advances in the determination of a high spatial resolution geopotential model using chronometric geodesy	295
Di Fiore, L.	Perspective to measure forces between macroscopic flat parallel plates	199
Do, T.	Testing the gravitational theory with short-period stars around our galactic center	283
Dufour, G.	Casimir-Polder shifts on quantum levitation states	179
Ebran, J.-P.	Low-energy tests of Lorentz symmetry: new constraints with nucleons in a cold atom clock	169
Endeve, E.	Gravitational wave signals from multi-dimensional Core-collapse Supernova explosion simulations	37
Endeve, E.	Gravitational wave signals from multi-dimensional Core-collapse Supernova explosion simulations	37
Essayeh, M.	Studies of general relativity with quantum sensors	105
Faye, G.	Conservative Dynamics of Binary Systems of Compact Objects at the Fourth Post-Newtonian Order	251
Fienga, A.	Universality of free fall versus ephemeris	101
Finetti, N.	PETER: a double torsion pendulum to test quasi free-fall on two degrees of freedom	97
Francou, G.	Constraints on Lorentz symmetry violations with Lunar Laser Ranging	93
Frey, V.	All sky search for long duration gravitational-wave transients	31
Gai, M.	The Astrometric Gravitation Probe Concept	173
Gallego Cadavid, A.	Primordial power spectrum and local features	297
Gallego-Cano, E.	Testing the gravitational theory with short-period stars around our galactic center	283
Garufi, F.	PETER: a double torsion pendulum to test quasi free-fall on two degrees of freedom	97
Gautam, A.	Testing the gravitational theory with short-period stars around our galactic center	283
Geiger, R.	Studies of general relativity with quantum sensors	105
Ghez, A.	Testing the gravitational theory with short-period stars around our galactic center	283
Giersz, M.	Black holes binaries from globular clusters as sources of gravitational waves	21
Gondek-Rosinska, D.	Black holes binaries from globular clusters as sources of gravitational waves	21
Grado, A.	PETER: a double torsion pendulum to test quasi free-fall on two degrees of freedom	97
Grado, A.	Perspective to measure forces between macroscopic flat parallel plates	199

Guéna, J.	Searching for scalar dark matter using six years of LNEe-SYRTE fountain clock comparison data	165
Guérout, R.	Casimir-Polder shifts on quantum levitation states	179
Guerlin, C.	Progress on testing Lorentz symmetry with MICROSCOPE	75
Guerlin, C.	ACES MWL data analysis center at SYRTE	149
Guerlin, C.	Low-energy tests of Lorentz symmetry: new constraints with nucleons in a cold atom clock	169
Guerlin, C .	Recent advances in the determination of a high spatial resolution geopotential model using chronometric geodesy	295
Harris, J.	Gravitational wave signals from multi-dimensional Core-collapse Supernova explosion simulations	37
Hees, A.	Constraints on Lorentz symmetry violations with Lunar Laser Ranging	93
Hees, A.	Universality of free fall versus ephemeris	101
Hees, A.	Searching for scalar dark matter using six years of LNEe-SYRTE fountain clock comparison data	165
Hees, A.	Testing the gravitational theory with short-period stars around our galactic center	283
Heisenberg, L.	Generalised Proca Theories	233
Heske, A.	The Quantum Sensor Challenge - Designing a System for a Space Mission	117
Hix, W.	Gravitational wave signals from multi-dimensional Core-collapse Supernova explosion simulations	37
Holleville, D.	Studies of general relativity with quantum sensors	105
Huang, F.	P Probing the hidden gauge symmetry breaking of the early universe and new physics by the phase transition gravitational waves	287
Ivanov, M.	Integrals of quasi-linear equations of gravitating dark matter at the space thermostat presence: gravitation frequency and scale	299
Jetzer, P.	Detecting additional polarization modes with LISA	69
Jia, S.	Testing the gravitational theory with short-period stars around our galactic center	283
Jovanović, P.	Different ways for graviton mass evaluations	247
Khan, E.	Low-energy tests of Lorentz symmetry: new constraints with nucleons in a cold atom clock	169
Kleihaus, B.	Neutron stars with realistic equations of state in scalar-tensor theories of gravity	279
Kosmo, K.	Testing the gravitational theory with short-period stars around our galactic center	283
Kunz, J.	Neutron stars with realistic equations of state in scalar-tensor theories of gravity	279
López, D.	de Sitter-invariant special relativity and the dark energy problem	293
Lambrecht, A.	Casimir-Polder shifts on quantum levitation states	179
Landragin, A.	Studies of general relativity with quantum sensors	105
Langlois, D.	Degenerate Higher-Order Scalar-Tensor (DHOST) theories	221
Lansonneur, P.	AEgIS experiment: status & outlook	87
Laskar, J.	Universality of free fall versus ephemeris	101
Lasseri, R.-D.	Low-energy tests of Lorentz symmetry: new constraints with nucleons in a cold atom clock	169
Lattanzi, M.	The Astrometric Gravitation Probe Concept	173
Laurent, P.	Atomic Clock ensemble in space	139
Laurent, P.	ACES MWL data analysis center at SYRTE	149
Le Poncin-Lafitte, C.	Constraints on Lorentz symmetry violations with Lunar Laser Ranging	93
Le Poncin-Lafitte, C.	ACES MWL data analysis center at SYRTE	149
Lefèvre, G.	Studies of general relativity with quantum sensors	105
Leite, A.	Preparing ESPRESSO's fundamental physics tests	123
Leite, A.	Stability of Fundamental Couplings and Dark Energy: a pre-ESPRESSO analysis and forecast	229
Lentz, E.	Gravitational wave signals from multi-dimensional Core-collapse Supernova explosion simulations	37
Levi, M.	Effective Field theory of post-newtonian gravity including spins	263
Lion, G .	Recent advances in the determination of a high spatial resolution geopotential model using chronometric geodesy	295
Lodewyck, J.	Optical clocks and fiber links	153
Lodewyck, J.	Test of special relativity using a fibre network of optical clocks	159
Lu, R.	Testing the gravitational theory with short-period stars around our galactic center	283
Lucchesi, D.	LARASE: Testing General Relativity with Satellite Laser Ranging	203

Magnafico, C.	LARASE: Testing General Relativity with Satellite Laser Ranging	203
Majid, W.	Millisecond Pulsars at the Center of the Galaxy	275
Marchand, T.	4.5 Post-Newtonian order gravitational radiation	259
Marconi, L.	PETER: a double torsion pendulum to test quasi free-fall on two degrees of freedom	97
Marronetti, P.	Gravitational wave signals from multi-dimensional Core-collapse Supernova explosion simulations	37
Marsat, S.	Conservative Dynamics of Binary Systems of Compact Objects at the Fourth Post-Newtonian Order	251
Martinez, G.	Testing the gravitational theory with short-period stars around our galactic center	283
Martins, C.	Preparing ESPRESSO's fundamental physics tests	123
Martins, C.	Stability of Fundamental Couplings and Dark Energy: a pre-ESPRESSO analysis and forecast	229
Matthews, K.	Testing the gravitational theory with short-period stars around our galactic center	283
Menzel, R.	Gravitational Properties of Light	127
Messer, O.	Gravitational wave signals from multi-dimensional Core-collapse Supernova explosion simulations	37
Meynadier, F.	ACES MWL data analysis center at SYRTE	149
Mezzacappa, A.	Gravitational wave signals from multi-dimensional Core-collapse Supernova explosion simulations	37
Mielec, N.	Studies of general relativity with quantum sensors	105
Milano, L.	PETER: a double torsion pendulum to test quasi free-fall on two degrees of freedom	97
Minazzoli, O.	Universality of free fall versus ephemeris	101
Molaro, P.	Preparing ESPRESSO's fundamental physics tests	123
Morris, M.	Testing the gravitational theory with short-period stars around our galactic center	283
Mota, D.	Cosmic Tsunamis : Wrecking Screening Mechanisms in Modified Gravity	217
Motahar, Z.	Neutron stars with realistic equations of state in scalar-tensor theories of gravity	279
Moucherek, F.	Stability of Fundamental Couplings and Dark Energy: a pre-ESPRESSO analysis and forecast	229
Mynenkov, Y.	PETER: a double torsion pendulum to test quasi free-fall on two degrees of freedom	97
Naoz, S.	Testing the gravitational theory with short-period stars around our galactic center	283
Panet, I.	Recent advances in the determination of a high spatial resolution geopotential model using chronometric geodesy	295
Pardini, C.	LARASE: Testing General Relativity with Satellite Laser Ranging	203
Patricelli, B.	Electromagnetic follow-up of gravitational wave transients: first results and perspectives	43
Pereira, J.	de Sitter-invariant special relativity and the dark energy problem	293
Pereira dos Santos, F.	Trapped atom interferometry for the study of Casimir forces and Gravitation at short range	185
Peron, R.	LARASE: Testing General Relativity with Satellite Laser Ranging	203
Philippoz, L.	Detecting additional polarization modes with LISA	69
Pihan-Le Bars, H.	Progress on testing Lorentz symmetry with MICROSCOPE	75
Pihan-Le Bars, H.	Low-energy tests of Lorentz symmetry: new constraints with nucleons in a cold atom clock	169
Pinho, A.	Stability of Fundamental Couplings and Dark Energy: a pre-ESPRESSO analysis and forecast	229
Prevedelli, M.	Studies of general relativity with quantum sensors	105
Pucacco, G.	PETER: a double torsion pendulum to test quasi free-fall on two degrees of freedom	97
Pucacco, G.	LARASE: Testing General Relativity with Satellite Laser Ranging	203
Rätzel, D.	Gravitational Properties of Light	127
Rabault, M.	Studies of general relativity with quantum sensors	105
Reynaud, S.	Casimir-Polder shifts on quantum levitation states	179
Riou, I.	Studies of general relativity with quantum sensors	105
Riva, A.	The Astrometric Gravitation Probe Concept	173
Sakai, S.	Testing the gravitational theory with short-period stars around our galactic center	283
Sakr, Z.	Testing general relativity from curvature & energy contents at cosmological scale	243
Salomon, C.	Atomic Clock ensemble in space	139
Schödel, R.	Testing the gravitational theory with short-period stars around our galactic center	283
Sesana, A.	Multi-band gravitational wave astronomy: science with joint space- and ground-based observations of black hole binaries	59

Silva, T.	Preparing ESPRESSO's fundamental physics tests	123
Silva, T.	Stability of Fundamental Couplings and Dark Energy: a pre-ESPRESSO analysis and forecast	229
Solaro, C.	Trapped atom interferometry for the study of Casimir forces and Gravitation at short range	185
Stanga, R.	PETER: a double torsion pendulum to test quasi free-fall on two degrees of freedom	97
Stanga, R.	LARASE: Testing General Relativity with Satellite Laser Ranging	203
Szczpanczyk, M.	Gravitational wave signals from multi-dimensional Core-collapse Supernova explosion simulations	37
Szkudlarek, M.	Black holes binaries from globular clusters as sources of gravitational waves	21
Tolley, A.	Theories of Modified Gravity	209
Vecchiato, A.	The Astrometric Gravitation Probe Concept	173
Visco, M.	PETER: a double torsion pendulum to test quasi free-fall on two degrees of freedom	97
Visco, M.	LARASE: Testing General Relativity with Satellite Laser Ranging	203
Viswanathan, V.	Universality of free fall versus ephemeris	101
Walters, A.	Prospects for probing fundamental physics with the radio sky	133
Weltman, A.	Prospects for probing fundamental physics with the radio sky	133
Wilkens, M.	Gravitational Properties of Light	127
Witzel, G.	Testing the gravitational theory with short-period stars around our galactic center	283
Witzemann, A.	Prospects for probing fundamental physics with the radio sky	133
Wolf, P.	Progress on testing Lorentz symmetry with MICROSCOPE	75
Wolf, P.	ACES MWL data analysis center at SYRTE	149
Wolf, P.	Searching for scalar dark matter using six years of LNEe-SYRTE fountain clock comparison data	165
Wolf, P.	Low-energy tests of Lorentz symmetry: new constraints with nucleons in a cold atom clock	169
Wolf, P .	Recent advances in the determination of a high spatial resolution geopotential model using chronometric geodesy	295
Yakunin, K.	Gravitational wave signals from multi-dimensional Core-collapse Supernova explosion simulations	37
Zakharov, A.	Different ways for graviton mass evaluations	247
Zanolin, M.	Gravitational wave signals from multi-dimensional Core-collapse Supernova explosion simulations	37

List of Participants

List of Participants

First Name	Family Name	Institution	Country	Email address
Wilmer	Alfonso-Pardo	University of Antioquia	Colombia	wilmer.alfonso@udea.edu.co
Adriana	Araujo	IFT - UNESP	Brazil	adrianaaraujo@ift.unesp.br
Eugeny	Babichev	LPTO	France	eugeny.babichev@th.u-psud.fr
Massimo	Bassan	INFN Tor Vergata	Italy	bassan@roma2.infn.it
Andrew	Beckwith	Chongqing University	China	rwill9955b@gmail.com
Michal	Bejger	Copernicus Astronomical Center	Poland	bejger@camk.edu.pl
Joël	Bergé	ONERA	France	joel.berge@onera.fr
Marie Anne	Bizouard	LAL	France	mabizoua@lal.in2p3.fr
Luc	Blanchet	IAP	France	blanchet@iap.fr
Yannick	Boetzel	University of Zurich	Switzerland	boetzel@physik.uzh.ch
Camille	Bonvin	University of Geneva	Switzerland	camille.bonvin@unige.ch
Adrien	Bourgoin	University of Bologna	Italy	adrien.bourgoin@obspm.fr
Philippe	Bouyer	LP2N - Institut d'Optique	France	philippe.bouyer@institutoptique.fr
Dmitry	Budker	Helmholtz Institute	Germany	budker@uni-mainz.de
Damir	Buskulic	LAPP	France	buskulic@lapp.in2p3.fr
Luigi	Cacciapuoti	ESA	Netherlands	Luigi.Cacciapuoti@esa.int
Julia	Casanueva Diaz	LAL	France	casanuev@lal.in2p3.fr
Nelson	Christensen	Artemis - OCA	France	nelson.christensen@oca.eu
Pierre-Philippe	Crépin	Laboratoire Kastler-Brossel	France	pierre-philippe.crepin@lkb.upmc.fr
Axel	de la Macorra	UNAM	Mexico	a.macorra@gmail.com
Pascal	Debu	CEA - Saclay DRF	France	pascal.debu@cea.fr
Pacôme	Delva	Observatoire de Paris - UPMC	France	pacome.delva@obspm.fr
Luciano	Di Fiore	INFN	Italy	difiore@na.infn.it
Jacques	Dumarchez	LPNHE	France	jacques.dumarchez@cern.ch
Sheila	Dwyer	Caltech	USA	dwyer_s@ligo-wa.caltech.edu
Eirik	Endeve	University of Tennessee	USA	endevee@ornl.gov
Guillaume	Faye	IAP	France	faye@iap.fr
Luigi	Ferraioli	ETH	Switzerland	luigi.ferraioli@erdw.ethz.ch
Valentin	Frey	LAL	France	frey@lal.in2p3.fr
Mario	Gai	INAF	Italy	gai@oato.inaf.it
Alexander	Gallego Cadavid	Universidad de Antioquia	Colombia	alexander.gallego@udea.edu.co
César	Gattano	SYRTE	France	cesar.gattano@obspm.fr
Ferran	Gibert	University of Trento	Italy	ferran.gibert@unitn.it
Aniello	Grado	INAF	Italy	agrado@na.astro.it
Christine	Guerlin	LKB	France	christine.guerlin@lkb.ens.fr
Philipp	Haslinger	UC Berkeley	USA	haslinger@berkeley.edu
Aurélien	Hees	UCLA	USA	ahees@astro.ucla.edu
Gerhard	Heinzel	MPI Albert Einstein Institute	Germany	gerhard.heinzel@aei.mpg.de
Lavinia	Heisenberg	ETH	Switzerland	lavinia.heisenberg@eth-its.ethz.ch
Astrid	Heske	ESA - ESTEC	Netherlands	astrid.heske@esa.int
Jason	Hogan	Stanford University	USA	hogan@stanford.edu
FaPeng	Huang	IHEP	China	huangfp@ihep.ac.cn
Paul	Indelicato	Laboratoire Kastler-Brossel	France	paul.indelicato@lkb.upmc.fr
Mikhail	Ivanov	Central Institute of Aviation Motors	Russia	ivanov@ciam.ru
Marc-Thierry	Jaekel	LPT - ENS	France	jaekel@lpt.ens.fr
Matthew	Jaffe	UC Berkeley	USA	mjaffe@berkeley.edu
David	Langlois	APC	France	langlois@apc.univ-paris7.fr
Pierre	Lansonneur	IPN Lyon	France	pierre.lansonneur@cern.ch
Alexandre	Le Tiec	Observatoire de Paris	France	letiec@obspm.fr
Ana Catarina	Leite	Inst. Astrofísica e Ciências do Espaço	Portugal	Ana.Leite@astro.up.pt
Michele	Levi	CEA - Saclay IPhT	France	michele.levi@cea.fr
Jérôme	Lodewyck	LPNE - SYRTE Observatoire de Paris	France	jerome.lodewyck@obspm.fr
Walid	Majid	Jet Propulsion Lab.	USA	majidw@gmail.com
Tanguy	Marchand	IAP	France	marchand@iap.fr
Carlos	Martins	CAUP	Portugal	carlos.martins@astro.up.pt
Gilles	Métris	OCA - Geoazur	France	Gilles.Metris@geoazur.unice.fr
Frédéric	Meynadier	SYRTE - Observatoire de Paris	France	Frederic.Meynadier@obspm.fr
Olivier	Minazzoli	Centre Scientifique de Monaco	Monaco	ominazzoli@gmail.com
David F.	Mota	University of Oslo - Th. Astrophysics	Norway	d.f.mota@astro.uio.no
Zahra	Motahar	Oldenburg University	Germany	zahra.motahar@uni-oldenburg.de
Jeff	Murugan	University of Cape Town	South Africa	jmurugan@ias.edu
Alessandro	Nagar	INFN	Italy	alex@nagarsoft.com
Valery	Nesvizhevsky	Institut Laue-Langevin	France	nesvizhevsky@ill.eu

Barbara	Patricelli	INFN	Italy	barbara.patricelli@pi.infn.it
Franck	Pereira dos Santos	SYRTE	France	franck.pereira@obspm.fr
Lionel	Philippoz	University of Zurich	Switzerland	plionel@physik.uzh.ch
Hélène	Pihan-Le Bars	SYRTE	France	helene.pihan-lebars@obspm.fr
Michele	Punturo	INFN	Italia	michele.punturo@pg.infn.it
Sabi r	Ramazanov	Gran Sasso Science Institute	Italy	sabir.ramazanov@gssi.infn.it
Ernst	Rasel	Leibniz Univ. - Inst. of Quantum Optics	Germany	rasel@iqo.uni-hannover.de
Dennis	Rätzel	University of Vienna	Austria	raetzel.dennis@gmail.com
Serge	Reynaud	Laboratoire Kastler-Brossel	France	serge.reynaud@lkb.upmc.fr
Manuel	Rodrigues	ONERA	France	manuel.rodrigues@onera.fr
Dorota	Rosinska	University of Zielona Gora	Poland	dorota@camk.edu.pl
Avetis Abel	Sadoyan	Yerevan State University	Armenia	asadoyan@gmail.com
Ziad	Sakr	IRAP	France	zsakr@irap.omp.eu
Francesco	Salemi	AEI	Germany	francesco.salemi@aei.mpg.de
Martin	Schnabl	Institute for Physics	Czech Republic	schnabl@fzu.cz
Christian	Schubert	Institut für Quantenoptik	Germany	schubert@iqo.uni-hannover.de
Alberto	Sesana	University of Birmingham	UK	asesana@star.sr.bham.ac.uk
Fiodor	Sorrentino	INFN	Italy	fiodor.sorrentino@ge.infn.it
Yevgeny	Stadnik	University of New South Wales	Australia	y.stadnik@unsw.edu.au
Andrew	Tolley	Imperial College	UK	a.tolley@imperial.ac.uk
Alexander	Vikman	Institute of Physics	Czech Republic	vikman@fzu.cz
Alexey	Voronin	P. N. Lebedev Institute	Russia	dr.a.voronin@gmail.com
Peter	Wass	Imperial College	UK	p.wass@imperial.ac.uk
Amanda	Weltman	University of Cape Town	South Africa	awelti@gmail.com
Victoria	Xu	UC Berkeley	USA	vxu@berkeley.edu
Alexander	Zakharov	ITEP	Russia	alex_f_zakharov5@mail.ru